Lecture Notes in Electrical Engineering 1129

Yusheng Xue
Yuping Zheng
Antonio Gómez-Expósito *Editors*

Proceedings of the 8th PURPLE MOUNTAIN FORUM on Smart Grid Protection and Control (PMF2023)

Springer

Lecture Notes in Electrical Engineering 1129

Series Editors

Leopoldo Angrisani, *Department of Electrical and Information Technologies Engineering, University of Napoli Federico II, Napoli, Italy*
Marco Arteaga, *Departament de Control y Robótica, Universidad Nacional Autónoma de México, Coyoacán, Mexico*
Samarjit Chakraborty, *Fakultät für Elektrotechnik und Informationstechnik, TU München, München, Germany*
Jiming Chen, *Zhejiang University, Hangzhou, Zhejiang, China*
Shanben Chen, *School of Materials Science and Engineering, Shanghai Jiao Tong University, Shanghai, China*
Tan Kay Chen, *Department of Electrical and Computer Engineering, National University of Singapore, Singapore, Singapore*
Rüdiger Dillmann, *University of Karlsruhe (TH) IAIM, Karlsruhe, Baden-Württemberg, Germany*
Haibin Duan, *Beijing University of Aeronautics and Astronautics, Beijing, China*
Gianluigi Ferrari, *Dipartimento di Ingegneria dell'Informazione, Sede Scientifica Università degli Studi di Parma, Parma, Italy*
Manuel Ferre, *Centre for Automation and Robotics CAR (UPM-CSIC), Universidad Politécnica de Madrid, Madrid, Spain*
Faryar Jabbari, *Department of Mechanical and Aerospace Engineering, University of California, Irvine, CA, USA*
Limin Jia, *State Key Laboratory of Rail Traffic Control and Safety, Beijing Jiaotong University, Beijing, China*
Janusz Kacprzyk, *Intelligent Systems Laboratory, Systems Research Institute, Polish Academy of Sciences, Warsaw, Poland*
Alaa Khamis, *Department of Mechatronics Engineering, German University in Egypt El Tagamoa El Khames, New Cairo City, Egypt*
Torsten Kroeger, *Intrinsic Innovation, Mountain View, CA, USA*
Yong Li, *College of Electrical and Information Engineering, Hunan University, Changsha, Hunan, China*
Qilian Liang, *Department of Electrical Engineering, University of Texas at Arlington, Arlington, TX, USA*
Ferran Martín, *Departament d'Enginyeria Electrònica, Universitat Autònoma de Barcelona, Bellaterra, Barcelona, Spain*
Tan Cher Ming, *College of Engineering, Nanyang Technological University, Singapore, Singapore*
Wolfgang Minker, *Institute of Information Technology, University of Ulm, Ulm, Germany*
Pradeep Misra, *Department of Electrical Engineering, Wright State University, Dayton, OH, USA*
Subhas Mukhopadhyay, *School of Engineering, Macquarie University, Sydney, NSW, Australia*
Cun-Zheng Ning, *Department of Electrical Engineering, Arizona State University, Tempe, AZ, USA*
Toyoaki Nishida, *Department of Intelligence Science and Technology, Kyoto University, Kyoto, Japan*
Luca Oneto, *Department of Informatics, Bioengineering, Robotics and Systems Engineering, University of Genova, Genova, Genova, Italy*
Bijaya Ketan Panigrahi, *Department of Electrical Engineering, Indian Institute of Technology Delhi, New Delhi, Delhi, India*
Federica Pascucci, *Department di Ingegneria, Università degli Studi Roma Tre, Roma, Italy*
Yong Qin, *State Key Laboratory of Rail Traffic Control and Safety, Beijing Jiaotong University, Beijing, China*
Gan Woon Seng, *School of Electrical and Electronic Engineering, Nanyang Technological University, Singapore, Singapore*
Joachim Speidel, *Institute of Telecommunications, University of Stuttgart, Stuttgart, Germany*
Germano Veiga, *FEUP Campus, INESC Porto, Porto, Portugal*
Haitao Wu, *Academy of Opto-electronics, Chinese Academy of Sciences, Haidian District Beijing, China*
Walter Zamboni, *Department of Computer Engineering, Electrical Engineering and Applied Mathematics, DIEM—Università degli studi di Salerno, Fisciano, Salerno, Italy*
Junjie James Zhang, *Charlotte, NC, USA*
Kay Chen Tan, *Department of Computing, Hong Kong Polytechnic University, Kowloon Tong, Hong Kong*

The book series *Lecture Notes in Electrical Engineering* (LNEE) publishes the latest developments in Electrical Engineering—quickly, informally and in high quality. While original research reported in proceedings and monographs has traditionally formed the core of LNEE, we also encourage authors to submit books devoted to supporting student education and professional training in the various fields and applications areas of electrical engineering. The series cover classical and emerging topics concerning:

- Communication Engineering, Information Theory and Networks
- Electronics Engineering and Microelectronics
- Signal, Image and Speech Processing
- Wireless and Mobile Communication
- Circuits and Systems
- Energy Systems, Power Electronics and Electrical Machines
- Electro-optical Engineering
- Instrumentation Engineering
- Avionics Engineering
- Control Systems
- Internet-of-Things and Cybersecurity
- Biomedical Devices, MEMS and NEMS

For general information about this book series, comments or suggestions, please contact leontina.dicecco@springer.com.

To submit a proposal or request further information, please contact the Publishing Editor in your country:

China

Jasmine Dou, Editor (jasmine.dou@springer.com)

India, Japan, Rest of Asia

Swati Meherishi, Editorial Director (Swati.Meherishi@springer.com)

Southeast Asia, Australia, New Zealand

Ramesh Nath Premnath, Editor (ramesh.premnath@springernature.com)

USA, Canada

Michael Luby, Senior Editor (michael.luby@springer.com)

All other Countries

Leontina Di Cecco, Senior Editor (leontina.dicecco@springer.com)

**** This series is indexed by EI Compendex and Scopus databases. ****

Yusheng Xue · Yuping Zheng ·
Antonio Gómez-Expósito
Editors

Proceedings of the 8th PURPLE MOUNTAIN FORUM on Smart Grid Protection and Control (PMF2023)

Springer

Editors
Yusheng Xue
NARI Group Co., Ltd.
Nanjing, Jiangsu, China

Yuping Zheng
NARI Group Co., Ltd.
Nanjing, Jiangsu, China

Antonio Gómez-Expósito
Department of Electrical Engineering
University of Sevilla
Seville, Spain

ISSN 1876-1100 ISSN 1876-1119 (electronic)
Lecture Notes in Electrical Engineering
ISBN 978-981-99-9250-8 ISBN 978-981-99-9251-5 (eBook)
https://doi.org/10.1007/978-981-99-9251-5

© State Grid Electric Power 2024

This work is subject to copyright. All rights are solely and exclusively licensed by the Publisher, whether the whole or part of the material is concerned, specifically the rights of translation, reprinting, reuse of illustrations, recitation, broadcasting, reproduction on microfilms or in any other physical way, and transmission or information storage and retrieval, electronic adaptation, computer software, or by similar or dissimilar methodology now known or hereafter developed.
The use of general descriptive names, registered names, trademarks, service marks, etc. in this publication does not imply, even in the absence of a specific statement, that such names are exempt from the relevant protective laws and regulations and therefore free for general use.
The publisher, the authors, and the editors are safe to assume that the advice and information in this book are believed to be true and accurate at the date of publication. Neither the publisher nor the authors or the editors give a warranty, expressed or implied, with respect to the material contained herein or for any errors or omissions that may have been made. The publisher remains neutral with regard to jurisdictional claims in published maps and institutional affiliations.

This Springer imprint is published by the registered company Springer Nature Singapore Pte Ltd.
The registered company address is: 152 Beach Road, #21-01/04 Gateway East, Singapore 189721, Singapore

Paper in this product is recyclable.

Contents

Optimal Allocation Strategy of Electro-Hydrogen Hybrid Energy Storage Capacity Based on Empirical Mode

Gong Shanggao[1,2], Wang Chenglin[1,2], Xu Hui[1,2], Wang Hui[1,2](✉), Zhang Jiajun[1,3], and Ji Xiu[1,2]

[1] Changchun Institute of Technology, Changchun 130012, China
wanghui841013@ccit.edu.cn
[2] Innovation Department of Jilin Electric Power Co., Ltd, Changchun 130012, China
[3] National and Local Joint Engineering Research Center for Measurement, Control and Safe Operation of Intelligent Distribution Networks, Changchun 130012, China

Abstract. With the continuous increase of the proportion of wind power access, the energy coordination capacity in the power system is weakened and the power quality is reduced. Based on this, this paper proposes a method to solve the problem of flattening energy fluctuations in the synergistic power system of electro-hydrogen hybrid energy storage, and uses the hybrid energy storage capacity optimization method composed of supercapacitor and PEM electrolyzer to solve the problem of optimal allocation of wind power fluctuations in grid-connected. Firstly, the structure model of hybrid energy storage system with supercapacitor is proposed, and on this basis, the original signal of wind power is decomposed by empirical mode method to obtain the low-frequency component directly connected to the grid and the high-frequency component that needs to be flattened by hybrid energy storage. Then, the high-frequency fluctuation of wind power in grid-connected is solved by optimizing the hybrid energy storage capacity with supercapacitors. Finally, based on the actual wind power data in Northeast China in 2022 as an example, combined with the example analysis in the MATLAB2018B + Gurobi solution environment, the effectiveness of the flattening strategy is verified by the example analysis, which provides an effective scheme for the flattening of wind power fluctuations, which can effectively improve the system economy.

Keywords: Wind power fluctuation flattening · Hybrid energy storage optimization · Energy management strategies · Supercapacitors · Variable baselines

1 Introduction

With the rapid development of new energy and energy Internet related technologies, large-scale new energy sources are continuously integrated into the power grid, which brings severe challenges to the power system. However, wind power is the most widely used of the most widely developed new renewable energy sources [1]. However, in the

Y. Xue et al. (Eds.): PMF 2023, LNEE 1129, pp. 1–16, 2024.
https://doi.org/10.1007/978-981-99-9251-5_1

process of wind power development, due to the rapid development of wind power, it has brought great challenges to the power system, and the operation of the system has also been affected. This paper proposes that hybrid energy storage to stabilize high-frequency fluctuations provides an effective way to improve the power quality and energy synergy optimization level of grid-connected, and has become one of the hot issues in the field of hybrid energy storage flattening high-frequency components at home and abroad. However, due to the rapid development of modern power systems, higher requirements are put forward for energy storage devices, and traditional energy storage technologies cannot meet the requirements of modern power systems at the same time. However, now the hybrid energy storage system (HESS) can be formed through different storage unit combinations, which can complement each other in the performance of each storage unit, solve the defects of single energy storage unit energy storage, improve the integrity of energy storage in modern power systems [2], and improve the volatility of wind power output. The hybrid energy storage system is mainly composed of supercapacitors and hydrogen energy storage, in which the supercapacitors are responsible for flattening the high-frequency components of wind power signals, and the high-frequency components that cannot be connected to the grid are flattened to meet the requirements of grid connection; Hydrogen energy storage system has the advantages of long storage time, clean and efficient, and is considered to be a potential large-capacity energy storage under the “big environment” [3].

At present, the research on hybrid energy storage to stabilize wind power mainly focuses on the high-frequency component signal of wind power, and the literature [4] proposes that the low-frequency component and high-frequency component of wind power should be dealt with by adiabatic compressed air energy storage and flywheel energy storage system respectively to alleviate wind power fluctuations and enhance wind power permeability. Literature [5] Construct a hybrid energy storage system composed of battery and hydrogen energy storage, use batteries to suppress short-term fluctuations in photovoltaic and load power, and when the battery SOC reaches 99.5%, the control algorithm transfers the excess power to the electrolyzer. Literature [6] Hybrid energy storage capacity configuration and control strategy to smooth wind power fluctuations, put forward the use of electrolyzer and supercapacitor for wind power flattening, through wavelet decomposition of wind power signal, decomposition into high-frequency signal and low-frequency signal, and then use energy-type energy storage element electrolyzer is mainly used to absorb low-frequency power, power-type energy storage element supercapacitor undertakes the task of absorbing high-frequency power and releasing power to the power grid, and finally achieves the purpose of leveling wind power.

For the current research on electro-hydrogen hybrid energy storage, it is mainly based on batteries, supplemented by hydrogen storage, and hybrid energy storage is mainly used in microgrids, and few supercapacitor-based hybrid energy storage is applied in large grid systems [7]. In this paper, the strategy of using PEM electrolyzer combined with supercapacitor to smooth the high-frequency fluctuation of wind power is formulated by considering the use of hydrogen energy storage as the main body and supercapacitor as the supplement to smooth the high-frequency fluctuation of wind power. Firstly, the original signal of wind power is decomposed based on empirical mode decomposition (EMD) into several intrinsic mode function (IMF) signals of various orders, and then the signal reconstruction is realized by using C2F, and the fluctuation amount that needs energy storage is eliminated according to the maximum fluctuation limit, and then the supercapacitor is used to achieve flattening. Then, based on the charge and discharge power constraints and storage state constraints of supercapacitor energy storage and hydrogen energy storage, an energy management strategy considering the operating characteristics of PEM electrolyzers is formulated. Based on this strategy, it is established that the total cost of HESS is the smallest objective function, and the basic symmetry characteristics of the EMD high-frequency component envelope are used combined with the supercapacitor for capacity configuration, aiming at the problem that the negative fluctuation after the high-frequency component 0 reference line is still very large, by improving the variable reference line, and obtaining the value of the optimal reference line, as well as the optimal value of the capacity configuration, the final grid-connected power fluctuation is the same as the low-frequency component fluctuation of EMD, that is, completely controllable. In summary, this paper solves the wind power output by introducing a hybrid energy storage system composed of electrolyzer and supercapacitor, proposes a flattening effect evaluation method, formulates a coordinated operation control strategy of the energy storage system, and combines the actual operation data of the wind farm to verify that the proposed method can not only smooth the fluctuation of wind power, improve power quality, but also prevent overcharge and overdischarge of supercapacitors, and improve the service life of hybrid energy storage systems.

2 Coordinated Operation Framework of Electro-Hydrogen Hybrid Energy Storage

2.1 Structural Model of Hybrid Energy Storage System with Supercapacitor

Aiming at the fluctuation problem caused by large-scale grid integration of wind power, an optimal and coordinated operation framework of electricity-hydrogen hybrid energy storage is proposed, as shown in Fig. 1, the structure model of hybrid energy storage system with supercapacitor is composed of super capacitor (SC), hydrogen energy storage (Hydrogen Energy Storage), and power grid.

An electric-hydrogen hybrid energy storage system (HESS) containing supercapacitors and hydrogen energy storage was established, and the deviation between the actual output of wind power and the expected target power was used as the flattening object, in which the supercapacitor bore the high-frequency fluctuation and the hydrogen energy storage bore the low-frequency change. A schematic diagram of the structural model of the combined operation system of electro-hydrogen hybrid energy storage (HESS) and wind farm is shown in Fig. 1.

2.2 Configuration Analysis of Hybrid Energy Storage System of Supercapacitor and Proton Exchange Membrane Electrolyzer

(1) Relevant data of a variety of electrolyzers

By comparing the three electrolysis in Table 1, this paper comprehensively considers the system operating cost and the characteristics of the electrolyzer to make a tradeoff comparison, and finally selects the proton exchange membrane electrolyzer as the electro-hydrogen container.

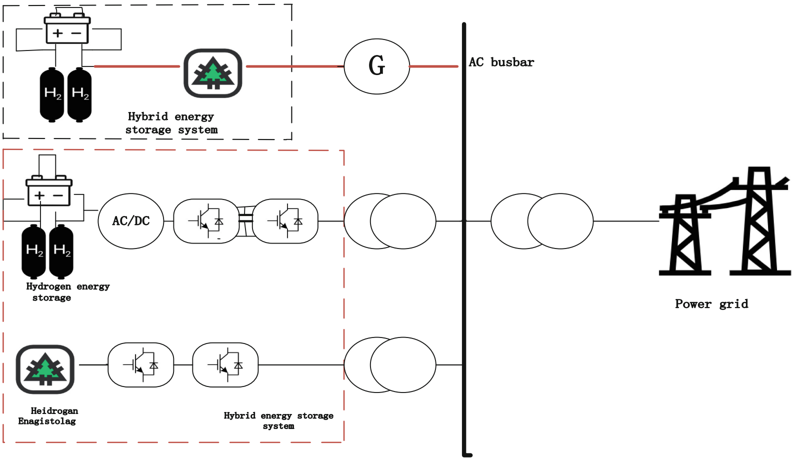

Fig. 1. Structure model of hybrid energy storage system with super capacitor

(2) Data related to supercapacitors

The number of charge and discharge times of supercapacitors can reach up to 1 million times, and the working life can reach 15 years. And compared with other storage batteries, the advantages of supercapacitors are: supercapacitors will not burn when short-circuited and punctured, and supercapacitors are safer than lithium batteries that are prone to spontaneous combustion or even explosion when punctured; And the energy value of the supercapacitor's energy storage device is related to the initial energy value of the supercapacitor's charge and discharge efficiency:

$$E_v(\mathrm{t}) = E_v, 0 + \sum_{i=0}^{N} P(\mathrm{b})(ti)\Delta\mathrm{t} \tag{1}$$

where, $E_{v,0}$; $\mathrm{E_v(t)}$, the energy value of the initial moment and moment of the supercapacitor; N is the number of points sampled from the start t moment to the moment.

Supercapacitor due to the frequency of charge and discharge is too frequent, will make the service life of the supercapacitor greatly shortened, in order to make the supercapacitor storage power life longer, by changing the upper and lower limits of the charge state of the energy storage system running the set value, so that the supercapacitor energy storage value is always in the set range with the equipment end, and finally can make the life loss of the energy storage system smaller, so that the system becomes more economical, the rated capacity of the supercapacitor is:

$$E'\mathrm{c} = \frac{\max\{E(t)\} - \min\{Eb(t)\}}{\overline{sc}} \tag{2}$$

where E'_{c} is the rated capacity of the supercapacitor.

The maximum charge and discharge power is the infinite norm of the real-time power sequence of energy storage;

$$P + G = ||P + G||\infty \tag{3}$$

Table. 1 Data related to three types of electrolyzers

	Alkaline electrolysis	PEM electrolysis	SOC electrolysis
Scale of hydrogen production by a single unit	0.5–1000 Nm/h^2	00.1–200 Nm/h^2	\
Electrolyzers consume energy	4.5–5.5 kwh/Nm^2	3.8–5.0 kwh/Nm^2	2.6–3.6 kwh/Nm^2
System conversion efficiency	60–75%	70–90%	85–100%
System life	Up to 20–30 years	Up to 10–20 years	\
Speed of downtime	The start and stop are fast, in minutes	Fast start-stop, milliseconds	Slow start-stop
Dynamic responsiveness	Strong	Strong	Weaker
Load regulation range	15–100% rated load	0–160% rated load	\
Floor space	Larger	Smaller	\
Electrolyzer price	2000–3000 yuan/kw	1200–20000 yuan/kw	\
Peculiarity	The technology is mature, the cost is low, and it is easy to apply on a large scale, but the actual power consumption is large and a stable power supply is required	It is easy to realize miniaturization and weight reduction, high cost, and small scale	\

$$P - G = ||P - G||\infty$$

where $P + G$, $P - G$ are the maximum charging and discharging powers of the supercapacitor, both of which are positive numbers greater than zero; $P + G$, $P - G$ are the charging power collection and discharge power collection of the supercapacitor.

Finally, by comparing the characteristics of supercapacitor and proton exchange membrane electrolyzer, this paper fully considers the economy of the system and the life of the energy storage system, and finally selects the PEM electrolytic cell as the electrolyzer of electro-hydrogen, and the supercapacitor as the energy storage element for smoothing the high-frequency components of wind power.

2.3 EMD-Based Wind Power Allocation Strategy

The EMD based wind power allocation decision first uses the empirical mode decomposition (EMD) method to decompose the original signal of wind power into a multi-order intrinsic mode function (IMF) signal, and obtains the C2F reconstruction signal through the superposition reconstruction of the IMF signal. According to the maximum fluctuation limit, the high-frequency fluctuations that need to be stabilized by hybrid energy storage are obtained, and the supercapacitors are used to eliminate the fluctuations and realize the smoothing of wind power signals (Fig. 2).

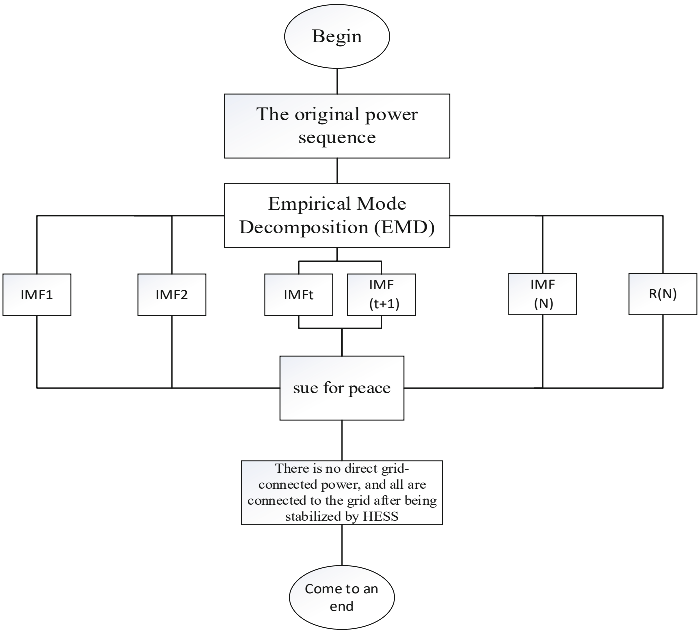

Fig. 2. Flow chart of wind power allocation strategy based on EMD

The wind power signal is decomposed by EMD to obtain the IMF signal of each order, and the decomposed signal includes high-frequency signal and low-frequency signal, and then the high-frequency signal and low-frequency signal are superimposed and calculated respectively to obtain low-frequency components and high-frequency components. That is, the reconstructed signals are: high-frequency reconstruction (Fine to coarse, f2c) and low-frequency reconstruction (Coarse to fine, c2f), and the specific EMD decomposition wind power high and low frequency reconstruction signals are shown in Fig. 3.

High-frequency reconstruction is to decompose the wind power signal through EMD to obtain the IMF signal, and then the high-frequency reconstruction components of each order are generated by superimposing the IMF signal from top to bottom, and the specific reconstruction method is as follows:

$$\begin{gathered} f_{2c(1)} = IMF1 \\ f_{2c(2)} = IMF1IMF2 \\ f_{2c(p+1)} = IMF1IMF2.\dots\dots IMFp + res \end{gathered} \tag{4}$$

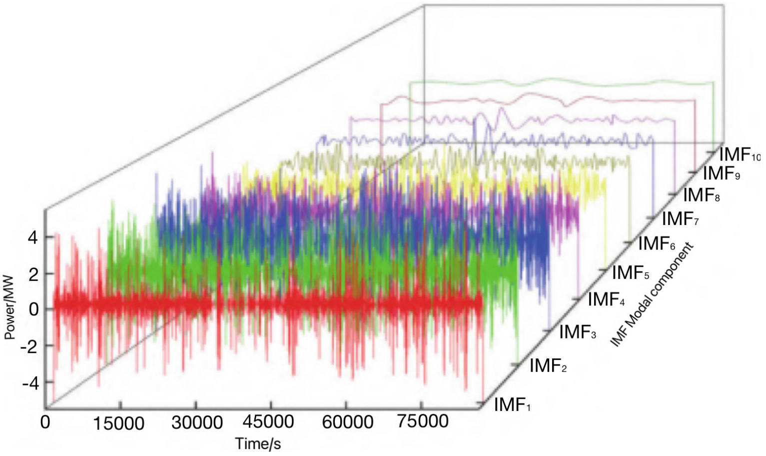

Fig. 3. IMF modal components after decomposition

3 Capacity Configuration Model of Hybrid Energy Storage System with Supercapacitor

3.1 Objective Function

The objective function consisting of the supercapacitor energy storage cost, the hydrogen energy storage cost, and the opportunity compensation cost of wind power is shown in Eq. (5).

$$\min C = C_{CAT} + C_{HESS} + C_{w}^{comp} \tag{5}$$

Formula: C is the annual comprehensive cost; $\mathrm{C_{CAT}}$ is the cost of supercapacitor energy storage; $\mathrm{C_{HESS}}$ is the cost of hydrogen energy storage; $\mathrm{C_{w}^{comp}}$. Compensate for the opportunity to compensate for wind power fluctuations. Where $\mathrm{C_{CAT}}$, $\mathrm{C_{HESS}}$ and as shown in Eq. (6).

$$\begin{aligned} C_{CAT} &= C_{CAT}^{inv} + C_{CAT}^{oper} \\ C_{HESS} &= C_{HESS}^{inv} + C_{HESS}^{oper} \end{aligned} \tag{6}$$

Formula: $\mathrm{C_{CAT}^{inv}}$ and $\mathrm{C_{CAT}^{oper}}$ are the investment cost and operation and maintenance cost of supercapacitor energy storage, respectively; $\mathrm{C_{HESS}^{inv}}$ and $\mathrm{C_{HESS}^{oper}}$ the investment cost and operation and maintenance cost of hydrogen energy storage, respectively.

1. Total investment cost

$$C_{CAT}^{inv} = \left(C_{CATP}^{inv} P_{CAT}^{rated} + C_{CATE}^{inv} E_{CAT}^{rated} \right) \frac{r(1+r)^{\beta}}{(1+r)^{\beta} - 1} \tag{7}$$

$$C_{HESS}^{inv} = \left(C_{EL}^{inv} P_{EL}^{stabrated} + C_{FC}^{inv} P_{FC}^{stabrated} + C_{STO}^{inv} P_{STO}^{stabrated} \right) \frac{r(1+r)^{\beta}}{(1+r)^{\beta} - 1} \tag{8}$$

Formula: C_{CATP}^{inv} and C_{CATE}^{inv} are the power and capacity investment cost coefficients of supercapacitor energy storage, respectively; C_{EL}^{inv}, C_{FC}^{inv}, C_{STO}^{inv} the power and capacity investment cost coefficients of electrolyzers, fuel cells and hydrogen storage tanks, respectively; *r* is the discount rate, the value is 7%; β for the operating cycle of the system, it is set at 30 years.

2. Operation and maintenance costs

The operation and maintenance costs are estimated in proportion to the investment cost, as shown in Eqs. (9), (10) and (11).

$$C_{CAT}^{oper} = \alpha\, C_{CAT}^{inv} \tag{9}$$

$$C_{HESS}^{oper} = \beta\, C_{HESS}^{inv} + C_{on} \tag{10}$$

$$C_{on} = N_{EL}\, C_{SLL} \tag{11}$$

Formula: α and β are the proportion of operation and maintenance costs of supercapacitor energy storage and hydrogen energy storage systems to their investment costs; C_{ON} is the start-stop cost, N_{EL} is the number of electrolyzer start-ups C_{SLL}; Cost per start-up for the electrolyzer.

3.2 Constraints

(1) Hydrogen energy storage flattening fluctuation module configuration boundary constraints

Hydrogen energy storage should leave part of the power and capacity space for smoothing wind power fluctuations, so the power and capacity of the module need to be kept within the total power and capacity of hydrogen energy storage, as shown in Eqs. 12, 13 and 14 respectively.

$$0 \le P_{el}^{stabrated} \le P_{el}^{rated} \tag{12}$$

$$0 \le P_{bc}^{stabrated} \le P_{bc}^{rated} \tag{13}$$

$$0 \le K_{sto}^{stabrated} \le K_{sto}^{rated} \tag{14}$$

(2) Power balance constraints

The hybrid energy storage power task is divided P_{HESS} into two parts: positive fluctuation and negative fluctuation, positive fluctuation at $P_{HESS} \ge 0$, at which time supercapacitor energy storage charging or electrolytic cell start absorption fluctuation is required, and when $P_{HESS,n} \le 0$is negative fluctuation, supercapacitor energy storage discharge or fuel cell start-up compensation fluctuation is required, as shown in Eq. (15).

$$P_{HESS,n} = P_{el,n}^{stab} + P_{bat,n}^{cn} + P_{P-uncomp,n} - P_{N-uncomp,n} - P_{FC,n}^{stab} - P_{BAT,n}^{disch} \tag{15}$$

(3) Charge and discharge power constraints
1. Supercapacitor energy storage

$$\begin{gathered}\eta_x(t)=\frac{P_x(t)}{P_x^-},P_x(t)\geq 0\\ \eta_x(t)=-\frac{P_x(t)}{P_x^+},P_x(t)\leq 0\\ W_x(t)=SOC_x(t)\end{gathered}\tag{16}$$

where $\mathrm{P_x^+}$ and $\mathrm{P_x^-}$ are the maximum charging power and maximum discharge power of the energy storage element, respectively; Real-time power for the moment; Timing indicates a supercapacitor.

2. Hydrogen energy storage

$$P_{EL}^{stab\min}\leq P_{EL,n}^{stab}\leq 1.2P_{EL}^{stab\max}\tag{17}$$

$$P_{EL,n}^{stab}\leq 0$$

Formula: $\mathrm{P_{EL}^{stabmin}}$ is the minimum operating power of the electrolyzer.

(4) Energy storage state constraints
1. Supercapacitor energy storage

$$\begin{gathered}E(t)=E(t-1)+\left\{P_{SC}(t)\alpha b\Delta t,P_{SC}(t)\right\}\geq 0\\ E(t)=E(t-1)+\left\{\frac{P_{SC}(t)}{\beta v}\Delta t,P_{SC}(t)\right\}\geq 0\end{gathered}\tag{18}$$

2. Hydrogen energy storage

In addition to the conversion characteristics of electrolyzers and fuel cells, hydrogen energy storage constraints include the following constraints:

$$\begin{gathered}SOH_n^{stab}-SOH_{n-1}^{stab}\left(\frac{G_{STO,n}^{stain}}{Y_{STO}^{stabin}}+\frac{G_{STO,n}^{stain,out}}{Y_{STO}^{stabin}}\right)\Delta t\\ SOH_{\min}^{stab}\leq SOH_n^{stab}\leq SOH_{\max}^{stab}\end{gathered}\tag{19}$$

Formula: $\mathrm{SOH_n^{stab}}$ is the hydrogen storage state at *n* moments; $\mathrm{SOH_{min}^{stab}}$ and $\mathrm{SOH_{min}^{stab}}$ are the upper and lower limits of the hydrogen storage state of the hydrogen storage tank, respectively.

4 Example Analysis

4.1 Basic Data

Taking an installed capacity of 5588 MW in Northeast China, of which the installed capacity of wind power is 2348 MW, the wind farm with the total capacity of hydrogen energy storage system is selected according to 6–12% of the total installed power supply as an example, and the actual operation data of the wind farm in 2022 is selected with a time interval of 5 min, and the hybrid energy storage composed of PEM electrolyzer and super capacitor is used to smooth out wind power fluctuations. Firstly, the K-means algorithm is used to cluster the wind power data for the whole year of 2022, and eight wind power output scenarios are obtained as shown in Fig. 4.

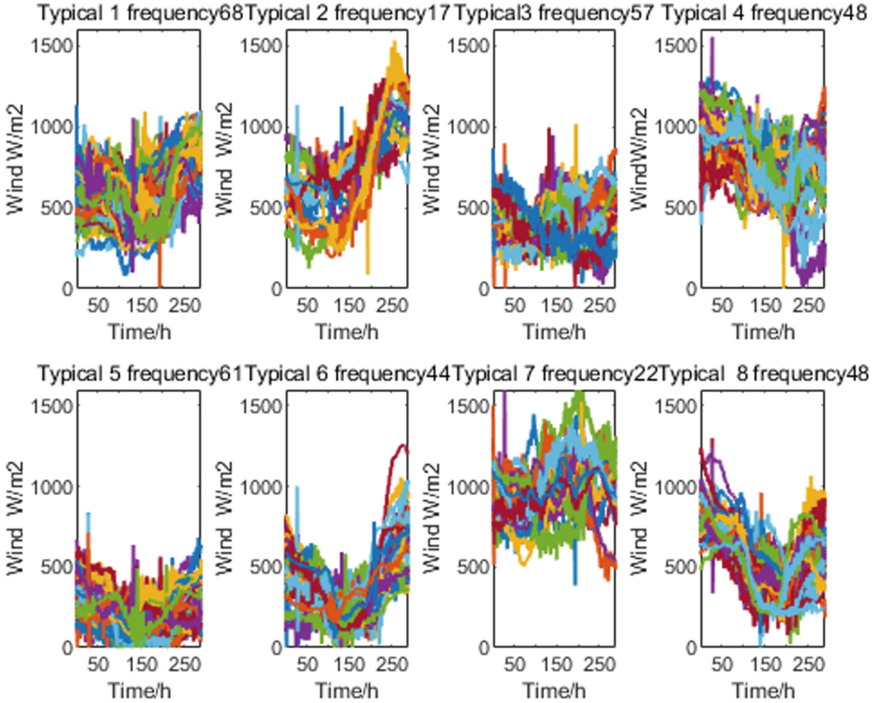

Fig. 4. Eight wind power output scenarios

Table 2 shows the number of days corresponding to each scenario and the probability of each scenario. Compared with the traditional K-means algorithm in solving the clustering scenarios of extreme wind power output data, cluster center distortion often occurs, so in order to solve the situation of cluster center distortion, this paper uses the median cumulative fluctuation as an indicator, selects typical days of various scenarios, and calculates the sum of fluctuations of all days of wind power output in K-means clustering scenarios, and arranges them in order according to the size of the fluctuations. And select the corresponding median as the typical day of the corresponding number of days for this type of scenario. The typical day selected by this method solves the influence of extreme data on the probability result and has strong persuasive power.

4.2 Power Distribution and Selection of Optimal Grid-Connected Fluctuations

The dividing line between the low-frequency grid-connected component and the high-frequency component of hybrid energy storage flattening is selected as the wind power

Table. 2 Days for different scenarios

Scenario	一	二	三	四	五	六	七	八
Total number of days	68	17	57	48	61	44	22	48
Probability	0.07	0.16	0.11	0.05	0.13	0.16	0.05	0.27

grid-connected fluctuation limit. Taking Typical Day 7 as an example, the maximum fluctuation of the low-frequency reconstruction component (5) is greater than the fluctuation limit of grid-connected, and (4) is selected as the low-frequency reconstruction component as the direct grid-connected component as shown in Fig. 5a, and (1) is selected, that is, IMF1 is used as the hybrid energy storage power task, and the reconstructed high-frequency component and low-frequency reconstruction component are obtained, as shown in (b, c) in the figure.

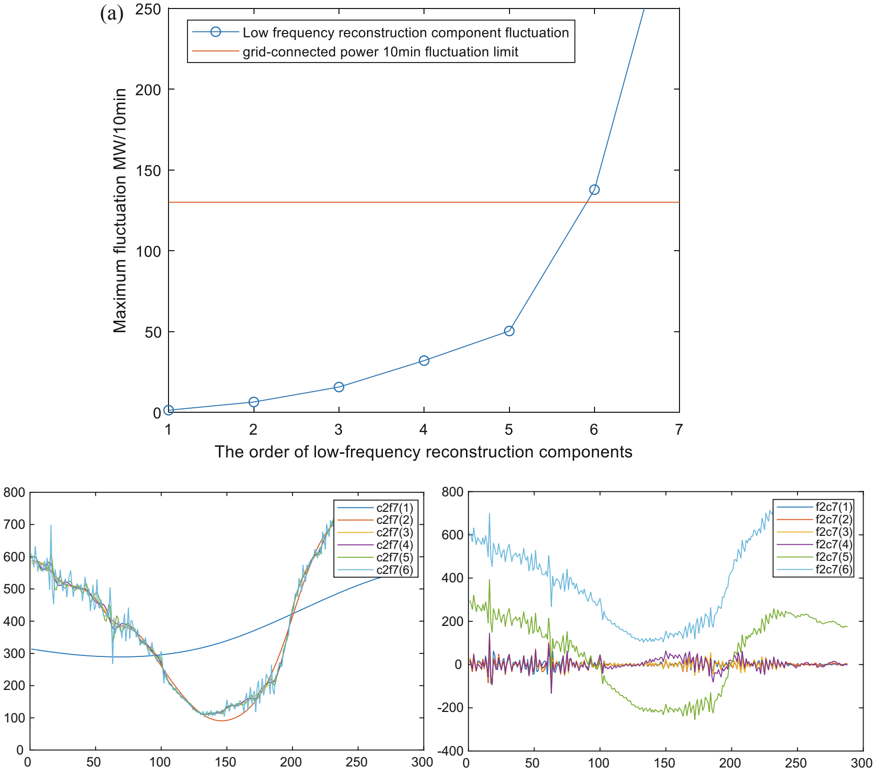

(b) Low-frequency reconstruction components (c) High-frequency reconstruction components

Fig. 5. Direct grid-tied component filtering. **b** Low-frequency reconstruction components. **c** High-frequency reconstruction components

The typical day seven of the wind power scene is obtained by K-means clustering, and the wind power signal is decomposed into low-frequency reconstruction component signal and high-frequency reconstruction component signal by EMD. The power maps of 120MW, 50MW and 20 MW were selected for comparison, and the power maps of low-frequency direct grid-connected components and high-frequency energy storage flattening components were compared, and the optimal grid-connected fluctuation limit was selected.

As shown in Fig. 6, as the fluctuation limit decreases, the direct grid-connected component becomes smoother and smoother, and the energy storage flattening component becomes more and more coarse and the amplitude is getting larger and larger. By comparing the direct grid-connected components, the curve with the fluctuation limit to 50 MW is smoother, so 50 MW is selected as the direct grid-connected component value.

4.3 The Variable Reference Line Flattens the High-Frequency Component

It can be seen from Fig. 7a, b that the high-frequency component signal is flattened by changing the variable reference line, and when the reference line is −6.2319 and the capacity configuration of the supercapacitor is configured to 42.07 MW, the result of hybrid energy storage flattening and the capacity configuration of the supercapacitor are optimal.

It can be seen from Fig. 8a, b that when the capacity of the supercapacitor is 42.07 MW and the reference line is −6.2319, the initial grid-connected power and high-frequency flattening component power map become smoother, and the flattening result is optimal.

4.4 Configure Result Analysis

This paper uses the MATLAB2018B + Gurobi platform algorithm to solve the problem. The capacity configuration of hybrid energy storage system is mainly analyzed into two scenarios:

Scenario 1: Traditional HESS energy management strategy;

Scenario 2: The energy management strategy mentioned in this article.

Table 3 shows that compared with the traditional strategy, the annual comprehensive cost of the capacity configuration solution under the strategy proposed in this article has been reduced by 5.732 million yuan, a decrease of 7.21%. The main reason is that the traditional strategy relies more on supercapacitor energy storage when leveling wind power fluctuations, and supercapacitor energy storage as a power energy storage, its capacity cost is higher than hydrogen energy storage, in addition, leveling wind power fluctuations also has requirements for the scale of energy storage capacity, in scenario 2, more emphasis on hydrogen energy storage as the main body, supercapacitor energy storage only undertakes auxiliary tasks. As a capacity-based energy storage, hydrogen energy storage has a larger capacity, but the total investment cost of scenario 2 is still 4.30% lower than that of scenario 1 due to its low capacity cost.

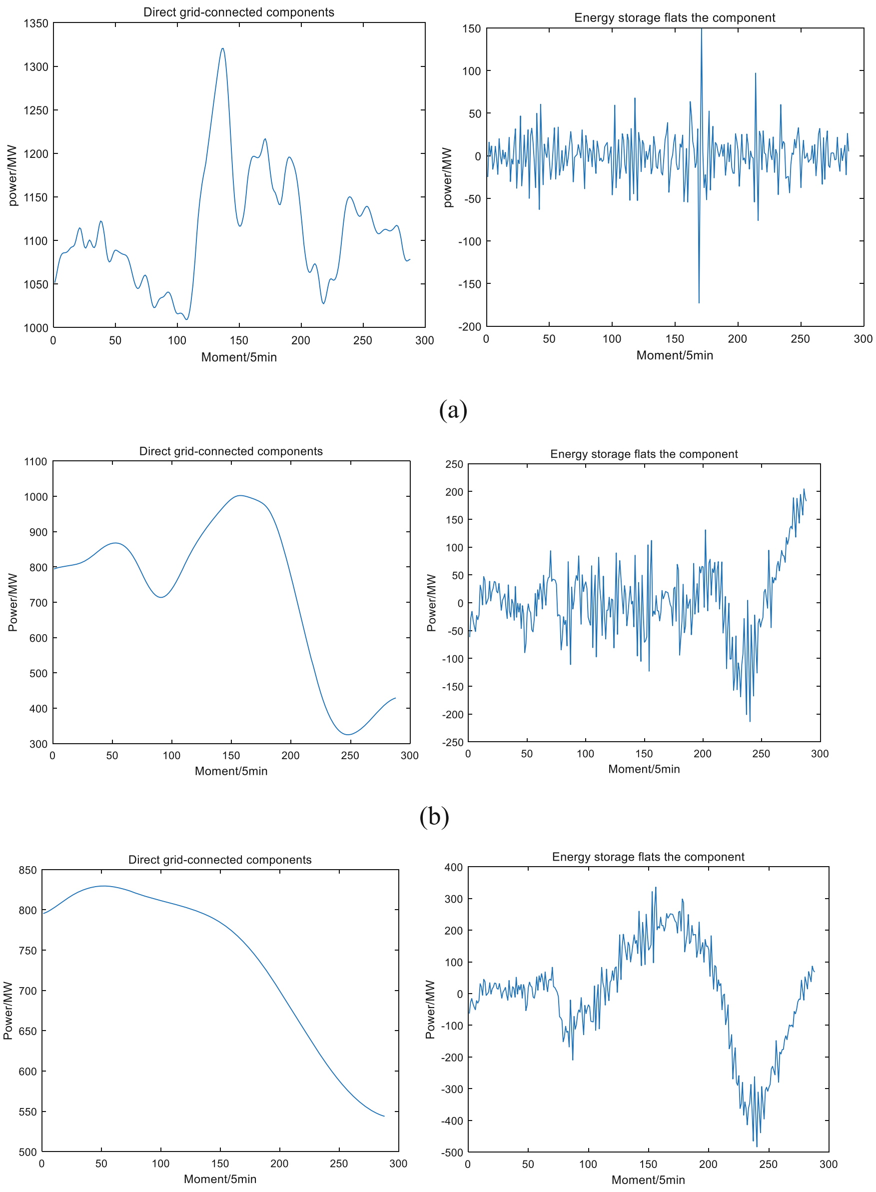

(a)

(b)

(c)

Fig. 6. Optimal direct grid-connected component screening. **a** Direct grid-connected component diagram and hybrid energy storage flattening component diagram when the fluctuation amount is limited to 120 WM. **b**Direct grid-connected component diagram and hybrid energy storage flattening component diagram when the fluctuation amount is limited to 50 WM. **c** Direct grid-connected component diagram and hybrid energy storage flattening component diagram when the fluctuation amount is limited to 20 WM

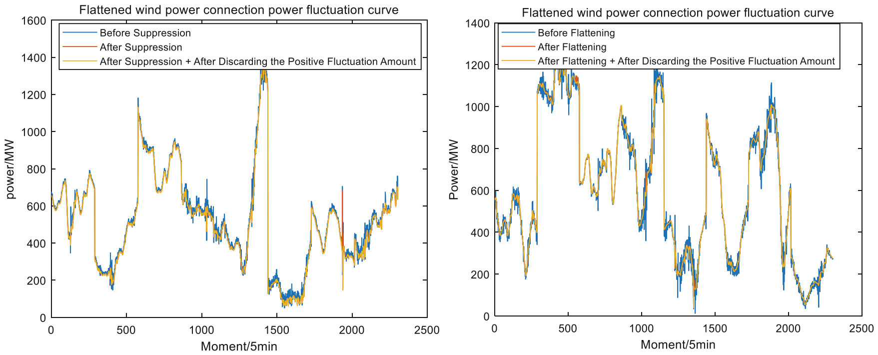

(a) (b)

Fig. 7. Selection of super capacitor variable reference line. **a** Unfolds the fluctuation curve of wind power connected to the grid after the supercapacitor capacity is configured to 36.22 MW. **b** Unfolds the fluctuation curve of grid-connected power of wind power after the supercapacitor capacity is configured to 42.07 MW

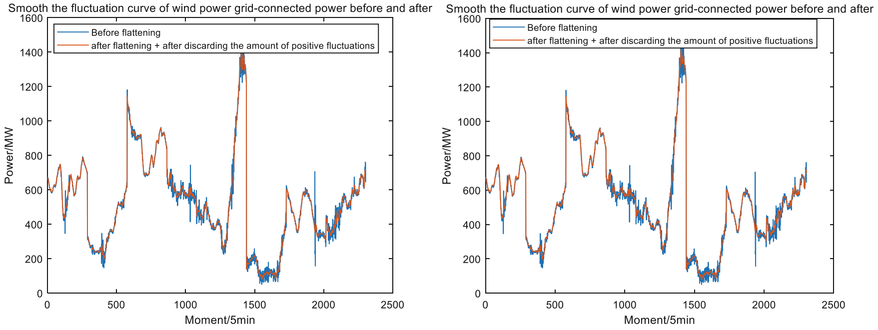

(a) (b)

Fig. 8. Initial grid-connected power and high-frequency flattening component power diagram. **a** The supercapacitor capacity is configured with 36.22 MW of initial grid-connected power low-frequency component and flattened grid-connected power. **b** The supercapacitor capacity is configured with 42.07 MW of initial grid-connected power, low-frequency component and flattened grid-connected power

5 Conclusion

(1) Compared with the traditional strategy, the strategy proposed in this paper (removed) hybrid energy storage capacity has lower cost and better economy; Moreover, the smoothing effect on wind power fluctuations is better, which can effectively reduce the amount of under compensation.

Table. 3 Capacity configuration results

Category	Parameter	Scenario 1	Scenario 2
Device capacity	Supercapacitor energy storage power/MW	83.79	33.53
	Supercapacitor capacitive energy power/MWh	44.60	159.45
Cost	Investment cost/million yuan	5612.8	5371.3
	Operation and maintenance cost/10,000 yuan	107.8	91.34
	Power fluctuation opportunity compensation cost/million yuan	2225.5	1910.5

(2) The HESS complementary mechanism is added to the proposed strategy, which improves the utilization rate of hydrogen energy storage, improves the service life of the supercapacitor, and leaves sufficient power and capacity space for subsequent compensation of high-frequency components.

(3) After changing the capacity configuration of the supercapacitor to stabilize the high-frequency component of wind power, the large value of the retained small amount of electricity fluctuates positively. Through the analysis of the example, the optimal configuration of the supercapacitor capacity is obtained.

References

1. Li, R., Li, Q., Pu, Y., et al.: Optimal configuration of an electric-hydrogen hybrid energy storage multi-microgrid system considering power interaction constraints. Power Syst. Protect. Control **50**(14), 53–64 (2022). (in Chinese)
2. Huang, X., Chen, Z.: Design and implementation of heterogeneous web platform based on JSON. Comput. Technol. Dev. **31**(3), 120–125 (2021)
3. Ma, W., Wang, W., Wu, X., et al.: Optimal dispatching strategy of hybrid energy storage system to smooth the fluctuation of photovoltaic grid-connected power. Autom. Electr. Power Syst. **43**(3), 58–66 (2019)
4. Ma, L., Huang, W., Ke, Li., et al.: Photovoltaic ultra-short-term power prediction model based on attention-LSTM. Electr. Meas. Instrum. **58**(2), 146–152 (2021)
5. Lei, Y., Lin, X.: Application of super magnetic energy storage-battery hybrid energy storage system in smoothing power fluctuations in wind power plants. High Volt. Eng. **45**(3), 983–992 (2019)
6. Li, Y., Wang, Q., Song, W., et al.: Variational mode decomposition-fuzzy control strategy for smooth wind power output of hybrid energy storage system. Power Syst. Prot. Control **47**(7), 58–65 (2019)
7. Tan, J: Research on optimal reconstruction method of distribution network benefit for new energy access. Encyclopedia For. Electron. J. (19), 2475 (2021)
8. Fu, J., Chen, J., Deng, H., et al.: Control strategy of hybrid energy storage system to smooth wind power fluctuation. Electr. Meas. Instrum. **57**(5), 94–100 (2020)
9. Tian, L.: Design and analysis of early warning monitoring system for photovoltaic power station based on Web platform. Shandong Electr. Power Technol. **47**(7), 60–63 (2020)
10. Yang, J., Zhang, J., Gui, X.: Capacity optimization configuration of hybrid energy storage system in grid-connected wind power generation. Power Syst. Technol. (5), 2019–1216 (2013)

11. Wen, Z., Sun, H.: MATLAB Intelligent Algorithm, vol. 58, no. 2, pp. 146–152. Tsinghua University Press, Beijing (2017)
12. Huang, X., Zhang, M.: Simulation of synchronous transmission method of spatial data based on thread pool technology. Comput. Simul. **38**(7), 148–152 (2021)
13. Li, Y., Wang, Q., Song, W., et al.: Optimal configuration of smooth wind power output hybrid energy storage capacity based on basic variational mode decomposition and Hilbert transform. Electr. Meas. Instrum. **56**(1):90–96–103 (2019)
14. Jiang, Q., Hong, H.: Wavelet-based capacity configuration and coordinated control of hybrid energy storage system for smoothing out wind power fluctuations. IEEE Trans. Power Syst. **28**(2), 1363–1372 (2012)
15. Li, X., Hui, D., Wu, L., et al.: Control straegy of battery state of charge for wind/battery hybrid power system. In: 2010 IEEE, International Symposium on Industrial Electronics, pp. 2723–2726. IEEE (2010)
16. Ursua, A., Barrios, E.L., Pascual, J., et al.: Integration of commercial alkaline water electolysers with renewable energies: Limitations and improvements. Int. J. Hydrogen Energy **41**(30), 12852–12861 (2016)

Analysis on the Impact of Locational Marginal Price of Wind-Thermal and Pumped-Storage Complementary Power Generation System

Zhicheng Xu(✉), Jun Xie, Xinyi Zhao, Yifan Chang, Denghui Fu, and Shanxi Xing

College of Energy and Electrical Engineering, Hohai University, Nanjing 211100, China
`211306080040@hhu.edu.cn`

Abstract. Consider the availability of remaining reservoir resources to pumped-storage reserve ancillary services, and establish a day-ahead market clearing model for the wind-thermal and pumped-storage complementary power generation system. Based on the optimality conditions, the energy service price and reserve ancillary service price are decomposed into shadow price components and water value components. The scarcity of reservoir and installed resources is reflected through the shadow price. The influence of pumped-storage constraints on the water value was analyzed from the perspective of power supply and load. The cross-time relationship between water value and shadow price is derived, and the impact of reservoir capacity on water value and remaining reservoir resource value is analyzed. Taking the modified IEEE-39 system as an example, different cases are designed to analyze the changing characteristics of various resource values in different periods, as well as the impact of scarcity of remaining resources on reserve auxiliary service price. Analyze the impact of pumped-storage installed capacity, reservoir capacity, and wind power penetration rate on clearing electricity price and its main components.

Keywords: Wind-thermal and pumped-storage complementary power generation system · Locational marginal price · Day-ahead market · Cross-time reservoir constraint · Value of reservoir resources

1 Introduction

The relevant document points out that: to further develop day-ahead, intra-day and real-time electricity trading and auxiliary service trading such as reserve and frequency regulation, form market clearing prices, and coordinate the spot market and auxiliary service market.

Considering environmental resource constraints, the wind penetration rate in the system is constantly increasing, gradually transforming thermal units into reserve auxiliary service providers. However, the increasing fluctuating wind power and demand for electricity put forward higher requirements for the flexibility of the system, and the demand for auxiliary services is constantly growing [1], which increases the difficulty of operation of the system and the power market. Pumped-storage power stations are

Y. Xue et al. (Eds.): PMF 2023, LNEE 1129, pp. 17–32, 2024.
https://doi.org/10.1007/978-981-99-9251-5_2

flexible and reliable, and can provide energy, reserve, storage and other services, which is an important support for realizing the goal of dual carbon [2].

Therefore, it is of great significance to fully consider the characteristics of pumped-storage and study the corresponding spot market clearing model and price formation mechanism. Literature [3] uses reserve to cope with wind power fluctuations, but it is difficult to avoid the subjectivity of the selection of reservation. Literature [4] establishes a double-layer optimization model by using relevant indexes of energy and reserve, but lacks analysis of the influence of external factors. Aiming at the reserve demand of renewable energy, literature [5] puts forward a market clearing model considering the declaration of reserve demand and demand elasticity. Literature [6] enhances the effectiveness of joint optimization of reserve and energy through partitioning of reserve demand. The above studies rarely consider the availability of remaining reservoir resources for reserve auxiliary service of pumped-storage, and lack the analysis of the price of reserve auxiliary service of pumped-storage.

Locational marginal price (LMP) has been widely implemented as an effective pricing scheme because it can reasonably measure energy value, reflect power supply and demand situation and network congestion [7, 8].

Researches on the LMP of thermal units have been relatively mature [9, 10], which can be expressed as system energy price, network congestion price and other components, or analyzed from the perspective of units, which are influenced by output, reserve, ramp and other constraints. Literature [11] analyzes the influence of load distribution law on clearing price. Literature [12] introduces a risk price component that considers the overload risk of lines. Literature [13] establishes a prospective dispatching model and analyzed the influence of thermal unit's cross time ramp ability on the price volatility, but does not consider the influence brought by the constraints of pumped-storage and transmission. Literature [14] studies the influence of thermal unit operation constraints on day-ahead price and main components. In literature [15], wind power uncertainty is suppressed by real-time balance adjustment, which reflects the balance value of reserve, but does not consider the influence of cross-time constraints. Literature [16] expounds the physical meaning of price signals according to the connection between dual multipliers and LMP, and deduces the extensible unified expression of price. The quantitative analysis of the influence of pumped-storage operation constraints on LMP is rarely seen in the above studies, especially the reservoir constraints that lead to output constraints. The cross-time characteristics of reservoir water volume lead to the coupling of optimization results in different periods, and the fluctuation of water value. The analysis of the influence of pumped-storage operation on LMP is of significance for the construction of the new power system.

In this paper, considering the availability of remaining reservoir resources to the auxiliary service of pumped-storage, the day-ahead market clearing model of wind-thermal and pumped-storage complementary power generation system is established. According to the optimality condition (Karush-Kuhn-Tucker, KKT), the price of energy service and reserve auxiliary service are decomposed into the shadow price components and water value components. The influence of pumped-storage constraints on the water value is analyzed from the perspective of power supply and load, the cross-time relationship between the water value and the shadow price of reservoir capacity constraints is deduced, and the influence of scarcity of reservoir capacity resources on the value of remaining reservoir resources is analyzed. Different cases are designed to analyze the changing characteristics of the value of various resources at different periods and the influence of the scarcity of remaining resources on the price of reserve auxiliary service, and to analyze the influence of the installed capacity of pumped-storage, reservoir capacity and wind power penetration on the price and its main components.

2 Day-Ahead Market Clearing Model with Wind-Thermal and Pumped-Storage

The objective function is the minimum total cost, which includes thermal power cost, reserve capacity cost, wind power cost and load shedding cost.

$$\min \sum_{t=1}^{NT} \left[\sum_{i=1}^{NG} (C_i(P_{i,t}) + C_i^{RU}(RU_{i,t}) + C_i^{RD}(RD_{i,t})) + \sum_{q=1}^{NQ} (C_q^w(P_{q,t}) + \sum_{n=1}^{NB} V^D D_{n,t}^s \right] \tag{1}$$

where NT, NG, NQ and NB are the number of scheduling periods, thermal units, wind farms and nodes. $P_{i,t}$ and $P_{q,t}$ are the generating power of thermal unit i and wind farm q at time t, $RU_{i,t}$ and $RD_{i,t}$ are the upward and downward reserve capacity of thermal unit i at time t, $D_{n,t}^s$ is the shedding load power of node n at time t. C_i, C_i^{RU} and C_i^{RD} are respectively the generation cost, upper and lower reserve capacity cost declared by thermal unit i, C_q^w is the power generation cost declared by wind farm q, V^D is the load shedding penalty cost factor.

(1) *Power balance constraint*

$$\sum_{i=1}^{NG} P_{i,t} + \sum_{q=1}^{NQ} P_{q,t} + \sum_{h=1}^{NH} (P_{h,t}^g - P_{h,t}^p) - \sum_{n=1}^{NB} (D_{n,t} - D_{n,t}^{sh}) = 0 : \lambda_t, \forall t \tag{2}$$

where NH is the number of pumped-storage stations. $P_{h,t}^g$ and $P_{h,t}^p$ represent the generating and pumping power of station h at time t; $D_{n,t}$ is the load power of node n at time t. λ_t is the corresponding dual multiplier.

(2) *Upper and lower reserve demand constraints*

$$\sum_{i=1}^{NG} RU_{i,t} + \sum_{h=1}^{NH} (RU_{h,t}^g + RD_{h,t}^p) \geq \alpha \sum_{n=1}^{NB} D_{n,t} + \beta \sum_{q=1}^{NQ} P_{q,t} : \lambda_t^u, \forall t \tag{3}$$

$$\sum_{i=1}^{NG} RD_{i,t} + \sum_{h=1}^{NH} (RD_{h,t}^g + RU_{h,t}^p) \geq \beta \sum_{q=1}^{NQ} P_{q,t} : \lambda_t^d, \forall t \tag{4}$$

where $RU_{h,t}^g$ ($RU_{h,t}^p$) and $RD_{h,t}^g$ ($RD_{h,t}^p$) are respectively the upward and downward reserve capacity reserved by the pumped-storage station h at time t under generating (pumping) state. α and β are the reserve demand coefficients of load and wind power. λ_t^{ru} and λ_t^{rd} are the corresponding dual multipliers respectively.

(3) *Operation constraints of thermal unit*

$$P_{i,t} \le P_{i,t} + RU_{i,t} \le P_i^{\max} : \underline{\varepsilon}_{i,t}^{u}, \overline{\varepsilon}_{i,t}^{u}, \forall i, \forall t \tag{5}$$

$$P_i^{\min} \le P_{i,t} - RD_{i,t} \le P_{i,t} : \underline{\varepsilon}_{i,t}^{d}, \overline{\varepsilon}_{i,t}^{d}, \forall i, \forall t \tag{6}$$

$$-P_i^r \le P_{i,t} - P_{i,t-1} \le P_i^r : \underline{\theta}_{i,t}, \overline{\theta}_{i,t}, \forall i, \forall t \tag{7}$$

where $P_i^{\max}$ and $P_i^{\min}$ are the upper and lower limits of output, P_i^r is the ramp rate. Equations (5)–(7) are the total output constraints and ramp constraint. $\underline{\varepsilon}_{i,t}^{u}$, $\overline{\varepsilon}_{i,t}^{u}$, $\underline{\varepsilon}_{i,t}^{d}$, $\overline{\varepsilon}_{i,t}^{d}$, $\underline{\theta}_{i,t}$ and $\overline{\theta}_{i,t}$ are the corresponding dual multipliers.

(4) *Operation constraints of thermal unit*

$$P_{h,t}^g \le P_{h,t}^g + RU_{h,t}^g \le I_{h,t}^g P_{h,\max}^g : \underline{\vartheta}_{h,t}^{g,u}, \overline{\vartheta}_{h,t}^{g,u}, \forall h, \forall t \tag{8}$$

$$I_{h,t}^g P_{h,\min}^g \le P_{h,t}^g - RD_{h,t}^g \le P_{h,t}^g : \underline{\vartheta}_{h,t}^{g,d}, \overline{\vartheta}_{h,t}^{g,d}, \forall h, \forall t \tag{9}$$

$$P_{h,t}^p \le P_{h,t}^p + RU_{h,t}^p \le I_{h,t}^p P_{h,\max}^p : \underline{\vartheta}_{h,t}^{p,u}, \overline{\vartheta}_{h,t}^{p,u}, \forall h, \forall t \tag{10}$$

$$I_{h,t}^p P_{h,\min}^p \le P_{h,t}^p - RD_{h,t}^p \le P_{h,t}^p : \underline{\vartheta}_{h,t}^{p,d}, \overline{\vartheta}_{h,t}^{p,d}, \forall h, \forall t \tag{11}$$

$$I_{h,t}^g + I_{h,t}^p \le 1, \forall h, \forall t \tag{12}$$

where $I_{h,t}^g$ and $I_{h,t}^p$ represent the pumped-storage operating state; $I_{h,t}^g = 1$, indicating generating state; $I_{h,t}^p = 1$, indicating pumping state; If $I_{h,t}^g = I_{h,t}^p = 0$, the station is stopped. $P_{h,\max}^g$ ($P_{h,\max}^p$) and $P_{h,\min}^g$ ($P_{h,\min}^p$) are the upper and lower limits for generating or pumping output. Equations (8)–(11) are the total output constraints for generating and pumping, Eq. (12) indicates that it cannot be in both generating and pumping state at the same time. $\underline{\vartheta}_{h,t}^{g,u}$, $\overline{\vartheta}_{h,t}^{g,u}$, $\underline{\vartheta}_{h,t}^{g,d}$, $\overline{\vartheta}_{h,t}^{g,d}$, $\underline{\vartheta}_{h,t}^{p,u}$, $\overline{\vartheta}_{h,t}^{p,u}$, $\underline{\vartheta}_{h,t}^{p,d}$ and $\overline{\vartheta}_{h,t}^{p,d}$ are the corresponding dual multipliers respectively.

(5) *Reservoir constraints*

$$V_{h,t} = V_{h,t-1} + \eta_h^p P_{h,t}^p - \frac{P_{h,t}^g}{\eta_h^g} : \upsilon_{h,t}, \forall h, \forall t \tag{13}$$

$$V_{h,\min} \le V_{h,t} \le V_{h,\max} : \underline{\delta}_{h,t}, \overline{\delta}_{h,t}, \forall h, \forall t \tag{14}$$

$$V_{h,NT} = V_{h,0} : \sigma_h, \forall h \tag{15}$$

$$V_{h,t} + V_{h,t}^u \le V_{h,\max} : \overline{\ell}_{h,t}, \forall h, \forall t \tag{16}$$

$$V_{h,t} - V_{h,t}^{d} \geq V_{h,\min} : \underline{\ell}_{h,t}, \forall h, \forall t \tag{17}$$

$$V_{h,t}^{u} = \eta_{h}^{p} RU_{h,t}^{p} + \frac{RD_{h,t}^{g}}{\eta_{h}^{g}} : \upsilon_{h,t}^{u}, \forall h, \forall t \tag{18}$$

$$V_{h,t}^{d} = \eta_{h}^{p} RD_{h,t}^{p} + \frac{RU_{h,t}^{g}}{\eta_{h}^{g}} : \upsilon_{h,t}^{d}, \forall h, \forall t \tag{19}$$

where $V_{h,t}$ is the reservoir water volume of the station h at time t. η_{h}^{g} and η_{h}^{p} are conversion efficiencies of water-to-electricity and electricity-to-water. $V_{h,\max}$ and $V_{h,\min}$ are the maximum and minimum reservoir capacity. $V_{h,NT}$ and $V_{h,0}$ are the final and initial reservoir water volume. $V_{h,t}^{u}$ and $V_{h,t}^{d}$ are the remaining storage space and available water saved for reserve. Equation (13) is the water balance constraint. Equation (14) is the upper and lower limit constraint of reservoir capacity. Equation (15) is the start-end water volume constraint. Equations (16)–(19) are reservoir constraints that take into account the remaining reservoir resources margin required for all reserves in real-time dispatching. $\upsilon_{h,t}$, $\underline{\delta}_{h,t}$, $\overline{\delta}_{h,t}$, σ_{h}, $\overline{\ell}_{h,t}$, $\underline{\ell}_{h,t}$, $\upsilon_{h,t}^{u}$ and $\upsilon_{h,t}^{d}$ are the corresponding dual multipliers respectively.

(6) *Wind power and shedding load constraints*

$$0 \leq P_{q,t} \leq P_{q,t}^{f}, \forall q, \forall t \tag{20}$$

$$0 \leq D_{n,t}^{sh} \leq D_{n,t}, \forall n, \forall t \tag{21}$$

where $P_{q,t}^{f}$ is the predicted value of wind power. Equation (20) indicates that wind power dispatching output cannot exceed the predicted value, Eq. (21) indicates that the load shedding power cannot exceed the actual load power.

(7) *Transmission capacity constraints*

$$\begin{aligned} - C_{l}^{\max} \leq & \sum_{n \in NB} T_{l,n} [\sum_{i \in MG_{n}} P_{i,t} + \sum_{q \in MQ_{n}} P_{q,t} + \sum_{h \in MH_{n}} (P_{h,t}^{g} - P_{h,t}^{p}) - (D_{n,t} - D_{n,t}^{sh})] \\ & \leq C_{l}^{\max} : \underline{\omega}_{l,t}, \overline{\omega}_{l,t}, \forall l, \forall t \end{aligned} \tag{22}$$

$$\begin{aligned} - C_{l}^{\max} \leq & \sum_{n \in NB} T_{l,n} [\sum_{i \in MG_{n}} (P_{i,t} + RU_{i,t}) + \sum_{h \in MH_{n}} (P_{h,t}^{g} + RU_{h,t}^{g} - P_{h,t}^{p} + RD_{h,t}^{p}) \\ & + (1 - \beta) \sum_{q \in MQ_{n}} P_{q,t} - (1 + \alpha)(D_{n,t} - D_{n,t}^{sh})] \leq C_{l}^{\max} : \underline{\omega}_{l,t}^{u}, \overline{\omega}_{l,t}^{u}, \forall l, \forall t \end{aligned} \tag{23}$$

$$\begin{aligned} - C_{l}^{\max} \leq & \sum_{n \in NB} T_{l,n} [\sum_{i \in MG_{n}} (P_{i,t} - RD_{i,t}) + \sum_{h \in MH_{n}} (P_{h,t}^{g} - RD_{h,t}^{g} - P_{h,t}^{p} - RU_{h,t}^{p}) \\ & + (1 + \beta) \sum_{q \in MQ_{n}} P_{q,t} - (1 - \alpha)(D_{n,t} - D_{n,t}^{sh})] \leq C_{l}^{\max} : \underline{\omega}_{l,t}^{d}, \overline{\omega}_{l,t}^{d}, \forall l, \forall t \end{aligned} \tag{24}$$

where $C_l^{\max}$ is the upper limit of transmission capacity of transmission line l, $T_{l,n}$ is the generation transfer distribution factor. MG_n, MQ_n and MH_n are sets of thermal units, wind farms, pumped-storage stations located at node n. Equation (22) is the transmission capacity constraint, Eqs. (23) and (24) are the transmission capacity constraint that considers the reserved capacity margin required to dispatch all reserves under the maximum upward or downward reserve demand. $\underline{\omega}_{l,t}, \overline{\omega}_{l,t}, \underline{\omega}^u_{l,t}, \overline{\omega}^u_{l,t}, \underline{\omega}^d_{l,t}$ and $\overline{\omega}^d_{l,t}$ are corresponding multipliers respectively.

3 Price Decomposition

3.1 Optimality Condition

In this system, pumped-storage can be regarded as negative power source when pumping. Wind power is not only an uncontrollable power entity, but also a reserve demand entity, which can be regarded as load with negative electricity demand. By taking partial derivatives of extended Lagrange function, the KKT condition of the pumped-storage under different state is obtained, which is used as the basis of price decomposition, as shown below.

$$\begin{aligned}\frac{\partial L}{\partial P^g_{h,t}} &= -\lambda_t + (\bar{\vartheta}^{g,u}_{h,t} - \underline{\vartheta}^{g,d}_{h,t}) + \upsilon_{h,t}/\eta^g_h \\ &\quad + \sum_l T_{l,n}(\bar{\omega}_{l,t} - \underline{\omega}_{l,t} + \bar{\omega}^u_{l,t} - \underline{\omega}^u_{l,t} + \bar{\omega}^d_{l,t} - \underline{\omega}^d_{l,t}) = 0, \forall h \in MH_n \end{aligned} \tag{25}$$

$$\begin{aligned}\frac{\partial L}{\partial P^p_{h,t}} &= \lambda_t + (\bar{\vartheta}^{p,u}_{h,t} - \underline{\vartheta}^{p,d}_{h,t}) - \eta^p_h \upsilon_{h,t} \\ &\quad - \sum_l T_{l,n}(\bar{\omega}_{l,t} - \underline{\omega}_{l,t} + \bar{\omega}^u_{l,t} - \underline{\omega}^u_{l,t} + \bar{\omega}^d_{l,t} - \underline{\omega}^d_{l,t}) = 0, \forall h \in MH_n \end{aligned} \tag{26}$$

$$\begin{aligned}\frac{\partial L}{\partial RU^g_{h,t}} &= -\lambda^u_t + (\bar{\vartheta}^{g,u}_{h,t} - \underline{\vartheta}^{g,u}_{h,t}) + \upsilon^d_{h,t}/\eta^g_h \\ &\quad + \sum_l T_{l,n}(\bar{\omega}^u_{l,t} - \underline{\omega}^u_{l,t}) = 0, \forall h \in MH_n \end{aligned} \tag{27}$$

$$\begin{aligned}\frac{\partial L}{\partial RD^g_{h,t}} &= -\lambda^d_t - (\bar{\vartheta}^{g,d}_{h,t} - \underline{\vartheta}^{g,d}_{h,t}) + \upsilon^u_{h,t}/\eta^g_h \\ &\quad - \sum_l T_{l,n}(\bar{\omega}^d_{l,t} - \underline{\omega}^d_{l,t}) = 0, \forall h \in MH_n \end{aligned} \tag{28}$$

$$\begin{aligned}\frac{\partial L}{\partial RU^p_{h,t}} &= -\lambda^d_t + (\bar{\vartheta}^{p,u}_{h,t} - \underline{\vartheta}^{p,u}_{h,t}) + \eta^p_h \upsilon^u_{h,t} \\ &\quad - \sum_l T_{l,n}(\bar{\omega}^d_{l,t} - \underline{\omega}^d_{l,t}) = 0, \forall h \in MH_n \end{aligned} \tag{29}$$

$$\frac{\partial L}{\partial RD_{h,t}^{p}} = -\lambda_t^u - (\bar{\vartheta}_{h,t}^{p,d} - \underline{\vartheta}_{h,t}^{p,d}) + \eta_h^p \upsilon_{h,t}^d + \sum_l T_{l,n}(\bar{\omega}_{l,t}^u - \underline{\omega}_{l,t}^u) = 0, \forall h \in MH_n \tag{30}$$

3.2 Price Decomposition of Load Node

According to the definition of LMP, the price at time t and node n can be obtained by partial derivative of Lagrange function on the energy or reserve demand of load-like entity (load, wind power), as shown in Eqs. (31)–(33).

$$LMP_{n,t} = \lambda_t - \sum_l T_{l,n}(\overline{\omega}_{l,t} - \underline{\omega}_{l,t} + \overline{\omega}_{l,t}^u - \underline{\omega}_{l,t}^u + \overline{\omega}_{l,t}^d - \underline{\omega}_{l,t}^d), \forall n \tag{31}$$

$$LMP_{n,t}^U = \lambda_t^u - \sum_l T_{l,n}(\overline{\omega}_{l,t}^u - \underline{\omega}_{l,t}^u), \forall n \tag{32}$$

$$LMP_{n,t}^D = \lambda_t^d + \sum_l T_{l,n}(\overline{\omega}_{l,t}^d - \underline{\omega}_{l,t}^d), \forall n \tag{33}$$

where Eq. (31) represents the energy price, and Eqs. (32) and (33) represent the upward and downward reserve price, including the system energy price component, system reserve price component and congestion price component.

3.3 Energy Price Decomposition of Pumped-Storage Node

The energy price can be decomposed into generating (pumping) capacity constraint price component and water consuming (pumping) value component through corresponding pumped-storage KKT conditions, as shown below.

$$LMP_{h,t}^g = (\overline{\vartheta}_{h,t}^{g,u} - \underline{\vartheta}_{h,t}^{g,d}) + \upsilon_{h,t} \big/ \eta_h^g, \forall h \in MH_n \tag{34}$$

$$LMP_{h,t}^p = -(\overline{\vartheta}_{h,t}^{p,u} - \underline{\vartheta}_{h,t}^{p,d}) + \eta_h^p \upsilon_{h,t}, \forall h \in MH_n \tag{35}$$

The characteristic of pumped-storage price lies in the value of limited reservoir resource. The reservoir water volume is cumulative variable, the target water volume V_t can be decomposed into basic volume + variable volume. For example, it can be expressed as basic water volume V_{t-1} plus variation $\Delta V_{t-1 \to t}$ during $t - 1 \sim t$. From this, it can be seen that the changes of water volume in the previous time will continuously accumulate to the existing reservoir water volume, and have an impact on the subsequent operation, which is a progressive relation.

Pumped-storage can be regarded as source or load under different states. In generating state, the remaining water of previous time is consumed, while in pumping state, the current water is increased. The reservoir water volume can be equivalent to the the available supply electricity or the load demand electricity. Therefore, the water value

υ must be discussed in terms of power source and pumping load. In generating state, the basic water volume V_{t-1} is the available generation resource, and the water value υ_t can be expressed as the economic benefit increased to the system by unit increase of basic water volume V_{t-1}. $1/\eta^g$ water is consumed per unit increment of generating power, and the water-electricity conversion price (water consumption value) is υ_t/η^g. In pumping state, the target water volume V_t is the load demand electricity, and υ_t can be expressed as the economic cost increased to the system by unit increase of the target water volume V_t. η^p water can be stored per unit increment of pumping power, and the electricity-water conversion price (pumping value) is $\eta^p\upsilon_t$.

The relationship between water consumption value (pumping value) and system energy price, shadow prices constrained by installed capacity and transmission capacity is shown in Eqs. (36) and (37).

$$\begin{aligned}\upsilon_{h,t}/\eta_h^g = \lambda_t - (\bar{\vartheta}_{h,t}^{g,u} - \underline{\vartheta}_{h,t}^{g,d}) \\ - \sum_l T_{l,n}(\bar{\omega}_{l,t} - \underline{\omega}_{l,t} + \bar{\omega}_{l,t}^u - \underline{\omega}_{l,t}^u + \bar{\omega}_{l,t}^d - \underline{\omega}_{l,t}^d), \forall h \in MH_n\end{aligned} \tag{36}$$

$$\begin{aligned}\eta_h^p\upsilon_{h,t} = \lambda_t + (\bar{\vartheta}_{h,t}^{p,u} - \underline{\vartheta}_{h,t}^{p,d}) \\ - \sum_l T_{l,n}(\bar{\omega}_{l,t} - \underline{\omega}_{l,t} + \bar{\omega}_{l,t}^u - \underline{\omega}_{l,t}^u + \bar{\omega}_{l,t}^d - \underline{\omega}_{l,t}^d), \forall h \in MH_n\end{aligned} \tag{37}$$

If the installed capacity of pumped-storage is greatly reduced and becomes a scarce resource, the ability of water-electricity conversion will be limited, affecting the value of water consumed or stored in different states. In generating state, limited installed capacity makes water cannot be rapidly consumed, and cannot provide enough electricity at peak load time to achieve the most economical water consumption, resulting in the decline of water consumption value. Similarly, in pumping state, it takes longer for water to accumulate, and it is not possible to extract enough water at low load time to achieve the most economical storage, resulting in higher pumping cost. Similarly, a similar conclusion can be obtained when line transmission capacity resources are scarce.

Through the KKT condition corresponding to V_t, the relationship between the water value υ and the shadow price δ constrained by reservoir capacity accumulated over time is obtained, as shown in Eqs. (38) and (39).

$$\upsilon_{h,t} = \upsilon_{h,t-1} + (\bar{\delta}_{h,t-1} - \underline{\delta}_{h,t-1} + \bar{\ell}_{h,t-1} - \underline{\ell}_{h,t-1}) = \upsilon_{h,1} + \sum_{\tau=1}^{t-1}(\bar{\delta}_{h,\tau} - \underline{\delta}_{h,\tau} + \bar{\ell}_{h,\tau} - \underline{\ell}_{h,\tau}) \tag{38}$$

$$\upsilon_{h,t} = \upsilon_{h,t+1} - (\bar{\delta}_{h,t} - \underline{\delta}_{h,t} + \bar{\ell}_{h,t} - \underline{\ell}_{h,t}) = \sigma_h - \sum_{\tau=t}^{NT}(\bar{\delta}_{h,\tau} - \underline{\delta}_{h,\tau} + \bar{\ell}_{h,\tau} - \underline{\ell}_{h,\tau}) \tag{39}$$

Due to the resource scarcity, reservoir capacity constraint is closely coupled with the output of pumped-storage. When the installed capacity is low, the ability of water storage or consumption becomes weak, the water volume changes little, the reservoir capacity constraint is loose. When the installed capacity is high, the ability of water regulation is improved, and it is easier to reach the boundary value. At this time, the reservoir capacity constraint is tight constraint, which is the main constraint condition affecting the value of reservoir water.

Shadow price of reservoir capacity constraint $\delta(\ell)$ represents the scarcity of reservoir capacity resources, and represents the economic benefits increased to the system by unit increment (decrease) of the upper (lower) limit of reservoir capacity. According to Eqs. (38) and (39), if the reservoir capacity resources are sufficient and the constraint does not work, then the water value is fixed, which is only determined by the dual multiplier σ of the excess or insufficient water storage at the last operation period. In generating state, if the basic water volume V_{t-1} reaches the upper limit, the multiplier $\overline{\delta}_{t-1} > 0$. In such cases, the water value υ_t is the superposition of the fixed value and the upper limit resource value of reservoir, and represents the total benefits generated by unit increment of water volume and upper limit. If V_{t-1} reaches the lower limit, the multiplier $\underline{\delta}_{t-1} > 0$. In such cases, υ_t represents net cost generated by the unit decrease of water volume and lower limit, as shown in Eq. (38). Similarly, in pumping state, if the target water volume V_t reaches the upper limit, υ_t after superposition can be expressed as net cost generated by unit increment of water volume and upper limit. If V_t reaches the lower limit, υ_t can be expressed as total benefits generated by unit decrease of water volume and lower limit, as shown in Eq. (39).

3.4 Reserve Price Decomposition of Pumped-Storage Node

On the premise of meeting the demand for energy service, the unused reservoir resources are used to provide reserve auxiliary service. The corresponding price is shown as follows, which can be decomposed into the component of reserve constraint price and conversion value of the remaining reservoir resources.

$$LMP_{h,t}^{g,ru} = (\bar{\vartheta}_{h,t}^{g,u} - \underline{\vartheta}_{h,t}^{g,u}) + \upsilon_{h,t}^{d}/\eta_h^g, \forall h \in MH_n \tag{40}$$

$$LMP_{h,t}^{g,rd} = -(\bar{\vartheta}_{h,t}^{g,d} - \underline{\vartheta}_{h,t}^{g,d}) + \upsilon_{h,t}^{u}/\eta_h^g, \forall h \in MH_n \tag{41}$$

$$LMP_{h,t}^{p,ru} = (\overline{\vartheta}_{h,t}^{p,u} - \underline{\vartheta}_{h,t}^{p,u}) + \eta_h^p \upsilon_{h,t}^{u}, \forall h \in MH_n \tag{42}$$

$$LMP_{h,t}^{p,rd} = -(\overline{\vartheta}_{h,t}^{p,d} - \underline{\vartheta}_{h,t}^{p,d}) + \eta_h^p \upsilon_{h,t}^{d}, \forall h \in MH_n \tag{43}$$

Through relevant KKT conditions, the relationship between residual reservoir resource value $\upsilon^d(\upsilon^u)$ and the shadow price ℓ considering availability of reserve service is obtained, as shown below.

$$\begin{cases} \frac{\partial L}{\partial V_{h,t}^{u}} = \overline{\ell}_{h,t} - \upsilon_{h,t}^{u} = 0, \forall h \in MH_n \\ \frac{\partial L}{\partial V_{h,t}^{d}} = \underline{\ell}_{h,t} - \upsilon_{h,t}^{d} = 0, \forall h \in MH_n \end{cases} \tag{44}$$

If the reservoir capacity resources are scarce, the reserve service and energy service will squeeze in the allocation of reservoir resources, resulting in the value of the residual reservoir resources. Combining with Eq. (44), it can be seen that its value is the same as ℓ, indicating the benefits generated by the unit increment of available residual resources to the system. A similar conclusion is drawn for the allocation of installed capacity resources to reserve and energy service. Similar to υ, residual value after water-electricity can also be obtained.

4 Example Analysis

The simulation is based on the IEEE-39 node system, including one pumped-storage station and six wind farms. The load curve is shown in Fig. 1. The wind farm adopts zero quotation strategy. The influences of the installed capacity of pumped-storage, reservoir capacity and the wind power penetration rate on the price in different cases.

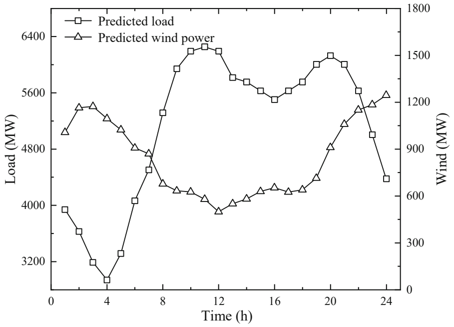

Fig. 1. Predicted values of wind power and load.

The case is set as follows. Case 1: No pumped-storage. Case 2: There is a pumped-storage power station with installed capacity of 1000 MW, reservoir capacity of 2000 MW h, water-electricity conversion efficiency of 94%, and electricity-water conversion efficiency of 75%. Case 3: On the basis of Case 2, the installed capacity is reduced to 40 MW. Case 4: Reduce the reservoir capacity to 200 MW h based on Case 2.

4.1 Energy Service Price Decomposition and Analysis

When the wind penetration rate is 26.38%, compare the energy price of the pumped-storage node in Case 1 and Case 2, as shown in Fig. 2. Figure 3 shows the wind curtailment rate of four cases under different scenarios. Table 1 shows the 24h average price and the price difference between the maximum and minimum in different cases.

From Figs. 2, 3 and Table 1, the integration of the pumped-storage into the system restrains the price peak, reduces the price gap, improves the system's ability to absorb wind power. By comparing Cases 2, 3 and 4, it can be seen that reducing the installed capacity or reservoir capacity will limit the regulation ability of pumped-storage, increase the price difference and wind abandonment rate. In other words, the scarcity of the resources of installed capacity and reservoir capacity is the main factor affecting regulation ability of pumped-storage and its price.

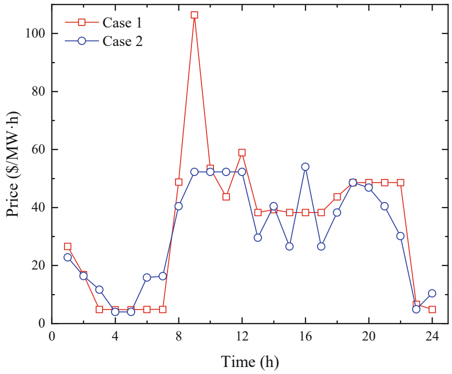

Fig. 2. Energy price in different cases.

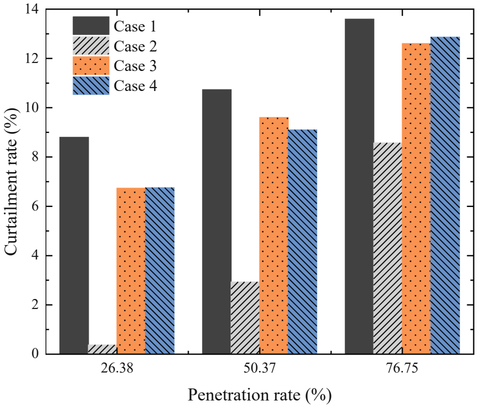

Fig. 3. Wind curtailment rate in different cases.

Table 1. Average price and price difference in different cases ($/MW h).

Case	Energy price	Price difference
1	34.18	101.63
2	30.72	50.05
3	33.45	92.81
4	33.31	98.58

Table 2 shows the energy price decomposition in Case 2 and 3 at pumping time 3 and generating time 9.

Combined with Table 2 and Sect. 3.3, Case 3 reduces the installed capacity, resulting in a significant increase in the upper capacity price. Meanwhile, it limits the ability of water-electricity conversion, which increases the cost of pumping and reduces the

Table 2. Energy price decomposition for pumped-storage in Cases 2 and 3 ($/MW h).

Hour	Case	Upper pumping capacity price	Lower pumping capacity price	Electricity-water conversion price	Energy price
3	2	0	7.68	3.98	11.66
	3	23.27	12.39	15.73	4.85
Hour	Case	Upper generating capacity price	Lower generating capacity price	Water-electricity conversion price	Energy price
9	2	0	0	52.30	52.30
	3	87.09	11.85	22.32	97.55

benefit of water consumption. The conversion between water and electricity is not the most economical, resulting in a widening of the price gap between the two times.

For Case 3 with limited installed capacity, its ability of water storage or consumption becomes weak, and the water cannot reach the upper and lower limits. Therefore, reservoir capacity resource is not scarce, reservoir capacity is not the main factor affecting the price. The corresponding shadow price is 0, and the water value remains unchanged. The changes of reservoir capacity value and water value in case 2 and Case 4 are shown in Fig. 4.

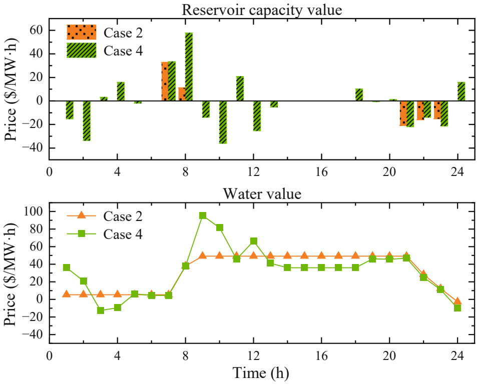

Fig. 4. Changes in reservoir capacity value and water value in Cases 2 and 4.

Case 4 with limited reservoir capacity, which limits the variation space of water. It is easier for water storage and consumption to reach the upper and lower limits, resulting in the actual converted water resources are in shortage, leading to the increase of price difference. From Fig. 4, it can be seen that in Case 4, the price of reservoir capacity fluctuates with a higher frequency and a larger amplitude, reflecting the scarcity of reservoir capacity resource. The corresponding water value also fluctuates under the superposition of additional capacity value.

Compared with Case 2, in Case 4, the ability of pumped-storage to absorb wind power and peak shaving and valley filling is weakened, and the the demand for pumping and power supply is increased, and uses the water value as a signal to guide pumped-storage for water conversion. For example, at pumping time 3 and 4 when wind power is high and load is low, water value is in the form of pumping cost and is negative, so as to stimulate pumped-storage to pump more water to absorb excess electricity. At generating time 9 and 10 when wind power is low and load is high, and the available water becomes scarce, the water value significantly increases and is in the form of water consumption benefit, so as to guide pumped-storage to invest more available water for supply.

4.2 Reserve Auxiliary Service Price Decomposition and Analysis

The changes in the value of residual reservoir resources in Case 2 and 4 are compared, as shown in Fig. 5.

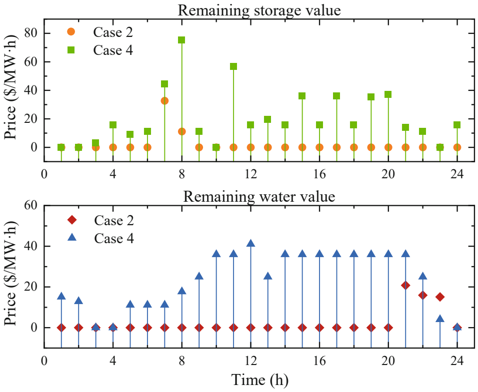

Fig. 5. Changes in the value of residual resources in Cases 2 and 4.

Figure 5 shows that there are insufficient residual resources available in Case 2 and Case 4. In Case 4, the reservoir capacity resources is the most short, and the value of residual resources fluctuates sharply and increases the most, reflecting the scarcity and guiding pumped-storage to provide more residual resources. However, in case 3, due to the limitation of installed capacity, On the contrary, the available reserved storage resources are relatively rich and not scarce, so the value of the residual resources is always zero.

When residual reservoir resources are scarce, reserve service and energy service will crowd out each other in the allocation of reservoir capacity resources. Similarly, the same phenomenon occurs when installed capacity resources are scarce, resulting in reserve price closer to energy price. This is evident in upward reserve service with higher demand. Table 3 shows the 24 h average reserve prices. Table 4 describes the relevance between price of reserve and energy through Euclidean distance (ED) and correlation coefficient (PCC). The shorter the ED, the higher the relevance, the closer the PCC is to

1 (−1), the stronger the positive (negative) correlation is, the closer it is to 0, the weaker the correlation is.

Table 3. Average reserve service price ($/MW h).

Case	Upward reserve price	Downward reserve price
2	6.16	4.68
3	28.63	11.85
4	26.84	10.47

Table 4. Relevance between upward reserve price and energy price.

Case	ED	PCC
2	156.93	−0.2819
3	74.99	0.8121
4	89.20	0.7055

Combined with the characteristics of each case and Tables 1 and 3, it can be seen that in Case 3 and Case 4, the resource crowding is serious, and the reserve price increases. Due to the larger demand, the price of upward reserve service is relatively close to energy price, as shown in Tables 3 and 4, while Case 2 shows that adequate resources will facilitate the division of energy service and reserve auxiliary service.

4.3 Influence of Wind Penetration Rate on the Value of Pumped-Storage Reservoir Resources

Tables 5 and 6 show various costs and average prices in Case 2 under different wind penetration rates.

Table 5. Costs in different wind power penetration ($).

Penetration rate (%)	Total cost	Fuel cost	Reserve cost
26.38	1901,705	1869,032	32,674
50.37	1505,956	1441,701	64,255
76.75	1179,581	1087,280	92,301

From Tables 5 and 6, the increase of wind penetration rate has both advantages and disadvantages. Although fuel cost is saved and energy price is reduced, the demand for

Table 6. Average prices in different wind power penetration rates ($/MW h).

Penetration rate (%)	Energy price	Upward reserve price	Downward reserve price
26.38	30.72	6.16	4.68
50.37	25.01	7.14	5.31
76.75	20.26	8.26	8.57

reserve service is increased, and other units in the system are gradually transformed into the reserve source, and the reserve cost and reserve price increase.

On the basis of Case 2, the installed capacity is further increased, and the value changes of various reservoir resources under different wind penetration rate from low to high are compared, as shown in Fig. 6.

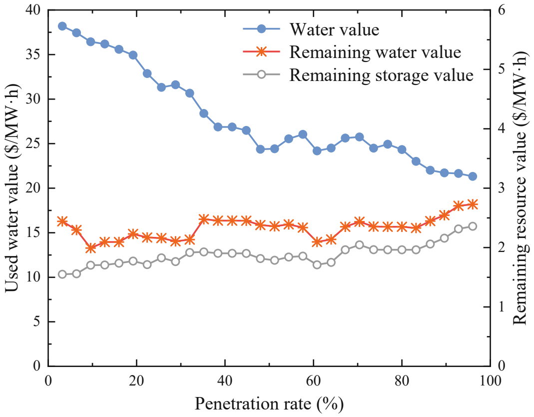

Fig. 6. Changes in the value of reservoir resource in different wind penetration rates.

Combined with the overall trend of the curve in Fig. 6, it can be seen that the increase of wind penetration rate reduces the cost or benefit of the water-electricity conversion in energy service, and its corresponding value decreases. As a result, the proportion of reserve service provided by pumped-storage gradually increases compared with energy service, while the value of remaining reservoir resources used to provide reserve service increases.

5 Conclusion

In this paper, considering the availability of remaining reservoir resources to the auxiliary service of pumped-storage, the day-ahead market clearing model of wind-thermal and pumped-storage complementary power generation system is established. The energy service price and reserve auxiliary service price of pumped-storage node are decomposed into shadow price components and water value components. From the perspective of power supply and load, this paper analyzes the influence of pumped-storage constraints on water value, deduces the relationship between water value and shadow price of reservoir capacity constraint in time, and analyzes the influence of reservoir capacity scarcity on water value and residual resource value. The variation characteristics of reservoir resource value at different times and the influence of residual resource scarcity on the price of reserve auxiliary service were analyzed with a variety of cases, and the influence of pumped-storage installed capacity, reservoir capacity and wind penetration rate on electricity price and its main components was analyzed.

References

1. Liu, D., Li, Q., Qin, L., et al.: Evaluation of grid accepting renewable energy in multi-time scale. Electr. Power Constr. **38**(07), 44–50 (2017)
2. Javed, M., Ma, T., Jurasz, J., et al.: Solar and wind power generation systems with pumped hydro storage: review and future perspectives. Renewa. Energy **148**, 176–192 (2020)
3. Chen, C.: Optimal wind-thermal generating unit commitment. IEEE Trans. Energy Convers. **23**(1), 273–6118 (2008)
4. Huang, D., Han, X., Lei, M., et al.: Bilevel optimal model of energy and spinning reserve in electricity market. Power Syst. Prot. Control **39**(21), 110–114 (2011)
5. Liu, S., Zhang, M., Xia, Q., et al.: The mechanism design of spot market based on the bidding of reserve requirement. Autom. Electr. Power Syst. **46**(22), 72–82 (2022)
6. Zhou, H., Hu, Y., Nie, Y., et al.: Co-optimization model of energy and reserve auxiliary service for regional interconnected power grid. Power Syst. Technol. **44**(03), 991–1001 (2020)
7. Ding, Q., Chang, L., Tu, M.: Key technologies of technical support system for electricity spot market. Autom. Electr. Power Syst. **42**(23), 7–14 (2018)
8. Fang, X., Yang, Z., Yu, J., et al.: Theoretical analysis and extension of locational marginal price. Proc. CSEE **40**(02), 379–390 (2020)
9. Yang, Z., Bose, A., Zhong, H., et al.: LMP revisited: a linear model for the loss-embedded LMP. IEEE Trans. Power Syst. **32**(5), 4080–4090 (2017)
10. Bai, L., Wang, J., Wang, C., et al.: Distribution locational marginal pricing for congestion management and voltage support. IEEE Trans. Power Syst. **33**(4), 4061–4073 (2018)
11. Conejo, A., Castillo, E., Minguez, R., et al.: Locational marginal price sensitivities. IEEE Trans. Power Syst. **20**(4), 2026–2033 (2005)
12. He, Y., Guo, J., Shen, J., et al.: Decentralized synergetic dispatch of interconnected power systems with risk-based locational marginal price. Power Syst. Technol. **41**(8), 2462–2468 (2017)
13. Anupam, A., Dae, C., Le, X.: Analysis of locational marginal prices in look-ahead economic dispatch. In: 2014 Power Systems Computation Conference (2014)
14. Shi, X., Zheng, Y., Xue, B., et al.: Effect analysis of unit operation constraints on locational marginal price of unit nodes. Power Syst. Technol. **43**(08), 2658–2665 (2019)
15. Juan, M., Antonio, J., Kai, L., et al.: Pricing electricity in pools with wind producers[J]. IEEE Trans. Power Syst. **27**(3), 1366–1376 (2012)
16. Wang, Y., Yang, Z., Yu, J., et al.: Analysis and extension of internal relationship between locational marginal price and dual multiplier. Autom. Electr. Power Syst. **45**(06), 82–91 (2021)

Coupling Model and Cooperative Optimization Operation of Multi-energy Complementary Integrated Energy System

Chen Yizhi[1,2,3], Tang Chenghong[1,2,3](✉), Yang Dongmei[1,2,3], Ye Wenjie[1,2,3], Xu Wenjun[4], and Meng Yuxiang[4]

[1] State Key Laboratory of Smart Grid Protection and Control, Nanjing 211106, China
tangchenghong@sgepri.sgcc.com.cn
[2] Nari Group Corporation (State Grid Electric Power Research Institute), Nanjing 211106, China
[3] NARI Technology Development Co., Ltd., Nanjing 211106, China
[4] Nanjing Normal University, Nanjing 210023, China

Abstract. Driven by the goal of "carbon peak and carbon neutrality", a comprehensive energy system that integrates multiple energy structures has emerged. How to realize multi-energy complementarity and collaborative optimization among different sources, effectively improve energy utilization efficiency and promote the consumption of renewable energy has become a research hotspot. In this paper, the architecture of the user-side multi-energy complementary integrated energy system is studied, and the coupling equipment and energy supply network are analyzed. A multi-time scale coupling model, including a static coupling model and dynamic coupling model, is established for the multi-energy conversion equipment, Furthermore, the multi-energy coupling integration model is described. Then, a multi-energy coupling collaborative optimization method was proposed, and the objective function and constraint conditions of the system optimization operation were established. Finally, based on the coupling model and optimization method proposed in this paper, a multi-energy complementary comprehensive energy management and control system is developed. The system has been piloted and applied in several typical comprehensive energy scenarios across the country. Through data analysis and practical application verification, energy efficiency and the economy can be effectively improved.

Keywords: Integrated energy system · Multi-energy coupling · Collaborative optimization · Economic operation

1 Introduction

Driven by the goal of "carbon peak and carbon neutrality", improving energy utilization efficiency and strengthening the comprehensive utilization of renewable energy has become the focus and research hotspot of the whole society. The integrated energy system (IES), especially near the user side, can realize the coupling and complementary and optimized operation of various energy sources, effectively improve energy utilization efficiency [1, 2] and promote the consumption of renewable energy [3, 4].

Y. Xue et al. (Eds.): PMF 2023, LNEE 1129, pp. 33–47, 2024.
https://doi.org/10.1007/978-981-99-9251-5_3

Realizing multi-energy complementarity and promoting the utilization of renewable energy is an important means to improve system energy efficiency and economy, as well as an important goal of comprehensive energy operation optimization [5–7]. Reference [8] studied the different control modes of producing hydrogen with electricity, and proposed the optimization model of the comprehensive energy system containing the hydrogen-producing units. Reference [9] designed the optimal scheduling method of the integrated energy system to find a low-cost and low-carbon operation scheme for the integrated energy system of office buildings. Reference [10] puts forward two operation modes of grid-connected wind-hydrogen interconnected coupled power generation system, and puts forward the operation strategy of isolated operation system. Reference [11] proposed an optimal scheduling model for hydrogen storage stations considering demand response. Reference [12] establishes an integrated energy system optimization scheduling model that takes into account the opportunity income of electric storage and the penalty cost of thermal storage. Reference [13] established a multi-agent cooperative operation model based on Nash negotiation theory, which can greatly improve the operation benefits of each agent and the overall benefits of the cooperative alliance. However, the current research is still focused on power systems or single coupling forms, and further research is needed in the aspects of multi-time scale coupling model and cooperative optimization operation considering multi-agent and multi-mode.

In this paper, the system architecture of user-side multi-energy complementary energy system is studied first, and the coupling equipment and energy supply network are analyzed. Furthermore, a multi-time scale coupling model, including static and dynamic coupling models, is established for the multi-energy conversion equipment, and the multi-energy coupling integration model is described. Then, a multi-energy coupling collaborative optimization method is proposed, which improves energy utilization efficiency and promotes the consumption of new energy. Finally, the software of the multi-energy complementary comprehensive energy management and control system is developed based on the model and optimization method in this paper. The system has been pilot-applied in several typical scenarios of comprehensive energy systems across the country. Through data analysis and practical application verification, energy efficiency and the economy can be effectively improved.

2 Multi-energy Complementary Integrated Energy System Architecture

As a new generation of energy system, the comprehensive energy system is an integrated energy system with deep integration and close interaction of source, network, and load network. The structure of the comprehensive energy system is shown in Fig. 1, which is generally composed of the following parts: energy supply network unit (such as power supply, gas supply, cooling, and heating supply network); Energy exchange units (such as combined cooling heating and power (CCHP) units, generating units, boilers, air conditioners, heat pumps, etc.), energy storage units (such as electricity, gas, heat and cold storage, etc.), terminal integrated energy supply units (such as microgrid) and end users. The power network transfers electricity from the power supply side to the load side; The thermal system is composed of heat source, heating network, heat recovery network, and heat load. High-temperature hot water transfers heat from the heat source to heat load through the heating pipe, transfers heat to the user through the radiator, turns into low-temperature hot water, and then flows back to the heat source through the heat recovery pipe. The natural gas system consists of a gas source, a gas supply pipeline, a compressor, and a load. A compressor driven by a gas turbine or a motor is used to increase the gas supply pressure to ensure the gas supply. Equipment such as combined heat and power (CHP) units, electric boilers, and gas-fired boilers can be converted between different energy sources according to demand.

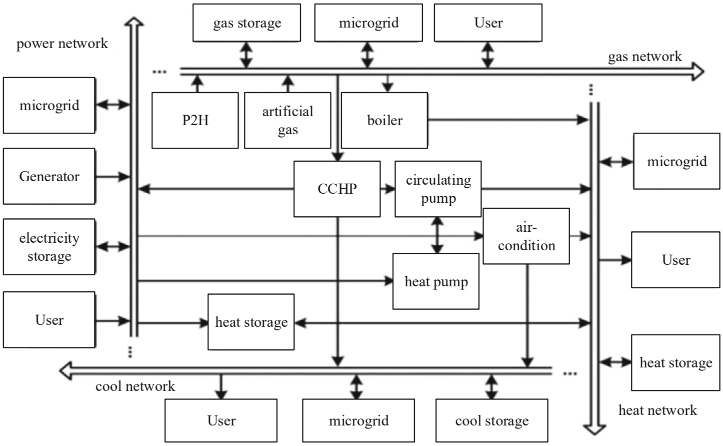

Fig. 1. Architecture of integrated energy system

Although the power supply network, heat supply network, and gas network are different in form, they all provide energy for users, which can be collectively referred to as the energy network. Therefore, the comprehensive energy system is essentially a multi-energy flow system. IES includes a variety of coupling devices, among which the main device for coupling conversion of power to heat (P2H) is the electric heat pump, which can convert electricity into heat with very high efficiency. It is a typical device for realizing electric heating conversion. The main device for power-to-cold coupling conversion (P2C) is the refrigerator. The main device for power-to-gas (P2G) is the electric hydrogen production unit. P2G is usually achieved by electrolyzing water to produce hydrogen, in which electrical energy is converted into hydrogen energy and heat energy. There are three main technologies for hydrogen production by electrolysis from water: alkaline electrolysis from water (ALK), proton exchange membrane electrolysis from water (PEM), and solid oxide electrolysis from water (SOEC). The cost of ALK is the most economical among the technical routes of electrolytic water hydrogen production. ALK and PEM technology, also known as low-temperature electrolysis, have been commercialized at present, and the efficiency of electricity to hydrogen can reach 60% ~ 70%. SOEC technology is expected to increase the efficiency of electric-hydrogen conversion to more than 85% under the condition of high temperature (600–800 °C), also known as high-temperature electrolysis, but the technology is not yet fully mature.

Through these coupling devices, the coupling transformation of electricity, heat, and gas energy networks in the integrated energy system is realized.

3 Multi-energy Conversion (P2X) Coupling Model

In the system architecture in Fig. 1, the model of the unit device can be referred to Ref. [14, 21]. Due to space limitations, this paper only introduces the electrothermal coupling model, electrocooling coupling model, and electrical coupling model in detail. The modeling of electric-heat transfer (cold) system mainly includes two aspects: the thermodynamic model and the electric power model to realize the interaction with the power system. The former establishes the quantitative relationship between the amount of electricity converted to heat (cold) and power (i.e. the energy efficiency ratio), while the latter focuses on the time-varying relationship between the amount of refrigeration (heat) and the power system, and the two jointly establish the internal relationship between temperature and power. In the electrolysis process, electric energy is converted into hydrogen energy and heat energy. The modeling of electric hydrogen production includes the electrochemical model and the relationship model between the voltage of the reaction process and the running state of the electrolytic cell.

3.1 Electrothermic Coupling (P2H) Model

Electrothermic coupling technology (including CCHP) has been applied in many fields because of its advantages of cleanliness and environmental protection.P2H mainly consists of electric heat pumps, which play an important role in utilizing low-grade waste heat resources and improving its grade. The electric heat pump uses the high-temperature heat source, to improve the heat energy from low-temperature to medium temperature, and it is often used for heating, domestic hot water, and industrial hot water; The electric heat pump can also use to produce high-temperature heat from the medium-temperature heat source, at the same time discharge some low-temperature heat to the low-temperature heat sink, used to prepare high-temperature hot water or steam.

The static coupling model of the electric heat pump can be expressed by the energy efficiency ratio coefficient, as shown in Eq. (1).

$$H_{\mathrm{HP\_M}}^{t} = C_{\mathrm{HP}} \cdot P_{\mathrm{HP}}^{t} \tag{1}$$

where, $H_{\mathrm{HP\_M}}^{t}$ is the heating power of the electric heat pump; P_{HP}^{t} is the electric heat pump power consumption; C_{HP} is the energy efficiency ratio of the electric heat pump.

During the system operation, the P2H equipment will run in different operating conditions, so the dynamic model of transformation under different operating conditions should be considered. The thermodynamic dynamic process of the electric heat pump is shown in Fig. 2, which is the fluctuation process of the electric heat pump in different periods.

The dynamic process of an electric heat pump can be represented by the equivalent thermodynamic parameter model in Fig. 3. The corresponding dynamic model is shown in Eq. (2–3).

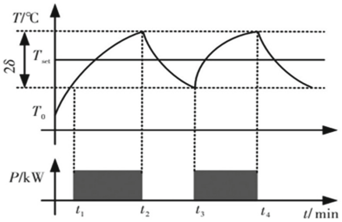

Fig. 2. Dynamic process of electric heat pump

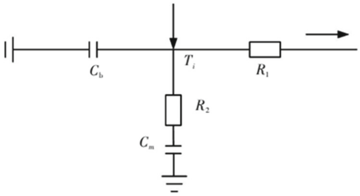

Fig. 3. Equivalent thermodynamic parameter model

$$T^{t+1} = T_a^{t+1} + s(t)QR - (T_a^{t+1} + s(t)QR - T^t)e^{-\frac{\Delta t}{RC}} \tag{2}$$

$$s(t) = \begin{cases} 1 & T^{t-1} \le T_{set} - \delta \\ 0 & T^{t-1} \ge T_{set} - \delta \\ s(t-1) & \text{others} \end{cases} \tag{3}$$

where, T^{t+1} is the output temperature, °C; C is equivalent thermoelectric capacity, J/°C; R is equivalent thermal resistance, °C/W; Q is equivalent heat ratio, W; Ta is the outdoor ambient temperature, °C; t is the simulation time; Δt is the simulation step size; $s(t)$ is the switching state of the electric heat pump at time t; Tset sets the working temperature of the electric heat pump; δ is the temperature control range.

3.2 Electrocooling Coupling (P2C) Model

P2C can convert electric energy into cold energy, mainly containing electric refrigeration and air conditioning. Electric refrigeration uses liquid refrigerant to absorb the heat load of the carrier coolant through evaporation and vaporization at low temperatures and low pressure, resulting in the cooling effect.

The static coupling model of electric refrigeration is shown in Eq. (4):

$$H_{RE,C}^t = C_{RE} \cdot P_{RE}^t \tag{4}$$

where, $H_{RE,C}^t$ is the refrigeration power of electric refrigeration; P_{RE}^t is the power consumed by electric refrigeration; C_{RE} is the energy efficiency ratio of electric refrigeration, which is generally 3;

The compressor is an important component of the electric refrigeration system, and its structural parameters directly affect the refrigeration capacity of the system. During the actual operation of the system, the compressor is not always in rated working conditions, so the dynamic model should consider the parameter changes of the compressor under unrated working conditions, and its dynamic equation is shown in Eq. (5):

$$\frac{dP_c^{out}}{dt} = \frac{R_g T_c^{in}}{V_c}(G_c^{in} - G_c^{out}) \tag{5}$$

where, V_c is the corresponding volume of the compressor cavity, m^3; G_c is air mass flow rate, kg/s; R_g is the gas constant of air, J/(kg K).

3.3 Electrical Coupling (P2G) Model

P2G is usually achieved by electrolysis of water to produce hydrogen, in which electrical energy is converted into hydrogen energy and heat energy. Through the analyse of the three main technologies for hydrogen production by electrolysis from water (ALK, PEM, and SOEC). Both ALK and PEM technologies can accept fluctuating power supply. The PEM is more flexible, It can accept load variation range from 0 to 100% of rated power (some devices even allow short-term operation at 160% of rated power), climb rate is 100%/ s, hot start time is only 1 s, and cold start time is 5 min. It's an ideal resource for flexibility.

The static coupling model of electric hydrogen production can be expressed as Eq. (6–8):

$$P_{ec} = \eta_{ec} P_{ec,in} = U_{ec}(i_{ec}, T_{ec}) \cdot i_{ec} = P_{ec,out} + Q_{ec} \tag{6}$$

$$Q_{ec} = [U_{ec}(i_{ec}, T_{ec}) - U_{tn}(T_{ec})] \cdot i_{ec} = \eta_h P_{ec} \tag{7}$$

$$P_{ec,out} = U_{tn}(T_{ec}) \cdot i_{ec} = \eta_{h2} P_{ec} \tag{8}$$

where, $P_{ec,out}$ is hydrogen production power, Q_{ec} is heat production power, P_{ec} is the actual input power, $P_{ec,in}$ is input AC power, η_{ec} is AC/DC conversion efficiency, and i_{ec} is current. T_{ec} is the temperature of the electrolytic cell; U_{ec} (i_{ec}, T_{ec}) is a function of electrolytic cell voltage, and its value varies with the changes of i_{ec} and T_{ec}. $U_{tn}(T_{ec})$ is a thermoneutral voltage function, and its value varies with T_{ec}; η_{h2} for electrolytic cell hydrogen production efficiency; η_h is the heat production efficiency of the electrolytic cell.

Both ALK and PEM technologies can accept fluctuating power supply, among which PEM has better flexible performance. Based on the electrochemical theory, when the equipment parameters and the external environment are set, the hydrogen and heat output of the electrolytic cell during operation depends on its input power and temperature. The hydrogen and heat output of the electrolytic cell can be adjusted by controlling these two variables. The relationship between hydrogen production power and heat production power, input power, and temperature of the electrolyzer is linearized, and its dynamic output is shown in Eq. (9):

$$\begin{cases} P_{ec,out,t} = \mu_1 P_{ec,in,t} + \nu_1 \delta_{ec,t} T_{ec,t} \\ Q_{ec} = \mu_2 P_{ec,in,t} + \nu_2 T_{ec,t} \end{cases} \tag{9}$$

where, μ_1, μ_2, ν_1 and ν_2 are the coefficients after linearization of the operation region of the thermo-hydrogen co-production in the electrolytic cell; $\delta_{ec,t}$ is the 0–1 state variable representing the running state of the electrolytic cell at time t.

Where, $P_{ec,out,t}$ is the hydrogen production power at time t, Q_{ec} is the heat production power, μ_1, μ_2, ν_1, ν_2 are the coefficients after linearization of the thermo-hydrogen co-production operation area of the electrolytic cell. $\delta_{ec,t}$ is the 0–1 state variable representing the running state of the electrolytic cell at time t.

3.4 Multi-Energy Coupling Integration Model

The multi-energy coupling integration model can be regarded as a generalized multi-port network node in the comprehensive energy system. By connecting with different energy networks, it can play the roles of converting, regulating, supplementing, relieving, and storing different energies. The input port is connected to the energy network and is responsible for energy exchange with the energy network (the input energy exchange includes positive energy and negative energy); The output ports supply the energy required by various loads (when there is a distributed power supply access, it can be considered to output negative energy to it). For a comprehensive energy system containing multiple energy conversion devices and various forms of energy, the coupling relationship between input and output can be described by matrix C, as shown in Eq. (10):

$$\underbrace{\begin{bmatrix} L_e \\ L_h \\ L_0 \end{bmatrix}}_{L} = \underbrace{\begin{bmatrix} C_{ee} & C_{ge} & C_{0e} \\ C_{eh} & C_{gh} & C_{0h} \\ C_{e0} & C_{g0} & C_{00} \end{bmatrix}}_{C} \underbrace{\begin{bmatrix} P_e \\ P_g \\ P_0 \end{bmatrix}}_{P} \tag{10}$$

where, matrix P is the input of each energy, matrix L is the output of each energy, and matrix C is the coupling coefficient between the input and output of each energy.

4 Multi-energy Cooperative Optimization Method for Integrated Energy System

With the development of P2X coupling technology, the coupling between electric power networks and various industries is deepening. Different energy sub-networks no longer operate alone, but realize the coupling interaction between different energy sub-networks through P2X equipment. Based on the P2X coupling model introduced in the previous section, the cooperative optimal scheduling operation of the integrated energy system can be realized by establishing the objective function and constraint conditions of the system operation.

4.1 Objective Function

In this paper, a day is divided into 24 periods, and an optimization objective function of the operation cycle of the multi-energy coupled equipment system is established. In order to realize the low-carbon economic operation of the comprehensive energy system, the optimization objective mainly includes the optimal objective function of the total operation energy efficiency and total operation cost considering the multi-energy coupling.

4.1.1 Optimal Function of Total Operational Energy Efficiency

When energy efficiency is considered, the objective function is the ratio of input power and output power of energy. Energy coefficients of different values are used to describe different energy sources, and then quantitative and qualitative energy losses in the production and conversion process are quantified to obtain energy utilization efficiency. The objective function is shown in Eq. (11).

$$\max \eta_{\text{ex}} = \frac{\sum\limits_{i \in \Omega_{\text{out}}} E_{\text{out},i}\lambda_i}{\sum\limits_{i \in \Omega_{\text{in}}} E_{\text{in},i}\lambda_i} = \frac{\sum\limits_{t} (P_{\text{el}}(t)\lambda_{\text{e}} + P_{\text{hl}}(t)\lambda_{\text{h}} + P_{\text{gl}}(t)\lambda_{\text{g}})}{\sum\limits_{t} (P_{\text{in,e}}(t)\lambda_{\text{e}} + P_{\text{in,g}}(t)\lambda_{\text{g}} + P_{\text{in,pw}}(t)\lambda_{\text{pw}})} \tag{11}$$

where, $E_{\text{in},i}$, $E_{\text{out},i}$ represents the input power and output power of the I-th energy; $P_{\text{el}}(t)$, $P_{\text{gl}}(t)$, $P_{\text{hl}}(t)$ represents the load power of electrical, gas, and heat at the time period t; $P_{\text{in,e}}(t)$, $P_{\text{in,g}}(t)$, $P_{\text{in,pw}}(t)$ represents the input power of electrical, gas, solar/wind in time period t; λ_{e}, λ_{g}, λ_{h}, λ_{pw} respectively represent mass coefficients of electrical, gas, heat, and solar/wind energy.

4.1.2 Optimal Function of Total Operating Cost

Considering the multi-energy coupling equipment, the total operation cost includes the operation cost of the traditional generator set, electric-heat-cold-gas coupling equipment, and the output cost of the natural gas source. The objective function is shown in Eq. (12):

$$\min \sum_{i \in T} \left[\sum_{i \in N_e^c} \left(a_i + b_i P_i^G(t) + c_i P_i^{G2}(t) \right) + \sum_{i \in N_g} \left(\beta_{i,t} Q_i^{ws}(t) \right) \right. \\ \left. + \sum_{i \in N_e^{CHP}} \varepsilon_{CHP} \left(\gamma_P P_i^{CHP}(t) + \gamma_H \Phi_i^{CHP}(t) \right) \right] \tag{12}$$

where, $\left(a_i + b_i P_i^G(t) + c_i P_i^{G2}(t)\right)$ is the operating cost of the generator, it is the equation for the quadratic function. To build a linear model, the equation is linearized by the piecewise linearization method; $\beta_{i,t} Q_i^{ws}(t)$ is the cost of natural gas source output; $\varepsilon_{CHP}\left(\gamma_P P_i^{CHP}(t) + \gamma_H \Phi_i^{CHP}(t)\right)$ is the operating cost of the CHP unit; Among them, a_i, b_i and c_i are the cost coefficients of the generator respectively; $P_i^G(t)$ is the active power output of the generator i at time t; β is the cost coefficient of natural gas, $Q_i^{ws}(t)$ is the output value of natural gas source at time t; ε_{CHP} is the fuel cost coefficient of CHP unit. $P_i^{CHP}(t)$, $\Phi_i^{CHP}(t)$ respectively represents the electrical power and thermal power emitted by CHP unit i at time t. γ_P, γ_H respectively CHP machine power consumes fuel of setting a unit electric power and thermal.

4.2 Constraint Condition

In order to ensure the safe and normal operation of the integrated energy system, it is necessary to set reasonable operation constraints. The operation constraints considered mainly include network constraints and equipment constraints. Network constraints mainly include energy constraints, Equipment constraints including the power constraints of upper and lower limits, and climbing power constraints, during the operation of the various equipment, such as unit equipment, energy storage equipment, coupling equipment, and other equipment.

4.2.1 Network Constraint

The network constraints in this paper mainly consider the constraints of energy supply and demand balance, including power system constraints, natural gas system constraints, and thermal system constraints. Network constraints are uniformly converted to power balance constraints, as shown in Eq. (13):

$$\begin{cases} P_{\mathrm{EL}}(t) + P_{\mathrm{HP}}(t) + P_{\mathrm{HTHP}}(t) = P_{\mathrm{GT}}(t) + P_{\mathrm{ES}}(t) + P_{\mathrm{wv}}(t) + P_{\mathrm{EX}}(t) \\ P_{\mathrm{SL}}(t) = H_{\mathrm{GT,S}}(t) + H_{\mathrm{HTHP,out}}(t) \\ P_{\mathrm{HL}}(t) + H_{\mathrm{HTHP,heated}}(t) = H_{\mathrm{HP,H}}(t) + H_{\mathrm{M}}(t) \end{cases} \tag{13}$$

where, $P_{\mathrm{EL}}(t)$, $P_{\mathrm{SL}}(t)$ and $P_{\mathrm{HL}}(t)$ are the electric load, steam gas load, and hot load of time t respectively; $P_{\mathrm{wv}}(t)$, $P_{\mathrm{ES}}(t)$ and $P_{\mathrm{EX}}(t)$ are the wind power generation power, battery power, and the interaction power between the system and the main network at the time t respectively. $P_{\mathrm{HP}}(t)$, $H_{\mathrm{HP,H}}(t)$ is the electric energy consumed by the electric heat pump and its heating power during the time t respectively. $H_{\mathrm{GT,S}}(t)$ is the steam thermal power output by the gas turbine during the period t.

4.2.2 Equipment Constraints

Equipment constraints include that all kinds of equipment, such as unit equipment, energy storage equipment, and coupling equipment, must meet the upper and lower limits of power constraints and climbing power constraints during operation, as shown in Eq. (14).

$$\begin{cases} P_j^{\min} \le P_j(t) \le P_j^{\max} \\ -D_j^{\mathrm{down}} \Delta t \le P_j(t) - P_j(t-1) \le D_j^{\mathrm{up}} \Delta t \end{cases} \tag{14}$$

where, $P_j^{\min}$ and $P_j^{\max}$ are the upper and lower limits of the output power of device j respectively; D_j^{down} and D_j^{up} are the upper and lower limits of the climbing power of device j respectively.

5 Multi-energy Complementary Integrated Energy System and Application

5.1 Architecture Diagram of Multi-energy Complementary Comprehensive Energy Management and Control System

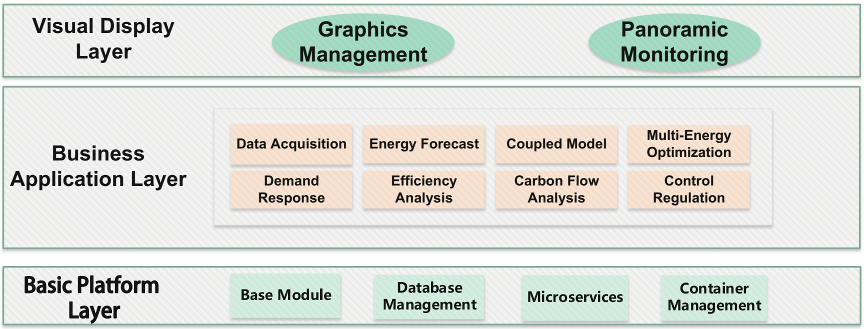

Fig. 4. Software architecture of multi-energy complementary integrated energy management and control system

The software package is developed based on the model and optimization method in this paper. The system software architecture is shown in Fig. 4, which adopts C/S architecture and follows the design idea of micro-service architecture. The multi-energy complementary integrated energy system architecture includes the basic platform layer, business application layer, and visual display layer.

(1) Basic platform layer: Based on the microservice software architecture mode, it supports the whole life cycle management from development to deployment, operation, and maintenance, which can be divided into basic modules, database management modules, microservice modules, container management modules, etc.
(2) Business application layer: Provide users with various business functions and applications through the user interface, including data acquisition module, energy forecast module, coupled model module, multi-energy optimization module, demand response module, energy efficiency analysis module, carbon flow analysis module, control regulation module, etc.
(3) Visual display layer: provide the interaction window between the system and users through visual means such as Web interface; Including graphics management module, panorama monitoring module, and so on.

5.2 Typical Scenario Application

The multi-energy and complementary integrated energy management and control system has been piloted in several integrated energy demonstration zones across the country. Including user-side scenes such as commercial CBD, schools, hospitals, industrial parks, etc., and area scenes such as urban energy Internet scenes, covering a variety of different primary and secondary energy types such as electricity, heat, and natural gas, to meet the different applications needs of heating in the north and green electricity consumption in the south. Through the energy efficiency analysis module of the system and the analysis of economic benefits, the energy efficiency and economy of typical scenarios have been significantly improved.

5.3 Scenario Application Example

In order to further verify the advantages of the proposed model and the collaborative control method, a case study was carried out in the integrated energy system scenario of a multi-energy coupled and complementary industrial park represented by the textile industry. The main energy requirements are electricity, hot water, and steam, and the system includes CCHP units, photovoltaics, wind power, an upper power grid, storage batteries, electric heat pumps, and high-temperature steam heat pumps. The high-temperature steam heat pump consumes electric energy to produce steam. Table 1 lists the unit parameters.

Table 1. Unit parameter

Name	Gas turbine	Electrical heat pump	Steam heat pump	Wind power	Solar power	Main network	Rechargeable battery	Heat storage tank
Power/Capacity (kW/kWh)	800	100	30	400	300	200	300 (kWh)	100 (kWh)
Efficiency	0.35	3	4	–	–	–	0.001	0.002
Operation and maintenance unit price/(yuan /kWh)	0.053	0.026	0.024	0.029	0.025	–	0.051	0.049

The average power supply efficiency of the power plant in the main power network interacting with the industrial park is 0.35, and the average power transmission efficiency is 0.9. Unit wind abandonment penalty cost is 0.03 yuan/kWh; The price and low calorific value of natural gas are 2.54 yuan/m^3 and 9.7 kWh/m^3 respectively. Combined with the annual power generation data of the system, 22:00–24:00, 0:00–7:00 are selected as the valley period, 7:00–16:00 as the normal period, and 16:00–22:00 as the peak period. The model and method in this paper are adopted, and 1h is divided into the optimized sub-time segment, aiming at the maximum consumption of wind power and photovoltaic output, as well as the optimal energy saving and economy. The coupling conversion effect of high-temperature steam heat pumps on different grades of energy is fully considered. During the valley electricity price period, the high-temperature steam heat pump is full, and the wind power is absorbed to convert hot water into steam, which increases the hot water load during the period, improves the heat production of the high-temperature steam heat pump, realizes the efficient electrothermal coupling conversion, and improves the energy utilization efficiency of the system. From 7:00 to 9:00, there is wind abandonment in the system, and high-temperature steam heat pump is invoked to supply energy to absorb excess wind power. Due to its own energy loss, the hot water storage tank first releases water from 22:00 to 24:00, heats and stores hot water through an electric heat pump during the normal period of electricity price, and releases heat during the peak period of electricity price. The optimization results of power, steam, and hot water are shown in Fig. 5a–c respectively:

The model and method in this paper are adopted to calculate and analyze the indicators of the system before and after optimization, as shown in Table 2:

Through the calculation example, after the optimization model and method are adopted, the heat supply of the electric heat pump is increased by increasing the hot water load to improve the load rate, and the load rate is increased by 9.71%. The thermal power optimization of the high-temperature steam heat pump is carried out, decoupling the operation constraint of the CCHP unit, promoting the wind power consumption in the system, and avoiding the wind abandonment penalty. The energy efficiency is increased by 16.25%, which verifies the effectiveness of the model and method in this paper.

6 Conclusion

This paper focuses on improving the energy utilization efficiency of IES, and realizing coupling complementarity and cooperative optimization among various energy sources, Based on the analysis of coupling equipment and energy supply network, the multi-time scale coupling model of the multi-energy conversion equipment is established, including static model, dynamic coupling model and multi-energy flow unified model. Furthermore, the multi-energy coupling collaborative optimization method was proposed, and the objective function and constraint conditions of the system optimization operation were established. Finally, the software of the multi-energy complementary comprehensive energy management and control system is developed. The system has been piloted and applied in several typical comprehensive energy scenarios across the country. Through data analysis and practical application verification, energy efficiency and economy can be effectively improved. With the continuous deepening of energy reform, the multi-energy complementary comprehensive energy management and control system developed in this paper will continue to be promoted and applied in comprehensive energy projects, constantly expand the typical application scenarios of the system, continue to carry out algorithm optimization and engineering experience accumulation, to further improve the optimization and scheduling ability of the multi-energy complementary comprehensive energy system.

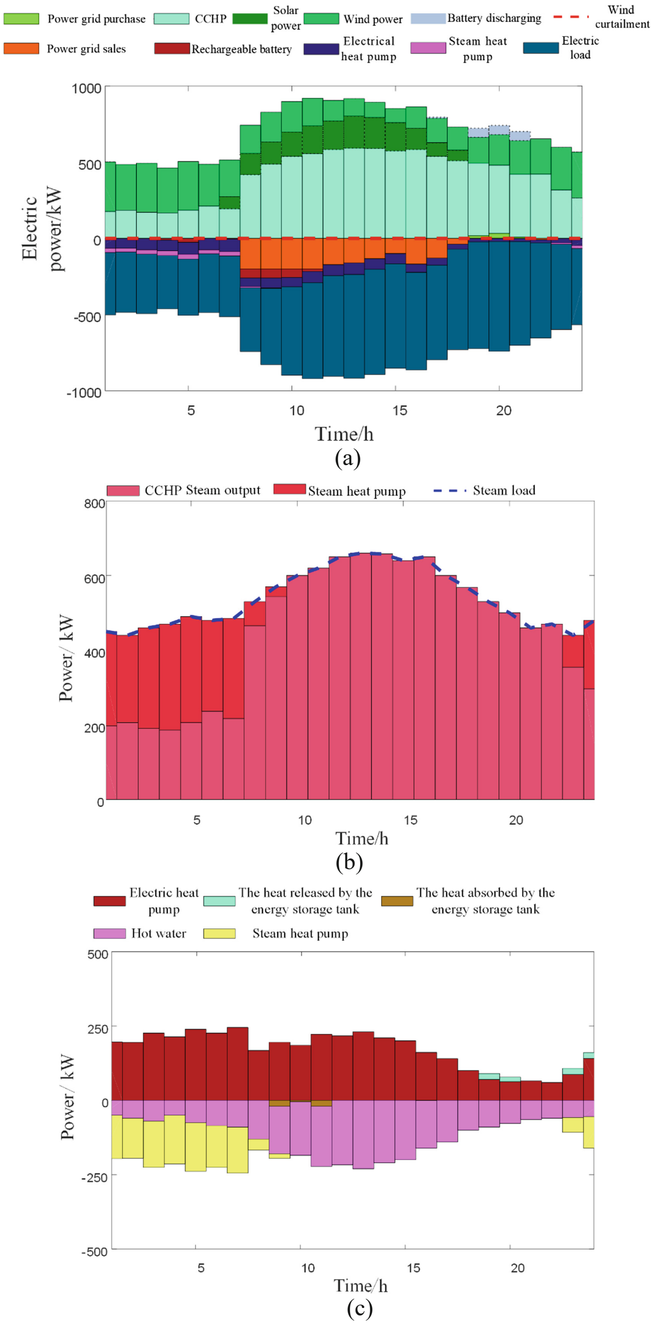

Fig. 5. **a** Results of power optimization scheduling. **b** Results of steam optimization scheduling. **c** Results of hot water optimal scheduling

Table 2 Comparison of indicators before and after optimization

Optimal scheduling	Before optimization	Post-optimization	Compare
Curtailment penalty cost/yuan	27.5	0	
Total cost/yuan	8953.3	7760.3	−13.3%
Load rate (%)	68.29	78.00	+9.71
Energy efficiency (%)	83.59	99.84	+16.25

Acknowledgment. This research is supported by Key Research and Development Program of Jiangsu Province (BE2020081).

References

1. Ding, T., Mu, C., Bie, Z., et al.: Review of energy Internet and its operation. Proc. CSEE **38**(15), 4318–4328 (2018)
2. Cheng, H., Hu, X., Wang, L., et al.: Review on research of regional integrated energy system planning. Autom. Electr. Power Syst. **43**(7), 2–13 (2019)
3. Tang, C., Wang, J., Zeng, B., et al.: Optimal dispatch for integrated energy considering energy grade conversion in industrial park with steam heat pumps. Autom. Electr. Power Syst. **47**(2), 191–199 (2023)
4. Yang, J., Zhang, N., Wang, Y., et al.: Multi-energy system towards renewable energy accommodation: review and prospect. Autom. Electr. Power Syst. **42**(4), 11–24 (2018)
5. Yao, G., Li, L., Zhou, L., et al.: A review on integrated household energy utilization in urban residential areas. Modern Electric Power **37**(2), 152–162 (2020)
6. Geng, J., Yang, D., Gao, Z., et al.: Optimal operation of distributed integrated energy microgrid with CCHP considering energy storage. Electr. Power Eng. Technol. **40**(1), 25–32 (2021)
7. Ding, Y., Chen, H., Wu, J., et al.: Multi-objective optimal dispatch of electricity-gas-heat integrated energy system considering comprehensive energy efficiency. Autom. Electr. Power Syst. **45**(2), 64–73 (2021)
8. Guo, M., Yan, Z., Zhou, Y., Zhang, P., et al.: Optimized operation design of integrated energy system with wind power hydrogen production. Electr. Power **53**(01), 115–123+161 (2020)
9. Dong, F., Zhang, Y., Shang, M.: Multi-criteria comprehensive evaluation of distributed energy system. Proc. CSEE **36**(12, :3214–3223 (2016)
10. Bernalagustin, J., Dufolopez, R.: Hourly energy management for grid-connected wind hydrogen systems. Int. J. Hydrogen Energy **33**(22), 6401–6413 (2008)
11. Khani, H., El-Taweel, N.A., Farag, H.E.: Supervisory scheduling of storage-based hydrogen fueling stations for transportation sector and distributed operating reserve in electricity markets. IEEE Trans. Ind. Inf. **16**(3), 1529–1538 (2019)
12. Yong, J., Zhao, J., Huan, J., et al.: Multi-energy system optimal dispatch based on chaos enhanced firework algorithm in grid connection. Power Syst. Technol. **43**(10), 3725–3732 (2019)
13. Ma, T., Pei, W., Xiao, H., et al.: Cooperative operation method for wind-solar-hydrogen multi-agent energy system based on Nash bargaining theory. Proc. CSEE, pp. 1–24 [2020-09-27]. https://doi.org/10.13334/j.0258-8013.pcsee.200956

14. Cui, Y., Jiang, T., Zhong, W., et al.: Source-load coordination economic dispatch method for regional integrated energy system considering wind power accommodation. Power Syst. Technol. **44**(7), 2474–2483 (2020)
15. Jin, H., Sui, J., Xu, C., et al.: Research on theory and method of multi-energy complementary distributed CCHP system. Proc. CSEE **36**(12), 3150–3161 (2016)
16. Shaoqing, W.E.I., Jiangping, H.A.O., Hemin, H.U., et al.: Thermal energy cascade utilization technology of coordinated waste heat and regenerative systems. Therm. Power Gen. **47**(6), 111–115 (2018)
17. Xu, H., Dong, S., He, Z., et al.: Multi-energy cooperative optimization of integrated energy system in plant considering stepped utilization of energy. Autom. Electr. Power Syst. **42**(14), 123–130 (2018)
18. Huang, W., Wang, X., Tai, N., et al.: Energy coupling conversion model and cascade utilization method for microgrid with heat and power system. Proc. CSEE **40**(21), 6804–6815 (2020)
19. Diao, H., Li, P., Wang, J., et al.: Optimal dispatch of integrated energy system considering complementary coordination of electric/thermal energy storage. Trans. China Electrotech. Soc. **35**(21), 4532–4543 (2020)
20. Wang, C., Liu, H., Gong, J., et al.: Joint scheduling of different energy storage for improving wind power accommodation ability in integrated community energy system. Electr. Power Constr. **39**(4), 35–44 (2018)
21. Xue, Y., Guo, Q., Sun, H., et al.: Comprehensive energy utilization rate for park-level integrated energy system. Electr. Power Autom. Equip. **37**(6), 117–123 (2017)

Research on the Architecture and Key Technologies of Remote Online Protection Testing System in Smart Substation

Yi Tang[1], Zhe Yu[2], Hang Lv[2], Jun Du[2], and Zhiguo Wang[2](✉)

[1] Shandong Electric Power Dispatching and Control Center, Jinan 250001, China
[2] NR Electric Co. Ltd., Nanjing 211102, China
`wangzg@nrec.com`

Abstract. In recent years, the technology in smart substation has been rapidly developed in China, and core technical advantages such as digitalization and standardization of information sharing in smart substation have been further demonstrated. However, the advantages of smart stations such as logical isolation and process layer data sharing are not fully utilized in the maintenance of protection device in smart substation. At present, isolator link mechanism is still widely used in the maintenance of protection device in smart substation, and plugging and unplugging of equipment fibers are often required during the testing process, which brings potential risks to the safe operation of the protection equipment. In order to solve these problems, this paper proposes a technical solution of remote online relay protection testing system architecture by deeply exploring the digital advantages of smart substations. Firstly, the virtual circuit logical isolation technology for relay protection devices based on IEC61850 ED2 is discussed in detail. Secondly, it focuses on the design and functional application of the smart substation remote online testing APP; Based on the current technical situation, the feasibility of realizing network remote secure access from the dispatching center to the smart substation side and the entire test data flow are emphatically analyzed. Combined with the pilot project, the remote online relay protection testing system is preliminarily verified. The results show that remote online testing of relay protection can effectively improve the efficiency of operation and maintenance of relay protection in smart substations.

Keywords: Smart substation · Online testing system · Logical isolation of virtual circuit · IEC61850

1 Introduction

In recent years, with the extensive application of smart substations, the technology of smart substations has developed rapidly. The core technical advantages of smart substation, such as digitalization of the whole substation information, networking of communication platforms, standardization of information sharing, and intelligence of high-voltage equipment, are further highlighted [1–4]. However, for a long time, the maintenance of

Y. Xue et al. (Eds.): PMF 2023, LNEE 1129, pp. 48–60, 2024.
https://doi.org/10.1007/978-981-99-9251-5_4

the protection device in smart substation still uses isolator link mechanism. Although this mechanism ensures that the maintained device does not affect the normal operation of other device,, multiple devices' optical fibers need to be plugged and unplugged during the testing, and repeated plugging and unplugging of optical fibers will bring potential risks to the safe operation of the protection device [5]. It can be seen that the maintenance of smart substations has not fully utilized the outstanding advantages of the logical isolation realization through protection device software and data sharing in process layer.

Different from IEC61850 ED1, IEC61850 ED2 has made more detailed and complete adjustments to the definition and application of GOOSE. This provides strong technical support for making full use of the advantage of data sharing in the whole smart substation, achieving online testing, and even remote online testing of remote smart substations. The advantages of information opening and data sharing in smart substations are also being widely used by engineers. Through the relay protection online monitoring and detection of smart substation, the realization of operation and maintenance without power outage has gradually become a new technology research hotspot [6, 7]. Literature [8] designed an non-invasive automatic testing system to solve the problems of low testing efficiency and insufficient safety of the secondary circuit in smart substation. The test of the secondary circuit of the protection device can be completed not changing the device configuration and physical link in the substation, which significantly improved the efficiency of engineering test. Literature [9] proposes a solution for automatic acceptance of substation monitoring information that is oriented to dispatcher control and meets the requirements of full circuit acceptance, which breaks through the technical bottleneck of automatic acceptance of interactive information between master and substations and greatly improves the efficiency of acceptance testing. Literature [10] has effectively solved a series of problems in the actual operation and maintenance of secondary equipment of smart substation by configuring online monitoring and intelligent diagnosis device of secondary equipment in the substation, and status monitoring and remote operation and maintenance system of secondary equipment in the control center. The above research has improved the operation and maintenance efficiency of smart substation to a certain extent, but there is still a certain distance from online testing. Literature [11, 12] proposes to establish a remote test engineer station, allow test experts to access software to control substation test computer through high-level security network, establish a more convenient test channel through the network, and solve the remote test problem under the two states of relay protection undesired operating and incorrect operating. However, remote access based on the public network can not guarantee the data security.

Based on the IEC61850 ED2 technical standard, this paper proposes a solution for the relay protection remote testing system architecture by deeply exploring the digital advantages of current smart substations in China. Under the premise of following relevant standards, the scheme is established based on the existing information interaction system between the dispatching side and the intelligent substation. Firstly, based on the IEC61850 ED2 technical standard, the safety and controllability of the logic link used by the protection device maintenance in smart substations and the logical isolation of virtual circuit between protection devices are realized, which ensures the safety and feasibility of the scheme in the technical level. Secondly, using the proprietary communication network from the dispatching side or centralized control substation to the substation, the secure data interaction between the dispatching side or centralized control substation and the testing APP of the substation can be achieved by expanding the IEC104/IEC101 protocol. Finally, a fully controlled testing APP is deployed in the smart substation monitoring and control system based on the container technology to achieve automatic control over the start and stop of online testing terminals. Based on this scheme, a remote online testing system for relay protection has been established in a 220 kV smart substation in Shandong Province, and the feasibility and convenience of the system have been preliminarily verified.

2 Simulation Mechanism and Isolation Technology by Software

The biggest change of the GOOSE message parameter definition in the IEC61850 ED2 compared to the ED1 is the addition of the "Simulation" parameter. The "Simulation" parameter is used to identify whether the GOOSE message is sent by a simulation device or by an actual operating device. The Simulation reception processing mechanism of the "Simulation" parameter refers to the processing behavior of the GOOSE receiving element when the "Simulation" parameter of the GOOSE message received by the IED is TRUE. This technology provides necessary technical support for smart substations to truly achieve online testing of relay protection without plugging in and unplugging the optical fiber of the tested equipment.

2.1 Simulation Mechanism

The data object "Sim" of the logical node "LPHD" of the IED is used to determine whether the IED receives a normal subscription message or simulation message. When the value of the "Sim.stVal" parameter is FALSE, the IED receives a normal subscription message. When the value of the "Sim.stVal" is TRUE, the IED receives a test message simulating the subscription message.

After adopting the new maintenance mechanism, the operating equipment sends a GOOSE/SV message with the simulation quality of FALSE to the IED, and the test equipment sends a GOOSE/SV message with the simulation quality of TRUE to the IED. When the IED is in the operating state, that is, the value of "Sim.stVal" is FALSE, then the IED only receives the normal subscription message. When the IED device is in the testing state, that is, the value of "Sim.stVal" is TRUE, then the IED only receives test messages of analog quality. To reflect the message receiving status, the parameters "LGOS" and "LSVS" are set to respectively reflect the receiving status of GOOSE and SV messages. When the value of "LGOS.St" is TRUE, it indicates that the subscription message is in the receiving status. When the value of "LGOS.St" is FALSE, it indicates that the subscription message has not been received or is not in the receiving status. When the value of "LGOS.SimSt" is TRUE, it indicates that the subscription message with the simulation quality of TRUE is processed. When the value of "LGOS.SimSt" is FALSE, it indicates that the subscription message with the simulation quality of FALSE is processed. The processing of the Simulation message by the GOOSE receiving element needs to be judged based on the status of the “LPHD.Sim”. The processing logic is shown in Fig. 1.

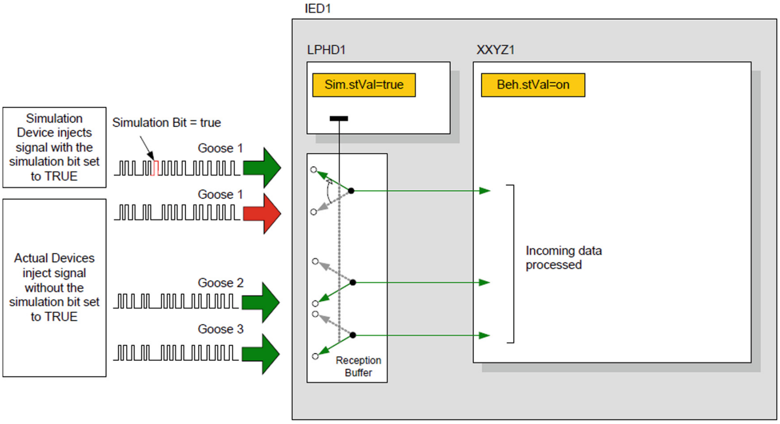

Fig. 1. The processing mechanism of GOOSE simulation message

2.2 Logical Isolation Technology of Virtual Circuit

In order to ensure that the message from maintenance equipment does not affect the operating equipment, the protection device must achieve reliable logical isolation of virtual circuit to ensure the safety of online testing. Hence, the existing TEST maintenance mechanism and the GOOSE receiving logic link of related protection equipment can be used in smart substation.

The existing maintenance mechanism of smart substations is as follow: the maintained protection equipment and acquisition execution unit need to connect the isolator link of the maintenance, and the maintenance quality of the GOOSE/SV message sent by these devices is TRUE. All devices that subscribe to these device messages obtain their maintenance status based on the maintenance quality of the message, and process the message according to the consistency rules by comparing with their own maintenance status. If the maintenance quality of the two devices is consistent, effective treatment shall be taken, and if not, invalid treatment shall be taken. In order to achieve remote online testing, the logic link of the maintenance of the protection device can be controlled remotely.

According to the requirements of online testing, it is necessary to enable and disable the GOOSE receiving logic link related to maintained equipment protection. If the line protection is in maintenance state, it is necessary to disable the logic link used to initiate breaker failure protection of the corresponding bay of the bus bar protection. When the GOOSE receiving logic link is disabled, the protection device no longer processes the GOOSE message, but automatically sets a fixed value based on the logic of the received signal. For example, the device resets the breaker failure initiation signal and breaker failure inter-tripping signal to prevent the protection device from under side operating. The GOOSE sending logic link, SV and GOOSE receiving logic link of the tested protection device are always enabled. Before the test, the protection device is put into "Simulation" mode, that is, the value of "Sim.stVal" in LPHD is set to TRUE, and the test terminal sends simulation SV and GOOSE message with the Simulation quality of TRUE. At this time, the tested protection device accepts the simulation message sent by the test terminal.

The reliability of virtual circuit logic isolation technology is related to the simulation and test status of the tested protection device, the test status of the station-layer message between the protection device and the protection tester, and the bay receiving link of the protection device, etc. Before the test is performed, the isolation effectiveness can be evaluated by the following methods:

$$\mathrm{M} = \left(\mathrm{M_r}\&\overline{\mathrm{S}}\&\overline{\mathrm{T} \oplus \mathrm{T_r}} + \mathrm{M_t}\&\mathrm{S}\&\overline{\mathrm{T} \oplus \mathrm{T_t}}\right)\&\mathrm{LP} \tag{1}$$

T: the local test status.
Tr: the test status of the message from the subscription device.
Tt: the test status of the message from the testing device.
S: the local simulation status.
M: the actual application message of the protection device.
Mr: the message of subscription device.
Mt: the message of test device.
LP: Receiving link.

3 Software Design of Online Testing APP

The online testing APP is the control core of remote online testing system for the relay protection in the smart substation, and plays a connecting role in the entire business data flow. In order to ensure the safety and controllability of the output data of the whole test APP, the existing hardware equipment of the smart substation is used to deploy the test APP in the substation monitoring and control system based on the container technology. Using the container technology to deploy test APP can effectively ensure the data security and controllability of the substation monitoring and control system. When the test APP is in service, no matter whether the test APP crashes or not, it will not have an essential impact on the substation monitoring and control system. At the same time, the container uses limited hardware resources, the network environment can be separated, the application program in the container can be bound to the local port, it is not necessary to worry about conflict with the host system or other software in the container. The test APP is developed by QT, a cross-platform C++ graphical user interface application development framework, which is convenient for debugging and transplantation of the test APP, and meets the technical requirements of deploying APP in the container of Linux operation system.

3.1 Function Design of Test APP

In order to quickly process test business data, the test APP is divided into the following function modules based on testing applications, including virtual device module, device configuration data editing module, device test data editing module, test case management module, test data management module, test process control module, IEC103 communication module, and test terminal communication module. The data flow of each module in the test APP is shown in Fig. 2.

The virtual device module receives the test setup data sent from the test master station located on the dispatching center or the centralized control station, including the test case group number (remote regulation type data) and the test case number inside the group. If it is 0, the entire group of test cases (remote regulation type data) and test start/stop control commands (remote control type data) will be executed, and these data will be transferred to the test process control module. The virtual device module receives the test results uploaded by the test APP and the test result is sent to the remote test engineer station.

The device configuration data editing module and the device test data editing module are mainly used to quickly edit the channel configuration data and test data of the tested device and save the test project through a graphical interface.

The test case management module is mainly used to manage test cases through a graphical interface, open device channel configuration data, open device test data, and create and delete test cases.

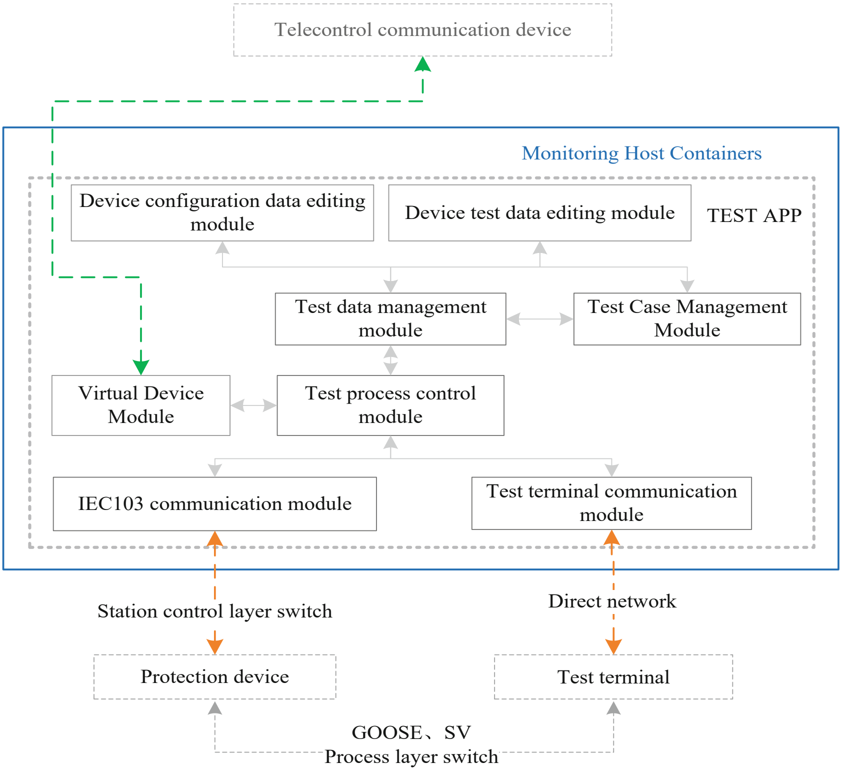

Fig. 2. Test APP software architecture

The test data management module is mainly used to form a test data flow which is sent to the signal output terminal based on the channel configuration data and test data designed by the tester.

The test flow control module mainly has two main functions:

1. Receive the command from the virtual device module, and read local test cases into memory according to the mapping relationship, and implement test start/stop control operations.
2. Receive the status change message of the tested device sent by the communication module of the test terminal, and compare it with the monitoring message to form a test briefing. If it is a remote operation, the test briefing is upload to the virtual device module.

The test terminal communication module uses private protocols and signal output terminals for data communication to achieve the sending of test command data and the automatic upload of the device test status change message. The communication module of the test terminal adopts the direct network connection with the signal output terminal, so as to avoid the influence of test data on the network.

The device IEC103 communication module can automatically modify and verify the device protection settings online, thus assisting the test system to complete the verification of the logical functions of the protection device one by one.

3.2 Function Application of Test APP

Based on the above system functional division, the online testing APP of smart substation relay protection has been developed. The right side of Fig. 3 shows the graphical configuration interface for testing APP analog and binary data, and the left side of Fig. 3 shows the project management center interface for testing APP. The test APP provides a maximum of 6 state analog graph data editing functions or remote analog data mapping functions, and finally realizes the engineering file saving of progressive test data. Through the test management center, you can quickly open the test project can be quickly open to carry out the relay protection online test.

The test APP can realize the relay protection online test analysis in two modes, one is to launch the online test remotely, and the other is to launch the online test in the substation locally. For remote online test, the test initiating end is at the dispatch center or the test engineer station of the centralized control station. For the test in the substation locally, the test APP can be directly opened, establish the test case through the graphical interface, or select the test case to perform the test. Although the operation method of two modes is different, the test dataflow is exactly the same after testing the APP data endpoint.

4 Test Data Security Access

Domestic and foreign experts and scholars have made certain research on remote online detection of relay protection in smart substations. Unlike foreign countries, data communication between substations and control centers in China adopts dedicated network

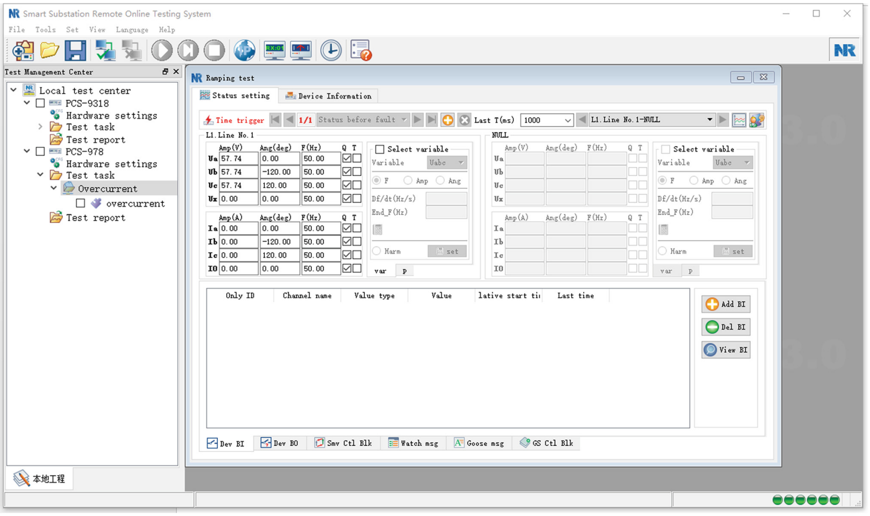

Smart Substation Remote Online Testing System

Ramping test

Time trigger 1/1 Status before fault

Last T(ms): 1000

L1. Line No. 1-NULL

L1. Line No. 1

	Amp(V)	Ang(deg)	F(Hz)	Q	T
Ua	57.74	0.00	50.00	☑	☐
Ub	57.74	-120.00	50.00	☑	☐
Uc	57.74	120.00	50.00	☑	☐
Ux	0.00	0.00	50.00	☑	☐

	Amp(A)	Ang(deg)	F(Hz)	Q	T
Ia	0.00	0.00	50.00	☑	☐
Ib	0.00	-120.00	50.00	☑	☐
Ic	0.00	120.00	50.00	☑	☐
I0	0.00	0.00	50.00	☑	☐

☐ Select variable

Variable: Uabc

● F ○ Amp ○ Ang

Fig. 3. Remote online test APP of relay protection

to transmit power data, typically using longitudinal encryption devices on the substation side, so as to achieve safe and reliable transmission of power data. The idea of this paper is to add a remote test engineer work station in the dispatching control center or centralized control center, and utilize the existing network architecture to establish test communication link only by limited expansion of the IEC104/IEC101 communication data point table. Measured bay data (e.g.: voltage, current, phase angle, frequency…) will be transmitted by using remote regulation data type. Enabling/disabling data of the logic links will be transmitted by using the binary input data type. The start/stop control data of the test APP will be transmitted by using the remote control data type. On the substation side, the test APP is designed in the SCADA (Supervisory Control and Data Acquisition) HMI system container, so as to receive test data from the test engineer workstation. Moreover, the test data will be parsed and forwarded to the signal output terminal, and the device status change message received by the signal output terminal will be sent to the test engineer workstation. As shown by the red dotted line in Fig. 4, a test closed-loop link is established through the test APP, so as to achieve the safe transmission of test command data, and the reception and upward feedback of the result data, as well as the remote detection of the relay protection circuit. The network connection relationship between the test APP and the test engineer workstation is shown in Fig. 4.

Figure 5 shows the detailed data interaction diagram of the remote test engineer workstation, station manager, test APP, and test terminal in the remote online testing process of the smart substation. The test expert initiates the online test in the dispatching center, and the test APP automatically opens local test cases by parsing IEC 60870-5-104 mapping data. The test case data are configured according to state sequences based on the device settings of the protection devices under test. After the test terminal outputs the measurements for the pre-configured time, the output will stop automatically. If a single test case is executed, the test APP opens the test case according to the mapping data

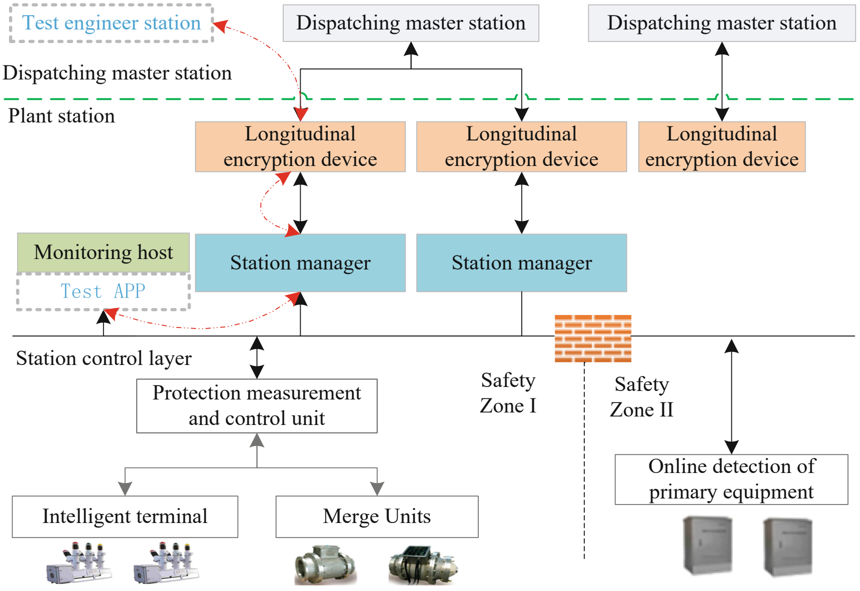

Fig. 4. Schematic diagram of smart substation system structure

to execute the test. If full set of tests are required, the test APP automatically performs the loop test according to the number of test cases in 1 set. For example, the remote test master station tests and verifies the overcurrent protection function of the protection device. The protection device has overcurrent stage I/II/III functions that require to be tested one by one. After the remote test master station issues the test command, the test APP executes the over current stage I test, completes the test and uploads the test report, and then cyclically executes the overcorrect stage II and stage III until all the test cases of the entire test group have been tested.

5 Trial Project Application

The smart substation remote online testing system developed based on the smart substation remote testing system architecture proposed in this paper has been implemented in a 220 kV smart substation in Shandong province. All the protection devices of the smart substation are designed based on IEC61850 Edition 2 standard, and the remote online testing APP is deployed in the SCADA HMI system container. Figure 6 is a schematic diagram of the online testing of the main transformer protection device of the substation. The test terminal communicates directly with the APP through direct network cable, obtains the device GOOSE status change message through the substation process level Ethernet switch, and uploads the test status change message to the APP. The test APP filters the monitoring messages according to the test cases, and organizes them locally into a test report, which is displayed on the main interface of the test APP. In case of remote test operation, the test APP will upload the test report to the remote test engineer workstation.

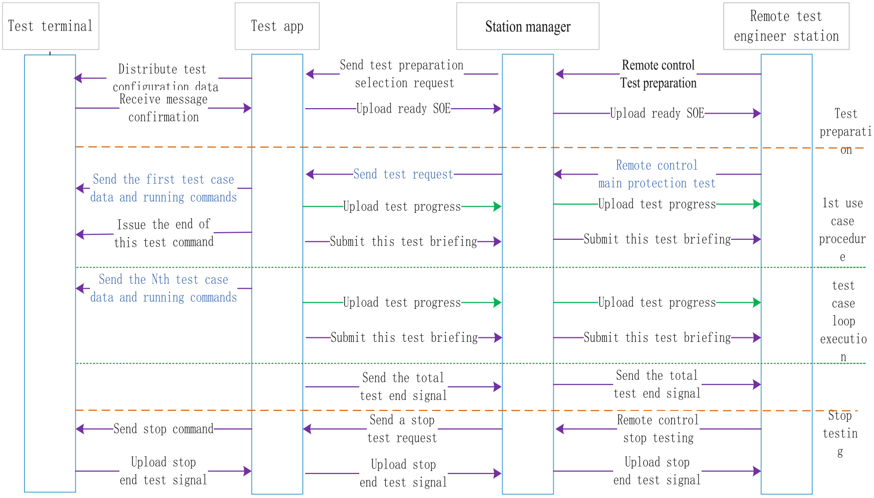

Fig. 5. Typical test data interaction flow chart of relay protection remote detection

The protection devices in the substation have great differences in bays and protection components, so the test engineering is configured independently for each protection device. The test engineering diagram is shown in Fig. 7, including two parts: test environment and test case. The test environment is mainly equipped with the information of each bay's analog channel, protection setting, binary input, tripping output of the protection device, etc., which is used to simulate the working condition of normal hot standby when the tested device is under the logic isolation condition, so as to avoid the link disconnecting. According to the different tested protection components, the test case verifies the key factors such as protection accuracy, the operating time, and enabling/disabling control by means of state sequence.

In order to realize remote control, for test cases configuration, the tested protection components are grouped in principle, and each test case group corresponds to a remote control point, which is used to perform for a group of test cases by remote control of the master station. In the test case group, test cases are added, including changing setting, state sequence, and operating criteria to realize functional tests such as protection operating accuracy, operating time, and blocking logic. Each test case corresponds to a remote point for sending the result of whether the test passes. After all the test cases are configured, the test APP traverses the test project and generates an communication list including remote control of the test group and remote communication of the test cases for remote control.

After the configuration of the test project is completed, the test APP remains online. The test process is divided into three stages: test preparation, test execution and test reset.

In the test preparation stage, there are two operations: (1) Remote control or manual control to enable the Simulation and Maintenance logic link of the tested protection device to make the tested protection device enter the test state; (2) Remote or manual control the test APP, and the test system enters the test mode. If the protection device

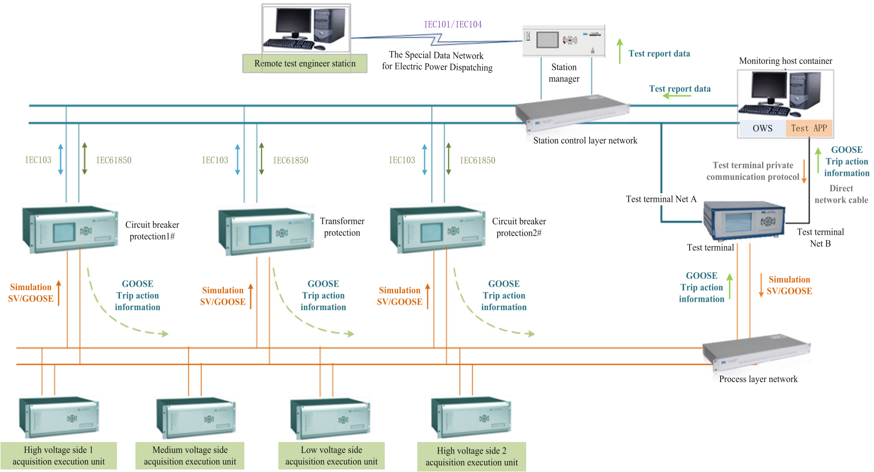

Fig. 6. Diagram of main transformer protection test of a 220 kV substation in Shandong

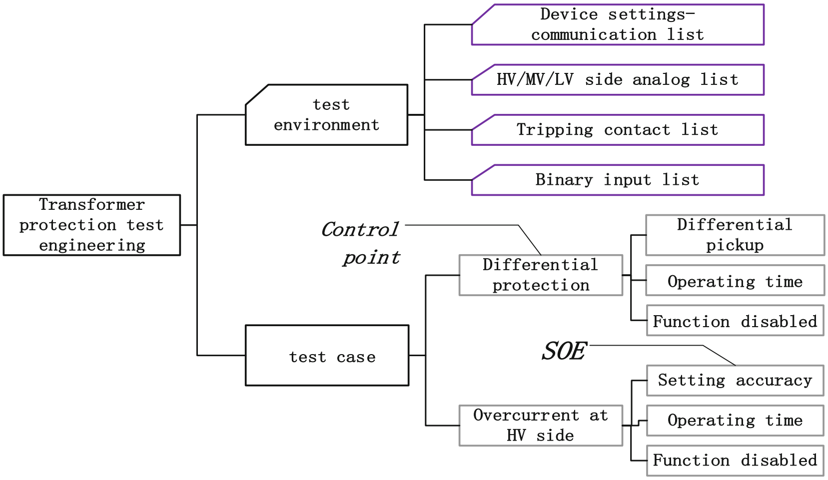

Fig. 7. Schematic diagram of test engineering structure

first enters the test state, at this time the protection device no longer receives normal SV message, the alarm of process layer disconnect is issued. If the test system first enters the test mode and sends a message with Simulation flag, then the protection device enters the test state. Within a period of time, the sampling of the protection device will contain both the received normal SV message and the newly received Simulation message, and there is the sudden change in the sampling calculation results, and there is the possibility of alarm or operating. The output contact may be affected. After several validations, it is decided that the tested protection device enters the test state first, and the test system enters the test mode again. After the test system enters the test mode, the process layer data should ensure output rated voltage and zero current before and after the test case is applied to ensure that the process layer disconnection will not occur in the test execution stage.

In the test execution stage, the test APP repeatedly receives the test command, executes the test process, sends the test progress, and judges and upload the test result. Receive remote or local test commands, match them to the corresponding test group, and execute test cases sequentially. Before and after the test cases are executed, the number of test cases is counted, and the number of completed test cases and the total number of test cases are sent as SOE, so that the test progress can be known in remote end. After the execution of each test case, the test APP collects operating information, compares it with the preset result of the test case, and make a conclusion on whether the test case passes, and sends it through remote message. After the entire group of test cases is executed, send the total result of whether all test cases pass the test.

Typical execution process of a test case:

Step 1: Modify the device protection settings;

Step 2: Wait for the device running;

Step 3: The test APP control the test terminal to output analog data, and execute the test;

Step 4: Stop the output, and verify whether the preset results are satisfied;

Step 5: Modify the device settings to the original value, and verify them;

Step 6: Upload the test report and progress.

After the completion of all tests, remote or manual control test APP to terminate the test and enters the test reset stage. According to the sequence of steps in the test preparation stage, to avoid the sudden change of SV messages, the test system exits the test state first; Then, according to the safety regulations related to the protection device routine check, after confirming that the current protection setting is consistent with the operating setting, disable the Simulation and Maintenance link of the protection device and restore the normal operation of the protection device. During the test, in order to ensure the effectiveness of logic isolation, the status of the simulation link and the test link of the tested protection device are mapped to the GOOSE message. By receiving the GOOSE message, the tester obtained the link status of the tested device, and verified whether the logic isolation is reliable according to formula (1). If the status of logic isolation is inconsistent with the expected status, stop sending process layer data and exit the test state.

It has been verified that there is no difference between the test result and the routine check of the protection device. During the test preparation and reset phase, the process layer message in optical fibers can be configured within one minute by using software because optical fibers do not need to be plugged and unplugged. It is ensured that the correct test environment is prepared and manual involvement is reduced.

6 Conclusion

Based on the IEC61850 Edition 2 standard, the scheme in this paper fully utilizes the simulation mechanism, maintenance mechanism, and SV/GOOSE receiving/sending logic link mechanism of smart substations, so as to achieve safe and reliable isolation of the virtual circuits between the maintenance devices and the running devices. The testing terminal always outputs SV and GOOSE messages with the simulation quality, so as to ensure the safe transmission of simulation messages in the process level. The smart substation relay protection remote online testing system can be applied to the remote periodic inspection, as well as the functional verification after remote upgrading of the protection device programs. The system can quickly achieve online testing of relay protection functions for the remote dispatching control center, the centralized control center, or the local SCADA HMI system.

Deeply exploring the digital advantages of smart substations and promoting the rapid application of new technologies in smart substations, still remains an important direction for the development of smart substation technology in the future. Remote online test system of smart substations undoubtedly creates more convenient and faster online automatic test conditions, which will also make a beneficial attempt and exploration for the in-depth practice of relay protection remote test in smart substations within China.

Acknowledgment. This work is supported by National Key R&D Program of China (2021YFB2401000).

References

1. Yang, Z., Zhou, B., Zhang, H., et al.: Discussion on novel scheme of smart substation automation system. Autom. Electr. Power Syst. **40**(14):1–7 (2016). https://doi.org/10.7500/AEPS20150825008
2. Luo, L., Peng, Q., Wang, D., et al.: Monitoring method of process level network in smart substation. Autom. Electr. Power Syst. **42**(11), 151–156 (2018). https://doi.org/10.7500/AEPS20170728006
3. Liu, H., Gao, X., Du, L., Yu, J.: Modular design of intelligent substation SCD file management and control system. Power Syst. Prot. Control **47**(3), 154–159 (2019)
4. Chen, D., Xu, L., Zhao, X.: Development and analysis of core IEC standards for smart substation automation and relay protection. Autom. Electr. Power Syst. **43**(21), 229–239 (2019). https://doi.org/10.7500/AEPS20190401004
5. Hu, S., Li, L., Zhu, X., et al.: Auxiliary safety measures of protection relay in smart substation based on switching of maintenance states. Autom. Electr. Power Syst. **43**(1), 242–247 (2019). https://doi.org/10.7500/AEPS20180409011
6. Liu, K., Huang, M., Li, Y., et al.: Fault information model and online monitoring method for relay protection system in smart substation. Power Autom. Equip. **38**(2), 210–216 (2018)
7. Ye, Y., Sun, Y., Huang, T., Guo, M., Huang, Y.: Online state detection and fault diagnosis technology of relay protection secondary circuits in smart substation. Power Syst. Prot. Control **44**(20), 148–153 (2016)
8. Zhou, C., Wu, H., Hu, G., et al.: Non-intruding development of automatic test system based on IEC 61850 edition2.0. Power Syst. Prot. Control **45**(14), 143–147 (2017)
9. Peng, Z., Liu, Y., Luo, J., Xiong, H, Fan, Q.: Architecture and key technologies of smart substation's monitoring and control information automatic acceptance system. Power Syst. Prot. Control **48**(7), 174–181 (2020)
10. Qin, H., Wu, F., Peng, S., Ge, L., You, T.: New technology research on secondary equipment operation maintenance for smart grid. Power Syst. Prot. Control **43**(22), 35–40 (2015)
11. Apostolov, A.: Remote testing of digital substations. In: CIGRE Chengdu Symposium 2019, Chengdu (2019)
12. Apostolov, A.: Functional testing of centralized protection systems. In: CIGRE Session 2022, Paris (2022)

Design of Coupling Robust Damping Controller for AC-DC Interconnection System

Tianyi Sun[1], Baohong Li[1](✉), Qin Jiang[1], Min Zhang[2], and Tengxin Wang[2]

[1] College of Electrical Engineering, Sichuan University, Chengdu 610065, China
scu_lbh@163.com
[2] State Grid Shanxi Electric Power Research Institute, Taiyuan 030001, China

Abstract. The robust control method is effective in suppressing the phenomenon of low frequency oscillations (LFOs) in power systems. Aiming at the problem of LFOs in AC/DC transmission system, a coupling robust damping controller design method based on multiple input multiple output (MIMO) system model is proposed to enhance the damping of specific oscillation modes by utilizing the interaction between different control loops instead of decoupling the control loops. Firstly, the global least squares—rotation invariant (TLS-ESPRIT) technique is used to identify the reduced order model of MIMO system and the oscillation modes of the system. Then a kind of hybrid H_2/H_∞ method is used to design coupling robust damping controller based on different control loops. The balanced truncation method is used to reduce the order of the controller, which has both robust performance and practical engineering application. Finally, a four-machine two-area AC/DC test system is built in PSCAD/EMTDC. The time domain simulation results show that the coupling robust controller can effectively suppress the LFOs under various disturbances and faults, and the system can quickly recover stable operation. At the same time, output feedback control is utilized, which is convenient for engineering practice.

Keywords: AC-DC interconnected power grid · Low frequency oscillation · Hybrid H_2/H_∞ method · Coupling robust damping control

1 Introduction

The characteristics of the reverse distribution of energy resources and load in China determine the basic pattern of "West-East electricity transmission project". High voltage direct current (HVDC) transmission technology, which is suitable for long distance and large capacity transmission, provides an effective solution for the rational development, optimal allocation and efficient utilization of domestic resources, and has huge economic, environmental and social benefits. With the increasing scale and complexity of interconnected power system, inter-area LFOs occur from time to time, which brings great challenges to the safe and stable operation of power system. Divergent inter-area oscillations caused by insufficient damping may even lead to power failure.

Y. Xue et al. (Eds.): PMF 2023, LNEE 1129, pp. 61–72, 2024.
https://doi.org/10.1007/978-981-99-9251-5_5

The most common measure used to suppress LFOs is to add a power system stabilizer (PSS) to the excitation regulator of a synchronous generator to offset the negative damping generated by an automatic voltage regulator (AVR) with simple voltage deviation regulation and provide a positive damping torque to the generator. However, some studies have shown that PSS is not always effective for LFOs, especially inter-area oscillations. At present, the main function of PSS is still to suppress local oscillations. In recent years, with the increasing maturity of HVDC, the additional control based on HVDC has been widely studied, especially in damping inter-area oscillations has more flexible control modes and faster response speed than the traditional damping control. At present, for the research of additional damping control of power system, the more mature analysis methods include robust control, optimal control, adaptive control and fuzzy control. A bilinear matrix inequality design method for MIMO robust controller is proposed in [1]. In [2], a decentralized and coordinated control method for large-scale nonlinear process control systems based on dissipative system theory is proposed, but it is complicated to construct and solve the Hamiltonian Jacobi inequality. In [3], An improved D-K iterative method is used to design a decentralized H_∞ robust controller for suppressing urban building oscillations. In [4], communication network constraints such as signal delay and signal loss are taken into account, and a dynamic output feedback controller with wide-area signal as feedback signal is designed to suppress inter-area oscillations.

Most of the existing design methods of robust damping controller are in the form of single input single output (SISO). There is only one robust damping controller feedback signal in a single control loop, which is difficult to demonstrate its robustness in complex power systems or when the fault point is far from the installation site of the controller. In addition, the existing MIMO controller based on decoupling design of multiple control loops is difficult to eliminate the coupling between loops when there are more control devices, and the relative gain array (RGA) method may be difficult to find a suitable control loop for pairing, thus affecting the effect of the controller.

In this paper, the current control terminal of HVDC system is taken as input, and the speed difference of generators in different regions is taken as output. Without decoupling design of different control loops, the TLS-ESPRIT algorithm is used to obtain the state space equation and oscillation mode of the MIMO system directly. Then the coupling robust controller is designed based on the hybrid H_2/H_∞ robust control method. The simulation results of the four-machine two-area AC/DC test system show that the designed controller can effectively suppress the LFOS of the system and show strong robustness.

2 Hybrid H_2/H_∞ Robust Control Theory for MIMO System

2.1 Design Objectives of Controller

The system structure of hybrid H_2/H_∞ robust control is shown in Fig. 1. For the system shown in the figure, its state-space equation can be described as

$$\begin{cases} \dot{\boldsymbol{x}} = \boldsymbol{A}\boldsymbol{x} + \boldsymbol{B}_1\boldsymbol{w} + \boldsymbol{B}_2\boldsymbol{u} \\ z_\infty = \boldsymbol{C}_\infty\boldsymbol{x} + \boldsymbol{D}_{\infty 1}\boldsymbol{w} + \boldsymbol{D}_{\infty 2}\boldsymbol{u} \\ z_2 = \boldsymbol{C}_2\boldsymbol{x} + \boldsymbol{D}_2\boldsymbol{u} \\ \boldsymbol{y} = \boldsymbol{C}\boldsymbol{x} + \boldsymbol{D}_{y1}\boldsymbol{w} + \boldsymbol{D}_{y2}\boldsymbol{u} \end{cases} \tag{1}$$

where $\boldsymbol{x}$ is the state variable of the system, $\boldsymbol{A}$ is the state matrix, $\boldsymbol{B}_1$ is the disturbance gain matrix, $\boldsymbol{B}_2$ is the control input matrix, $\boldsymbol{u}$ is the control variable, $\boldsymbol{y}$ is the output of the system, $\boldsymbol{w}$ is the external perturbation of the system, and z_2 and z_∞ represent the output variable corresponding to the perturbation $\boldsymbol{w}$. $\boldsymbol{C}_\infty$, $\boldsymbol{D}_{\infty 1}$ and $\boldsymbol{D}_{\infty 2}$ represent the variables associated with the H_∞ index, while $\boldsymbol{C}_2$ and $\boldsymbol{D}_2$ represent the variables associated with the H_2 index. For the described system, the controller designed is required to meet the following three objectives:

(a) The closed-loop system is asymptotically stable;

(b) H_∞ performance: The H_∞ norm of the closed-loop transfer function $\boldsymbol{T}_\infty$(s) from $\boldsymbol{w}$ to z_∞ does not exceed the given upper bound $\gamma_\infty(\gamma_\infty > 0)$, so that the system has robust stability to the disturbance uncertainty caused by $\boldsymbol{w}$;

(c) H_2 performance: The H_2 norm of the closed-loop transfer function $\boldsymbol{T}_2$(s) from w to z_2 does not exceed the given upper bound $\gamma_2(\gamma_2 > 0)$ to achieve the optimal system performance.

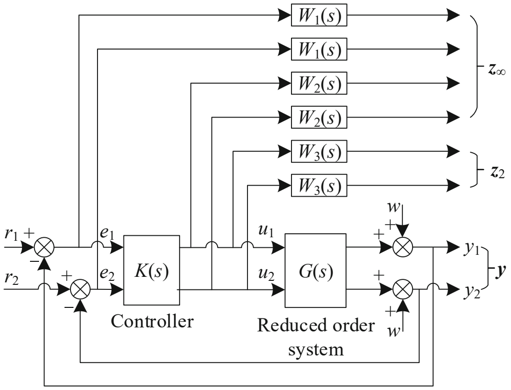

Fig. 1. Diagram of hybrid H_2/H_∞ control system

2.2 Implementation of Controller Objectives

A. *Regional Pole Assignment*

The structure of actual power system is complex, so there must be uncertainty of model and disturbance. It is difficult to ensure the stable operation of power grid for a long time. However, as long as the closed-loop poles of the system are assigned to region D of the complex plane as shown in Fig. 2, the system can be asymptotically stable and has certain dynamic and steady-state properties.

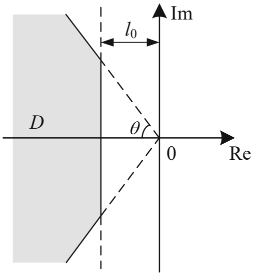

Fig. 2. Pole configuration area

The closed-loop pole of the system is required to be located in the given region in Fig. 2, which is described by matrix inequality as

$$D = \left\{ s \in C \middle| L + sM + s^{*}M^{T} < 0 \right\} \tag{2}$$

where C is the complex field, s^* is the conjugate of s, and $\boldsymbol{L}$ and $\boldsymbol{M}$ satisfy

$$\begin{cases} \boldsymbol{L} = \begin{bmatrix} 2l_0 & 0 \\ 0 & 0 \end{bmatrix} \\ \boldsymbol{M} = \begin{bmatrix} \sin\theta & -\cos\theta \\ \cos\theta & \sin\theta \end{bmatrix} \end{cases} \tag{3}$$

For the suppression of low-frequency oscillation, the characteristic values of the closed-loop system should be located in the region where the damping ratio ζ is greater than cosθ, and the characteristic values of the closed-loop system should not be too close to the virtual axis, so that the adjustment time of the system back to stability after failure is shorter. The regional pole assignment problem can be solved using the LMI toolbox in MATLAB.

B. *Mixed H_2/H_∞ Control*

H_∞ performance index reflects the suppression effect of the system on interference. The H_∞ norm of the closed-loop transfer function $\boldsymbol{T}_\infty(s)$ from $\boldsymbol{w}$ to z_∞ is defined as

$$\|\boldsymbol{T}_\infty(s)\|_\infty = \underset{\omega}{p_k}\{\sigma_{\max}(\boldsymbol{T}_\infty(\mathrm{j}\omega))\} \tag{4}$$

where $\|\boldsymbol{T}_{\infty}(s)\|_{\infty}$ represents the peak value (p_k) of the maximum singular value of the frequency response of the system.

The H_2 performance index reflects the asymptotic change of the corresponding output when the system is interfered by white noise. The H_2 norm of the closed-loop transfer function $\boldsymbol{T}_2(s)$ from $\boldsymbol{w}$ to z_2 is defined as

$$\|\boldsymbol{T}_2(s)\|_2 = \sqrt{\frac{1}{2\pi}\int_{-\infty}^{\infty} t_{\mathrm{r}}\big(\boldsymbol{T}_2^{*}(\mathrm{j}\omega)\boldsymbol{T}_2(\mathrm{j}\omega)\big)\mathrm{d}\omega} \tag{5}$$

where $t_{\mathrm{r}}(\cdot)$ represents the trace of the matrix.

The mixed $\mathrm{H}_2/\mathrm{H}_{\infty}$ control problem is a multi-objective control problem, and the performance index J should meet the following requirements.

$$J = \min\{\alpha\|\boldsymbol{T}_{\infty}(s)\|_{\infty} + \beta\|\boldsymbol{T}_2(s)\|_2\} \tag{6}$$

where α represents robust performance, β represents weight coefficient of control cost, and the sum of the two is equal to 1. α and β can be set to different values according to the controller effect designed. For fixed weights, the controller should be designed to minimize the performance index J.

3 Example Analysis

3.1 Example System

This paper will take the four-machine two-area AC-DC interconnection system shown in Fig. 3 as an example for simulation verification. The generators in this system all contain excitation and speed control systems. The control modes of the two DC lines are rectifier side setting current control and inverter side setting voltage control.

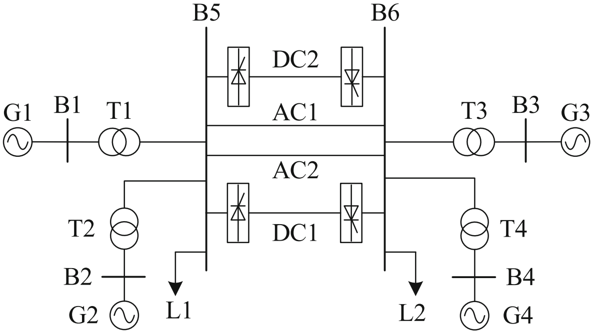

Fig. 3. Topology of four-machine two-area system

Table 1. Oscillation mode of the system

Signal	Mode	Frequency/Hz	Eigenvalue	Damping ratio/%
$\Delta\omega_{13}$	1	1.9822	$-1.7478 \pm 12.4545i$	13.90
	2	0.8043	$-0.7486 \pm 5.0536i$	14.65
	3	0.7126	$-1.1457 \pm 4.4772i$	24.79
$\Delta\omega_{24}$	1	2.4970	$-2.2438 \pm 15.6894i$	14.16
	2	1.2572	$-2.8753 \pm 7.8993i$	34.20
	3	0.8777	$-0.8562 \pm 5.5146i$	15.34
	4	0.3216	$-1.0442 \pm 2.0208i$	45.90

TLS-ESPRIT algorithm is a signal parameter estimation method with high resolution. Compared with Prony algorithm, it has higher computational efficiency and stronger anti-interference ability. The algorithm mainly samples the operating data of the system, thus forming the autocorrelation and cross-correlation matrix, and then finds the frequency and attenuation of the signal. It is suitable for model identification and oscillation characteristic analysis of system with small disturbance.

The TLS-ESPRIT algorithm is used to identify the oscillation modes contained in the system shown in Fig. 3. A step disturbance of 0.02 p.u. is applied at the control point of DC1 rectifier siding current as input, and the speed difference $\Delta\omega_{13}$ between G1 and G3, and the speed difference $\Delta\omega_{24}$ between G2 and G4, respectively, are used as outputs to obtain the oscillation mode of the system, as shown in Table 1.

3.2 Identification of MIMO System Model

The input-output relationship of the system open-loop model can be expressed as

$$\begin{bmatrix} y_1(s) \\ y_2(s) \end{bmatrix} = \begin{bmatrix} G_{11}(s) & G_{12}(s) \\ G_{21}(s) & G_{22}(s) \end{bmatrix} \begin{bmatrix} u_1(s) \\ u_2(s) \end{bmatrix} \tag{7}$$

where $u_1(s)$ and $u_2(s)$ represent the input at the constant current control terminal of DC1 and DC2 respectively, and $y_1(s)$ and $y_2(s)$ represent the output of generator speed difference $\Delta\omega_{13}$ and $\Delta\omega_{24}$ respectively.

As can be seen from Eq. (7), if $u_2(s)$ equals 0 and the original system linearization condition is not changed, the transfer functions $G_{11}(s)$ and $G_{21}(s)$ from $u_1(s)$ to $y_1(s)$ and $y_2(s)$ can be obtained by applying small perturbation excitation at the input $u_1(s)$ and TLS-ESPRIT identification. Similarly, both G_{12}(s) and $G_{22}(s)$ can be identified by applying a perturbation to $u_2(s)$. The identification results of reduced order transfer function are shown in (8).

$$\begin{cases} G_{11}(s) = \dfrac{-0.0002594s^6 + 0.00866s^5 - 0.1189s^4 +}{s^6 + 7.284s^5 + 222.3s^4 + 868.9s^3 + 8927s^2 +} \rightarrow \\ \quad \leftarrow \dfrac{0.7112s^3 + 2.529s^2 + 9.25s}{1.647 \times 10^4 s + 8.817 \times 10^4} \\ G_{12}(s) = \dfrac{-5.617 \times 10^{-6}s^8 + 0.0003659s^7 + 0.0006862s^6 + 0.0224s^5 +}{s^8 + 13.19s^7 + 277.1s^6 + 1175s^5 + 1.618 \times 10^4 s^4 + 3.304 \times 10^4 s^3 +} \rightarrow \\ \quad \leftarrow \dfrac{0.03799s^4 + 0.3906s^3 + 0.4193s^2 + 1.758s}{3.431 \times 10^5 s^2 + 2.956 \times 10^5 s + 2.428 \times 10^6} \\ G_{21}(s) = \dfrac{0.0002123s^8 - 0.01446s^7 + 0.4154s^6 - 6.586s^5 +}{s^8 + 14.04s^7 + 426.5s^6 + 3565s^5 + 3.923 \times 10^4 s^4 + 1.651 \times 10^5 s^3 +} \rightarrow \\ \quad \leftarrow \dfrac{55.42s^4 - 106.8s^3 + 110.7s^2 + 125.5s}{8.943 \times 10^5 s^2 + 1.596 \times 10^6 s + 2.86 \times 10^6} \\ G_{22}(s) = \dfrac{-5.599 \times 10^{-6}s^4 + 0.000514s^3 - 0.002251s^2 + 0.002658s}{s^4 + 11.91s^3 + 177.6s^2 + 493.8s + 3869} \end{cases} \tag{8}$$

3.3 Design of Coupling Robust Controller

In order to satisfy the requirements of H_2 and H_∞ performance indexes, appropriate weight functions should be selected for the system model when designing the controller. Generally, $W_1(s)$ is a high-pass filter. $W_2(s)$ is a low-pass filter. $W_3(s)$ can be set as a small constant. The order of the selected weight function should not be too high. There is no fixed method for the selection of the weight function. After repeated tests, the weight function is

$$\begin{cases} W_1(s) = \dfrac{5s}{s+100} \\ W_2(s) = \dfrac{100}{s+100} \\ W_3(s) = 1 \end{cases} \tag{9}$$

After the weight function is given, the robust toolbox is used in MATLAB, and let the weight coefficient $\alpha = \beta = 0.5$ in Eq. (6). A pole assignment area is set with a damping ratio greater than 30%. The hinfmix function is used to solve the controller without γ_2 and γ_∞ constraints. The relationship between system input, output and controller transfer function matrix can be expressed as

$$\begin{bmatrix} u_1(s) \\ u_2(s) \end{bmatrix} = \begin{bmatrix} K_{11}(s) & K_{12}(s) \\ K_{21}(s) & K_{22}(s) \end{bmatrix} \begin{bmatrix} y_1(s) \\ y_2(s) \end{bmatrix} \tag{10}$$

Considering the difficulty of controller implementation, the balance truncation method is used to reduce the order, and the expression after reducing order of the controller is

$$\begin{cases} K_{11}(s) = \dfrac{-485.6s^3 - 26780s^2 - 73200s - 576600}{s^4 + 20.09s^3 + 310.5s^2 + 1342s + 4426} \\ K_{12}(s) = \dfrac{2.75 \times 10^{-7}s^3 - 2.053 \times 10^{-5}s^2 - 8.649 \times 10^{-5}s + 1076000}{s^4 + 173.4s^3 + 2582s^2 + 9037s + 27550} \\ K_{21}(s) = \dfrac{-1943s^3 - 12520s^2 - 135300s - 218600}{s^4 + 23.39s^3 + 519.5s^2 + 1823s + 4689} \\ K_{22}(s) = \dfrac{6814s^3 + 79820s^2 + 877500s + 1738000}{s^4 + 12.56s^3 + 168.9s^2 + 607.4s + 3046} \end{cases} \tag{11}$$

Each SISO controller designed is 10 orders when considering the weight function. The expression reduced by the balanced truncation method is only 4 orders. Figure 4 shows the Bode diagram of the controller before and after reducing order. In the concerned low frequency band, Bode diagrams before and after reducing order are consistent, meeting the requirements.

3.4 Simulation Verification

The structure of the coupled robust controller is shown in Fig. 5. *G*(s) in the figure is the controlled system. $K(s)$ is the coupling robust controller. Four SISO controllers are added to the corresponding constant current control loop of the system, and different disturbances are applied in the PSCAD for comparison and verification.

A. *Disturbance 1*

At the first second, single-phase ground fault occurs in bus 6, and the fault lasts 0.1 s. The speed difference signals $\Delta\omega_{13}$ and $\Delta\omega_{24}$ are taken as the observation objects. The suppression effect of the controller on oscillation is shown in Figs. 6 and 7. In the figure, all ordinates are per unit value, the same below.

B. *Disturbance 2*

At the first second, three-phase ground fault occurs in bus 6, and the fault lasts 0.1s. The speed difference signals $\Delta\omega_{13}$ and $\Delta\omega_{24}$ are taken as the observation objects. The suppression effect of the controller on oscillation is shown in Figs. 8 and 9.

4 Conclusion

In this paper, a coupling robust controller design method based on MIMO model is proposed by using HVDC converter devices in AC/DC network. On the basis of identifying the reduced order model of the system, using the mixed H_2/H_∞ robust control theory, the problem of solving the controller is transformed into solving the linear matrix inequality,

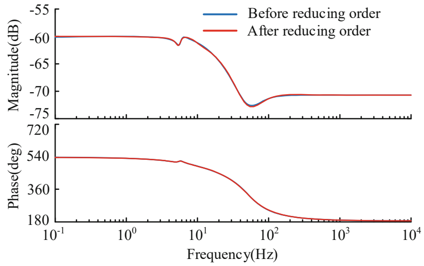

(a)$K_{11}(s)$

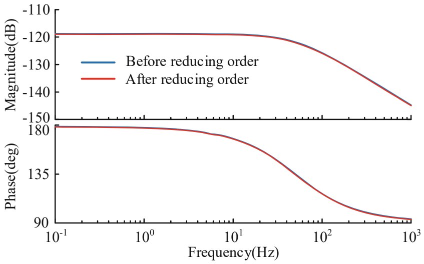

(b)$K_{12}(s)$

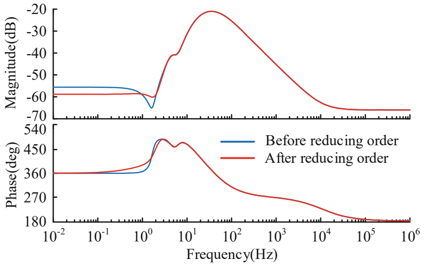

(c)$K_{21}(s)$

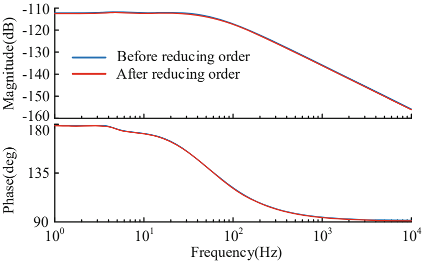

(d)$K_{22}(s)$

Fig. 4. Bode diagram of controller and reduced-order controller

and the performance index is optimized. The designed controller has low order, which is convenient for engineering practice and popularization. In addition, due to the complex topology structure and variable working conditions of the actual system, the method based on control loop decoupling is difficult to play its advantages when the coupling between the control devices is tight. Therefore, in this paper, the low-order model of MIMO system is obtained by directly identifying the state space of MIMO system, and

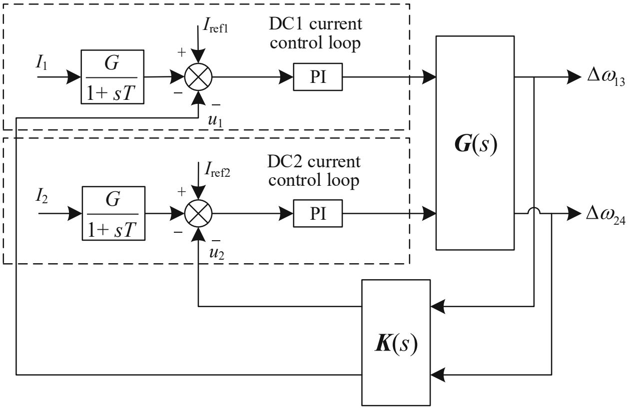

Fig. 5. Control system structure

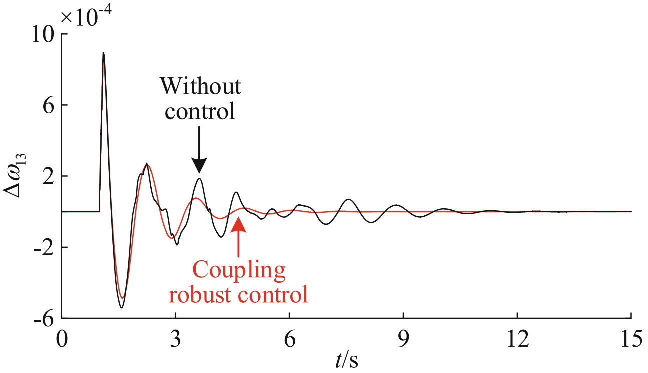

Fig. 6. Dynamic response of $\Delta\omega_{13}$ for the disturbance 1

the decoupling of the complex control loop is avoided. The method has good inhibition effect under various working conditions. The method can effectively suppress the LFOs of the system under various disturbances and faults, and shows strong robustness. The control method proposed in this paper can be extended to the system with more inputs and outputs, and provides a reference for the stable operation of complex power grid. In the future, this method will be used to further study the problem of interval oscillation of inter-regional interconnected power grids, and the influence of wide area signal delay will be further considered.

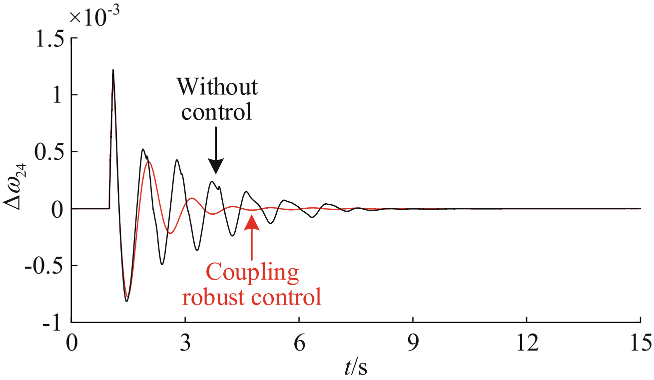

Fig. 7. Dynamic response of $\Delta\omega_{24}$ for the disturbance 1

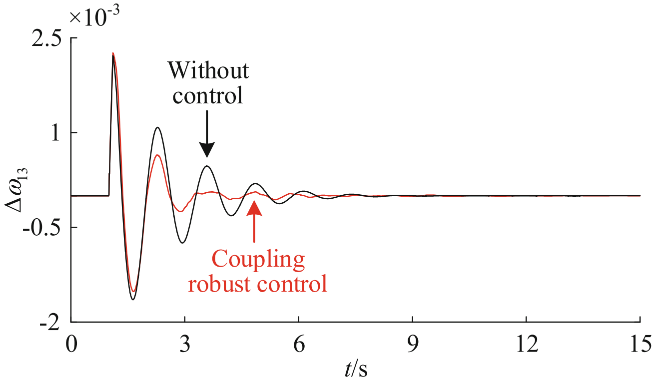

Fig. 8. Dynamic response of $\Delta\omega_{13}$ for the disturbance 2

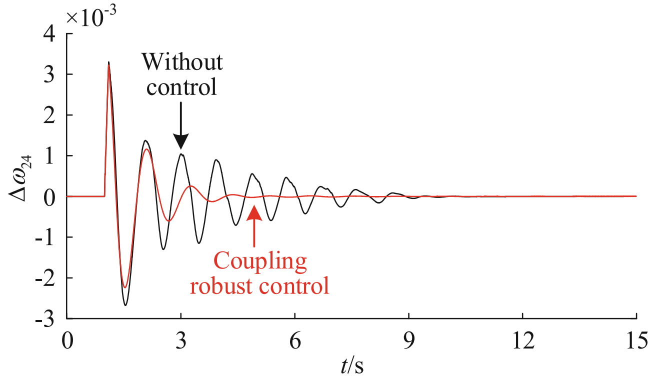

Fig. 9. Dynamic response of $\Delta\omega_{24}$ for the disturbance 2

Acknowledgement. Project supported by the Science and Technology Project of State Grid Corporation of China: Cloud energy storage framework-based AI dispatching strategy of renewable energy integration and contingency response (5100-202199274A-0-0-00).

References

1. Rosa, P., Balas, G.J., Silvestre, C., Athans, M.: A synthesis method of LTI MIMO robust controllers for uncertain LPV plants. IEEE Trans. Autom. Control **59**(8), 2234–2240 (2014)
2. Hioe, D., Hudon, N., Bao, J.: Decentralized nonlinear control of process networks based on dissipativity-A Hamilton-Jacobi equation approach. J. Process. Control. **24**(3), 172–187 (2014)
3. Qu, C., Huo, L., Li, H.: A modified D-K iteration approach for the decentralized H_∞ control of civil structures with parametric uncertainties. In: *Mathematical Problems in Engineering*, vol. 2014 (2014)
4. Obaiah, M.C., Subudhi, B.: Robust damping controller design for damping enhancement of inter-area oscillations considering communication network constraints. In: TENCON 2017—2017 IEEE Region 10 Conference, Penang, Malaysia, pp. 1131–1136 (2017)

Emergency Disposal Optimization of Power Grid Cascading Failure Risk Under Multiple Wildfire Points

Chang Kang(✉), Xue Feng, Yu Chen, Li Wei, Huang Yan, and Liu Shaofeng

State Grid Electric Power Research Institute (NARI Group Corporation), Nanjing 211106, China
changkang@sgepri.sgcc.com.cn

Abstract. Wildfire disasters can cause transmission line failures characterized by low re-closing rate and high breaker rejecting rate, which dramatically increase the risk of cascading failures in power grids. Firstly, the characteristics of power grid cascading failures under multiple wildfire disasters are analyzed from the perspectives of multi fire high impedance faults, evolution pathways of power grid cascading reactions, and emergency disposal requirements for power grid cascading failures under multi-fire disasters. Secondly, establish quantitative decision-making indicators for emergency disposal on cascading failures risk, such as, the probability of transmission line cascading failures, the risk of power grid cascading failures, and the weight of transmission line cascading failures risk. Thirdly, an optimal decision-making method for emergency disposal of cascading failures risk was proposed, which considered the deployment of fire extinguishing equipment and the adjustment of power grid operation mode. Finally, the effectiveness of the proposed method is verified by a practical case of power grid.

Keywords: Wildfire disasters · High impedance faults · Cascading failures · Failure probability · Risk assessment · Fire extinguishing equipment · Emergency disposal

1 Introduction

A large number of power transmission lines pass through forests and mountains with dense vegetation, and wildfire disasters are prone to concentrated outbreaks in a short period of time due to man-made, lightning, spontaneous combustion and other reasons. In China, there are more than 20,000 wildfire points every year [1], causing multiple power grid transmission lines to trip simultaneously or sequentially, which seriously threatens the operational reliability of the transmission network [2].

Once the transmission line trip accident occurs due to wildfire disasters, it is difficult to re-close the transmission line breakers because of the pollution produced by combustion. It is easy to cause several important lines to trip at the same time when multiple wildfire points occur, and further lead to grid cascading failures and large area blackout accidents. Therefore, it is of great significance to study the emergency disposal of power grid cascading failure risks under multiple wildfire points.

Y. Xue et al. (Eds.): PMF 2023, LNEE 1129, pp. 73–86, 2024.
https://doi.org/10.1007/978-981-99-9251-5_6

A large amount of research has been conducted on power grid cascading failures based on random simulation, complex system theory and accident chain models [3–5]. In article [4], a dynamic fault tree analysis model of cascading failures is established based on the accident chain set. In article [5], a risk assessment model and blocking strategy of cascading failure considering the influence of bad weather are established. However, the existing studies have not taken into account the characteristics of multiple wildfire points and their high impedance faults feature, which lead to breakers rejection and multiple cascading failures, resulting in inaccurate probability assessment and identification of cascading failure paths.

Different transmission line trips have different impacts on the power grid. Places with multiple wildfire points are not necessarily high-risk areas of the power grid. And the number of fire extinguishing equipment is limited. It is not effective to reduce the impact of wildfire disasters on the power grid only by the deployment of fire extinguishing equipment. In article [6], a wildfire disaster power grid fire extinguishing equipment optimization allocation method is proposed. Further in article [7], optimal dispatch strategy of fire extinguishing equipment, for minimizing risk of power grid, is studied in case of wildfire disaster with multiple fire points near transmission lines. However, only from the perspective of allocation and dispatch of fire extinguishing equipment, it is not possible to quickly deal with the cascading failure risks caused by multiple wildfire points in a short time, so it is necessary to comprehensively consider both the deployment of fire extinguishing equipment and the adjustment measures of power grid operation mode.

In this article, the characteristics of cascading failures in power grid under multiple wildfire points are analyzed firstly. Secondly three quantitative decision-making indicators for emergency disposal of cascading failure risks are established. And then an optimal decision-making method for emergency disposal of cascading failure risks considering both fire extinguishing equipment deployment and power grid operation mode adjustment is proposed. Finally the effectiveness of the proposed method is verified with an actual case in HN power grid.

2 Characteristics Analysis on Cascading Failures of Power Grid Under Multi-wildfire Points

2.1 Characteristics of High Impedance Faults Under Multi-wildfire Points

The reasons for the decrease in insulation strength of power transmission lines due to wildfire are divided into three types [2]. (1) The high temperature of the flames causes a decrease in air density, leading to a decrease in insulation level. (2) Charges in the flames cause distortion of the electrical field near the conductors. (3) Discharge triggered by particles. Therefore, power transmission lines faults caused by wildfire exhibit the characteristics of low re-closing rate.

Wildfire faults are typical single-phase high-impedance grounding faults [8]. As a nonlinear high-impedance grounding fault, the fault quantity caused by wildfire is not significantly changed, and the relay protection may not be recognized and started. The fault type may be transformed from a single-phase grounding short circuit fault to a phase-to-phase fault, which enlarges the fault scope. The high-impedance feature makes the wildfire faults exhibit the characteristics of high breakers rejecting rate.

The characteristics of low re-closing rate and high breakers rejecting rate of power transmission lines faults caused by wildfire disasters increase the probability of cascading failures, which is a greater threat to the security and stability of the power grid.

2.2 Evolutionary Characteristics of Cascading Failures in Power Grid

According to the temporal and electrical characteristics of subsequent cascading failures triggered by initial faults, the evolutionary pathways of cascading failures in the power grid can be divided into three categories. (1) Overload-type cascading failures, which are often induced by current transfer caused by electromagnetic network faults. (2) Voltage-type AC/DC cascading failures, which are generally caused by insecure steady-state or transient voltages of some buses after the initiation of DC faults or partial current transfer, triggering action of automatic control devices. (3) Unstable decoupling-type cascading failures, which generally occur in inter-regional power grid and are accompanied by system instability and decoupling induced by the automatic control devices failures.

2.3 Emergency Disposal Characteristics of Cascading Failures in Power Grid Under Multi-wildfire Points

Cascading failures of the power grid under multi-wildfire points exhibit the following characteristics, such as massive and uncertain evolutionary paths, fast evolution, and high probability and risk. Therefore, the corresponding emergency disposal requires the following abilities. 1) The ability to identify the evolutionary paths of cascading failures induced by wildfire online. 2) The ability to quantify the impact of power transmission lines under wildfire disasters on the risk of cascading failures in the power grid. 3) The ability to coordinate the deployment of fire extinguishing equipment and the adjustment of the power grid operation mode to optimize the risk of cascading failures.

3 Evaluation of Decision-Making Indicators for Emergency Disposal of Cascading Failures Risk

3.1 Assessment of Cascading Failure Probability of Transmission Lines

Initial Faults under Multi-Wildfire Points. Based on the fire points distribution and the geographic location of the transmission lines and towers, the failure probability p_{l_i} of transmission line i is calculated [2]. Then, based on the failure probabilities of the transmission lines, the failure contingency set is generated [9] to produce an initial contingency set $\{F_1{}^0, \ldots, F_i{}^0, \ldots F_N{}^0\}$, where $F_i{}^0$ represents the i-th initial contingency in the set, and N is the number of initial contingency.

Impact of Power Flow Transfer on Cascading Failure Probability. The cascading failure probability $p_{CLi,j}$ of the j-th cascading failure component after the initial contingency ${F_i}^0$ causes power flow transfer can be calculated according to Eq. (1).

$$p_{CL_{i,j}}=\begin{cases} \alpha_1 \cdot P_{l_j}/P_{l_{jN}}, & 0 \le P_{l_j} \le 0.8P_{l_{jN}} \\ \alpha_2 \cdot P_{l_j}/P_{l_{jN}}+\alpha_3, & 0.8P_{l_{jN}} < P_{l_j} \le 1.2P_{l_{jN}} \\ 1.0, & P_{l_j} > 1.2P_{l_{jN}} \end{cases} \tag{1}$$

where P_{lj} represents the power flow value before the fault of the j-th stage breaking component, P_{ljN} represents the rated power flow value of the j-th stage breaking component, and α_1, α_2 and α_3 are proportionality coefficients where $0 < \alpha_1 < 1$ and $1 < \alpha_2, \alpha_3 < 0$.

Impact of High Impedance Characteristics of Wildfire Faults on Cascading Failure Probability. The failure probability $p_{JDi,j}$ of the j-th cascading failure component, which is caused by the action of the backup protection due to the high-impedance faults characteristics of the wildfire and it is determined by the rejecting probability of the j-1 breaking component.

According to the vegetation type of the j-1 breaking component where the wildfire occurs, the corresponding impedance characteristics and rejecting rate level $\lambda_{jd\_k}(k = 1,\ldots,5)$ of the component are determined according to Table 1. Then, the probability of the j-th cascading failure component is determined according to Eq. (2).

Table 1. Relationship between vegetation type and breaker rejecting rate caused by wildfire.

Vegetation type	Impedance level	Rejecting rate λ_{jd_k}
Weeds/straw/reeds	Maximum	λ_{jd_1}
Shrubs	High	λ_{jd_2}
Mixed vegetation dominated by shrubs	Medium	λ_{jd_3}
Arbors	Low	λ_{jd_4}
Mixed vegetation dominated by arbors	Minimum	λ_{jd_5}

$$p_{JD_{i,j}}=1-e^{-\lambda_{jd\_k}} \tag{2}$$

Where $0 \le \lambda_{jd\_k} \le 1$ represents the rejecting rate of the k-th vegetation type, and λ_{jd_k} decreases with the increase of k.

Impact of Transmission Line Defects on Cascading Failure Probability. The failure probability $p_{QXi,j}$ of the overhead transmission line in each span, which includes eight components, namely foundation, tower, conducting wire and ground wire, insulator, armor clamp, grounding device, channel environment, and ancillary facilities, is considered based on the effects of component state defects, as shown in Eq. (3).

$$p_{\mathrm{QX}_{i,j}}=1-\prod_{l=1}^{L}p_{l\_qx} \tag{3}$$

where L represents the number of spans in the j-th cascading failure line, and p_{l_qx} represents the failure probability of the l-th span due to defects, as shown in Eq. (4).

$$p_{l\_qx} = 1 - e^{-\left(\sum_{n=1}^{N} \lambda_n + \lambda_0\right)} \tag{4}$$

where λ_0 is a constant that is generally of the same order of magnitude as the annual failure rate of transmission lines in the region. λ_n represents the normalized failure rate value corresponding to the state defect of the n-th component, as shown in Eq. (5).

$$\lambda_n = \min\left\{\sum_{k=1}^{K_n} \lambda_{nk}, \lambda_{n\_(\max+1)}\right\} \tag{5}$$

where K_n represents the number of state defects for the n-th component, λ_{nk} represents the failure rate value of the n-th component under the k-th state defect, and its value is set according to Table 2. $\lambda_{n\_(max+1)}$ represents the failure rate value of the n-th component corresponding to the previous level state defect of the current worst state defect level.

Identification and Probability Calculation of Transmission Lines in Cascading Failures. The probability of the cascading failure line is calculated by considering various factors such as power flow transfer, equipment state defects, and high-impedance faults caused by wildfire-induced breakers rejection. This allows for the online identification and probability calculation of the most likely cascading failure component in the power grid under wildfire disasters.

According to the principle of independent events, taking into account factors such as power flow transfer, equipment defect status, and breakers rejection caused by high resistance state of wildfire disasters, the probability of cascading failure $P_{SEi,j}$ in the j-th stage of the i-th initial contingency F_{i0} is calculated as follows (6).

Table 2. Failure rate values under transmission line status defects.

Status defect level description	Alarm level	Corresponding failure rate values λ_{nk}
Normal	0	λ_{nk_0}
Notice	1	λ_{nk_1}
Anomalies	2	λ_{nk_2}
Alerts	3	λ_{nk_3}
Failure	4	λ_{nk_4}

Where λ_{nk_0}–λ_{nk_4} show an increasing trend, and $0 \le \lambda_{nk} \le 1$.

$$p_{SE_{i,j}} = 1 - (1 - p_{CLi,j})(1 - p_{QXi,j})(1 - p_{JDi,j}) \tag{6}$$

By selecting the cascading failure component with the highest probability or a probability exceeding a threshold value as the j-th cascading failure component of the i-th initial contingency F_{i0}, the online search for the cascading failure path and probability assessment of the cascading failure line can be achieved.

3.2 Power Grid Cascading Failure Risk Assessment

Probability Assessment of Cascading Failure Path. The successive action events $SE_{i,j}$ of the initial contingency ${F_i}^0$ and its subsequent stages are considered as a set CF_{i_k}, which is referred to as the k-th cascading failure path of the i-th initial contingency. The cascading failure probability p_{CFi_k} of this k-th path is the product of the failure probabilities of each stage, as shown in Eq. (7).

$$p_{CF_{i\_k}}{=}p_{Fi0} \times \prod_{j=1}^{j=J} p_{SE_{i,j}} \tag{7}$$

where J is the number of successive breaking stages in the k-th cascading failure path of the i-th initial contingency, and p_{Fi0} is the failure probability of the i-th initial contingency ${F_i}^0$.

Cascading Failure Risk of Power Grid. The power grid operating risk R_{CKi_k} of the k-th cascading failure path is the product of the failure probability p_{CFi_k} and the severity of the failure S_{CFi_k}, as shown in Eq. (8).

$$R_{CF_{i\_k}}{=}p_{CF_{i\_k}} \times S_{CF_{i\_k}} \tag{8}$$

where the severity of the failure S_{CFi_k} can be determined by grading the corresponding accident events level based on the time-domain simulation of the cascading failure. In Ref. [10], the accident events of State Grid Corporation of China are divided into 8 levels. In Ref. [11], China Southern Power Grid Company divides accident events into 9 levels. Reference [12] provides a method for handling multiple severity levels caused by the same fault scenario.

The risk of cascading failure R_{CF} in the power grid under multi-wildfire disasters is evaluated by summing up the risks of all cascading failure paths, as shown in Eq. (9).

$$R_{CF} = \sum_{CF_{i\_k} \in CF} R_{CF_{i\_k}} \tag{9}$$

where CF represents the set of all cascading failure paths.

3.3 Calculation of Cascading Failure Risk Weight of Transmission Lines

If the risk of cascading failure in the power grid R_{CF} is greater than the acceptable risk threshold R_u, some emergency disposal need to be taken for the key transmission lines. Therefore, it is necessary to define the weight index of each transmission line in the cascading failure risk as a quantitative basis for the emergency measures priority.

The risk weight β_l of transmission line l is the weighted sum of the power grid operating risks of all cascading failure paths corresponding to the line, as shown in Eq. (10).

$$\beta_l = \sum_{l \in L, CF_{i\_k} \in CF} \gamma_{l\_CF_{i\_k}} \times R_{CF_{i\_k}} \tag{10}$$

where L represents the set of all transmission lines, CF represents the set of all cascading failure paths, CF_{i_k} represents the k-th cascading failure path triggered by the i-th contingency, R_{CFi_k} represents the power grid operating risk corresponding to the cascading failure CF_{i_k}, and $\gamma_{l\_CFi\_k}$ represents the weight factor of transmission line l in the cascading failure evolution path CF_{i_k}. When transmission line l belongs to the cascading failure path CF_{i_k}, $0 < \gamma_{l\_CFi\_k} \le 1$, and it is generally set as $\gamma_{l\_CFi\_k} = 1.0$. When transmission line l does not belong to the cascading failure path CF_{i_k}, $\gamma_{l\_CFi\_k} = 0$.

4 Optimization Decision-Making Method for Emergency Disposal on Cascading Failure Risks

4.1 Two-Level Optimization Process

The emergency disposal measures for cascading failure mainly include two aspects, namely equipment level and system level. The deployment of fire extinguishing equipment to reduce equipment failure probability needs to be given priority due to its long disposal time. While the adjustment of power grid operation mode used to reduce post-fault losses has a relatively short processing time and can be at the lower level of a two-level optimization framework.

The optimization process for emergency disposal on fire-induced cascading failures is shown in Fig. 1. Based on the distribution of wildfire points and transmission lines, the failure probability of each transmission line is obtained. The contingency sets are then generated based on the probability of transmission line failures. Based on the current power grid state data, the risk of cascading failures for the initial contingency sets is evaluated, and the risk weights of each transmission line in the power grid are obtained. Using the risk weights and a optimization model for the deployment of fire extinguishing equipment, the optimal deployment plan for fire extinguishing equipment is determined. Based on the optimal deployment plan for fire extinguishing equipment and an optimization model for power grid operation, the power flow of transmission lines involved in cascading failures is adjusted to reduce the probability of cascading faults.

4.2 Optimization of Wildfire Extinguishing Equipment Deployment

In the case of large-scale wildfires, the number of fire extinguishing equipment is often far less than the number of transmission lines that need to be extinguished. The optimization model for fire extinguishing equipment deployment is established with the objective of minimizing the cost of deploying fire extinguishing equipment per unit of risk, and subject to the constraint of the total number of available fire extinguishing equipment. The optimization model is as Eq. (11).

$$\begin{aligned} \min \quad & \sum_{l \in L} \lambda_l C_l / \beta_l \\ s.t. \quad & \sum_{l \in L} n_l \lambda_l = N_{ext} \end{aligned} \tag{11}$$

where β_l is the risk weight of transmission line l. C_l is the cost of deploying fire extinguishing equipment on transmission line l, and the cost of deploying fire extinguishing equipment on each transmission line is assumed to be a constant value. n_l is the number of wildfire points associated with transmission line l, λ_l is the decision variable that represents whether to deploy fire extinguishing equipment on transmission line l, with $\lambda_l = 1$ indicating deployment and $\lambda_l = 0$ indicating no deployment. L represents the set of all transmission lines, and N_{ext} represents the total number of fire extinguishing equipment available.

The decision variable λ_l is solved based on the optimization model to determine the set of transmission lines L_{ext} where fire extinguishing equipment should be deployed.

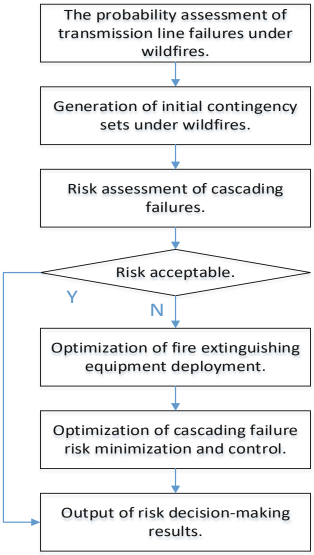

Fig. 1. Optimization process for emergency disposal on cascading failures caused by multiple wildfires.

4.3 Optimization of Decision-Making by Adjusting the Power Grid Operation Mode

The Optimization of the deployment of fire extinguishing equipment can reduce the failure probability of initial contingency. Based on this, the optimization of generators outputs and load values, which adjusts the power flow of transmission lines involved in cascading failures, can reduce the probability of cascading failures. And then it is achieved to comprehensively reduce the risk of cascading failures.

In the case of wildfires, the optimization model for adjusting power grid operation mode is established with the objective of achieving a cascading failure risk level that is below the acceptable risk threshold R_u. The optimization model takes into account the constraints on the adjustment space for generators and loads, as well as the constraints on the power flow limits of transmission lines. The optimization model is formulated as Eq. (12).

$$\begin{array}{ll}\min & \left|\sum_{CF_{i\_k}\in CF} R'_{CF_{i\_k}} - R_u\right| = \left|\sum_{CF_{i\_k}\in CF} p'_{Fi0}\times\prod_{j=1}^{j=J} p'_{SE_{i,j}}\times S'_{CF_{i\_k}} - R_u\right| \\ & P_{D.i.d}\le P'_{D.i}\le P_{D.i.u} \qquad i\in D \\ s.t. & P_{G.i.d}\le P'_{G.i}\le P_{G.i.u} \qquad i\in G \\ & P_{lj.d}\le P'_{lj}\le P_{lj.u} \qquad l_j\in L\end{array} \tag{12}$$

where $R'_{CF_{i\_k}}$ represents the risk value of the cascading failure path CF_{i_k} after optimization. p'_{Fi0} represents the failure probability of the i-th initial contingency ${F_i}^0$ after considering the deployment of fire extinguishing equipment. When the transmission lines involved in the initial contingency ${F_i}^0$ have fire extinguishing equipment deployed, $p'_{Fi0} = f(t)p_{Fi0}$, where $0\le f(t)\le 1$ represents a function that decreases with time. Otherwise, $p'_{Fi0} = p_{Fi0}$. $S'_{CF_{i\_k}}$ represents the severity of the cascading failure path CF_{i_k} after considering the combined effect of fire extinguishing equipment deployment and power grid operation mode adjustment. In general, $S'_{CF_{i\_k}} = \eta SC_{Fi\_k}$, where $0\le\eta\le 1$, and for simplicity, the change in failure severity can be ignored, i.e. $\eta = 1.0$. $p'_{SE_{i,j}}$ represents the failure probability of the j-th stage of the cascading event in the cascading failure path CF_{i_k} after considering power grid operation mode adjustment. $P_{D.\,i.d}$, $P_{G.\,i.d}$, and $P_{lj.\,d}$ respectively represent the lower limit of the i-th controllable load active power, the i-th generator active power output, and the active power flow limit of the l_j transmission line. $P_{D.i.u}$, $P_{G.i.u}$, and $P_{lj.u}$ respectively represent the upper limit of the i-th controllable load active power, the i-th generator active power output, and the active power flow limit of the l_j transmission line.

The failure probability $p'_{SE_{i,j}}$ of the j-th stage of the cascading failure path CF_{i_k} after considering power grid operation mode adjustment is calculated according to Eq. (13).

$$p'_{SE_{i,j}} = \begin{cases}\alpha_1\cdot P'_{l_j}/P_{l_{jN}}, & 0\le P'_{l_j}\le 0.8P_{l_{jN}} \\ \alpha_2\cdot P'_{l_j}/P_{l_{jN}}+\alpha_3, & 0.8P_{l_{jN}} < P'_{l_j}\le 1.2P_{l_{jN}} \\ 1.0, & P'_{l_j} > 1.2P_{l_{jN}}\end{cases} \tag{13}$$

where P'_{l_j} represents the power flow value of the transmission line lj before the fault occurs in the j-th stage of the cascading event after considering power grid operation mode adjustment.

The power flow value of the component l_1 in the first stage of the cascading event CF_{i_k} caused by the i-th initial contingency, after considering power grid operation mode adjustment, is calculated according to the following Eq. (14).

$$P'_{l1} = P_{l1} + \sum_{i\in G}[s_{G.i.l1}(P'_{G.i}-P_{G.i})] + \sum_{i\in D}[s_{D.i.l1}(P'_{D.i}-P_{D.i})] \tag{14}$$

where P_{l1}, P_{Gi}, and P_{Di} respectively represent the power flow value of the transmission line l_1 before the operation mode adjustment, the active output of the i-th generator, and the active value of the i-th load. P'_{l1}, P'_{Gi}, and P'_{Di} respectively represent the power flow value of the transmission line l_1 after adjusting the operation mode, the active output of the i-th generator, and the active value of the i-th load. $S_{G.i.l1}$ represents the active power sensitivity of the i-th generator output adjustment on the impact of power flow changes on the transmission line l_1. $S_{D.i.l1}$ represents the active power sensitivity of the i-th load active power adjustment on the impact of power flow changes on the transmission line l_1. G represents the number of generators participating in optimization adjustment, and D represents the number of controllable loads participating in active power adjustment.

For the k-th cascading failure path CF_{i_k} caused by the i-th initial contingency, without considering the impact of its power change, i.e. $p'_{SEi,j} = p_{SEi,j} (j > 1)$.

The decision variables $P'_{G.i}$ and $P'_{D.i}$ are solved based on the optimization model to determine the amount of power grid operation mode adjustment and its corresponding cascading failure risk under wildfire disasters. If there is no solution, measures need to be taken to expand the range of adjustable units and controllable loads, restore the operation of maintenance lines, and update the set G, D, and L in optimization Eq. (12) before re-optimizing the solution.

By integrating the optimization plan for fire extinguishing equipment deployment and the optimization plan for power grid operation mode adjustment, an optimized emergency disposal plan for cascading failure risk of power grid under multi-wildfire points can be obtained.

5 Case Study

5.1 Case Description

Based on the HN power grid actual operating data and the monitoring data of the wildfire that occurred on April 5th, 2019 at 10:45:00, the study focused on the southwest transmission sections of the HN power grid and its associated main power sources. The power grid network and the distribution of 10 wildfire points are shown in Fig. 2.

5.2 Assessment of Cascading Failures Risk in Power Grid Under Multiple Wildfire Points

The typical parameters in Eqs. (1), (2), and (5) in the case study are calculated for probability based on the following values: $\alpha_1 = 0.25, \alpha_2 = 2.0, \alpha_3 = -1.4$, $\lambda_{jd\_5} \sim \lambda_{jd\_1}$ are taken as 0.05, 0.1, 0.15, 0.2 and 0.25 in ascending order, $\lambda_{nk\_0} \sim \lambda_{nk\_4}$ are taken as 0, 0.2, 0.4, 0.7 and 1.0 in ascending order.

Table 3 shows the transmission lines and their corresponding failure probabilities under the 10 wildfire points. The transmission lines with failure probabilities greater than the threshold value (0.2 in this paper) are selected as initial contingency for security and stability simulation to determine the cascading failure paths. The failure probability, severity level, and risk of each path are evaluated using the method proposed in this paper. Seven cascading failure paths that require attention are selected and shown in Table 4.

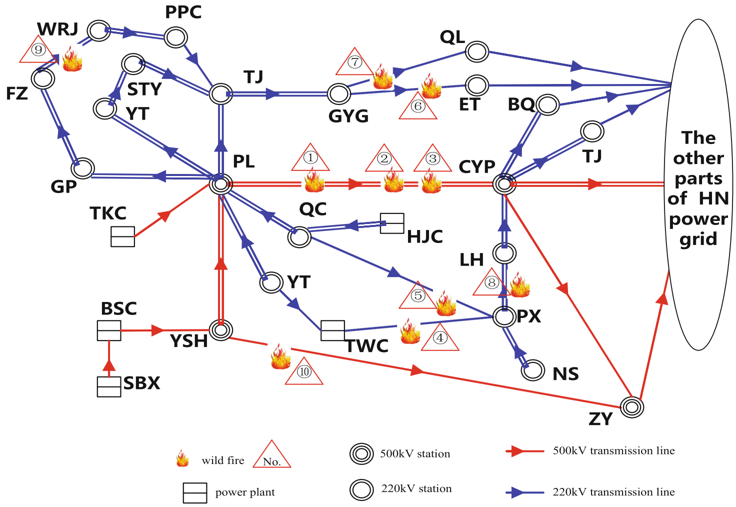

Fig. 2. The HN power grid network and the distribution of wildfire points.

According to the requirement of not occur Level 5 events [10], the acceptable risk threshold value is determined to be 5.0 in this paper. Currently, the total risk assessment value for cascading failures in the power grid is 21.00. Therefore, an optimized emergency disposal decision-making for cascading failure risk needs to be made in this case.

Table 3. Transmission lines and their corresponding failure probabilities under multiple wildfire points.

Line name	Corresponding wildfire point number	Failure probability
PL-CYP	①②③	0.63
TWC-PX	④⑤	0.47
GYG-ET	⑥⑦	0.42
GYG-QL	⑦	0.31
PX-LH	⑧	0.23
FZ-WRJ	⑨	0.21
QC-PX	⑤	0.21
YSH-ZY	⑩	0.20

5.3 Optimization of Emergency Disposal on Cascading Failure Risk

Based on a two-layer optimization model that first deploys fire extinguishing equipment to reduce the probability of initial faults, and then adjusts the operation mode to reduce

Table 4. Cascading failure paths and their power grid risks under multiple wildfire points.

Cascading failure path	p_{CFi_k}	S_{CFi_k}	R_{CKi_k}
PL-CYP → QC-PX → GYG-ET → GYG-QL → TWC-PX → YSH-ZY	0.57	9	5.10
PL-CYP → GYG-ET → GYG-QL → PX-LH → YSH-ZY	0.50	9	4.54
PL-CYP → GYG-ET → GYG-QL → PX-LH → FZ-WRJ → YSH-ZY	0.47	9	4.25
PL-CYP + TWC-PX → QC-PX → GYG-ET → GYG-QL → TWC-PX → YSH-ZY	0.27	9	2.40
PL-CYP + TWC-PX → GYG-ET → GYG-QL → PX-LH → YSH-ZY	0.24	9	2.13
PL-CYP + TWC-PX → GYG-ET → GYG-QL → PX-LH → FZ-WRJ → YSH-ZY	0.22	9	2.00
YSH-ZY → FZ-WRJ → YT-STY	0.14	4	0.58
Cascading failure risk of power grid			21.00

the probability of cascading faults, an optimized emergency disposal on cascading failure risk is carried out for this case study.

Assuming that only 6 fire extinguishing equipment sets are currently available, the optimized model that considers the weight of transmission lines cascading failure risk is used to determine the deployment of fire extinguishing equipment for wildfire points ⑩, ⑦, ⑥, ①, ② and ③, as shown in Table 5.

Table 5. Fire extinguishing equipment deployment based on transmission lines risk weights.

Line name	Corresponding wildfire point number	Risk weights	Number of fire extinguishing equipment
YSH-ZY	⑩	21.00	1
GYG-QL	⑦	20.42	1
GYG-ET	⑥⑦	20.42	1
PL-CYP	①②③	20.42	3
PX-LH	⑧	12.92	0
TWC-PX	④⑤	11.63	0
QC-PX	⑤	7.50	0
FZ-WRJ	⑨	6.83	0

Taking into account the impact of fire extinguishing equipment, the failure probabilities of the relevant transmission lines will decrease over time according to a decreasing pattern, thereby reducing the cascading failure risk to some extent, as shown in Table 6. According to the simulation results, after the fire extinguishing equipment starts to take effect, the cascading failure risk can be reduced to 16.92. But it is still higher than the acceptable risk threshold value. It can be seen that it is not possible to quickly suppress the cascading failure risk in the short term through fire extinguishing equipment deployment alone.

Based on this, it is necessary to further optimize the generators outputs and control the power flow of critical transmission channels to suppress the cascading failure evolution.

Table 6. Cascading failure paths and their power grid risks considering fire extinguishing equipment.

Cascading failure path	$p'_{CF_{i\_k}}$	$S'_{CF_{i\_k}}$	$R'_{CK_{i\_k}}$
PL-CYP → QC-PX → GYG-ET → GYG-QL → TWC-PX → YSH-ZY	0.45	9	4.08
PL-CYP → GYG-ET → GYG-QL → PX-LH → YSH-ZY	0.40	9	3.63
PL-CYP → GYG-ET → GYG-QL → PX-LH → FZ-WRJ → YSH-ZY	0.38	9	3.40
PL-CYP + TWC-PX → QC-PX → GYG-ET → GYG-QL → TWC-PX → YSH-ZY	0.21	9	1.92
PL-CYP + TWC-PX → GYG-ET → GYG-QL → PX-LH → YSH-ZY	0.19	9	1.71
PL-CYP + TWC-PX → GYG-ET → GYG-QL → PX-LH → FZ-WRJ → YSH-ZY	0.18	9	1.60
YSH-ZY → FZ-WRJ → YT-STY	0.14	4	0.58
Cascading failure risk of power grid			16.92

After optimizing the generators outputs as shown in Table 7 (where HJC is a run-of-river hydro-power station and is not included in the optimization), the cascading failure risk can be controlled to an acceptable level in a short time, as shown in Table 8.

Table 7. Generators outputs optimization to reduce cascading failure risk.

Name of power plant	Power output before optimization/MW	Optimized power output/MW
SBX	1140.00	866.40
BSC	540.00	410.40
TKC	800.00	576.80
TWC	78.00	59.28
HJC	130.00	130.00

Table 8. Cascading failure paths and their power grid risks considering both fire extinguishing equipment deployment and power grid operational adjustments.

Cascading failure path	$p'_{CF_{i\_k}}$	$S'_{CF_{i\_k}}$	$R'_{CK_{i\_k}}$
PL-CYP → QC-PX → GYG-ET → GYG-QL → TWC-PX → YSH-ZY	0.12	9	1.04
PL-CYP → GYG-ET → GYG-QL → PX-LH → YSH-ZY	0.13	9	1.21
PL-CYP → GYG-ET → GYG-QL → PX-LH → FZ-WRJ → YSH-ZY	0.10	9	0.86
PL-CYP + TWC-PX → QC-PX → GYG-ET → GYG-QL → TWC-PX → YSH-ZY	0.05	9	0.49
PL-CYP + TWC-PX → GYG-ET → GYG-QL → PX-LH → YSH-ZY	0.06	9	0.57
PL-CYP + TWC-PX → GYG-ET → GYG-QL → PX-LH → FZ-WRJ → YSH-ZY	0.05	9	0.41
YSH-ZY → FZ-WRJ → YT-STY	0.07	4	0.27
Cascading failure risk of power grid			4.85

6 Conclusion

Based on the analysis of the characteristics of cascading failures in power grid under multiple wildfire points, quantitative decision-making indicators for emergency disposal on cascading failure risks is established, and an optimized emergency disposal decision-making method that considers both the deployment of fire extinguishing equipment and power grid operational adjustments is proposed. The effectiveness of the proposed method is verified through a practical case study in HN power grid.

However, the evolution of cascading faults is an optimization problem in time period. This paper only provides a mechanism explanation and modeling optimization through various optimizations at a certain time section. In the future, it is necessary to further expand the optimization of the cascading failure evolution trajectory within a certain period of time.

Acknowledgement. This research work was funded by the China State Grid Corporation Project of Application Preparation Research on Power Grid Proactive Support for Dual Carbon Revolution (5108-202218280A-2-50-XG).

References

1. Lu, J., Liu, Y., Wu, C., et al.: Study on satellite monitoring and alarm calculation algorithm of wild fire near transmission lines. Proc. CSEE **35**(21), 5511–5519 (2015)
2. Wu, Y., Xue, Y., Lu, J., et al.: Space-time impact of forest fire on power grid fault probability. Autom. Electric Power Syst. **40**(3), 14–20 (2016)
3. Xue, Y., Xie, Y., Wen, F., et al.: A review on cascading failures in power systems. Autom. Electric Power Syst. **37**(19), 1–9, 40 (2013)
4. Ding, M., Xiao, Y., Zhang, J., et al.: Risk assessment model of power grid cascading failures based on fault chain and dynamic fault tree. Proc. CSEE **35**(4), 821–829 (2015)
5. Ding, M., Qian, Y., Zhang, J., et al.: Coordinated control model of power system cascading failures based on risk assessment. Autom. Electric Power Syst. **40**(7), 1–8 (2016)
6. Guo, J., Lu, J., Jian, Z., et al.: Optimal allocation of fire extinguish equipments for power grid under widespread fire disasters. Power Syst. Technol. **42**(8), 2687–2693 (2018)
7. Jian, Z., Lu, J., Guo, J., et al.: Optimal allocation of fire extinguish equipments for power grid under widespread fire disasters. Power Sys. Technol. **42**(7), 2324–2330 (2018)
8. Wang, B., Ni, J., Wang, H., et al.: Single-end fault location for high impedance arc grounding fault in transmission line. Proc. CSEE **37**(05), 1333–1341 (2017)
9. Chang, K., Huang, Y., Feng, C., et al.: Research on the screening of multiple contingency and its failure probability assessment technology in natural disasters. In: 4th Purple Mountain Forum on Smart Grid Protection and Control, Aug 18, pp. 23–35 (2019)
10. Investigation procedures of power accidents of State Grid Corporation of China. SGCC [2011] 2024 (2011)
11. Q/CSG 210020-2014 Investigation Procedures of Power Accidents of China Southern Power Grid. China Southern Power Grid Co., LTD. (2014)
12. Chang, K., Zhao, M., Yu, C., et al.: Discussion of power system operation risk control technology in natural disasters. In: 4th Purple Mountain Forum on Smart Grid Protection and Control, Aug 18, pp. 47–61 (2019)

Research on Grid Connection Control Strategy of Building Energy Router Based on Pre Synchronous VSG Control Technology

Baojin Guan[1], Hui Wang[1](✉), Xiaohua Zhang[2], Pan Yin[1,3], and Xiangping Meng[1]

[1] Safe Operation of Smart Distribution Network of the Measurement and Control Joint Engineering Research Center, Changchun Institute of Technology, Changchun, Jilin 130012, China
wanghui841013@ccit.edu.cn
[2] State Grid Jilin Electric Power Co., Ltd. Yanbian Power Supply Company, Jilin Yanji 130012, China
[3] Jilin Institute of Chemical Technology, Jinlin, Jilin 130012, China

Abstract. Aiming at the problem of unstable DC bus connection in building energy routers, this paper proposes a grid connection control strategy for building energy routers based on pre-synchronous virtual synchronous generator (VSG) control technology. Firstly, an energy router topology is designed, and secondly, the pre-synchronous VSG is analyzed. Pre-synchronous VSG control is adopted for the DC bus connection in the energy router to maintain the stability of the system and reduce the voltage and current impact of the common coupling point. In this paper, the simulation model of pre-synchronous VSG control energy router connected to the grid is established by MATLAB/simulink. In MATLAB, simulation results show that the pre-synchronous virtual synchronous machine (VSG) control has the characteristics of small overshoot. The proposed control strategy proposes a new solution for the grid-connected operation of energy routers.

Keywords: Energy router · Pre-synchronization · Virtual synchronization · Stable grid connection

1 Introduction

With the development of society, building energy consumption continues to rise, but fossil energy is gradually depleted. In 2018, global electricity accounted for 19.2% of final energy consumption, China's building energy consumption accounted for 46.5% of the country's total energy consumption, carbon emissions accounted for 51.3% of the country's carbon emissions [1], the world urgently needs an energy revolution. In this context, the EU and the United States have respectively proposed the goal of achieving 100 and 80% renewable energy utilization by 2050, China has proposed to peak carbon dioxide emissions before 2030, achieve carbon neutrality before 2060, and increase the level of electrification of terminal energy consumption in the building sector from the current 30% to about 75% by 2060. The electrification of the building sector will greatly

Y. Xue et al. (Eds.): PMF 2023, LNEE 1129, pp. 87–102, 2024.
https://doi.org/10.1007/978-981-99-9251-5_7

reduce carbon emissions, accelerate the goal of dual carbon, reduce the burden on the environment, reduce the pressure of fossil energy supply, and improve energy security.

Today, the impact of booming Internet technologies on people's lifestyles has greatly increased, and through the Internet of Information, its potential is changing more and more energy fields. The energy Internet is at the heart of the third industrial revolution in full swing. The development of society has promoted the development of the energy Internet, and a series of policies implemented by the state in the fields of economy and politics have provided great support for the development of the energy Internet [2]. As a key device of the new power system, the energy router can realize energy interconnection, two-way flow of energy, plug and play, and improve the stability of energy transmission, which has been widely recognized around the world [3].

However, most of the existing literature discusses power supply and distribution applications implemented using energy routers in large grids with medium and high voltages, or the operation and control of DC links in islanded mode of building-level energy routers. The literature [4] points out that the use of energy routers to realize medium and high voltage power supply and distribution applications is relatively mature, while the energy routers in building-level island mode limit their application due to poor system stability when the energy is excess or insufficient. Literature [5] proposes a multi-port energy router control strategy, but the power utilization rate is relatively low. Literature [6] proposes a small energy router control strategy, but the ports are limited. Literature [7] proposes a hierarchical control method for energy routers, but the line utilization rate is relatively low. Literature [8] proposes a phase-shift control strategy, but the control is complex. And there is little literature that discusses the topology and control of building-level energy routers. This paper elaborates the topology of the building-level energy router, and designs a building-level energy router DC grid-connected control mode, which can provide stable grid power support for the operation of the energy router in the building-level island mode at any time, and it can be said that the two-way flow of energy between the power grid and the energy router can be realized, and the stability of the operation of the energy router can be increased. It has certain theoretical value and practical application value.

2 Application Scenarios and Topology Analysis of Building Energy Routers

2.1 Building Energy Router Application Scenarios

As the core equipment of new energy power grid connection, energy routers play an important role in the stability of new energy grid connection and the interconnection of electricity between various buildings. This article designs a building group microgrid system with an energy router as the core device that can achieve energy interconnection between buildings, improving the integrity of electricity between buildings and improving the stability of community electricity interconnection [9]. The architecture of the building energy internet is shown in Fig. 1.

After the power grid is connected to the distribution and transformation room of the residential area, power is supplied to the residential buildings through the residential

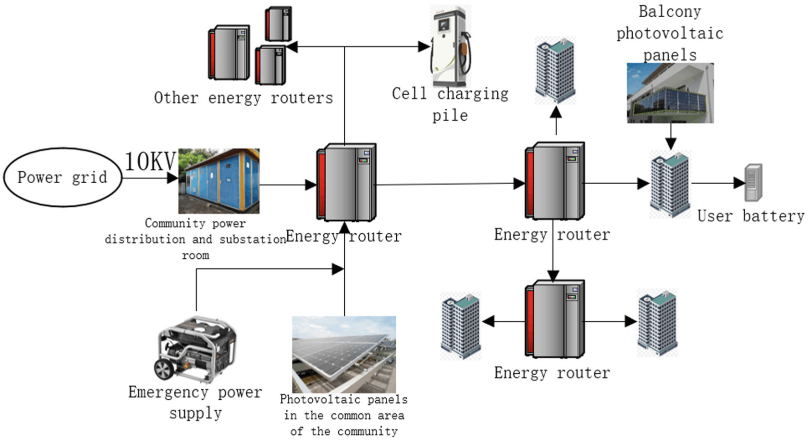

Fig. 1. Building energy internet architecture diagram.

distribution line. Energy routers are connected between the residential building groups, forming a microgrid system with energy routers as the core between one or more residential areas. It can not only maintain the stability of electricity in residential areas, but also connect clean energy such as photovoltaics to the grid, increasing the proportion of clean energy in the grid. At the same time, it can connect DC loads such as electric vehicles through energy routers to provide more stable voltage for the charging of electric vehicles. If the electricity generated by clean energy sources such as photovoltaics exceeds the electricity generated by the load, it can be stored through batteries. The excess energy can be sold to the power grid company in the form of clean energy grid connection in residential areas, providing both electricity to the grid and income for residents.

2.2 Building Energy Router Topology Analysis

2.3 Building Power Supply System Topology Based on Building Energy Router

From Fig. 2, it can be seen that the topology of the energy router is a three-level topology structure, namely the input stage, isolation stage, and output stage. The input stage is connected to 220 V and 380 V/220 V AC power, which can achieve bidirectional energy flow between the energy router and the community power grid. The two ports generate 400 and 750 V DC power through single-phase DC/AC inverters and three-phase DC/AC inverters, respectively, and are connected to two DC buses. The voltage on both sides is connected and interconnected through the intermediate stage high-frequency isolated DC/DC converter DAB. The 400 V DC bus is connected to the photovoltaic panel and household battery on the balcony. The 750 V DC bus is connected to the rooftop photovoltaic panels, as well as photovoltaic panels in the common area of the community, centralized energy storage boxes in the community, emergency power supplies, and other energy routers.

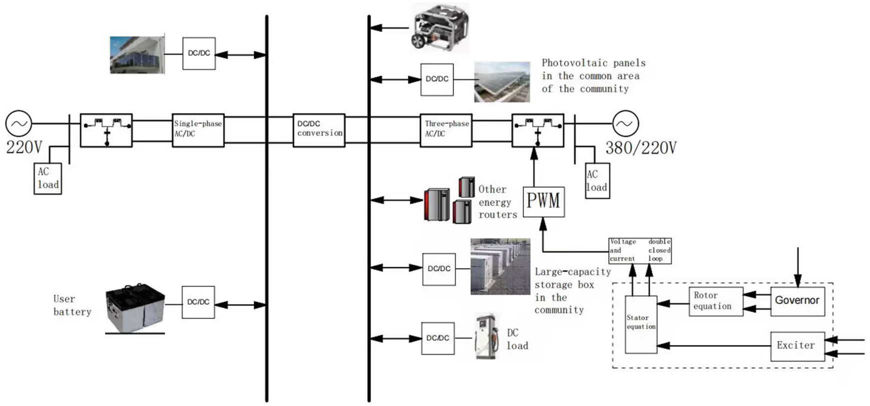

Fig. 2. Building power supply system topology based on energy router.

2.4 Building Energy Router Solid-State Topology

According to the description of the power supply system structure of the energy router above, the solid-state topology of the building energy router is shown in Fig. 3.

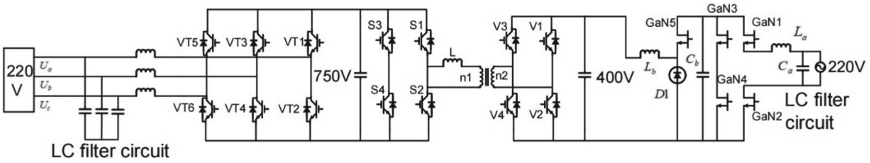

Fig. 3. Solid-state topology of building-powered energy routers.

(1) *Single-phase AC/DC converter*

Here, the single-phase AC/DC converter adopts the PFC with totem pole structure, which is a bidirectional AC/DC converter with high efficiency and high power density [10]. It has the following characteristics.

Based on GaN devices; Closed loop control, when working in the forward direction, the AC side is connected to a 220 V AC source, and the DC side is the 400 V DC bus of the energy router, requiring constant current output from the converter; When working in reverse, the DC side is connected to the 400 V DC bus of the energy router, and the AC side is connected to the 220 V power grid. The effective value of the output current of the converter is constant, and the current phase and frequency follow the input side signal.

L_a is 2 Mh, C_b is 190 Uf, L_b is 1 Mh, C_c is 90 Uf.

As shown in Fig. 4, 220 V AC rectification is generally around 311 V, so a secondary converter is required. The secondary converter used here is a buck circuit that can boost the voltage to 400 V, which can meet the standard of 400 V DC bus voltage in the energy router.

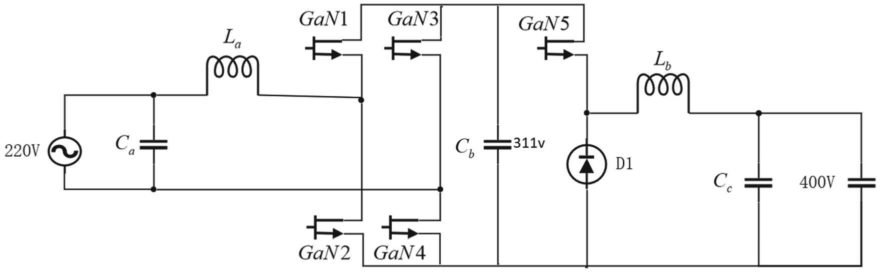

Fig. 4. PFC structure of totem pole structure.

(2) *Three phase DC/AC inverter.*

The three-phase DC/AC inverter adopts virtual synchronous machine pre-synchronization control technology to achieve parallel and off grid switching. This is the focus of this article's research, and simulation of the grid connection process is conducted in the following text.

In order to ensure that the energy router outputs the same waveform as the large power grid and reduce the impact losses generated during grid connection. The 750 V DC bus of the energy router is connected to the grid using pre-synchronized VSG control technology, which can ensure that the energy router can still achieve stable and offline operation in the event of system load increase or decrease or fluctuations [11].

The three-phase AC grid connection port of the energy router adopts a three-phase full bridge inverter, and the topology of the DC/AC AC port is shown in Fig. 5.

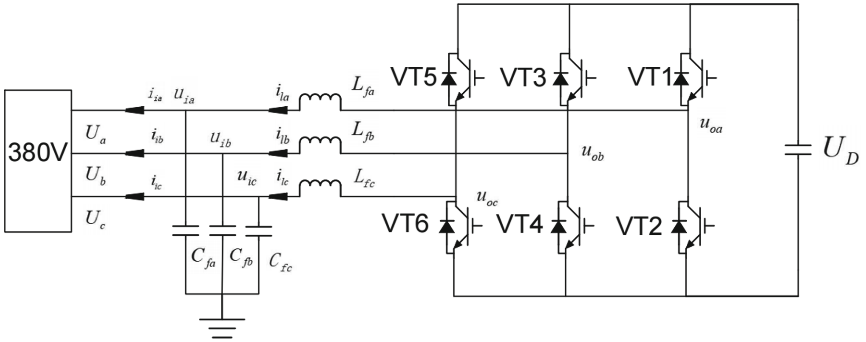

Fig. 5. Three-phase full-bridge inverter structure

As shown in Fig. 5, with the midpoint u_{d} as the reference potential, this topology can be seen as a combination of three single-phase half bridge inverters. The upper and lower switch tubes of the same bridge arm complement each other in making and breaking. When the upper tube VT1 of the A-phase bridge arm is connected, the lower tube VT4 is cut off; When VT4 is on, VT1 is off. When VT1 (D1) is conducting, node A is connected to the positive end of the DC power supply, $m_{\mathrm{ia}} = m_{\mathrm{d}}/2$; ; When T4 (D4) is conducting, node A is connected to the negative terminal of the DC power supply, $m_{\mathrm{ia}} = -u_{\mathrm{d}}/2$.

Similarly, points B and C also determine their potentials based on the conduction of the upper and lower tubes. The driving method for each bridge arm is 180° conductivity and 120° phase difference.

Among them, VT is IGBT, u_{ix}, i_{ix} (x = a, b, c) represents the output voltage and current of the inverter port; L_{fx}, C_{fx} (x = a, b, c) represents the system's filtering inductance and filtering capacitor, which are used to reduce the impact of various harmonics; 380 V represents the load connected to the grid or system.

3 Energy Router DC Bus Connected VSG Control Method

3.1 Virtual Synchronous Generator Modeling

The establishment of a virtual synchronous generator model involves knowledge points from three disciplines: power electronics technology, electrical engineering, and circuits [12]. This study combines traditional virtual synchronous generators. Generators generally have a multi order model. In order to simplify control and make it more practical, a second-order virtual synchronous generator model is established here. The virtual synchronous generator simulates the function of traditional synchronous generators achieving the same frequency on both sides of the grid during grid connection, which can achieve stable grid voltage during grid connection and reduce the impact of energy routers on grid stability during grid connection. The control block diagram of the virtual synchronous generator is shown in Fig. 6.

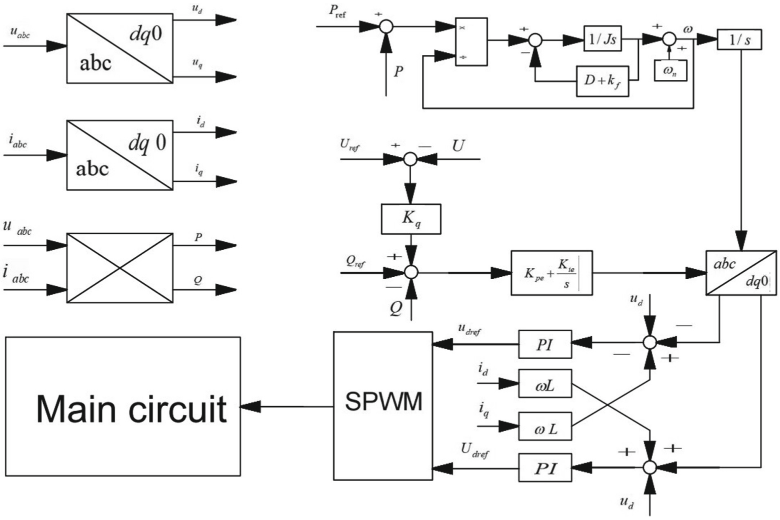

Fig. 6. Control block diagram of virtual synchronous machine

3.2 Virtual Stator Voltage Model

The reference source for the control principle of virtual synchronous generators is the ideal working principle of traditional synchronous generators, which have uniform air gaps and hidden pole machines, without distinguishing between direct axis and quadrature axis reactances. The stator voltage equation of an ideal synchronous generator is as follows:

$$\dot{U} = \dot{E}_0 - \mathrm{j}\dot{I}_{\mathrm{a}}X_S \tag{1}$$

Among them, there is a voltage drop in the excitation electromotive force and port voltage, which is generated by the armature resistance and synchronous reactance, and the resulting voltage drop is represented by $\mathrm{j}\dot{\mathrm{I}}_{\mathrm{a}}X_{\mathrm{S}}$. The excitation electromotive force is represented by $\dot{\mathrm{E}}_0$, and the port voltage is represented by $\dot{\mathrm{U}}$ express.

T The stator voltage control block diagram can be obtained from the stator voltage equation, and it can be seen from Fig. 7 that the stator voltage link can receive the signal output by the rotor mechanical link and the virtual excitation link, and generate a reference voltage input to the PWM signal generator. The simulation diagram of the stator voltage link is shown in Fig. 12.

3.3 Virtual Rotor Mechanical Model

The rotor model of an ideal synchronous generator is shown in Fig. 7.

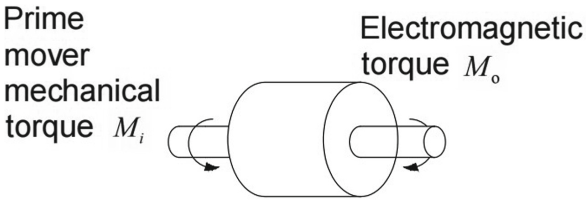

Fig. 7. Synchronous generator rotor model

Here, we need to analyze the force acting on the rotor during rotation, which is affected by the mechanical torque of the prime mover and the electromagnetic torque generated by the rotor itself due to the influence of stator current. The rotor equation is as follows:

$$M_{\mathrm{i}} - M_{\mathrm{o}} = J\frac{d\omega_{\mathrm{m}}}{d\mathrm{t}} + \frac{D}{\omega_{\mathrm{m}}}\left(\omega_{\mathrm{m}} - \omega_{\mathrm{g}}\right) \tag{2}$$

The physical meaning of the formula is that the mechanical torque of the prime mover minus the electromagnetic torque is equal to the moment of inertia multiplied by angular acceleration plus the damping prime mover mechanical torque, which is expressed in M_{i}, and the electromagnetic torque of the rotor is expressed in M_{o}. The moment of inertia is represented by J, the damping coefficient is represented by D, and the grid angular frequency is represented by ω_0 represents.

The corresponding rotor mechanical equation can be obtained by converting the torque success rate, as shown in the following formula.

$$P_{\mathrm{m}} - P_e = J\omega\frac{d\omega}{d\mathrm{t}} + D(\omega - \omega_{\mathrm{g}}) \tag{3}$$

According to the rotor mechanical equation, the rotor control block diagram can be obtained, from Fig. 7, the rotor mechanical link generates the output frequency and initial phase through the control of active-frequency, the output frequency generated by the rotor mechanical link is multiplied by the excitation electromotive force amplitude generated by the phase angle and stator voltage link to obtain a reference wave, and then the command value of the inverter output port PCC is generated through the stator voltage link, and then the corresponding pulse is generated through the voltage and current double closed-loop SPWM, which is output to the inverter to produce a waveform similar to the characteristics of the power grid [13].

3.4 Virtual Excitation Link Model

The control block diagram of the virtual excitation link is shown in Fig. 8.

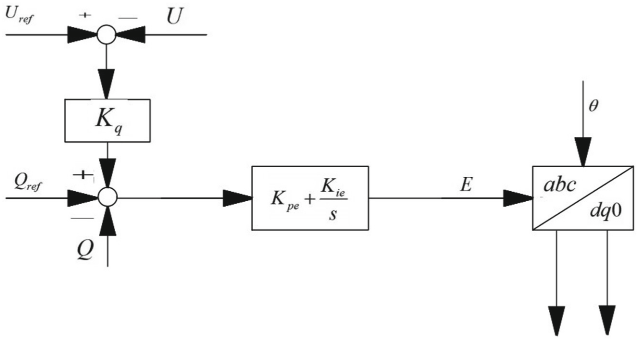

Fig. 8. Control block diagram of virtual excitation link

It can be seen from the control block diagram that the virtual excitation link generates the excitation electromotive force through reactive-voltage control. The input to the virtual stage is the difference between the reactive power reference value minus the reactive feedback value plus the voltage droop control coefficient multiplied by the voltage reference value and the voltage feedback value.

The amplitude generated by the virtual excitation link and the frequency and initial phase generated by the rotor mechanical link synthesize the reference wave, and then through the stator voltage link, the command value at the output port of the inverter is obtained, and then the pulse input to the inverter is generated by the voltage and current double closed loop below, and finally the characteristics of the inverter are the demand characteristics.

3.5 Voltage and Current Dual Closed-Loop Control

Figure 9 shows the voltage and current dual closed-loop control block diagram.

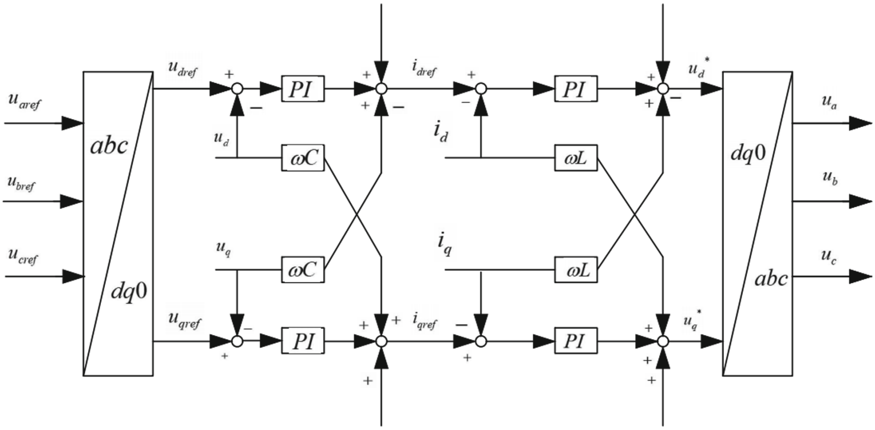

Fig. 9. Voltage and current dual closed loop control block diagram

Where $u_{(\text{aref,bref,cref})}$ represents the three-phase reference voltage, ω is the output angular frequency of the inverter, derived from the virtual generator algorithm equation. i_q and i_d are the d_q components of the inverter output current, u_q and u_d are the d_q components of the inverter output current, u_d* and u_q* represent the d_q components of the generated voltage modulation signal, L and C represent the filtering inductance and filtering capacitance. The voltage and current dual closed-loop circuit generates modulation waves and sends them to the inverter to ultimately generate an ideal waveform.

3.6 Inverter Grid Connection Circuit Structure

The DC bus voltage is converted into AC voltage through an inverter controlled by SPWM, and then integrated into the power grid after LC filtering. The circuit structure is shown in Fig. 10.

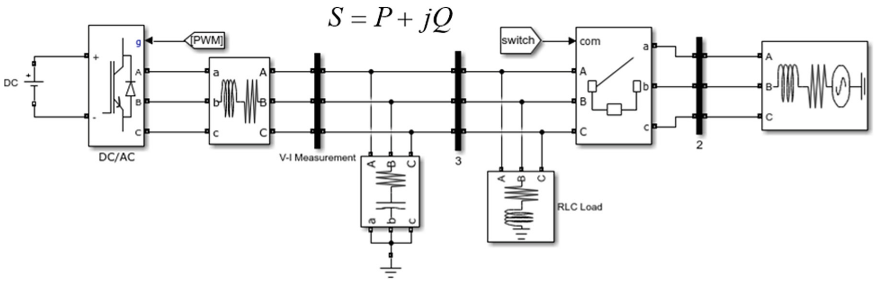

Fig. 10. Main circuit diagram

The apparent power of VSG is represented by S, the voltage of the inverter output port, i.e. the grid voltage, is represented by UL, and the current of each phase is represented by i_a, i_b, $i_\mathrm{c} =$ I represents, and the expressions for P, Q, and I are shown in Fig. 10.

$$\begin{cases} P = \dfrac{E_0 U_\mathrm{i}}{Z}\cos(\alpha - \theta_0) - \dfrac{U_i^2}{Z}\cos\alpha \\ Q = \dfrac{E_0 U_\mathrm{i}}{Z}\sin(\alpha - \theta_0) - \dfrac{U_i^2}{Z}\sin\alpha \\ Z = \sqrt{(\omega L_t)^2 + (R_t)^2} \\ \alpha = \arctan\left(\dfrac{\omega L_t}{R_t}\right) \end{cases} \tag{4}$$

$$i_a, i_b, i_c \text{ Corresponding line current } I = \frac{E_0 \angle \theta_0 - U_i \angle 0^\circ}{R_\mathrm{t} + j\omega L_t} \tag{5}$$

Among them, the circuit properties are expressed by Z, and E_0 and θ_0 can be determined by giving PQ, so that the power transmitted by the inverter and the power of the grid can be matched, and finally the controllable and low-loss VSG-controlled DC inverter can be stably connected to the grid.

4 Simulation Analysis of Grid-Connected Pre-synchronous VSG Control of Energy Router

The standard for measuring the performance of pre-synchronous VSG control of building energy routers is whether the energy output by the inverter can be integrated into the grid to control the power disturbance to achieve safe grid connection.

4.1 Simulation Model Establishment

This article establishes a simulation model for the grid connection operation of an energy router, which integrates 750 V DC power into the grid after being inverted by an inverter controlled by the VSG algorithm.

In the simulation built, the VSG algorithm control simulation diagram is shown in Fig. 11.

4.2 Simulation of Grid-Connected Mode Under the Control of Building Energy Router VSG

Next, analyze the grid connection simulation under normal conditions, and the main simulation parameters of the inverter are shown in Table 1.

The grid-connected signal generated after automatic pre-synchronization judgment conditions. After VSG pre-synchronization, it will automatically connect to the grid at about 0.29 S. Figure 12 shows the voltage amplitude pre-synchronization process, which reaches the grid-connected condition in about 0.29 s, and then automatically connects to the grid.

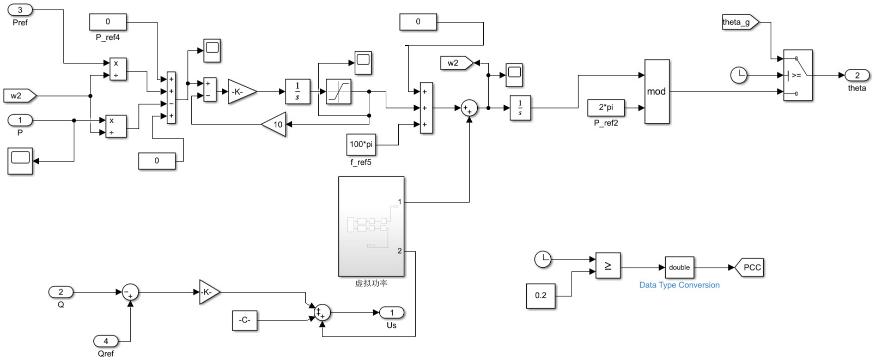

Fig. 11. VSG algorithm control simulation diagram

Table 1. Simulation parameters of three-phase bidirectional DC/AC converter.

Parameter	Numerical value
Rated power P(W)	25
The inverter measures the filter inductor Lm/Mh	7
Load measurement filter inductor Lg/Mh	1.9
Filter capacitors Ct/F	24e-6
Damping resistance Ro/Ω	4e-3
AC output line voltage (V)	220
Valid values U_{abc} (V)	220
Output frequency f(Hz)	50
Factor	0.8
Switching frequency f(Hz)	4000
Damping factor D	50
Inertia J(kg m/s^2)	0.15
Stator armature resistance $Ro/m\Omega$	12
Stator armature inductor L/Mh	0.06

Figure 13 is the system grid-connected frequency waveform diagram, the premise that the energy router and the large power grid can run smoothly is that the waveforms of the two should be consistent, as can be seen from the figure, the system starts to connect and close the grid in 0.29 s, and after the VSG control pre-synchronization, it is officially connected to the grid in about 0.3 s. At this time, the output frequency of the system and the frequency of the power grid have basically been consistent, which meets the requirements of the power grid for the power quality output of the inverter, and it can be seen from the simulation waveform that the frequency after the completion of grid

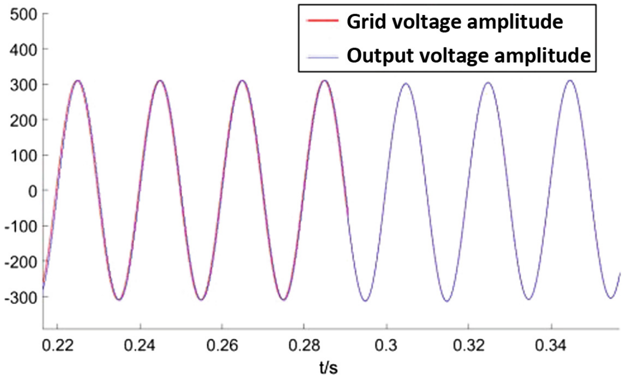

Fig. 12. Voltage amplitude pre-synchronization process

connection has been stable at 50 ± 0.05 Hz, which greatly improves the stability of the DC bus connection of the energy router.

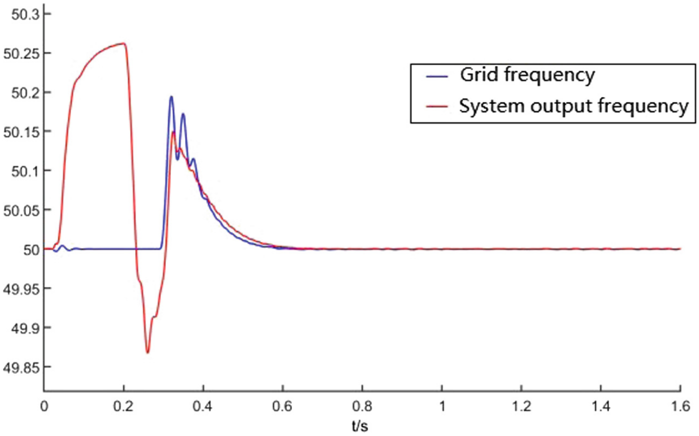

Fig. 13. Grid-connected frequency waveform

Figure 14 represents the three-phase voltage waveform output by the inverter, and it can be seen from the simulation results that the voltage fluctuation is stable, which is about 12% lower than the voltage fluctuation of the traditional grid-connected method.

Figure 15 represents the waveform of the three-phase current output by the inverter.

From the simulation results, it can be seen that the current overshoot under VSG control is small, the adjustment time is relatively short, and the virtual synchronous generator has the functions of primary frequency regulation and active power following. It can maintain the stability of the grid-connected system.

Figure 16 represents the active and reactive waveform output by the inverter.

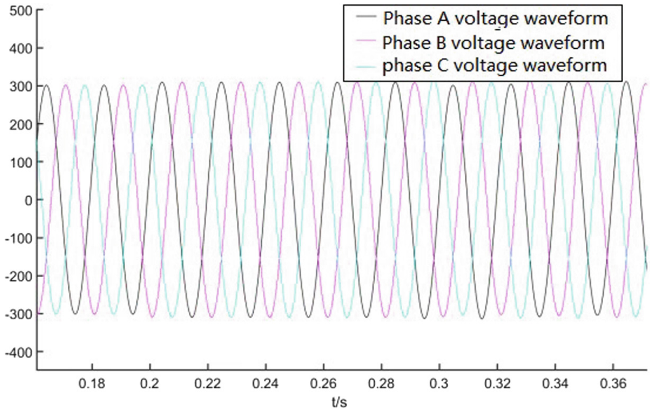

Fig. 14. Grid-connected voltage simulation diagram

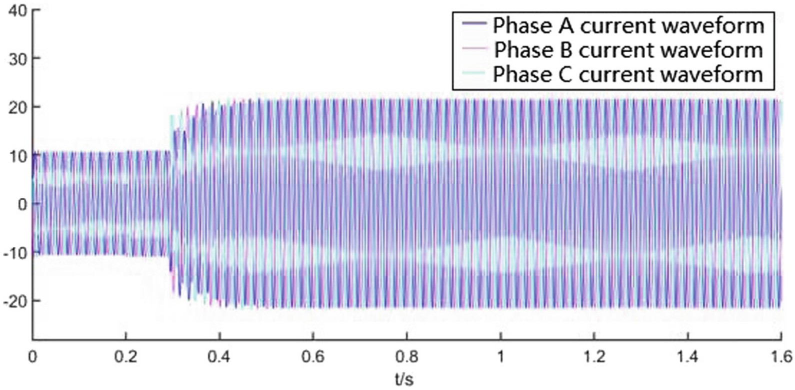

Fig. 15. Grid-connected current simulation.

From the simulation results, it can be seen that the active power rises to 5000 W during the grid connection process, and the reactive power can always be maintained at 0 W, ensuring the stability of the system.

4.3 Sag Control Simulation Comparative Analysis

The inertia and damping of the power system largely determine its stability, although the traditional droop control can make the microgrid automatically adjust the power distribution and find a stable operation point whether it is connected to the grid or when the island is running, but the simple sag characteristics ignore the inertia and damping of the system, which reduces the stability of the system to a certain extent [14].

In this paper, the grid connection under droop control is also simulated and compared with VSG control. Figure 17 shows the waveform of a phase current output by the system under droop control.

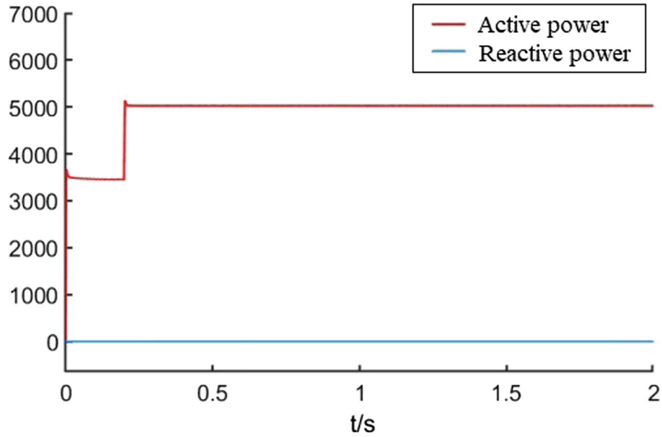

Fig. 16. The active-dead waveform output by the inverter

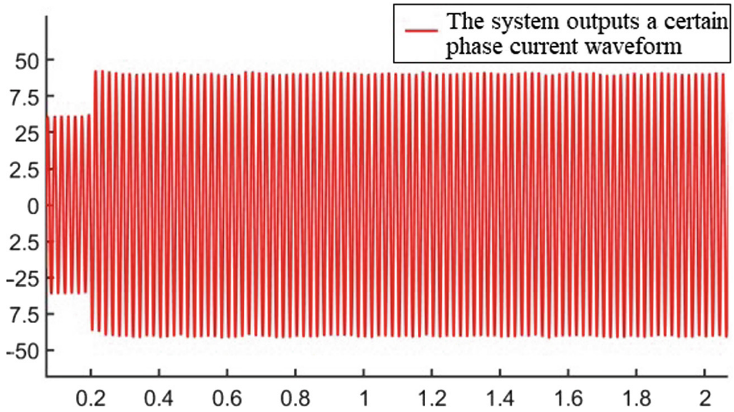

Fig. 17. A phase current waveform output by the system

In order to more, here the system output of a certain phase current waveform for analysis, Figure 15 is the grid-connected current simulation waveform under droop control, from the figure it can be seen that 0.2 gives the grid-connected control signal, directly connected to the grid, and does not go through the pre-synchronization link, at 0.2 S caused the current waveform offset, and the current overshoot compared to the current overshoot under VSG control increased, causing a certain degree of impact on the large power grid, obviously VSG control is more stable than the droop control when connected to the grid.

Figure 18 shows the active reactive waveform after grid connection under droop control.

It can be seen from the simulation results that the droop control reactive power is still about 700 W, compared with the reactive power waveform under VSG control, it is obvious that the use of VSG control can make the system more stable. It can be seen

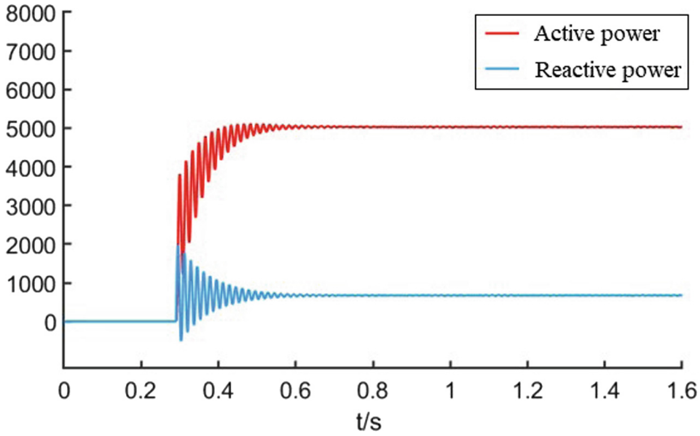

Fig. 18. Active and reactive waveform

that compared with the sag control, VSG control has less impact on the large power grid when connected to the grid, and can maintain the stable operation of the power grid after grid connection.

5 Conclusion

In this paper, a building energy router topology and DC bus grid-connected pre-synchronous VSG control method are designed, which are summarized as follows:

1. Around the building energy router, its application scenarios and topology are expounded, which ensures the rationality and practicality of the energy router topology.
2. Aiming at the stability of DC bus connection of building energy routers, a pre-synchronous VSG control method is designed to reduce the voltage and current impact of common coupling points when connected to the grid.
3. The simulation model of energy router grid connection under pre-synchronous VSG control established by MATLAB/simulink, and comparative analysis with droop control, verify the correctness of the proposed energy router topology and grid connection mode.

Acknowledgement. This article is supported by the Jilin Science and Technology Development Plan(20220101229JC).

References

1. China Building Energy Consumption Research Report 2020. Build. Energy Efficiency (Chinese and English) **49**(02), 1–6 (2021)
2. XuGongsan: Shandong Ind. Technol. **222**(16), 149 (2016)

3. Wang, J, Li Y., Lu Z., et al.: Research on local energy Internet based on energy switch and router. Proc. CSEE **36**(13), 3433–3439+3362 (2016)s
4. Huang, K., Li, Y., Zhang, X., et al.: Research on power control strategy of household-level electric power router based on hybrid energy storage droop control. Prot. Control Mod. Power Syst. **6**, 13 (2021)
5. Shi, L., Liu, G.: Research on switching control strategy of multi-LAN port energy router. J. Electric Power Sci. Technol. **34**(02), 84–90 (2019)
6. Zhou, L.: Research on Circuit Topology and Control Strategy of Small Energy Router. University of Electronic Science and Technology of China (2017)
7. Wei, L., Liu, T., Liu, L., et al.: Research on structure and control strategy of new multi-terminal energy router. J Taiyuan Univer. Scie. Technol. **41**(03), 183–189 (2020)
8. Pan, B., Wang, H., Zhang, Y., Gui, X., Wan, Y.: Research on reconstruction strategy of active distribution network with distributed power source. Power Syst. Protect. Control **48**(15), 102–107 (2020)
9. Chen, H.: Development of 5KW Household Multi-port Energy Router. Nanjing University of Aeronautics and Astronautics (2020)
10. Li, T.: Research on Topology and Control Strategy of Multi-port Building Power Supply Energy Router. Harbin Institute of Technology (2021)
11. Chen, M., Li, Y., Tian, H., et al.: Microgrid application technology of household energy router. Solar Energy **285**(01), 58–61 (2018)
12. Liu, X., Guo, Z., Jia, J., et al.: Stability analysis and virtual impedance design of microgrid VSG based on single-input single-output equivalent sequential impedance. Trans. China Electrotech. Soc. 1–18[2023–05–11]
13. Ma, C.: Application of VSG Technology in Dual DC Link Energy Router. Shanxi University (2021). https://doi.org/10.27284/d.cnki.gsxiu.2021.000288
14. Yang, X., Zhang, J.: Coordinated control strategy of AC/DC multi-port household energy router. Electric. Eng. **23**(03), 31–38 (2022)
15. Shen, Y., Huang, X., Zhou, R.: Rational application of low-voltage DC distribution technology in civil buildings. Build. Electric. **38**(07), 9–14 (2019)

Correction of Wind Power Prediction Error Under the Extreme Weather Based on K-nearest Neighbor Algorithm

Wenjie Ye[1,2,3](✉), Gang Liu[1,2,3], Dongmei Yang[1,2,3], Yiheng Liang[1,2,3], Yize Yang[1,2,3], Chenghong Tang[1,2,3], and Yizhi Chen[1,2,3]

[1] State Key Laboratory of Smart Grid Protection and Control, Nanjing 211106, China
wanghui841013@ccit.edu.cn
[2] Nari Group Corporation (State Grid Electric Power Research Institute), Nanjing 211106, China
[3] NARI Technology Development Co., Ltd, Nanjing 211106, China

Abstract. Extreme weather, such as cold waves and frosts, can significantly impact the output of wind farms. To address this issue, this paper proposes a short-term power prediction and correction method suitable for wind farms during extreme weather, based on the K-nearest neighbor algorithm and multiple linear regression model. By verifying that wind power output is affected by wind speed, temperature, humidity, wind power kurtosis, and other factors, the K-nearest neighbor algorithm is used to obtain the sample set of similar days on the day to be measured. The regression model of influencing factors and output errors is established to improve the power prediction accuracy. A wind farm in northwest China is used as a test example to verify the effectiveness of the output correction method.

Keywords: Extreme weather · Wind power prediction · K-nearest neighbour algorithm

1 Introduction

Under the goals of carbon peaking and carbon neutrality, the key task is to construct a power system dominated by new energy. Photovoltaic and wind power are two rapidly developing representations of new energy over the last decade, and are expected to replace conventional energy sources [1]. However, the randomness and fluctuating nature of new energy not only results in substantial defects in the reliability and stability of the power system but also diminishes the accommodation of new energy. Therefore, reserving capacity based on new energy power prediction at different time scales is an effective measure to solve this problem. In recent years, extreme weather events such as cold waves, frosts, and freezing rain have occurred frequently in China, greatly reducing the accuracy of new energy power prediction. With the significant expansion of wind farms, the impact of extreme weather will be further exacerbated [2]. It is urgent to analyze the factors that limit wind power output and take countermeasures in advance to address these problems.

Y. Xue et al. (Eds.): PMF 2023, LNEE 1129, pp. 103–111, 2024.
https://doi.org/10.1007/978-981-99-9251-5_8

In extreme weather conditions, such as cold waves, the ice load can cause changes to the geometrical shape of wind turbine blades, ultimately leading to a reduction in lift and drag. This decrease in aerodynamic performance results in a reduced wind utilization coefficient and ultimately affects the output of wind turbines [3, 4]. Sensors are fundamental to detecting changes in wind power output. Jin S has introduced the development and application of several types of electric weather sensing and proposed an application framework for sensing monitoring [5]. By analyzing meteorological factors, utilizing fuzzy recognition of data as input for a neural network can accurately predict meteorological conditions [6]. To predict new energy power output during extreme weather, the distance analysis method can be used to effectively identify the correlation between meteorological factors and wind power output. By combining this approach with SOM clustering to categorize sample types, a prediction model based on weather-type clustering recognition can be established [7]. In Ref. [8], the relationship between average output under different weather conditions is mapped to a weather type index, which serves as the input for a neural network to obtain an accurate correlation between meteorological factors and wind power output. Additionally, an extraction model for holiday power load characteristics is proposed based on historical load and meteorological data [9]. Currently, predicting wind power output during extreme weather conditions has become a key area of focus. However, traditional algorithms are not effective in correcting power prediction error during extreme weather. Therefore, there is a need to improve the accuracy of power prediction in extreme weather conditions.

This paper presents a novel approach for correcting short-term power prediction error in wind farms in extreme weather conditions. The proposed method is based on the K-nearest neighbor algorithm and multiple linear regression model. By analyzing the correlation factors of power prediction error, a regression model and a sample set of similar days were established. Additionally, the least square method was utilized to estimate the regression model parameters and modify the power prediction.

2 Methodology

Wind power prediction error refers to the difference between predicted and measured wind power during a specific period [10]. The proposed method for correcting these errors and related parameters using the K-nearest neighbor algorithm is outlined as follows:

(1) Obtain historical data related to extreme weather, including historical meteorological forecast data, historical power prediction data, and historical measured power data.
(2) Utilize the Pearson correlation coefficient method to analyze the correlation factors of power prediction error in extreme weather conditions.
(3) Utilize the K-nearest neighbor algorithm to select historical data strongly correlated with the prediction days. Additionally, establish a regression model for power prediction error and correlation factors using the multiple linear regression method.
(4) Calculate the multiple linear regression parameters and obtain the power prediction error for the prediction days based on their meteorological data.

3 Influencing Factors and Correction Models

3.1 Analysis of Influencing Factors

Extreme weather conditions can have a significant impact on wind power output. To illustrate this, this paper examines a wind farm located in northwest China, and analyzes the effects of meteorological factors such as wind speed, temperature, humidity, and power fluctuation on power prediction error. Specifically, the study focuses on the scenarios of gale, icing, and low temperature during cold wave weather.

The correlation between impact factors and prediction errors can be described using the Pearson correlation coefficient, as follows:

$$\mathrm{r} = \frac{\sum_{i=1}^{n}(x_i - \overline{x})(y_i - \overline{y})}{\sqrt{\sum_{i=1}^{n}(x_i - \overline{x})^2}\sqrt{\sum_{i=1}^{n}(y_i - \overline{y})^2}} \tag{1}$$

3.1.1 The Influence of Wind Speed Cubic on Prediction Error

Wind poweris determined by wind speed v, wind utilization coefficient C_p and other factors, which is related to the cubic of wind speed [11].

$$\mathrm{P} = 0.5\rho AC_p(\lambda, \beta)v^3 \tag{2}$$

By analyzing historical data from the wind farm, the study examined the impact of wind speed on prediction errors in extreme weather conditions. Figure 1 depicts the relationship between power prediction error and the cubic of wind speed. The correlation coefficient of 0.7107 indicates a strong correlation between the cubic of wind speed and power prediction error.

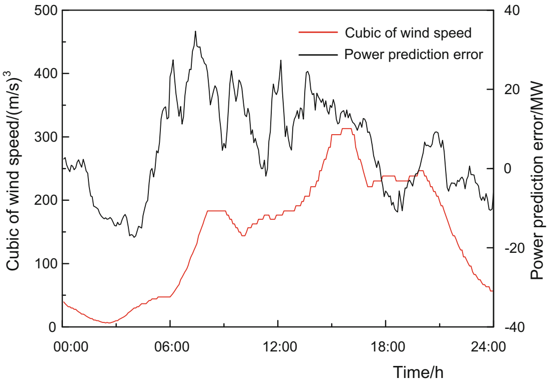

Fig. 1. The relation curve between wind power prediction error and wind speed cubic

3.1.2 The Effect of Temperature on Prediction Error

Cold waves, frost and so on which are forms of extreme weather, are often accompanied by drops in temperature. During such conditions, wind turbine blades and sensing equipment, such as engine room anemometers, are prone to large-scale icing. However, the accumulation of ice on blades can lead to unbalanced blade loads or changes in aerodynamic characteristics. Additionally, ice accumulation on anemometers in the engine room can cause the detected wind speed to be lower than the actual wind speed, resulting in unit shutdowns [12]. Temperature also has a significant impact on prediction errors. Figure 2 illustrates the relationship between wind power prediction error and temperature, with a correlation coefficient of 0.45589, indicating a moderate correlation between wind power prediction error and temperature.

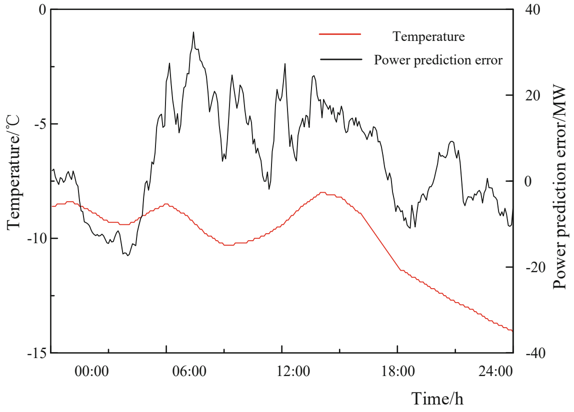

Fig. 2. The relation curve between wind power prediction error and temperature

3.1.3 Influence of Relative Humidity on Prediction Error

Extreme weather conditions such as cold waves and frost can cause ice cover on wind turbines, often requiring a combination of high humidity environments. Consequently, in extreme weather conditions such as cold waves and frost, relative humidity has a significant impact on wind power prediction error. Figure 3 displays the relationship between wind power prediction error and relative humidity, with a correlation coefficient of 0.6054, indicating a strong correlation between wind power prediction error and relative humidity.

3.1.4 The Influence of Power Fluctuation on Prediction Errors

Kurtosis, also referred to as the peak coefficient, is a statistical measure that represents the degree of peakedness of a curve at its average value. It reflects the sharpness of the peak [13] and can be defined as follows:

$$\mathrm{K} = \frac{\sum_{i=1}^{n} (X_i - \overline{X})^4}{(n-1)s^4} \tag{3}$$

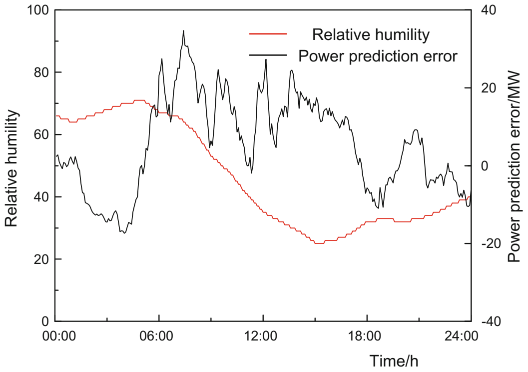

Fig. 3. The relation curve between wind power prediction error and relative humidity

where X_i is the sample, $\overline{X}$ is the sample mean, and s is the standard deviation. Figure 4 displays the relationship between wind power prediction error and wind power kurtosis, with a correlation coefficient of 0.3093, indicating a moderate correlation between wind power prediction error and wind power kurtosis.

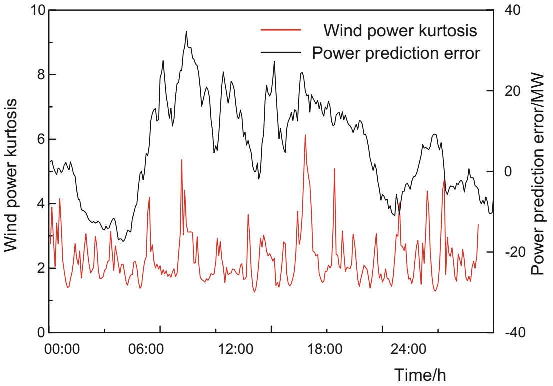

Fig. 4. The relation curve between wind power prediction error and wind power kurtosis

3.2 K-Nearest Neighbor Optimization Algorithm

This article filters similar days based on curve features to find power curves that are similar to the target power curve features. Initially, various indexes were defined to describe the curve characteristics, and the K-nearest neighbor algorithm was utilized to calculate the feature distance. The similarity between the predicted and historical daily power curves was judged by comparing the feature distance. The comprehensive feature vector $F = [P_{max}, P_{max, hour}, P_{avg}, Q]$ is defined to describe a daily power curve. P_{max} is the maximum daily fluctuation; $P_{max, hour}$ is the maximum intra-day hourly fluctuation; P_{avg} is the daily average fluctuation; Q is daily power generation.

Daily maximum fluctuation P_{max} refers to the maximum peak valley difference of power within 24 h; $\Delta P_{max,\ hour}$ is the maximum hourly fluctuation within a day, the frequency of power data is 5 min.

The static coupling model of electric refrigeration is shown in Eq. (4).

$$\begin{aligned} &\Delta P_{\text{max,hour}} = \max\{\max[p(i)] - \min[p(i)]\} \\ &i = n, 2n...., 12n; \quad n \in (1, 24) \end{aligned} \tag{4}$$

where *p(i)* is the ith time series power point on the daily power curve.

Daily average fluctuation ΔP_{avg} is average value of the peak-valley power difference in an hour of the daily power.

$$\begin{aligned} &\Delta P_{\text{avg}} = \text{avg}\{\max[p(i)] - \min[p(i)]\} \\ &i = n, 2n...., 12n; \quad n \in (1, 24) \end{aligned} \tag{5}$$

Normalizing the feature vector, F_1 and F_2 are the daily predicted and historical curves respectively, and the characteristic distance L_{12} is the Euclidean distance of the comprehensive feature vector are defined as:

$$\begin{aligned} L_{12} = [(\mathrm{P}_{1,\max} - \mathrm{P}_{2,\max})^2 + (\Delta P_{1,\text{max,hour}} - \Delta P_{2,\text{max,hour}})^2 \\ + (\Delta P_{1,\text{avg}} - \Delta P_{2,\text{avg}})^2 + (\mathrm{Q}_1 \text{ - } \mathrm{Q}_2)^2] \end{aligned} \tag{6}$$

The feature vector that is most similar to the target feature vector can be selected by sorting the feature distance from small to large.

3.3 Multiple Linear Regression Error Correction Model

Multiple linear regression method is used to establish the prediction error estimation model. It is to establish the corresponding relationship between prediction error and influencing factors based on historical data, and calculate the parameters to predict future error values. Based on the above research, wind power prediction influencing factors during extreme weather include wind speed cubic, temperature, relative humidity, and wind power kurtosis. In multiple linear regression analysis, the recorded variable (prediction error) is Y, and the set of influencing factors is $X = \{x_1, x_2, \ldots, x_p\}$. Where p is the number of influencing factors, n is the sample size, the matrix is defined as:

$$\mathrm{x} = \begin{bmatrix} x_{11} & x_{12} & \ldots & x_{1p} \\ x_{21} & x_{21} & \ldots & x_{2p} \\ \ldots & \ldots & \ldots & \ldots \\ x_{n1} & x_{n2} & \ldots & xp \end{bmatrix}_{n \times p} \quad \mathrm{y} = \begin{bmatrix} y_1 \\ y_2 \\ \ldots \\ y_n \end{bmatrix}_{1 \times n} \tag{7}$$

The multiple linear regression model can be expressed as:

$$\mathrm{Y} = XB \tag{8}$$

Select K nearest neighbor algorithm to obtain *multiple* datas in historical datas similar to prediction datas during extreme weather, and the prediction error E, wind speed cubic

V, wind power kurtosis k, temperature T and relative humidity H in each period are calculated respectively. Then $Y = E$, $X = [V, k, T, H]$, B is calculated according to the equation. Finally, according to the weather forecast and power prediction, the prediction error E is solved to correct the power prediction.

4 Case Analysis

This paper takes the extreme weather datas of a wind farm in northwest China in 2018–2022 as a sample. The wind farm capacity was 200 MW, with a time interval of 5 min. Firstly, identify and process the wind farm's abnormal data. Secondly, confirm the extreme weather type of prediction day and obtain similar daily data by K nearest neighbor optimization algorithm. Finally, curve fitting each parameter respectively, and combined with meteorological data and conventional power prediction results, the prediction error was obtained, then correct the prediction results (Table 1).

Table 1. Statistical table of extreme weather in 2018–2022 for a wind farm in Northwest China

Date of occurrence	End date	Extreme weather type
2018/1/9	2018/1/10	Frost
2018/1/21	2018/1/23	Cold wave
…	…	…
2022/6/28	2022/6/28	Frost
…	…	…
2022/11/29	2022/12/1	Cold wave

Taking December 28, 2020 as the prediction day, Fig. 5 shows the comparison between the wind power prediction value before and after correction and the measured power.

Table 2 shows the statistical results of the wind power prediction before and after correction. The root mean square error RMSE is calculated as follows:

$$\mathrm{RMSE} = \sqrt{\frac{1}{n}\sum_{k=1}^{n}\left(\frac{P_{m,k} - P_{p,k}}{C_k}\right)^2} \tag{9}$$

where $P_{m,\,k}$ is the actual average power during period k; $P_{p,\,k}$ is the predicted average power during period k; C_k is the total boot capacity during period k; n is the total number of periods in the statistics time range.

Figure 5 and Table 2 demonstrate that the proposed method for modifying wind power predictions based on the K-nearest neighbor algorithm and multiple linear regression has significantly improved prediction accuracy. The modified power curve is consistent with the measured power curve, and the root mean square error (RMSE) has been reduced by 3.5%.

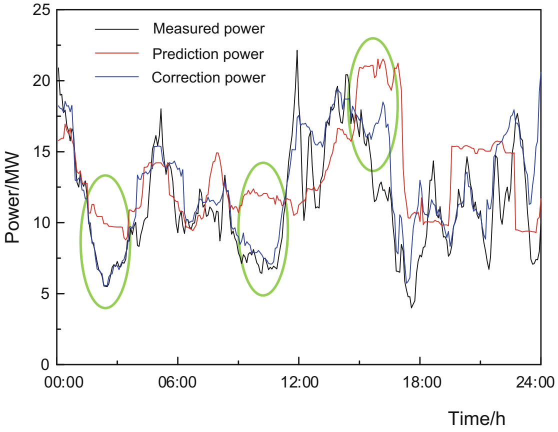

Fig. 5. The relation curve between wind power prediction error and wind power kurtosis

Table 2. Root mean square error and correlation coefficient of predicted power before and after correction

	RMSE	Correlation coefficient *r*
Before correction	0.089	0.402
After correction	0.054	0.814

5 Conclusion

This paper proposes a novel approach for correcting short-term power predictions for wind farms in extreme weather conditions. The method leverages the K-nearest neighbor algorithm and multiple linear regression model, and identifies key factors such as wind speed, temperature, humidity, and wind power kurtosis that affect wind power output during cold waves. Specifically, the K-nearest neighbor algorithm is utilized to identify a sample set of similar days on the day of measurement, and a regression model is established to examine the relationship between the influencing factors and output errors. This approach has been demonstrated to improve the accuracy of power predictions and has practical implications for optimizing the performance and reliability of wind power systems in extreme weather conditions.The conclusions are as follows:

(1) Based on a large amount of measured datas from wind farms in the northwest region, the prediction error of wind power in extreme weather conditions such as cold waves and frost to be influenced by factors such as wind speed cubic, temperature, humidity, and wind power kurtosis is analyzed;

(2) The power prediction error model and influencing factor model are established by using multiple linear regression method,. The K-nearest neighbor algorithm was applied to obtain a sample set of similar days on the test day, solve the parameters, and correct the predicted results.

(3) The prediction error correction model was verified using actual data, resulting in a 3.5% reduction in root mean square error (RMSE) compared to the uncorrected predictions.

In general, the wind power prediction error model based on the K-nearest neighbor algorithm effectively improves prediction accuracy, which is significant in ensuring the reliability and stability of power systems and facilitating the integration of new energy sources.

Acknowledgment. This research is supported by State Grid Corporation of China (No. 5108-202218280A-2–68-XG).

References

1. Lin, C., Chen, C., Bie, C., et al.: Post-disaster load restoration method for urban distribution network with dynamic uncertainty and frequency-voltage control. Autom. Electric Power Syst. **46**(17), 56–64 (2022)
2. Cong, F., Shi, P., Fang, J., et al.: Advances and prospects of spatiotemporal pattern variation of extreme precipitation and its affecting factors under the background of global climate change. J. Catastrophol. **32**(2), 165–174 (2017)
3. Virk, M.S., Homola, M.C., Nicklasson, P.J.: Effect of rime ice accretion on aerodynamic characteristics of wind turbine blade profiles. Wind Eng. **34**(2), 207–218 (2010)
4. Zanon, A., De Gennaro, M., Kühnelt, H.: Wind energy harnessing of the NREL 5 MW reference wind turbine in icing conditions under different operational strategies. Renew. Energy **115**, 760–772 (2018)
5. Jin, S., Chi, Y., Wang, B., et al.: Application research of meteorological sensing and monitoring technology in power grid. Electric Power Inf. Commun. Technol. **4**, 84–90 (2020)
6. Chen, C., Duan, S., Cai, T., et al.: Short-term photovoltaic generation forecasting system based on fuzzy recognition. Trans. China Electrotech. Soc. **26**(7), 83–89 (2011)
7. Dai, Q., Duan, S., Cai, T., et al.: Short-term PV generation system forecasting model without irradiation based on weather type clustering. Proc. CSEE **31**(34), 28–35 (2011)
8. Yuan, X., Shi, J., Xu, J.: Short-term power forecasting for photovoltaic generation considering weather type index. Proc. CSEE **33**(34), 57–64 (2013)
9. Yang, B., Dou, Q., Bai, X., et al.: Holidays and extreme weather power load feature extraction model. Heilongjiang Electric Power **6**, 409–412 (2009)
10. Wu, X., Lu, Z., Qiao, Y.: Estimation of day-ahead wind power distribution based on power forecast error correction. Yunnan Electric Power **47**(3), 6 (2019)
11. Yang, P., Hu, Q., Fu, P., et al.: Wind-farm equivalent study considering the utilization factor of wind energy. China Sci. Paper **11**(23), 2711–2715 (2016)
12. Shu, L., Ren, X., Hu, Q., et al.: Influences of environmental parameters on icing characteristics and output power of small wind turbine. Proc. CSEE **36**(21), 6 (2016)
13. Joanes, D.N., Gill, C.A.: Comparing measures of sample skewness and kurtosis. J. Royal Stat. Soc.: Ser. D (The Statistician) **47**(1), 183–189 (1998)

Research on Fault Characteristics of DFIG Wind Farm with Flexible DC Integration

Fei Mo(✉), Wen Gu, Jie Ji, Lei Guan, and Jiaxing Huang

Jiangsu Frontier Electric Technology Co., LTD., Jiangning District, Nanjing 211102, China
799620947@qq.com

Abstract. At present, China's offshore wind power generation technology has a lot of room for development. As the offshore distance of offshore wind farms grows, the traditional AC integration approach has gradually been replaced by the flexible DC transmission integration approach. The difference from the traditional AC integration approach is that there are a multitude of power electronic devices in the VSC-HVDC system, which makes the fault characteristics of the system greatly changed. This paper mainly studies the fault properties of doubly-fed induction generator (DFIG) with flexible DC integration. Firstly, the topology and control strategy of DFIG Wind Farm with flexible DC integration are analyzed, and a mathematical model of the system control part is established. Secondly, the DFIG short-circuit current is calculated, and the factors affecting the size of the short-circuit current are found through analysis. Finally, the fault characteristics are analyzed by building a DFIG Wind Farm model with flexible DC integration on the PSCAD/EMTDC simulation platform.

Keywords: Flexible DC transmission technology · Doubly-fed induction generator (DFIG) · Fault characteristics · Electromagnetic transient simulation

1 Introduction

With the worsening of environmental degradation and energy scarcity, carbon neutrality and carbon peak were written into the government's report, building a model of power system with abundant sustainable energy is one of the key measures to attain the goal of shifting to a clean and low-carbon electricity. One of the most established and promising technological methods of producing new energy power among them is wind power generation [1–3]. Offshore wind energy is rich in resources, and offshore wind power generation still has great potential for development [4, 5].

Offshore wind farms are usually far from land. At this time, the power losses caused by long-distance and large-capacity transmission must be considered. As the scale of wind farm projects and offshore distances continue to rise, the prevailing trend for the future development of grid-connected wind farms is the utilization of flexible DC transmission technique, i.e. the voltage-sourced converter based HVDC (VSC-HVDC) [6, 7]. Compared to high-voltage AC transmission technology, flexible DC transmission technology has the advantages of long transmission distance, low power loss, and low

Y. Xue et al. (Eds.): PMF 2023, LNEE 1129, pp. 112–125, 2024.
https://doi.org/10.1007/978-981-99-9251-5_9

communication interference. However, there are plenty of highly nonlinear power electronic devices in the flexible and straight system, and the control strategies of the system are diverse, which leads to greater changes in the fault characteristics of the system than that of traditional AC systems [8–10]. Therefore, study of the fault characteristics of double-fed wind farms under flexible DC grid-connected mode holds practical significance.

In [11], the influence of flexible DC converters of different structures on the fault voltage and current output of wind farms and flexible DC converters is summarized through simulation analysis. In [12], the AC-side fault characteristics of the flexible DC system of different types of wind turbines are studied through simulation models and a current transfer strategy for offshore wind farms is proposed. However, this type of method lacks theoretical analysis and it is difficult to accurately characterize the fault characteristics. However, the above-mentioned research is mainly aimed at the fault analysis of inverter power supplies, and it is rare to investigate the various fault properties of the system, especially the fault characteristics of the AC side.

In this paper, the topology and control strategy of DFIG wind farm with flexible DC integration are firstly analyzed. Furthermore, a mathematical model is established for the system control segment. Subsequently, the DFIG short-circuit current is derived, with an emphasis on determining factors affecting the magnitude of the short-circuit current through analysis. Finally, the model of DFIG with flexible DC integration is developed on the PSCAD/EMTDC simulation platform to analyze t wind farm side fault characteristics of DFIG with flexible DC integration.

2 Topology and Control Strategy of DFIG with Flexible DC Integration

2.1 Topology of DFIG with Flexible DC Integration

Presently, the development of offshore wind power resources has taken the lead as the future development path for wind power generation in our country due to the utilization of offshore wind power resources is reaching saturation. With the growth of offshore distance, the loss and construction costs caused by the use of AC submarine cables are getting continuously rising, while the construction cost of the use of DC submarine cables is relatively low, and the grid-connected through flexible direct current transmission technology has the advantages of low communication interference and asynchronous networking. Therefore, when using far-sea wind power resources, the use of flexible DC grid-connected has more advantages. Through the collation and analysis of the structure of the offshore flexible DC wind farm that has been built in China, the topology of the DFIG with flexible DC integration is illustrated in Fig. 1.

The wind turbine's output voltage, which measures at 0.69 kV, is tied into the 35 kV bus bar via the fan box variable boost. By means of the step-up transformer installed in the offshore substation, the voltage of the 35 kV-bus is elevated to 220 kV, a connection is established to the offshore converter station, which is then linked to the onshore converter through DC submarine cable. Finally, the onshore converter station is connected to the power grid. In Fig. 1, the onshore converter station is integrated to power grid, which is

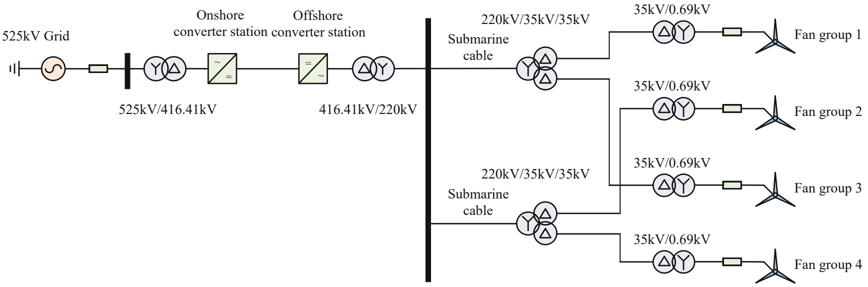

Fig. 1. Topology of DFIG with flexible DC integration

typically achieved with constant DC voltage/constant reactive power (V_{dc}/Q), and the offshore converter station is connected to wind generation, which is generally controlled by constant AC voltage/frequency (V_{ac}/f).

2.2 Topology and Control Strategy of DFIG

The DFIG consists of a fan blade, a gearbox, a double-fed induction motor, a rotor/grid-side converter (RSC/GSC). The DIFG is one type of the winding rotor induction generator, and its rotor circuit is connected to the power grid through a converter attached to the rotor slip ring. In contrast, the stator of DFIG is directly connected to the power grid. The topology of the DFIG is shown in Fig. 2.

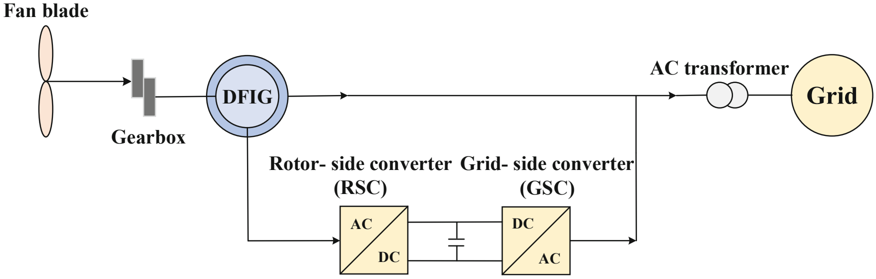

Fig. 2. Topology of DFIG

The active power output of the DFIG to the power grid consists of two parts, namely the active power output from the RSC and GSC. For wind turbines, the decoupling control strategies of the RSC and GSC are often considered to model them [13, 14].

(1) Rotor-side converter control strategy

The stator voltage vector direction U_s serves as a reference for the orientation of the d-axis, and the control methods of feedforward compensation and PI adjustment are adopted at the same time. The expression of the rotor voltage control equation for DFIG is as follows:

$$\begin{cases} u_{rd} = \left(k_{riP} + k_{riI}\big/ s\right)\left(i^*{}_{rd} - i_{rd}\right) + \omega_2\left(\dfrac{L_m U_s}{\omega_1 L_s} - \sigma L_r i_{rq}\right) \\ u_{rq} = \left(k_{riP} + k_{riI}\big/ s\right)\left(i^*{}_{rq} - i_{rq}\right) + \omega_2 \sigma L_r i_{rd} \end{cases} \tag{1}$$

where the rotor voltage's components are broken down into u_{rd}/u_{rq} along the d/q-axis, while the rotor current's components are similarly divided into i_{rd}/i_{rq} along the d/q-axis; k_{riP}/k_{riI} are the proportional/integral adjustment coefficient of the inner loop of the rotor current; The d/q-axis parts of the rotor current's command values are represented by $i^*{}_{rd}$ and $i^*{}_{rq}$, respectively; $\omega_1/\omega_2 = \omega_1$-$\omega_r$ are the synchronous angular frequency/angular frequency of deviation.

In addition, the active/reactive power output of the DFIG stator can be approximately decoupled and adjusted by the d/q-axis components of the rotor current, respectively. Therefore, the RSC control schematic diagram based on the outer power/inner rotor current loop is shown in Fig. 3 can be obtained.

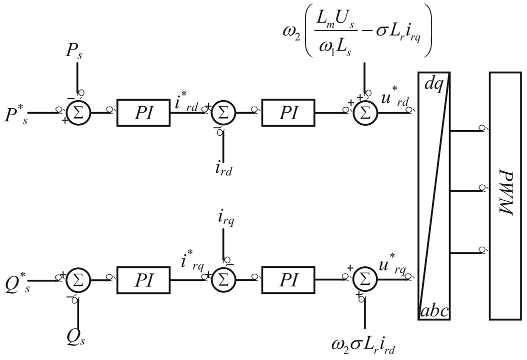

Fig. 3. Rotor side converter control schematic

(2) Grid-side converter control strategy

The stator voltage vector direction U_s serves as a reference for the orientation of the d-axis, and the control method of feedforward compensation and PI adjustment is adopted. The current inner loop controller of GSC can be expressed as:

$$\begin{cases} u_{gcd} = \left(k_{giP} + k_{giI}\big/ s\right)\left(i^*{}_{gcd} - i_{gcd}\right) + Ri_{gcd} + \omega_1 L_g i_{gcq} + U_s \\ u_{gcq} = \left(k_{giP} + k_{giI}\big/ s\right)\left(i^*{}_{gcq} - i_{gcq}\right) + Ri_{gcq} - \omega_1 L_g i_{gcd} \end{cases} \tag{2}$$

where u_{gcd}/u_{gcq} are the d/q-axis components of the output voltage on the GSC AC-side; i_{gcd} /i_{gcq} are the d /q-axis components of the output current on the GSC AC-side; L_g /R_g are the connection inductance/resistance; k_{giP}/k_{giI} are the proportional/integral adjustment coefficients of the current inner loop of GSC; $i^*{}_{gcd}$ /$i^*{}_{gcq}$ are the command values of the Grid-side current d/q-axis components.

The control goal of GSC is to ensure the stability of the DC voltage. Therefore, the control block diagram of the GSC composed of the dual-loop is demonstrated in Fig. 4.

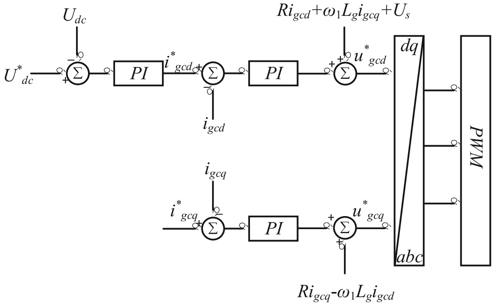

Fig. 4. Grid side converter control schematic

3 Transient Characteristics of DFIG with Flexible DC Integration

3.1 Transient Characteristics of DFIG

When a wind turbine is used as a power supply, it is very different from the traditional synchronous generator power supply. When considering the fault characteristics of the system, it is imperative to first explore the factors that affect the fault characteristics of the wind farm [15–17]. Taking the voltage drop at the stator terminal as an example, the fault current characteristics of DFIG are analyzed, and the stator voltage/magnetic chain equation of DFIG can be derived by contacting them.

$$\begin{cases} p\psi_{sd} = u_{sd} + R_s \frac{L_m i_{rd} - \psi_{sd}}{L_s} + \omega_1 \psi_{sq} \\ p\psi_{sq} = u_{sq} + R_s \frac{L_m i_{rq} - \psi_{sq}}{L_s} - \omega_1 \psi_{sd} \end{cases} \tag{3}$$

Assuming that the stator winding voltage $U_f = (1 - \lambda)U_{sn}$ after the voltage drops, and considering $u_{sd} = U_f$ and $u_{sq} = 0$, the Laplace transform and the inverse Laplace transform can be solved by applying the Laplace transform.

$$\begin{cases} \psi_{sd}(t) = -\dfrac{U_{sn} - U_f}{\omega 1} \mathrm{e}^{-R_s t/L_s} \sin \omega_1 t \\ \psi_{sq}(t) = -\dfrac{U_f}{\omega_1} - \dfrac{U_{sn} - U_f}{\omega_1} \mathrm{e}^{-R_s t/L_s} \cos \omega_1 t \end{cases} \tag{4}$$

During the fault transient process, $p\psi_{sd} \neq 0, p\psi_{sq} \neq 0$. At the same time, the outer loop of the power is locked, and the given rotor current reference values $i^*{}_{rd}$ and $i^*{}_{rq}$ remain unchanged. The stator magnetic chain d/q-axis fault components can be obtained by the derivation of the closed-loop transfer function:

$$\begin{cases} \Delta\psi_{sd} = \psi_{sd}(t) - \psi_{sd0} = -\dfrac{U_{sn} - U_f}{\omega_1} \mathrm{e}^{-R_s t/L_s} \sin \omega_1 t \\ \Delta\psi_{sq} = \psi_{sq}(t) - \psi_{sq0} = \dfrac{U_{sn} - U_f}{\omega_1} (1 - \mathrm{e}^{-R_s t/L_s} \cos \omega_1 t) \end{cases} \tag{5}$$

The difference e_d/e_q of the closed-loop transfer function are:

$$\begin{cases} \Delta i_{rd} \approx \dfrac{e_d}{k_{riP}} \\ \Delta i_{rq} \approx \dfrac{e_q}{k_{riP}} \end{cases} \tag{6}$$

Applying the above formula to the DFIG stator magnetic chain equation:

$$\begin{cases} \Delta\psi_{sd} = -L_s\Delta i_{sd} + L_m e_d/k_{rip} \\ \Delta\psi_{sq} = -L_s\Delta i_{sq} + L_m e_q/k_{rip} \end{cases} \tag{7}$$

$$\begin{cases} \Delta\psi_{sd} = -L_s\Delta i_{sd} - \dfrac{\omega_r L_m^2 p\Delta\psi_{sd}}{\omega_1 L_s k_{riP}} \\ \Delta\psi_{sq} = -L_s\Delta i_{sq} - \dfrac{\omega_r L_m^2 p\Delta\psi_{sq}}{\omega_1 L_s k_{riP}} \end{cases} \tag{8}$$

where $k_1 = \omega_r L_m/(\omega_1 L_s K_{riP})$, which can be obtained by simplifying the above formula:

$$\begin{cases} \Delta I_{sd}(s) = \Delta U_s(s)\frac{-(sL_m k_1+1)sL_s}{(sL_s+R_s)^2+(L_s\omega_1)^2} \\ \Delta I_{sq}(s) = \Delta U_s(s)\frac{(sL_m k_1+1)[sL_sR_s+R_s^2+(L_s\omega_1)^2]}{[(sL_s+R_s)^2+(L_s\omega_1)^2]L_s\omega_1} \end{cases} \tag{9}$$

The Laplace inverse change is made to the above formula, and the following is the time-domain expression for the d/q-axis fault components of the stator winding current:

$$\begin{cases} \Delta i_{sd}(t) = D\sin(\omega_1 t + \varphi)\mathrm{e}^{-R_{st}/L_s} \\ \Delta i_{sq}(t) = -\frac{\lambda U_{sn}}{\omega_1 L_s} + D\cos(\omega_1 t + \varphi)\mathrm{e}^{-R_{st}/L_s} \end{cases} \tag{10}$$

where, $\varphi = \arctan(\omega_1 L_m K_1)$. Therefore, after the voltage drops, the stator winding current d and q axis fault current are: $i_{sd0} + \Delta i_{sd}(t)$ and $i_{sq0} + \Delta i_{sq}(t)$.

Under the failure of the power grid, since the stator magnetic chain cannot undergo sudden changes, the transient DC component attenuated by the time constant determined by the stator resistance and inductance is generated, and finally attenuated to zero. This component will sense the back electromotive force of the rotor in the rotor, affecting the rotor transient characteristics.

Considering the transient process of the controlled motor/rotor short-circuit current, it can be divided into three parts, which are the periodic components determined by the rotor current reference; the rotor current response to the back electromotive force, the size of which is determined by the value of the back electromotive force, that is, affected by the degree of voltage drop; the rotor current natural component is associated to the control parameters.

Expressing the short-circuit current component of the DFIG stator requires consideration of both the stator magnetic chain and the rotor current. Among them, the periodic component corresponds to the stator magnetic chain periodic component and has nothing to do with the initial state of the DFIG. It is just related to the stator voltage and the stator inductance after the fault is generated; the DC transient component corresponds to the DC transient component of the stator magnetic chain, which is affected by the initial operating conditions of DFIG and power grid failure time, the more serious the stator voltage drop under DFIG failure, the greater the DC transient component initial value; the current transient characteristics are controlled by the rotor side converter Impact, if the control bandwidth of the RSC is sufficient, the excitation voltage provided by the rotor-side converter can follow the command value well. When the response time of the converter is fast enough, the rotor current periodic component can be approximated as a reference value.

3.2 Transient Characteristics of Flexible DC Transmission

Ignoring factors such as signal sampling and filtering delay, converter switching delay, etc., after decoupling, the converter control closed-loop transfer function's d-axis current can be expressed as:

$$G(s) = \frac{i_d}{i^*{}_d} = \frac{k_P s + k_I}{Ls^2 + (R + k_P)s + k_I} \tag{11}$$

Select $k_P/k_I = L/R$, and the current control's closed-loop transfer function can be expressed as follows:

$$G(s) = \frac{k_P}{k_P + Ls} = \frac{1}{1 + \frac{s}{\omega_c}} \tag{12}$$

where, ω_c is the angular frequency, $\omega_c = k_P/L$.

At this time, the inner loop of the current is a first-order inertial link. So that the active power command before the fault is $i^*{}_{d0}$, $i^*{}_{d1}$ is the active current command after the voltage drops, and the output converter d-axis fault component current can be obtained:

$$\begin{aligned} \Delta i_{df}(s) &= G(s)i^*{}_{d1}(s) - G(s)i^*{}_{d0}(s) \\ &= \frac{1}{1 + \frac{s}{\omega_c}} \frac{i^*{}_{d1} - i^*{}_{d0}}{s} \\ &= \left(i^*{}_{d1} - i^*{}_{d0}\right)\left(\frac{1}{s} - \frac{1}{s + \omega_c}\right) \end{aligned} \tag{13}$$

Through the Laplace transform, the fault current component's time domain expression can be obtained as:

$$\Delta i_{df}(t) = \left(i^*{}_{d1} - i^*{}_{d0}\right)\left(1 - \mathrm{e}^{-\omega_c t}\right) \tag{14}$$

Neglecting the transient process is advisable when the switching frequency is large and the current inner loop with speedy response time. At this time, the fault current of the d/q axis is:

$$\begin{cases} i_{df}(t) = i^*{}_{d1} \\ i_{qf}(t) = i^*{}_{q1} \end{cases} \tag{15}$$

Before the failure, the inverter station operates in a unit power factor state, and the converter output three-phase current can be obtained as:

$$\begin{cases} i_{a0}(t) = i^{*}{}_{d0}\cos(\omega t + \theta_1) \\ i_{b0}(t) = i^{*}{}_{d0}\cos\left(\omega t + \theta_1 - \dfrac{2\pi}{3}\right) \\ i_{c0}(t) = i^{*}{}_{d0}\cos\left(\omega t + \theta_1 + \dfrac{2\pi}{3}\right) \end{cases} \tag{16}$$

where, θ_1 denotes the a-phase current initial phase angle.

Since the converter station's inertial time constant is so small, its transient output component is expected to be disregarded, and according to the constrained converter overcurrent capacity, the current reference limit is generally set in the inner loop of the current. When the current exceeds the limit i_{lim}, the active/reactive reference of the current will be limited. The short-circuit current amplitude of the flexible DC wind farm is lower than that of the AC wind farm under the converter current-limiting control. When the converter current limiting control conditions are reached, the converter output short-circuit current is expressed as:

$$\begin{cases} i_{a1}(t) = i_{lim}\cos(\omega t + \theta_1 + \varphi) \\ i_{b1}(t) = i_{lim}\cos\left(\omega t + \theta_1 - \dfrac{2\pi}{3} + \varphi\right) \\ i_{c1}(t) = i_{lim}\cos\left(\omega t + \theta_1 + \dfrac{2\pi}{3} + \varphi\right) \end{cases} \tag{17}$$

where, $\varphi = \arctan(i^{*}{}_{q1}/i^{*}{}_{d1})$. The above equation indicates that the active/reactive current reference $i^{*}{}_{d1}/i^{*}{}_{q1}$ determine the converter short-circuit current amplitude. The short-circuit current amplitude is slightly greater than the steady-state operating current amplitude when the controller current limit i_{lim} is reached; the short-circuit current phase angle φ rises with the growth of the reactive current reference ${i_{q1}}^{*}$.

When the wind farm adopts flexible direct current and is connected to the grid, a failure occurs on the system side. Flexible direct current transmission technology can reduce the harmonic component of the current in the system. For flexible direct current transmission systems, wind turbines have more generator characteristics; in AC transmission systems, since the AC transmission line's other side is connected to the infinite system, wind farms have more load characteristics. Therefore, the short-circuit current supplied by the system side varies under the two grid-connected modes after a short-circuit failure. The short-circuit current provided by the VSC-HVDC system is lower than that of the AC system in the event of a system fault. In the event of a fault on the system, because of the influence of the current inner loop limiting link, the short-circuit current supplied by the VSC-HVDC system is less than that under a failure occurs on the wind farm side.

4 Simulation Analysis

4.1 Simulation System

The VSC-HVDC system with DFIG integration is illustrated in Fig. 5, where f_1 is the system-side failure point, and f_2 is the wind farm-side failure point.

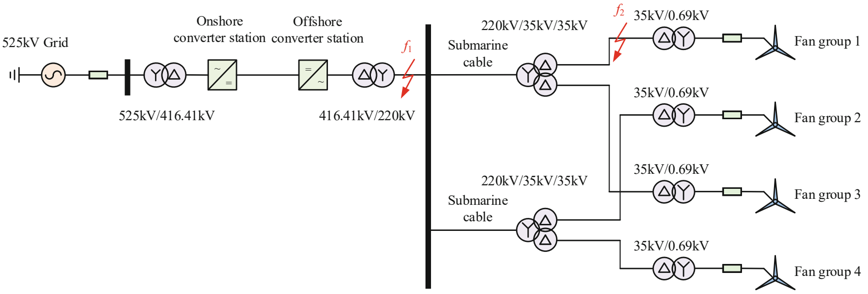

Fig. 5. The simulation of VSC-HVDC system with DFIG integration

Through the equivalent calculation of the wind farm internal collector circuit parameters and the equivalent wind farm module inside the PSCAD, the wind farm can be equivalent to a single wind turbine connected to the power grid through the equivalent wind farm module. The parameters of the flexible DC grid-connected wind farm simulation system are shown in Table 1.

4.2 Simulation of Fault at System Side (f_1)

In Fig. 5, point f_1 has a AB interphase short circuit fault at 10 s, and the short-circuit point is a 220 kV bus bar. Figure 6a–c show the instantaneous fault voltage, the instantaneous fault current supplied by the power grid, and the instantaneous fault current supplied by wind turbines.

It can be noted from Fig. 6a that the fault phase voltage (AB phase) instantaneous value is equal after the fault occurs. The fault phase voltage (AB phase) peak value drops from 202.11 to 96.77 kV within 10 ms after the fault occurs, and the non-fault phase voltage (C phase) peak value rises from 203.21 to 215.80 kV within 10 ms after the fault occurs. Due to the failure to remove the fault in time, the three-phase voltage began to oscillate in a period of 0.1s after the fault occurred. Figure 6b shows that the fault phase peak current provided by the grid system rises from 1.93 to 6.37 kA (3.32 times the rated value) within 10 ms, and the phase difference of the waveform of the fault phase (AB phase) is 180º, and the non-fault phase current rises to 2.50 kA, the increase is much lower than that of the fault phase. Figure 6c shows that the peak fault phase current provided by wind turbines rises from 2.06 to 10.44 kA (5.07 times the rated value) within 10 ms.

In summary, when a two-phase interphase (AB phase) short-circuit fault occurs at point f_1, the fault phase peak voltage is lower than the steady-state value, and the non-fault phase peak voltage is slightly higher than the steady-state value. Under normal

Table 1. Parameters of flexible DC grid-connected wind farm simulation system

System parameters	Value
Rated capacity of grid S_N/MVA	1100
Rated voltage of grid U_N/kV	525
Grid equivalent resistance R_S/Ω	1.3779
Grid equivalent inductance L_S/mH	24.9
Transformer ratio of onshore converter station /(kV/kV)	525/416.41
Converter station capacity S_C/MVA	1100
Rated AC voltage of converter station U_{AC}/kV	416.41
Rated DC voltage of converter station U_{DC}/kV	800
DC submarine cable resistance between stations R_{DC}/Ω	1.404
DC submarine cable inductance between stations L_{DC}/mH	100
Transformer ratio of offshore converter station /(kV/kV)	416.41/230
AC submarine cable resistance R_1/Ω	0.558
AC submarine cable inductance L_1/mH	4.3417
Split transformer 1/2 variable ratio /(kV/kV/kV)	230/35/35
Fan box type transformer variable ratio /(kV/kV)	35/0.69
Fan rated capacity S_G/MVA	4.25
Fan rated voltage U_G/kV	0.69
Fan converter DC voltage U_{dc}/kV	1.2

circumstances, the short-circuit current supplied by the power grid is 10–15 times the rated value, while the short-circuit current supplied by the VSC-HVDC system is 3.32 times the rated value, which is less than that of the power grid.

4.3 Simulation of Fault at Wind Farm Side (f_2)

In Fig. 5, point f_2 has a AB interphase short circuit fault at 10s, and the short-circuit point is a 35 kV bus bar. Figure 7a–c show the instantaneous fault voltage/current supplied by the power grid, and the instantaneous fault current supplied by wind turbines.

It can be noted from Fig. 7a that the fault phase voltage (AB phase) instantaneous value is equal after the fault occurs. Its peak value is reduced from 32.41 to 13.12 kV within 10 ms of the fault, and the non-fault phase voltage (C phase) is reduced from 32.32 to 31.53 kV within 10 ms of the fault. Due to the failure to remove the fault in time, the three-phase voltage began to oscillate in a period of 0.1s after the fault occurred. As shown in the graphical representation in Fig. 7b, the peak current of the fault phase provided by the grid system rises from 3.03 to 32.2 kA (10.63 times the rated value) within 10 ms, and the phase difference of the waveform of the fault phase (AB phase) is 180°, and the non-fault phase current increases to 3.44 kA, the increase is lower than that of the fault phase. As shown in the graphical representation in Fig. 7c, the peak

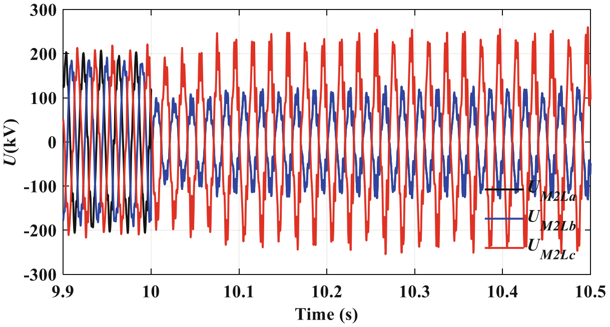

(a) Instantaneous fault voltage

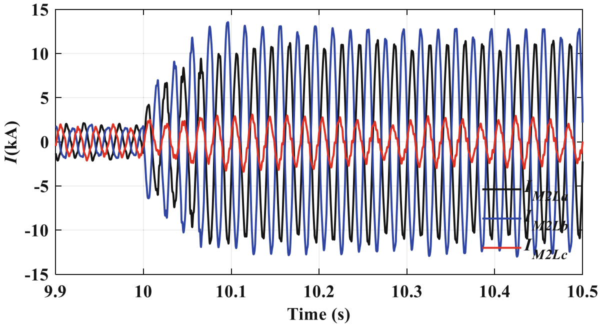

(b) Instantaneous fault current supplied by the power grid

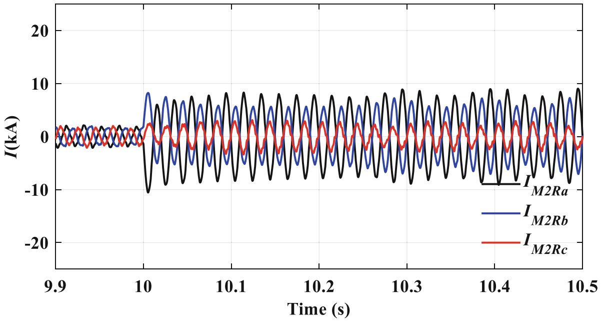

(c) Instantaneous fault current provided by wind turbines

Fig. 6. Fault characteristics of AB interphase short circuit at point f_1

three-phase current provided by wind turbines rises from 2.96 to 5.06 kA (1.71 times the rated value) within 10 ms.

In summary, a conclusion similar to Sect. 4.2 can be obtained.

When a fault arises at point f_1, the grid system will generate a fault current 3.32 times the rated value; when a fault happens at point f_2, the current will surge to 10.63 times the rated value. The short-circuit current generated by the power grid of f_1 is less than that of f_2. This is due to the fact that the control strategy adopted by the offshore converter station is V_{ac}/f control. When a failure occurs on the system side, the AC

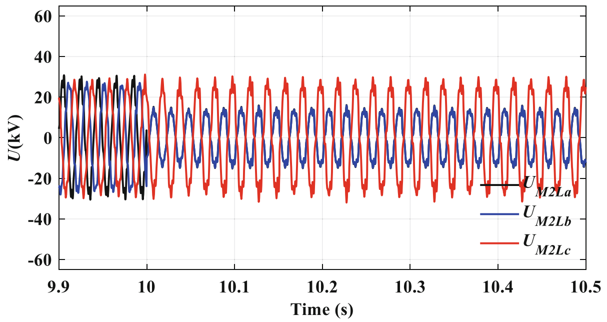

(a) Instantaneous fault voltage

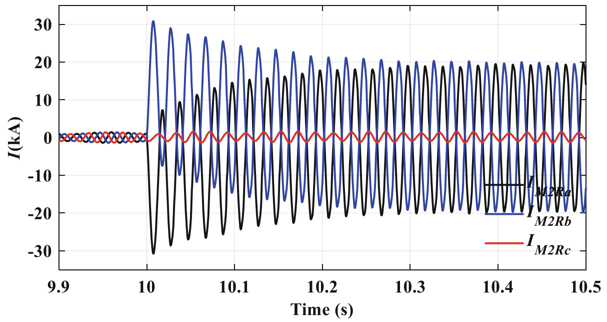

(b) Instantaneous fault current supplied by the power grid

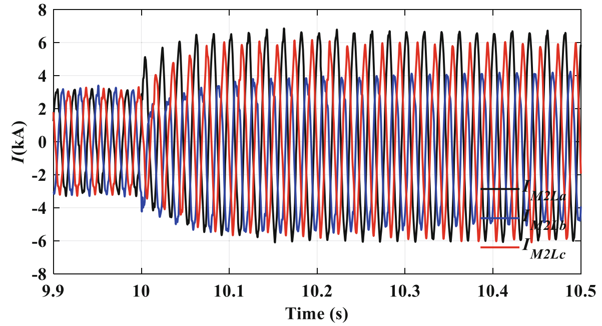

(c) Instantaneous fault current provided by wind turbines

Fig. 7. Fault characteristics of AB interphase short circuit at point f_2

voltage amplitude will change and the fault phase voltage will drop. At this time, the constant AC voltage control used by the offshore converter station will be affected. The control system's current inner loop regulation constrains the amplitude of the fault current component in the *d*/*q* axis, as a result, the occurrence of such faults leads to a decrease in the outlet current of the offshore converter, which is significantly lower than the short-circuit current supplied by the power grid when the wind farm side fails.

5 Conclusion

(1) In this paper, a study is conducted on the topology and control method of a flexible DC grid-connected wind generation. The analysis delves into the structure of DFIG, and a mathematical model of DFIG converter is subsequently established.

(2) This paper derived the formula of the short-circuit circuit of DFIG, and analyzed the main factors that affecting the system short-circuit current. The short-circuit current of the system is related to three parts: the periodic component determined by the rotor current reference, the rotor current response to the back electromotive force, and the rotor current natural component.

(3) In this paper, the short-circuit current formula of the flexible DC converter output is derived, and the short-circuit current characteristics are analyzed. When a fault occurs at the system side, the short-circuit current provided from the VSC-HVDC system is less than that of the AC system. And it can be concluded that when a system side fault occurs, due to the influence of the current inner loop limiting link, the short-circuit current supplied by the VSC-HVDC system is less than that under a failure occurs on the wind farm side.

(4) In this paper, a DFIG model with flexible DC integration in PSCAD/EMTDC is constructed, and the fault characteristics of the system when the AB phase of the 35 kV bus bar and the 220 kV bus bar of the model are analyzed. To assess the impact of such faults on both the system side and the wind farm side, a comparison is made between the short-circuit currents supplied by the power grid. It is concluded that the inner loop control of the current in the control system limits the amplitude of the fault current component of the d/q axis and reduces the outlet converter short-circuit current.

Acknowledgement. Supported by Science and Technology Project of Jiangsu Frontier Electric Technology Co., LTD (No. KJ202201).

References

1. Wu, C., Zhang, X.-P., Sterling, M.: Wind power generation variations and aggregations. CSEE J. Power Energy Syst. **8**(1), 17–38 (2022)
2. Sun, C., Chen, J., Tang, Z.: New energy wind power development status and future trends. In: 2021 International Conference on Advanced Electrical Equipment and Reliable Operation (AEERO), Beijing, China, pp. 1–5 (2021)
3. Qazi, A., et al.: Towards sustainable energy: a systematic review of renewable energy sources, technologies, and public opinions. IEEE Access **7**, 63837–63851 (2019)
4. International Energy Agency: Global Offshore Wind Report 2019. International Energy Agency, Paris (2019)
5. He, Q., Zhang, F., Liu, D., Gao, C., Shi, S., Xi, P.: Analysis on the development status and problems of China's offshore wind power. In: 2018 2nd IEEE Conference on Energy Internet and Energy System Integration (EI2), Beijing, China, pp. 1–4 (2018)
6. Ji, K., Tang, G., Pang, H., Yang, J.: Impedance modeling and analysis of MMC-HVDC for offshore wind farm integration. IEEE Trans. Power Delivery **35**(3), 1488–1501 (2020)

7. Meng, P., Xiang, W., Chi, Y., Wang, Z., Lin, W., Wen, J.: Resilient DC voltage control for islanded wind farms integration using cascaded hybrid HVDC system. IEEE Trans. Power Syst. **37**(2), 1054–1066 (2022)
8. Wang, P., Liu, P., Gu, T., Jiang, N., Zhang, X.: Small-signal stability of DC current flow controller integrated meshed multi-terminal HVDC system. IEEE Trans. Power Syst. **38**(1), 188–203 (2023)
9. Wang, P., Wang, Y., Jiang, N., Gu, W.: A comprehensive improved coordinated control strategy for a STATCOM integrated HVDC system with enhanced steady/transient state behaviors. Int. J. Electr. Power Energy Syst. **121**, 1–12 (2020)
10. Wang, P., et al.: Equivalent model of multi-type distributed generators under faults with fast-iterative calculation method based on improved PSO algorithm. Protect. Control Mod. Power Syst. **6**, 1–12 (2021)
11. Chen, X., Hou, Y., Wen, J.: Fault characteristics analysis of two HVDC technologies for wind power integration. In: ISGT 2014, Washington, DC, pp. 1–6 (2014)
12. Prignitz, C., Eckel, H.-G., Achenbach, S.: A fault handling current control strategy for offshore wind turbines in interconnected offshore wind farms with different types of HVDC transmission. In: 2017 IEEE 8th International Symposium on Power Electronics for Distributed Generation Systems (PEDG), Florianopolis, Brazil, pp. 1–6 (2017)
13. Mohammadi, J., Vaez-Zadeh, S., Afsharnia, S., Daryabeigi, E.: A combined vector and direct power control for DFIG-based wind turbines. IEEE Trans. Sustain. Energy **5**(3), 767–775 (2014)
14. Arani, M.F.M., Mohamed, Y.A.-R.I.: Analysis and impacts of implementing droop control in DFIG-based wind turbines on microgrid/weak-grid stability. IEEE Trans. Power Syst. **30**(1), 385–396 (2015)
15. Wang, P., et al.: Impact of the PV location in distribution networks on network power losses and voltage fluctuations with PSO analysis. CSEE J. Power Energy Syst. **8**(2), 523–534 (2022)
16. Sheng, X., Wan, S., Han, X., He, Y., Wang, X.: Impact of actual wind speed distribution on the fault characteristic of DFIG rotor winding asymmetry. In: IEEE Transactions on Instrumentation and Measurement, vol. 71, pp. 1–14,Art no. 3507714 (2022)
17. Ma, Y., Zhu, D., Zou, X., Kang, Y., Guerrero, J.M.: Transient characteristics and quantitative analysis of electromotive force for DFIG-based wind turbines during grid faults. Chin. J. Electric. Eng. **8**(2), 3–12 (2022)

Coordination and Optimization Control for Stable Load Shedding Control and Dynamic Zoning of Power Grid

Donghao Wu(✉), Lixiang Jin, Zhenjia Li, and Lei Zheng

State Grid Jiaxing Power Supply Company, Jiaxing 31400, Zhejiang, China
0808190209@163.com

Abstract. For the steady under voltage problem of the system, currently, measures such as switching on/off capacitors and reactors, adjusting transformer taps, etc. are generally taken to make the voltage rise firstly. When the control measures are insufficient, it is necessary to cut off some of the load. Considering that when the local steady under voltage level of the system is above 0.8 p.u, the control time requirement is not high, it is proposed to use dynamic zoning technology to coordinate with load shedding control and improve the refinement level of load shedding control. The impact evaluation indicators for dynamic zoning and the comprehensive cost indicators for load shedding are defined, and the direct search method of rotating variables is adopted to reduce the complexity of optimization search. Firstly, a zoning scheme is determined, and based on the control sensitivity index of the load, available load shedding points are selected. Furthermore, based on the evaluation results of load shedding priority, load shedding points are selected sequentially, and the minimum comprehensive control cost under this zoning scheme is calculated. Finally, by rotating the zoning points sequentially and iterating continuously, the optimal comprehensive control strategy is obtained. The effectiveness of this method in reducing load shedding and comprehensive control costs has been verified based on actual power grid examples.

Keywords: Dynamic zoning · Load shedding · Direct search method · Power grid · Sensitivity index

1 Introduction

Building a new type of power system with new energy as the main body is an important way to help achieve the "dual carbon" goal. With the doubling of the scale and scope of the interconnected power grid and the rapid increase in the proportion of new energy, the characteristics of the power grid have undergone fundamental changes [1]. The electricity market has led to diverse changes in operating modes, greatly increasing the probability of power grid loss of safety and stability due to successive events. Load shedding control is an important means to cope with severe power grid failures and emergencies, prevent the collapse of the power system, and thus prevent the occurrence of large-scale power outages [2]. The implementation of load shedding control mainly

Y. Xue et al. (Eds.): PMF 2023, LNEE 1129, pp. 126–136, 2024.
https://doi.org/10.1007/978-981-99-9251-5_10

includes the second and third lines of defense of the power system, namely the safety and stability control system, under frequency and under voltage load shedding devices, load control systems, etc. [3]. However, according to Order No. 599 of the State Council "Ordinances of Electrical Security Accident Emergency Disposal and Investigation", an excessively high proportion of regional load shedding can lead to serious power grid safety accidents and subsequent accountability. Therefore, in order to reduce the losses caused by severe faults to the system, it is necessary to take all available measures to reduce the risk of power safety accidents.

Layering and zoning operation is a trend in the development of power grids., The "Guidelines for Security and Stability of Power Systems" clearly stipulate that, the power grid structure should adhere to the basic principle of layering and zoning operation. Zoning is the division of the entire power grid into several sub regions, characterized by strong relationships between internal nodes and weak relationships between nodes in different sub regions [4, 5]. At present, most transmission network zoning is based on voltage level, while distribution network zoning is mostly based on electrical distance. The domestic provincial power grid has realized zoning operation basically, and there are some backup communication channels between adjacent districts for post-incident power grid support [6]. Dynamic zoning is a special operation mode adjustment that changes the distribution of system power flow by switching on or off backup communication channels and changing the network topology. The dynamic zoning adjustment is usually realized by switching operation, and has a certain time-delay. According to on-site experience, the operation time of a single line is mostly within the range of 1–5 min.

Due to the fact that reactive power compensation devices in the system are also configured according to the principles of layering and zoning operation and local balancing, dynamic zoning is usually closely related to the demand for reactive power control. Reference [7] proposes a dynamic zoning method for distribution networks based on the dynamic reactive power regulation characteristics of renewable distributed power sources such as wind power and photovoltaic. Firstly, the optimal zoning scheme that can meet dynamic reactive power regulation is formed, and then real-time reactive voltage regulation of the zoning is executed. In addition, dynamic zoning can also achieve the redistribution of active power flow in the power grid [8, 9]. Reference [10] addresses the transmission congestion problem that may exist in the backup scheduling process of power systems containing wind power. Based on the probability distribution characteristics of system power flow, the blocking risk index of the line is calculated, and a dynamic zoning backup configuration method is proposed to improve the backup schedule ability effectively. Reference [11] proposes a dynamic zoning technology to reduce the risk of power safety accidents by considering the coordination and cooperation of dynamic zoning technology and emergency load shedding measures in response to the risk of local line overload after a fault. Reference [12] suggests that the emergency load shedding strategy should also consider the changes in the system network topology and the mutual influence of frequency and voltage stability to achieve dynamic adaptability of load shedding. However, there is no quantitative analysis of the impact of changes in network topology on the emergency load shedding strategy.

This article focuses on the problem of slow decrease or long-term suspension of voltage in local power grids under large disturbance faults. Considering the time requirements of steady-state voltage control and the operational delay of dynamic zoning, it is proposed to utilize the dynamic zoning capability of the power grid fully, and achieve rapid voltage recovery while avoiding load shedding and triggering under voltage load shedding actions as much as possible. The index system for dynamic zoning and load evaluation index for load shedding are defined, and the direct search method of variable rotation is used to provide the optimal dynamic zoning and load shedding strategies. This ensures that the voltage is restored to a safe range while minimizing the control cost of the system.

2 Evaluation Indexes for Dynamic Zoning and Load Shedding

The "Guidelines for Security and Stability of Power Systems" clearly stipulate that, during the transient process of power system disturbance, the load bus voltage can recover to 0.80 p.u. within 10 s, which means that the voltage allowed by the user should be above 0.8 p.u; During the medium to long term process of power system disturbance, the load bus voltage can be maintained or restored above 0.90 p.u. The "Technical Regulations for Automatic Under Voltage Load Shedding in Power Systems" stipulate that after disturbances occur in the system or during the continuous increase of load, automatic under voltage load shedding measures are configured to cut off a portion of the load automatically before the voltage of certain bus in the power grid drops to an unacceptable level, ensuring that voltage collapse does not occur, thereby ensuring the safe and stable operation of the system and uninterrupted power supply to important users. Considering extremely serious faults in the power grid, the operating voltage setting of the under voltage load shedding device configured in the power grid is generally lower than 0.8 p.u. When the system voltage drops to between 0.8 and 0.9 standard unit values, the under voltage load shedding device does not operate generally. At this time, the system can still operate for a long time, but its ability to resist disturbances is weakened. Generally, measures such as switching on or off capacitors and reactors, adjusting transformer taps, etc. can be taken to make the voltage rise. When control measures are insufficient, cut off part of the load urgently.

Due to the fact that this scenario allows for a longer continuous running time, dynamic zoning can be considered as a solution. However, it can generally solve the problem of under voltage of backup channels or stations near the loop breaking point. For the under voltage of the entire zone, the control effect may be limited, and coordination with load shedding is necessary. Compared to cutting off the load directly, adopting dynamic zoning can reduce the impact on power supply safety and reduce the economic cost. However, it is necessary to consider the impact of dynamic zoning operation on system security and stability, as well as the reliability of the operation. For example, the dynamic zoning of power network may also affect the short-circuit current of the system because it involves the open-close loop of the electromagnetic ring network. A proper dynamic zoning scheme will reduce or avoid the use of load shedding measures by alleviating the extent of equipment overload, voltage overshoot, frequency offset, etc.

In order to evaluate the advantages and disadvantages of different dynamic zoning schemes fully, it is necessary to establish the evaluation indexes covering the economy, security and reliability of the power grid (Table 1).

Table 1. Index system of dynamic zoning

Index category	Evaluation indicators
Economy	Network loss
	Number of operations
Security	Short circuit current
	Safety margin
Reliability	Capacity-to-load ratio

The specific meaning of the indicator is as follows:

Network loss: due to the change of power flow distribution.
Number of operations: reflect the cost of performing dynamic zoning.
Short circuit current: check the impact of power grid topology changes.
Safety margin: reflect the degree of emergency resolution.
Capacity-to-load ratio: reflect the load rate of each partition after dynamic zoning.

Usually, relying on dynamic zoning solely may not avoid cutting off loads completely. Therefore, taking into account the performance ratio of dynamic zoning operations, it is necessary to determine the cutting priority of each load point under different zoning schemes further. Propose to consider four dimensions of attributes: interruption loss, electricity department, operational performance, and electrical distance, as evaluation indicators for each switchable load. By assigning a weight to each evaluation indicator and multiplying the score of each evaluation indicator of the load by its weight, the weighted comprehensive score of each load is obtained. The evaluation indicators are shown in Table 2.

Table 2. Load evaluation index

Evaluation indicator	Specific meanings
Interruption loss	Reflect the cost of electricity loss
Electricity department	Reflect the power usage condition of the users
Operational performance	Reflect the physical performance of the device
Electrical distance	Reflect the geographical location of load points

3 Coordinated Control of Load Shedding and Dynamic Zoning

3.1 Optimization Objectives

The dynamic zoning problem is an optimization problem aimed at finding a set of parameter values to achieve optimal system performance actually. The formulation of the objective function mainly considers minimizing the control cost of the system while ensuring that the voltage is restored to a safe range. The control cost includes two parts mainly. One part is the operational cost of dynamic zoning, which is reflected by the economic losses corresponding to zoning operations in the dynamic zoning evaluation indicators.

$$C=\sum_{i=1}^{N} D_i \tag{1}$$

In the formula, D_i is the economic cost calculated from the loss caused by a single operation, and N is the total number of zoning operations.

The other part is the economic cost of load loss caused by load shedding, including the cost of power outage loss and the cost of power safety accident liability, which can be represented by the following equation [11].

$$F = F_1 + \beta F_2 \tag{2}$$

In the formula, F_1 is the economic cost of power outage loss due to load shedding.β is the weight coefficient of the responsibility cost F_2.

Taking into account the costs of both types of control, the comprehensive control cost is defined as follows.

$$C = \omega C + \alpha F \tag{3}$$

In the formula, ω and α are the weight coefficients of the dynamic zoning operation cost and load shedding cost, respectively.

In theory, the optimal scheme of dynamic zoning and load shedding should satisfy min(C), that is, load shedding measures should minimize the control cost after considering both dynamic zoning and load shedding.

Among them, the optimal control needs to meet both the safety and reliability constraints of the system, and the optimization problem can be expressed as follows.

Objective function:

$$\min(C) \tag{4}$$

Constraint condition:

I. Power flow constraints of the line:

$$\eta_{L,i} = 1 - \frac{I_{L,i}}{I_{L,i,\lim}} > 0 \tag{5}$$

II. Capacity constraints of transformers:

$$\eta_{T,i} = 1 - \frac{S_{T,i}}{S_{T,i,\lim}} > 0 \tag{6}$$

III. Short circuit current constraint:

$$\eta_{k,j} = 1 - \frac{I_{k,j}}{I_{k,j,\lim}} > 0 \tag{7}$$

In the formula: $I_{L,i}$ represents the current value of the line; $I_{L,i,\lim}$ is the thermal stability limit of the line; $S_{T,i}$ is the apparent power of the transformer; $S_{T,i,\lim}$ is the rated capacity of the transformer; $I_{K,j}$ is the maximum short-circuit current of the bus; $I_{k,j,\lim}$ is the breaking current limit of the bus.

IV. Voltage safety margin constraints

$$\eta_{V,j} = \min\left(T_{cr} - T_{b,j}, V_{\min,j} - V_{cr} + k_t\left(T_{cr} - \frac{T_{b,j}V_{cr}}{V_{R,j}}\right)\right) > 0 \tag{8}$$

In the formula, V_{cr}, T_{cr} is the voltage setting value and the maximum acceptable duration below the corresponding setting value; $V_{\min}$ is the transient minimum voltage of the central bus after fault clearing; V_R is the steady-state recovery voltage after a fault; T_b is the longest duration during which the bus voltage is lower than V_{cr} in actual faults; k_t is the critical voltage offset time factor. If $T_{b,i} > T_{cr}$, then $\eta_{V,j} < 0$, it is judged as instability directly; If $T_{b,i} \leq T_{cr}$, then stability is characterized by two parts of information weighting: firstly, the difference between the minimum transient voltage and the set voltage; The second is the difference between the time below the critical voltage and the set time after calibrating the steady-state recovery voltage after a fault.

3.2 Coordinated Control Method

It can be seen that the variables of the objective function are nonlinear and discrete for dynamic zoning operations. Therefore, this problem is an optimization problem of discrete variables with nonlinear constraints. Due to the complexity of power system problems, which result in huge computational complexity and poor real-time performance, this article considers using the direct search method to solve the problem. The direct search method is to use a numerical solution to generate a feasible sequence of problems through a series of iterations, and gradually achieve the optimal solution. Among them, the variable rotation method is the most effective direct search method for solving dynamic zoning optimization problems. The basic idea is: to change one variable at a time while keeping the other variables unchanged, that is, to seek the best along the coordinate axis of this variable, and rotate each variable until the best is found.

For this problem, since the operation of dynamic zoning is discrete and the number of operations should not be too many, it is possible to determine the dynamic zoning operation first, and only operate one zoning point at a time, while keeping the other zoning points unchanged. Furthermore, transform multidimensional search into a one-dimensional search problem for each partition.

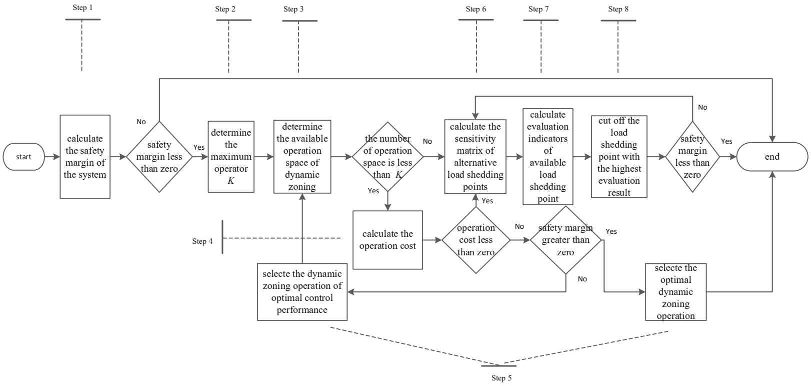

Fig. 1. Coordinate control method flow

Check the performance of the integrated control under the constraint of the maximum operand to see if it can solve the under voltage under the expected fault after the execution of the dynamic zoning operation. If it can solve the problem, then the optimal dynamic zoning operation combination scheme is selected according to the direct search method. If it cannot be solved, then the dynamic zoning operation combination with the best load shedding scheme is chosen, on this basis of control sensitivity of each alternative load shedding point is calculated. Remove the load with the highest weighted comprehensive score iteratively until the under voltage problem under the expected fault is resolved.

The specific method flow is as follows (Fig. 1):

Step 1: Simulate and calculate the voltage response trajectory of the power grid after the expected fault occurs. According to Eq. (8), calculate the voltage safety margin of key bus nodes in the system. If there are buses with a safety margin less than zero, proceed to step 2. Otherwise, end this method.
Step 2: Determine the zone of the bus with a voltage safety margin less than zero, and based on the network topology between adjacent zones, determine the maximum number of operations K for dynamic zoning operations, with a value of K not exceeding 3.
Step 3: Determine the available dynamic zone operating space based on the operation of backup channels and switching points between different zones in the power grid. If there is no available operating space, proceed to step 6; otherwise, proceed to step 4.
Step 4: For different dynamic zoning schemes, simulate and calculate the response curve, and calculate the safety margin of the system using dynamic zoning only based on Eq. (5)–(8).
Step 5: If the safety margin is greater than zero, calculate the operation cost C of the dynamic zoning directly, select the dynamic zoning scheme with the lowest operation cost as the final control, and end this method; Otherwise, proceed to step 6.
Step 6: Using the parameter perturbation method, calculate the improvement of voltage safety margin of bus nodes with the margin less than zero for each alternative load

shedding point, and generate a sensitivity matrix.

$$M = \begin{bmatrix} \frac{\Delta\eta_1}{\Delta P_1} \cdots \frac{\Delta\eta_n}{\Delta P_1} \\ \cdots \cdots \cdots \\ \frac{\Delta\eta_1}{\Delta P_m} \cdots \frac{\Delta\eta_n}{\Delta P_m} \end{bmatrix} \quad (9)$$

where, ΔP_m is the power perturbation of load point m, and $\Delta\eta_n$ is the increase in voltage safety margin of the nth bus after load shedding operation.

Determine whether there are elements in each row of the matrix with values greater than the sensitivity threshold: if so, use the corresponding load point in that row as a means of load shedding. All available load shedding points constitute the set of available load shedding points for this fault.

Step 7: Calculate the evaluation indicators for each available load point, and obtain the weighted comprehensive score for each load based on the weight of each evaluation indicator. The calculation formula for the weighted comprehensive score is

$$X_n = \sum_{i=1}^{4} R_i X_{in} \quad (10)$$

In the formula, X_n is the comprehensive score of the nth load; R_i is the weight of the ith evaluation indicator; X_{in} is the score of the ith indicator of the nth load. The shedding priority evaluation result of each load is the weighted comprehensive score.

Step 8: Based on the evaluation results of the shedding priority, search in order of priority from high to low until the under voltage state is resolved. Provide control measures for the expected fault under different zoning schemes, calculate the comprehensive control cost, and end this method.

On the basis of considering dynamic zoning, this method improves the refinement level of load control further, reduces the impact and economic losses on normal production and life, and has significant economic and social benefits.

4 Example Analysis

The effectiveness of the proposed method in ensuring system safety and stability and reducing load shedding after accident is verified by an actual UHVDC power grid, the power grid is shown in Fig. 2.

The region is independently powered by three zones: WZ, TZN, and TZN. NS, SM, YH, YQ, and CN are the main generator set connected to the 500 kV bus directly. The thick and solid lines are 500 kV voltage level lines, and the dashed lines T1, T2, and T3 are three backup channels.

When a short circuit grounding fault occurs on the 500 kV line between Bus F and Bus I and is cut off, a large amount of power flow shifts to the line between Bus I and Bus G, resulting in the long-term suspension of bus voltage in the WZ area between 0.8 and 0.9 p.u, posing a risk of triggering under voltage load shedding actions. At the same

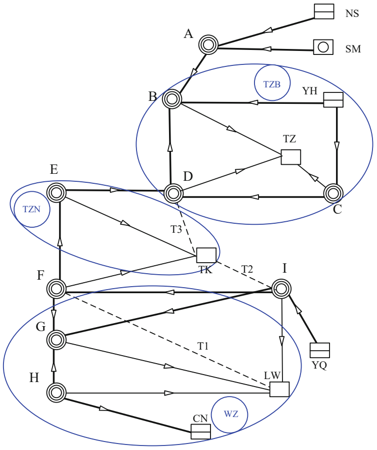

Fig. 2. Wiring diagram of a local power grid

time, it has led to insufficient transient support capacity of YQ units for TZN area. Due to the lack of support from main units, there is also a problem of slow voltage recovery in TZN area. After the fault, the voltage curve of some bus is shown in Fig. 3.

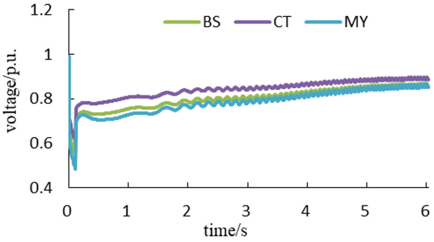

Fig. 3. The bus voltage curve after fault

If only load shedding measures are adopted, first select the load points that can be cut off based on the sensitivity matrix, and determine the final control strategy by calculating the cutting priority evaluation results of these load points. The total comprehensive control cost is shown in the Table 3.

Table 3. The cost of load shedding scheme

Zone	The amount of load shedding/MW	The ratio of load shedding/%	Comprehensive control cost
TZB	0	0	0.85
TZN	589	15.1	
WZ	1890	48.6	

To reduce the cost of system load shedding, considering that the system voltage is above 0.8 pu and the system can withstand a time of more than 10 min, dynamic zoning and load shedding coordination can be considered. Through iterative calculation, it is finally determined that emergency standby channels T1 and T2 have the best effect on system voltage recovery control, but some loads still need to be cut off. Similarly, the final load shedding amount and control cost can be obtained as shown in the Table 4.

Table 4. The comprehensive cost of load shedding scheme with dynamic zoning

Zone	The amount of load shedding/MW	The ratio of load shedding/%	Comprehensive control cost
MD	0	0	0.43
CF	245	6.3	
WJ	782	20.1	

It can be seen that considering the coordinated control of dynamic zoning and load shedding, the load shedding of the power grid is reduced significantly, and the comprehensive control cost is also reduced significantly.

5 Conclusion

In this paper, the application of dynamic zoning steady-state control of power grid is studied in order to reduce load loss, and the following results and conclusions are obtained:

When the steady-state under voltage level of the system is above 0.8 p.u, the under voltage load shedding device usually does not operate, and the system can still operate for a long time. Only when the voltage of certain buses in the power grid drops to an unacceptable level or cannot be restored for a long time, will a part of the load be cut off automatically to ensure the safe and stable operation of the system and uninterrupted power supply to important users. Therefore, dynamic zoning operations can be considered in this situation to reduce load shedding.

This article proposes a method for coordinating and optimizing dynamic zoning and load shedding measures based on direct search method. Firstly, the zoning strategy of the system is determined. Then, by defining the control sensitivity index and comprehensive weighting index of the load, the refinement level of load control is further improved, reducing the impact and economic losses on normal production and life, and has significant economic and social benefits. The effectiveness of the proposed method was verified through simulation in actual power grids.

Acknowledgements. This study is supported by the Mass entrepreneurship and innovation Program of State Grid Zhejiang Electric Power Company, Research and Demonstration of Key Technologies for Load Side Stability Coordination Control of New Power Systems in 2022,No.B711JZ220008.

References

1. Yao, L., Zhu, L., Zhou, M., et al.: Prospects of coordination and optimization for power systems with high proportion of renewable energy. Autom. Electric Power Syst. **41**(9), 36–43 (2017)
2. Zhang, H., Tian, H., Ding, C., et al.: A low-frequency and low-voltage load shedding method based on centralized coordination and real-time distributed control. Power Syst. Clean Energy **38**(4), 37–43 (2022)
3. Xue, Y., Ren, X., Wei, H.: Comments on the optimization and coordination of low- frequency and low-voltage load shedding decision-making. Autom. Electric Power Syst. **33**(9), 100–107 (2009)
4. Lin, S., Wu, J., Mo, C., et al.: Dynamic partition and optimization method for reactive power of distribution networks with distributed generation based on second-order cone programming. Power Syst. Technol. **42**(1), 238–246 (2018)
5. Yan, X., Xu, Y.: Multi-time scale reactive power optimization of distribution grid based on model predictive control and including RDG regulation. Trans. China Electro Tech. Soc. **34**(10), 2022–2037 (2019)
6. Lei, X., Pan, S., Guan, X., et al.: Transmission safety margin constrained unit commitment in power systems. Proc. CSEE **34**(31), 5651–5658 (2014)
7. Xu, Y., Yan, X., et al.: Dynamic partitioning real-time reactive power optimization method for distribution network with renewable distributed generators participating in regulation. Mod. Electric Power **37**(1), 42–50 (2020)
8. Yang, J., Yan, Z., Feng, D.: Equilibrium model for integrated energy-reserve electricity market with regional reserve constraints. Autom. Electric Power Syst. **33**(11), 13–17 (2009)
9. Zhou, X., Xu, W., Xu, C., et al.: The assistant decision making for power grid equipment overloading considering load transfer actions. Power System Protect. Control **41**(23), 61–66 (2013)
10. Yu, H., Xu, Q., Xu, B., et al.: Graph cut method for dynamic zonal reserve allocation in power grid with wind power integration. Proc. CSEE **40**(12), 3765–3774 (2020)
11. Li, Z., Liu, F., Cui, X., et al.: Coordinate control study for dynamic division and load shedding considering electrical security accident risk. Power Syst. Protect. Control **45**(1), 35–40 (2017)
12. Zhu, L., Zhou, X., Tang, L., et al.: Multi-objective optimal operation for micro-grid considering interruptible loads. Power Syst. Technol. **41**(6), 151–158 (2017)

Forecasting-Aided Graphical Learning for Robust State Estimation of Distribution System

Cao Di[1(✉)], Junbo Zhao[2], Jiaxiang Hu[1], Yuehui Huang[3], Qi Huang[1], Zhe Chen[4], and Weihao Hu[1]

[1] University of Electronic Science and Technology of China, Chengdu, China
caodi@uestc.edu.cn
[2] Department of Electrical and Computer Engineering, University of Connecticut, Storrs, CT 06269, USA
[3] State Key Laboratory of Operation and Control of Renewable Energy and Storage Systems, China Electric Power Research Institute, Beijing, China
[4] Department of Energy Technology, Aalborg University, Pontoppidanstraede 111, Aalborg, Denmark

Abstract. The forecasting of of pseudo-measurements play an important role in distribution system state estimation (DSSE). This paper proposes robust DSSE method based on forecasting-aided graphical learning method. The nodal power consumption models are first built to produce pseudo-measurements based on deep neural network. Then, the pseudo-measurements and real-time measurements are represented as a graph according to the topology of the distribution network, which are further processed by a graph attention network to capture the mapping relationship between the graphical measurements and the state variables based on the error modeling of pseudo-measurements. The robustness against anomalous measurements is achieved through the embedding of structural information of DN. The modeling of pseudo-measurements further enhance its robustness by guiding the formulation of edge weights of the graph neural network. Comparative tests are carried out on a IEEE 119-node system to demonstrate the effectiveness and robustness of the proposed method.

Keywords: Forecasting-aided state estimation · Graph neural network · Distribution network

1 Introduction

The penetration of distributed renewable energy sources are continuously increasing in recent years, which causes huge challenges for the stable and secure operation of the distribution networks (DN). State estimation can provide reliable data supporting real-time monitoring analysis, voltage control, and economic dispatching of distribution system [1–3]. However, the distribution system state estimation (DSSE) faces huge challenges owing to the limited real-time measurements, imprecise physical parameters, and variablility of renewable energy sources [4].

Y. Xue et al. (Eds.): PMF 2023, LNEE 1129, pp. 137–148, 2024.
https://doi.org/10.1007/978-981-99-9251-5_11

Various methods have been porposed in literature. Among them, weighted least squares (WLS) is the one of the most studied DSSE method. A WLS-based DSSE method is proposed for a three-phase network [5]. Reference [6] proposed a DSSE method based on WLS and the developed three-phase model. It also introduced the concept of stochastic results and conducted analysis in detail. A DSSE method that can deal with complex variables was proposed in [7] based on Wirtinger calculus and WLS method.

When the errors of all measurements obey the Gaussian distribution, the WLS method is equivalent to maximum likelihood estimation. However, the WLS-based methods are not suitable for unobservable distribution system since large estimation error may persist when there is a small model fitting error [8]. This bring huge challenges for the implementation of WLS method in practice. To enhance the observability of the distribution system, various forecasting methods have been proposed to produce pseudo-measurements, which fall into the category of forecasting-aided DSSE method. Reference [9] proposed a WLS-based DSSE method that employed an deep neural network for pseudo-measurement modeling. Simulation results demonstrated that the generated pseudo-measurements allow the WLS method to achieve better quality estiamtes. The exact line parameters and network topology are typically assumed to be perfectly known for the WLS method. But, such a fact does not hold for DN owing to the scarcity of measurements and the aging of the network [10].

Another way to deal with DSSE is to employ discriminative learning to capture the regression rule from the measurements to state variables [11]. The learning-based methods can exploit valuable information from the abundant historical data, thus holding the promise to enhance performance of DSSE. Reference [8] proposed a Bayesian state estimation method for unobservable distribution system based on deep learning method. A deep neural network is employed to directly learn the mapping relationship between measurements and state variables in [12, 13].

The learning-based methods can exhibit satisfactory performance when sufficient historical data are available. However, typical learning-based methods treat the measurements as a vector that ignores the structural correlation between different measurements [14–16]. In addition, they employ black-blox network to capture the mapping relationship between measurements and state variables from data, resulting in poor generalizability and interpretability of DSSE model. This decrease their robustness to anomalous situations such as missed measurements due to the cyber-attacks or sensor malfunctions. Additionally, most forecasting-aided DSSE methods utilized various pseudo-measurement modeling methods to enhance estimate accuracy of iteration-based WLS method, the impact of the quality of generated pseudo-measurements on the performance of learning-based methods has been seldom studied.

To this end, this paper propose a forecasting-aided graphical learning for robust state estimation of unobservable DN where the measurements may be missing, noisy, and unreliable. The main contributions are

- The proposed DSSE method is robust to noisy and unreliable measurements. This is achieved by representing the measurements as a graph and employing a graph attention network (GAT) to capture the regression rule between measurements and state variables. The embedding of topology information enable the proposed method to restore the missed or noisy measurements utilizing information of its neighbouring nodes.

- The forecasting of pseudo-measurements enhance the quality of estimates, as well as its robustness to anomalous events. The modeling of pseudo-measurements induce the formulation of edge weight and allow the GAT to pay attention to nodes with low forecasting error. This allow the proposed method to better exploit the value of the pseudo-measurements to deal with the data acquisition errors.

2 Problem Formulation and Proposed Method

2.1 Neural Network-Based Load Forecasting Model

Consider a distribution system with $N + 1$ buses that are collected in $\mathcal{N} := \{1, ..., N\}$, where the substateion is at the bus indexed by $n = 0$. Collect all the lines into $\mathcal{L} := \{(n, n')\} \subseteq N \times N$. Let $p_n^c + jq_n^c$ represents the active and reactive power of load demand at bus *n*; and $x_n = v_n \angle \theta_n$ denotes the state of bus *n*, where v_n and θ_n represent its voltage magnitude and angle, respectively.

The nodal active/reactive power injection can be denoted as a time series $\{p_{n,t}^c, q_{n,t}^c\}$, where $p_{n,t}^c$ represent the active power of load demand of bus *n* at time-step *t*. Historical consumption data and other variables such as time index and node index are used as the input features that are denoted as $a_{n,t}$. The aim of the forecasting of pseudo-measurements is to look for a function $f_n(\cdot)$ that maps from the input features $a_{n,t}$ to $p_{n,t}^c$ that is formulated as

$$\hat{p}_{n,t}^c = f_n(a_{n,t}),\ n \in \mathcal{N} \tag{1}$$

where $\hat{p}_{n,t}^c$ represents the predicated power of bus *n* by the forecasting model at time-step *t*. We employ deep neural network-based learning method to capture the regression rule from $a_{n,t}$ to $\hat{p}_{n,t}^c$. Then, the mapping relationship between them is denoted as

$$\hat{p}_{n,t}^c = z_l[...z_1(a_{n,t})] \tag{2}$$

$$z_i = g(W_i * o_{i-1} + b_i),\ i = 2, 3, ..., l \tag{3}$$

where z_i denotes the mapping relation of the ith layer of NN; o_{i-1} is the output of *(i-1)*th layer of the NN; W_i and b_i denote the weights and bias of ith layer, respectively; g is the activation function; l represents the number of layer of the forecasting model. The variables of the model θ_n are optimized according to the following loss based on the gradient rule:

$$Loss(\theta_n) = \sum_{i=1}^{B} |\hat{p}_{n,i}^c - p_{n,i}^c|, \tag{4}$$

$$\theta_n' \leftarrow \theta_n - \eta_n \nabla_{\theta_n} J(\theta_n) \tag{5}$$

where B is the number of batch size; and η_n denotes the learning rate for the forecasting model of bus *n*.

2.2 GAT-Based State Estimator

Traditionally, learning-based methods just stack the measurements of DN and treat them as a vector, which ignores the structural correlations between the measurements. To exploit the valuable structural information of the real-time and pseudo-measurements, we represent them as a graph-stuctured data and embed the topology knowledge in the GAT-based estimator.

Specifically, the input features of the GAT is denoted as $X = (M, A)$, where $M \in R_{k\times n}$ represents the nodal feature matrix, and $A \in R_{n\times n}$ is the adjacency matrix. Instead of predetermining the weights of adjacent nodes, the GAT learns to attend to the specific nodes that contributes most to the enhancement of estimate quality by introducing the attention model into the graph network. The hidden state of node i is calculated as

$$h_{att,i} = \sigma_{GAT}\left(\sum_{j\in N(i)} \alpha_{ij} g_j(m_j)\right), \tag{6}$$

where $h_{att,i}$ denotes the output representation of node i by the GAT layer; σ_{GAT} represents the activation function of the GAT layer; $g_j(\cdot)$ denotes the embedding function, which is a multi-layer perception; α_{ij} is the attention score that represents the correlation between node i and j. It can be derived according to

$$eij = \sigma_{LR}(w^T(g_i(m_i)||g_i(m_i))), \tag{7}$$

$$\alpha ij = \frac{\exp(eij)}{\sum_{k\in N(i)} \exp(eik)}, \tag{8}$$

where σ_{LR} represents the leaky rectified linear function; || denotes the concatenation operation. To stabilize the training process of the GAT-based state estimator, mulit-ahead attention model is adopted in the proposed method. There are L independent attention models that are utilized to obtain the hidden features, which are concatenated for further processing. Then, (6) is revised to

$$h_{att,i} = \overset{L}{\underset{l=1}{||}} \sigma_{GAT}\left(\sum_{j\in N(i)} \alpha^l_{ij} g_j(m_j)\right), \tag{9}$$

where α^l_{ij} denotes the attention score calculated by the lth attention model.

To extract common features of the whole system, a convolution neural network (CNN) is employed after the GAT layer, the output of which are further processed by a fully-connected neural network (FCN) to embed features. The GAT layer, CNN, and FCN layer together comprise the first graph module. Then, the output representations are processed by the two graph modules that share the same architecture with the first module. The two graph modules are task-specific that corresponds to the estimation of voltage magnitude and angel, respectively. After that, we concatenate the embedding of two task-specific modules and fed them into a CNN and FCN for estimation of state variables.

Remark: Note that the pseudo-measurements are generated according to the mean percentage error of nodal forecasting models during the training process. The graph-structured input data and the GAT method allow the structural information to be embedded in the neural network, the aid of forecasting model further enable it to assign proper weights to discriminate the importance of each neighbor. The embedding of physical knowledge and the aid of forecasting allow it to achieve better robustness than traditional learning-based methods.

2.3 Training of the Load Forecasting Model and GAT-Based State Estimator

The training of the proposed method can be divided into two steps: the training of the nodal load forecasting model based on historical data and the learning of GAT-based state estimator according to the forecasting errors of pseudo-measurements. The detailed training procedure are listed in Algorithm 1.

Algorithm 1 Training of the proposed method

```
1: Randomly initialize the variables of the load forecasting model and the state estimation
   model
 for epoch $e = 1, 2, \ldots N$
2:       sample a batch of data from the training set
3:       calculate the loss value according to (4)
4:       update the variables of forecasting model according to (5)
End for
5:   Calculate the forecasting errors of each node on test set
   for epoch $e = 1$: $M$
6:       randomly sample a batch $B$ from the training data, obtain a sample of the
   pseudo-measurement according to the error distribution of each node and concatenate them
   with the real-time measurement
7:     calculate the loss value and optimize the parameters based on the gradient rule
  End for
```

3 Numerical Results

3.1 Experimental Setting

The diagram of the test sytem [17] is shown in Fig. 1. The realistic power consumption data published by Irish Commission for Energy Regulation Smart Metering Project [18] are used in this test. 536 days of smart meter measurements of 4095 customers are utilized. The interval of the measurements is 30 min. We aggragate the power consumption data from 35 customers as the load demand of one node. The nodal load demand data are first normalized to preserve the randomness of the power consumption behavior of customers. Then, they are multiplied with the base value of each node to match the scale of IEEE 119-node system. A constant power factor is assumed. In the test system,

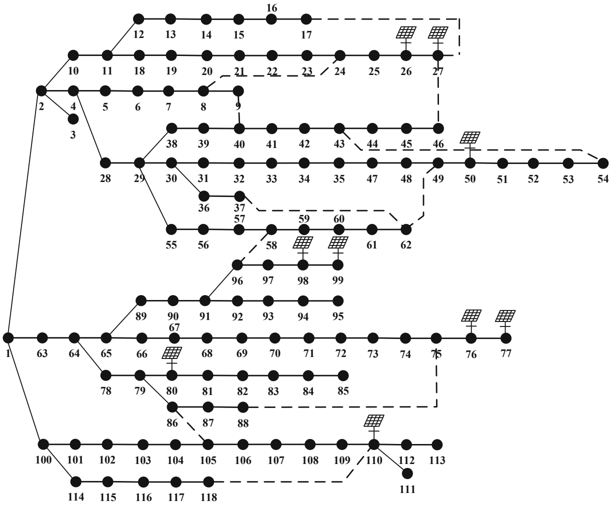

Fig. 1. The diagram of the IEEE 119-node system.

we have six PV units that are located at node 26, 27, 76, 77, 98, and 99, respectively. The active power capacity of the PV units is set to 1.8 MW. The field PV generation data from a pilot project in southwest China is utilized to reflect the variance. The real measurements include the active/reactive power flow in 25% lines of the system. The error distributions of the real-time measurements are assumed to be Gaussian with 0 mean and 1% of the measurements as the deviation. The pseudo-measurements include the active/reactive power consumptions of all the nodes. The measurement errors are modeled based on the load forecasting models.

For the training of the load forecasting model, 4000 instances of samples are used. The input of the forecasting model of node i include $\{p^c_{i,t-336}\}_{i\in\mathcal{N}}$, $p^c_{i,t-672}$, $p^c_{i,t-1344}$, $p^c_{i,t-2688}$, and the one-hot encoding of time index and node index. The output is $p^c_{i,t}$. 800 instances of samples are utilized as the test set to model the forecasting error of each node. Then, the 800 instances of samples are used by the GAT model, where 600 instances are used for training and the rest for performance evaluation.

The neuron numbers of the hidden layers of the load forecasting model are set to 400, 200, and 200, respectively. The batch size and learning rate are set to 32 and 1e-4, respectively. For the attention model in the GAT module, 8 attention heads are used. Both the kernel size and stride length of the CNN in the GAT module are set to 1. For the CNN in prediction module, they are set to 3 and 1, respectively. The AdamW optimizer is selected for the optimization of the state estimator.

3.2 Evaluation of the Load Forecasting Model

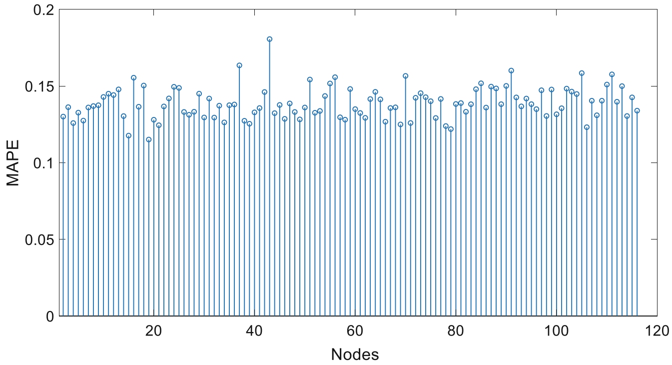

Fig. 2. MAPE of the forecasting models on different nodes.

The performance of the load foreasting model on different nodes are shown in Fig. 2. The mean absolute percentage error (MAPE) is selected as the evaluation index. That the largest forecasting error is 18.1% of node 44, and the lowest error is 11.5% of node 20. The average MAPE of all the nodes is 13.9%. That the difference of nodal forecasting error motivate the design of the forecasting-aided DSSE method by inducing the formulation of edge weights of GAT to better incorporate the uncertainties of the forecasting error of nodal injection.

3.3 Evaluation of the Robustness of the Proposed DSSE Method

To evaluate the accuracy of and robustness of the proposed forecasting-aided GAT method, we compare it with several benchmark DSSE methods: (1) WLS method, where accurate physical parameters of DN are assumed to be known. The forecasting values of nodal load consumption are used as the pseudo-measurements; (2) the back-proppagation neural network method (BP), where a deep neural network is utilized as the state estimator that is trained according to the forecasting error of each node; (3) the GAT method, where GAT is employed to learn the repression rule from the measurements to the state variables. The error of the pseudo-measurements is set to 50%, as is often the case.

Two experiments are designed to investigate the robustness of the proposed method to typical data acquisition errors. The first experiment is implemented to evaluate the robustness to noisy observations. 5 cases where different proportions of real-time measurements are randomly selected and added with 20% uniform noise are considered in this test. The performance of different DSSE methods under various noise level are shown in Table 1. The best performance of each case is shown in a bold color. As is shown in the table, the accuracy of different methods are relatively high under the normal condition. The proposed method outperforms other benchmarking methods in both voltage magnitude and angle. When random noises are added to the 10% randomly selected real-time measurements, the estimation accuracy of all DSSE method decrease.

When we continuous to increase the proportion of noisy measurements, more obvious performance degradation can be observed. The performance drag of the iteration-based WLS method is the most apparent. The MAE of voltage magnitude and angle decrease 93.1% and 257.7% when compared with the normal condition. This implies that the WLS method is sensitive to the data acquisition error. By contrast, the learning-based methods are more robust to the noisy observations. The advantage of learning-based methods in dealing with measurement misalignment is observed here. Compared with the GAT method, the proposed forecasting-aided GAT method can learn discriminative weights to attentive to credible nodal injection values through the guidance of node-specific forecasting error. Therefore, it can maintain its accuracy even when half of the real-time measurements are corrupted. The results imply the advantage of the proposed method in dealing with the data acquisition errors.

Table 1. MAE for different DSSE methods when different proporations of real-time measurements are noised.

Method	0		10%		20%		50%	
	Mag	Ang	Mag	Ang	Mag	Ang	Mag	Ang
WLS	5.09	10.4	6.60	18.7	7.31	25.9	9.83	37.2
BP	4.59	5.9	4.69	6.26	4.94	7.14	5.15	7.05
GAT	6.19	5.62	6.37	6.48	6.44	6.73	6.68	8.59
Pro	*4.48*	*4.95*	*4.59*	*5.46*	*4.65*	*5.53*	*4.93*	*7.05*

The second test is carried out to investigate the robustness of various DSSE methods to missing observations and noisy measurements. Four cases are considered: (1) Case 1, where the real-time measurements located at branch 4–28 are lost; (2) Case 2, where the real-time measurements located at branches 4–5 and 65–66 are lost; (3) Case 3, where the real-time measurements located at branches 2–10, 4–28, and 100–101 are lost; (4) Case 4, where the real-time measurements located at branch 2–4, 30–31, 4–28, 69–70, 100–101 are lost. For the four cases, 20% uniform noise is added to 50% randomly selected nodes to simulate measurement misalignment.

The performances for different DSSE methods on test data are shown in Table 2. That significant performance degradation of BP method can be observed when some real-time measurements are lost. Its accuracy decrease 628.6 and 589.8% for voltage magnitude and angle under Case 4, respectively. The negative impact of missing measurements on the learning-based method is observed here. Since the GAT method embed the topology information of DN in the neural network, it can fill in the missing values using the information of neighboring nodes. Therefore, it outperforms the BP method in both voltage magnitude and angle under the four cases. This illustreates the advantages of physics-informed neural network in dealing with the anomalous measurements. The proposed method incorporate the forecasting errors of nodal power consumpiton, which allow it to better exploit the values of pseudo-measurements. Therefore, it outperforms BP and GAT methods under four cases. Although the WLS method achieve better performance than the proposed method in voltage magnitude under Case 3 and 4, its performances on voltage angle are much worse than the proposed method under all cases. In addition, it rely on the accurate physical line parameters that are difficult to obtain in practice, while the proposed method can learn from historical data and reduce reliance on physical circuit parameters.

Table 2. MAE for different DSSE methods when some real-time measurements are lost.

Method	Case 1		Case 2		Case 3		Case 4	
	Mag	Ang	Mag	Ang	Mag	Ang	Mag	Ang
WLS	10.2	39.7	10.5	42.3	*10.6*	42.2	*10.8*	44.4
BP	11.3	16.1	13.0	12.5	25.5	27.9	33.9	40.7
GAT	9.19	9.78	10.1	10.1	16.2	15.1	29.8	31.6
Pro	*6.70*	*7.82*	*7.90*	*8.50*	13.2	*12.0*	*23.1*	*26.2*

The voltage profiles of a time-slot on test data for various DSSE methods under normal conditions are plotted in Fig. 3. That all the DSSE methods can provide accurate state estimation results when there are no data acquisition errors. This is consistent with the result in Table 1.

The voltage profiles obtained by different methods under Case 2 are shown in Fig. 4. That the estimate accuracies of all DSSE methods have different degree drop when compared with that in Fig. 3. The data acquisition errors significantly decrease the accuracy of WLS-based method. It struggles to provide accurate estimation of voltage angle under this condition, see node 68–99 in Fig. 4b for example. The BP method also suffers from obvious performance degradation when some real-time measurements are lost, see node 70–77 and 90–99 in Fig. 4a. The disadvantage of ignoring the physical knowledge is observed here. By contrast, the GAT and proposed method embed the structural information in the neural network, which enable them to restore the missing or noisy values utilizing the information of adjacent nodes. Thus, they outperform the WLS and BP methods. The incorporation of uncertainties of noal power consumption further enable the proposed method to pay attention to pseudo-measurements with low forecasting errors, which allow the proposed method to better deal with data acquisition errors by rationally exploiting the value of pseudo-measurements. The comparative results illustrate the benefits of embedding the topology information and forecasting errors of pseudo-measurements.

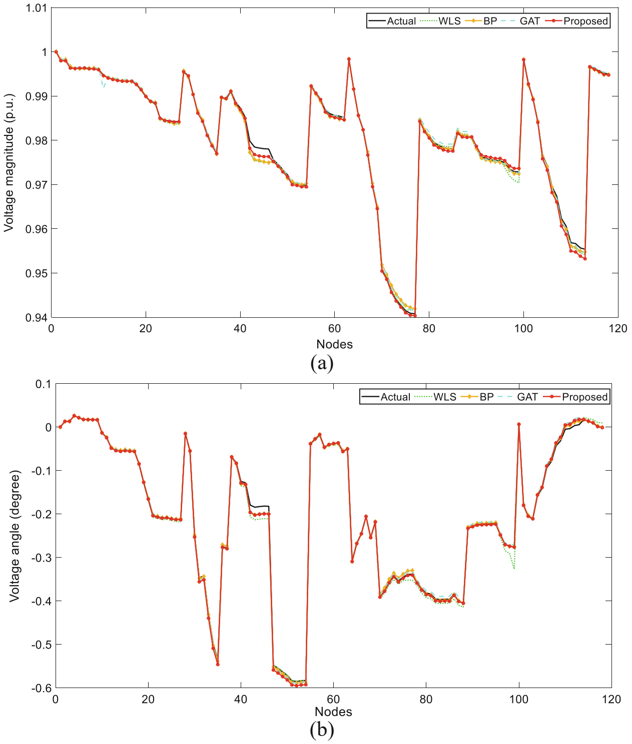

(a)

(b)

Fig. 3. Voltage profiles for different DSSE methods under normal condition: **a** voltage magnitude; **b** voltage angle.

4 Conclusions

This paper proposes a forecasting-aided robust DSSE method based on physics-informed GNN. The nodal power consumption forecasting is first built to capture the uncertainties of pseudo-measurements, followed by a GAT-based state estimator that is trained according to the forecasting errors. Comparative tests on IEEE 119-node system demonstrate that: (1) the embedding of structural information enable the proposed method to achieve better robustness to missing measurements than typical learning-based methods; (2) the aid of the forecasting models of pseudo-measurements further enhance the robustness of the proposed DSSE method in deal with data acquisition errors.

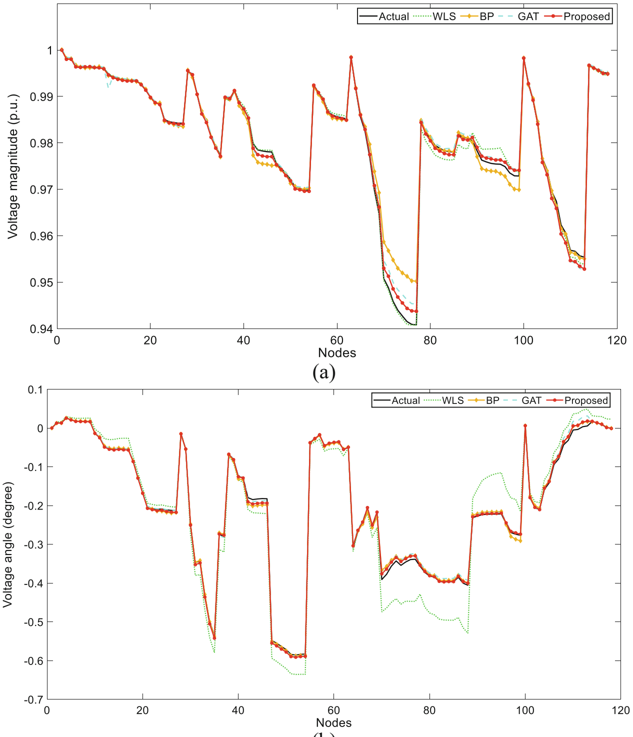

(a)

(b)

Fig. 4. Voltage profiles for different DSSE methods under Case 2: **a** voltage magnitude; **b** voltage angle.

References

1. Primadianto, A., Lu, C.N.: A review on distribution system state estimation. IEEE Trans. Power Syst. **32**(5), 3875–3883 (2017)
2. Zhao, J., et al.: Power system dynamic state estimation: motivations, definitions, methodologies, and future work. IEEE Trans. Power Syst. **34**(4), 3188–3198 (2019)
3. Zhang, Y., Wang, J., Li, Z.: Interval state estimation with uncertainty of distributed generation and line parameters in unbalanced distribution systems. IEEE Trans. Power Syst. **35**(1), 762–772 (2020)
4. Ngo, V., Wu, W.: Linear programming contractor for interval distribution state estimation using RDM arithmetic. IEEE Trans. Power Syst. **36**(3), 2114–2126 (2021)
5. Baran, M.E., Kelley, A.W.: State estimation for real-time monitoring of distribution systems. IEEE Trans. Power Syst. **9**(3), 1601–1609 (1994)
6. Li, K.: State estimation for power distribution system and measurement impacts. IEEE Trans. Power Syst. **11**(2), 911–916 (1996)
7. Džafić, I., Jabr, R.A., Hrnjić, T.: Hybrid state estimation in complex variables. IEEE Trans. Power Syst. **33**(5), 5288–5296 (2018)
8. Mestav, K.R., Luengo-Rozas, J., Tong, L.: Bayesian state estimation for unobservable distribution systems via deep learning. IEEE Trans. Power Syst. **34**(6), 4910–4920 (2019)

9. Manitsas, E., Singh, R., Pal, B.C., Strbac, G.: Distribution system state estimation using an artificial neural network approach for pseudo measurement modeling. IEEE Trans. Power Syst. **27**(4), 1888–1896 (2012)
10. Cao, D., Zhao, J., Hu, W., Liao, Q., Huang, Q., Chen, Z.: Topology change aware data-driven probabilistic distribution state estimation based on Gaussian process. IEEE Trans. Smart Grid **14**(2), 1317–1320 (2023)
11. Zamzam, A.S., Fu, X., Sidiropoulos, N.D.: Data-driven learning-based optimization for distribution system state estimation. IEEE Trans. Power Syst. **34**(6), 4796–4805 (2019)
12. Barbeiro, P. N. P., Krstulovic, J., Teixeira, H., Pereira, J., Soares, F.J., Iria, J.P.: State estimation in distribution smart grids using autoencoders. In: Proceeding IEEE 8th International Power of Engineering Optimal Conference, March 2014, pp. 358–363 (2014)
13. Zhang, L., Wang, G., Giannakis, G.B.: Real-time power system state estimation and forecasting via deep neural networks. IEEE Trans. Sig. Process. **67**(15), 4069–4077 (2019)
14. Liao, W., Bak-Jensen, B., Pillai, J.R., Wang, Y., Wang, Y.: A review of graph neural networks and their applications in power systems. J. Mod. Power Syst. Clean Energy **10**(2), 345–360 (2022)
15. Cao, D., et al.: Physics-informed graphical representation-enabled deep reinforcement learning for robust distribution system voltage control. IEEE Trans. on Smart Grid. https://doi.org/10.1109/TSG.2023.3267069
16. Cao, D., Zhao, J., Hu, W., Yu, N., Hu, J., Chen, Z.: Physics-informed graphical learning and Bayesian averaging for robust distribution state estimation. IEEE Trans. Power Syst. https://doi.org/10.1109/TPWRS.2023.3282413
17. Ghasemi Damavandi, M., Krishnamurthy, V., Martí, J.R.: Robust meter placement for state estimation in active distribution systems. IEEE Trans. Smart Grid **6**(4), 1972–1982 (2015)
18. Commission for Energy Regulation (CER): CER smart metering project- electricity customer behaviour trial, 2009–2010. 1st edition. Irish social science data archive. SN: 0012-00. www.ucd.ie/issda/CERelectricity

Energy Storage Battery Life Prediction Based on CSA-BiLSTM

Ruofan Zhao[1], Shaoze Zhou[2], Xinzhe Xu[3], and Shuxin Zhang[1](✉)

[1] School of Electrical Engineering, Northeast Electric Power University, Jilin 132012, China
`zhang_shu_xin@126.com`
[2] NARI Group Corporation (State Grid Electric Power Research Institute), Nanjing 211106, China
[3] State Grid Beijing Electric Power Company, Beijing 100031, China

Abstract. Life prediction of energy storage battery is very important for new energy station. With the increase of using times, energy storage lithium-ion battery will gradually age. Aging of energy storage lithium-ion battery is a long-term nonlinear process. In order to improve the prediction of SOH of energy storage lithium-ion battery, a prediction model combining chameleon optimization and bidirectional Long Short-Term Memory neural network (CSA-BiLSTM) was proposed in this paper. The maximum discharge capacity of the battery was used to define the battery SOH. The chameleon optimization algorithm was introduced into the architecture of the bidirectional short-short memory network to optimize the network. The percentages of *MAE* and *RMSE* were 2.501 and 2.511% before optimization, and 1.292 and 1.420% after optimization, respectively. The optimized model has high prediction accuracy.

Keywords: Energy storage battery · State of health · Bidirectional long short-term memory neural network · Chameleon Swarm Algorithm

1 Introduction

In recent years, along with the proposal of "double carbon" goal, reducing the proportion of fossil energy has become a hot topic under the background of "double carbon". In the near future, new energy storage stations will make great achievements. As the "heart" of new energy storage stations, it is particularly important to accurately estimate the health of energy storage batteries.

Lithium-ion battery is the heart of energy storage power station with its advantages of high energy density, low self-discharge rate, good cycling performance and no memory effect [1]. State of health (SOH) indicates the extent to which a battery's performance and capacity change over time and over time. When the SOH of the battery drops to about 70%, it is necessary to replace the battery in time to ensure the safe and stable operation of the electrical equipment. Therefore, accurate SOH estimation is of great significance for the safe and stable operation of lithium-ion batteries.

Nowadays, SOH acquisition methods for lithium-ion batteries are mainly divided into three categories, namely direct measurement method [2–4], model-based method

Y. Xue et al. (Eds.): PMF 2023, LNEE 1129, pp. 149–157, 2024.
https://doi.org/10.1007/978-981-99-9251-5_12

[5–8] and data-driven method [9–12]. Literature [13] use artificial neural network to characterize the nonlinear relationship between battery terminal voltage and SOH, but it is easy to fall into local minimum. Literature [14] use support vector machine (SVM) to predict SOH, and uses PSO to optimize the kernel function, but the SVM method is time-consuming and difficult to determine the kernel function.

At present, the common definition method is to take the internal resistance and capacity of lithium-ion battery as the definition index. In practice, since the capacity of lithium-ion batteries is difficult to be directly measured, this paper defines the battery SOH from the perspective of capacity, and uses the maximum discharge capacity of the battery instead of the capacity to define the battery SOH as:

$$SOH=\frac{Q_{\max}}{C_{\mathrm{r}}} \tag{1}$$

where, $Q_{\max}$ represents the current maximum discharge capacity of the battery, and C_{r} represents the capacity of the lithium-ion battery when it leaves the factory. The definition is more consistent with the use of energy storage devices.

2 Introduction to Prediction Model

2.1 BiLSTM Neural Network

Bidirectional Long Short-Term Memory neural network is a variant of Recurrent Neural Network (RNN), Bi stands for bidirectional. LSTM stands for Long Short-Term Memory. In traditional RNN, information flows in only one direction, front to back or back to front. But in BiLSTM, uses past and future contextual information to predict the current output by processing the input sequence in both directions simultaneously. It consists of two LSTM layers, a forward (front to back) and a reverse (back to front), whose outputs are spliced or merged at each time step to form the final output.

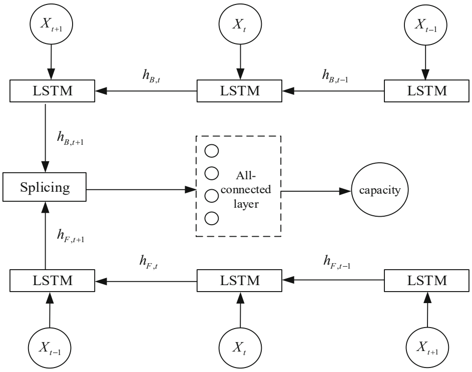

Fig. 1. BiLSTM Network structure diagram

The output of the two layers is spliced to form a new output, and the splicing formula is:

$$h=\left\{h_{F,t},h_{B,t}\right\} \tag{2}$$

where, $h_{F,t}$ are time t the time series is input forward; $h_{B,t}$ are time t the time series is input backward. In the Fig. 1, LSTM consists of a forgetting gate, an input gate and an output gate:

$$\begin{aligned} f_t &= \sigma(W_f[h_{t-1}, x_t] + b_f)\pi \\ i_t &= \sigma(W_i[h_{t-1}, x_t] + b_i) \\ \overline{C_t} &= \tanh(W_c[h_{t-1}, x_i] + b_c) \\ C_t &= f_t \odot C_{t-1} + i_t \odot \overline{C_t} \\ O_t &= \sigma(W_o[h_{t-1}, x_t] + b_o) \\ h_t &= O_t \odot \tanh(C_t) \end{aligned} \tag{3}$$

where C_t is the state of the memory unit, f_t, i_t and O_t are the forgetting gate, input gate and output gate respectively, b_f, b_i and b_o are the corresponding bias of each gated unit, b_c is the input state bias, W_f, W_i and W_o are the corresponding weight of each gated unit. W_c for input state Heavy, $\sigma(\cdot)$ as the sigmoid function.

2.2 Chameleon Swarm Algorithm

Chameleon Swarm Algorithm (CSA) is an optimization algorithm which simulates the dynamic behavior of chameleon when it comes to finding food. Chameleon Swarm Algorithm is an optimization algorithm with excellent performance. It simulates the behavior characteristics of chameleon to optimize the problem. The algorithm has excellent performance in optimization ability, convergence speed and accuracy, and is suitable for solving various optimization problems. The algorithm principle is divided into the following four steps:

(1) Initialization: randomly initialize within the search range.
(2) Searching for prey: The chameleon's way of searching for prey can be expressed as follows:

$$y_{t+1}^{i,j} = \begin{cases} y_{t,i}^{i} + p_1(P_t^{i,j} - G_t^j)r_2 + p_2(G_t^j - y_t^{i,j})r_1, r_i \geq P_p \\ y_t^i + \mu\Big((u^j - l^j)r_3 + l_b^j\Big)\mathrm{sgn}(rand - 0.5), r_i < P_p \end{cases} \tag{4}$$

where:, $y_{t,i}^{i}$, $y_{t+1}^{i,j}$ represents the position of chameleon i at the t and $t + 1$ iterations in J-dimensional space; G_t^j represents the position of the optimal individual in the t iteration of the chameleon in the J-dimensional space; $P_t^{i,j}$ represents the position of the best individual of chameleon i in J-dimensional space so far; u^j and l^j represent the upper and lower limits of the spatial dimension of chameleon hunting prey. $\mathrm{sgn}(rand - 0.5)$ indicates the direction of rotation of the chameleon; r is the random number of [0,1]; p_1 and p_2 represent the parameters of the chameleon's ability to find prey, and P_p represents the probability of the chameleon's perception of prey. When $r_i \geq P_p$ is present, the chameleon will change its position in space to better find prey. When $r_i \leq$ Pp, the chameleon changes direction to search for prey.

(3) eye rotation of chameleon: position update when simulating the eye rotation of chameleon to locate prey:

$$y_{t+1}^{i} = yr_{t}^{i} + \overline{y_{j}^{i}} \tag{5}$$

where y is the average position coordinates of the chameleon eyes before rotation, and y_{t+1} is the coordinates after rotation.

(4) Capture prey: the speed of the chameleon tongue capturing prey is defined as:

$$v_{t+1}^{i,j} = wv_{t}^{i,j} + c_1(G_t^j - y_t^{i,j})r_1 + c_2(P_t^{i,j} - y_t^{i,j})r_2 \tag{6}$$

where c_1 and c_2 control G and P to influence the tongue-snapping speed of chameleon, generally taking the empirical value $c_1 = c_2 = 1.75$.

2.3 CSA-BiLSTM Optimization Prediction Model

In this paper, a CSA-BiLSTM optimization prediction model is proposed. By combining chameleon optimization algorithm with BiLSTM neural network algorithm, a better prediction effect can be obtained. The flow of this model is shown in the Fig. 2.

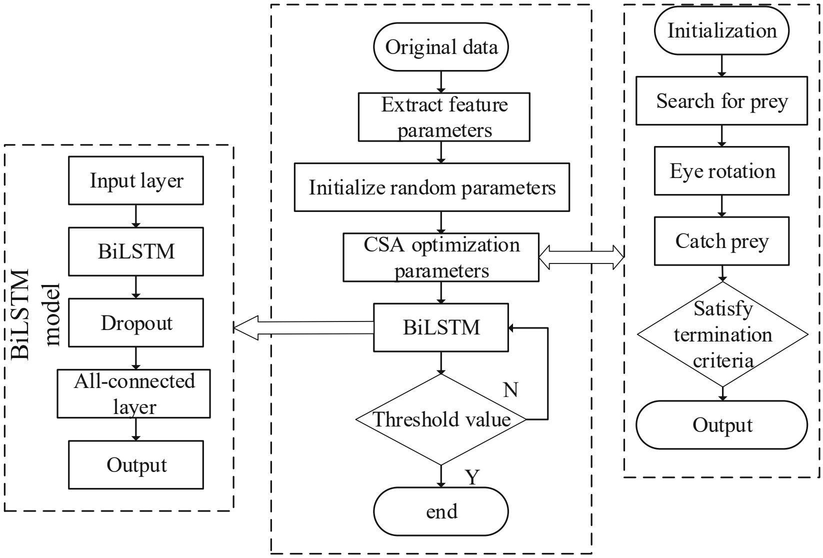

Fig. 2. Flow chart of the CSA-BiLSTM model

In summary, the proposed CSA-BiLSTM optimization prediction model combines chameleon optimization algorithm with BiLSTM neural network algorithm to achieve more accurate and rapid prediction effect. This model has potential application value in prediction problems and provides new ideas and methods for the research of related fields.

3 Method Verification

In this paper the proposed method for the effectiveness of the method for estimating the battery SOH, this section USES the Oxford battery aging data set [15] (Oxford Battery Degradation Dataset) results show, the data set used batteries for lithium-ion batteries, battery rated capacity of 740 mA·h. The constant current discharge is repeated on the lithium-ion battery, and the battery is charged again after complete discharge. The complete process is one cycle. After 100 cycles, a capacity calibration was carried out and its current capacity was measured by ampere-hour integration method. The purpose of battery aging is achieved through multiple cycles of charging and discharging. When the battery capacity reaches about 70%, the cycle test is stopped.

It is worth noting that the voltage, temperature, and capacity curves recorded during each cycle correspond to a SOH. As the constant current charging mode is adopted, it is not suitable for current to be used as input parameters. The average voltage and average temperature at the time of charging are selected as input characteristics, and the maximum discharge capacity of the battery is selected as output characteristics. Some of the data are shown in the Table 1.

Table 1. Part of the experimental data

SOH%	Amount of charge/mA·h	Discharging current/A	Temperature/°C
99.88	739.11	0.74	40.93
93.28	690.36	0.74	40.91
85.37	631.74	0.74	40.86
78.05	577.59	0.74	41.43
75.76	560.65	0.74	41.37

The network construction and data processing tools all adopt matlab2021a. Parameter settings of neural network model are shown in Table 2.

3.1 Evaluation Criteria

In order to reflect the superiority of the proposed algorithm, the reference value of battery SOH is compared with the predicted values of CSA-BiLSTM, BiLSTM and other algorithms, and the comparison results are shown in Fig. 3.

Table 2. Neural network model parameters

Parameter name	Parameter value
BiLSTM layer	Unit = 128
Dropout	Node loss probability is 0.2
Epochs	200
Batchsize	568
Options	Adam
Learning rate	0.0002
CSA algorithm population number	5
CSA algorithm evolution number	5

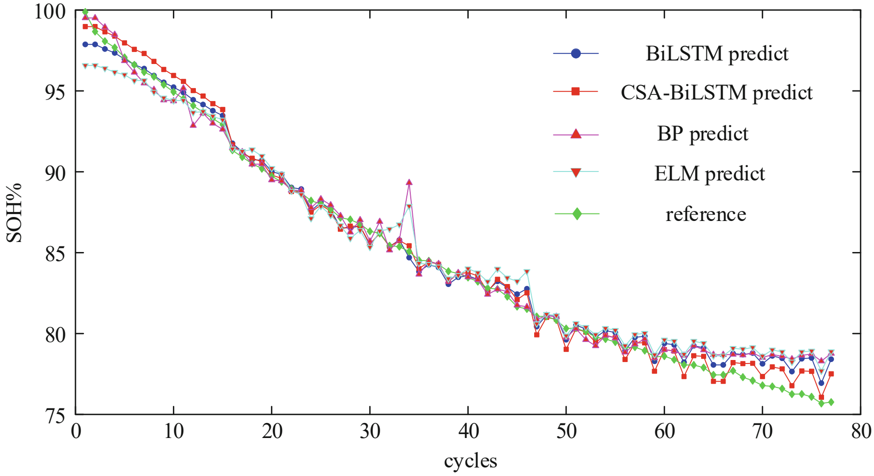

Fig. 3. Comparison of SOH predicted values and measured values of different algorithms

In order to compare the predictive effect of battery SOH before and after the optimization model, mean absolute error (*MAE*) and root mean squared error (*RMSE*) were used for evaluation. *MAE* and *RMSE* formulas are as follows:

$$MAE = \frac{1}{n}\sum_{i=1}^{n}\left|(y_i - \hat{y}_i)\right| \tag{7}$$

$$RMSE = \sqrt{\frac{1}{n}\sum_{i}^{n}(y_i - \hat{y}_i)^2} \tag{8}$$

where y_i is the *i* predicted maximum discharge quantity, and that $\hat{y}_i$ is the *i* true maximum discharge quantity.

Firstly, the relative error curve before and after optimization is calculated, and the calculation result is as shown in the Fig. 4.

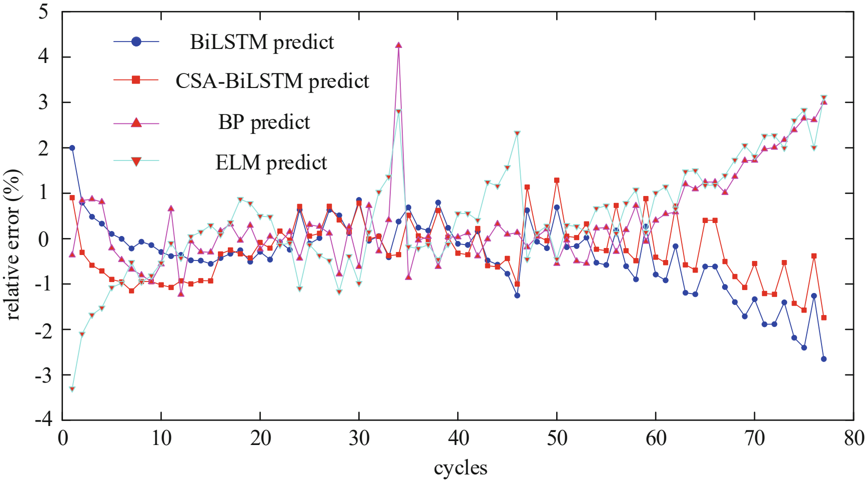

Fig. 4. Comparison of SOH relative error curves of different algorithms

As we can see in the Fig. 4, the relative error before optimization is mainly distributed in [−2.5, 2%]. After optimization, the relative error is mainly distributed in [−1, 1%]. The relative error of BP neural network prediction value is mainly distributed in [−1, 4%]. The relative error of ELM neural network prediction value is mainly distributed in [−1, 3%]. The relative error after optimization is relatively small.

According to the definition of SOH in this paper, *MAE* and *RMSE* of different algorithms can be calculated. The calculation results are shown in Table 3.

Table 3. Error results of different algorithms

Algorithm type	MAE	RMSE
BiLSTM	2.501	2.551
CSA-BiLSTM	1.292	1.420
BP	2.537	2.624
ELM	2.521	2.596

The calculation results show that the prediction error of the proposed algorithm is obviously reduced.

4 Conclusion

In this paper, a bidirectional Long Short-Term Memory neural network is proposed, and the CSA-BiLSTM prediction model optimized by chameleon optimization algorithm is used to predict the SOH of energy storage lithium-ion batteries. By comparing the errors before and after optimization, it is found that the optimized prediction results have high accuracy and robustness. In this study, Oxford battery aging data set is used for verification, which is off-line aging data. In the next step, the SOH prediction of energy storage batteries in actual use can be further studied.

Acknowledgments. This work is supported by National Key Research and Development Program of China (2022YFB2402700): "Key technologies for stable operation and direct current transmission of large-scale new energy power generation bases without conventional power supply support".

References

1. Huang, X., Zhang, X., Wei, T., et al.: Development and applications status of supercapacitors. Adv. Technol. Electrical Eng. Energy **36**(11), 63–74 (2017)
2. Ng, K.S., Moo, C.S., Chen, Y.P., et al.: Enhanced coulomb counting method for estimating state-of-charge and state-of-health of lithium-ion batteries. Appl. Energy **86**(9), 1506–1511 (2009)
3. Love, C.T., Virji, M.B.V., Rocheleau, R.E., et al.: State of-health monitoring of 18650 4S packs with a single point impedance diagnostic. J. Power Sources **266**, 512–519 (2014)
4. Galeotti, M., Cinà, L., Giammanco, C., et al.: Performance analysis and SOH (state of health) evaluation of lithium polymer batteries through electrochemical impedance spectroscopy. Energy **89**, 678–686 (2015)
5. Doyle, M., Newman, J.: Modeling the performance of rechargeable lithium-based cells: design correlations for limiting cases. J. Power Sources **54**(1), 46–51 (1995)
6. Doyle, M., Newman, J.: Analysis of capacity-rate data for lithium batteries using simplified models of the discharge process. J. Appl. Electrochem. **27**(7), 846–856 (1997)
7. Zou, C., Manzie, C., Nesic, D., et al.: Multi-time-scale observer design for state-of-charge and state-of-health of a lithium-ion battery. J. Power Sources **335**, 121–130 (2016)
8. Deshpande, R., Verbrugge, M., Cheng, Y.T., et al.: Battery cycle life prediction with coupled chemical degradation and fatigue mechanics. J. Electrochem. Soc. **159**(10), A1730–A1738 (2012)
9. Andre, D., Appel, C., Soczka-Guth, T., et al.: Advanced mathematical methods of SOC and SOH estimation for lithium-ion batteries. J. Power Sources **224**, 20–27 (2013)
10. Wang, D., Miao, Q., Pecht, M.: Prognostics of lithium-ion batteries based on relevance vectors and a conditional three-parameter capacity degradation model. J. Power Sources **239**, 253–264 (2013)
11. Richardson, R.R., Birkl, C.R., Osborne, M.A., et al.: Gaussian process regression for in-situ capacity estimation of lithium-ion batteries. IEEE Trans. Ind. Inf. **15**(1), 127–138 (2018)
12. Richardson, R.R., Osborne, M.A., Howey, D.A.: Gaussian process regression for forecasting battery state of health. J. Power Sources **357**, 209–219 (2017)
13. He, F., Hu, Y., Guo, G., et al.: State of health estima-tion for lithium-ion batteries based on ANN. Power Technol. **41**(5), 708–710 (2017)

14. Qin, T., Zeng, S., Guo, J.: Robust prognostics for state of health estima-tion of lithium-ion batteries based on an improved PSO-SVR model. Microelectron. Reliab. **55**(9–10), 1280–1284 (2015)
15. Birkl, C.R.: Diagnosis and Prognosis of Degradation in Lithium-ion Batteries. University of Oxford, Oxford (2017)

Quantitative Analysis on the Impact of Coal Power Carbon Emission Cost and Capacity Price Revenue on the Long-Term Power Generation Balance of the System

Bin Cai, Jiahui Chen, Yusheng Xue(✉), Feng Xue, and Enfan Lu

NARI Group Corporation (State Grid Electric Power Research Institute), Nanjing 211106, China
xueyusheng@sgepri.sgcc.com.cn

Abstract. The long-term evolution of coal power installed capacity in the physical dimension is affected by social factors such as coal-related policy mechanisms (carbon pricing and capacity electricity prices) and the decommissioning decision of existing coal power. Under the guidance of the Cyber-Physical-Social system in Energy (CPSSE), a hybrid simulation model covering coal power policy, existing coal power decommissioning decision, and long-term evolution of coal power installed capacity is established. The evolution process of the long-term financial condition and decommissioning time of each coal power plant with different carbon emission costs and capacity price revenue are obtained by the simulation model. And impact of coal power plant decommissioning on the long-term power generation balance of the whole system are analyzed. The results show that high carbon emission costs may have a fatal impact to the financial condition of coal power plants, and the resulting large-scale decommissioning in advance of coal power plants can cause long-term power generation balance risks of the whole system, and a reasonable capacity price can help to address the above risks.

Keywords: CPSSE · Energy transition · Hybrid simulation · Carbon emission cost · Capacity price · Coal power plant decommissioning · Long-term power generation balance

1 Introduction

Influenced by factors such as resource endowment and development history, China's power structure has been long dominated by coal power. With the advancement of the energy revolution and the "dual carbon" target, new energy sources such as wind and photovoltaic have become the main drivers of power generation growth, but coal power is still the largest power source in China, and the proportion of coal power installed capacity and power generation is still about 50% and 60% respectively. Since the average service life of coal power units in China is relatively short [1], coal power will still be the most major power source for a long time in the future if it servers as its design life. More importantly, the support of flexible and controllable coal power is inseparable for the

Y. Xue et al. (Eds.): PMF 2023, LNEE 1129, pp. 158–172, 2024.
https://doi.org/10.1007/978-981-99-9251-5_13

construction of new-type power system with new energy as the main sources. Therefore, the relevant power and climate policy mechanisms must be able to ensure the healthy development of coal power.

As one of the largest sources of carbon emissions, coal power has already been covered in China's carbon emission market and began to afford the cost of carbon emissions. Studies on carbon markets has received widespread attention. Studies on the short-term scales mainly involves the total carbon emission setting and carbon quota allocation methods, as well as the market fairness, market efficiency, market game behavior, market efficiency, and the interaction between the carbon market and other policies and mechanisms under different methods [2]. Studies on the long-term scale mainly focuses on the lowest carbon price required by a country or a region to achieve emission reduction targets, and the qualitative principle for the decline of carbon quota benchmark value [5].

On the other hand, because the value of coal power in ensuring the flexible adjustment ability of the new-type power system cannot be fully reflected by relying on power generation revenue solely, the establishment of capacity compensation mechanism or capacity market for coal power has been paid more and more attention. At present, the UK, the US PJM, Sweden, Denmark, Norway, Finland, and other electricity markets are running capacity markets [7]. At the beginning of 2022, the government of China issued a guidance which proposed to explore capacity compensation mechanisms, capacity markets, scarcity electricity prices and other ways to ensure the recovery of power capacity investment and long-term power supply security [8].

However, there are few quantitative research addressing the impact of carbon emission cost and capacity price benefit of coal power long-term power generation balance for the carbon emission cost and capacity price revenue of coal power, and the related important issues have not been paid enough attention. For example, what impact will the growing cost of carbon emissions have on the long-term financial condition of the existing coal power plants? Will the decision makers decommission coal power plants in advance due to the deterioration of financial condition caused by high carbon emission costs? If the coal power plants are decommissioned in advance, how will it affect the long-term power supply security of the whole system? How will different level of capacity price compensation offset the adverse impact of carbon emission cost increase on power supply security?

The above problems not only involve the long-term evolution of power generation installed capacity, carbon emission of power system and other physical dimension factors, but also have a close interaction with social dimension factors such as electric power economy, coal power policy mechanism and decision-making behaviors of coal power operators. It is necessary to integrate policy mechanism and participant behavior into the overall research of electric power technology, economy, and emissions [9]. The concept of CPSSE (Cyber-Physical-Social System in Energy) proposed in [10] provides a research framework for cross-domain dual carbon revolution issues that integrate information, physical, and social elements. The sand-table deduction based on the hybrid simulation of technology, economy, emission, and participant behavior is an effective means to study the above complex problems [11].

Based on the CPSSE framework, this paper establishes a hybrid simulation model covering the policy mechanism of coal power, the retirement decision-making behavior of stock coal power, and the long-term evolution of coal power installed capacity. Based on the sand-table deduction, the effects of different coal power policy mechanisms (carbon pricing reflecting the negative externalities of coal power environment, capacity price reflecting the flexible adjustment value of coal power) on the long-term economic operation index of coal power plants, the retirement time of coal power plants, and the power balance of the whole system are analyzed.

2 Model and Method

2.1 The Interaction of Policy, Company Decision-Making and Long-Term Power Generation Balance

Government affects the game behavior of companies in various markets by formulating economic society, setting "dual carbon" and energy development plans, adjusting various policies, regulation, and market mechanisms. Generation companies (GENCOs) game in energy, electricity, capacity, carbon emissions and capital markets, and determine the construction and decommission of installed power capacity, thus affecting the available power generation capacity and long-term power generation balance of the whole system in the physical dimension (Fig. 1).

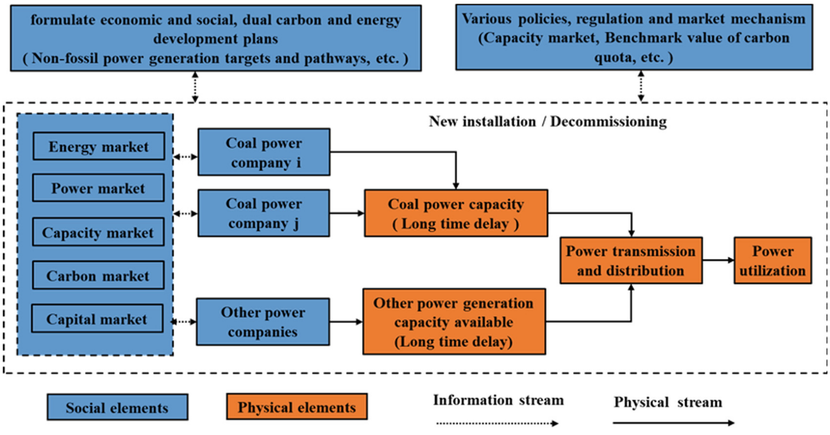

Fig. 1. Technical-economic-emission model of power system

The facility-level simulation model of coal power generation and non-coal power generation is established with year as the simulation step size. It can simulate the investment, construction, operation and decommission stages of power facilities, calculating the dynamic evolution process of installed capacity, power generation, coal consumption, carbon emission, carbon emission quota, power generation cost (fuel, emission, operation and maintenance, finance, etc.), power generation revenue (electricity, capacity), power generation profit and other characteristic quantities of each facility. Only the annual power generation balance is considered in the model, and the power balance and grid security and stability constraints are ignored. Detailed introduction for the simulation model, please refer to References [13].

2.2 Model of Policies

The policies in this study are exogenously given in the form of scenario parameters, including: ① The development target and pathway planning value of non-fossil power generation in the whole system; ② The electricity price of various types of power generation and the capacity price of coal power; ③ The carbon pricing scenario of each year describes by “carbon quota benchmark value & carbon emission price”.

2.3 Model of New Installation and Decommission Behavior of GENCOs

The new installation and decommission of power plants are affected by a large number of factors, including but not limited to: environment (i.e. emission pollution), technical performance (i.e. energy consumption), economy (i.e. profitability) and other factors. However, it is impossible to consider all the factor in models. In this study, simplified behavioral models are constructed for coal power and non-fossil energy.

Coal power

1. New installation: It is assumed that no new coal power will be installed in the research period.
2. Decommission: A simplified model of coal power decommissioning in advance due to poor financial condition is constructed.

- For each coal power plant, after the end of each simulation year t, it is calculated and determined whether its service year reaches the designed life.
- For coal power plants that have not reached the designed life, it is calculated and determined whether the following inequalities are satisfied.

$$p_t/c_t < \alpha_t \tag{1}$$

$$\text{Or} \quad \mathrm{n}_t < \beta_t \tag{2}$$

- Among them, p_t means power generation profit, c_t means power generation cost, and n_t means net assets. α_t and β_t can be set as specific values according to research objectives. The smaller α_t and β_t is, the less likely it is for the coal power plant to be decommissioned in advance.
- If the condition for decommissioning in advance of any coal power plant is met, the agent of that coal power plant will be removed from the simulation for the next simulation year.

Non-Fossil energy

1. New installation: New power capacity of each year is installed according to the non-fossil energy power generation targets and paths set by the government.
2. Decommission: All the non-fossil energy power facilities serve as designed life.

3 Simulation Scenarios and Parameter Settings

To focus on the interaction between coal-related policies, decision-making behavior of coal power companies and long-term power generation balance of the whole system, this paper uses a simplified hypothetical system for simulation and analysis. The simulation process is as follows Fig. 2.

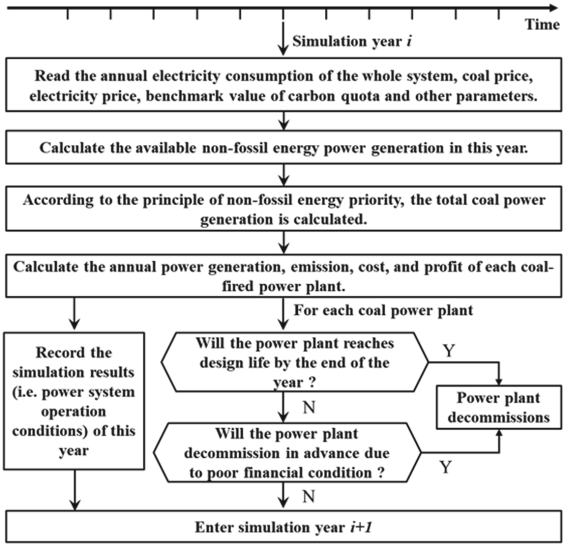

Fig. 2. The process of the dynamic simulation

The key scenarios and parameter settings are as follows:

1. Research period: from 2018 to 2035 (hereinafter referred to as "transition period"), with year as the simulation step.
2. Type of power generation: only coal power and non-fossil energy power generation are considered (non-fossil energy power generation is not subdivided temporarily).
3. Installed power generation capacity of the whole system in the initial year: the installed years of power generation capacity are distributed from 2001 to 2017; all coal power plants installed in the same year are clustered into one coal power object(i.e. Coal_01 represents all the coal power installed in 2001), the capacity and coal consumption rate of each coal power object can be seen in Table 1; all non-fossil energy power sources installed in the same year are clustered into one object as well. It should be noted that this clustering method is a simplified processing to accelerate the simulation speed, and each power generation object does not represent the actual coal power plants or non-fossil energy power sources.
4. Lifespan of generators: 30 years for coal power, 20 years for non-fossil energy.
5. Annual utilization hours of power generation: 1800 h for non-fossil energy power generation; the principle of non-fossil energy priority is adopted in the simulation; the remaining power generation demand of the whole system is supplied by the

Table 1. Main parameters of power generator objects

Year of installation	Coal power			Non-fossil energy power	
	Serial number	Capacity (MW)	Coal consumption rate (g/kWh)	Serial number	Capacity (MW)
2001	Coal_01	2000	320.0	/	/
2002	Coal_02	3000	317.8	/	/
2003	Coal_03	4800	315.6	/	/
2004	Coal_04	4800	313.4	/	/
2005	Coal_05	4800	311.3	Non-fossil_01	300
2006	Coal_06	4800	309.1	Non-fossil_02	500
2007	Coal_07	8000	306.9	Non-fossil_03	800
2008	Coal_08	8000	304.7	Non-fossil_04	1600
2009	Coal_09	8000	302.5	Non-fossil_05	3200
2010	Coal_10	8000	300.3	Non-fossil_06	4000
2011	Coal_11	9600	298.1	Non-fossil_07	4800
2012	Coal_12	9600	295.9	Non-fossil_08	5600
2013	Coal_13	9600	293.8	Non-fossil_09	6400
2014	Coal_14	9600	291.6	Non-fossil_10	7200
2015	Coal_15	8000	289.4	Non-fossil_11	8000
2016	Coal_16	8000	287.2	Non-fossil_12	8800
2017	Coal_17	4800	285.0	Non-fossil_13	9600

coal power, and the power generation is distributed by proportional according to the installed capacity of each coal power plant, the maximum value of annual utilization hours of coal power plant is set as 6000 h.

6. In 2018, the total power generation of the system was 640 billion kWh, and the electricity consumption of the whole system respectively increased by 4.5%, 4.0%, 3.5% and 3.0% in 2019–2020, 2021–2025, 2026–2030 and 2031–2035.
7. The proportion of non-fossil energy power generation in the whole system: increases linearly from 20% in 2018 to 60% in 2035.
8. Carbon emission factor of coal: 2.8 tons of CO_2 per ton of standard coal.
9. Costs of coal power: including financial, depreciation, operation and maintenance, fuel, and carbon emissions costs.
10. Coal power price: The electricity price was set at 355 CNY/MWh during the study period. Referring to the current situation that China does not implement two-part electricity price for coal power, the capacity price is set as 0 in the basic scenario, and the effects of different capacity prices on improving the economic benefits of coal power and supporting the long-term power balance of the system are analyzed.
11. Coal price: set at 800 CNY/ton during the research period.

12. Long-term loan interest rate: 4.9%.
13. Repayment and depreciation: The loan repayment period of each power plant is 15 years, and the depreciation period is 18 years.
14. Benchmark value of power supply carbon emission quota: Three quotas scenarios are set, named *High Quota*, *Mid Quota*, and *Low Quota*; Referring to China's national carbon market launched in 2021, this study assumes that coal power plants start to participate carbon market from 2021, benchmark values of power supply carbon emission quota of the three scenarios are all set as 0.877 t/MWh in 2021 [14], and will respectively be reduced to 0 by 2040, 2045 and 2050 (linear decline among the middle year) in *High Quota*, *Mid Quota*, and *Low Quota* scenarios, and the benchmark values of 2035 are 0.454, 0.365 and 0.231 t/MWh respectively.
15. Carbon emission price: Three carbon emission price scenarios are set, named *High Price*, *Mid Price* and *Low Price*; the carbon emission price in 2021 is set as 60 CNY/ton; the price will increase by 30 CNY/ton, 20 CNY/ton and 10 CNY/ton per year in *High Price*, *Mid Price* and *Low Price* scenarios, and the carbon price will rise to 480,340 and 200 CNY/ton by 2035 respectively.

4 Analysis of Simulation Results

4.1 Impact of Carbon Emission Costs

Analysis of *Mid Quota & Low Price* Scenario

This section analyzes the scenario in which the carbon quota takes the median value and the carbon price takes the low value (recorded as "*Mid Quota & Low Price*").

The total installed power capacity of the whole system during the transition period is shown in Fig. 3. The installed capacity of non-fossil energy power generation will increase significantly to 390 million kW by 2035; Coal_01 to Coal_05 will reach their design life and will be decommissioned one by one after 2031, and the total installed capacity of coal power will decrease to 96 million kW by 2035.

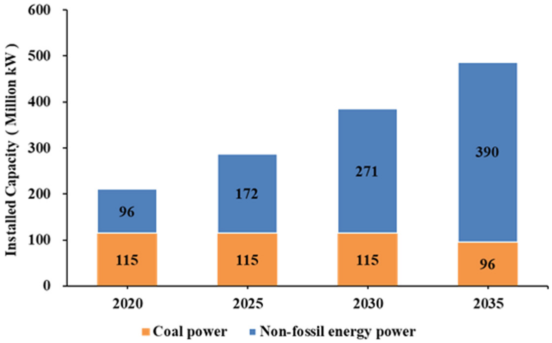

Fig. 3. Installed power generation capacity (2020–2035)

Figure 4 shows the relationship between the total carbon emissions and the total carbon emission quotas of all coal power plants from 2021 to 2035. The actual carbon emissions in 2021 and 2022 are lower than the allocated carbon emission quotas, with a small surplus. In 2023, there will be a gap in carbon emission quotas, and the gap will increase to 217 million tons by 2035.

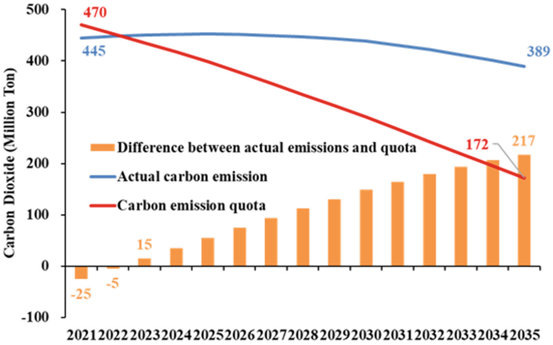

Fig. 4. Total actual CO_2 emissions and quotas for all coal power plants (2021–2035)

In terms of the total carbon emission cost of all the coal power plants, due to the surplus of 25.3 and 5.2 million tons carbon emission quotas in 2021 and 2022, and the emission cost will be −15 and −400 million CNY respectively. Then, the emission costs will be positive value and rise to 43.5 billion CNY by 2035.

The power generation profit (see Fig. 5) and carbon emission cost of all coal power plants in the whole system show the opposite trend. Without considering the cost of carbon emissions (carbon price is 0), as the depreciation cost and financial cost of coal power decrease year by year, the power generation profit of coal power increases to 13.9 billion CNY by 2035. In the scenario of "*Mid quota & Low price*", due to the rapid growth of total emission costs, the growth trend of power generation profits will be reversed after 2023, declining to −29.6 billion CNY by 2035.

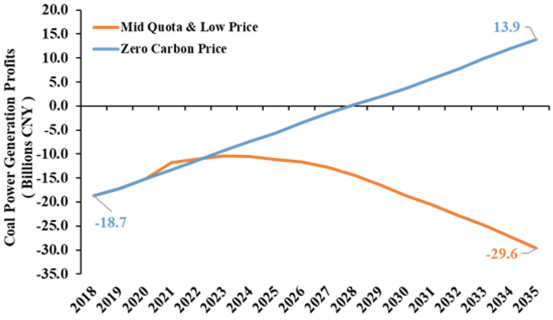

Fig. 5. Generation profit of all the coal power plants (2018–2035)

Due to the difference in coal consumption rate of each power plant, the carbon emissions per unit power supply and carbon emission cost of different coal power plants are different. Figure 6 shows the emission cost of Coal_01, Coal_07 and Coal_17.

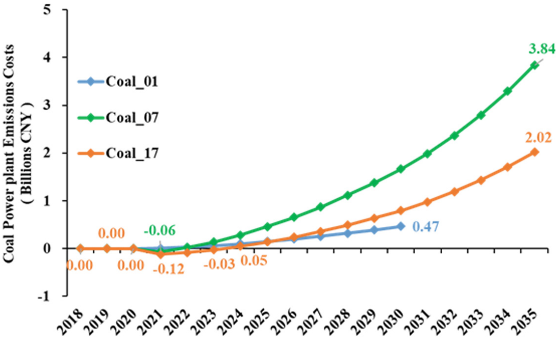

Fig. 6. CO_2 emissions costs of Coal_01, Coal_07 and Coal_17 (2018–2035)

In 2021, the benchmark value of power supply carbon emission is 877 g/kwh. The unit power supply carbon emission of Coal_01 is 896 g/kwh, and the unit power supply carbon emissions of Coal_07 and Coal_17 coal power are 859 and 798 g/kwh, respectively. Therefore, Coal_01 will have a carbon quota gap in 2021, and the carbon emission cost is 0.05 billion CNY. Coal_07 and Coal_17 coal power have carbon quota surplus in 2021, and the carbon emission costs are -60 and -120 million CNY respectively. Subsequently, the carbon emission cost of them increases year by year, and the carbon emission cost of Coal_01 rises to 0.47 billion CNY by 2030. Coal_07 has carbon quota gaps since 2022, and the carbon emission cost will rise to 3.84 billion CNY by 2035. Coal_17 has carbon quota gaps since 2025, and the carbon emission cost will rise to 2.02 billion CNY by 2035.

Due to the combined effect of power generation, depreciation cost, carbon emission cost and other factors, the generation profit of each coal power shows different dynamic evolution characteristics during the transition period. It will not be detailed here.

Analysis of multiple carbon market scenarios

Carbon emission costs will have a negative impact on power generation profits. The decline rate of the benchmark value of power supply carbon emission quota and carbon emission price are important factors affecting the financial conditions of coal power plants. This section analyzes nine carbon market scenarios composed of three carbon quota scenarios and three carbon emission price scenarios (see Sect. 3).

Scenarios without decommissioning in advance of coal power plant

Figure 7 shows the power generation cost of Coal_17 in different scenarios. In general, for the nine carbon market scenarios, except for a small amount of carbon emission quota surplus in the early years, the total power generation cost increase to varying degrees due to the additional increased carbon emission cost.

In the scenario of "*Low Quota & High Price*", coal power plant will afford the highest carbon emission cost, the power generation cost of Coal_17 will rise to 13.7 billion CNY by 2035. In the scenario of "*High Quota & Low Price*", coal power plant will afford the lowest carbon emission cost, the power generation cost of Coal_17 will rise to 8.9 billion CNY by 2035. In the above two scenarios, the power generation cost of Coal_17

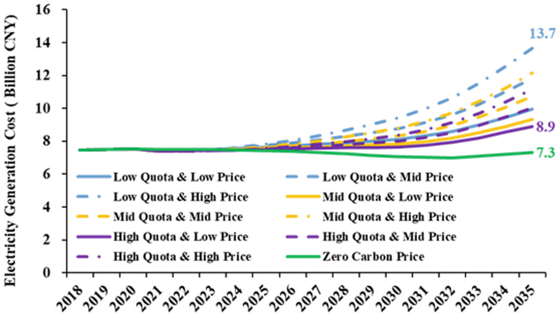

Fig. 7. Generation costs of Coal_17 in different scenarios

is 6.4 billion CNY and 1.6 billion CNY higher than that in scenario of "*Zero Carbon Price*" respectively.

Figure 8 shows the net assets of Coal_17 in different scenarios. The net assets of Coal_17 in 2035 are positive only in the two modest scenarios "*High Quota & Low Price*" and "*Mid Quota & Low Price*", which are 3 billion CNY and 0.7 billion CNY respectively. The net assets of Coal_17 in 2035 for the remaining scenarios are negative. In the scenario of "*Low Quota & High Price*", Coal_17 will afford the highest carbon emission cost, and its net assets will decline to -22.5 billion CNY by 2035.

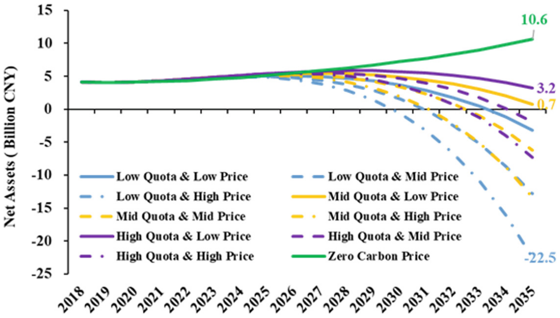

Fig. 8. Net assets of Coal_17 in different scenarios

Scenarios with decommissioning in advance of coal power plant

This section analyzes the impact of different carbon market scenarios if coal power plants decommissioning in advance due to poor financial condition. In the simulation case, the α_t and β_t in formula (1) are set as -25% and 0 respectively, and both remain unchanged during the research period.

Figure 9 shows the situation of decommissioning in advance of coal power and power shortage of the whole system in nine carbon market scenarios. There is no decommissioning in advance of coal power only in two modest scenarios of "*High Quota & Low*

Price" and "*Mid Quota & Low Price*". For the other seven scenarios, there are decommissioning in advance of coal power, and different amount of power shortage occurs except for the scenario of "*High Quota & Mid Price*".

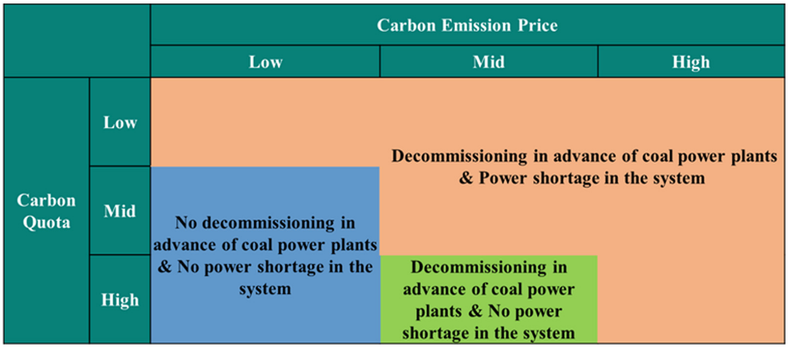

		Carbon Emission Price		
		Low	Mid	High
Carbon Quota	Low	Decommissioning in advance of coal power plants & Power shortage in the system		
	Mid	No decommissioning in advance of coal power plants & No power shortage in the system		
	High		Decommissioning in advance of coal power plants & No power shortage in the system	

Fig. 9. Decommissioning in advance of coal power and power shortage in different scenarios

There are great differences in the decommissioning situation of coal power plants between 9 scenarios. In the scenario of "*Low Quota & High Price*" with the highest carbon emission cost, only Coal_01 will decommission in 2031 when it reaches its design life, the other coal power will all decommission in 2033 due to the serious deterioration of financial condition (that is, the ratio of power generation profit to power generation cost is less than -25%, or the net assets declines to negative).

Figure 10 shows the average service duration of all the coal power plants by 2035 in 9 scenarios. For the two most modest scenarios of "*High Quota & Low Price*" and "*Mid Quota & Low Price*" without decommissioning in advance of coal power, the average service duration of coal power is 26.1 years, the same as that of "*Zero Carbon Price*" scenario. And for the other seven scenarios, the average service duration of coal power decline to 22.0 years –25.8 years.

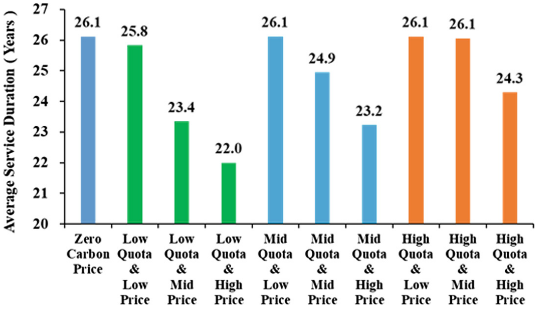

Fig. 10. Average service duration of coal power in different scenarios

Figure 11 shows the power shortage of 6 scenarios with decommissioning in advance of coal power. In the scenario of "*Low Quota & High Price*" with the highest carbon emission cost, power shortages will occur in 2030 and continue to 2035. The power shortage in the "*Low Quota & Low Price*" scenario is relatively light, with a power shortage of 74.7 billion kW in 2035.

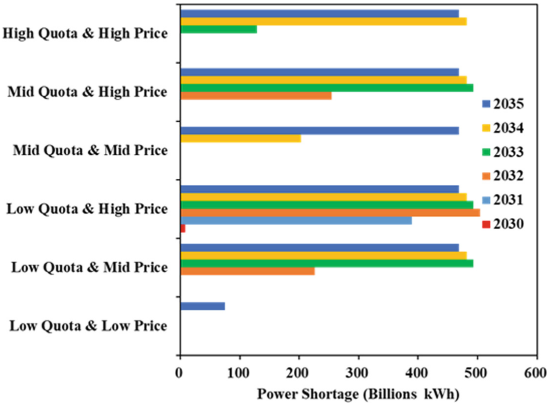

Fig. 11. Power shortage of 6 scenarios with decommissioning in advance of coal power

It should be pointed out that, coal power plants need to meet many other constrains (such as government approve) for decommissioning in advance due to poor financial condition. Therefore, it is impossible to decommission such a large proportion of coal power capacity within a few years. However, based on simulation deduction, the evolution of financial indicators of coal power plants in different scenarios can be quantitatively analyzed (i.e. insolvency or serious losses), which provides decision support for optimizing other policies and scheme that can reflect the value of coal power (i.e. improving financial indicators of coal power through capacity price).

4.2 The Combined Effect of Carbon Emission Cost and Capacity Price Revenue

This section takes the scenario of "*Mid Quota & Mid Price*" as an example to analyze the combined impact of carbon emission cost and capacity price revenue. The capacity price of each year during the transition period is set as follows: from 2018 to 2020, the price is set as 0; from 2021 to 2035, the price increase linearly to *P_CAP* (the higher the value of *P_CAP* is, the higher revenue for the coal power).

The capacity revenue can improve the financial condition of coal power, thus alleviating the trend of decommissioning in advance of coal power. Figure 12 shows the coal power installed capacity of the whole system in different capacity price scenarios. When the capacity price is 0, all the coal power will decommission in advance by 2033 due to the poor financial condition. When *P_CAP* rises to 105 thousand CNY/MW·Year, the total amount of decommissioning capacity of coal power has been greatly reduced, 75 million kW of coal power will be in service by 2035, but it is still lower than the installed capacity of coal power required to ensure power generation balance (78 million kW). When *P_CAP* rises to 110 thousand CNY/MW·Year, 88 million kW of coal power will be in service by 2035, but the annual power generation utilization hours of coal power will reach to 5322 h, therefore, the power supply pressure is still relatively tight. When *P_CAP* rises to 125 thousand CNY/MW·Year, no any decommissioning in advance will occur during the transition period, 75 million kW of coal power will be in service by 2035, and the annual power generation utilization hour of coal power will be reduced to 4878 h.

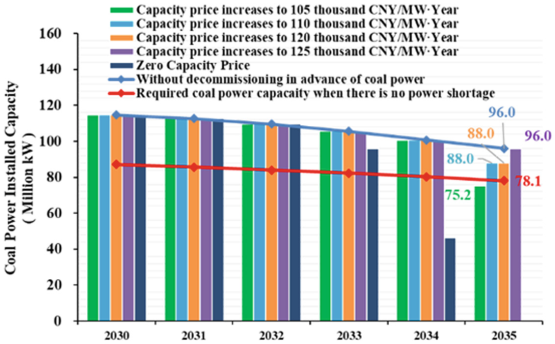

Fig. 12. Installed coal power capacity in different capacity price scenarios

The total capacity price revenue and carbon emission cost of all coal power plants in different capacity price scenarios are shown in Table 2. There is not any decommissioning in advance in above scenarios, and the cumulative carbon emission cost during the transition period is 418 billion CNY. When *P_CAP* rises to 545 thousand CNY/MW·Year, the cumulative capacity price revenue reaches to 421 billion CNY, which can fully cover the carbon emission cost.

Table 2. Capacity revenues and carbon costs in different capacity price scenarios

Cumulative Capacity Price Revenue in different capacity price scenarios (Billion CNY)				Cumulative carbon emission cost (Billion CNY)
$P\_CAP = 150$ thousand CNY/MW·Year	$P\_CAP = 450$ thousand CNY/MW·Year	$P\_CAP = 540$ thousand CNY/MW·Year	$P\_CAP = 545$ thousand CNY/MW·Year	
116	347	417	421	418

5 Conclusion

The evolution process of the long-term financial condition and decommissioning time of each coal power plant, and the impact of coal power plant decommissioning on the long-term power generation balance of the whole system are analyzed in different carbon cost scenarios. On this basis, the effects of different capacity price levels on improving the finiancal condition of coal power plants and the long-term power generation balance of the whole system under the background of low-carbon transition are preliminarily analyzed. The following conclusions are obtained:

1. With the decline of benchmark value of carbon emission quotas and the rising carbon emission price, carbon emission cost will become one of the important factors affecting the financial indicators of coal power plants, such as generation cost, generation profit and net assets.
2. If the benchmark value of carbon emission quota declines too fast and the carbon emission price rises too fast, it may lead to extreme deterioration of the finiancal condition of coal power plants, such as serious losses and insolvency. If the coal power plants decommission in advance without other new installed power supply sources, it will seriously endanger the long-term power generaiton balance.
3. Reasonable capacity price can improve the finiancal indicators, and avoide extensive decommissioning in advance of coal power plants, ensuring power generation balance of the whole system is within a safe margin range.
4. In the future research, it is necessary to consider the influence of coal power installed capacity requirement for power balance and peak regulation balance, and deepen the research on the interaction between benchmark value regulation of carbon emssion quota, coal power capacity price scheme and new energy policies.

Acknowledgement. This work is supported by the China State Grid Corporation Project of Application Preparation Research on Power Grid Actively Supporting Dual Carbon Revolution (No. 5108-202218280A-2-50-XG).

References

1. China Electricity Council: Research on flexible operation and life extension operation of coal-fired power plants [EB/OL]. https://www.cec.org.cn/upload/1/pdf/1609833032589.pdf. Accessed 20 April 2022 (in Chinese)
2. Partnership for Market Readiness (PMR) and International Carbon Action Partnership (ICAP): Emissions Trading in Practice: A Handbook on Design and Implementation. World Bank, Washington, DC (2016)
3. Zhou, P., Wang, M.: Carbon dioxide emissions allocation: a review. Ecol. Econ. **125**, 47–59 (2016)
4. Jiuping, X., Xin, Y., Zhimiao, T.: A tripartite equilibrium for carbon emission allowance allocation in the power-supply industry. Energy Policy **82**, 62–80 (2015)
5. Xiliang, Z., Xiaodan, H., Da, Z., et al.: Research on the pathway and policies for China's energy and economy transition toward carbon neutrality. Manage. World **38**(1), 19 (2022)
6. Zhang, X., Zhang, D., Yu, R.: Theory and practice of China's national carbon emissions trading system. Manage. World **37**(08), 80–95 (2021)
7. Furui, H., Xiuli, W., Tao, S., et al.: Capacity market design in the United Kingdom and revelation to China's electricity market reform. Autom. Electr. Power Syst. **39**(24), 1–7 (2015)
8. National Development and Reform Commission National Energy Administration: Guiding Opinions on Accelerating the Construction of a Unified National Electricity Market System

(Development Reform Structural Reform [2022] No.118) [EB/OL] https://www.ndrc.gov.cn/xxgk/zcfb/tz/202201/t20220128_1313653.html?code=&state=123. Accessed 28 January 2022 (in Chinese)

9. Xue, Y.: The new-type power system actively supporting the dual carbon target of China via CPSSE[EB/OL]. The 6th Purple Mountain Forum, 14th Aug 2021, Nanjing, China. https://mp.weixin.qq.com/s/zhH6HUI40jnaBNqpXjXaQ
10. Xue, Y., Yu, X.: Beyond smart grid—a cyber-physical-social system in energy future. Proc. IEEE **105**(12), 2290–2292 (2017)
11. Xue, Y.: The integration of holistic thinking and reductive thinking, and common progress of basic research and applied research [EB/OL]. The 7th Purple Mountain Forum, 12th Aug 2022, Nanjing, China. https://mp.weixin.qq.com/s/LBZZZiVjxkjF-besux4BA
12. Yinbiao, S., Yusheng, X., Bin, C., et al.: A review of energy transition analysis: elements and paradigms. Autom. Electr. Power Syst. **42**(9), 1–15 (2018)
13. Yan, W., Bin, C., Xinxin, Y., et al.: Quantitative analysis of China's low-carbon energy transition. Int. J. Electr. Power Energy Syst. **119**, 1–9 (2020)
14. Ministry of Ecology and Environment of the PRC: 2019–2020 National Carbon Emissions Trading Quota Setting and Allocation Implementation Plan (Power Generation Industry) [EB/OL]. https://www.mee.gov.cn/xxgk2018/xxgk/xxgk03/202012/W020201230736907121045.pdf. Accessed 20 April 2022 (in Chinese)
15. Cai, B., Xue, Y., Fan, Y., et al.: Optimization on trans-regional electricity transmission scale of China's western renewable energy base: the case study of Qinghai province. In: 2nd International Symposium on Architecture Research Frontiers and Ecological Environment, December 20–22, Guilin, China (2019)
16. Xinxin, Y., Bin, C., Yusheng, X., et al.: Quantitative assessment of clean transition of GenCo considering other participants' generation investment. Energy Proc. **156**, 23–27 (2019)

Analysis of the Status Quo and Coupling Mechanisms of the Ancillary Services Market with Carbon Market, Green Certificate Market and Green Electricity Market Under the Green Energy Transformation

Jiahao Wang[1], Hengrui Ma[1](✉), Bo Wang[2,3], Abdullah Alharbi[4], Hongxia Wang[2,5], and Xiaozhu Li[6,7]

[1] New Energy (Photovoltaic) Industry Research Center, Qinghai University, Xining 810016, China
`henry3764@foxmail.com`
[2] School of Electrical and Automation, Wuhan University, Wuhan 430072, Hubei, China
[3] Hubei Key Laboratory of Power Equipment and System Security for Integrated Energy, School of Electrical Engineering and Automation, Wuhan University, Wuhan, China
[4] Prince Sattam Bin Abdulaziz University, Al-Kharj, Kingdom of Saudi Arabia
[5] Department of Electrical and Computer Engineering, University of Denver, Denver, USA
[6] Engineering Research Center of Ministry of Education for Renewable Energy Generation and Grid Connection Technology, Xinjiang University, Urumqi 830047, Xinjiang, China
[7] School of Electrical and Automation, Xinjiang University, Urumqi 830047, China

Abstract. Against the backdrop of the “dual carbon” goal and the green of energy transformation, the volatility and randomness issues of the new power system dominated by wind and solar power are becoming increasingly prominent, affecting the safe and stable operation of the power system. Therefore, the role of auxiliary services in promoting the use of alternative energy sources and ensuring power quality is becoming increasingly. In this context, this article summarizes and organizes the current development and operations status of the auxiliary services market, carbon market, green certificate market, and green electricity market in mature foreign markets, as well as the experience that can be used for reference. It also sorts out the relationship between the interaction and influence of the auxiliary services market and various other markets. Finally, based on the practical needs for market development to facilitate China’s green energy transformation, development recommendations are provided for the design of the auxiliary services market and various market coupling mechanisms, to fully leverage the synergistic effect of the auxiliary services market with the carbon market, green certificate market, and green electricity market, support China’s green energy transformation.

Keywords: Auxiliary services market · Carbon trading market · Green certificate market · Green electricity market · Market coupling

Y. Xue et al. (Eds.): PMF 2023, LNEE 1129, pp. 173–187, 2024.
https://doi.org/10.1007/978-981-99-9251-5_14

1 Introduction

The 14th National People's Congress (NPC) emphasized the need for China to focus on the promotion of energy conservation and carbon reduction, coordinate energy security by ensuring supply stability and the development of green low-carbon energy sources, examining how to best promote carbon peaking and carbon neutrality. The country's energy development over the next 5 years and beyond must pay more attention to promoting green transformation [1]. Orderly promoting the carbon neutrality work of carbon peaking, implementing the action plan of carbon peaking, and studying a safe, stable and efficient new power market are important ways to promote the construction of new power systems. At present, the design of market mechanism in the relevant research on the power market is still one of the concerns [2].

There is a high correlation between the electricity market, carbon market, green certificate market, and green electricity market in terms of construction purpose, transaction type, transaction subject and transaction object. Against the backdrop of vigorous reforms in the electricity market, an increasing proportion of renewable energy entities are participating in the market and a decline in renewable energy subsidies [3]. Studying the coupling mechanism of diversified markets can provide a coordinated and closely connected trading environment for the diversified market-oriented trading system of entities, enhance the power grid's ability to absorb renewable energy generation, and form a joint force to solve the problem of "difficult to enter the market" when participating in the market due to the intermittency and instability of some renewable energy sources.

With the access of more and more new energy sources, the demand for power quality is gradually increasing. As a part of the power market, the ancillary services market mainly ensures the safe operation of the grid through frequency modulation, peak shaving, standby and other measures, which not only has the particularity of specific power functions, but also has the commonalities that ultimately affect market prices and power generation costs. Therefore, explore the ancillary services market and the carbon market the coupling relationship between the green certificate market and the green electricity market provides new ideas for the coordinated operation of various trading mechanisms in the new power system.

2 The Current State of the Energy-Related Market in the Domestic and Foreign Markets

Among mature markets abroad, there are more applications and data that can be discussed and analyzed for reference, whereas in China, there is more development and theoretical research on the current situation.

2.1 Coupling Relationship Between the Current Operation Status of the European Carbon Market and the Electricity Market

The European Union Emission Trading System (EU ETS) is the world's earliest legally binding carbon market established for enterprises, it is the main tool used by the EU to control Green House Gas emissions (GHG) such as carbon dioxide [4]. The system is closely related to the European electricity market as the power generation industry is the main beneficiary and polluter of the system. EU ETS encourages emission reduction and the development and use of innovative technologies by setting prices for GHG such as carbon dioxide and encourages market participants to invest in low-carbon technologies. The European electricity market is a trading platform for electricity production and consumption among European countries. The EU ETS is coupled with the European electricity market, allowing power companies to be influenced by emission trading systems in decision-making, investment, and electricity production.

The EU ETS dictates the production cost of power generation enterprises shall not exceed 2% of the enterprise's production cost; Therefore, the cost of carbon emissions can lead to higher production costs for coal-fired power generation companies versus those of gas power generation companies. When the European Union Allowance (EUA) price is high enough, power generation companies may change their fuel types, switch from coal-fired power generation to gas power generation and save costs by changing the original clearing order; After conducting carbon trading, the electricity prices of the 20 member states of the European Union will increase by an average of 10–13 euros per megawatt hour, an increase of 12–27% [5].

The EU green certificate trading mechanism is a product of the liberalization of the electricity market, mainly to ensure that renewable energy power producers obtain additional benefits. The competition mechanism of this mechanism has attracted many EU countries to participate. Taking the Netherlands as an example, the local green certificate market follows the principle of voluntary demand, which comes in part from collective power producers who promise to supply green electricity, The other part is the end users who have reduced taxes due to the use of green electricity [6].

2.2 Coupling Relationship Between the Current Operation Status of the US Carbon Market and the Electricity Market

Similar to the carbon market in the European Union, the carbon market in the United States is closely coupled with the electricity market. Each state promotes emissions reduction through the implementation of carbon trading, with the most representative being California's carbon trading market and regional GHG reduction plans (RGGI) [7].

The California carbon market has set limits on total emissions, allowing emission entities such as power plants to choose between emission reduction and trading. The initial goal of construction was to reduce carbon emissions to 1990 levels by 2020. For the majority of carbon quotas allocated to the power sector, the government first issued free quotas to enterprises and requires them to submit them. Then, the submitted quotas are auctioned off, and the auction revenue is returned to the enterprises. It is stipulated that there will be no increase in user costs and prices will not be transmitted to consumers [8].

The RGGI regional carbon market also adopts the method of entrusted auction, but the RGGI carbon emission quota is divided into two levels. The first level is to allocate the quota of the entire region to each state, and the second level is to allocate the quota of each state to each power plant; It affects the spot market trading of electricity and the medium to long-term investment of power producers, thereby changing the power structure of the electricity market. It also changes the electricity market trading between RGGI regions and non RGGI regions, and there is a possibility of carbon leakage to non RGGI regions; The establishment of the RGGI carbon market has led member states to achieve over 40% reduction in carbon emissions from the power industry, despite achieving 8% GDP growth [9].

The green certificate system in the United States implements state level management. The federal government has not implemented a nationwide green certificate policy, and most states that implement carbon quota systems have established renewable energy certificate (REC) trading systems, which include green certificate certification, trading, and regulatory agencies. Renewable energy electricity produced by power producers can be traded through renewable energy certificates, and the trading scope can be conducted across the state [10]. The green certificate standards vary among different states, but there is some flexibility, and some states can also allow green certificate transactions to take place across states.

2.3 Current Situation of Energy-Related Markets in China

Facing the goal of "dual carbon", under a unified governance framework system, China is also coordinating the correlation between various markets (e.g. the carbon market, electricity market, and green certificate market) to effectively connecting them at the market mechanism level; At present, China has made progress through academic research on the relevant electricity market, implementing key measures such as multi market collaborative operation, medium to long-term and spot trading linkage, auxiliary services market construction, and high demand response mechanism construction.

Development status of auxiliary services market. In the process of transitioning from planned to market-oriented and from free to paid, China's power auxiliary services market has gradually opened up various competitive businesses, improving the ability of unit regulation and the quality of auxiliary services. The development and status experience of China's auxiliary services market is shown in Fig. 1 [11]; By the end of 2022, China's power auxiliary services had achieved full coverage of power grids in 6 major regions and 33 provinces, and the basics of a unified auxiliary services rule system have been established. In 2022, through the market-oriented mechanism of auxiliary services, a total of over 90 million kW of regulation capacity will be excavated throughout the country, promoting an annual increase in clean energy generation of over 100 billion kW h; Coal power enterprises have received compensation benefits of approximately 32 billion yuan due to auxiliary services [12].

"Through the creation of auxiliary services markets, the construction and development of renewable energy plants is encouraged, which results in more stable and reliable renewable energy generation "The development of the auxiliary services market further enhances the scale and types of auxiliary services, thereby better ensuring the reliability and stability of renewable energy generation in the electricity market, reducing operational risks, volatility, and uncertainty. The marginal cost of renewable energy power generation enterprises is almost zero. In the carbon market, through trading carbon quotas and policy measures, renewable energy revenue is promoted. The profit space of new energy installation is increased." Due to the market-oriented resource allocation attribute, investment in and construction of renewable energy facilities increases." The

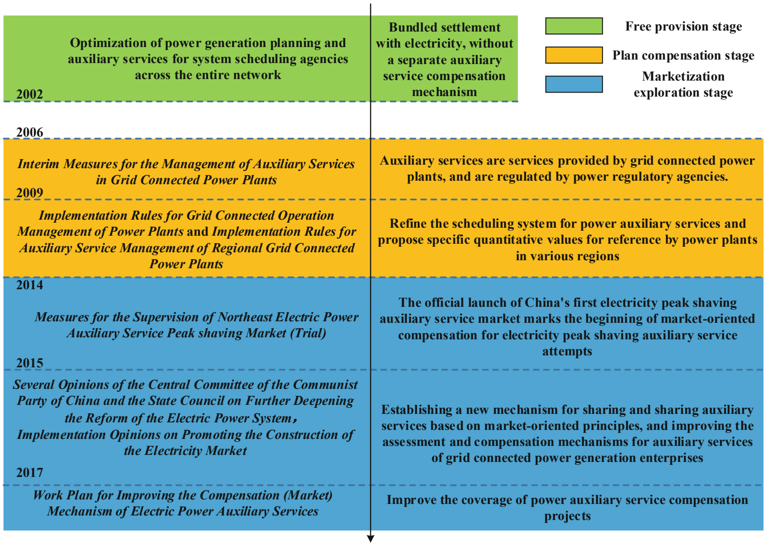

Fig. 1. The development experience of China's auxiliary services market

market-oriented resource allocation attribute makes the investment and construction of renewable energy related power generation installations increase, and the demand for auxiliary services market also increases, as shown in Fig. 2.

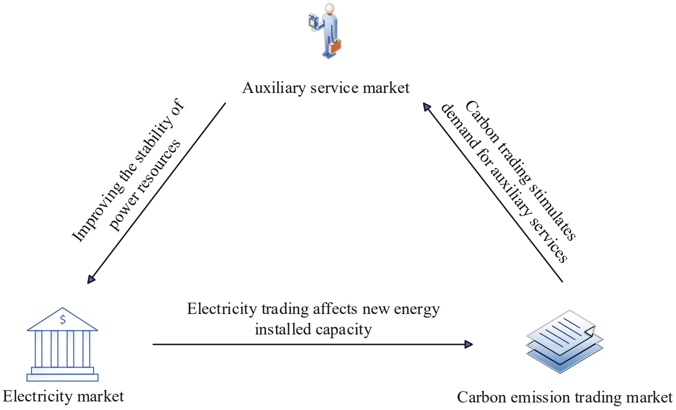

Fig. 2. The mechanism of auxiliary services in power systems

2.4 Current Development Status of Carbon Trading Market

Carbon emissions trading market. The carbon market can be achieved by limiting the total amount and issuing or auctioning carbon emission permits. Carbon quotas are issued by the government, and the market entities are mainly key emission units. The key emission units in the national carbon market refer to large enterprises in industries such as chemical manufacturing, construction materials, steel, and electricity production, whose annual emissions reach or exceed 26,000 tons, or whose total energy consumption reaches or exceeds 5000 tons of standard coal, the value was 10,000 tons from 2019 to 2020.

"The original plan, developed, was for the original eight pilot markets (i.e., Beijing, Shanghai, Guangzhou, state all 8 cities) would gradually transition to an online national carbon market. However, the "Interim Regulations on the Management of Carbon Emission Trading (Revised Draft)," released in March 2021, stated that no local pilot markets were being constructed. In March 2023, the Ministry of Ecology and Environment issued the "Implementation Plan for Setting and Distributing the Total Amount of National Carbon Emission Trading Quotas for 2021 and 2022 (Power Generation Industry)", which clarified the total amount and allocation plan of carbon emission trading quotas; The plan points out that in 2021, the total quota of the power generation industry in the national carbon emission trading market will be 560 million tons of carbon dioxide, including 386 million tons of coal power and 174 million tons of gas power [13].

At present, the original 8 pilot markets in Beijing, Shanghai, Guangzhou and other places will gradually transition to the online national carbon market, and in March 2021, the "Interim Regulations on the Management of Carbon Emission Trading (Revised Draft)" stated that no local pilot markets are being constructed [14]. Currently, the 8 pilot markets still exist. At present, carbon quotas are only carried out through spot trading, without introducing financial trading products such as carbon futures and options. Only when the future carbon emission trading market enters a certain mature stage and the economic attributes of carbon emission trading are clearer, will we consider providing market entities with corresponding financial risk management tools to avoid spot risks in the carbon emission trading market.

As of February 2023, the trading volume of carbon emission quotas in the national carbon emission trading market was 1.8543 million tons, with a total trading volume of 104 million yuan and an average trading price of 55.87 yuan/ton. Among them, the trading volume of listed agreements was 2,54,300 tons, with a trading volume of 14.2958 million yuan, with a maximum trading price of 57.50 yuan/ton and a minimum trading price of 55.00 yuan/ton; The bulk agreement transaction volume is 1.6 million tons, with a transaction amount of 89.3 million yuan. The highest transaction price is 57.50 yuan/ton, and the lowest transaction price is 55.00 yuan/ton [15].

CCER. China Certified Emission Reduction (CCER) is another trading entity in China's carbon market that is beyond carbon quotas. It refers to the carbon emissions reduced through projects such as clean energy, energy conservation and emission reduction, and forest carbon sinks. These reductions can be traded in the carbon trading market or used to offset corresponding carbon quotas [16]. Its low price can meet the carbon emission reduction needs of different types of enterprises and institutions, promoting low-carbon development throughout the entire society (Fig. 3).

As of February 2023, the cumulative trading volume of CCER in the domestic carbon market was 317900 tons, with only Tianjin, Sichuan, Shanghai, and Shenzhen having transactions, with Tianjin being more active with a transaction volume of 1,99,300

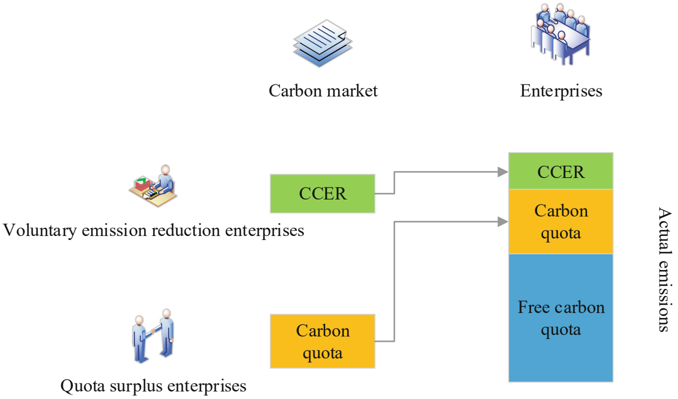

Fig. 3. Actual total emissions of carbon market emission control enterprises

tons. As of February 28, 2023, the cumulative trading volume of CCER in the domestic regional carbon market is 452 million tons; Among them, Tianjin CCER has a cumulative trading volume of 66.67 million tons, ranking third in China [15].

Current development status of green certificate market. Green certificates are the confirmation and attribute proof of renewable energy generation capacity, as well as the only proof of consumption of green electricity. Based on market subscription conditions, renewable energy power quota assessment and mandatory trading of green electricity certificates will be launched in a timely manner starting from 2018 [17]. Due to the dual value of electricity and the environment in renewable energy generation, its abstract environmental value can be specifically characterized by green certificates. Green certificates are the monetization of the environmental value of renewable energy, they are marketable securities that can be transferred and traded with the production of renewable energy [18].

As of April 2023, the cumulative issuance volume of wind power on the green power trading platform was 45,548,841 cases, of which only 8,684,227 cases were listed, with a listing rate of only about 19.1%. Similarly the cumulative issuance of photovoltaic energy or capacity was 30,492,495 cases, of which only 4,908,710 cases or 16.1% were listed. This issue is mirrored in the trading volume of green certificates is 7,579,298 cases, accounting for only 16.6% of the listed volume, while the trading volume of photovoltaic green certificates is 11,913,954, with a trading rate of about 30.1%. This lack of participation might in part be due to current issues in, China's green certificate market including high prices, poor tracking mechanisms, and the lack of an open secondary market for green certificates, which allows for only single direction green certificate transfer. Although some enterprises have a green consumption awareness, energy costs are still the main consideration factor under industry competition pressure. Voluntary purchase of green certificates in the market requires stronger awareness and higher costs [19].Moreover, there is no corresponding punishment mechanism for green energy consumption, and there is no clear punishment measure for entities that do not meet the responsibility weight for renewable energy consumption.

Current development status of Green electricity market. Green electricity operates within the framework of medium to long term electricity. It does not involve curve decomposition issues and prioritize clearing and settlement in the spot market. Green electricity is a physical commodity with electrical energy attributes, and also it has the corresponding environmental value of being environmentally friendly. Therefore, in the green electricity market, it achieves both the utility value of electricity and the simultaneous delivery of environmental value of green electricity.

The green electricity market differs from the green certificate market due to two main factors, Firstly the green electricity market distinguishes the environmental value of green electricity from its inherent electricity commodity value, creating a clearer boundary between the two values, Secondly, the green electricity market addresses the limitations of green certificate trading. When subscribing to green certificates, one only has the right to declare the corresponding quantity of green electricity, meaning that claiming to have used green electricity does not mean that the enterprise has consumed the corresponding green electricity. This is not conducive to tracking and recording the consumption situation of the enterprise. In green electricity trading, green electricity consumption vouchers are directly issued to end users, achieving the unity of green electricity consumption and green certificates; At the same time, the green electricity market can serve as a support for the development of new power systems, building a bridge for direct trading between renewable energy generation enterprises and end users, expanding trading channels, and promoting the development of the new electricity market; The establishment of a national green electricity trading market can provide more convenient channels for the consumption of renewable energy electricity, while also alleviating the market situation of oversupply of green electricity and effectively promoting the consumption of renewable energy [20].

As of November 2022, the trading volume of green electricity has exceeded 20 billion kW h, with over 50 million green certificates issued, equivalent to over 50 billion kW h of electricity.

3 Analysis of the Impact Mechanism Between the Auxiliary Services Market and Various Markets

3.1 The Interactive Impact of Auxiliary Services Market and Carbon Market

There are differences in the trading mechanisms between the auxiliary services market and the carbon market. The former is a market driven by demand for auxiliary services, while the latter policy required mandatory or non-mandatory performance market with carbon emission quotas as the trading subject. However, there may be overlap among market participants, as power generation companies involved in the auxiliary services market are likely to be participants in the carbon market. Additionally, as the proportion of new energy access market increases, the demand for auxiliary services market increases, further raising the possibility of overlapping market participants in both markets. There is mutual influence between the auxiliary services market and the carbon market, but it is not singular or direct.

An increasing proportion of renewable energy is being integrated into the market, leading to a rise in the demand for auxiliary services due to the quality requirements of new energy power generation. Changes in supply and demand result in higher prices for auxiliary services, and as a consequence electricity costs. This, in turn, leads to an overall increase in electricity prices. The shifting supply and demand relationship within the electricity market subsequently causes a decrease in electricity supply, which in turn reduces the demand for carbon quotas in the carbon market ultimately affecting carbon prices. The reduction of carbon prices, especially the reduction of electricity costs for power generation enterprises that are required to control emissions, leads to dynamic changes in electricity costs. Since carbon costs are relatively higher than auxiliary services costs, electricity prices experience a greater decrease than increase, thereby stimulating electricity supply in the market. The increase in electricity supply further stimulates demand in the auxiliary services market, thus creating dynamic cycle in the market. Auxiliary services prices, carbon prices, and electricity prices achieve a a reasonable price range in the market through dynamic market-oriented allocation, resulting in a dynamic balance, as shown in Fig. 4.

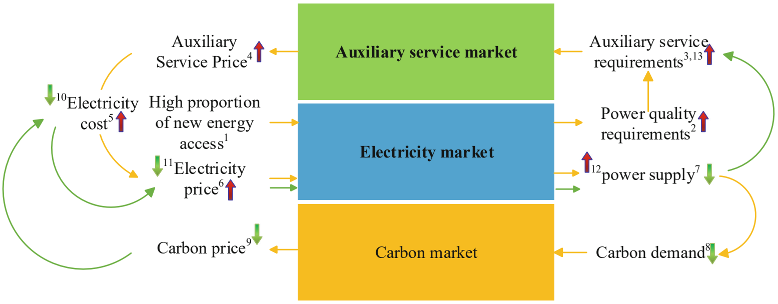

Fig. 4. The impact of auxiliary services prices on carbon prices

Currently, the impact of carbon prices on electricity costs is generally more significant due to the inclusion of emission costs associated with electricity production. Carbon prices are implemented to incentivize electricity producers to adopt environmentally friendly power generation technologies and reduce carbon emissions. When carbon prices increase, power producers are required to pay higher fees for emitting the same amount of carbon dioxide, thereby increasing the production cost of electricity.

Simultaneously, with the continuous development and maturity of clean energy technology, power generation companies can also reduce carbon dioxide emissions by implementing more environmentally friendly technologies thereby reducing the impact of carbon prices on costs. At the same time, government management is actively promoting various policies and different types of green trading markets, such as green electricity, green certificates, and other trading markets, but they are still in the pilot or early stage of development in China. The price of auxiliary services is mainly set up to ensure the stability and reliability of the power system. Although the price of auxiliary services also affects the production cost of electricity, its impact is usually much smaller than the carbon price.

3.2 The Interactive Impact of Auxiliary Services Market and Green Certificate Market

In the electricity market, renewable energy power generation enterprises can use the green certificate market to obtain profits, and the price of green certificates will directly affect the investment returns of renewable energy power generation enterprises. At the same time, renewable energy power generation enterprises can also earn profits by providing auxiliary services, and the price and demand of auxiliary services will also affect the operating costs and profits of the enterprise. Therefore, although the auxiliary services market and green certificate market are two different markets, their mutual influence is becoming increasingly close in the context of green energy transformation, which plays an important role in promoting the stable operation of the electricity market and the development of the renewable energy industry.

The installed capacity and output of renewable green energy electricity are key factors affecting the supply of green certificate markets. If the production of green electricity is large, it may lead to oversupply in the green certificate market and a decrease in prices, and vice versa. The price and load fluctuations in the electricity market affect the supply and demand relationship between the auxiliary services market and the green certificate market. When the price and load fluctuations in the electricity market are significant, the demand in the auxiliary services market increases, and changes in the generation cost side affect the demand in the green certificate market, thereby affecting the supply of the green certificate market.

The policy environment has a certain impact on the development of the auxiliary services market and the green certificate market. The non mandatory nature of China's current green certificate market is one of the reasons why enterprises have low enthusiasm. If a developed green certificate market can drive enterprises to profit from it, power generation enterprises will prioritize clearing the green electricity portion when choosing auxiliary services or providing auxiliary services to obtain green certificates. This can promote green transformation and strengthen the coupling between the services market, electricity market, and green certificate market.

3.3 Interactive Impact of Auxiliary Services Market and Green Electricity Market

In order to meet the demand for renewable energy consumption, green power enterprises need to purchase auxiliary services to ensure the safe and stable operation of the power grid. Therefore, with the continuous development of the green power market, the demand for auxiliary services in the market will correspondingly increase. This reflects the necessity of coupling the two from a macro perspective of development. At the same time, the income from providing auxiliary services is one of the important sources of income for green power enterprises. The income from auxiliary services can be used to compensate for the profits of green power enterprises and promote their development.

For the development of both markets, relevant policies are also one of the important factors. Encouraging green power enterprises to participate in the auxiliary services market through policies, such as obtaining priority clearance in power dispatch, including in the auxiliary services market. The formulation of green certificate prices and the order of green power clearance will affect the development of the green power market, thereby affecting the auxiliary services market.

4 Suggestions on the Coupling Mechanism Between the Auxiliary Service Market and Various Markets

The green certificate market and green electricity market promote the substitution of green energy for fossil energy through load side consumption of green electricity to achieve 'carbon control'; the 'carbon market' promotes the low-carbon transformation of fossil energy by increasing the production costs of carbon emitting enterprises to achieve 'carbon control'. The construction of auxiliary services markets aims to achieve 'carbon control' by replacing fossil energy more with green energy and promoting the low-carbon transformation of fossil energy 'Carbon control' provides a supporting role, utilizing the 'regulator' function of the auxiliary services market to effectively promote the optimal allocation of power resources and the large-scale development of renewable energy. Therefore, how to effectively connect various market mechanisms and policy tools, fully leverage the comprehensive regulatory and mutually supportive role of auxiliary services, carbon, green certificates, and other markets in a good institutional mechanism environment, leverage their respective advantages, overcome their own shortcomings, achieve the connection and integration between different markets, and assist China's energy transformation is the focus and difficulty of future research.

4.1 Coupling of Auxiliary Services Market and Carbon Market

The coupling mechanism design between the auxiliary services market and the carbon market can mainly encourage the production and use of low-carbon electricity through the transmission of carbon prices, and improve the economic benefits of auxiliary services. The following are the key points to pay attention to:

Determine the carbon price level. The coupling mechanism between the auxiliary services market and the carbon market should determine an appropriate and reasonable carbon price level to encourage the production and use of low-carbon electricity and improve the economic benefits of auxiliary services.

Pay attention to the carbon emissions of auxiliary services themselves. When designing a coupling mechanism, consideration should be given to the carbon emissions of auxiliary services, and carbon quotas and offset mechanisms should be introduced into the auxiliary services market to ensure that low-carbon auxiliary services receive more returns.

Clarify the interaction between the carbon market and the auxiliary services market. The price of the carbon market can be used as a price guide for auxiliary services, and carbon trading and carbon performance can be introduced in the auxiliary services market to enhance the price correlation between the two markets, which can achieve better coupling between the markets.

Distinguish between market participants and market behavior. When designing a coupling mechanism, it is necessary to identify the roles of market participants and make different incentive measures based on their functions and roles in the market, such as electricity production, electricity market, auxiliary services supply, and carbon market operation.

Specify policy objectives. When designing a coupling mechanism, policy objectives should be clearly defined, such as reducing carbon emissions, improving energy efficiency, encouraging the development of renewable energy, and ensuring that the coupling mechanism complies with policy guidelines.

4.2 Coupling of Auxiliary Services Market and Green Certificate Market

There is a mutual influence relationship between the auxiliary services market and the green certificate market, and there is an increasing possibility of coupling between market entities and situations. The following are the key points that can be paid attention to when coupling the auxiliary services market and the green certificate market:

Mobilize green electricity to interact and provide new auxiliary services. Research the parts of auxiliary services that can be provided by green electricity, and compare these auxiliary services with traditional auxiliary services to form a stable new type of green electricity auxiliary services for the market. At the same time, clarify the source of green electricity and the way to convert green certificates, and complete the coupling between the auxiliary services market and the green certificate market through green electricity.

Develop new trading rules and policy environment. Mainly targeting the relatively slow developing green certificate market, the policy environment will directly affect the supply and demand relationship and price level of the auxiliary services market and green certificate market. One important reason is that the green certificate market is already driven by policies at the current stage. At present, the green certificate market in China is not fully active, and the investment decision-making enthusiasm of renewable energy power generation enterprises is not high; However, from the perspective of the interactive relationship between the auxiliary services market and the green certificate market, it is necessary to develop the green certificate market in the context of the decline of national subsidies and the green transformation of energy. Therefore, there is a need for research on the coupling between the auxiliary services market and the green certificate market. How to enhance the enthusiasm of the main participants in the green certificate market, including enhancing international recognition of green certificates, solving the problem of double counting with the carbon market, and accelerating the development of the green certificate market, requires new trading rules and policies to provide a prerequisite for the coupling of auxiliary services and the green certificate market.

The design of a coupling mechanism between the auxiliary services market and the green certificate market also requires consideration of market regulation and compliance, regular evaluation of market development, in order to make necessary adjustments and improvements.

4.3 Coupling of Auxiliary Services Market and Green Electricity Market

To design a coupling mechanism between the auxiliary service market and the green power market, it is necessary to clarify how green power generation enterprises participate in the auxiliary services market, as well as the threshold and standards for participation. At the same time, clarify the service content and requirements provided by green power enterprises to participate in the auxiliary service market, ensuring fair competition and product quality in the market. Consider the benefits that green power enterprises can obtain after participating in the auxiliary service market and develop corresponding revenue mechanisms; This can be achieved by introducing policy subsidies or incentive mechanisms to encourage more green power enterprises to participate in the market. Establish a forecasting system for load and price, with reliable green power certification and generation data provided by green power enterprises. Fully consider the advantages and disadvantages of green power to make optimal clearance decisions, ensuring the quality and revenue of auxiliary services. Due to the significant overlap between the green certificate market and the green electricity market, it is possible to fully integrate the characteristics of the synergistic mechanism between the green certificate market and the auxiliary services market for multi market collaborative operation.

5 Summary

Since the proposal of China’s electricity market reform in 2015, the electricity market has provided a more relaxed market environment for the integration of renewable energy into the power system. The 2020 “dual carbon” goal has also provided the “fuel” for the rapid development of the new electricity market. In March 2023, Premier Li Qiang emphasized that China should promote the green transformation of energy and take the “reassurance” for the rapidly developing and increasingly high proportion of renewable energy integration in the new electricity market.

In order to accelerate the integration of renewable energy into the power system, the carbon market, green certificate market, and green electricity market are receiving increasing attention. The carbon market achieves emission reduction goals by increasing the cost of corporate carbon emissions and transmitting prices to the user side. The green certificate market and green electricity market promote low-carbon transformation by actively consuming green electricity on the load side and reflecting environmental premiums. In the new electricity market dominated by wind and solar power generation, the issues of volatility and randomness urgently need to be addressed. At this time, the auxiliary services market, as an important part of the electricity market, provides assistance for the safe and stable operation of microgrids through peak shaving, frequency regulation, backup, and other services.

Combining the functions of auxiliary services in the power market, effectively connecting and comprehensively regulating the auxiliary services market with various market mechanisms can promote the optimal allocation of power resources and the large-scale development of renewable energy. Therefore, studying the coupling relationship and synergistic effects between the auxiliary services market and the carbon market, green certificate market, and green electricity market can effectively assist in the consumption of renewable energy and the development of the market. The role of the auxiliary services market in the new electricity market is also becoming increasingly evident.

References

1. Li, Q.: Attends Press Conference and Answers Questions from Chinese and Foreign Journalists (2023). Rolling News. Government of China. Retrieved from http://www.gov.cn/xinwen/2023-03/13/content_5746555.htm#allContent
2. Guo, H., Zheng, K., Tang, Q., et al.: Data-driven research on electricity markets: challenges and prospects. Autom. Electr. Power Syst. **47**(1), 200–215 (2023)
3. He, J., Liu, Q., Zhao, W., et al.: Market—oriented trading system considering renewable energy under the goal of carbon peak and neutrality. Sci. Technol. Eng. **21**(36), 15476–15484 (2021)
4. Zhang, J., Wang, Z., Lei, Y.: The Enlightenment of the EU carbon market experience to the construction of China's carbon market. Price Theor. Prac. **2020**(1), 32–36+170 (2020)
5. Zhao, M., Jiang, K., Xu, H., et al.: Impacts of EU ETS on European power industry and its implications. Clim. Change Res. **8**(6), 462–468 (2012)
6. Zeng, M., Sun, X., Li, N., et al.: The design of renewable source policy on the condition of power market-learning from the EU. Sci. Technol. Indust. **12**(4), 14–18 (2012)
7. Liu, H., Zheng, S.: Construction of the US carbon market and its implications for China. China Econ. Trade Herald **2014**(8), 7–8 (2014)
8. Wang, B., Fang, H.: Consignment auction mechanism in carbon markets: a review and prospects. Ecol. Econ. **36**(10), 34–40 (2020)
9. Wu, D., Zhao, X., Wang, L.: Operating performance of U.S. regional carbon market: a case study of regional greenhouse gas initiative. Ecol. Econ. **33**(2), 49–53 (2017)
10. Ren, D., Xie, X.: International experience in establishing a green certificate trading system for renewable energy. Energy of China, **35**(9), 12–15+21 (2013)
11. Yuan, J., Xi, X.: Current situation and issues of China's power ancillary service market construction. China Power Enterp. Manage. **2020**(7), 34–38 (2020)
12. Deepening the Reform of Power Marketization [EB/OL] (2023) Global Times. Retrieved from https://www.huanqiu.com/article/49CpceyGlCz
13. Relevant Officials from the Ministry of Ecology and Environment Answered Journalists' Questions on the "Draft Implementation Plan for the Setting and Allocation of Carbon Emission Trading Quotas for 2021 and 2022" [EB/OL] (2023, April 7). Ministry of Ecology and Environment of the People's Republic of China. Retrieved from https://www.mee.gov.cn/ywdt/zbft/202211/t20221103_1000246.shtml
14. Notice on Public Solicitation of Opinions on the "Provisional Regulations on Carbon Emission Trading Management (Revised Draft)" [EB/OL] (2023). Ministry of Ecology and Environment. Retrieved from https://www.mee.gov.cn/xxgk2018/xxgk/xxgk06/202103/t20210330_826642.html
15. Carbon Emission Trading Market Dynamics in February 2023: China Paper Newsletters, **2023**(3), 29–31 (2023)
16. Wang, K., Chen, M.: Review and prospect of China's carbon trading system. J. Beijing Inst. Technol. (Soc. Sci. Ed.) **20**(2), 24–31 (2018)
17. National Development and Reform Commission: Notice on the Trial of Green Power Certificate Issuance and Voluntary Trading System (Development and Reform Energy [2017] No. 132) [EB/OL] (2017). Retrieved from https://www.ndrc.gov.cn/xxgk/zcfb/tz/201702/t20170203_962895_ext.html

18. Zhang, X., Chen, Zheng., Ma, Z., et al.: Study on electricity market trading system adapting to renewable portfolio standard. Power Syst. Technol. **43**(8), 2682–2690 (2019)
19. Shi, J.: Comparison and enlightenment: advantages and disadvantages of green certificate mechanisms in Europe, the United States, and China. Energy **2019**(11), 37–40 (2019)
20. You, X.: Development trends of domestic green certificates and strategies for power generation enterprises. Energy **2022**(11), 34–36 (2022)

Port Energy Management Optimization Method Based on Demand Response and Internal and External Collaboration

Xinyu Duan[1], Zhijian Wu[2], Guodong Huang[2], Xiaofeng Dong[2], and Wei Wang[1](✉)

[1] NARI School of Electrical and Automation Engineering Nanjing Normal University,
Nanjing 210046, China
2399189044@qq.com, wangw_seu@163.com

[2] Suzhou Power Supply Company, State Grid Jiangsu Electric Power Co, Suzhou 215004, China
1014426538@qq.com, 652208077@qq.com, 419475750@qq.com

Abstract. At present, due to the characteristics of many kinds of port loads, large scale and large differences in load timing, it makes the ship shore power with large uncertainty. To address such problems, this paper researches the prediction method of port load, and proposes the prediction method of ship shore power load based on Monte Carlo simulation by analyzing the law of ship port call; and for the problem of port system energy scheduling and optimization, it considers the optimal scheduling of each unit within the port, and proposes the optimization model based on demand response and internal and external cooperation with the goal of minimizing system operation cost. The optimization model of port energy management based on demand response and internal and external cooperation is proposed. The proposed method is validated with the example of Taihu Port Terminal and Tongli Lake Port Terminal in Suzhou City, Jiangsu Province, which shows that the proposed method reduces the operating cost of the port words.

Keywords: Monte Carlo · Demand response · Energy management optimization

1 Introduction

With the popularization of port shore power technology, reasonable port energy planning and stable energy supply have been emphasized, and port energy and load are the primary considerations for port energy system planning. Compared with traditional port industrial parks, port loads are characterized by many types (cold, heat, electricity, etc.), large scale, and large differences in load timing in each port area, which put forward higher requirements for energy planning and operation [1]. Therefore, it is important to explore load prediction methods applicable to ports, to carry out reasonable energy planning, and to reduce the operating costs of ports.

Scholars at home and abroad have conducted more studies on energy management issues, and the literature [2] is to review the current energy saving technologies and measures for port container terminals, including the optimization and upgrading of terminal equipment and the application of energy management systems. The literature [3]

Y. Xue et al. (Eds.): PMF 2023, LNEE 1129, pp. 188–197, 2024.
https://doi.org/10.1007/978-981-99-9251-5_15

takes the port of Singapore as an example and analyzes the port energy consumption situation. In the literature [4], it is proposed that the fluctuation of renewable energy and load can be effectively smoothed by different energy storage units, and the energy management and optimization model of the energy system is established based on this. In the literature [5], the impact of wind-light-storage on the management and optimization of energy local area network system was considered comprehensively, and a model for minimizing system investment and fuel cost and maximizing renewable energy utilization was established and solved by an improved particle swarm optimization method. Most of the aforementioned studies have adopted individual planning, individual design and independent operation for ports, which cannot achieve efficient supply of overall energy from the perspective of the overall port energy system, which raises the problem of high cost of planning and operation of port energy systems.

In this context, this paper proposes an optimization model of port energy management based on demand response and internal and external collaboration. Firstly, the uncertainty of port load is analyzed and the ship shore power load forecast is predicted based on Monte Carlo simulation according to the law of ship call; secondly, the port energy management optimization model is proposed with the objective of minimizing the system operation cost, and the demand response mechanism is introduced in the internal coordination of the port, and on the basis of realizing the coordination and balance of each unit inside the port, the energy supply and demand is optimized through the interaction with external ports or The demand response mechanism is introduced in the internal coordination of the port, and the balance of energy supply and demand is achieved through the interaction with external ports or power grids. The feasibility and economy of the proposed method are demonstrated by the example of the Taihu Port Terminal and Tongli Lake Port Terminal in Suzhou City, Jiangsu Province.

2 Port System Model Construction

2.1 Wind and Light Output Forecast

(1) Wind Power Model

The output power of the wind turbine is closely related to the magnitude of the wind speed, which is described using the Weibull two-parameter distribution curve, which is a single-peaked curve with two parameters [6]. The wind speed probability density function can be expressed as:

$$f(V) = (\frac{k}{c})(\frac{V}{c})^{k-1} \exp\left[-\left(\frac{V}{c}\right)^{k}\right] \tag{1}$$

where, V is the wind speed at the hub of the fan impeller (m/s); k and c denote two important parameters in the wind speed distribution, the shape parameter and the scale parameter, respectively; the magnitude of their values can be calculated or estimated using wind speed history data, etc.

(2) Photovoltaic Power Generation Model

The output power of photovoltaic power generation is affected by a variety of factors, and there are large differences in the output power under different lighting conditions. Considering the solar radiation value and ambient temperature, the PV power plant output can be expressed as:

$$\begin{cases} P_{\mathrm{V}} = L_{\mathrm{X}} P_{\mathrm{STC}} \dfrac{1 + k(T_{\mathrm{c}} - T_{\mathrm{r}})}{G_{\mathrm{STC}}} \\ T_{\mathrm{c}} = T_{\mathrm{e}} + 0.0256 L_{\mathrm{X}} \end{cases} \tag{2}$$

where, L_X is the light intensity; P_{STC} is the maximum test power of the standard test; G_{STC} standard test light intensity, k is the power temperature coefficient; T_c and T_r are the operating temperature of the panel and the reference ambient temperature (25 °C); T_e is the actual ambient temperature.

2.2 Load Forecasting

Since the use of shore power by ships has a large uncertainty, Monte Carlo simulation is used to predict the daily load of shore power use by ships. The behavior of shore power use after port call is analyzed from three aspects: the time of port call, the length of port call and the power of shore power use after port call, according to the law of ship port call [7].

(1) Port of Call Time Distribution

The time of ships passing through a specific water has uncertainty, and there is a sequential order of ships' arrival, which satisfies the condition of random arrival. Therefore, the moments of port calls are assumed to obey normal distribution.

$$f(t) = \frac{1}{\sigma_t \sqrt{2\pi}} \exp\left[-\frac{(t - \mu_t)^2}{2\sigma_t^2}\right] \tag{3}$$

where, μ_t and σ_t are the mean and standard deviation of the moment t when shore power starts to be used after port call, respectively.

(2) Length of Port Call Distribution

The length of port calls varies for different types of ships. Even for the same type of ships, their docking length varies when they receive the influence of shipowner and port docking arrangement. Assuming that the length of each type of ship calls obeys the exponential distribution, its probability density function can be expressed as follows:

$$f(d) = \lambda e^{-\lambda d}, d > 0 \tag{4}$$

where, λ denotes the distribution parameter and its inverse is the mathematical expectation of the ship's port call duration d.

(3) Shore Power Size Distribution

A normal distribution is used to model the distribution of power magnitude for different types of ships using shore power with a probability density function of:

$$f(p) = \frac{1}{\sigma_p\sqrt{2\pi}} \exp\left[-\frac{(p - \mu_p)^2}{2\sigma_p^2}\right] \tag{5}$$

where, μ_p and σ_p are the mean and standard deviation of the shore power p, respectively.

3 Port Energy Management Optimization Model

Considering a port as an energy system, it consists of numerous directly connected and interconnected units, which are divided into capacity, energy use, storage and interconnection units according to the energy richness after multi-time node interaction, and are responsible for energy production, call, storage and interaction respectively. The energy production unit consists of wind and photovoltaic generators; the energy use unit includes critical loads, interruptible loads and transferable loads; the energy storage unit includes storage batteries, etc. The port's energy management is achieved through internal self-regulating balances and through buying and selling of electricity traded through the external grid. The internal regulation of the port considers the demand response mechanism and achieves supply and demand balance by regulating the production energy of each internal controllable capacity unit, the charging/discharging status of the energy storage unit, the power and the interruption ratio of the interruptible load.

3.1 Optimization Model

(1) Objective Function

The optimization of the port energy system is aimed at minimizing the operating cost in time T. The cost function is the operating expense cost of each unit.

$$C_{\mathrm{T}} = \sum_{t=1}^{\mathrm{T}} (C_{\mathrm{P}}(t) + C_{\mathrm{C}}(t) + C_{\mathrm{B}}(t) + C_J(t)) \tag{6}$$

$$C_{\mathrm{P}}(t) = \sum_{W_i=1}^{W_n} (\alpha_{W_i} P_{W_i}(t) + \beta_{W_i}) + \sum_{S_i=1}^{S_n} (\alpha_{S_i} P_{S_i}(t) + \beta_{S_i}) \tag{7}$$

$$C_{\mathrm{C}}(t) = -\sum_{C_i=1}^{C_n} (P_{C_i}(t) p_{C_i}^r(t)) + \sum_{I_i=1}^{I_n} \left[-P_{I_i}(t)(1 - R_{I_i}(t)) p^r(t) + P_{I_i}(t) R_{I_i}(t) p_{I_i}^o(t)\right] \tag{8}$$

$$C_{B_i}(T) = \sum_{t=1}^{T} p^r(t)(P_{B_i}^{\mathrm{C}}(t) - P_{B_i}^{\mathrm{D}}(t) R_{B_i}^{\mathrm{D}}(t)) + (N_{B_i}^{\mathrm{C}}(T) + N_{B_i}^{\mathrm{D}}(T)) R_{B_i}^{\mathrm{T}} \tag{9}$$

$$C_{\mathrm{J}}(t) = \sum_{J_i=1}^{J_n} \left[\left(P_{J_i}^{\mathrm{I}}(t) R_{J_i}^{\mathrm{I}}(t) - P_{J_i}^{\mathrm{O}}(t) R_{J_i}^{\mathrm{O}}(t)\right) p^r(t)\right] \tag{10}$$

where, C_{T} is the total internal operating cost of the system (a negative value is considered as a gain); $C_{\mathrm{P}}(t)$, $C_{\mathrm{C}}(t)$, and $C_{\mathrm{B}}(t)$, $C_J(t)$ are the operating costs of each capacity, energy-using, storage, and interconnection unit in time period t. W_n and S_n are the number of wind and PV capacity units; α_{W_i}, β_{W_i} and α_{S_i}, β_{S_i} are the primary and constant term coefficients of the operating cost versus output power equation for the i-th wind capacity unit and PV capacity unit, respectively. C_n, I_n are the number of critical loads and interruptible loads; $P_{r(t)}$ is the system base tariff; $p^r_{C_i}(t)$ and $p^o_{I_i}(t)$ are the payable rate for critical loads and the compensation rate for interruptible loads, respectively [8]; $R^{\mathrm{D}}_{B_i}(t)$ is the discharge rate; $R^{\mathrm{T}}_{B_i}$ is the single state transition rate; J_n is the number of interaction ports; $R^{\mathrm{I}}_{J_i}(t)$, $R^{\mathrm{O}}_{J_i}(t)$, $R^{\mathrm{I}}_{Y_i}(t)$, $R^{\mathrm{O}}_{Y_i}(t)$, $R^{\mathrm{I}}_{\mathrm{G}}(t)$, and $R^{\mathrm{O}}_{\mathrm{G}}(t)$ are the corresponding buy and sell rates in time period t, respectively [9].

(2) Binding Condition

1) Power Constraints for Each Unit

$$P^{\mathrm{m}}_i(t) \le P_i(t) \le P^{\mathrm{M}}_i(t) \tag{11}$$

where, $P_i(t)$ is the actual power generated by each unit in time period t. $P^{\mathrm{m}}_i(t)$, $P^{\mathrm{M}}_i(t)$ and are the lower and upper limits of the output power of each unit in time period t, respectively.

2) Supply and Demand Power Balance Constraint

$$\begin{aligned}
&\sum_{W_i=1}^{W_n} P^{\mathrm{A}}_{W_i}(t)+\sum_{S_i=1}^{S_n} P^{\mathrm{A}}_{S_i}(t)+\sum_{B_i=1}^{B_n} P^{\mathrm{D}}_{B_i}(t)+\sum_{J_i=1}^{J_n} P^{\mathrm{I}}_{J_i}(t)\\
&=\sum_{C_i=1}^{C_n} P_{C_i}(t)+\sum_{I_i=1}^{I_n} P_{I_i}(t)+\sum_{B_i=1}^{B_n} P^{\mathrm{C}}_{B_i}(t)+\sum_{J_i=1}^{J_n} P^{\mathrm{O}}_{J_i}(t)
\end{aligned} \tag{12}$$

where, the first 3 terms on the left side of the equation are the output power of each capacity unit, the 4th term is the discharge amount of each energy storage unit, and the 5th-7th terms are the power input from the interconnected port or grid; the first 2 terms on the right side of the equation are the energy consumption of each energy use unit, the 3rd term is the charging amount of each energy storage unit, and the 4th-6th terms are the power output to the interconnected port or grid.

3.2 Solution Strategy

The model is solved by a combination of Lagrange multiplier method and co-evolutionary algorithm [10]: the former transforms the constrained optimization problem into an unconstrained optimization problem; the latter solves the transformed unconstrained optimization problem, and the flow chart is shown in Fig. 1.

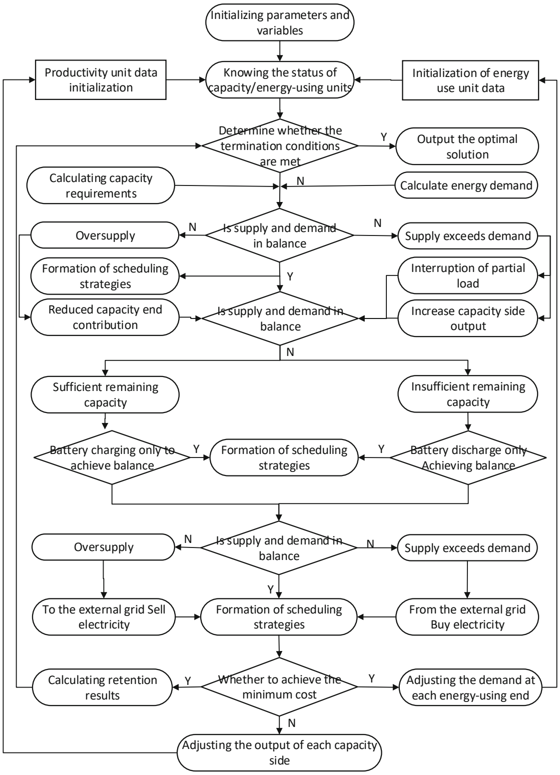

Fig. 1. Flowchart of model solving.

4 Example Analysis

4.1 Example of Calculation

In this paper, the actual data of Dusanting Terminal and Luoxingzhou Terminal of Tongli Lake in Suzhou City, Jiangsu Province are selected to validate the optimization model, and the configuration parameters of each component unit of the port system [11] are selected for the calculation cases as shown in Tables 1, 2, 3 and 4, respectively, and all tests are considered for 24 time periods of 1 h each.

4.2 Analysis of Results

Analysis of energy output and load forecast results. The Assuming the simulated number of ships is 1000. in calculating the time to use shore power, since it takes some time to connect the ship to the shore power cable and to switch the ship's electricity from the auxiliary engine to the shore power system, it is assumed that the actual time to use shore power is 3h less than the berthing time for each ship at each call. The predicted values are shown in Figs. 2 and 3.

Table 1. Productivity unit parameter configuration.

Type	Serial number	Coefficient	Constant term	Power rating
Wind power	WDG1	0.35	2.5	125
	WDG2	0.35	2.5	125
	WDG3	0.32	4	125
	WDG4	0.32	4	125
	WDG5	0.30	5	125
Photovoltaic	PVG1	0.55	5×10^{-4}	100
	PVG2	0.55	5×10^{-4}	100
	PVG3	0.50	1×10^{-4}	100
	PVG4	0.50	1×10^{-4}	100
	PVG5	0.50	10^{-3}	100

Table 2. Configuration of energy-using unit parameters.

Type	Expense reimbursement rate		
Critical loads	1.15		
Interruptible load	0.25 (high)	0.15 (medium)	0.10 (low)

Table 3. Energy storage unit parameters configuration.

Initial capacity (kW)	Rated capacity (kW)	Charge/discharge power	Charge/discharge efficiency (%)	Self-discharge power (kW h)	Charge rate
50	100	[0, 50] kW	98.5	0.001	2

Table 4. Energy storage unit parameters configuration.

Type	Buy/sell electricity rates	Interaction power/kW
Neighbourhood energy local area network	1.05/0.95	[−50, 50]
Utility grid	1.20/0.80	No restrictions

Analysis of port energy management results. In order to more intuitively analyze the impact of port interconnection on system economics, this paper sets up the following two scenarios for comparative analysis:

Scheme I: Public grid direct interconnection mode, where energy is directly exchanged with the public grid on demand, i.e., the internal supply/demand demand

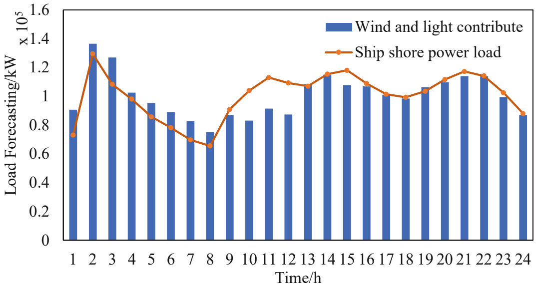

Fig. 2. Trans mountain pavilion terminal scenic output and load demand.

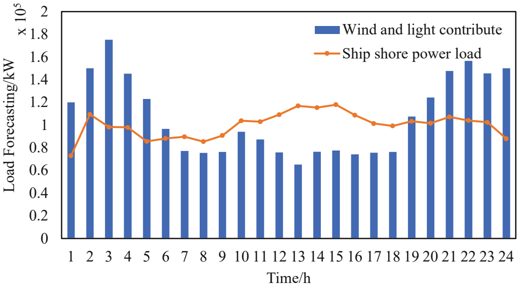

Fig. 3. Tongli lake Luoxingzhou terminal scenic output and load demand.

of the port is met on a priority basis, and the excess or shortage is met by direct energy exchange with the external grid.

Scheme II: Demand response mode, in the process of energy interaction within the port, it is achieved by adjusting the energy production of each internal controllable capacity unit, the charging/discharging state of the energy storage unit, the power and the interruption ratio of the interruptible load, and if it cannot be balanced by self-regulation, then interaction with the external grid is carried out.

Based on the above parameter settings, the above two scenarios are tested and the results are shown in Fig. 4. Where the positive values are the power and cost of the port bought from the external grid and the negative values are the power and revenue sold. It can be seen from the figure that scheme II has significantly lower power purchase compared to scheme I.

Table 5 shows the results of the total daily operating costs of the port system. From the results, it can be seen that the port operating costs can be effectively reduced by using the demand response coordination optimization model.

5 Summary

In order to realize the optimal operation of the port, the load demand of vessels is predicted according to the uncertainty of the port, and an optimization method of port energy management based on demand response and internal and external cooperation

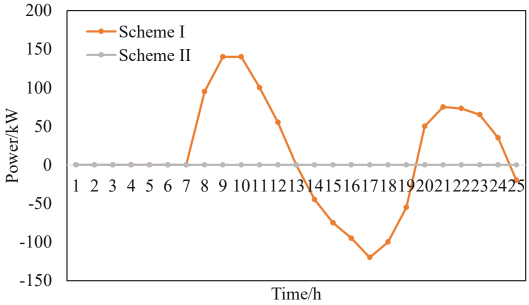

Fig. 4. Real-time power curve.

Table 5. Total system cost under different scenario architectures.

Type	Cost of the Watanabe pavilion terminal	Tongli lake Luoxingzhou pier cost
Scheme I	2084.74	2015.4
Scheme II	1971.96	1923.92

is proposed, and the effectiveness of the method is verified by taking the Taihu Lake Lingang Terminal and Tongli Lake Lingang Terminal in Suzhou City, Jiangsu Province as examples. The main conclusions are as follows:

(1) The prediction of ship shore power load is carried out by Monte Carlo method according to the law of ship port call from three aspects of port call time, port call duration and shore power used after port call respectively, and the accuracy of the prediction is improved.
(2) Considering the self-regulation balance of port energy and the interaction with other ports or power grids, and introducing the demand response mechanism in the internal self-regulation to realize the economic dispatch and optimal allocation of energy and reduce the operation cost.

References

1. Lv, X., Xu, F., Guan, H.: Study on low-carbon clean energy supply in ports. China Water Transp. (Second half month) **22**(09), 28–29 (2022). (in Chinese)
2. Wang Y, Zhang J, Wu W, Zeng C.: A review of energy-efficient measures at container terminals: potential, constraints and directions. Energy (2021)
3. Ozan, E.: Economic impacts of small-scale own generating and storage units and electric vehicles under different demand response strategies for smart households. Appl. Energy **126**, 142–150 (2014)
4. Nagarajan, A., Ayyanar, R.: Design and strategy for the deployment of energy storage systems in a distribution feeder with penetration of renewable resources. IEEE Trans. Sustain. Energy **6**(3), 1085–1092 (2015)

5. Abedini, M., Moradi, M., Hosseinian, S.: Optimal management of microgrids including renewable energy sources using GPSO-GM algorithm. Renew. Energy **90**, 430–439 (2016)
6. Hu J, Chen C, Zhu Q.: Energy consumption and emission reduction in ports: A case study of the Port of Singapore. J. Clean. Prod. (2017)
7. Zeng, M., Yang, Y., Liu, D.: "Generation-grid-load storage" coordinative optimal operation mode of energy internet and key technologies. Power Syst. Technol. **40**(1), 114–124 (2016). (in Chinese)
8. Song, T.: Research on the integrated energy system of harbor with counting and demand response. Southeast Univ. (2020). https://doi.org/10.27014/d.cnki.gdnau.2020.000137
9. Zhang, Y., Liu, B., Zhang, T.: An intelligent control strategy of battery energy storage system for microgrid energy management under forecast uncertainties. Int. J. Electrochem. Sci. **9**, 4190–4204 (2014)
10. Sun, Y., Kirley, M., Halgamuge, S.: Extended differential grouping for large scale global optimization with direct and indirect variable interactions. In: Genetic and Evolutionary Computation Conference 2015(GECCO).Madrid, Spain: the Association for Computing Machinery Special Interest Group on Genetic and Evolutionary Computation, pp. 313–320 (2015)
11. Hong, T., Pinson, P., Fan, S.: Probabilistic energy forecasting: global energy forecasting competition 2014 and beyond. Int. J. Forecast. **32**, 896–913 (2016)

Impedance Modeling and Impedance Characteristics Analysis of SVI Multi-unit Parallel System

Wei Chen[1,2](✉), Shaoze Zhou[1], Xinyu Lei[1], Xinzhe Song[1], Zheng Wei[1], and Wei Wang[1]

[1] NARI Group Corporation (State Grid Electric Power Research Institute), Nanjing 211106, China
`Chenwei2023@foxmail.com`
[2] School of Electrical and Automation Engineering, Nanjing Normal University, Nanjing 210023, China

Abstract. Various stability problems have arisen in the current renewable energy generation systems based on Self-synchronous Voltage-source Inverters (SVI). Therefore, there is an urgent requirement to analyze the impedance characteristics of SVI multi-unit parallel systems. Firstly, the impedance model of a single unit is derived based on the control strategy of SVI using the harmonic linearization method. Then, an SVI multi-unit parallel equivalent impedance modeling method is proposed based on the condition that the parameters are consistent. The multi-unit system is equated to the parallel connection of SVIs with the same parameters, so as to derive the SVI multi-unit parallel equivalent impedance model. Meanwhile, the impedance is verified by MATLAB sweep-frequency simulation. Finally, according to the established impedance model, the effects of LC filter parameters, parallel line impedance, and the number of parallel units on the equivalent impedance characteristics are analyzed, which provides a reference for the stability analysis and optimization of renewable energy generation systems.

Keywords: Renewable energy generation · Self-synchronous voltage source · SVI · Impedance model · Impedance characteristics

1 Introduction

As the core force of the current energy transformation, renewable energy will replace traditional energy to gradually develop into the main support power [1]. At the same time, energy conversion devices are to be gradually shifted from traditional synchronous generators to grid-following inverters and other power electronic devices, and this brings a series of stability problems in power systems [2].

The main control strategy of grid-following inverters today is virtual synchronous generator (VSG) control [3], which can meet the grid-following conditions under a weak grid and also actively provide voltage and frequency support. Meanwhile, the self-synchronous voltage-source inverter (SVI) with improved VSG as the control core has

Y. Xue et al. (Eds.): PMF 2023, LNEE 1129, pp. 198–209, 2024.
https://doi.org/10.1007/978-981-99-9251-5_16

become one of the current research hotspots [4]. Today, the main method to analyze the stability of new energy generation systems is the impedance analysis method [5]. Therefore, based on the VSG impedance modeling and analysis, it is necessary to perform impedance modeling for SVI-based power generation systems. At the same time, the influence of various factors on its impedance characteristics is analyzed to provide a reference for stability analysis and optimization of renewable energy power generation.

There has been a large amount of literature on impedance modeling and analysis of new energy generation systems. In the literature [6], a small-signal equivalent circuit of grid-connected system with split channels was established based on the dq impedance model. Then, the impedance ratio is defined based on the harmonic-impedance relationship and the dominant characteristics of harmonic oscillation are extracted based on the equivalent second-order oscillation link. The literature [7] compared the state-space method and impedance analysis method, and found that the impedance analysis method can effectively simplify the system stability analysis. Secondly, the impedance models and application characteristics of dq-axis linearization and harmonic linearization were compared. Impedance modeling methods in dq coordinate system have many drawbacks in practical applications. Therefore, the small-signal model of the three-phase grid-connected inverter is processed in the literature [8] based on the abc coordinate system using harmonic linearization to establish the positive and negative sequence impedance model. In the literature [9], the small-signal wide-band positive and negative sequence impedance models of isolated PWM inverters were established, and the influence of control method, load type, and load power magnitude on the stability of isolated microgrid systems was analyzed using Nyquist stability criterion. In the literature [10], a modified three-phase LCL-type grid-connected inverter sequential impedance model is established and stability analysis is performed from the resonance principle and log frequency stability perspective. Meanwhile, the impedance characteristic curve is considered for damping link parameter selection. In the literature [11], the small-signal sequential impedance models of voltage-controlled VSG and current-controlled VSG are established using harmonic linearization method, and the sequential impedance characteristics of these two different types of VSG are compared and analyzed. In the paper [12], a VSG sequential impedance model including reactive loop is established and the VSG sub-synchronous oscillation mechanism is analyzed based on the impedance ratio stability criterion.

Based on the above literature analysis, this paper conducts impedance modeling and impedance characteristics analysis for SVI multi-unit parallel system. Firstly, the SVI single-unit impedance model is established based on the harmonic linearization method. Then, an SVI multi-unit impedance equivalent model is proposed and verified by sweep-frequency simulation. Finally, the effects of LC filter parameters, parallel line impedance, and the number of parallel units on the impedance characteristics of the SVI multi-unit parallel system are analyzed to provide a reference basis for stability analysis and optimization of renewable energy generation systems.

2 Topology and Control Strategy O SVI

The topology of SVI is a three-phase bridge circuit as shown in Fig. 1a. The control strategy of SVI is centered on the improved VSG control [13], while the virtual impedance part is added to optimize the current output characteristics, and the control block diagram is shown in Fig. 1b.

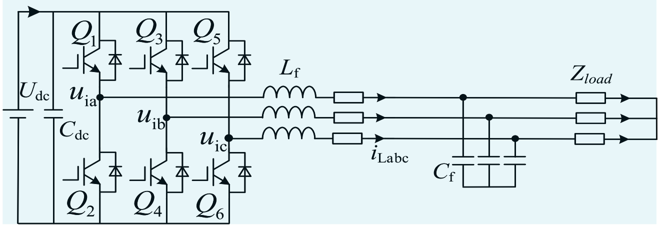

(a) Topology of SVI

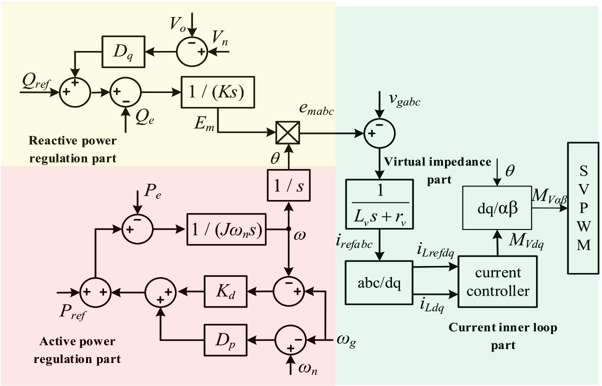

(b) Control strategy of SVI

Fig. 1. Topology and control strategy diagram of SVI

The SVI simulates a synchronous generator by converting the mechanical power of the prime mover into electromagnetic power and the rotor's rotational inertia to obtain the active regulation part as shown below:

$$P_{\text{ref}} - P_{\text{e}} + D_{\text{p}}\omega_{\text{n}}(\omega_{\text{n}} - \omega) \approx J\omega_{\text{n}}\frac{d\omega}{dt} \tag{1}$$

where P_{ref} is the reference power command, P_{e} is the output electromagnetic power, D_{p} is the frequency-active power sag factor, J is the rotational inertia, ω is the generated angular frequency, and ω_{n} is the rated angular frequency of the grid.

Simulating the excitation control equation of a synchronous generator and regulating the excitation current in real time, the reactive power regulation part can be obtained as shown in the following equation:

$$E_{\text{m}} = \left[D_{\text{q}}(V_{\text{n}} - V_{\text{o}}) + (Q_{\text{ref}} - Q_{\text{e}})\right]/(Ks) \tag{2}$$

where E_{m} is the generated internal potential, Q_{ref} is the reactive power given; Q_{e} is the real-time reactive power, D_{q} is the voltage-reactive power sag factor, K is the reactive integration factor, V_{n} is the rated voltage amplitude, and V_{o} is the output voltage amplitude.

The virtual impedance is introduced to obtain the reference for the current inner loop command in the abc coordinate system as shown in the following equation:

$$i_{Lrefabc} = \left(e_{mcbc} - e_{gabc}\right)/(sL_v + R_v) \tag{3}$$

where i_{Lrefabc} is the current inner loop command value, e_{mabc} is the inverter three-phase modulated wave generation internal potential; e_{gabc} is the three-phase grid voltage; L_{v} and R_{v} are the virtual reactance and virtual resistance respectively.

The obtained current in-loop command reference is coordinate transformed with the three-phase inductor current feedback signal obtained by sampling, and the current in-loop controller is constructed in the dq coordinate system to achieve closed-loop control of the inverter output inductor current, as follows:

$$\begin{cases} M_{Vd} = \left(i_{dref} - i_{Ld}\right)\left(K_p + \frac{K_i}{s}\right) - \omega L_f i_{Lq} + E_d \\ M_{Vq} = \left(i_{qref} - i_{Lq}\right)\left(K_p + \frac{K_i}{s}\right) + \omega L_f i_{Ld} + E_q \end{cases} \tag{4}$$

where i_{dqref}, i_{Ldq}, E_{gdq} and M_{Vdq} are the inductor current reference signal, inductor current feedback signal, grid voltage and current inner loop output signal, respectively, and K_{p} and K_{i} are the proportionality and integration coefficients of the current inner loop regulator, respectively.

3 Impedance Modeling and Verification of SVI Multi-unit Parallel System

3.1 Impedance Modeling of SVI Multi-unit Parallel System

According to the harmonic linearization method, a three-phase balanced positive and negative sequence disturbance voltage is injected at the common point, and then the impedance is derived based on the SVI impedance modeling process shown in Fig. 2.

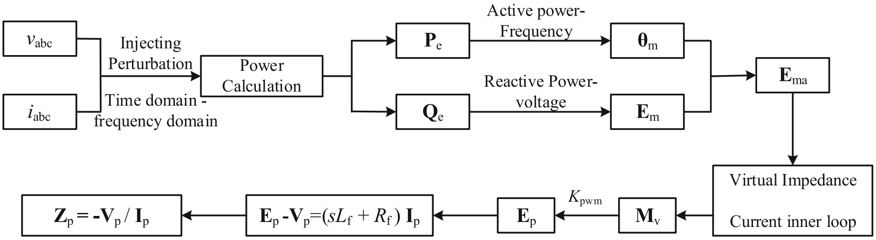

Fig. 2. Process of SVI impedance modeling

The time domain expressions for the voltage and current of phase A after voltage disturbance injection are shown below:

$$\begin{cases} v_\mathrm{a}(t) = V_1\cos(2\pi f_1 t) + V_\mathrm{p}\cos(2\pi f_\mathrm{p}t + \varphi_\mathrm{vp}) + V_\mathrm{n}\cos(2\pi f_\mathrm{n}t + \varphi_\mathrm{vn}) \\ i_\mathrm{a}(t) = I_1\cos(2\pi f_1 t + \varphi_\mathrm{i1}) + I_\mathrm{p}\cos(2\pi f_\mathrm{p}t + \varphi_\mathrm{ip}) + I_\mathrm{n}\cos(2\pi f_\mathrm{n}t + \varphi_\mathrm{in}) \end{cases} \tag{5}$$

where V_1, I_1 and f_1 denote the fundamental voltage amplitude, current amplitude and frequency, respectively, and φ_i1 denotes the power factor angle; V_p, I_p, f_p, φ_vp and φ_ip denote the positive sequence disturbance voltage amplitude, current amplitude, frequency, voltage initial phase angle and current initial phase angle, respectively; V_n, I_n, f_n, φ_vn and φ_in denote the negative sequence disturbance voltage amplitude, current amplitude, frequency, voltage initial phase angle and current initial phase angle, respectively.

By transforming the phase A voltage and current in the time domain-frequency domain, the expressions are obtained as follows:

$$\mathbf{V}_\mathrm{a}[f] = \begin{cases} \mathbf{V}_1, f = \pm f_1 \\ \mathbf{V}_\mathrm{p}, f = \pm f_\mathrm{p} \\ \mathbf{V}_\mathrm{n}, f = \pm f_\mathrm{n} \end{cases}, \ \mathbf{I}_\mathrm{a}[f] = \begin{cases} \mathbf{I}_1, f = \pm f_1 \\ \mathbf{I}_\mathrm{p}, f = \pm f_\mathrm{p} \\ \mathbf{I}_\mathrm{n}, f = \pm f_\mathrm{n} \end{cases} \tag{6}$$

where $\mathbf{V}_1$, $\mathbf{V}_\mathrm{p}$ and $\mathbf{V}_\mathrm{n}$ are the frequency domain expressions for the fundamental, positive sequence and negative sequence voltages, respectively; $\mathbf{I}_1$, $\mathbf{I}_\mathrm{p}$ and $\mathbf{I}_\mathrm{n}$ are the frequency domain expressions for the fundamental, positive sequence and negative sequence currents, respectively.

According to the active power-frequency characteristics of SVI, the expression for the phase angle of the potential within SVI can be obtained as:

$$\boldsymbol{\theta}_\mathrm{m}[f] = \begin{cases} M(s)[\omega_\mathrm{n}D_\mathrm{p} + P_\mathrm{ref}/\omega_\mathrm{n} - 3(\mathbf{V}_1\mathbf{I}_1^* + \mathbf{V}_1^*\mathbf{I}_1)/\omega_\mathrm{n}], \ \mathrm{dc} \\ -3M(s)(\mathbf{V}_1^*\mathbf{I}_\mathrm{p} + \mathbf{V}_\mathrm{p}\mathbf{I}_1^*)/\omega_\mathrm{n}, f = \pm(f_\mathrm{p} - f_1) \\ -3M(s)(\mathbf{V}_1\mathbf{I}_\mathrm{n} + \mathbf{V}_\mathrm{n}\mathbf{I}_1)/\omega_\mathrm{n}, f = \pm(f_\mathrm{n} + f_1) \end{cases} \tag{7}$$

where $M(s) = 1/(Js^2 + D_\mathrm{p}s)$.

According to the reactive power-voltage characteristics of SVI, the expression for the potential amplitude within SVI can be obtained as:

$$\mathbf{E}_\mathrm{m}[f] = \begin{cases} N_\mathrm{v}(s)[D_\mathrm{qv}(\sqrt{2}V_\mathrm{n} - V_1) + Q_\mathrm{ref} - 3j(-\mathbf{V}_1\mathbf{I}_1^* + \mathbf{V}_1^*\mathbf{I}_1)], \mathrm{dc} \\ N_\mathrm{v}(s)[-D_\mathrm{qv}\mathbf{V}_\mathrm{p} \mp 3j(\mathbf{V}_1^*\mathbf{I}_\mathrm{p} - \mathbf{V}_\mathrm{p}\mathbf{I}_1^*)], f = \pm(f_\mathrm{p} - f_1) \\ N_\mathrm{v}(s)[-D_\mathrm{qv}\mathbf{V}_\mathrm{p} \pm 3j(\mathbf{V}_1\mathbf{I}_\mathrm{n} - \mathbf{V}_\mathrm{n}\mathbf{I}_1)], f = \pm(f_\mathrm{n} - f_1) \end{cases} \tag{8}$$

where $N_\mathrm{v}(s) = 1/K_\mathrm{v}s$.

When small signal perturbations are injected, the A-phase modulated signal of SVI can be expressed as:

$$e_\mathrm{ma} = (E_\mathrm{m1} + \Delta E_\mathrm{m})\cos(\theta_\mathrm{m1} + \Delta\theta_\mathrm{m}) \tag{9}$$

Neglecting the small signal component of the phase angle, the corresponding expression is obtained as:

$$\cos(\theta_{\mathrm{m1}} + \Delta\theta_{\mathrm{m}}) \approx \cos\theta_{\mathrm{m1}} - \Delta\theta_{\mathrm{m}}\sin\theta_{\mathrm{m1}} \tag{10}$$

This yields the small signal component of the modulated signal as:

$$\Delta e_{\mathrm{ma}} = \Delta E_{\mathrm{m}}\cos\theta_{\mathrm{m1}} - E_{\mathrm{m1}}\Delta\theta_{\mathrm{m}}\sin\theta_{\mathrm{m1}} \tag{11}$$

Bringing Eqs. (7) and (8) into Eq. (11), the positive sequence component of the A-phase modulated signal can be obtained as:

$$\begin{aligned}\mathbf{E}_{\mathrm{ma}}[\pm f_{\mathrm{p}}] = &-\frac{3}{4}je^{j\theta_{\mathrm{m1}}}[E_{\mathrm{m1}}\frac{M(s\mp j\omega_1)}{\omega_{\mathrm{n}}}\\ &+N_{\mathrm{v}}(s\mp j\omega_1)]V_1\cdot\mathbf{I}_{\mathrm{p}} + \{-\frac{3}{4}je^{j\theta_{\mathrm{m1}}}[E_{\mathrm{m1}}\frac{M(s\mp j\omega_1)}{\omega_{\mathrm{n}}}\\ &-N_{\mathrm{v}}(s\mp j\omega_1)]I_1e^{-j\varphi_{\mathrm{i1}}} - \frac{1}{2}e^{j\theta_{\mathrm{m1}}}D_{\mathrm{qv}}N_{\mathrm{v}}(s\mp j\omega_1)\}\cdot\mathbf{V}_{\mathrm{p}}\end{aligned} \tag{12}$$

According to the virtual impedance characteristics of SVI, the expression of the current inner loop reference in positive sequence is obtained as:

$$\mathbf{I}_{\mathrm{aref}}[\pm f_{\mathrm{p}}] = (\mathbf{E}_{\mathrm{ma}}[\pm f_{\mathrm{p}}] - \mathbf{V}_{\mathrm{p}})/(s/L_{\mathrm{v}} + R_{\mathrm{v}}) \tag{13}$$

According to the current inner loop characteristic of SVI, the expression of the modulated signal in positive sequence is obtained as:

$$\mathbf{M}_{\mathrm{v}}[\pm f_{\mathrm{p}}] = \{(\mathbf{E}_{\mathrm{ma}}[\pm f_{\mathrm{p}}] - \mathbf{V}_{\mathrm{p}})T_{\mathrm{v}} - \mathbf{I}_{\mathrm{p}}\}G_{\mathrm{PI}}(s\mp j\omega_1) \tag{14}$$

where $T_{\mathrm{v}} = 1/(s/L_{\mathrm{v}} + R_{\mathrm{v}})$, $G_{\mathrm{PI}}(\mathrm{s})$ is the current inner loop PI transfer function.

In general, the modulation link transfer function can be expressed as:

$$K_{\mathrm{pwm}}(s) = K_{\mathrm{m}}V_{\mathrm{dc}}G_{\mathrm{d}}(s) \tag{15}$$

where $G_{\mathrm{d}}(s) = e^{-T_{\mathrm{s}}s}$, T_{s} is the sampling period and K_{m} is the PWM gain.

The KVL equation of the main circuit in positive sequence can be given as:

$$K_{\mathrm{pwm}}(s)\cdot\mathbf{M}_{\mathrm{v}}[\pm f_{\mathrm{p}}] - \mathbf{V}_{\mathrm{p}} = (sL_{\mathrm{f}} + R_{\mathrm{f}})\mathbf{I}_{\mathrm{p}} \tag{16}$$

Bringing Eqs. (14) and (15) into Eq. (16), the SVI positive sequence impedance can be obtained. Similarly, the negative sequence impedance can be obtained. Therefore, the positive and negative sequence impedance of SVI is:

$$\begin{aligned}
\mathbf{Z}_{\mathrm{p}}{}'(s) &= -\mathbf{V}_{\mathrm{p}}/\mathbf{I}_{\mathrm{p}} \\
&= \left\{\begin{aligned} &(sL_{\mathrm{f}}+R_{\mathrm{f}}) - \{-\frac{3}{4}je^{j\theta_{\mathrm{m1}}}[E_{\mathrm{m1}}\frac{M(s-j\omega_1)}{\omega_{\mathrm{n}}} \\ &+N_{\mathrm{v}}(s-j\omega_1)]V_1T_{\mathrm{v}}-1\}G_{\mathrm{PI}}(s-j\omega_1)K_{\mathrm{pwm}}(s)\end{aligned}\right\} \\
&/\left\{\begin{aligned} &1-\{\{-\frac{3}{4}je^{j\theta_{\mathrm{m1}}}[E_{\mathrm{m1}}\frac{M(s-j\omega_1)}{\omega_{\mathrm{n}}}-N_{\mathrm{v}}(s-j\omega_1)]I_1e^{-j\varphi_{\mathrm{i1}}} \\ &-\frac{1}{2}e^{j\theta_{\mathrm{m1}}}D_{\mathrm{qv}}N_{\mathrm{v}}(s-j\omega_1)\}-1\}T_{\mathrm{v}}G_{\mathrm{PI}}(s-j\omega_1)K_{\mathrm{pwm}}(s)\end{aligned}\right\}
\end{aligned} \tag{17}$$

$$\begin{aligned}
\mathbf{Z}_{\mathrm{n}}{}'(s) &= -\mathbf{V}_{\mathrm{n}}/\mathbf{I}_{\mathrm{n}} \\
&= \left\{\begin{aligned} &(sL_{\mathrm{f}}+R_{\mathrm{f}}) - \{\frac{3}{4}je^{-j\theta_{\mathrm{m1}}}[E_{\mathrm{m1}}\frac{M(s+j\omega_1)}{\omega_{\mathrm{n}}} \\ &+N_{\mathrm{v}}(s+j\omega_1)]V_1T_{\mathrm{v}}-1\}G_{\mathrm{PI}}(s+j\omega_1)K_{\mathrm{pwm}}(s)\end{aligned}\right\} \\
&/\left\{\begin{aligned} &1-\{\{\frac{3}{4}je^{-j\theta_{\mathrm{m1}}}[E_{\mathrm{m1}}\frac{M(s+j\omega_1)}{\omega_{\mathrm{n}}}-N_{\mathrm{v}}(s+j\omega_1)]I_1e^{j\varphi_{\mathrm{i1}}} \\ &-\frac{1}{2}e^{-j\theta_{\mathrm{m1}}}D_{\mathrm{qv}}N_{\mathrm{v}}(s+j\omega_1)\}-1\}T_{\mathrm{v}}G_{\mathrm{PI}}(s+j\omega_1)K_{\mathrm{pwm}}(s)\end{aligned}\right\}
\end{aligned} \tag{18}$$

In addition, considering the effect of filtering capacitor filtering, the complete SVI positive and negative sequence impedance expression is:

$$\begin{cases} \mathbf{Z}_{\mathrm{p}}(s) = \mathbf{Z}_{\mathrm{p}}{}'(s)\|[1/(sC_{\mathrm{f}})+\mathrm{R_d}] \\ \mathbf{Z}_{\mathrm{n}}(s) = \mathbf{Z}_{\mathrm{n}}{}'(s)\|[1/(sC_{\mathrm{f}})+\mathrm{R_d}] \end{cases} \tag{19}$$

In the renewable energy grid-following scenario, the parameters between multi-unit parallel units are usually kept consistent to facilitate unified management and control. Therefore, based on the condition that the parameters between SVI multiple parallel units are consistent, an SVI multiple parallel equivalent impedance modeling method is proposed. According to the SVI parallel impedance modeling method, the SVI parallel impedance model is constructed as shown in Fig. 3.

Based on the consistency of parameters between multiple units of SVI, it is obtained that:

$$\begin{cases} \mathbf{Z}_{\mathrm{SVI1}} = \mathbf{Z}_{\mathrm{SVIi}} = \mathbf{Z}_{\mathrm{SVIn}} \\ \mathbf{Z}_{\mathrm{Line1}} = \mathbf{Z}_{\mathrm{Linei}} = \mathbf{Z}_{\mathrm{Linen}} \end{cases} \tag{20}$$

At the same time, let $\mathbf{Z}_{\mathrm{M}} = \mathbf{Z}_{\mathrm{SVI}} + \mathbf{Z}_{\mathrm{Line}}$, we can obtain the equivalent impedance $\mathbf{Z}_{\mathrm{mul}}$ of multiple units in parallel as follows:

$$\mathbf{Z}_{\mathrm{mul}} = \mathbf{Z}_{\mathrm{M1}}\|\mathbf{Z}_{\mathrm{M2}}\|\cdots\|\mathbf{Z}_{\mathrm{Mn}} = \frac{\mathbf{Z}_{\mathrm{M1}}}{\mathrm{N}} \tag{21}$$

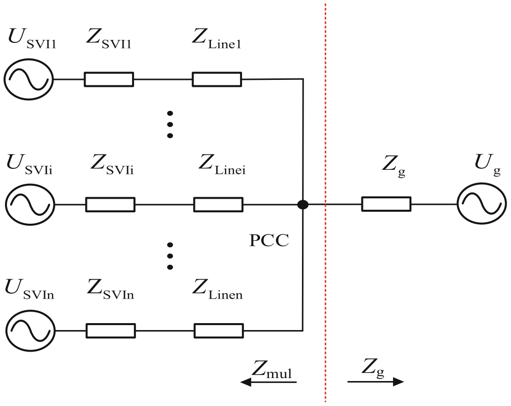

Fig. 3. Equivalent impedance model of SVI multi-unit parallel system

Table 1. Simulation main parameters table.

Parameter	Value	Parameter	Value
U_{dc}/V	700	J	0.3
V_{n}/V	180	D_{p}	250
f_0/Hz	50	K_{v}	300
L_{f}/uH	150	D_{q}	20000
C_{f}/uF	600	L_{v}/uH	150
L_{g}/uH	100	R_{v}/mΩ	1.5

3.2 Sweep-Frequency Verification of Multi-unit Parallel Impedance Model

To verify the accuracy of the established SVI multi-unit parallel impedance model, the simulation was built in MATLAB/Simulink for sweep-frequency verification. The main parameters of the simulation are shown in Table 1.

According to the above parameters, the simulation is performed for 3 units in parallel, and the amplitude and phase of positive and negative sequence impedance at different frequencies are recorded. At the same time, the positive and negative sequence impedance characteristic curves are plotted according to the derived SVI parallel impedance model, and the simulation data are compared with the model curves for verification, as shown in Fig. 4.

The simulated data basically fit the impedance model curve, thus verifying the accuracy of the derived SVI impedance model. The specific analysis shows that above 100 Hz, the SVI impedance characteristic curve is similar to that of LC filter; in the low frequency band below 50 Hz, the impedance is inductively negatively damped.

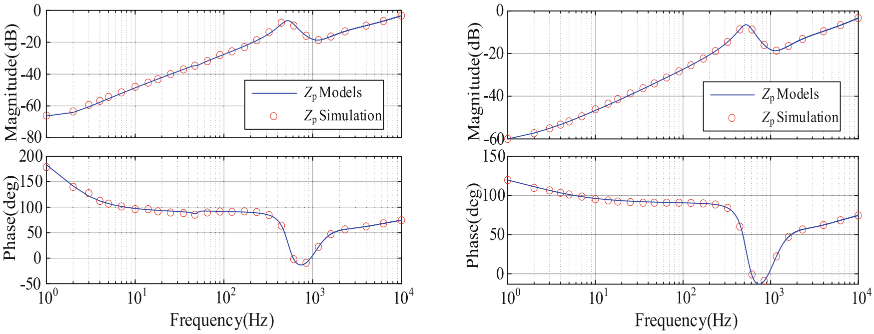

(a) Positive sequence impedance (b) Negative sequence impedance

Fig. 4. Validation diagram of 3 units impedance model

4 Effect of Factors on Impedance Characteristics

From the SVI impedance model curve can be seen: positive and negative sequence impedance is only slightly different in the low frequency band. Among them, the positive sequence impedance low frequency band phase exists in the capacitive region, while the negative sequence impedance is inductive. Therefore, the following will analyze the impact of various influencing factors on the SVI impedance characteristics through the positive sequence impedance.

4.1 Effect of Filter Parameters on Impedance Characteristics

The effect of the filter inductance parameter L_f on the SVI impedance characteristics is shown in Fig. 5. The size of the filter inductor parameter has an important effect on the SVI impedance characteristics in the 0.2–2 kHz frequency band. When the inductance value increases, the resonant frequency of the output impedance of the SVI shifts to the left, while the resonant peak increases. In addition, in the low-frequency band of 1–50Hz, an increase in the inductance value will result in an increase in the impedance amplitude and may cause the low-frequency oscillation frequency to shift to the left. Therefore, proper selection of the filter inductor size is essential to improve the grid stability of multi-stage parallel systems.

The effect of the filter capacitance parameter C_f on the SVI impedance characteristics is shown in Fig. 6. The size of the filter capacitor parameter in the main circuit has an effect only for the part of the high-frequency band above 100 Hz. When the capacitance value increases, the resonant frequency of the output impedance of the SVI shifts to the left, and the resonant peak value decreases. Therefore, by properly selecting the size of the filter capacitor in the high-frequency band, the impedance characteristics of the SVI can be adjusted to achieve the desired design requirements.

4.2 Effect of Parallel Line Impedance on Impedance Characteristics

The effect of the parallel line impedance Z_{Line} on the SVI multi-unit parallel impedance characteristics is shown in Fig. 7. The effect of parallel line impedance on the multi-unit

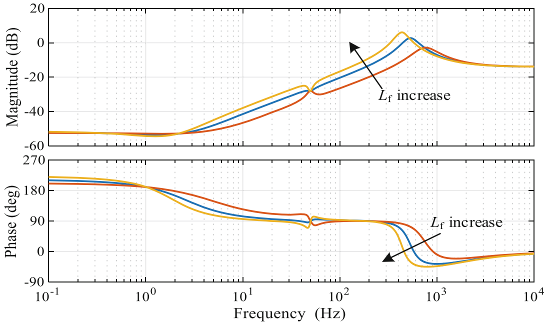

Fig. 5. Effect of L_f on impedance characteristics

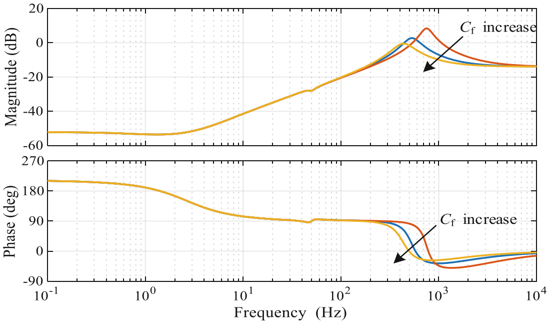

Fig. 6. Effect of C_f on impedance characteristics

parallel system is equivalent to the series line impedance on the SVI, so the high-frequency band characteristics change from the LC filter to the LCL filter; while the low-frequency band is improved due to the introduction of the resistive part in the feeder impedance, which improves the negative damping in the low-frequency band and facilitates the stability of the multi-unit parallel system.

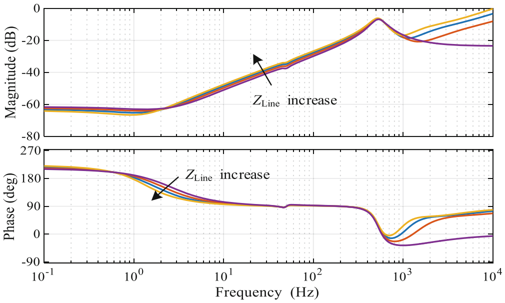

Fig. 7. Effect of Z_{Line} on impedance characteristics

4.3 Effect of Number of Parallel Units on Impedance Characteristics

The effect of the number of parallel units *N* on the impedance characteristics of the SVI multiple parallel system is shown in Fig. 8. As the number of parallel units N increases, the overall amplitude-frequency characteristic curve of multi-unit parallel system impedance shifts down; the phase frequency characteristic curve shifts down slightly in the low frequency band (1–10 Hz) and shifts up slightly in the high frequency band (1–10 kHz). This is due to the fact that when N increases, the impedance of multi-unit parallel system is equivalent to the SVI single-unit impedance for parallel connection, and the impedance of multi-unit parallel system is 1/*N* of the single.

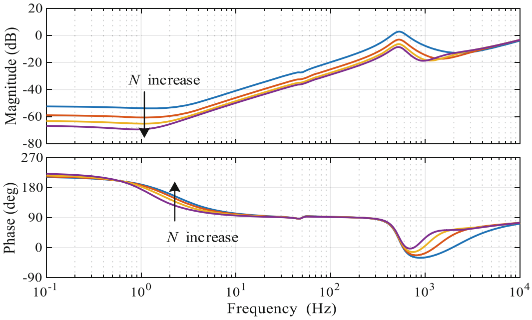

Fig. 8. Effect of *N* on impedance characteristics

5 Conclusion

In this paper, impedance modeling based on SVI control strategy, a multi-unit parallel equivalent impedance modeling method is proposed and verified by impedance sweep-frequency simulation. In addition, the influence of various factors on impedance characteristics is analyzed according to the established impedance model. The following conclusions are drawn as a result:

The swept-frequency simulation verifies the accuracy of the established SVI multi-unit equivalent impedance model. Among them, the impedance is inductively negatively damped in the low-frequency band below 50 Hz; above 100 Hz, the SVI impedance characteristic curve is similar to the LC filter characteristics.

Analysis of the factors affecting impedance characteristics shows that: LC filter parameters mainly affect the high-frequency band of impedance characteristics; parallel line impedance will increase will change the LC filter into an LCL filter; the increase in the number of parallel units will cause the overall downward shift of the impedance amplitude-frequency characteristics curve of the multi-unit parallel system.

Acknowledgments. This work is supported by the Project of National Key Research and Development Program of China (2022YFB2402700).

References

1. Hui, L.I., Dong, L.I.U., Danyang, Y.A.O.: Analysis and reflection on the development of power system towards the goal of carbon emission peak and carbon neutrality. Proc. CSEE **41**(18), 6245–6259 (2021)
2. Xiaorong, X.I.E., Jingbo, H.E., Hangyin, M.A.O., et al.: New issues and classification of power system stability with high shares of renewables and power electronics. Proc. CSEE **41**(02), 461–475 (2021)
3. Zhang, X., Li, M., Guo, Z., et al.: Review and perspectives on control strategies for renewable energy grid-connected inverters. J. Glob. Energy Interconnection **4**(05), 506–515 (2021)
4. Wang, W., Wei, Z., Chen, J., et al.: A seamless transfer strategy between grid-connected and islanding operation for microgrid inverters. Power Electron. **55**(07), 123–125+133 (2021)
5. Zhang, X., Yang, S., Wang, J., et al.: Impedance-based method used for stability analysis of multi-paralleled converter system. Electr. Drive **49**(09), 12–15+21 (2019)
6. Zhijie, Z.E.N.G., Huafeng, X.I.A.O., Bo, G.A.O., et al.: Stability analysis method of harmonic resonance of grid-connected generation system based on impedance ratios and oscillation damping. Proc. CSEE **40**(22), 7201–7212 (2020)
7. Chen, X., Wang, Y., Gong, C., et al.: Overview of stability research for grid-connected inverters based on impedance analysis method. Proc. CSEE **38**(7), 2082–2094, 2223 (2018)
8. Li, Y., Zhao, S., Ma, Y., et al.: Impedance modeling and characteristic analysis of three-phase LCL-type grid-connected inverters. Electr. Power Autom. Equip. **39**(07), 107–113 (2019)
9. Jinming, L., Dongchen, Y., Wenhua, W., et al.: Sequence impedance modeling and high-frequency oscillation suppression method for island microgrid. Trans. China Electrotech. Soc. **35**(7), 1538–1552 (2020)
10. Yuhong, W.A.N.G., Wei, Y.E., Ruihua, S.O.N.G., et al.: Design of additional active damping for three-phase LCL grid connected inverter based on impedance analysis method. High Volt. Eng. **47**(8), 2645–2656 (2021)
11. Wu, W., Chen, Y., Zhou, L., et al.: Sequence impedance modeling and stability analysis for virtual synchronous generator connected to the weak grid. Proc. CSEE **39**(06), 1560–1571+1853 (2019)
12. Wang, Y., Zhang, X., Guo, Z., et al.: Suppression strategy of sub synchronous oscillation of virtual synchronous generator. Power Electron. **55**(04), 20–25 (2021)
13. Zheng, W.E.I., Qiuhua, J.I., Wei, W.A.N.G., et al.: Control strategy of self-synchronous voltage source inverter for asymmetric power grid. Autom. Electr. Power Syst. **45**(10), 124–131 (2021)
14. Jie, C., Xinying, Z., Zhenyu, Y., et al.: Dead-time effect and background grid-voltage harmonic suppression methods for inverters with virtual impedance control. Trans. China Electrotech. Soc. **36**(8), 1671–1680 (2021)

A Wind-Solar-CSP Complementary Real-Time Control Decision-Making Method with Future Trend Consideration

Jianlin Zheng[1(✉)], Haotian Zhang[2], and Tian Zhou[2]

[1] CGDG-COSINSOLAR Engineering Technology CO. LTD, Hangzhou 310000, China
11186631@qq.com
[2] State Grid Electric Power Research Institute, Nanjing 211106, China

Abstract. Wind and solar power generation, as well as the entire power system, are accompanied by randomness and fluctuations. With the continuous improvement of renewable energy forecasting accuracy, in the process of grid operation, online real-time optimization with further trend consideration can provide relatively reasonable real-time instructions based on the trend of renewable energy changes. This paper gives the adjustable space of CSP between adjacent time points according to ultra-short-term wind and solar forecasting and the active power regulation rate of CSP. By discretizing the adjustable space, different combinations of active power of power plants are obtained in each time point. From the set of power plant combinations that simultaneously satisfy all constraints of real-time power generation control optimization decisions, the power plant combination with the weighted optimal objective function value alone is selected as the coordinated optimization decision result for real-time power generation control, and instructions are issued to solve the problem of prediction correction and rolling optimization caused by the sharp increase in random factors in grid operation, and improve the decision accuracy of real-time power generation control.

Keywords: First keyword · Second keyword · Third keyword

1 Introduction

Randomness and volatility are two inherent attributes of wind and solar generation, and even the entire power system [1]. Due to the fast development and large-scale construction of new energy in China, as well as the prominent issues of power system conditions and market mechanisms, some regions have encountered the problem of consuming wind and solar resources [2]. With the set goal in "14th Five-Year Plan", the number of RES can be expected to increase continuously in China [3].

Multi-energy complementarity refers to the combination of multiple renewable energy sources, such as solar energy, wind energy, hydropower, to provide stable energy supply at different times and locations, which can solve the issues of the instability and seasonality of renewable energy [4]. Besides, it can also improve energy utilization efficiency, reduce energy costs, and decrease environmental pollution and dependence

Y. Xue et al. (Eds.): PMF 2023, LNEE 1129, pp. 210–221, 2024.
https://doi.org/10.1007/978-981-99-9251-5_17

on fossil fuels. Concentrating Solar Power (CSP) generation is a clean and highly controllable energy technology. Currently, newly-built solar CSP plants are equipped with thermal energy storage devices [5]. The decoupling of light and electricity in solar-thermal power generation gives the output of the power plant the characteristics of being time-shifted and adjustable. The adjustment speed and depth are superior to conventional thermal power units, making it a high-quality new energy source with system peak-shaving capabilities.

Real-time generation control, as a key link in the automation of power system dispatch, plays a crucial role in ensuring the safe, reliable, efficient, low-carbon and high-quality operation of the power grid [6]. As one of the key components of power system dispatch automation, real-time generation control can monitor and control the operation of generating units to ensure stable operation of the power system under any load changes. By monitoring and analyzing parameters such as load, voltage, and frequency in real time, real-time generation control can achieve automatic start-stop, active and reactive power regulation, grid connection and disconnection of generating units to meet user requirements and grid stability requirements. At the same time, real-time generation control can optimize the operation efficiency of the power system, reduce power production costs, reduce environmental impact, and improve the reliability and security of the power system.

Currently, the existing real-time active power control optimization decisions in the power system are aimed at making single-point decisions [7–11] for the timing of issuing instructions for the next control cycle based on the data obtained from the current state of the grid, usually including predicted data for renewable energy and load, and planned data for renewable and conventional energy [12]. However, these decisions do not take into account the changing trends of renewable energy and load. Although this optimization method can achieve the optimal command value at a given time point, it cannot guarantee the optimal sum of commands over a period of time, that is, to maximize the total amount of electricity generated. In addition, the single-point optimization used in the current AGC system of the power system cannot consider the unsatisfactory scheduling results caused by prediction errors and control deviations in real-time stage, but only punishes each power plant based on a scoring mechanism after the fact. Although this mechanism seems fair, it cannot make each power plant clear about its own regulation problems in real-time stage, nor can it make the power grid receive timely feedback from each power plant, resulting in an inability to improve the control effect. As the accuracy of load and renewable energy generation capacity forecasting improves, it is more practical for power grid operation to predict the output trend of future periods through load and new energy forecasting [13–15], and make power generation control optimization decisions accordingly, rather than relying on single-point control at the current moment. When there are large fluctuations in load and wind-solar energy generation capacity in the short term, the safety and stability characteristics of the power grid will also change accordingly. If real-time power generation control optimization decisions are made only for a single time point, the real-time control optimization results for subsequent time points may be unsatisfactory due to the limitations of the active power regulation speed of power plants. Under the condition of high accuracy of ultra-short-term load and wind-solar energy generation capacity forecasting, if their future trends can be considered for real-time power generation control coordination optimization decisions, and by rolling forward, the control effect will be better than that of only focusing on single-point real-time power generation control.

This paper proposes a novel wind-solar-CSP decision-making method by automatically adjusting space of CSP based on the active power regulation speed of CSP and tracing the variability of wind and solar farm in order to reduce curtailment. By discretizing the adjustable space, it selects the optimal combination of active power of power plants that satisfies all constraints for real-time power generation control optimization decisions at different time points, taking into account the active power combination of wind farms and CSP. The selected combination of power plant active power, which has the highest weighted value of the objective function of real-time power generation control optimization decisions, is used as the result of real-time power generation control coordination and optimization decisions, thus improving the decision accuracy of wind-solar-CSP real-time power generation control at the resource end.

The rest of paper is organized as follows. Section II illustrates the main steps of the proposed method, Section III explains the real-time control decision-making model, Section IV expresses the optimization algorithm for section security, and a brief case study is demonstrated in Section V. Section VI concludes the paper.

2 The Proposed Method

With the addition of energy storage systems, CSP power generation can increase the consumption of renewable energy in the power system and reduce wind and solar curtailment. In recent years, solar thermal power generation has gradually become a research focus in the field of power systems [16–20]. The CSP power plant consists of three components: Solar Field, Thermal Energy Storage, and Power Block. These three components are connected with each other by heat-transfer flow (HTF). The transfer fluid is used as a medium to achieve energy flow and conversion between the subsystems within the power plant. The internal energy flow of the heating process is added to the traditional CSP power plant, as shown in Fig. 1.

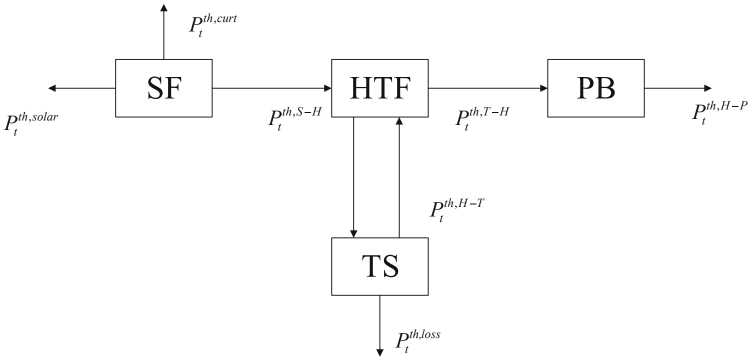

Fig. 1. Simplified structure of solar power station

Taking into account the random factors encountered during power grid operation and the inflexibility of power source regulation, this paper proposes a new wind and CSP complementary real-time control decision-making method based on ultra-short term wind power forecasting coordinated optimization control. Through predictive correction and rolling optimization, it adapts to the rapid increase of random factors in modern power grid operation. The main idea of this method (Fig. 2) is as follows:

Firstly, based on ultra-short-term forecasting and intra-day planning values, with the maximum output of new energy as the target and considering section and peak regulation constraints, calculate the real-time active power command values of wind and CSP at t0 + T, t0 + 2T, …, and t0 + nT as the initial values for the time points in the ultra-short-term forecasting sheet.

Secondly, all participating stations in the active command calculation are grouped according to whether they meet the active regulation rate requirements. The initial values of the instructions calculated by the stations that meet the requirements are issued as the final values. The value range of the final values of the two time points is determined for the stations that do not meet the regulation rate requirements based on the size relationship of the initial values of the instructions at t0 + T, t0 + 2T, …, and t0 + nT.

Then, the value range of the instruction final values at t0 + T, t0 + 2T, …, and t0 + nT is divided into different levels to obtain a combination set of control instruction tentative values for the time points. The combinations that do not meet the active regulation rate are eliminated.

Finally, the combination that is independently solved and weighted optimally for the time points is selected as the final value of the active instruction after this time point optimization decision-making.

Compared with other existing methods, the method mentioned in this article has the following two characteristics:

By solving the power generation control optimization decision-making model that reflects the comprehensive index of the impact of power plant output on the safety and stability characteristics, economic and environmental performance, predictive performance, and regulation performance of the power grid.

Taking the weighted optimal value of the independent decision-making objective function of real-time power generation control for adjacent two time points as the overall goal, and adapting to the more complex practical needs of the safety and stability characteristics of the modern power grid operation through predictive correction and rolling optimization methods.

To reduce the time cost caused by the enumeration method, this article adopts the Latin hypercube sampling method based on Cholesky decomposition to reduce the correlation of the sampling matrix. The results of this method are compared with those of the enumeration method to verify the effectiveness of the proposed method.

3 Real-Time Control Decision-Making Model

This paper combines the variability and instability of new energy generation and its impact on the power grid, with the goal of maximizing real-time output of new energy as the objective function. Meanwhile, considering the balance constraints, section constraints, and power generation and reserve of the power plant as conditions, a real-time

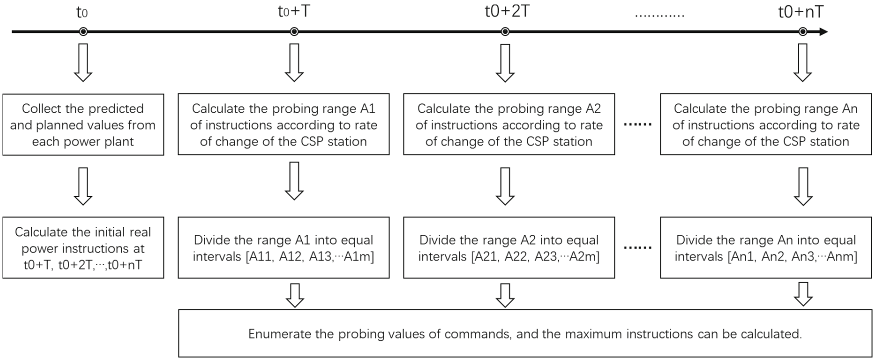

Fig. 2. Time point rolling Method

scheduling model of the power grid is established. Therefore, the objective function can be expressed as:

$$F_{MAX} = \sum_{k \in G} \beta_{c.k} \cdot P_{k.1} \tag{1}$$

where: βc.k is the comprehensive index of real-time control optimization decision-making for power plant k, and its calculation formula is:

$$\begin{aligned} \beta_{c.k} = k_s \frac{\beta_{s.i}}{\max(\beta_{s.i}, i \in C)} + k_e \frac{\beta_{e.i}}{\max(\beta_{e.i}, i \in C)} + \\ k_p \frac{\beta_{p.i}}{\max\left(\beta_{p.i}, i \in C\right)} + k_c \frac{\beta_{c.i}}{\max(\beta_{c.i}, i \in C)}\ i \in \mathrm{C} \end{aligned} \tag{2}$$

In the equation, βs.i, βe.i, βp.i, and βc.i are the safety and stability performance indicators, economic and environmental performance indicators, ultra-short-term power generation capability prediction performance indicators, and active regulation performance indicators of power plant i obtained by the current dispatch automation system analysis of the control center. ks, ke, kp, and ki are the corresponding coefficients for the safety and stability performance indicators, economic and environmental performance indicators, ultra-short-term power generation capability prediction performance indicators, and active regulation performance indicators. This can change the coefficients corresponding to the indicators based on the type of power plant and its state in the power grid. In this paper, the prediction performance indicator specifically refers to the error between actual output and predicted power under unrestricted conditions for wind and solar power plants; the control performance indicator specifically refers to the error between actual output and real-time command under restricted conditions for wind and solar power plants.

The constraint conditions include:

Power balance constraint

$$-K_f \frac{\varepsilon_f}{f_r} \sum_{i4 \in L} P_{i4.1} \leq \sum_{k \in G} P_{k.1} + \sum_{i1 \in B} P_{i1.1} + \sum_{i2 \in D} P_{i2.1} + \sum_{i3 \in TL} P_{i3.1} - (1+\gamma) \sum_{i4 \in L} P_{i4.1}$$
$$+K_f \frac{(f_0 - f_r)}{f_r} \sum_{i4 \in L} P_{i4.1} \leq K_f \frac{\varepsilon_f}{f_r} \sum_{i4 \in L} P_{i4.1} \tag{3}$$

Section power flow constraint

$$-P_{sl.l.lmt.OD} \leq P_{sl.l.0} + \sum_{k \in G} [S_{C.l.k}(P_{k.1} - P_{k.0})] + \sum_{i1 \in B} [S_{B.l.i1}(P_{i1.1} - P_{i1.0})]$$
$$+ \sum_{i2 \in D} [S_{D.l.i2}(P_{i2.1} - P_{i2.0})] + \sum_{i3 \in TL} [S_{TL.l.i3}(P_{i3.1} - P_{i3.0})] + \sum_{i4 \in L} [S_{L.l.i4}(P_{i4.1} - P_{i4.0})$$
$$+ \sum_{i5 \in DC} [S_{DC.l.i5}(P_{i5.1} - P_{i5.0})] \leq P_{sl.l.lmt.FD} \; l \in SL \tag{4}$$

Output power constraint

$$P_{k.1.d} \leq P_{k.1} \leq P_{k.1.u} k \in G \tag{5}$$

Reserve constraint

$$\sum_{k \in G} (P_{k.1.us} - P_{k.1}) + \sum_{i1 \in B} (P_{i1.1.us} - P_{i1.1}) + \sum_{i2 \in D} (P_{i2.1.us} - P_{i2.1}) \geq \mu_u \sum_{i4 \in LD} P_{i4.1}$$
$$\sum_{k \in G} (P_{k.1} - P_{k.1.ds}) + \sum_{i1 \in B} (P_{i1.1} - P_{i1.1.ds}) + \sum_{i2 \in D} (P_{i2.1} - P_{i2.1.ds}) \geq \mu_d \sum_{i4 \in LD} P_{i4.1} \tag{6}$$

In the equation, Pk.0 and Pk.1 are the actual and command values of active power for each power plant at t0 + T, t0 + 2T, …, and t0 + nT, respectively. Pi1.0 and Pi1.1 are the actual and planned active power values for power plant i1 according to the scheduling plan at t0 + T, t0 + 2T, …, and t0 + nT. Pi2.0 and Pi2.1 are the actual and planned active power values for power plant i2 controlled in real-time by other control centers at t0 + T, t0 + 2T, …, and t0 + nT. Pi3.0 and Pi3.1 are the real-time and planned active power values injected into the internal grid by the connection line i3 in the set of inner and outer grid connection lines TL. Pi4.0 and Pi4.1 are the actual and predicted active power values for the concentrated load i4 in the load L. Pi5.0 and Pi5.1 are the actual and command values of active power at the AC side node i5 in the set of DC nodes DC. γ is the network loss coefficient within the control range of the dispatch center at t0. f0 and Kf are the frequency and static frequency characteristic coefficient of active power within the control range of the dispatch center, fr is the rated frequency within the control range of the dispatch center, and εf is the preset allowable deviation value of frequency within the control range of the dispatch center. For the overloaded monitoring transmission equipment in the set of stable sections SL, the values of Psl.l.lmt.FD and

Psl.l.lmt.OD are equal, which is the active overload limit of the transmission equipment *l* calculated based on the power factor of the transmission equipment *l* at t0. For the overloaded monitoring stable sections in the SL set, Psl.l.lmt.FD and Psl.l.lmt.OD are the forward and backward stability limits of the stable section at t0 + T, respectively. Psl.l.0 is the active power of the overloaded monitoring transmission equipment or stable section in the current time t0 within the control range of the dispatch center. SC.l.k is the active power sensitivity of the overloaded monitoring transmission equipment or stable section to the grid-connected active power of each power plant. SB.l.i1 and SD.l.i2 are the active power sensitivities of the overloaded monitoring transmission equipment or stable section to the grid-connected active power of all power plants participating in real-time control and scheduling plan, respectively, within the control range of the dispatch center at t0. STL.l.i3 is the active power sensitivity of the overloaded monitoring transmission equipment or stable section to the injected active power of the connection line i3 in the TL set within the control range of the dispatch center at t0. SL.l.i4 is the active power sensitivity of the overloaded monitoring transmission equipment or stable section to the active power of the concentrated load i4 in the network within the control range of the dispatch center at t0. SDC.l.i5 is the active power sensitivity of the overloaded monitoring transmission equipment or stable section to the grid-connected active power of the AC side node i5 in the DC set within the control range of the dispatch center at t0. μu and μd are the preset positive and negative reserve capacity coefficients of active power for t0 + T, respectively.

By maximizing the sum of the product of the comprehensive index and the active power control command of power plants, taking into account the real-time adjustable space and adjustment speed of active power of power plants, transmission equipment limits, stable section forward and backward limits, frequency regulation and peak shaving constraints, etc., this method comprehensively reflects the various factors that need to be considered in real-time power generation control optimization decisions, including safety and stability, economic efficiency, low-carbon environmental protection, and scientific management. It meets the requirements of multi-level scheduling and coordination optimization and real-time control of multi-type power sources in the large-scale power grid.

As the inherent factors in modern power system, intermittence and variability are companied with wind and solar power generation in life-cycle. Generally, the normal operation period for wind and solar generation can be classified into capping period and non-capping period.

In a high renewable penetration level power grid, forecasting accuracy needs to be concerned in non-capping period, and control response accuracy needs to be concerned in capping period, because the renewable power fluctuation could influence the traditional power generation scheduling. To quantify these two factors, prediction precision indices and operation performance indices [21] are used in this paper.

4 Optimization Algorithm for Section Security

The impact characteristics of power plant output on power grid security and stability are only reflected in the sensitivity of power plant output to transmission equipment/stable section power in the constraint equation of transmission equipment/stable section power.

This cannot fully reflect the impact characteristics of power plant output on various types of power grid safety and stability.

When the system needs to reduce active power, the grid power of renewable energy power plants with smaller safety and stability control performance costs should be prioritized for reduction, taking into account the lower limit value of active power execution and the prediction accuracy. When the system needs to increase active power, the upper limit value of the grid active power control instruction execution value of the renewable energy power plant should be considered comprehensively, and the grid active power of the renewable energy power plant with a larger comprehensive performance index of prediction accuracy and adjustment performance indicators should be prioritized for increase.

Based on the real-time flow of the outgoing section, control limit, real-time output of new energy and new energy consumption space, the load rate of the outgoing section can be calculated, denoted as L_j^{net}, shown in Fig. 3. The warning and emergency thresholds are pre-set to $\mu_{yj.j}$ and $\mu_{tz.j}$. Which dividing the outgoing section into three interval zones.

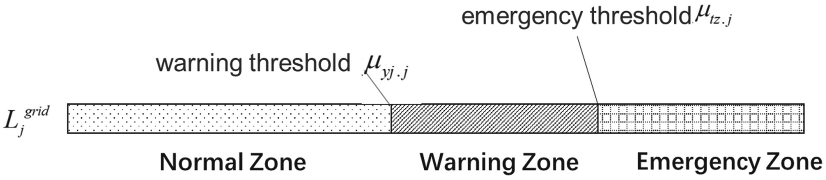

Fig. 3. Sketch map of interval scene division

$$L^{grid} = \sum_{i \in C} P_{n.i'} / P_{grid'} \tag{7}$$

(a) Normal Zone: all sections related to renewable energy plants $L^{grid} < \mu_{yj.j}$,

$$P_{tl.j}(T)/P_{tl.j.\max} < \mu_{yj.j} \;\; T > T_{1.\min} \tag{8}$$

(b) Warning Zone: At least one section whose loading is between $\mu_{yj.j}$ and $\mu_{tz.j}$,

$$\mu_{yj.j} \le P_{tl.j}(T)/P_{tl.j.\max} \le \mu_{tz.j} \;\; T > T_{2.\min} \tag{9}$$

(c) Emergency Zone: At least one section whose loading is larger than $\mu_{tz.j}$

$$P_{tl.j}(T)/P_{tl.j.\max} > \mu_{tz.j} \;\; T > T_{3.\min} \tag{10}$$

where $T_{1.\min}$, $T_{2.\min}$, $T_{3.\min}$ are the time threshold in each zone.

Considering various factors such as fluctuations in power grid load and renewable energy output may cause fluctuations in section. To avoid frequent adjustments of renewable energy instructions caused by fluctuations, a duration longer than the threshold value will be set as a necessary condition for determining the safety interval. The time thresholds for different sections can be flexibly configured, and the minimum interval holding time can be set for the warning and emergency zones. During this period, the safety interval can only be maintained or extended towards a smaller margin, to avoid frequent switching between the warning, emergency zone and the safety zone, which would cause repeated adjustments of renewable energy instructions.

This control method ensures the stability of the system while changing the same magnitude of output, and improves the real-time, reliability, and accuracy of the grid active power control of renewable energy power plants, as well as the initiative of renewable energy power plants to improve the level of grid active power prediction and control technology equipment.

5 Case Study

To illustrate the effectiveness of the algorithm proposed in this paper, a case study is conducted on the operation curve of a certain region with wind, solar and CSP during 24 h. The operational parameters of all power sources are from the actual power grid and have been anonymized. In this case study, there are 6 wind farms, 4 solar farms and 2 CSPs, all of which are connected to the grid through the same transmission line. The relevant data is shown in Table 1.

Table 1. Grid and generation parameters

	Capacity (MW)	Daily maximum value (MW)	Daily minimum value (MW)
WF1	100	27.87	–
WF2	402	209.8	–
WF3	300	176.87	–
WF4	201	61.69	–
WF5	201	92.7	–
WF6	25	127.29	–
PV1	100	45	–
PV 2	100	67.5	–
PV 3	100	45	–
PV 4	100	45	–
CPS 1	50	–	–
CPS 2	50	–	–
Tie-line	1000	450.54	295.43

The dispatch operation curve of the power grid in this case study is shown in Fig. 4, where the total predicted curve of wind and solar power is the weighted curve of the predicted curves of the mentioned wind and solar power plants, the tie-line curve is the

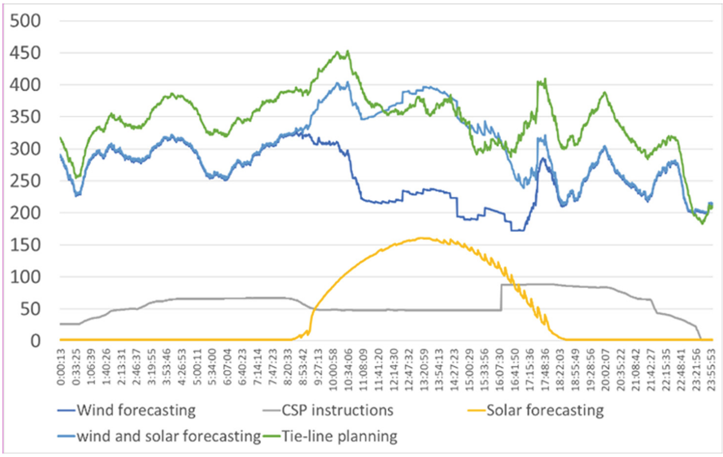

Fig. 4. Dispatch commands curves under normal operation

planned curve of the external transmission line for the day, and the real-time instructions for CSP and wind-solar power are the total instruction curves of CSP and wind-solar power participating in real-time optimization control using single time-point optimization. As seen from the figure, based on the single time-point optimization of the proposed objective function, the instructions for wind-solar-CSP power can be adjusted according to the outgoing demand of the transmission line. CSP power can match the instructions of wind-solar power while satisfying its own ramping constraint. However, this algorithm only optimizes the instructions based on the known information of the next time point at the current time point, without considering the uncertainty and trend of wind-solar power sources, so it cannot achieve the optimal sum of instructions within a certain period.

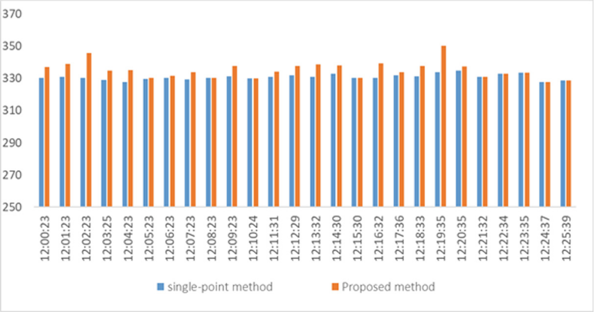

Fig. 5. Single time-point optimization curve versus proposed optimization curve

Figure 5 shows a comparison of the tie-line channel curve, the total predicted curve of wind and solar power, and the instruction curves obtained by single time-point and the proposed optimization from 12:00 to 12:25. As seen from Fig. 5, during the period, due to the high wind power generation and the low level of the tie-line, the planned output of CSP was reduced to 50 MW. In the previous time period from 8:30, the planned output of CSP was reduced in advance based on the wind and solar power prediction information to ensure that wind power had enough space for consumption, which ensured that the control effect was better than that of single time-point control. It can be seen that the instruction values given by the proposed optimization algorithm are slightly larger than those obtained by the single time-point optimization.

6 Conclusions and Future Work

Randomness and volatility are inherent properties of wind and solar resources, as well as the entire power system. In the process of power grid operation, optimization with further trend consideration can give relatively reasonable real-time instructions based on the trend of renewable energy changes. This paper provides a novel wind-solar-CSP complimentary real-time control method based on the active power regulation rate of power plants and future trends of the renewable energy. The active power of different power plants at all time points in the forecasting sheet is combined through discretization, and the power plant combination with the weighted optimal value of the objective function alone is selected from the active power combinations of power plants that simultaneously satisfy all constraint conditions, which is used as the coordinated optimization decision result for real-time power generation control, and instructions are issued to improve the decision accuracy of real-time power generation control.

Further research will be conducted on the model in this paper. Since the research in this paper is based on real-time control strategies made when the forecasting accuracy reaches a certain level, it has a strong dependence on the forecasting accuracy of renewable energy. The uncertainty level of renewable energy will be evaluated in the future, and an adaptive real-time power generation control optimization decision method for the uncertainty of new energy will be proposed.

Acknowledgement. Financial support by State Grid Corporation of China, Science and Technology Projects "Research and application of key technologies for integrated optimization of wind power, photovoltaic, CSP and energy storage in multi-energy complementary demonstration" is very much appreciated.

References

1. Wang, W., Huang, S., Zhang, G., et al.: Optimal operation of an integrated electricity-heat energy system considering flexible resources dispatch for renewable integration. J. Mod. Power Syst. Clean Energy **9**(4), 699–710 (2021)
2. Yinbiao, S., Zhigang, Z., Jianbo, G., et al.: Study on key factors and solution of renewable energy accommodation. Proc. CSEE **37**(1), 1–9 (2017)
3. Renewables 2022, https://www.iea.org/, last accessed 2023/5/16
4. Dai Liyuan, X., Taishan, W.M., et al.: A survey of real time control technology for multi-source power grid coordination. Electr. Power Sci. Eng. **33**(5), 16–23 (2017)

5. Chen, R., Sun, H., Guo, Q., et al.: Reducing generation uncertainty by integrating CSP with wind power: an adaptive robust optimization-based analysis. IEEE Trans. Sustain. Energy **6**(2), 583–594 (2015)
6. Hui, D., Yanfang, Z., Maxiang, W., et al.: Design and application of intelligent power control system for integration of renewable energy. Autom. Electr. Power Syst. **43**(2), 105–120 (2019)
7. Fan, X., Zhixu, C., Yong, Z., et al.: Real-time generation scheduling model and its application. Autom. Electr. Power Syst. **38**(6), 117–122 (2014)
8. Zhang, Z., Xia, Q.: Architecture and key technologies for generation scheduling of smart grid. Power Syst. Technol. **33**(20), 1–8 (2009)
9. Yin, J., Z, D.: Closed-loop control model for real-time generation scheduling considering source-side and load-side prediction error. Autom. Electr. Power Syst. **42**(6), 99–105 (2018)
10. Lin, L., Zhu, C., Zheng, T.: Active power control of wind farm cluster and its strategy. Autom. Electr. Power Syst. **38**(14), 9–16 (2014)
11. Haohao, W., Tian, Z., Zhao, Y., et al.: Review of real-time complementary active power control of multi-type power resources for large scale renewable energy. Mod. Electr. Power **36**(4), 1–10 (2019)
12. Yang, B., Haiwang, Z., Qing, X., et al.: An intraday rolling scheduling with unit energy coordination and operating cost control. Power Syst. Technol. **37**(10), 2965–2972 (2013)
13. Choi, D.H., Le, X.: Data perturbation-based sensitivity analysis of real-time look-ahead economic dispatch. IEEE Trans. Power Syst. **32**(3), 2072–2082 (2017)
14. Peng, L., Danwen, Y., Ming, Y., et al.: Flexible look-ahead dispatch realized by robust optimization considering CVaR of wind power. IEEE Trans. Power Syst. **33**(5), 5330–5340 (2018)
15. Yingzhong, G., Xie, L., et al.: Stochastic look-ahead economic dispatch with variable generation resources. IEEE Trans. Power Syst. **32**(1), 17–29 (2017)
16. Yingyu Wang, X.: Influence of concentrating solar power on new energy consumption of Qinghai power grid. Distrib. Energy **7**(6), 68–72 (2022)
17. Liu, Y., Li, G., Qi, J., et al.: Characteristics and development direction of Molten salt trough CSP technology. Energy Energy Conserv. **210**(3), 1–6 (2023)
18. Fang, Y., Zhao, S., et al.: Joint optimal operation and bidding strategies of concentrating solar power plants with wind farms. Proc. CSEE **40**(1), 39–50 (2020)
19. Zhang, T., Shu, T., Chengwei, G.: Scheduling strategy for concentrating solar power plant and wind power system considering controllable load. Proc. CSU-EPSA **34**(9), 32–39 (2022)
20. Xiao, B., Wang, T.: Optimal coordinated operation model considering photovoltaic power and concentrating solar power. Mod. Electr. Power **37**(2), 163–170 (2020)
21. Zhang, H.T., Wang, H., et al.: A novel strategy for wind-solar-hydro complimentary real-time scheduling and control. In: 2019 IEEE Innovative Smart Grid Technologies - Asia (ISGT 2019), pp. 3782–3787 (2019)

A Model Predictive Control for Gird-Forming Voltage Source Converter

Xinzhe Song[1(✉)], Shaoze Zhou[1], Wei Wang[1], Wei Chen[1,2], Zheng Wei[1], and Dongmei Yang[1]

[1] NARI Group Corporation (State Grid Electric Power Research Institute), Nanjing 211106, China
`2623387153@qq.com`
[2] School of Electrical and Automation Engineering, Nanjing Normal University, Nanjing 210023, China

Abstract. In response to the issue of insufficient frequency and voltage regulation capability in high-penetration renewable energy system, a control strategy combining grid-forming voltage source converter (GFM-VSC) with model predictive control (MPC) is proposed. Based on the main circuit topology of the converter, a power prediction model is established. Then a cost function concerning both inductor current and power output is constructed and a control strategy based on the which is introduced. A fast dynamic response to frequency and voltage variations has been achieved. Simulations have confirmed the effectiveness of the proposed control strategy.

Keywords: Voltage source converter · Grid forming · Model predictive control

1 Introduction

Conventional grid-connected converters use grid-following (GFL) control methods that employ a phase lock loop (PLL) to synchronize with the grid [1]. Unfortunately, this strategy lacks inertia and damping. That means converters using GFL control cannot operate independently and will decrease the stability of power system. This risk intensifies as more electronic devices are brought online, as studies have shown [2–4].

Scholars tried to address the aforementioned issue by developing control strategies that imitate the operational characteristic of synchronous generators [5, 6]. The grid-forming voltage source converter (GFM-VSC) is a notable inverter control strategy that mirrors synchronous machine characteristics within the power control loop [7]. It enables the manifestation of voltage source properties externally, which grants GFM-VSC units the ability to actively respond to changes in grid voltage and frequency [8, 9]. This attribute facilitates the provision of power support and contributes to enhancing the operational stability of power grids that feature a significant share of renewable energy devices. Furthermore, it should be noted that the GFM-VSC adopts a power synchronous method, which supports the system voltage and frequency by adjusting the output active

Y. Xue et al. (Eds.): PMF 2023, LNEE 1129, pp. 222–232, 2024.
https://doi.org/10.1007/978-981-99-9251-5_18

power and reactive power [10]. Therefore, the response speed of GFM-VSC to power signals greatly affects its performance.

Amidst the swift advancements of digital signal processors (DSPs), model predictive control (MPC) algorithm has been widely implemented in the fields of power electronics converters and motor control due to its exceptional discrete control quality [11, 12]. The MPC algorithm is characterized by its high response speed, high-quality control performance [13–15]. By constructing a reasonable cost function, it is possible to achieve coordinated control of multiple control objectives [16].

This article proposes a GFM-VSC power prediction control strategy. Based on the main circuit structure of the converter, a power prediction model for the grid-forming VSC unit is established. The combination of power prediction control and virtual synchronous control, which simulates the operating characteristics of synchronous machines, enables the MPC control method for grid-connected VSC voltage source converters. While maintaining voltage source characteristics, the dynamic response speed of the unit is ensured. A simulation model was built on MATLAB/Simulink platform to confirm the effectiveness of the proposed control strategy.

2 Control Strategy of GFM-VSC

2.1 System Modeling

When equipped with appropriate correction circuits and energy storage devices, the voltage on the DC side of the inverter can be approximately considered to be constant. Therefore, this proposed control strategy will be illustrated through the example of a conventional energy storage converter. The main circuit topology of a GFM-VSC is shown in Fig. 1.

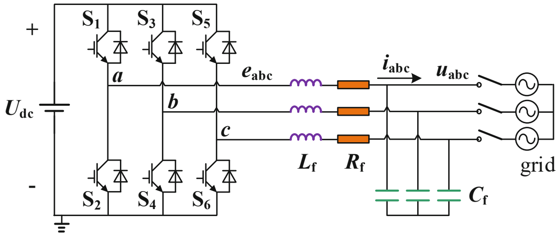

Fig. 1. Main circuit topology of GFM-VSC

As is shown above, U_{dc} is the DC side bus voltage; u_{abc} and i_{abc} represent the three-phase voltage and current output at the AC side; e_{abc} represents the output voltage of the three-phase bridge arm; L_{f}, R_{f} and C_{f} form a LC filter. According to Kirchhoff voltage law, it can be concluded that:

$$L_{\mathrm{f}}\frac{di_{\mathrm{abc}}}{dt} = e_{\mathrm{abc}} - R_{\mathrm{f}}i_{\mathrm{abc}} - u_{\mathrm{abc}} \tag{1}$$

By applying Clark transformation to Eq. (1), it can be obtained that current rate of change model in αβ coordinate system is:

$$\begin{cases} \frac{\mathrm{d}i_\alpha}{\mathrm{d}t} = \frac{1}{L_\mathrm{f}}(e_\alpha - R_\mathrm{f} i_\alpha - u_\alpha) \\ \frac{\mathrm{d}i_\beta}{\mathrm{d}t} = \frac{1}{L_\mathrm{f}}\left(e_\beta - R_\mathrm{f} i_\beta - u_\beta\right) \end{cases} \tag{2}$$

i_α, i_β are the current output of VSC in αβ coordinate system; u_α, u_β are the voltage output of VSC in αβ coordinate system; e_α, e_β are the inner potential of VSC in αβ coordinate system.

If u_abc is balanced, the voltage rate of change model can be presented as:

$$\begin{cases} \frac{\mathrm{d}u_\alpha}{\mathrm{d}t} = \omega \cdot U_\mathrm{m} \cdot \cos\omega t = -\omega u_\beta \\ \frac{\mathrm{d}u_\beta}{\mathrm{d}t} = \omega \cdot U_\mathrm{m} \cdot \sin\omega t = \omega u_\alpha \end{cases} \tag{3}$$

U_m is the amplitude of output voltage at AC side; ω represents the angular frequency.

The power output can be calculated in αβ coordinate system, Eq. (4) shows the output power model P_e and Q_e.

$$\begin{cases} P_\mathrm{e} = \frac{3}{2}\left(u_\alpha i_\alpha + u_\beta i_\beta\right) \\ Q_\mathrm{e} = \frac{3}{2}\left(u_\beta i_\alpha - u_\alpha i_\beta\right) \end{cases} \tag{4}$$

2.2 Reference Calculation of GFM-VSC

In order to simulate the operating characteristics of a synchronous generator, GFM-VSC generates a virtual inner potential e_m whose reference is calculated by active power loop and reactive power loop.

Based on the speed regulator equation and rotor motion equation of the synchronous machine, the control equation of the GFM-VSG active power loop can be listed as follow:

$$\begin{cases} P_\mathrm{e\_ref} = P_\mathrm{ref} + D_\mathrm{p}(\omega_\mathrm{n} - \omega_\mathrm{g}) - K_\mathrm{d}(\omega - \omega_\mathrm{g}) \\ J\omega_\mathrm{n}\dfrac{\mathrm{d}\omega}{\mathrm{d}t} \approx P_\mathrm{e\_ref} - P_\mathrm{e} \\ \dfrac{\mathrm{d}\theta}{\mathrm{d}t} = \omega \end{cases} \tag{5}$$

P_ref is the active power command; D_p is the frequency-active power droop coefficient; K_d is the mechanical damping coefficient; $P_\mathrm{e\_ref}$ is the total command of active power; P_e is the active power output of VSC; J is the virtual inertia of VSC; ω_g is the angular frequency of output voltage; ω_n is the rated angular frequency; θ is the phase reference of GFM-VSC inner potential.

The reactive power loop of GFM-VSC simulates the voltage regulation characteristic of the excitation system of a synchronous generator. The control equation can be given as:

$$\begin{cases} Q_\mathrm{e\_ref} = D_\mathrm{q}(U_\mathrm{n} - U_\mathrm{m}) + Q_\mathrm{ref} \\ \dfrac{\mathrm{d}E_\mathrm{m\_ref}}{\mathrm{d}t} = \dfrac{1}{K}(Q_\mathrm{e\_ref} - Q_\mathrm{e}) \end{cases} \tag{6}$$

Q_{ref} is the reactive power command; D_{q} is the voltage-reactive power droop coefficient; $Q_{\mathrm{e\_ref}}$ is the total command of reactive power; Q_e is the reactive power output of VSC; K is the integral coefficient of reactive power loop; U_{n} is the rated amplitude of phase voltage; E_{m} is the amplitude of GFM-VSC inner potential.

The reference value of inner potential in abc coordinate system, is calculated by Eq. (7), using the phase θ from the active power loop and amplitude E_{m} from reactive power loop.

$$\begin{cases} e_{a\_ref}(k) = E_m(k)\cos[\theta(k)] \\ e_{b\_ref}(k) = E_m(k)\cos[\theta(k) - 2\pi/3] \\ e_{c\_ref}(k) = E_m(k)\cos[\theta(k) + 2\pi/3] \end{cases} \tag{7}$$

Since the inner potential cannot be measured and used as a control target directly. Virtual impedance L_{v}, R_{v} are introduced to calculated the current reference $i_{\mathrm{abc\_ref}}$. By this way, the control objective for inner potential is transformed into a control objective for current which is measurable. Its value is obtained by Eqs. (8) and (9)

$$L_{\mathrm{v}}\frac{di_{\mathrm{abc\_ref}}}{dt} = e_{\mathrm{abc\_ref}} - R_{\mathrm{v}}i_{\mathrm{abc}} - u_{\mathrm{abc}} \tag{8}$$

$$\begin{cases} i_{\alpha\_ref}(k) = \dfrac{2}{3}\cdot\left[i_{a\_ref}(k) - \dfrac{1}{2}i_{b\_ref}(k) - \dfrac{1}{2}i_{c\_ref}(k)\right] \\ i_{\beta\_ref}(k) = \dfrac{\sqrt{3}}{3}\cdot\left[i_{b\_ref}(k) - i_{c\_ref}(k)\right] \end{cases} \tag{9}$$

The amplitude and angular frequency at PCC are measured through a frequency & amplitude measure model. Based on the Park transformation, when the d-axis coincides with the phasor of phase-A, the amplitude U_{m} and angular frequency ω_{g} can be obtained. The entire calculation process for the reference of GFM-VSC is concentrated in Fig. 2.

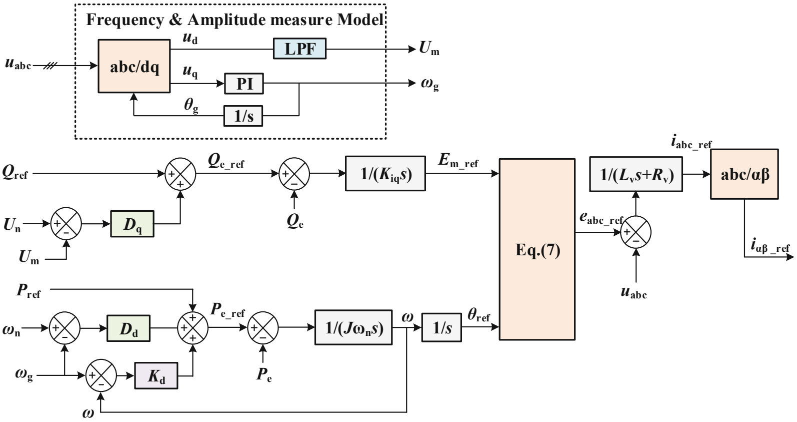

Fig. 2. Reference calculation of GFM-VSC

3 MPC Strategy of GFM-VSC

3.1 Predictive Model of MPC in GFM-VSC

In order to achieve the power prediction model of GFM-VSC, derivative calculation is applied to Eq. (4). The changing rate of active power P_e and reactive power Q_e are presented in Eq. (10).

$$\begin{cases} \frac{dP_e}{dt} = \frac{3}{2}\left(u_\alpha \frac{di_\alpha}{dt} + u_\beta \frac{di_\beta}{dt} + i_\alpha \frac{du_\alpha}{dt} + i_\beta \frac{du_\beta}{dt}\right) \\ \frac{dQ_e}{dt} = \frac{3}{2}\left(u_\beta \frac{di_\alpha}{dt} - u_\alpha \frac{di_\beta}{dt} + i_\alpha \frac{du_\beta}{dt} - i_\beta \frac{du_\alpha}{dt}\right) \end{cases} \tag{10}$$

Associating Eqs. (2), (3) and (10), the changing rate of active power P_e and reactive power Q_e can be calculated in the form of Eq. (11).

$$\begin{cases} \frac{dP_e}{dt} = \frac{3}{2L_f}\left(u_\alpha e_\alpha + u_\beta e_\beta - u_\alpha^2 - u_\beta^2\right) - \frac{R_f}{L_f}P_e - \omega Q_e \\ \frac{dQ_e}{dt} = \frac{3}{2L_f}\left(u_\beta e_\alpha - u_\alpha e_\beta\right) - \frac{R_f}{L_f}Q_e + \omega P_e \end{cases} \tag{11}$$

Through the discretization of Eqs. (2) and (11), the MPC model of GFM-VSC is:

$$\begin{aligned} P_e(k+1) = {} & \frac{3T_s}{2L_f}\left[u_\alpha(k)e_\alpha(k) + u_\beta(k)e_\beta(k) - u_\alpha^2(k) - u_\beta^2(k)\right] \\ & + \left(1 - \frac{R_f T_s}{L_f}\right)P_e(k) - T_s \omega Q_e(k) \end{aligned} \tag{12a}$$

$$\begin{aligned} Q_e(k+1) = {} & \frac{3T_s}{2L_f}\left[u_\beta(k)e_\alpha(k) - u_\alpha(k)e_\beta(k)\right] + T_s \omega P_e(k) \\ & + \left(1 - \frac{R_f T_s}{L_f}\right)Q_e(k) \end{aligned} \tag{12b}$$

$$i_\alpha(k+1) = \left(1 - \frac{R_f T_s}{L_f}\right)i_\alpha(k) + \frac{T_s}{L_f}\left[e_\alpha(k) - u_\alpha(k)\right] \tag{13a}$$

$$i_\beta(k+1) = \left(1 - \frac{R_f T_s}{L_f}\right)i_\beta(k) + \frac{T_s}{L_f}\left[e_\beta(k) - u_\beta(k)\right] \tag{13b}$$

T_s is the sampling period of the controller.

s_a, s_b, s_c are the switch function of three-phase bridge arm. Their values are given as below.

$$\begin{aligned} s_a &= \begin{cases} 1, & \text{when } S_1 = 1 \text{ and } S_2 = 0 \\ 0, & \text{when } S_1 = 0 \text{ and } S_2 = 1 \end{cases} \\ s_b &= \begin{cases} 1, & \text{when } S_3 = 1 \text{ and } S_4 = 0 \\ 0, & \text{when } S_3 = 0 \text{ and } S_4 = 1 \end{cases} \\ s_c &= \begin{cases} 1, & \text{when } S_5 = 1 \text{ and } S_6 = 0 \\ 0, & \text{when } S_5 = 0 \text{ and } S_6 = 1 \end{cases} \end{aligned} \tag{14}$$

The value of e_{α}, e_{β} depends on the switching signal at k moment. Using the switch function, inner potential of VSC in αβ coordinate system can be calculated by Eq. (15)

$$\begin{cases} e_{\alpha}(k) = \dfrac{2}{3} \cdot U_{\mathrm{dc}}(k) \cdot \left[s_{\mathrm{a}}(k) - \dfrac{1}{2} s_{\mathrm{b}}(k) - \dfrac{1}{2} s_{\mathrm{c}}(k) \right] \\ e_{\beta}(k) = \dfrac{\sqrt{3}}{3} \cdot U_{\mathrm{dc}}(k) \cdot [s_{\mathrm{b}}(k) - s_{\mathrm{c}}(k)] \end{cases} \tag{15}$$

Equations (12a), (12b), (13a) and (13b), has calculated the predicted values for power and current at time $k + 1$. The cost function for predictive control can be defined based on the sum of squared error between the predicted values of power and current at time k + 1 and the reference values of power and current at time k. The cost function can be concluded as follow:

$$\begin{aligned} J_w = {} & \lambda_1 \left\{ \left[P_{e\_ref}(k) - P_e(k+1) \right]^2 + \left[Q_{e\_ref}(k) - Q_e(k+1) \right]^2 \right\} \\ & + \lambda_2 \left\{ \left[i_{\alpha\_ref}(k) - i_{\alpha}(k+1) \right]^2 + \left[i_{\beta\_ref}(k) - i_{\beta}(k+1) \right]^2 \right\} \end{aligned} \tag{16}$$

λ_1 and λ_2 are the weighting factors. The flowchart of finite set MPC algorithm is shown in Fig. 3.

There are six none-zero switching state for GFM-VSC. By substituting Eq. (15) into Eq. (12a), the value function $J_{\mathrm{w}}(i)$ for each switching state can be calculated. By a rolling calculation method, the optimal switch state that minimizes the cost function can be obtained and outputted in each sampling period. The control block diagram of the proposed current MPC strategy for GFM-VSC units is shown in Fig. 4.

4 Simulation and Validation

In order to verify the effectiveness of the proposed control strategy, a 500 kW GFM-VSC simulation model on MATLAB/Simulink platform is built. Simulation parameters of controllers and main circuits are shown in Table 1.

4.1 Active Power—Frequency Droop Characteristic

To verify the autonomous frequency regulation feature of the control strategy under system frequency fluctuations, Fig. 5a, b respectively display the simulated waveforms of the GFM-VSC system response after transitioning to off-grid operation. In Fig. 5a and b, from top to bottom, the graphs show the active power output of the generator, the frequency of the output voltage, the three-phase output current, and the three-phase output voltage.

In scenario depicted in Fig. 5a: before 0.2 s, the GFM-VSC was operating in grid-connected mode, and the system frequency was maintained at 50 Hz, while the GFM-VSC output was 300 kW. At 0.2 s, the connection to the power grid was disconnected, and the GFM-VSC generator independently supported a 300 kW active load. At 0.5 s, a 50 kW active load was applied to simulate a decrease in system frequency. In the scenario depicted in Fig. 5b: The GFM-VSC output was increased to 350 kW, and at

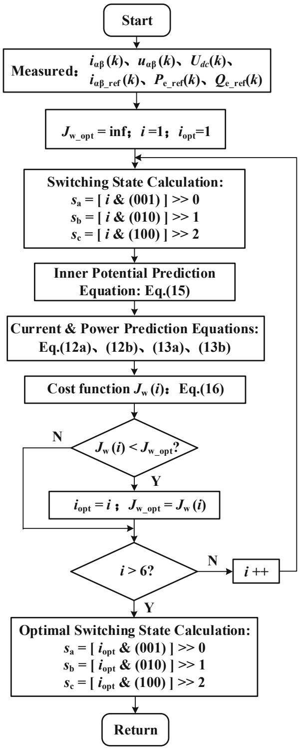

Fig. 3. Flowchart of finite set control algorithm

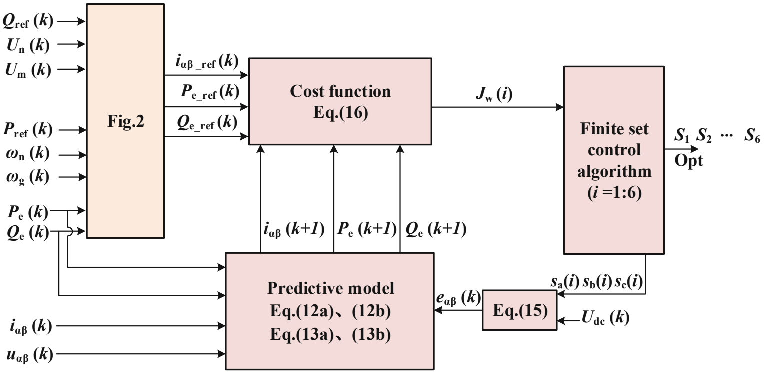

Fig. 4. MPC strategy for GFM-VSC

0.2 s it was disconnected from the grid. At 0.5 s, a 50 kW active load was disconnected to simulate an increase in system frequency.

As the waveforms show: Due to the inertia and damping characteristics simulated by the active loop, which correspond to the rotor motion equation of a synchronous

Table 1. Simulation parameters.

Parameters	Value	Parameters	Value
Un/V	220	Dp	16600
Lf/μH	150	Dq	11500
Rf/Ω	0.001	K	0.001
Cf/μF	100	J	0.138
ωn/(rad/s)	314	Kd	15600
Rg/Ω	0.001	λ1	1×10^{-8}
Lg/μH	5.8	λ2	1

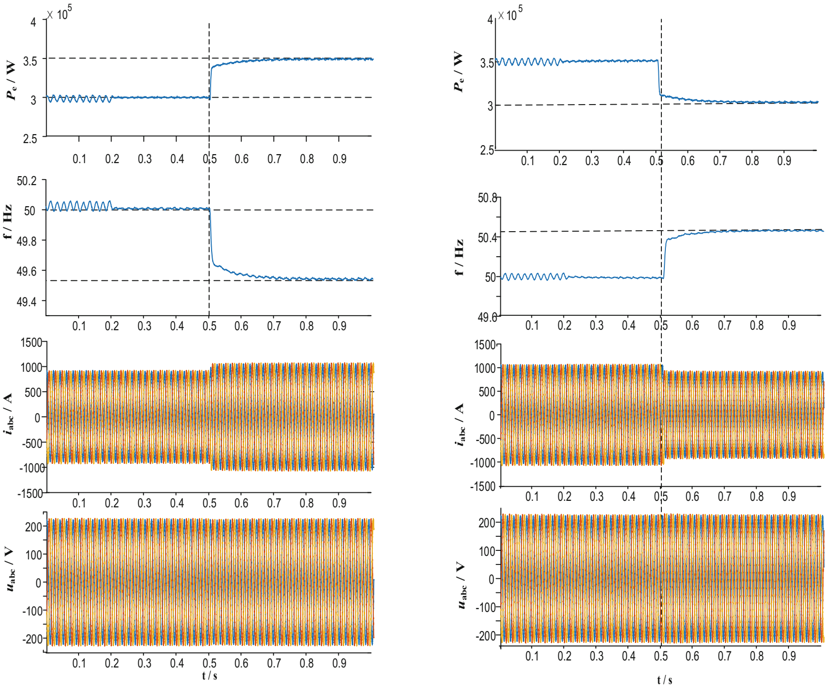

(a) frequency drop (b) frequency rise

Fig. 5. Waveform of GFM-VSC frequency regulation

generator, the GFM-VSC generator output frequency did not experience drastic changes as the grid frequency changed abruptly at the moment of the disturbance.

4.2 Reactive Power–Voltage Droop Characteristic

To verify the autonomous voltage regulation capability of the control strategy when subjected to voltage fluctuations in the system, Fig. 6a and b show the simulation waveforms of the GFM-VSC system response after switching to islanding mode. In Fig. 6a and b, from top to bottom, the graphs show the reactive power output of the generator, the amplitude of the output voltage, the three-phase output current, and the three-phase output voltage.

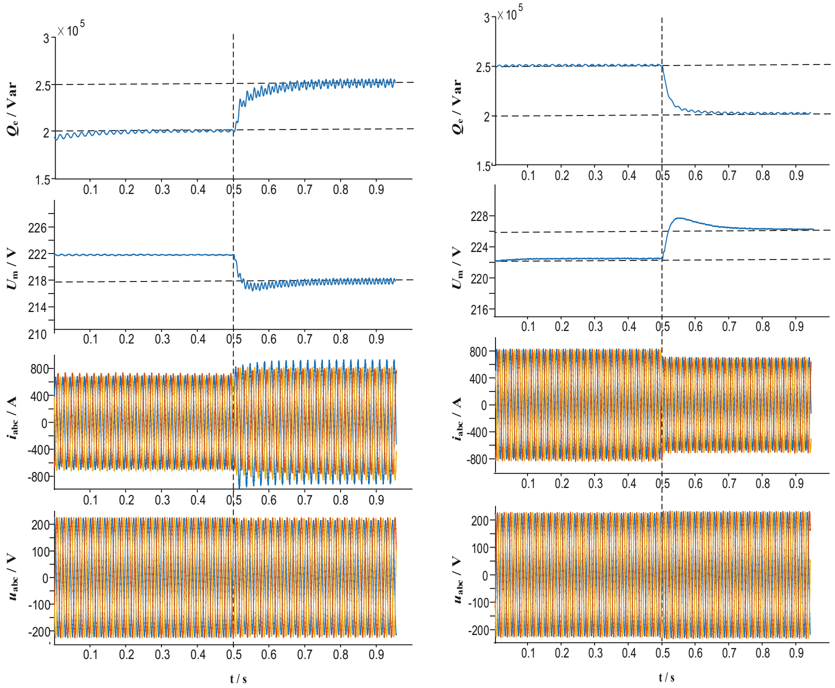

(a) voltage drop (b) voltage rise

Fig. 6. Waveform of GFM-VSC voltage regulation

In the scenario shown in Fig. 6a, prior to 0.2 s, the GFM-VSC was operating in grid-connected mode, and the system voltage was maintained near the rated voltage of 222 V, with a GFM-VSC output of 200 kVar. At 0.2 s, the connection with the grid was disconnected, and the GFM-VSC generator had to independently bear a 200 kW active load. At 0.5 s, a 50 kVar reactive load was added to simulate a decrease in system voltage. In the scenario shown in Fig. 6b, the GFM-VSC output was increased to 250 kVar, and it was disconnected from the grid at 0.2 s. At 0.5 s, the 50 kVar reactive load was disconnected to simulate an increase in system voltage.

As the waveforms show: The proposed control strategy, the GFM-VSC can autonomously respond to changes in grid voltage amplitude and provide reactive power support to the grid, automatically participating in grid primary regulation.

5 Conclusion

This paper proposed a model predictive control for gird-forming voltage source Converter. A cost function concerning both inductor current and power output is constructed. The combination of grid-forming voltage source control and model predictive control through power and current-based MPC has shown good dynamic performance and is beneficial for enhancing the dynamic support capability of grid-forming units. The simulation results verified the effectiveness of the proposed method.

Acknowledgments. This work is supported by National Key Research and Development Program of China (2022YFB2402700).

References

1. Xu, J., Liu, W., Liu, S., et al.: Current state and development trends of power system converter grid-forming control technology. Power Syst. Technol. **46**(09), 3586–3595 (2022)
2. Ding, M., Wang, W., Wang, X., et al.: A review on the effect of large-scale PV generation on power systems. Proc. CSEE **34**(1), 1–14 (2014)
3. Sun, J., Li, M., Zhang, Z., et al.: Renewable energy transmission by HVDC across the continent: system challenges and opportunities. CSEE J. Power Energy Syst. **3**(4), 353–364 (2017)
4. Zhuo, Z., Zhang, N., Xie, X., et al.: Key technologies and developing challenges of power system with high pro-portion of renewable energy. Autom. Electr. Power **45**(09), 171–191 (2021)
5. Wang, Y., Liu, B., Duan, S.: Transient performance comparison of modified VSG controlled grid-tied converter. In: 2019 IEEE Applied Power Electronics Conference and Exposition (APEC), Anaheim, USA, pp. 3300–3303 (2019)
6. Li, D., Zhou, Q., Lin, S., et al.: A self-adaptive inertia and damping combination control of VSG to support frequency stability. IEEE Trans. Energy Conv. **32**(01), 397–398 (2017)
7. Wei, Z., Ji, Q., Wang, W., et al.: Control strategy of grid-forming voltage source converter for asymmetric power grid. Autom. Electr. Power. **45**(10), 124–131 (2021)
8. Wang, J., Zhang, X., Zhu, Q., et al.: Transient stability analysis and control strategy of virtual synchronous generators. Electr. Mach. Control **26**(12), 28–37 (2022)
9. Huang, Q., Wang, W., Deng, X., et al.: Research on control strategy of grid type photovoltaic self-synchronous voltage source. Power Electron. Technol. **57**(04), 87–90 (2023)
10. Hu, J., Zhu, J., Dorrell, D.G.: Model predictive control of inverters for both islanded and grid-connected operations in renewable power generations. IET Renew. Power Gener. **8**(3), 240–248 (2014)
11. Yang, Y., Zhao, F., Ruan, Y., et al.: Model current predictive control for three-phase gridconnected inverters. Trans. China Electrotech. Soc. **26**(6), 153–159.
12. Zhou, Z., Liu, X., Yang, P.: Research on PMSM current predictive control system with double disturbance observer. Power Electron. **53**(10), 18–22 (2019)
13. Zhixian, D., Wensheng, S., Menghua, C.: Predictive current control algorithm for single-phase PWM rectifier model. Chin. J. Electr. Eng. **36**(11), 2996–3004 (2016)
14. Deng, Z., Song, W., Cao, M.: A model predictive current control scheme for single-phase PWM rectifiers. Proc. CSEE **36**(11), 2996–3004 (2016)
15. Dou, X., Xiao, Y., Yuan, X., et al.: Energy management strategy based on improved model predictive control for micgrid. Autom. Electr. Power Syst. **41**(22), 56–65 (2017)

16. Panten, N., Hoffmanm, N., Fuchs, F.W.: Finite control set model predictive current control for grid-connected voltage-source converters with LCL filters: a study based on different state feedbacks. IEEE Trans. Power Electron. **31**(7), 5189–5200 (2016)

Energy Storage Capacity Allocation of Renewable Energy Side Based on SSA-RNN Algorithm

Xingyuan Meng[1], Shaoze Zhou[2], Mengchun Wang[3], and Shuxin Zhang[1](✉)

[1] School of Electrical Engineering, Northeast Electric Power University, Jilin 132012, China
`zhang_shu_xin@126.com`
[2] NARI Group Corporation (State Grid Electric Power Research Institute), Nanjing 211106, China
[3] Electric Power Research Institute, State Grid Heilongjiang Electric Power Co., Ltd., Harbin 150030, China

Abstract. In order to optimize the storage capacity configuration to improve the utilization rate of renewable energy and improve the efficiency and reliability of system operation. This paper looks for effective ways to maximize the use of renewable energy resources. Combined with the requirements of power grid balance and stability, the sum of the cost of wind and solar energy resource waste and energy storage investment is taken as the objective function. Mathematical modeling and sparrow search algorithm optimization recurrent neural network are used to determine a reasonable energy storage capacity allocation scheme. At the same time, the energy storage scheduling strategy is designed, which can not only minimize the battery loss and deterioration, but also ensure that the system can meet the energy demand. The research results can provide guidance for the allocation of renewable energy storage capacity and promote the sustainable development of renewable energy power generation.

Keywords: Energy storage capacity configuration · Renewable energy utilization · Sparrow search algorithm · Recurrent neural network · Energy storage scheduling strategy

1 Introduction

Wind-solar complementary system has become an important energy supply mode. However, due to the instability and intermittency characteristics of wind and solar energy, rational planning of energy storage capacity allocation has become one of the current research hotspots. The energy storage system plays a crucial role in the wind-solar complementary system. It can balance the difference between energy supply and demand, improve the grid-connection capacity of renewable energy, and effectively absorb wind and solar energy [1, 2].

In the wind-solar complementary system, unreasonable battery capacity and scheduling will directly affect the fatigue degree of the battery [3], destroy the balance and

Y. Xue et al. (Eds.): PMF 2023, LNEE 1129, pp. 233–242, 2024.
https://doi.org/10.1007/978-981-99-9251-5_19

stability of the power grid operation, and cause adverse effects on the sustainable development of the renewable energy power generation industry, thus reducing the economic benefits. Therefore, rational capacity configuration of energy storage is the key to ensure its stable output. Literature [4–7] uses typical daily load and renewable energy scenarios, or typical carriers to calculate the allocation scale. In literature [8–10], production simulation method was adopted to obtain the final energy storage configuration scheme.

In this paper, the energy storage capacity configuration is optimized to improve the utilization rate of renewable energy on the renewable energy side and improve the operation efficiency and reliability of the system. This paper looks for effective ways to maximize the use of renewable energy resources. Combined with the requirements of power grid balance and stability, the sum of the cost of wind and solar energy resource waste and energy storage investment is taken as the objective function. Mathematical modeling and sparrow search algorithm optimization recurrent neural network are used to determine a reasonable energy storage capacity allocation scheme. At the same time, an energy storage charging and discharging strategy is designed, which can not only minimize battery loss and deterioration, but also ensure that the system can meet the energy demand. The research results can provide guidance for the allocation of renewable energy storage capacity and promote the sustainable development of renewable energy power generation. Through this study, we expect to provide valuable guidance and decision support for energy storage capacity allocation in wind-solar complementary systems. At the same time, by optimizing the storage capacity configuration, it will further improve the grid-connection capacity and consumption capacity of renewable energy, promote the wide application of clean energy, and make positive contributions to the realization of sustainable energy supply and environmental protection.

2 Renewable Energy Station System Structure

A typical combined wind and photovoltaic energy storage system is shown in Fig. 1

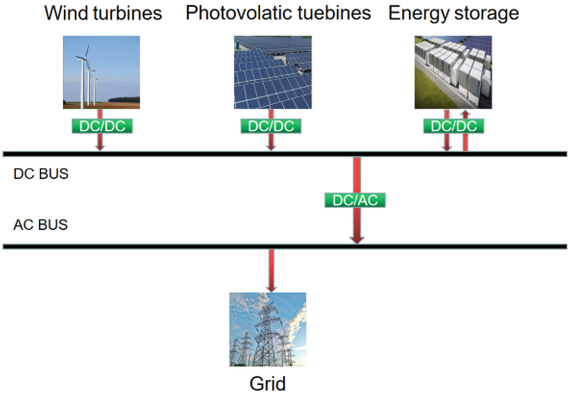

Fig. 1. Schematic diagram of the combined wind and photovoltaic energy storage system

As shown in Fig. 1, the power generation side includes the wind generator set and photovoltaic generator set, which are connected to the DC bus through the DC/DC converter, and then connected to the power grid through the inverter. When there is a surplus of wind or solar power, the energy storage battery can be charged and the excess energy stored. In addition, the energy storage battery can be used as a load to absorb energy from the generating side. This configuration enables efficient use and regulation of energy.

3 Energy Storage Capacity Configuration Model

3.1 Objective Function

In the optimization process, efficiency and economic benefits can be effectively improved by minimizing the profit lost from investment cost and resource waste as the objective function. Then the objective function can be expressed as:

$$C_{\min} = C_{Ps}P_{Sn} + C_{Es}E_{Sn} + \sum_{i=1}^{365}\left(\sum_{t=0}^{24} P_{Ct,i}\right)C_p \tag{1}$$

where C_{Ps} represents the average annual investment cost per unit power of the energy storage system, P_{Sn} represents the rated power of the energy storage system, C_{Es} represents the average annual investment cost per unit capacity of the energy storage system, E_{Sn} represents the rated capacity of the energy storage system, $P_{Ct,i}$ represents the wind and optical power abandonment power at time t on the ith day of the year, and C_p represents the on-grid price of renewable energy.

Wind and solar discard is the actual generated electricity, minus the actual applied electricity, including the electricity provided for load and energy storage. The expression is:

$$P_{Ct} = \mathrm{P}^{r}_{w,t} + \mathrm{P}^{r}_{pv,t} - P_{w,t} - P_{pv,t} \tag{2}$$

where $P_{w,t}$ is the wind power output at time t, and $P_{pv,t}$ is the photovoltaic output at time t. When there is a surplus of wind power output, it includes both the power provided to the power grid and the power charged for the energy storage system. $\mathrm{P}^{r}_{w,t}$ is the total power actually emitted by wind power at time t, and $\mathrm{P}^{r}_{pv,t}$ is the total power actually emitted by photovoltaic at time t.

3.2 Constraints

To ensure secure and stable system running, the following constraints must be met during system running.

(1) The actual power injected into the grid of wind power and photovoltaic power generation shall not exceed its generating capacity:

$$\begin{cases} 0 \le P_{w,t} \le \mathrm{P}^{r}_{w,t} \\ 0 \le P_{pv,t} \le \mathrm{P}^{r}_{pv,t} \end{cases} \tag{3}$$

(2) Energy storage charging and discharging power constraints:

$$\begin{cases} 0 \le P_{stc} \le P_{sn} \\ 0 \le P_{std} \le P_{sn} \end{cases} \tag{4}$$

(3) State constraints on charge and discharge of energy storage:

$$P_{stc} \times P_{std} = 0 \tag{5}$$

It means that the energy storage cannot be charged and discharged at the same time.

(4) In order to limit the charging and discharging depth of energy storage and improve the life of energy storage, the *SOC* state of energy storage is constrained:

$$SOC_{\min} \le SOC_t \le SOC_{\max} \tag{6}$$

where SOC_t is the battery charging state at time t. $SOC_{\max}$ and $SOC_{\min}$ are the upper and lower limits of the battery charging state respectively. *SOC* can be expressed as:

$$SOC_t = SOC_{t-1} + \frac{(\eta_c \times P_{stc} - \eta_d \times P_{std}) \times \Delta t}{E_{sn}} \tag{7}$$

where $SOC_{t\text{-}1}$ is the state of charge at the last moment of t; η_c is the energy storage charging efficiency; η_d is the energy storage discharge efficiency; Δt is the interval time.

(5) Constraints that the initial state and final state of each cycle of the energy storage system are equal:

$$SOC_0 = SOC_{end} \tag{8}$$

(6) Balance between supply and demand of power system:

$$P_{w,t} + P_{pv,t} + P_{std} = L_t \tag{9}$$

where P_{std} is the energy storage discharging power at time t, and L_t is the scheduling instruction. When the energy storage discharging, it is regarded as the power supply.

4 Sparrow Search Algorithm Optimized Recurrent Neural Network

Features of sparrow optimization algorithm: Inspired by sparrow's foraging and defense behavior, it has the characteristics of swarm intelligence, self-adaptability and distributed optimization. It can be applied to solve complex optimization problems, simulate sparrow's foraging and defense strategies, and realize global search and fast convergence.

RNN is a neural network model with cyclic connections, designed for sequential data and time-dependence. It introduces a loop structure to share information between time steps, capturing long-term dependencies. It uses a hidden state to store previous information and combines it with current input to produce the output and new hidden state. This loop structure enables RNN to process sequences of any length through time expansion.

At each time step t, the calculation process of RNN can be described as follows:

Input: Given input sequence X_t (can be a single input or multiple inputs).

Hidden state calculation:

$$h_t = f(W_{hx}X_t + W_{hh}h_{t-1} + b_h) \tag{10}$$

Calculation of output:

$$y_t = g\left(W_{yh}h_t + b_y\right) \tag{11}$$

Among them, the $f(\cdot)$ and $g(\cdot)$ is activation function, W_{hx}, W_{hh}, W_{yh} is weight matrix, b_h and b_y is the bias vector.

Combining Sparrow algorithm with RNN can adopt the following specific process (Fig. 2).

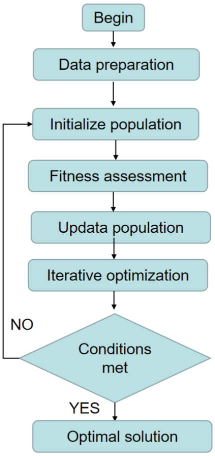

Fig. 2. Algorithm flow chart

Data preparation: Prepare time series data for training the RNN model.

Initialize population: Use SSA to initialize a population where each individual represents a set of parameters for the RNN model.

Fitness assessment: The RNN model is trained using a set of parameters for each individual and its fitness is assessed.

Update population: Based on fitness values, the population is updated using SSA operations such as selection, crossover and mutation.

Iterative optimization: The steps of fitness assessment and population renewal are repeated until a stop condition is reached.

Optimal solution extraction: the individual with the lowest fitness is selected as the optimal solution, and its corresponding RNN model parameters are extracted.

The combination of SSA-RNN (Sparrow Search Algorithm—Recurrent Neural Network) offers the following advantages:

(1) Global search capability: SSA as an optimization algorithm has the ability to perform global search and find optimal solutions. By integrating SSA with RNN, it becomes possible to optimize the parameters and structure of the RNN, thereby enhancing its performance in specific tasks. SSA helps in finding better initial parameters and more suitable network structures, which accelerates the training process and improves the accuracy of the model.

(2) Parameter optimization: RNN models often have a large number of parameters, and optimizing these parameters is a complex and time-consuming task. By using SSA for parameter optimization, it becomes possible to find optimal parameter combinations more quickly, speeding up the training process. The search mechanism of SSA effectively explores the parameter space, avoiding getting trapped in local optima.

(3) Improved convergence: RNN training can encounter challenges such as vanishing or exploding gradients, which can hinder convergence. By employing SSA as an optimization algorithm, these issues can be addressed. SSA adjusts parameters and search strategies appropriately, improving the convergence of the RNN model and enabling it to better adapt to the training data.

(4) Adaptability: SSA exhibits adaptive characteristics, allowing parameter adjustments and optimization strategy updates based on search results and experience. This adaptability enhances optimization efficiency and result quality. In the context of SSA-RNN, this adaptability provides better parameter and structure selection to suit different data and task requirements.

(5) Comprehensive optimization: The combination of SSA and RNN enables comprehensive optimization. SSA handles global search and parameter optimization, while RNN focuses on sequence modeling and prediction tasks. This comprehensive optimization improves the performance and generalization ability of the model, making it more suitable for real-world applications.

In summary, the combination of SSA-RNN offers advantages such as global search capability, parameter optimization, improved convergence, adaptability, and comprehensive optimization. This combined approach enhances the performance and training efficiency of the RNN model, making it suitable for various sequence modeling and prediction tasks.

5 Example Analysis

In this study, the annual actual on-grid power of a wind-solar combined power station is collected, and the energy storage capacity configuration simulation analysis is carried out by using the above algorithm. In order to conduct simulation analysis, we select the 24-h combined wind and photovoltaic output of a typical day, as shown in Fig. 3.

Simulation parameter settings are shown in the Table 1.

Input the actual output of the typical day and the grid dispatching instructions, as well as various parameters, and use the sparrow search algorithm to optimize the calculation method of recurrent neural network to solve the above nonlinear programming problems, and obtain the optimal energy storage rated power P_{Sn} and E_{Sn}. And typical daily wind

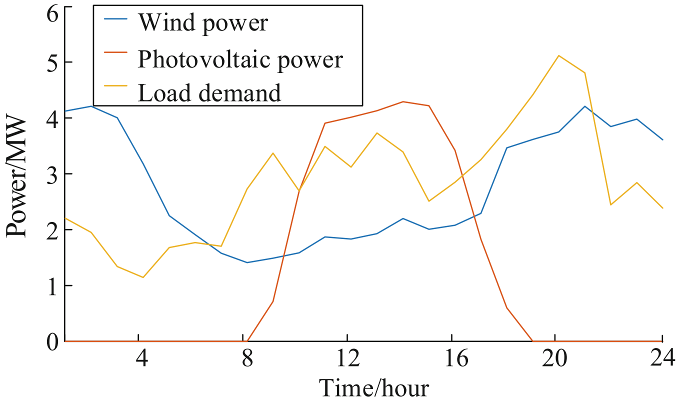

Fig. 3. Output characteristics of wind and photovoltaic power generation in typical days

Table 1. .

Parameters	Value
C_{Ps}	50,000 yuan/MW
C_{Es}	170,000 yuan/W h
C_p	1.08 yuan/kW h
$P_{Sn\_\max}$	5 MW
$E_{Sn\_\max}$	10 MW h
$SOC_{\min}$	0.1
$SOC_{\max}$	0.9
SOC_0	0.5
η_c	0.92
η_d	0.9

output, 24 h energy storage charging and discharging under the optimal energy storage capacity, and wind and solar discard is the smallest.

According to the simulation analysis results, the optimal energy storage capacity configuration solution is 1.5 MW/4.5 MW h. Figure 4 shows the wind and solar power output on a typical day, the dispatching required output, and the 24-h charging and discharging situation under the optimal energy storage capacity.

The initial storage capacity is set at 50% of the rated capacity. In the case of insufficient wind-power generation capacity, the difference between the energy storage system and the scheduling command is compensated by the discharge of the energy storage system, so as to reduce the SOC of the energy storage battery. If it is reduced to $SOC_{\min}$, the energy storage system stops discharging. In the case of surplus wind energy and solar energy output, energy storage is charged to reduce the waste of wind energy and

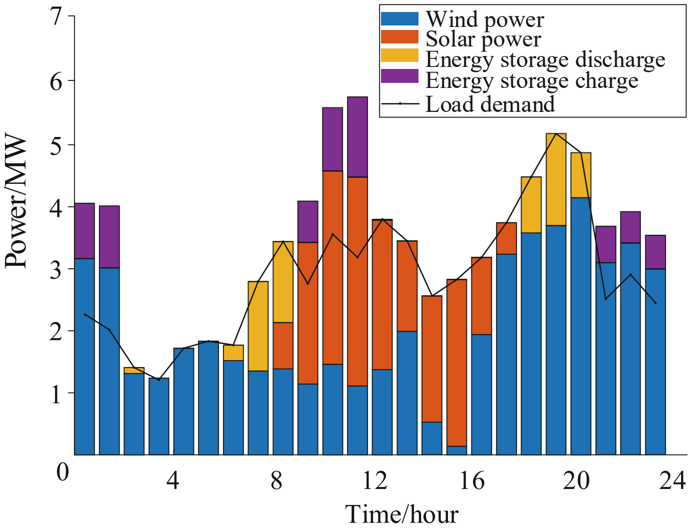

Fig. 4. Optimal energy storage capacity allocation scheme for wind and solar power station

solar energy resources, so that the SOC of energy storage battery keeps increasing. After reaching the $SOC_{\max}$, energy storage will not be charged. When the wind-solar combined output is the same as the dispatching instruction of the power grid, the energy storage neither charges nor discharges.

The amount of wind and solar discarded on a typical day is shown in Fig. 5 (Fig. 6).

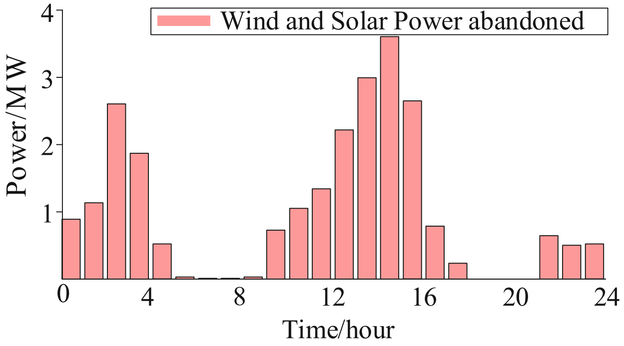

Fig. 5. Wind and solar abandonment in a typical day

The above is a comparison chart of the amount of abandoned wind and light when there is no energy storage, most of the time the amount of abandoned wind and solar without energy storage is higher than when there is energy storage, but sometimes it is may higher or equal in order to make the SOC of the battery meet the constraints. After energy storage is configured, the amount of wind and solar discarded is greatly reduced compared with that without energy storage, and it plays the role of peak cutting and

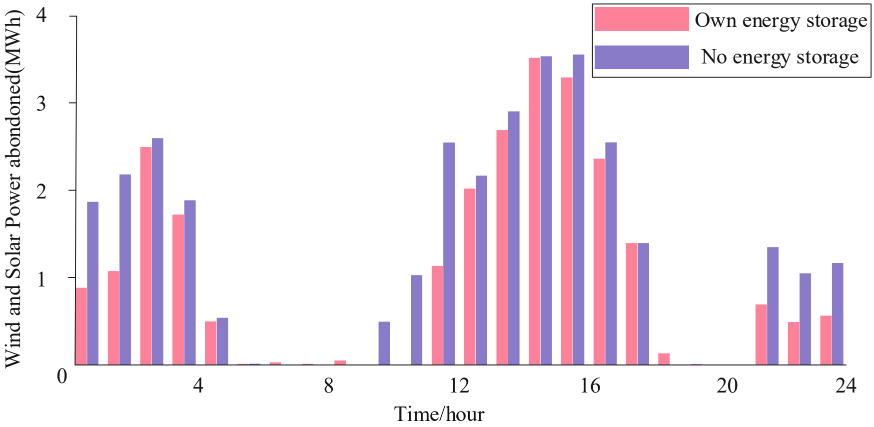

Fig. 6. Comparison of abandoned wind and solar with and without energy storage

valley filling. It can send about 2.29 million kW h more electricity to the grid every year. If the feed-in tariff of 1.08 yuan/kW h is calculated, the net profit of 1.63 million yuan a year is still obtained.

6 Conclusion

The main conclusions regarding maximizing the adjustment capacity and benefits of energy storage in large-scale energy storage of renewable energy power stations are as follows.

The single-objective energy storage capacity configuration model considers the economy of wind and solar abandonment and total annual investment in energy storage. Coordinating renewable energy and energy storage enables peak shaving, valley filling, and improved support to the power grid. The optimal energy storage capacity selection scheme effectively reduces wind and solar discard compared to other schemes. The study confirms the effectiveness of the method and its potential application in the economic field. Sparrow search algorithm optimization recurrent neural network is used to calculate the optimal energy storage configuration scheme, offering advantages such as efficient optimization, consideration of timing relationships, generalization ability, and improved energy utilization efficiency.

Acknowledgments. This work is supported by National Key Research and Development Program of China (2022YFB2402700): “Key technologies for stable operation and direct current transmission of large-scale new energy power generation bases without conventional power supply support”.

References

1. Jilei, Y., Bin, L., Zhang, Y., et al.: Energy storage requirements and configuration analysis based on typical characteristics of global energy internet[J]. Power Gener. Technol. **42**(1), 20–30 (2021)

2. Baomin, F., Hongzhi, L., Xiangpeng, K., et al.: Research on long-term distributed energy storage configuration with high proportion of photovoltaic output[J]. Power Syst. Prot. Control **49**(2), 121–129 (2021)
3. Liang Jian, Y., Gaocai, Y., et al.: Application of battery energy storage technology in peak regulating optimization of wind power system[J]. Power Inf. Commun. Technol. **18**(10), 67–73 (2020)
4. Qiu Ting, X., Bolun, W.Y., et al.: Stochastic multistage coplanning of transmission expansion and energy storage[J]. IEEE Trans. Power Syst. **32**(1), 643–651 (2017)
5. Jiuyi, G., Yang, L., Yanlin, G., et al.: Different typical user side energy storage configuration evaluation and operation optimization model[J]. Power Grid Technol. **44**(11), 4245–4253 (2020)
6. Jianlin, L., Binqi, G., Meng, N., et al.: Optimal allocation strategy of energy storage capacity in wind-wind storage system[J]. Trans. China Electrotechnical Soc. **33**(6), 1189–1196 (2018)
7. Wenxia, L., Shuting, Z., Xueqian, G., et al.: Optimal allocation of modular energy storage in distribution network considering comprehensive utility and subjective cognition[J]. Power Grid Technol. **46**(6), 2074–2083 (2022)
8. Wu Weiping, H., Zechun, S.Y.: Optimization and allocation of wind farm energy storage based on stochastic programming and sequential monte carlo simulation[J]. Power Grid Technol. **42**(4), 1055–1062 (2018)
9. Dong, Y., Gaofeng, F., Cun, D., et al.: Analysis and calculation method of energy storage in power system configuration[J]. China Electr. Power **55**(1), 26–36 (2022)
10. Xuebin, L., Hao, Z.: Energy storage configuration method for wind farm based on wiener stochastic process[J]. Power Grid Technol. **46**(9), 3437–3446 (2022)
11. Yang Xiaolei, X., Jianyuan, T.H., et al.: Research on optimal configuration of energy storage system based on improved whale algorithm[J]. Zhejiang Electr. Power **40**(3), 113–120 (2021)
12. Shixiao, X., Li, Y., Lina, L., et al.: A chance constrained programming based optimal configuration method of hybrid energy storage system[J]. Power Syst. Technol. **36**(5), 79–84 (2012)

Distributed Energy Storage Sharing Strategy for Microgrid: An Asymmetric Nash Bargain-Based Integration Approach

Xuan Kong[1], Lei Ma[1], Xiaozhu Li[2], and Laijun Chen[1,2](✉)

[1] New Energy (Photovoltaic) Industry Research Center, Qinghai University, Xining 810016, China
chenlaijun@tsinghua.edu.cn
[2] Department of Electrical Engineering and Applied Electronics Technology, Tsinghua University, Beijing 100084, China

Abstract. Energy storage is an effective tool in microgrids to absorb new energy output and smooth its fluctuations. Multiple users within a microgrid have their own distributed energy storage (DES). In this paper, we propose an energy storage sharing (ESS) model aggregated by a common platform within a microgrid to improve user benefits and energy storage utilization. The electricity cost of users and the benefits from sharing the owned energy storage are fully considered in the model, which effectively promotes the consumption of new energy in the microgrid and maximizes the benefit of users. The proposed operational strategy is divided into two phases: energy dispatch and transaction payment. The new energy consumption rate is effectively improved based on the energy dispatch in the shared mode, and the problem of profit distribution among multiple users is fairly addressed by a transaction payment method based on Asymmetric Nash Bargaining. The model is solved by the alternating direction multiplier method, which can effectively protect the privacy of each subject. The results shows that the benefits of the three users increased by 8.37, 0.1076 and 0.3375 times respectively through the proposed method. Users who share more power and energy storage have greater benefits, which proves that the fairness of the distribution is improved by the proposed distribution method. It is conducive to increasing the enthusiasm of users to participate in sharing.

Keywords: Microgrid · Energy storage sharing · Asymmetric Nash bargaining · Alternate direction multiplier method · Profit distribution

1 Introduction

Energy storage technologies play an important role in the absorption of new energy sources, the stabilization of power supply and the implementation of power system flexibility. It is a key technology to build a new power system based on new energy and achieve the goal of "Carbon Peaking and Carbon Neutrality" [1]. The introduction of energy storage at the microgrid side can effectively improve the power quality in the

Y. Xue et al. (Eds.): PMF 2023, LNEE 1129, pp. 243–258, 2024.
https://doi.org/10.1007/978-981-99-9251-5_20

microgrid, ensure the power balance and meet the flexible power demand of its load [2]. However, the overall investment cost of energy storage is relatively high and its utilization rate is low due to technical constraints [1–5]. Some experts and scholars have introduced the concept of sharing economy into the energy storage market and put forward the concept of "energy storage sharing".

In recent years, there has been a lot of research by scholars on operational mechanism and modes of ESS. In the generation side, the stability of the coalition is demonstrated in a ESS mechanism based on a cooperative game new energy field station [3]. The introduction of shared energy storage was found to reduce the operating costs of the industrial user base by analyzing the investment and return issues of energy storage plants [4]. The use of blockchain technology to construct non-cooperative game models not only enhances the security of energy storage sharing transactions, but also guarantees the maximization of the interest of the participating transaction nodes [5]. On the microgrid side, shared energy storage is equipped in the community [6]. The operation strategy for the shared energy storage is set to static allocation based on the data of the previous day. The impact of using shared energy storage in a residential environment on the cost of the community is also evaluated. In [7], the authors consider the demand response in the park and construct a bi-level optimal dispatch model for grid-connected microgrids, integrating the energy optimization factors at the grid level. Scholars have focused on the participation of shared energy storage in the energy dispatch of the system and the implementation of joint optimal dispatch among multiple microgrids [8]. In order to better manage multiple microgrids, the concept of cloud energy storage (CES) was proposed in literature [9]. The literature [10] analyzes their decisions in detail from the perspectives of CES and consumers. The example analysis shows that CES can benefit both investors and consumers.

Most of the existing studies focus on models where agents manage energy storage within microgrids in a centralized manner. Agents are responsible for purchasing power from the larger grid and then retailing it within the microgrid for a portion of the profit [7, 8]. Operators can also participate in auxiliary market peak regulation to obtain part of the benefits [11]. This model makes it difficult to take into account the revenue or cost of electricity for individual customers. It does not focus on the case of customers building their own energy storage. Moreover, the operators typically maximize their own revenue, thus increasing the payment burden of customers in the microgrid.

The main methods to redistribute the benefits of multiagent participation in cooperative games are VCG (Vickery-Clarke-Groves, VCG), Shapley Value algorithm, Nucleolus method, etc. [12]. The VCG mechanism is applicable to relevant scenarios involving policy incentives, where it is difficult to achieve market clearing. Therefore, it has not been applied to multiagent cooperation and shared trading models in microgrids. The Shapley Value algorithm is based on the marginal contribution of users to the benefit allocation. However, the calculation complexity of this method is large, and the maximization of global benefits cannot be guaranteed [13]. The satisfaction of the participating agents and the stability of the alliance are concerned by the Nucleolus method, but the complexity of the method grows geometrically with the number of participants [12]. The Nash bargaining game maximizes the coalition payoff and then bargains among the participating agents to allocate the cooperation payoff. This maximizes the coalition gain and remains relatively easy to solve when there are more participating agents [11]. Asymmetric Nash Bargaining can be better applied to the situation where each participant in the alliance has different contribution degrees because it overcomes the disadvantage that standard Nash bargaining cannot completely and fairly distribute the interests of participants [14].

According to the above analysis, this paper proposes an operational model based on a public platform to aggregate DES of users. The method can better aggregate DES within microgrids, reduce user costs and improve energy storage utilization. The specific technical contributions of this paper are as follows:

(1) A large number of DES within the microgrid are integrated by the proposed operational model. There are no aggregators in the decentralized platform model for benefit sharing. This mode uses power sharing and energy storage sharing for energy scheduling, which reduces the electric energy interaction between users and the grid, so it can increase the consumption of new energy in the microgrid and increase the revenue of the users.
(2) We use Asymmetric Nash Bargaining Game to distribute the benefits, which can address the unfairness arising from different degrees of contribution in the distribution of cooperative benefits.
(3) The model uses the alternating direction method of multiplier (ADMM) for distributed solving [12]. Privacy and security of users are strongly guaranteed as only a small amount of information needs to be uploaded for the platform to operate optimally. At the same time, the distributed solution method can also save a lot of computing resources, which is conducive to solving the game problem of a large number of participants.

2 Sharing Operation Mechanism of DES in Microgrid

2.1 Microgrid Energy Trading Model

Currently, microgrids operate in two main modes: a centralized purchasing and marketing model, and a self-produced and self-use model. In the first mode, agents (such as power grid enterprises or third-party operating companies) will purchase all the power generated by Distributed Generation (DG). In the second mode, the generation of DG is prioritized for prosumers, the excess power is purchased by the agent company, and the insufficient power is purchased from the agent.

Prosumers equipped with energy storage in microgrids have small PV or wind generation units. They are given priority to use the new energy to generate electricity, and excess power is sold to the grid. Some prosumers also have their own storage that can store excess new energy output. In practice, energy storage is often incompatible with the generation and consumption of electricity by prosumers due to cost and equipment implications.

Therefore, we propose a common platform aggregation model. This model aggregates the DES in the microgrid to improve the utilization of energy storage and reduce the cost of electricity for customers compared to the traditional trading model. There is no third party investment here and the various users in the microgrid entrust their own energy storage to the platform for management and scheduling, through which the energy transactions are carried out. Finally, the platform optimizes and generates the final electricity bill of the user.

Given the spatio-temporal coupling of multiagent participation and energy storage in the transaction, this paper splits the problem into two phases: power scheduling and revenue distribution. Firstly, the platform determines the electricity consumption decision of each user and the charging and discharging strategy of the aggregated energy storage based on the user's new energy generation data, load level and current aggregated energy storage SOC, spot price. In the second stage, the revenue distribution is based on an Asymmetric Nash Bargaining Game to determine the electricity bill for each subject.

2.2 Energy Flow in Microgrid

Figure 1 shows the energy and information flow in the microgrid under the proposed model.

First, the platform prioritizes the exchange of excess electricity among users through the generation and load information in the microgrid. The owner of the energy storage will no longer control the charging and discharging behavior of the energy storage itself, but will be managed by the platform in a unified manner. As a customer in the microgrid, it is sufficient to use electricity normally. The final electricity bill is affected by actions such as customers' excess power being fed back into the grid or current excess power consumption.

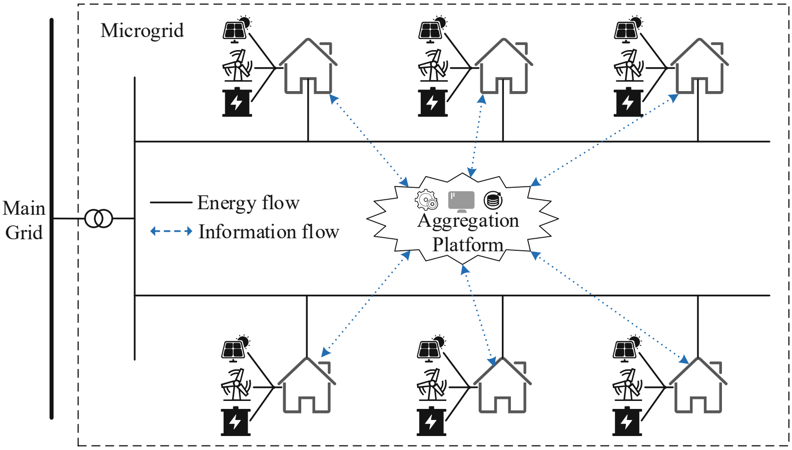

Fig. 1. Schematic diagram of the operation mode of DES based on a common platform aggregating users in a microgrid.

Second, the charging and discharging behavior of each energy storage is determined based on the state and net power of each energy storage in the microgrid. Similarly, the charging and discharging behavior of energy storage will bring benefits to the users, and the revenue ratio will eventually be optimized and uniformly settled by the platform.

Finally, the microgrid needs to interact with the external grid to ensure electrical power balance within the microgrid. The cost will also be shared by users.

2.3 System Modeling

The platform will make separate decisions on energy storage and electricity consumption. All the energy storage of the users are aggregated by the platform and they are unified as an energy storage pool. At this point, the user side only considers its electricity consumption strategy, where prosumers prioritize their own new energy output and balance their own loads. Finally, the revenue or payments associated with the sharing process between the user and the storage are finally settled in a unified manner. Thus, suppose that the power side user set I in the microgrid has i users and the energy storage set J contains j energy storages. For the sake of a uniform description, i and j correspond to one and the same.

Customer Side Model

According to the proposed model, the cost of user i is shown in Eq. (1). The electricity cost of the user i during the time period t mainly includes the electric energy interaction cost of the main grid $C_{i,gd}$ and the payment cost of participating in sharing π_i, after the energy dispatching of the platform.

$$U_i = C_{i,gd} + \pi_i \tag{1}$$

$$C_{i,gd} = \sum_{t=1}^{T} \left(\alpha_t^{mgb} P_{t,i}^{mgb} - \alpha_t^{mgs} P_{t,i}^{mgs} \right) \tag{2}$$

where, α_t^{mgb}, α_t^{mgs} refers to the electricity purchasing price from the microgrid and the electricity selling price to the microgrid in time period t respectively. $P_{t,i}^{mgb}$, $P_{t,i}^{mgs}$ is the electric power that user i buys or sells from the main network during time t.

The shared power $P_{i,t}^{u}$ and the interaction powers $P_{i,t}^{mgb}$ and $P_{i,t}^{mgs}$ with the primary network are the decision variables of user i. Equation (3) represents the power balance constraint of user i. $P_{i,t}^{u}$ represents power compensation sharing.

$$P_{i,t}^{G} - P_{i,t}^{L} + P_{i,t}^{mgb} - P_{i,t}^{mgs} + P_{i,t}^{u} = 0 \tag{3}$$

In fact, if $P_{i,t}^{u} > 0$, user i absorbs electricity from the microgrid; if $P_{i,t}^{u} < 0$, user i releases electricity to the microgrid.

Energy Storage Side Model

The objective function of energy storage j aggregated by platform is shown in Eq. (4):

$$G_{j,es} = C_{j,es} - w_j \tag{4}$$

$$C_{j,es} = \sum_{t=1}^{T} \mu \left(P_{t,j}^{\mathrm{ES}C} + P_{t,j}^{\mathrm{ES}D} \right) \tag{5}$$

where, w_j is the income of energy storage j; The loss during the use of energy storage is defined as $C_{j,es}$. Denote the depreciation cost per unit capacity of energy storage by μ. $P_{j,t}^{ESC}$, $P_{j,t}^{ESD}$ refers to the charging and discharging power of stored j in time period t respectively. Energy storage sharing is represented by $P_{j,t}^{es}$. Then there is:

$$P_{j,t}^{es} = P_{j,t}^{ESD} - P_{j,t}^{ESC} \tag{6}$$

If $P_{i,t}^{es} > 0$, energy storage j releases electricity to microgrid. The opposite means that energy storage j absorbs electricity from the microgrid.

Other Model Constraints

Power Balance Constraint

Equation (7) implies that the charge and discharge variability of the energy storage are balanced simultaneously.

$$\sum_{i=1}^{I} P_{i,t}^{u} - \sum_{j=1}^{J} P_{j,t}^{es} = 0 \tag{7}$$

Charge and Discharge Constraints of DES

The energy storage charging and discharging power must be within the maximum value are indicated by Eq. (8) and Eq. (9).

$$0 \le P_{j,t}^{\mathrm{ESC}} \le P_{es}^{\max} \tag{8}$$

$$0 \le P_{j,t}^{\mathrm{ESD}} \le P_{es}^{\max} \tag{9}$$

Energy Storage Operation Constraint

Energy storage system state of charge (SOC) values need to be between the maximum and minimum charge levels to prevent damage to the energy storage system from overcharging and discharging:

$$\mathrm{SOC}_{\min} E_j^{ES\max} \le E_{j,t}^{\mathrm{ES}} \le \mathrm{SOC}_{\max} E_j^{ES\max} \tag{10}$$

where, $E_j^{es\max}$ is the energy capacity of j. $SOC_{\min}$ and $SOC_{\max}$ are the minimum and maximum SOC of DES.

The capacity state E_t^{ES} of the energy storage j is shown as Eq. (11), where the energy storage losses during charging and discharging is taken into account. Set η_j^c and η_j^d to be the charging and discharging efficiency, respectively.

$$E_{j,t}^{\mathrm{ES}} = E_{j,t-1}^{\mathrm{ES}} + \left(\eta_j^c P_{j,t}^{\mathrm{ESC}} - \frac{1}{\eta_j^d} P_{j,t}^{\mathrm{ESD}} \right) \Delta t \tag{11}$$

3 Operational Model and Solution Process

3.1 Optimal Scheduling of DES

We have defined the mathematical model of the user as well as the energy storage. After platform aggregation, the global economic optimization target for electrical energy is defined as the sum of the costs of all customers on the electricity side and the energy storage side. This is for the purpose of prioritizing the consumption of new energy output in the microgrid and maximizing the global benefits in the microgrid.

$$\min \sum_{i=1}^{I} U_i + \sum_{j=1}^{J} G_{j,es} \tag{12}$$

$$\min \sum_{i=1}^{I} \left(C_{i,gd} + \pi_{\mathrm{i}}\right) + \sum_{j=1}^{J} \left(C_{j,es} - w_j\right) \tag{13}$$

For transactions within the entire microgrid, there is no third-party charge, so there is

$$\sum_{i=1}^{I} \pi_i - \sum_{j=1}^{J} w_j = 0 \tag{14}$$

Now the objective function can be transformed into

$$\min \sum_{i=1}^{I} C_{i,gd} + \sum_{j=1}^{J} C_{j,es} \tag{15}$$

In this case, the transaction payments and the flow of power between each player are decoupled, which simplifies the problem. The problem is formulated as an optimal scheduling problem for energy and energy storage among the participants of a microgrid. The optimal power dispatch strategies can be obtained by optimization, namely, the optimal power sharing P_i^{u*}; the optimal sale of electricity $P_{i,t}^{mgs*}$; the optimal power purchase P_i^{mgb*} and the optimal ESS decision P_j^{es*}.

3.2 Benefit Allocation Based on Asymmetric Nash Bargaining

The best ESS and power sharing scheduling strategy is optimized through the microgrid global energy economics goal. Prosumers will gain from the global optimization. The distribution of benefits after sharing cooperation is discussed below.

The Nash Bargaining model is widely used for cost or benefit allocation in cooperative game scenarios. In the standard Nash bargaining model, users are usually on equal footing and each agent ends up with the same amount of revenue, so it is difficult to take into account the difference in the contribution of each agent in cooperation. Therefore, we determine the bargaining power of users and their energy stores in a Nash bargaining game based on their contribution in sharing. Asymmetric bargaining is performed by calculating the bargaining position of the participants.

This paper uses energy sharing nonlinear mapping method, in order to ensure the fairness of power generation and consumption. It is generally considered that generation sharing bargaining power should be greater than the bargaining power of power consumption. The nonlinear mapping is performed using an exponential function with a natural constant e as the basis, for both electric energy sharing and energy storage sharing of users. The greater the amount of energy sharing, the stronger the bargaining power. The contribution degree is calculated as shown in Eq. (16). r_i defines the ability of user i to contribute to the entire sharing process.

$$r_i = \gamma_{\mathrm{p}}\left(e^{\beta_i \mathrm{C}} - e^{-\beta_i \mathrm{D}}\right) + \gamma_{es} e^{\beta_j \mathrm{ES}} \tag{16}$$

where, β_i^{C}, β_i^{D}, β_j^{ES} respectively represents the proportion of energy released and absorbed by user i to the microgrid, and the proportion between the shared capacity of energy storage j and the total shared capacity. γ_{p} and γ_{es} represent the weights of shared electric energy and shared energy storage respectively. Different weights directly affect the size of bargaining power. The determination of weight values should consider the relevant operating and investment costs of shared electricity and shared energy storage, to ensure the fairness of income distribution as much as possible. To simplify the model, we generally believe that the weight coefficient of shared energy storage is relatively large, which will motivate users to participate in the sharing of their energy storage.

$$\beta_i^{\mathrm{C}} = \frac{\sum_{t=1}^{T} P_{i,t}^{\mathrm{PC}}}{\sum_{t=1}^{T} \sum_{i}^{I} P_{i,t}^{\mathrm{PC}}} \tag{17}$$

$$\beta_i^{\mathrm{D}} = \frac{\sum_{t=1}^{T} P_{i,t}^{\mathrm{PD}}}{\sum_{t=1}^{T} \sum_{i}^{I} P_{i,t}^{\mathrm{PD}}} \tag{18}$$

$$\beta_j^{\mathrm{ES}} = \frac{\sum_{t=1}^{T} \left(P_{j,t}^{ESC} + P_{j,t}^{ESD}\right)}{\sum_{t=1}^{T} \sum_{j}^{J} \left(P_{j,t}^{ESC} + P_{j,t}^{ESD}\right)} \tag{19}$$

$$\gamma_{\mathrm{p}} + \gamma_{\mathrm{es}} = 1 \tag{20}$$

In the above formula, i and j are equal. $P_{i,t}^{\mathrm{PC}}$ and $P_{i,t}^{\mathrm{PD}}$ respectively represents sharing power to microgrid and using shared power from microgrid. This contribution represents that any sharing of user i (including electricity and energy storage) will improve the bargaining power. And the bargaining power of releasing electricity is stronger than that of absorbing it. The bargaining power of shared energy storage can be tuned by setting reasonable weights to better improve the incentives for users to participate in sharing.

The Asymmetric Nash bargaining model is constructed as shown in Eq. (21).

$$\begin{cases} \max \prod_{i=1}^{n} \left\{ C_i^0 - \left(U_i + G_{j,es} \right) \right\}^{r_i} \\ \text{s.t.}(7),\ (14) \end{cases} \tag{21}$$

$$C_i^0 - \left(U_i + G_{j,es} \right) > 0 \tag{22}$$

The cost of user i before participating in sharing is defined as C_i^0. Each user can obtain more revenue by participating in sharing, which is guaranteed by formula (22). Logarithm of the objective function of Eq. (21) is obtained.

$$\min \prod_{i=1}^{n} -r_i \ln \left\{ C_i^0 - \left(U_i + G_{j,es} \right) \right\} \tag{23}$$

This transformation makes the problem easier to solve.

3.3 Solving Algorithm

The mathematical models in Sect. 3.1 and Sect. 3.2 are solved by the ADMM algorithm in this paper. The problem solving in Sect. 3.1 is presented here as an example.

First, auxiliary variables Q^u and Q^{es} should be introduced to decouple the problem constraints, which will make the problem more amenable to the ADMM algorithm.

$$P_{i,t}^u - Q_{i,t}^u = 0 \tag{24}$$

$$P_{j,t}^{es} - Q_{j,t}^{es} = 0 \tag{25}$$

$$\sum_{i=1}^{I} Q_{i,t}^u - \sum_{j=1}^{J} Q_{j,t}^{es} = 0 \tag{26}$$

According to the ADMM algorithm, the augmented Lagrangian for this problem can be written as follows:

$$\begin{aligned} L = & \sum_{i=1}^{I} C_{i,gd} + \sum_{j=1}^{J} C_{j,es} \\ & + \frac{\mu_u}{2} \sum_{i=1}^{I} \sum_{t=1}^{T} \left(P_{i,t}^u - Q_{i,t}^u + \frac{\delta_{i,t}^u}{\mu_u} \right)^2 + \frac{\mu_{es}}{2} \sum_{j=1}^{J} \sum_{t=1}^{T} \left(P_{j,t}^{es} - Q_{j,t}^{es} + \frac{\delta_{j,t}^{es}}{\mu_{es}} \right)^2 \end{aligned} \tag{27}$$

where μ_u, μ_{es} is the penalty parameter; $\delta_{i,t}^u$, $\delta_{j,t}^{es}$ is the Lagrange multiplier.

Other operations are as follows:

(1) User side strategy updating

$$\min \ C_{i,gd} + \frac{\mu_u}{2}\sum_{t=1}^{T}\left(P_{i,t}^{u} - Q_{i,t}^{u}(k) + \frac{\delta_{i,t}^{u}(k)}{\mu_u}\right)^2 \tag{28}$$

(2) Energy storage side strategy updating

$$\min \ C_{j,es} + \frac{\mu_{es}}{2}\sum_{t=1}^{T}\left(P_{j,t}^{es} - Q_{j,t}^{es}(k) + \frac{\delta_{j,t}^{es}(k)}{\mu_{es}}\right)^2 \tag{29}$$

(3) Auxiliary variable updating

$$\begin{aligned}\min\frac{\mu_u}{2}\sum_{i=1}^{I}\sum_{t=1}^{T}\left(P_{i,t}^{u}(k+1) - Q_{i,t}^{u}(k+1) + \frac{\delta_{i,t}^{u}(k)}{\mu_u}\right)^2 \\ + \frac{\mu_{es}}{2}\sum_{j=1}^{J}\sum_{t=1}^{T}\left(P_{j,t}^{es}(k+1) - Q_{j,t}^{es}(k+1) + \frac{\delta_{j,t}^{es}(k)}{\mu_{es}}\right)^2\end{aligned} \tag{30}$$

(4) Lagrange multiplier updating

$$\delta_{i,t}^{u}(k+1) = \delta_{i,t}^{u}(k) + \mu_u\big(P_{i,t}^{u}(k+1) - Q_{i,t}^{u}(k+1)\big) \tag{31}$$

$$\delta_{j,t}^{es}(k+1) = \delta_{j,t}^{es}(k) + \mu_{es}\Big(P_{j,t}^{es}(k+1) - Q_{j,t}^{es}(k+1)\Big) \tag{32}$$

(5) Calculate the original residual and dual residual

$$\Psi_u = \sqrt{\sum_{i=1}^{I}\sum_{t=1}^{T}\left(P_{i,t}^{u}(k_1) - Q_{i,t}^{u}(k)\right)^2} \tag{33}$$

$$\Psi_{es} = \sqrt{\sum_{j=1}^{J}\sum_{t=1}^{T}\left(P_{j,t}^{es}(k_2) - Q_{j,t}^{es}(k)\right)^2} \tag{34}$$

$$\phi_u = \sqrt{\sum_{i=1}^{I}\sum_{t=1}^{T}\left(P_{i,t}^{u}(k_1) - P_{i,t}^{u}(k_1 - 1)\right)^2} \tag{35}$$

$$\phi_{es} = \sqrt{\sum_{j=1}^{J}\sum_{t=1}^{T}\left(P_{j,t}^{es}(k_2) - P_{j,t}^{es}(k_2 - 1)\right)^2} \tag{36}$$

(6) Penalty parameters updating

$$\mu_u = \begin{cases} \varepsilon \times \mu_u, if\ \phi_u > \varepsilon \Psi_u \\ \dfrac{1}{\varepsilon} \times \mu_u, if\ \phi_u < \varepsilon \Psi_u \\ \mu_u, otherwise \end{cases} \tag{37}$$

$$\mu_{es} = \begin{cases} \varepsilon \times \mu_{es}, if\ \phi_{es} > \varepsilon \Psi_{es} \\ \dfrac{1}{\varepsilon} \times \mu_{es}, if\ \phi_{es} < \varepsilon \Psi_{es} \\ \mu_{es}, otherwise \end{cases} \tag{38}$$

In ADMM, it is generally agreed that the convergence rate of the Lagrange multiplier is slow when the penalty parameter is small, and the convergence rate of the decision variable is slow when the penalty parameter is large. Therefore, the convergence rate of multiplier and decision variable can be accelerated by adjusting the penalty parameter adaptively.

The decision quantity of the user and the decision quantity of the energy storage are coupled to the auxiliary variables. Clearly the primal residual convergence rates of the two coupled constraints will be different. Therefore, in each iteration, we can compare the original remnants of the two coupling constraints and selectively update the decision, which can avoid the convergence of one coupling constraint too fast and the convergence of the other coupling constraint too slow. The above method can save computing resources [11].

4 Case Study

4.1 Basic Data

In this paper, the typical daily load data of three industrial users in a microgrid are selected [10]. Users 1 and 2 are two different types of discontinuous production users with varying levels of load fluctuations. User 3 is a continuous production user with large power consumption and small load fluctuations 24 h a day. The load curves of each user and the output curves of the distribution PV power generation and wind power generation equipped by users are shown in Fig. 2. User 1 is equipped with both photovoltaic and wind generation devices, user 2 only has PV generation devices, and user 3 only has wind generation devices.

The energy storage is equipped in all three users, and the power and capacity are shown in Table 1.

In operation, the energy storage SOC is set to be between 0.1 and 0.9, and the charge and discharge loss is 0.01/CNY kwh^{-1}. The purchase and sale price of electricity are shown as Table 2.

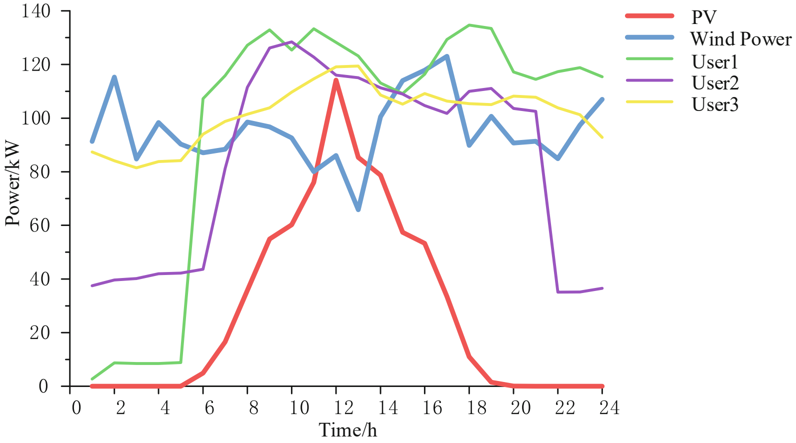

Fig. 2. The generation and load curves of users.

Table 1. User energy storage configuration

Number	Capacity/(kW h)	Power/kW
1	39	13
2	36	12
3	6	2

Table 2. The purchase and sale price of electricity during different period of time.

Time period	Electricity purchase price/CNY	Electricity sale price/CNY
08:00—12:00 17:00—21:00	1.1	0.44
12:00—17:00 21:00—24:00	0.66	0.26
00:00—8:00	0.32	0.13

4.2 Result Analysis

Energy Dispatch Results

The ADMM algorithm is used to find a distributed solution to the problem. The results of power scheduling are shown in Figs. 3 and 4.

As seen in Fig. 3, user 1 provides shared electric energy to the micro grid in more periods, because photovoltaic and wind power generation devices are both equipped, and the installed capacity of new energy is large, which can meet its load demand in more periods. The photovoltaic power generation equipped by user 2 fluctuates greatly. During 14:00–16:00 when PV power is sufficient and 1:00–5:00 when the load is small, the shared power from other customers can meet their own demand for electricity. Then, at other times, it not only needs to obtain shared energy, but also needs to purchase power from the microgrid to meet its own load balance.

The curves in Fig. 4 show the charging and discharging strategies of ES 1, ES 2 and ES 3 when they are shared. A negative value of the power indicates that the current energy storage battery is charging, and vice versa indicates that the energy storage is being discharged. The SOC states of three energy storage systems are shown in the bar chart. Based on the energy mutual economy pattern proposed in this model, the charging and discharging operations of all the energy storage systems are of the same type, so that the SOC of the storage systems change analogously. During one working day, the three energy stores achieve two charge and discharge behaviors.

Before sharing, all three users will sell their excess power online. Users reduce their interaction with the grid and thus increase the consumption rate of new energy in the microgrid through power sharing. At the same time, it offers conditions for users to reduce their own costs.

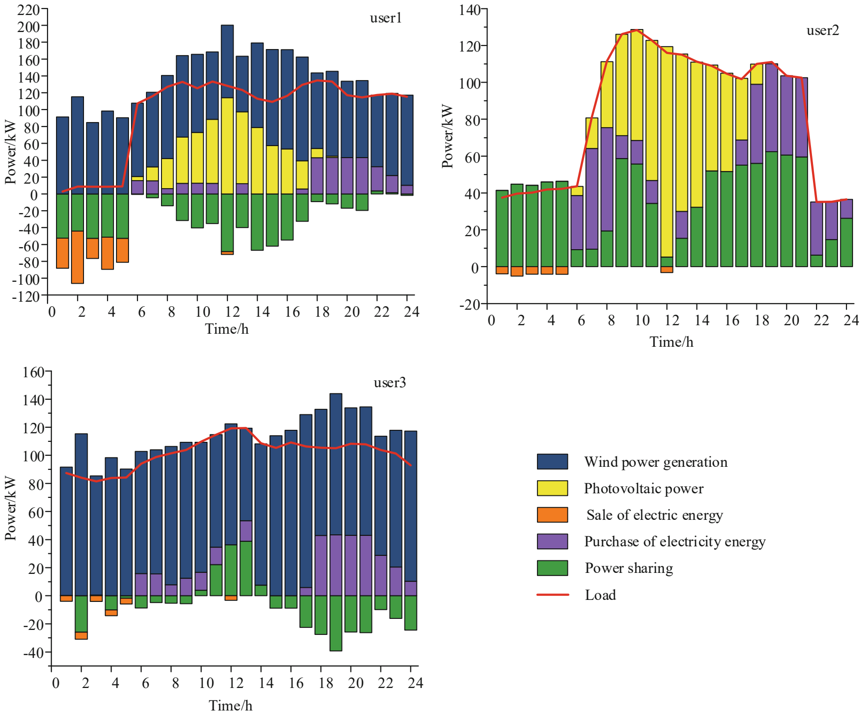

Fig. 3. The results of power balance and power sharing in user side.

Co-operation Benefit Distribution Results

The bargaining power of user 1, user 2 and user 3 is calculated to be 1.4604, 1.2703 and 0.8737, respectively, according to the power scheduling results in the previous section (when γ_p is set at 0.3, and γ_{es} is set at 0.7). The cost operation of the three users before and

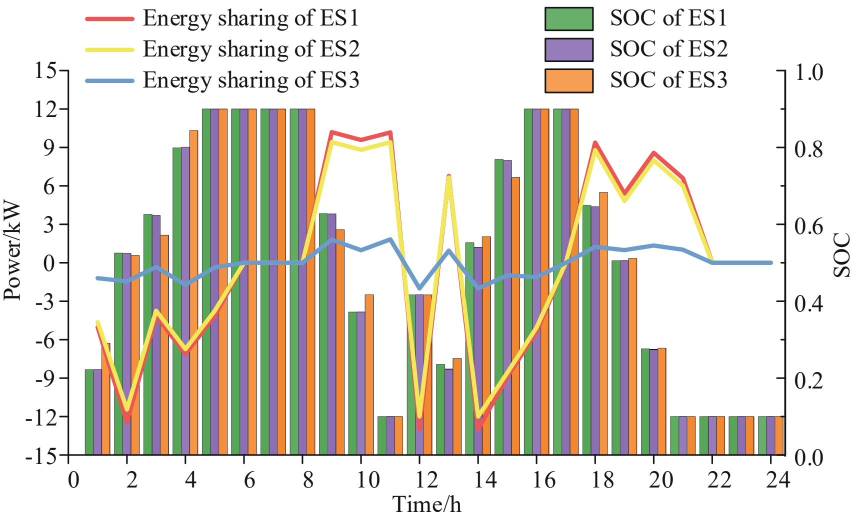

Fig. 4. ESS result and SOC state curve.

after participating in the sharing are shown in Table 3. All three users' gains are improved by 97.24 CNY, 105.57 CNY, and 65.14 CNY respectively, by using the Asymmetric Nash Bargaining method proposed in this paper to distribute benefits. Compared to the prior sharing, the benefits for each participant are improved by 8.37, 0.1076 and 0.3375 times respectively. It shows that by participating in sharing, the interests of all participating users are effectively improved. Among them, user 1 achieved the largest improvement because it has both photovoltaic and wind power, with large new energy generation capacity and an advantage in power sharing. At the same time, user 1 is equipped with a relatively large energy storage, so it has more advantage in sharing energy storage. Thus, it shows that each agent can obtain a fair distribution of benefits according to their contribution in the sharing process.

Table 3. Table captions should be placed above the tables.

Number	Cost before participating /CNY	Cost after participating /CNY	Income enhancement/CNY	Boosting ratio
1	−11.61	−108.85	97.24	8.37
2	980.96	875.38	105.57	0.1076
3	193.02	127.87	65.14	0.3375

The revenue enhancement for each user with different Nash bargaining power is shown in Table 4. Compared to conventional Nash Bargaining and Asymmetric Nash Bargaining, user 2 and user 3 have a larger payoff than the Asymmetric Nash bargaining distribution scheme. However, its actual contribution is smaller than that of user 1, which is clearly unfair to the other players. Regarding the different contribution weights, the revenue enhancement of user 2 decreases with the downward adjustment of the weights of the ESS contributions. This is due to the weakening of the bargaining advantage derived from its ESS. For user 1, its large new energy generation capacity improves revenue synchronization when power sharing is increased.

In summary, the Asymmetric Nash Bargaining scheme adopted in this paper can take into account the fairness of the allocation. It is necessary to set reasonable weighting coefficients to affect the bargaining power of the shared power and shared energy storage contributions, thus improving the incentive for users to engage in collaboration.

Table 4. Analysis of revenue enhancement of different Nash bargaining schemes.

Number	Standard Nash earnings boost/CNY	Asymmetric Nash earnings boost/CNY		
		$\gamma_p = 0.1, \gamma_{es} = 0.9$	$\gamma_p = 0.5, \gamma_{es} = 0.5$	$\gamma_p = 0.9, \gamma_{es} = 0.1$
1	84.65	91.952	98.701	117.59
2	113.23	108.25	98.79	99.252
3	69.90	67.81	70.47	50.96

5 Conclusion

In this paper, we propose an integrated DES optimization scheduling method based on Asymmetric Nash Bargaining in the context of new energy microgrids with high permeability, aiming at the operation scheduling requirements of multiple users owned energy storage in microgrids. The best scheduling strategy based on shared power and energy storage is solved by the ADMM algorithm The cooperative revenue sharing problem is solved fairly by the method of Asymmetric Nash Bargaining Game The main conclusions are as follows:

(1) A framework for aggregating and sharing DES of users within microgrids is proposed. Each user benefits from the proposed method compared to the previous model. The benefits of the three users are improved by 97.24 CNY, 105.57 CNY, and 65.14 CNY, respectively, and the benefits are improved by 8.37, 0.1076, and 0.3375 times.

(2) Users with high share participation can receive higher revenue by using Asymmetric Nash Bargaining for revenue allocation. Different weighting coefficients are assigned to the contributions of shared electricity and energy storage sharing, which can affect the bargaining power of users and regulate their revenue allocation. Therefore, the proposed method can effectively motivate users to participate in sharing.

(3) The problem is decomposed into two subproblems of power scheduling and revenue distribution and solved by ADMM algorithm, which can reduce the computational resources and protect the privacy and security of the user agent.

Acknowledgments. This work is supported by the State Grid Shanghai Electric Power Company Science and Technology Project Funding under the grant number (SGSHDK00DYJS2100670).

References

1. Zheng, Q., Jiang, L.X., Xu, Y.J., et al.: Research progress and development suggestions of energy storage technology under background of carbon peak and carbon neutrality [J]. Bull. Chin. Acad. Sci. **37**(4), 529–540 (2022)
2. Yang Xinfa, S., Jian, L.Z., et al.: Overview on micro-grid technology [J]. Proc. CSEE **34**(01), 57–70 (2014)
3. Cai, S., Laijun, C., Xinjie, Q., et al.: A generation-side shared energy storage planning model based on cooperative game[J]. J. Glob. Energy Interconnection **2**(04), 360–366 (2019)
4. Lin, L., Qingshan, X., Xiaoqing, W., et al.: Optimal economic scheduling of industrial customers on the basis of sharing energy-storage station[J]. Electr. Power Constr. **41**(05), 100–107 (2020)
5. Wang, X., Liu, J., Shen, W.: Non-cooperative game trading model of shared energy storage based on blockchain[J]. J. Nanjing Univ. Inform. Sci. Technol. (Nat. Sci. Ed.) **14**(05), 595–603 (2022)
6. Walker, A., Kwon, S.: Analysis on impact of shared energy storage in residential community: individual versus shared energy storage[J]. Appl. Energy 282 (2021)
7. Buxiang, Z., Jiahui, Z., Shen, D., et al.: Energy co-operative optimization of micro-grid campus system based on shared energy storage[J]. Electr. Drive **51**(18), 70–75 (2021)
8. Xianshan, L., Zijian, F., Fei, L., et al.: Game-based optimal dispatching strategy for distribution network with multiple microgrids leasing shared energy storage[J]. Proc. CSEE **42**(18), 6611–6625 (2022)
9. Liu, J., Zhang, N., et al.: Cloud energy storage for residential and small commercial consumers: a business case study—science direct[J]. Appl. Energy **188**(Feb.15), 226–236 (2017)
10. Zhang, S., Zhong, H.: Cloud energy storage capacity configuration for aggregated user energy storage and its transaction pricing[J]. South. Power Syst. Technol. **16**(11), 9–19 (2022)
11. Cui, S., Wang, Y.W., Liu, X.K., et al.: An economic storage sharing framework: asymmetric bargaining based energy co-operation[J]. IEEE Trans. Ind. Inf. (99), 1–1 (2021)
12. Li, X., Chen, L., Du, X., et al.: Research status and prospect of shared energy storage operation mechanism and trading mode on generation side[J]. J. Electr. Eng. **18**(01), 188–200 (2023)
13. Chis, A., Koivunen, V.: Coalitional game-based cost optimization of energy portfolio in smart grid communities[J]. IEEE Trans. Smart Grid **10**(2), 1960–1970 (2019)
14. Jinling, W., Ping, L., Minyuan, G., et al.: Operation optimization strategy of multi-microgrids energy sharing based on asymmetric Nash bargaining[J]. Power Syst. Technol. **46**(07), 2711–2723 (2023)
15. Lin, Z., Li, H., Fang, C.: Alternating Direction Method of Multipliers for Machine Learing[M], 1st edn. Science Press, Beijing (2023)

Evaluation Method for Source and Load Matching in User Side Active Distribution Network

Jiancheng Du, Jinda Zhu(✉), Jianfu Ni, Feng Liang, and Xin Wang

NARI Group Corporation (State Grid Electric Power Research Institute), Nanjing 211106, China
`153224962@qq.com`

Abstract. With the energy crisis and environmental problems highlighted, power users access distributed generation in the distribution network to achieve the goal of energy conservation and emission reduction, forming a user side active distribution network. However, the current active distribution network on the user side has caused source and load mismatch due to the dual fluctuation of source and load, resulting in issues such as voltage exceeding limits and power reverse transmission. Therefore, it is necessary to evaluate the source and load matching degree. However, existing evaluation methods lack the evaluation of source and load power quantity matching from the user side perspective. This article proposes a method for evaluating the source and load matching of user side active distribution networks. Firstly, an evaluation index system for source and load matching in user side active distribution networks was established from the perspectives of electricity matching and power matching; Secondly, the evaluation steps and methods for source and load matching in user side active distribution networks were proposed; Finally, the effectiveness of the proposed method in this paper is verified through numerical analysis of actual user side data.

Keywords: User side · Active distribution network · Electricity matching · Power matching · Evaluation index

1 Introduction

In recent years, with the deepening of the new round of power system reform, the scale of user side distribution networks invested and constructed by power users has rapidly expanded. The user side distribution network focuses on ensuring the normal operation of power users' electricity demand, and has extremely high requirements for the stability of power supply. With the development of the economy, the energy consumption and pollutant emissions in the production process of power users continue to increase. The green and low-carbon transformation of the user side distribution network has become an important task for the current and future energy sector in China [1, 2]. The integration of distributed generation (DG) such as wind and light into the user side distribution network has become a trend [3], forming an active user side distribution network. However, due to the dual fluctuation of load and DG on the user side, there may be a mismatch between

Y. Xue et al. (Eds.): PMF 2023, LNEE 1129, pp. 259–274, 2024.
https://doi.org/10.1007/978-981-99-9251-5_21

the source and load in the active distribution network on the user side, resulting in issues such as power reverse transmission and voltage exceeding limits [4–6]. Therefore, the evaluation of source load matching in user side active distribution networks has attracted the attention of scholars at home and abroad.

Recently indicators and methods related to distribution network evaluation have continuously emerged, and the perspectives on distribution network evaluation have become more diverse. Reference [7] evaluates the factors affecting the operation and inspection costs of distribution networks from aspects such as economy, equipment, and network structure; Reference [8] used the repetitive power flow calculation method to evaluate the power supply capacity of distribution networks containing DG; Reference [9] comprehensively evaluates the security situation of DG connected to the distribution network based on utility theory and ER algorithm; Reference [10] evaluates the energy-saving potential of distribution networks considering source load uncertainty; Reference [11] evaluates the wiring mode of distribution networks by constructing comprehensive efficiency and load distribution adaptation indicators based on average and maximum power supply capacity. Based on Lagrange shadow algorithm theory, literature [12] comprehensively evaluates the distribution network from two aspects of performance and benefit. However, the evaluation research on distribution networks mentioned above involves relatively little research on the source load matching method of active distribution networks.

In terms of evaluation methods for source load matching in distribution networks, existing research mainly focuses on the matching status between different types of DGs and between DGs and loads. References [13, 14] proposed an evaluation method for the complementary characteristics between wind and solar energy. Reference [15] proposed evaluation indicators for the matching degree between different DGs and loads, but the connotation of the matching is not perfect enough. References [16, 17] propose interactive evaluation indicators for building load and power grid. References [18, 19] studied the degree of matching between photovoltaic power generation and household loads. Reference [20] proposed a comprehensive matching evaluation method for DG integration into urban distribution networks from the perspective of the power grid, but lacked an evaluation of active distribution networks from the perspective of the user side. In summary, existing research only proposes a small number of indicators to evaluate the relationship between different DGs or DGs and loads, and rarely involves the quantification and analysis of DG and load electricity balance indicators. Moreover, the analysis perspective is mostly from the grid side, lacking analysis from the user side.

Based on the above analysis, this article proposes a method for evaluating the source load matching of user side active distribution networks. Firstly, an evaluation index system for source load matching in user side active distribution networks was established from the perspectives of electricity matching and power matching; Subsequently, the evaluation steps and methods for source load matching in user side active distribution networks were proposed; Finally, the effectiveness of the proposed method in this paper is verified through numerical analysis of actual user side data.

2 Evaluation Index System for Source Load Matching in User Side Active Distribution Network

2.1 Concept of Source Load Matching for Active Distribution Network on the User Side

The source load matching of the active distribution network on the user side refers to the matching of load, DG, and the size time space of the distribution network in terms of electricity quantity and power. In order to analyze the issues between energy and power matching after the user side active distribution network is connected to DG. This article proposes the concept of source load matching for user side active distribution networks, and its system is as follows.

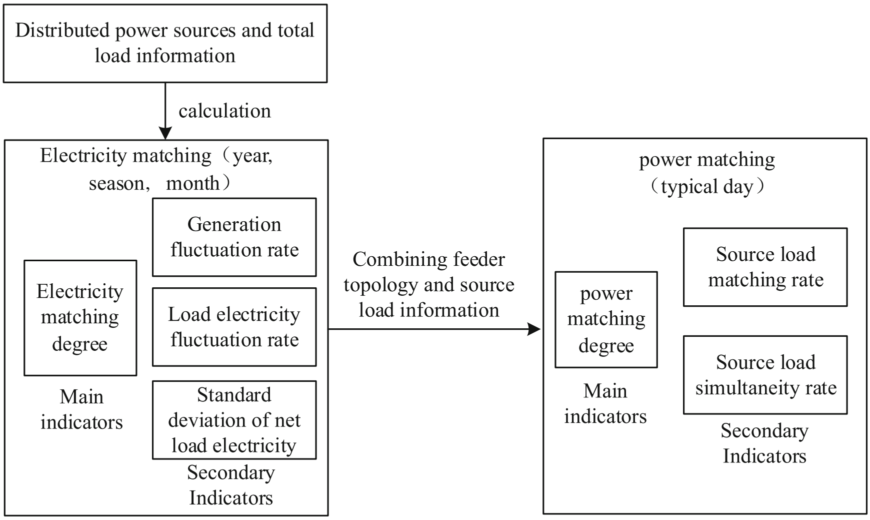

Fig. 1. Source and load matching system for user side active distribution network

From Fig. 1, it can be seen that the source load matching in this article is divided into electricity matching and power matching. Electricity matching refers to the matching of the total output of DG and the total load of the distribution network within a given range. The time includes multiple time scales such as year, quarter, and month, and the spatial scale includes each interval of line operation. The main evaluation indicator is electricity matching degree, and the auxiliary indicators are load electricity fluctuation rate, electricity generation fluctuation rate, and net load electricity standard deviation. Power matching refers to the matching of the distribution network DG and load within a given range on a typical daily power distribution. The main evaluation indicator is power matching degree, and the auxiliary indicators are source load matching rate and source load simultaneity rate. Electricity matching considers the size and spatial distribution of electricity, while power matching increases the distribution of load and DG at different times on typical days.

2.2 Evaluation Indicators for Source Load Matching in User Side Active Distribution Network

2.2.1 Electricity Matching Degree

The electricity matching degree of the user side active distribution network during time period t is defined as the evaluation value that reflects the matching between DG generation and load electricity based on the calculation of DG generation and load electricity in the region during this time period. The calculation formula is:

$$D_{\mathrm{E},t} = \begin{cases} \frac{\mu_{\mathrm{e}}}{\mu_1} & 0 \le \mu_{\mathrm{e}} \le \mu_1 \text{(low electricity penetration zone)} \\ 1 & \mu_1 < \mu_{\mathrm{e}} \le \mu_2 \text{(optimal Energy Consumption Zone)} \\ \frac{2\mu_{\mathrm{e}} - \mu_2 - 1}{\mu_2 - 1} & \mu_2 < \mu_{\mathrm{e}} \le 1 \text{(extremely high electricity penetration rate zone)} \\ k_1(\mu_{\mathrm{e}} - 1) - 1 & \mu_{\mathrm{e}} > 1 \text{(electricity return supply zone)} \end{cases} \tag{1}$$

among it:

$$\mu_{\mathrm{e}} = \frac{E_{\mathrm{DG}}}{E_{\mathrm{Load}} + E_{\mathrm{Loss}}} \tag{2}$$

In Eq. (1): μ_{e} is the proportion of DG electricity consumption at that time; μ_1 and μ_2 are respectively the boundary values for the low permeability area of electricity and the optimal consumption area of electricity, as well as the optimal consumption area of electricity and the extremely high permeability area of electricity, respectively; k_1 is penalty coefficient for electricity supply return.

In Eq. (2): E_{DG} is the power generation of DG in the region during this time period; E_{Load} is the load electricity consumption for this period of time in the region; E_{Loss} is the active power loss of the region. In this paper E_{Loss} can be determined by the statistical value of network loss, or through the given network loss rate which can simplify the calculation.

In order to meet the demand for a high proportion of clean energy consumption on the user side, to reasonably allocate adjustable resources, and to reduce backflow to the power grid, this paper considers the value of μ_1 is 30%, the value of μ_2 is 60% and the value of k_1 is −10. At this point, Eq. (1) is visualized as Fig. 2. At the same time, set the threshold value of $D_{\mathrm{E},t}$ is T_{E}. When $D_{\mathrm{E},t} > T_{\mathrm{E}}$, it means that the electricity matching is good. When $D_{\mathrm{E},t} < T_{\mathrm{E}}$, it means that the electricity matching is bad.

2.2.2 Electricity Matching Secondary Indicators

(1) Load electricity fluctuation rate

The load electricity fluctuation rate R_{lef} is the ratio of the standard deviation to the average of the daily load electricity curve for a certain period of time (month, season, year):

$$R_{\mathrm{lef}} = \frac{\sigma_{\mathrm{le}}}{\lambda_{\mathrm{le}}} \tag{3}$$

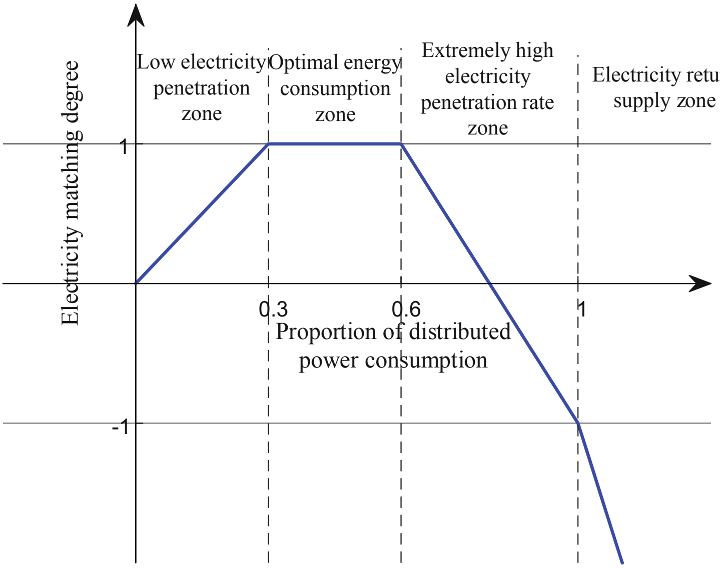

Fig. 2. Calculation basis for electricity matching degree

In Eq. (3): σ_{le} is the standard deviation of load daily electricity curve; λ_{le} is the average value of daily load electricity curve. At the same time, set the threshold value of R_{lef} is T_{lef}. When $R_{\text{lef}} > T_{\text{lef}}$, it means that the fluctuation rate of load electricity is high. When $R_{\text{lef}} < T_{\text{lef}}$, it means that the fluctuation rate of load electricity is low.

(2) Generation fluctuation rate

The generation fluctuation rate R_{gef} is the ratio of standard deviation to average of DG daily power generation curve during a certain time period (month, season, year):

$$R_{\text{gef}} = \frac{\sigma_{\text{ge}}}{\lambda_{\text{ge}}} \tag{4}$$

In Eq. (4): σ_{ge} is the standard deviation of DG daily power generation curve; λ_{ge} is the average value of DG daily power generation curve. At the same time, set the threshold value of R_{gef} is T_{gef}. When $R_{\text{gef}} > T_{\text{gef}}$, it means that the fluctuation rate of power generation is high. When $R_{\text{gef}} < T_{\text{gef}}$, it means that the fluctuation rate of power generation is low.

(3) Standard deviation of net load electricity

The standard deviation of net load electricity σ_{gle} is the standard deviation of the daily electricity generation curve of a certain time period (month, season, year) minus the daily electricity generation curve of DG.

2.2.3 Power Matching Degree

The power matching degree $D_{\text{GL},t}$ of the user side active distribution network at time t is defined as the evaluation value that reflects the matching between DG and load, as well as the matching between load and regional capacity, calculated based on the load rate of the region at that time. The calculation formula is as follows (5):

$$D_{\mathrm{GL},t} = \begin{cases} k_1\left(\mu_1 - \mu_{\mathrm{gl}}\right) + k_2 & \mu_{\mathrm{gl}} \le \mu_1 (\text{backward heavy or over load zone}) \\ \frac{k_2 \mu_{\mathrm{gl}}}{\mu_1} & \mu_1 < \mu_{\mathrm{gl}} \le 0 (\text{backhaul zone}) \\ 1 & 0 < \mu_{\mathrm{gl}} \le \mu_2 (\text{optimal absorption zone}) \\ \frac{\mu_3 - \mu_{\mathrm{gl}}}{\mu_3 - \mu_2} & \mu_2 < \mu_{\mathrm{gl}} \le \mu_3 (\text{main network power supply zone}) \\ \frac{k_3\left(\mu_{\mathrm{gl}} - \mu_3\right)}{1 - \mu_3} & \mu_3 < \mu_{\mathrm{gl}} \le 1 (\text{forward heavy load zone}) \\ k_1\left(\mu_{\mathrm{gl}} - 1\right) + k_3 & \mu_{\mathrm{gl}} > 1 (\text{forward over load zone}) \end{cases} \tag{5}$$

among it:

$$\mu_{\mathrm{gl}} = \frac{P_{\mathrm{gl},t}}{C_{\mathrm{B}} \cos\varphi} = \frac{P_{\mathrm{l},t} - P_{\mathrm{g},t} + P_{\mathrm{loss},t}}{C_{\mathrm{B}} \cos\varphi} \tag{6}$$

In Eq. (5): $D_{\mathrm{GL},t}$ is the power matching degree at time t; μ_{gl} is the regional load rate at that time; μ_1, μ_2, and μ_3 is respectively the boundary value between backward heavy or over lead zone and the backhaul zone; the optimal absorption zone and the main network power supply zone and the forward heavy load zone and the forward over load zone. k_1 is the penalty coefficient of the backward heavy or over lead zone and the forward heavy load zone. k_2 is the penalty coefficient of the backhaul zone. k_3 is the penalty coefficient of the forward heavy load zone.

In Eq. (6): $P_{\mathrm{l},t}$ is the active power of the area at time t, $P_{\mathrm{g},t}$ is the power generated in this area at time t, $P_{\mathrm{loss},t}$ is the active network loss at time t and it can be determined by the line impedance and the current that flow through the line. C_{B} is the regional capacity, $\cos\varphi$ is the power factor, $P_{\mathrm{gl},t}$ is the net load active power of the area at time t.

The range of power matching degree values is $(-\infty, 1]$. When the value is closer to 1, the higher the matching degree is. In this paper, the value of μ_1, μ_2, and μ_3 is -80%, 10%, 80% respectively and the value of k_1, k_2 and k_3 is -30, -15, -5 respectively. At this point, Eq. (5) is visualized as Fig. 3. At the same time, set the threshold value of $D_{\mathrm{GL},t}$ is T_{D}. When $D_{\mathrm{GL},t} > T_{\mathrm{D}}$, it means that the power matching is good. When $D_{\mathrm{GL},t} < T_{\mathrm{D}}$, it means that the power matching is bad.

After obtaining the power matching degree at a certain time, in order to evaluate the matching degree within a day, the average of each time is taken:

$$D_{\mathrm{GL}} = \frac{1}{n} \sum_{t=1}^{n} D_{\mathrm{GL},t} \tag{7}$$

In Eq. (7): D_{GL} is the power matching degree of the distribution network over a period of time. The research period is 1 day, 1 week, etc., with time scales of 5 min, 10 min, 15 min, 30 min, 1 h, etc.

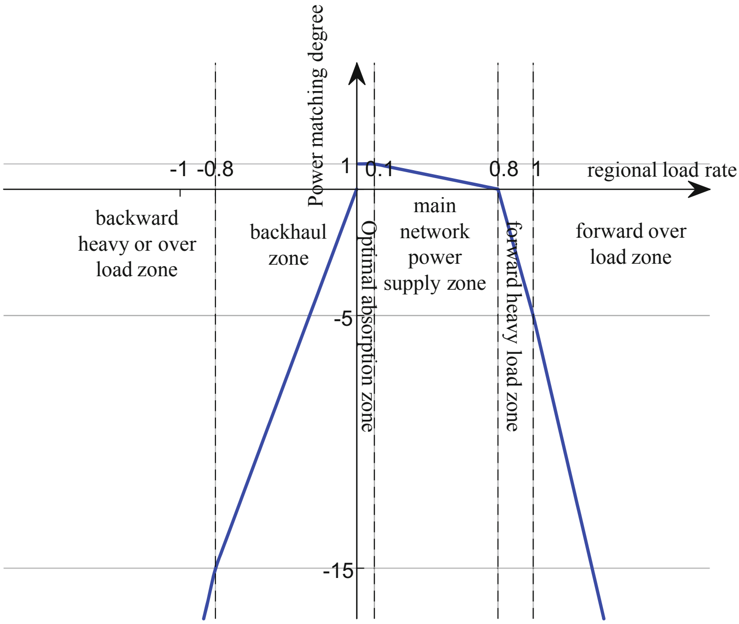

Fig. 3. Calculation basis for electricity matching degree

2.2.4 Secondary Indicators for Power Matching

(1) Source load matching rate

The source load matching rate R_{GL} is defined as the percentage of time during a certain time period when the matching degree of the internal load power is not lower than the threshold to the total time. The calculation formula is:

$$R_{\text{GL}} = \frac{t\left(D_{\text{GL},t} \geq T_{\text{D}}\right)}{n} \tag{8}$$

Set a threshold T_{R}, when $R_{\text{GL}} < T_{\text{R}}$ it means that the time of low $D_{\text{GL},t}$ is long.

(2) Source load simultaneity rate

The source load simultaneity rate R_{SGL} is defined as the synchronicity between the regional electricity load and the DG power curve, and the calculation formula is:

$$R_{\text{SGL}} = \frac{1 + r\left(P_{\text{l}}, P_{\text{g}}\right)}{2} \tag{9}$$

among it

$$r\left(P_{\text{l}}, P_{\text{g}}\right) = \frac{Cov\left(P_{\text{l}}, P_{\text{g}}\right)}{\sigma(P_{\text{l}})\sigma\left(P_{\text{g}}\right)} \tag{10}$$

P_{l} and P_{g} are respectively the active power vector of regional load and DG; $r\left(P_{\text{l}}, P_{\text{g}}\right)$ is the correlation coefficient between the two vectors; $\sigma(P_{\text{l}})$ and $\sigma\left(P_{\text{g}}\right)$ are the standard deviation of regional load and DG active power vector respectively.

Set a threshold T_{RS}, when $R_{\mathrm{SGL}} < T_{\mathrm{RS}}$ it means that synchronization between load and DG active power curve is good.

3 Evaluation Method for Source Load Matching in User Side Active Distribution Network

The evaluation method for source load matching in the user side active distribution network is as follows.

Firstly, prepare the data, including daily load data of the active distribution network on the user side, daily generation data of DG, transformer and feeder capacity, as well as network losses at various times calculated through power flow.

Next, calculate and analyze the evaluation indicators for source load matching in the user side active distribution network, and the specific steps are as follows.

To begin with, conduct an evaluation of electricity matching. If the electricity matching is poor, analyze the reasons for the poor electricity matching based on auxiliary indicators of electricity matching, load and DG distribution information. The main reason is that there are few or too many DGs installed, resulting in mismatches with the load. Next, conduct power matching evaluation. If the power matching is good, it indicates that the system is mainly operating in the DG low-permeability zone and mainly relies on the main network for power supply; If the power matching is poor, it indicates that the system is mainly operating in the high penetration zone of DG, and DG sends power back to the main network.

If the electricity matching is good, it indicates that the distribution of system DG and total load is relatively good, and power matching evaluation is conducted. If the power matching is good, then the system source load matching is good; If the power matching is poor, combined with the auxiliary indicators of power matching and the distribution information of load and DG, the main reason is the difference in source load matching rate and simultaneity rate, and the mismatch between DG and load time, causing DG to reverse power transmission to the main network. In special cases, there is a high source load matching rate and synchronization rate, but the DG power generation is small, making the system more dependent on the main network for power supply, resulting in slightly poor power matching.

Finally, when the source load matching of the active distribution network on the user side is not good, search for the dominant factors that affect the source load matching.

The flow chart of the evaluation method for source load matching in the user side active distribution network is shown in Fig. 4.

4 Example Analysis

4.1 Example Overview

Select a user side active distribution network as shown in Fig. 5 for example analysis. The 10 kV Sect. 1 has a heavy load and is connected to a wind turbine of 6.25 MW and a photovoltaic system of 3.66 MWp. The 10 kV Sect. 2 has a light load and is connected to a wind turbine of 6.25 MW. The annual load information and wind turbine

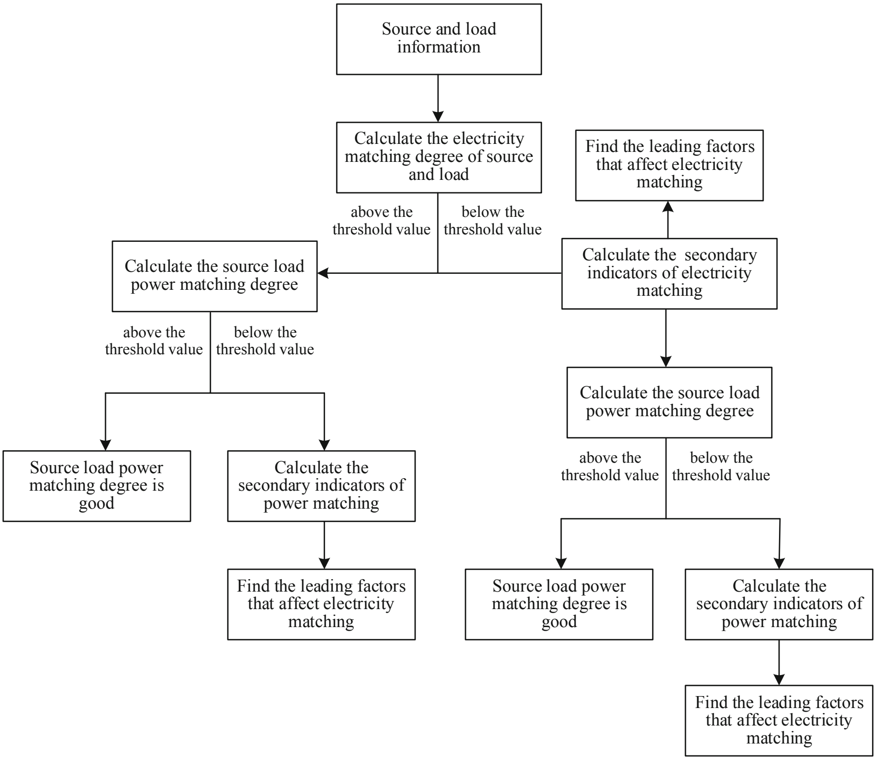

Fig. 4. Flow chart of source and load matching evaluation method for user side active distribution network

and photovoltaic power generation data of 10 kV Sects. 1 and 2 can be achieved by the real historical data in 2022. During normal operation, the 10 kV Sects. 1 and 2 bus tie circuit breakers are disconnected.

4.2 Source Load Matching Evaluation

Due to the heavy load and multiple DG installations in the 10 kV I section of the distribution network, the 10 kV I section was selected for evaluation of source load matching throughout the year. According to Eq. (1) to Eq. (2), calculate the annual, seasonly, and monthly electricity matching $D_{E,T}$ of the 10 kV Sect. 1 of the distribution network. The calculated annual electricity matching degree is 0.8596; The matching degrees of quarterly electricity consumption are 0.9503, 0.8484, 0.9870, and 0.6785, respectively; The monthly electricity matching degrees are 0.6796, 0.8692, 1, 1, 0.4807, 0.9316, 0.6076, 1, 1, 0.9640, 0.6773, and 0.6421, respectively. After getting the value of $D_{E,T}$, this example sets the threshold T_E. This example considers that when T_E is set to 0.6, it can achieve on-site consumption of user side DG, ensure that the user side DG and the power supply of the large power grid are in a reasonable proportion, and reduce reverse transmission and heavy load operation scenarios. At this point, the annual and

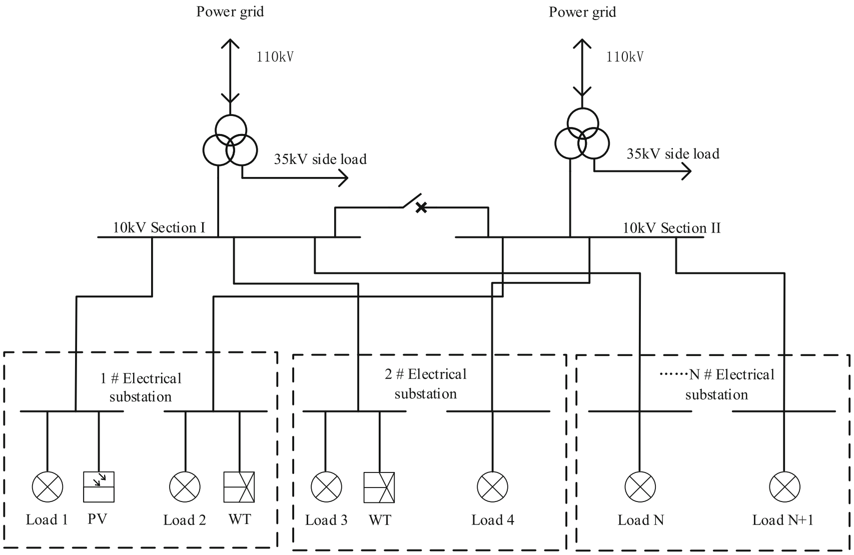

Fig. 5. Typical network structure of user side active distribution network

seasonly $D_{E,T}$ of the 10 kV Sect. 1 of the example distribution network is higher than T_E, with only May $D_{E,T}$ lower than T_E, indicating that the overall electricity matching of the 10 kV Sect. 1 of the example distribution network is good. Next, we will select May with a $D_{E,T}$ lower than T_E as Scenario 1, and March with a $D_{E,T}$ higher than T_E and the highest value as Scenario 2 for specific analysis of power matching first.

4.2.1 Scenario 1

For scenarios 1, $D_{E,T}$ is below T_E, this paper analyze the daily load and DG electricity quantity information in this scenario to assist in evaluating the source load matching situation of the distribution network and calculate auxiliary indicators R_{lef}, R_{gef}, and σ_{gle} for electricity quantity matching. According to calculations, in scenario 1, R_{lef} is 4.19%, R_{gef} is 51.14%, and σ_{gle} is 15.57. The daily load and DG energy information for scenario 1 is as follows.

The threshold of R_{lef} and R_{gef} in this paper is both 30%, when the value above 30% indicates a high volatility. From Fig. 6 and the auxiliary indicators of electricity matching, it can be seen that the fluctuation rate of load electricity in Scenario 1 is small, while the fluctuation rate of DG power generation is large. Due to the overall higher electricity consumption of Scenario 1 load than DG power generation, the line operates in the DG low permeability zone shown in Fig. 7. Therefore, the main reason for the low power matching in Scenario 1 is the small installed capacity and high load of DG. It is recommended to increase the installed capacity or transfer some transferable loads to other months.

On the basis of electricity matching analysis, calculate the daily power matching degree and power matching auxiliary indicators for scenario 1 according to Eqs. (5) – (10), and the curve is as follows.

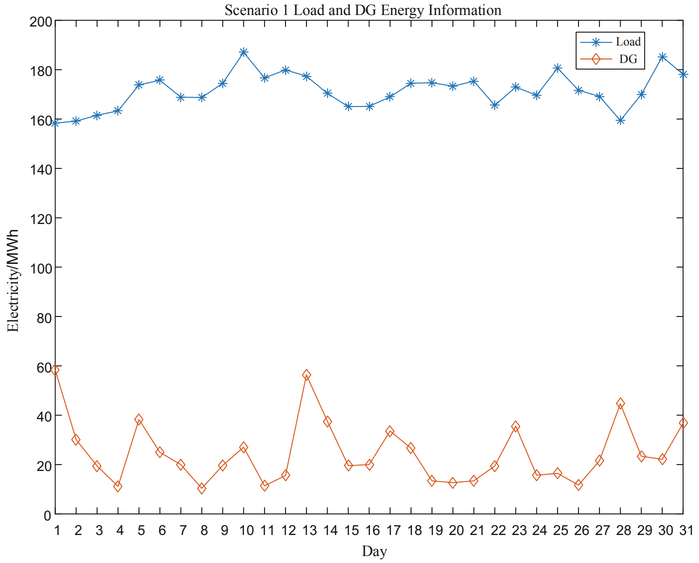

Fig. 6. Scenario 1 load and DG electricity information

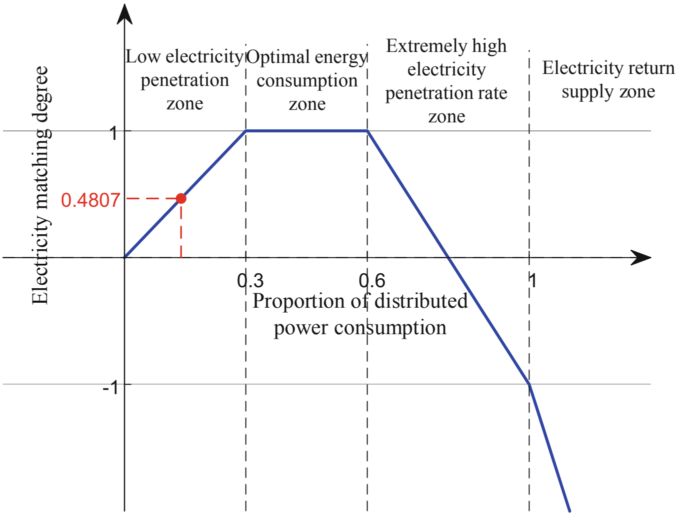

Fig. 7. Scenario 1 power matching diagram

From Fig. 8, it can be seen that in Scenario 1, D_{GL} is all higher than 0.5. In this example, considering that the user's expectation is mainly based on the optimal source load consumption state and the main network power supply state, with fewer cases of reverse transmission and overload. So the threshold T_D is set to 0.5. Therefore, in scenario 1, all are above the threshold. At the same time, considering the optimal absorption

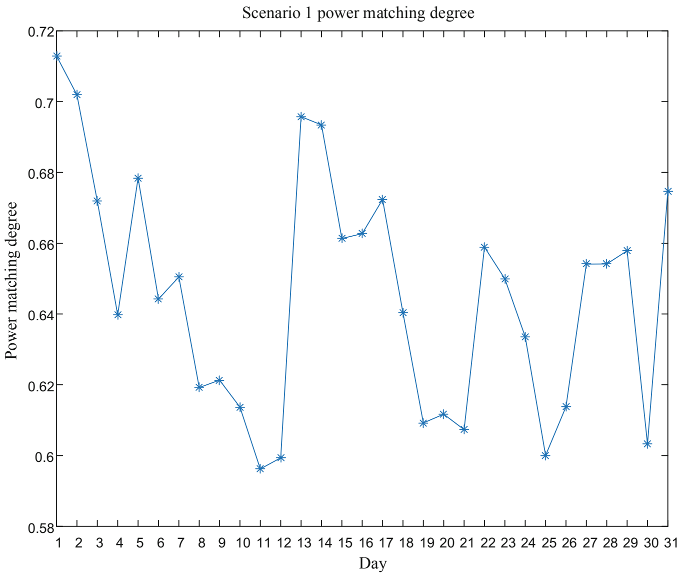

Fig. 8. Scenario 1 daily power matching diagram

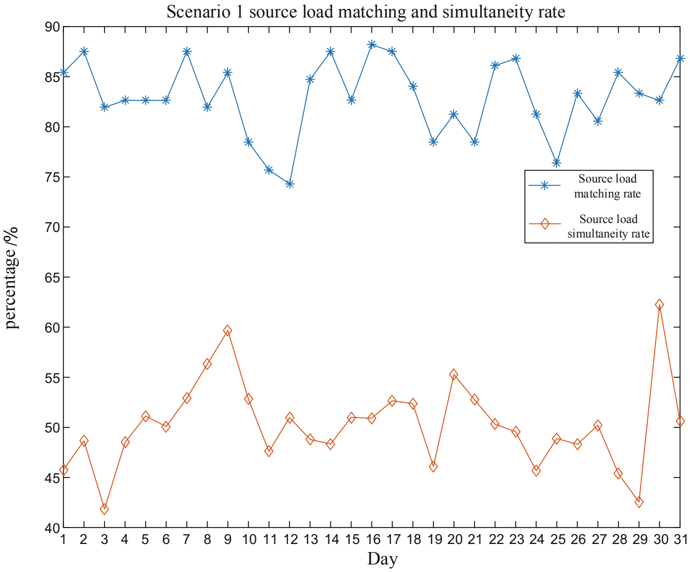

Fig. 9. Scenario 1 source and load matching and simultaneity rate

scenario of new energy, the source load matching rate and simultaneity rate should be relatively high. Set the threshold T_R to 50% and the threshold T_{RS} to 40%. From Fig. 9, it can be seen that although the electricity matching in this scenario is poor, due to both

T_R and T_{RS} are above the threshold, DG power generation is basically absorbed by the load. At this time, the system operates in the main grid power supply area and the power matching is good.

4.2.2 Scenario 2

For scenario 2, $D_{E,T}$ is higher than T_E and the value of $D_{E,T}$ is 1, indicating that the electricity level in this scenario matches well and the system is running in the optimal consumption zone. Calculate the daily power matching degree and auxiliary power matching indicators, and conduct specific evaluations based on the daily load and DG power information in Scenario 2.

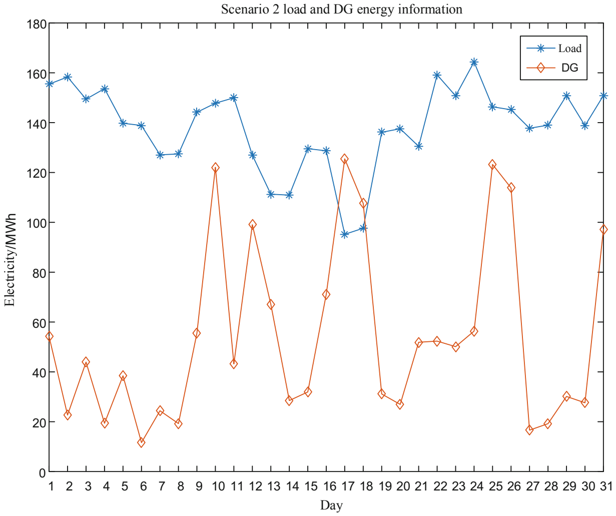

Fig. 10. Scenario 2 load and DG electricity information

As shown in Fig. 11, when the threshold T_D is set to 0.5, there are 8 days in Scenario 2 when the D_{GL} is below the threshold. Based on Figs. 10, 11 and 12, it can be seen that on days 10, 12, 16, 17, 18, 25, and 26, both R_{GL} and R_{SGL} are below the threshold, indicating poor power matching in such scenarios. Based on the specific combination of load and DG information, it can be seen that the daily DG generation is relatively high, but the matching between DG and load time is poor, and DG cannot be fully absorbed. Some parts of the system operate in the reverse transmission area. On the 13th day, both R_{GL} and R_{SGL} are high, but DG generated less electricity, and the system relied on the main grid for power supply, resulting in poor power matching.

Scenario 2 shows that other daily averages are above the threshold, indicating good power matching and source load matching. The system is operating in an ideal state and can achieve optimal DG absorption.

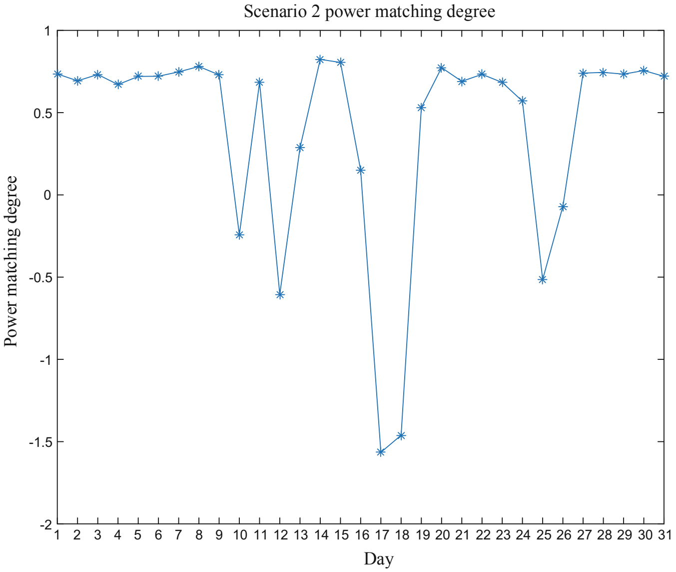

Fig. 11. Scenario 2 power matching degree

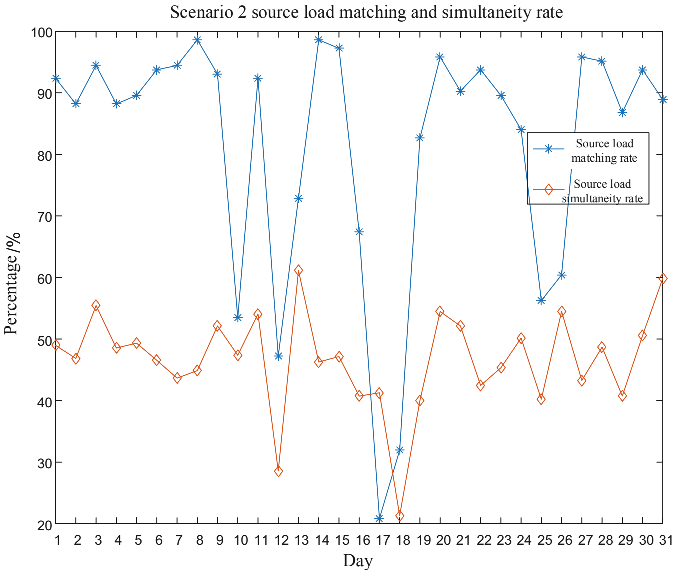

Fig. 12. Scenario 2 source and load matching and simultaneity rate

5 Conclusion

This article constructs an evaluation index system for the source load matching of the user side active distribution network, and proposes an evaluation method for the source load matching of the user side active distribution network. Through example analysis, the main conclusions are as follows:

(1) The evaluation method based on user side active distribution network source load matching can analyze the annual, quarterly, and monthly electricity matching situation of a typical user side active distribution network, and conduct monthly daily power matching analysis for typical months. The specific evaluation of the source load matching of a user side active distribution network was conducted through data and indicators.
(2) The evaluation method for source load matching in user side active distribution networks can provide guidance for user side load planning, DG location and capacity determination, and optimization of adjustable resources.
(3) Different from the traditional evaluation method of active distribution networks from the perspective of the grid side, this article evaluates the source load matching from the perspective of fully absorbing the DG of power users as much as possible.

The next step will be to propose a source load matching optimization method based on the topology information of active distribution networks on different user sides, and further verify the correctness of this method by evaluating the source load matching of active distribution networks on the user side before and after optimization.

Acknowledgments. This work is supported by the State Grid Corporation of China Science and Technology Project: Research and Demonstration of Key Technologies for Source Load Collaborative and Intelligent Operation and Maintenance of the Power Supply and Consumption System for the Whole County's Roof Photovoltaic Access. (No. 5400-202233168A-1-1-ZN).

References

1. Jinli, W., Fengsheng, L., Fang, X., et al.: Research on technical standard system of new distribution systems under double-carbon strategy [J]. China Electr. Power **56**(05), 22–31 (2023)
2. Fan, A., Xiong, Y., Yang, L., et al. Carbon footprint model and low–carbon pathway of inland shipping based on micro–macro analysis[J]. Energy 263(PE) (2023)
3. Lei, L., Tian, W.: Review of distribution network with distributed generation [J]. Commun. Power Technol. **36**(09), 20–21 (2019)
4. Le, L., Zhiyuan, M., Wenxiong, M., et al.: Voltage sag severity interval assessment method for user side considering tolerance characteristics of equipment of differing sensitivity [J]. Power Syst. Prot. Control **49**(02), 140–148 (2021)
5. Mingjie, L., Guoping, C., Cun, D., et al.: Research on power balance of high proportion renewable energy system [J]. Grid Technol. **43**(11), 3979–3986 (2019)
6. Lizhu, P., Shi, C.: Research on the impact of distributed photovoltaic power grid connection on the power quality of the power grid [J]. Sci. Technol. Innov. **31**, 38–39 (2020)

7. Luo, C.L., Li, Z., Xu, Z., et al.: Evaluation and analysis of factors affecting the operation inspection cost of distribution network equipment assets based on BMA-improved grey correlation method [J/OL]. China Electr. Power 1–13
8. Xin, Y., Gang, W., Lijun, Z., et al.: Probabilistic evaluation on power supply capability of distribution system with distributed generations [J]. J. Power Syst. Autom. **31**(04), 99–105 (2019)
9. Wu, B.: Comprehensive Security Evaluation of Distribution System with Distributed Generations [D]. Nanjing University of Posts and Telecommunications (2021)
10. Yang, Z., Wang, J., Wu, J., et al.: Assessment method of comprehensive energy saving potential of distribution network considering source-load power uncertainty [J]. China Electr. Power **55**(08), 151–156+164 (2022)
11. Jun, X., Buxin, S.: Comprehensive efficiency evaluation on connection modes in distribution networks [J]. Power Grid Technol. **43**(10), 3769–3781 (2019)
12. Wang, S., Wang, L., Chen, F., et al.: Comprehensive evaluation method of distribution network based on shadow price under big data environment [J]. Power Autom. Equipment **39**(10): 94–101 (2019)
13. Jin, Z., Jizhong, Z., Lai, X., et al.: Simulation of wind power output series based on space-time auto-regressive moving average model [J]. Power Syst. Autom. **43**(03), 101–107 (2019)
14. Monforti, F., Huld, T., Bodis, K., et al.: Assessing complementarity of wind and solar resources for energy production in Italy: a Monte Carlo approach[J]. Renew. Energy **63**(1), 576–586 (2014)
15. Ye Lin, Q., Xiaoxu, M.Y., et al.: Analysis on intraday operation characteristics of hybrid wind-solar-hydro power generation system [J]. Power Syst. Autom. **42**(04), 158–164 (2018)
16. Salom, J., Marszal, A.J., Widen, J., et al.: Analysis of load match and grid interaction indicators in net zero energy buildings with simulated and monitored data[J] Appl. Energy **136**, 119–131 (2014)
17. Ferraro, M., Sergi, F., Antonucci, V., et al.: Load match and grid interaction optimization of a net zero energy building through electricity storage: an Italian case-study[C]. IEEE 16th International Conference on Environment and Electrical Engineering, June 7–10, 2016, Florence, Italy, pp. 1–5
18. Cao, S., Siren, K.: Impact of simulation time-resolution on the matching of PV production and household electric demand[J]. Appl. Energy **128**, 192–208 (2014)
19. Luthander, R., Nilsson, A.M., Widen, J., et al.: Graphical analysis of photovoltaic generation and load matching in buildings: a novel way of studying self-consumption and self sufficiency[J]. Appl. Energy **250**, 748–759 (2019)
20. Jun, X., Hang, L., Bo, W., et al.: Comprehensive matching evaluation method for integration of distributed generator into urban distribution network [J]. Power Syst. Autom. **44**(15), 44–51 (2020)
21. Qionghui, L., Caixia, W.: Analysis on energy development based on the 13th five-year electric power planning[J]. China Electr. Power **50**(01), 30–36 (2017)

Icing Growth Model of Overhead Transmission Line on Multiple Machine Learning Algorithms

Yan Wang[1], Hui Hou[1](✉), Xiaolu Bai[2], Jianshuang Lv[2], Decheng Cai[2], and Yiyang Shen[2]

[1] Wuhan University of Technology, Wuhan, China
`husthou@126.com`
[2] Central Southern China Electric Power Design Institute co., Ltd. of China Power Engineering Consulting Group co., Ltd., Wuhan, China

Abstract. As the key equipment connecting regional power stations, substations and load, overhead transmission lines can be easily affected by ice disaster, which cause huge loss to the power system. Therefore, this paper establishes an icing growth model to predict the development trend of ice. First of all, the original data is preprocessed, and the feature variable with the most important rank is selected as the input. Secondly, nine machine learning algorithms are used to construct the prediction model, including three linear regression models (ridge regression, lasso regression, and elastic net regression), three single algorithm models (decision tree, K-nearest neighbors, and support vector regression), and three ensemble learning algorithms (gradient boosting regression, random forest, and adaptive boosting). Finally, the analysis is concluded that the decision tree, gradient lifting regression, random forest and adaptive lifting algorithm have demonstrated excellent performance on the test set. Furthermore, the predictive capability of these four optimal models is further validated by predicting new datasets.

Keywords: Overhead transmission line · Icing growth model · Influencing factor · Optimal model · Icing prediction

1 Introduction

Icing refers to the accumulation of ice on the surface of overhead transmission line (OHTL) under harsh weather conditions. Icing is easy to induce line breakage, ice flash, trip and other malignant accidents [1], leading to a large-scale power grid blackout phenomenon. Therefore, it is of great significance to study icing growth model of OHTL.

As the first step to explore the impact of ice disaster on the system, scholars at home and abroad have been carrying out research on icing prediction. Based on different emphasis, existing research has proposed various icing growth models for OHTL. Commonly used models mainly fall into two categories [2]: one is the physical model based on thermodynamics and aerodynamics [3–5], and the other is the machine learning model driven by historical data [6–9]. The realization method of physical model is to put forward a series of hypotheses and abstract the icing process with mathematical formula.

Y. Xue et al. (Eds.): PMF 2023, LNEE 1129, pp. 275–286, 2024.
https://doi.org/10.1007/978-981-99-9251-5_22

Among them, the selection of parameters has an important impact, which may lead to large differences in results under the same condition. Given the limitations of physical models, machine learning algorithms have been developed in recent years. The machine learning model seldom pays attention to the icing mechanism and chooses to ignore complex physical process. By gathering variable data associated with icing growth, this paper employs fuzzy processing techniques and chooses machine learning algorithms to train the collected data [10].

Considering the abundance of existing studies on predicting icing growth, this paper mainly uses online monitoring data to establish a data-driven machine learning algorithm model. Firstly, the factors affecting the icing are analyzed, which is used as the input feature vector in the following chapters. Secondly, a data-driven icing growth model is established based on nine machine learning algorithms. Finally, the optimal algorithmic model is selected through an analysis of a case and a comprehensive consideration of metrics such as MAE, MSE, and RMAE. Furthermore, the model is verified on different OHTLs to validate its performance.

2 Framework of Icing Growth Model

This section proposes an icing growth model framework, which is mainly divided into four parts: data collection, data processing, icing growth prediction, and optimal model selection. The overall framework is shown in Fig. 1.

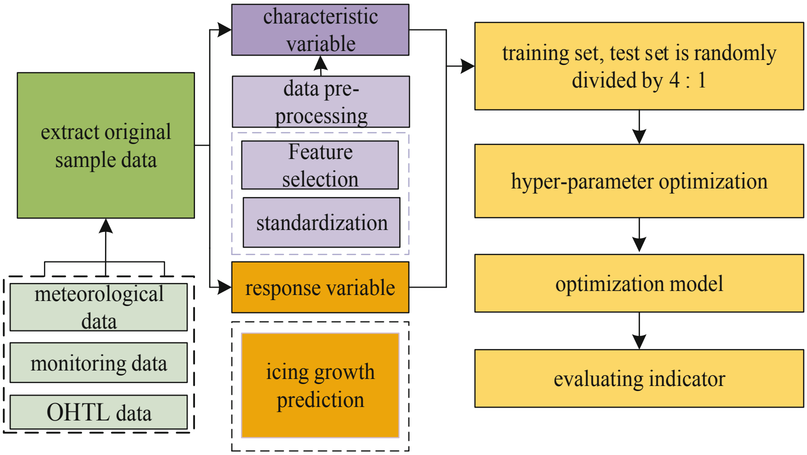

Fig. 1. Icing growth model framework

Firstly, data collection is carried out. Raw sample data such as meteorological and power grid data are extracted from multiple data sources, and historical icing data of Liuzhou Bureau in Guangxi, China is utilized as sample data.

Secondly, the original data is preprocessed and the correlation analysis of characteristic variables is carried out to eliminate some variables with strong correlation and construct the final input data set.

Finally, the study divides the preprocessed data into training set and test set according to 4:1 and establishes an icing growth prediction model based on nine commonly used machine learning algorithms. This study uses the validation set to evaluate and select the models. By comparing the prediction accuracy and stability of each model, the optimal model is selected and further optimized.

3 Data Space Construction

Icing growth prediction is a complex system problem based on data learning, and the premise is to have high quality sample data. When the sample quality is poor, the model is difficult to achieve the expected effect. Therefore, this paper initially performs data preprocessing on the original dataset to create a designated data space.

3.1 Data Preprocessing

This paper utilizes the data captured from the icing monitoring system of Liuzhou Bureau in Guangxi, China over recent years as the main sample for analysis. By carefully selecting and accumulating representative samples of icing events, scholars can identify key trends and statistical patterns impacting the formation and mitigation of ice. Therefore, this study emphasizes the importance of utilizing credible and comprehensive data collection methods that are essential for producing reliable results in scientific research. Affected by natural factors and human factors such as equipment failure, there are inevitably problems in the data. The original sample data may contain issues such as feature redundancy, noisy data and outliers, which can hinder the training and learning process of the model. Therefore, this paper analyzes the acquired data from the following three perspectives.

(1) Data cleaning. Some icing data are inaccurate and incomplete, which deviates from the actual value. According to the actual characteristics of such abnormal dates, one commonly uses approach is to treat them as missing values and replace them with either mean value [11].

(2) Data conversion. In practical application, the dimensionality of different characteristic variables in the collected original sample data is different. Incorporating a significant amount of historical data directly into a prediction model may impact its ability to fit the data and result in failing to achieve the desired accuracy. In order to eliminate the influence of dimensions among indicators, StandardScaler is used to conduct Min-Max standardization of data [12], to preserve the relationship existing in the original data and make different features comparable.

(3) Data balance. The dataset is highly unbalanced, with approximately 785,420 samples having zero values and only 29,025 samples having non-zero values, resulting in a ratio of approximately 27 to 1. Unbalanced data is easy to introduce noise and inaccurate prediction results, leading to data quality degradation. In this paper, the RandomUnderSampler module of the imblearn library in Python3.11 is applied to subsample most samples [13] to solve the problem. In addition, Mean Filtering is used to process data [14] to realize noise reduction on continuous features.

3.2 Feature Generation

After the above data preprocessing, input variables have 7 dimensions, including temperature, humidity, wind direction, inclination angle, tension, icing growth rate, and wind deflection angle. The characteristic variable in the existing original data lacks the key factor of wind speed [15], so it is difficult to achieve high accuracy with existing variables. In this section, through the selection and extraction of features, factors with a high comprehensive correlation coefficient are selected as sensitive parameters to reduce the redundancy of input data.

Icing thickness is affected by a variety of factors. Most scholars take wind speed as an important variable [13]. In extreme weather conditions, strong winds can quickly dry tiny water droplets, reducing icing formation. On the contrary, when the wind speed is low, the water droplets stay on the surface of objects and tend to form ice. Therefore, wind speed is one of the important characteristics of icing thickness prediction. The formula for calculating wind speed is generally derived from the subsonic theory in meteorology. The calculation formula and parameters are shown in Eq. (1).

$$v = \frac{P * R}{T + 273.15} \tag{1}$$

where, V is the wind speed, P is the air pressure, T is the temperature, and R is the gas constant of the gas at a specific mass. The original sample characteristic variable of Liuzhou Bureau in Guangxi, China lacks this important variable, but it also meets the parameter requirements in the above formula. Therefore, this paper considers using characteristic variable to generate the variable wind speed.

3.3 Variable Correlation Analysis

Pearson correlation coefficient is a commonly used statistical index, which is used to quantify the degree of linear correlation between variables to avoid feature redundancy [12]. With variable X and Y Pearson correlation coefficient $r(X, Y)$ is the standard deviation of its covariance ratio, as shown in Eq. (2).

$$r(X, Y) = \frac{\mathrm{cov}(X, Y)}{\sigma_X \sigma_Y} \tag{2}$$

A correlation heat map is used to visualize the relationships between continuous and binary variables, with the Pearson correlation coefficient indicating the strength of the correlation. Variables with a strong correlation are removed from consideration in order to comprehensively analyze all relevant factors. Finally, the combined consideration of correlation strength and variable type is used to eliminate corresponding variables.

4 Icing Growth Model

4.1 Algorithm Principle

In this paper, nine classical machine learning algorithms are selected for model training and testing, and the results are compared. The algorithms mainly include Ridge (L2 regularization), Lasso (L1 regularization) and Elastic Net (L1 regularization + L2 regularization) in linear regression (LR) [16]. There are three kinds of decision tree (DT), K-Nearest Neighbor Regression (KNNR) and Support Vector Regression (SVR) in a single algorithm model [17]; gradient Boosting Regression (GBR), Random Forest (RF) and Adaptive Boosting (AdaBoost) are three kinds of ensemble learning models [18, 19].

4.2 Parameter Optimization

This paper employs the cross-validation technique to assess the performance of various machine learning models and determine the ideal hyperparameter configuration. Specifically, for each model, the researcher utilizes the GridSearchCV method to systematically explore the hyperparameter space and identify the optimal configuration.

4.3 Evaluation Indicators

In order to objectively evaluate each model, it is necessary to evaluate and compare the indicators of the model. This chapter involves evaluating and comparing three metrics, namely Mean Absolute Error (MAE), Mean Square Error (MSE), and Root Mean Square Error (RMSE). Assuming a sample size of N, the computation methods are given by Eqs. (3) to (5).

$$MAE = \frac{1}{m}\sum_{i=1}^{m}\left|\left(y_i - \hat{y}_i\right)\right| \tag{3}$$

$$MSE = \frac{1}{m}\sum_{i=1}^{m}\left(y_i - \hat{y}_i\right)^2 \tag{4}$$

$$\mathrm{RMSE} = \sqrt{\frac{1}{m}\sum_{i=1}^{m}\left(y_i - \hat{y}_i\right)^2} \tag{5}$$

5 Case Study

5.1 Original Online Monitoring Data

The data source of icing prediction is the historical icing data of Liuzhou Bureau in Guangxi, China mainly including the meteorological data of each monitoring tower. The data variables include OHTL name, tower number, phase, monitoring time, temperature, humidity, wind direction, tension, wind deflection angle, inclination angle, icing growth rate and icing thickness. The original sample data set is shown in Table 1. The original sample data collected includes thirteen characteristic variables and one response variable.

Table 1. The original sample data set

Characteristic/response variable	Category	Variable name
Characteristic variable	Meteorological data	Temperature
		Humidity
		Wind direction
		Monitoring time
		Inclination angle
		Pull
		Icing growth rate
		Wind deflection angle
	OHTL data	OHTL name
		Tower no
		Phase
	Monitoring data	Monitoring device model
Response variable	Icing thickness	

5.2 Data Processing and Analysis

In correlation analysis, some feature variables may be highly correlated with response variables, so it is necessary to eliminate variables with strong correlations. After selecting feature variables in the previous section, a correlation heatmap is plotted for continuous variables (temperature, tension, inclination angle, icing growth rate, wind speed, humidity, wind deflection angle and wind direction), as shown in Fig. 2.

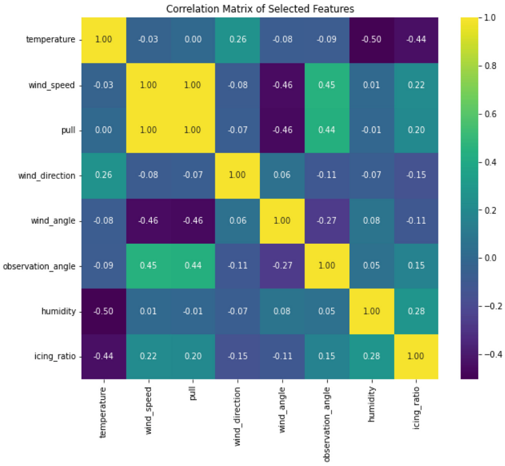

	temperature	wind_speed	pull	wind_direction	wind_angle	observation_angle	humidity	icing_ratio
temperature	1.00	-0.03	0.00	0.26	-0.08	-0.09	-0.50	-0.44
wind_speed	-0.03	1.00	1.00	-0.08	-0.46	0.45	0.01	0.22
pull	0.00	1.00	1.00	-0.07	-0.46	0.44	-0.01	0.20
wind_direction	0.26	-0.08	-0.07	1.00	0.06	-0.11	-0.07	-0.15
wind_angle	-0.08	-0.46	-0.46	0.06	1.00	-0.27	0.08	-0.11
observation_angle	-0.09	0.45	0.44	-0.11	-0.27	1.00	0.05	0.15
humidity	-0.50	0.01	-0.01	-0.07	0.08	0.05	1.00	0.28
icing_ratio	-0.44	0.22	0.20	-0.15	-0.11	0.15	0.28	1.00

Fig. 2. Variable heat map

From Fig. 2, it can be seen that tension shows a strong correlation with wind speed. Therefore, the variable tension is discarded, considering wind speed as the feature variable. Subsequently, an analysis is performed on the original sample data with seven feature variables remaining after removing strong correlation variables, as shown in the heat map of Fig. 3.

Fig. 3. Heat map after removing the strongly correlated variable

Feature Selection. Figure 4 is carried out by using random forest models to obtain the importance ranking of the seven descriptors through five repeated shuffles. Both wind speed and icing growth rate have correlation values with icing thickness. Wind deflection angle and temperature have similar correlation values of 0.42 and 0.46, respectively. Inclination angle, humidity and wind direction have weaker correlations. Consequently, this paper selects seven prioritized features, namely icing growth rate, wind speed, inclination angle, humidity, wind deflection angle and wind direction. With these seven feature variables selected as input, the model for predicting the icing thickness is established.

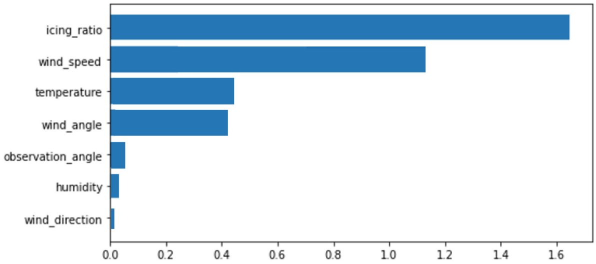

Fig. 4. Permutation importance of characteristic variables

5.3 Optimal Model Selection

Algorithm Selection. Based on the actual data of samples in Liuzhou Bureau in Guangxi, China, 5787 data points from the 2020–2021 period are used as training set. By training and optimizing the parameters of three linear models, this study obtained a preliminary comparison of predictive performance, as shown in Table 2.

Table 2. Preliminary comparison

Algorithm	Best_params	MSE	MAE	R^2
Ridge	{‘max_depth’: 15, ‘min_samples_split’: 2}	0.04687	0.16413	0.0786
Lasso	{‘learning_rate’: 0.1, ‘max_depth’: 5, ‘n_estimators’: 200}	0.23784	0.37742	0.01614
ENet	{‘max_depth’: 15, ‘min_samples_split’: 2, ‘n_estimators’: 200}	0.23780	0.37739	0.01528
SVR	{‘C’: 100, ‘epsilon’: 0.01, ‘gamma’: 0.1}	0.04819	0.15605	0.79252

Table 2 shows that compared with SVR, all three linear models performed poorly. Therefore, linear regression models are not suitable for predicting icing thickness. All three linear regression algorithms were deleted, and hyperparameters were optimized for the remaining six algorithms using k-fold cross-validation. The optimal parameters for each algorithm are shown in Table 3.

Table 3. The optimal parameters

Algorithm	Best_params
DT	{‘learning_rate’: 1, ‘n_estimators’: 200}
GBR	{‘n_neighbors’: 3, ‘weights’: ‘distance’}
RF	{‘C’: 10, ‘gamma’: ‘scale’, ‘kernel’: ‘rbf’}
KNNR	{‘activation’: ‘relu’, ‘alpha’: 0.001, ‘hidden_layer_sizes’: (150,), ‘solver’: ‘adam’}
SVR	{‘C’: 100, ‘epsilon’: 0.01, ‘gamma’: 0.1}
AdaBoost	{‘learning_rate’: 1, ‘loss’: ‘square’, ‘n_estimators’: 200}

Model Performance. Considering the practical application scenarios and the need to verify the generalization performance of the model, the trained model was applied to 52,725 data points from the 2021–2022 period to validate the model’s predictive performance. At the same time, to prove the superiority of our model, we extracted OHTL data with severe damage for prediction. First, we verified the performance of the six models on the 500 kV Guishan-B Transmission Line, which has the most complex situation. The basic information of the line is shown in Table 4.

Table 4. Basic information

OHTL name	Tower number	Phase	Start time	End time	Data
500 kV Guishan-B transmission line	56#	Optical cable	2022/1/30	2022/2/23	3939

The prediction set firstly selected 500 kV Guishan-B Transmission Line, with a period from January 3, 2022 to February 23, 2022, and a total of 3939 data points. From the comparison graph of predicted and actual values for the six models shown in Fig. 5, we can see that DT, GBR, RF, and AdaBoost algorithms fit well with the actual values, while KNNR and SVR have poor predictive performance. To present prediction errors and accuracy more accurately and intuitively, Fig. 6 shows a comparison of evaluation indicators for all algorithms. It is clear from Fig. 6 that compared with other algorithms, the evaluation indicators of DT, GBR, RF, and AdaBoost algorithms are relatively small, indicating that the deviation between predictions and actual values is small.

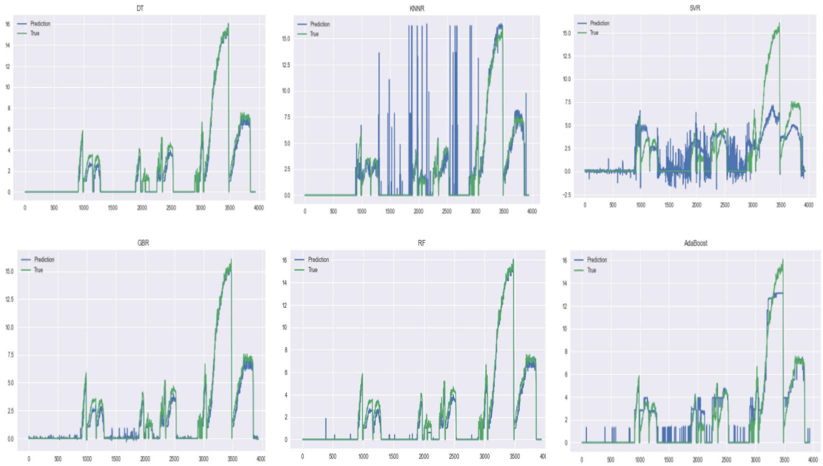

Fig. 5. Actual value and predicted value comparison

Generalization Study. To test the generalization ability of the model, the six algorithms are applied to the ±500 kV Niucong-B Transmission Line and 500 kV Huanrujia-A Transmission Line. The evaluation indicators of DT, GBR, RF, AdaBoost, KNNR, and SVR are compared, as shown in Figs. 7 and 8. It can be summarized from the figures that the conclusions drawn from the 500 kV Guishan-B Transmission Line are basically

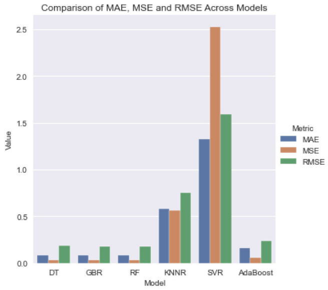

Fig. 6. Model evaluation index

applicable to other OHTLs. Among the six models, DT, GBR, RF, and AdaBoost algorithms achieve better predictive performance, indicating that the optimal model has good generality.

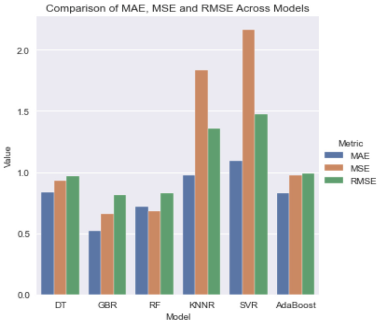

Fig. 7. DC line evaluation index comparison

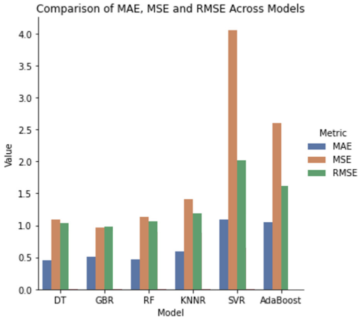

Fig. 8. AC line evaluation index comparison

6 Conclusion

This paper proposes a method for establishing an icing growth model during ice disaster and utilizing online monitoring data to predict ice thickness. The data are preprocessed, and the correlation of variables are analyzed to improve the quality of input. To ensure the accuracy and reliability of the selected model, we comprehensively consider indicators such as MAE, MSE, and RMSE, and selecting the optimal model based on multiple machine learning algorithms. Through case analysis, we predict the icing thickness at 500 kV Guishan-B Transmission Line and obtain good results with DT, GBR, RF and AdaBoost algorithms. Furthermore, we validate the universality of the four optimal models on other datasets such as the ±500 kV Niucong-B Transmission Line and 500 kV Huanrujia-A Transmission Line. The model proposed in this paper does not specifically consider the mechanism of actual icing process, and physical models can be introduced in the future to establish even more accurate predictive models that combine measured data with physical mechanisms. In the future, by combining machine learning algorithms with physical models and utilizing the dual feedback of data-driven and physical mechanisms, scientists can achieve more accurate and comprehensive predictive models in the future.

Acknowledgments. This work is supported by Central Southern China Electric Power Design Institute Co., Ltd. of China project 40-1A-KY202219-D102.

References

1. Heyun, L., Zhou, D., Fu, J., et al.: Heat transfer research on preventing critical current of conductor icing[J]. Electr. Power **34**(3), 42–44 (2001)
2. Xinbo, H., Lisha, O., Yana, W., et al.: Analysis of key influencing factors for overhead line icing[J]. High Voltage Eng. **37**(7), 1677–1682 (2011)
3. Imai, I.: Studies of ice accretion[J]. Res. Snow Ice **1**(3), 35–44 (1983)
4. Goodwin, E.J., et al.: Predicting ice and snow loads for transmission lines[C]. The 1st International Workshop on Atmospheric Icing of Structures pp. 267–273 (1983)
5. Makkonen, L.: Modeling power line icing in freezing precipitation[J]. Atmos. Res. **46**(1–2), 131–142 (1998)
6. Li, X., Zhang, X., Liu, J., Hu, J.: AMPSO-BP neural network prediction model for conductor icing in transmission lines[J]. Electr. Power Constr. **42**(09), 140–146 (2021)
7. He, L., Luo, J., Zhou, X.: A novel deep learning model for transmission line icing thickness prediction[C]. 2021 IEEE 5th Advanced Information Technology, Electronic and Automation Control Conference(IAEAC), vol. 5, pp. 733–738. IEEE, (2021)
8. Xiangdong, D., Huazhengwei, Z., et al.: Construction and application research of overhead line icing prediction model based on improved QFA-LSSVM[J]. Microcomput. Appl. **37**(01), 29–32 (2021)
9. Tong, Y., Yingna, L.: SSA-BiGRU overhead line icing growth prediction model guided by physics[J]. Electr. Power Sci. Eng. **38**(02), 28–36 (2022)
10. Xingliang, J., Fangyi, J., Quanlin, W., et al.: Prediction of overhead line icing caused by fog based on the optimal time step model[J]. Trans. China Electrotechnical Soc. **33**(18), 4408–4418 (2018)
11. Hui, H., Hao, G., Xiang, X., et al.: Prediction and evaluation of user power outage area under typhoon disaster[J]. Power Syst. Technol. **43**(06), 1948–1954 (2019)

12. Tianzhu, Y., Zhiping, Y.: Distribution network safety protection technology[M]. China Electric Power Press, Beijing (2015)
13. Zhang, W., Sheng, W., Du, S., et al.: Architecture and technical implementation of distribution network operation analysis system based on massive data[J]. Autom. Electr. Power Syst. **44**(03), 147–155 (2020)
14. Sheng, S., Jinfu, C., Xianzhong, D.: A review of mutual influence between global warming and power system[J]. Power Syst. Technol. **34**(02), 33–40 (2010)
15. Huang, X., Li, J.: Icing thickness prediction model using BP neural network[C]. 2012 International Conference on Condition Monitoring and Diagnosis (CMD), pp. 758–760. IEEE, (2012)
16. Bin, Z., Lingling, P., Yang, Z., et al.: Calculation of fault probability of overhead line icing considering de-icing factors[J]. Power Syst. Prot. Control **43**(10), 79–84 (2015)
17. Li, Z.: Research on the mechanism and prevention strategy of overhead line icing growth[D]. Harbin Institute of Technology, (2020)
18. Guote, L., Yanpeng, H., Lin, Y., et al.: Calculation of critical current for conductor anti-icing based on improved Messinger icing model and analysis of influencing factors[J]. Trans. China Electrotechnical Soc. **31**(18), 176–183 (2016)
19. Hui, Y., Jingjing, W.: Study on overhead line icing and micro-meteorological parameters and icing time[J]. High Voltage Apparatus **53**(12), 145–150 (2017)

Research on the Deployment Strategy of a Ring Sparse Array Camera Applied to Real-Time Scene Fusion of Digital Twins

Ziqian Zhang(✉), Shengsheng Li, Qingqiang Meng, Kang Shi, and Yunbo She

Nanjing NARI Information and Communication Technology Co., Ltd., Nanjing 211106, China
zhangziqian@sgepri.sgcc.com.cn

Abstract. A deployment strategy for a ring sparse array camera applied to digital twin real-time scene fusion is proposed to address the challenges of virtual and physical data synchronization and consistency in power grid equipment. Faced with the current situation of numerous components, diverse shapes, and complex occlusion relationships in power grid equipment, the optimization goal is to use the minimum number of cameras to cover the target area and synthesize any freely viewed synthetic image. The strategy described in this paper can improve the accuracy, fidelity and real-time of image acquisition while reducing the number of cameras to control the cost of image acquisition, thus breaking through the key difficulties of real-time replication and fusion of the main transmission and transformation equipment scene, promoting the mutual supplement of spatial data and live data, and strengthening the real-time perception and response capability of the physical state, Breaking the current low-level visualization application status of the digital twin "3D modeling, data hooking, and 3D display" in the power grid.

Keywords: Digital twin · Power system · Sparse camera array · Image synthesis technology · Multiple visual images

1 Introduction

The concept of digital twins originated in the United States and was first proposed by Professor Michael Grievous of the University of Michigan. It was initially named the "Information Mirror Model" and later evolved into the "Digital Twin". In the context of Industry 4.0, which focuses on digitization, networking, and intelligence, the concept of digital twins deeply integrating new generation information technology and digital models has attracted attention from both industry and academia. Simulation makes it possible to optimize physical entity in virtual space with high efficiency and low cost. The three-dimensional model in digital twins is a digital representation of the three-dimensional structure and appearance of natural and artificial entities in the physical world. It serves as the spatial foundation and unified spatial positioning framework and analysis basis for digital twins. Real time data used to perceive the real-time state of the physical world can compensate for the lack of realism in three-dimensional models, adding important real-time visual perception capabilities to digital twins, It greatly enhances people's perception and cognitive abilities towards complex scenes.

Y. Xue et al. (Eds.): PMF 2023, LNEE 1129, pp. 287–297, 2024.
https://doi.org/10.1007/978-981-99-9251-5_23

The requirements of power grid resources for information construction are also increasing synchronously, which requires the power grid to adapt to the development and improvement of new generation virtual reality technology, to quickly respond to changes in new demands and business expansion. Currently, the state perception and analysis technology of power transmission and transformation equipment is rapidly developing towards intelligence, and new technologies are constantly emerging, effectively improving the level of equipment intelligence. With the introduction of emerging machine learning technologies such as deep learning and reinforcement learning, the deep feature extraction and application capabilities of multidimensional heterogeneous data have been strengthened, greatly improving the efficiency of data analysis, and making it possible to construct complex digital twins of transmission and transformation equipment. In the power grid, digital twinning is not only about the perception of numbers, but also needs to reduce modeling costs through technologies and methods such as camera parameter calibration, free angle synthesis, virtual real fusion, Shadow Map algorithm, etc. It is still in its early stages in the power grid.

2 Analysis of Real-Time Scene Requirements for Digital Twins

The digital twin power grid needs to combine existing platforms and technological means to support the digitization of the power grid. At present, the landing application of digital twin technology in the Mechanical floor mainly focuses on the virtual model reconstruction and autonomous state management of power grid equipment. The 3D virtual reconstruction of power grid equipment is generally based on a variety of 3D data acquisition equipment, which measures the appearance of power equipment such as substations, towers, insulator strings, foundations, spacers, and shock absorbers. Then, various 3D model construction techniques are used to construct the 3D power grid equipment. Finally, the results are optimized through operations such as dynamic wire index creation or LOD processing. For example, the digital mirror evaluation system of Shanghai 35 kV Cailun Substation [1] established a digital twin model of the equipment inside the substation, and inputted real-time collected data from front-end sensors (such as real-time load, current, oil chromatogram, etc.) and historical data (such as historical sensor collection data, defect data, maintenance frequency, etc.) into the model to analyze the equipment operation status; The substation holographic model of Tianjin 110 kV Youle Port Intelligent Substation [2] forms a virtual spatial digital twin model by comprehensively collecting and updating IoT perception information and cloud lifetime information in real-time. The implementation and application of digital twin technology in the power grid layer mainly focus on online analysis and decision-making of the power grid. For example, the D5000 platform of Hunan Provincial Dispatch adds a power grid analysis model composed of physical and computational models, inputs real-time power grid measurement information collected by SCADA into the physical model [3], and relies on the computational model for state estimation calculation, Conduct power grid security and stability assessment based on real-time analysis models (physical and mathematical models).

In the process of achieving digital twins, static 3D models cannot reflect the limitations of scene reality, while real-time video is a widely used real-life data. Due to its simple deployment, low cost, and large perception range, it has become the most core perception data in current smart city construction. The two-dimensional video monitoring method is not conducive to controlling the overall situation of the monitoring video and the monitoring scene from a macro perspective. Therefore, many applications integrate videos as multimedia attribute data of 3D models. Italian scholars Navarrete and Blat, in their VideoGIS project [4], were the first to combine video images with geographical information to generate hyper video that can be called in the geographical environment. Korean scholars proposed to use video metadata to describe geographical locations [5], so that maps and video images can reference each other, and support the interactive operation between GIS and video images. The integration method of the above video and 3D model is relatively simple, and the 3D model and video are simply mounted. The video data is only used as attribute information of the 3D model and can only be used for low-level visualization applications. Only by deeply integrating video and 3D environment, combining static virtual 3D scenes with real-time dynamic 2D live videos, and strengthening coupling analysis with geographic environment, can the spatiotemporal attributes of surveillance videos be truly effectively utilized and application levels be improved. In power grid applications, by integrating live videos with 3D models, frequent updates of 3D models can be avoided, and the spatiotemporal relationship between digital models and power grid system entities can be fully explored for deeper applications.

The fusion modeling of video and virtual 3D scenes is mainly divided into two types: enhanced virtual environment and augmented reality. Augmented reality technology integrates virtual scenes into real videos, while augmented virtual environment technology embeds real videos into three-dimensional space. The key technology of augmented reality technology lies in the real-time superposition of virtual information on real scenes and the dynamic interaction between users and virtual information. With the help of intuitive and efficient human-computer interaction and the rich information that can be supplemented in real application scenarios, augmented reality technology has been integrated into the research of geographic data augmentation expression since the beginning of the last century, providing a 3D GIS visualization environment that seamlessly integrates with the real environment. Although the enhanced virtual environment supports the fusion of multiple videos and 3D scenes, it can easily lead to serious fusion deformation when there is a significant difference between the observation and projection perspectives. To ensure visual effects, the user's viewpoint is limited to pre-set viewpoints or roaming paths.

To overcome this limitation, free view synthesis technology provides the ability to synthesize scene views at any position in three-dimensional space. The "360-degree free view observation" technology for the Winter Olympics is a model of its successful application. By using a circular camera array, users can freely roam, and any virtual perspective video can be synthesized from a series of nearby camera videos. However, due to limitations such as sampling rate and image structure, there are often artifacts, voids, and other situations. In order to eliminate voids and occlusion errors in synthesized images, multiple camera video interpolation can be used for patching, but a densely deployed camera array scheme is required, which brings high cost, low efficiency, and heavy implementation workload.

Based on the above analysis, in order to achieve controllable cost and effect of automatic matching between real scene data and 3D scenes and eliminate the deformation problem during the fusion of video and 3D scenes, it is necessary to further develop a deployment strategy for circular sparse array cameras. This article will establish a mapping relationship between image/video space and geographic space by solving the internal and external parameters of the camera; Collect multi angle real-life images of a certain power grid device in the target area as sample images; Based on the collected sample images and the established mapping relationship, perform free view image synthesis based on light field reconstruction and free view image synthesis based on depth information to obtain multiple free view synthesized images; The optimization objective is to use the minimum number of cameras to cover the target area and synthesize any freely viewed synthesized image. The deployment optimization model of the circular camera array is solved to obtain the deployment results of the circular camera array.

3 Deployment Strategy for Circular Sparse Array Cameras

3.1 Virtual Real Fusion Method for Real Video and Free View Images

Camera parameter calibration

The prerequisite for accurate fusion of scene videos is to establish the correct geometric consistency relationship between the video data collected by the camera and the virtual 3D scene. Accurate camera parameters are required to establish the mathematical relationship between the three-dimensional geometric positions of spatial target surface points in the real world and the corresponding points in the image. The process of solving camera mapping parameters is called camera calibration, which includes internal and external orientation parameters. At present, the main methods for camera calibration can be divided into traditional calibration methods, active vision-based methods, and self-calibration methods. Traditional calibration methods require specific calibration objects, and common methods include DLT, Tsai, and Zhang Zhengyou's method [6]. Traditional calibration methods are relatively mature and have high calibration accuracy, which have been widely used. However, the process is time-consuming and laborious, and cannot be used for online calibration and situations where calibration objects cannot be used. The method based on active vision can obtain accurate 3D information without the use of standard reference objects. It only obtains an image sequence by controlling the motion of the turntable where the camera is installed. After matching the image sequence, certain constraint relationships are obtained to calculate parameters. However, this method cannot be used in situations where the camera motion is unknown or uncontrollable, and it requires a high precision and cost for the motion platform. The self-calibration method does not require a specific control field, and often relies on the relationship between the corresponding points of multiple images to directly calculate camera parameters. That is, using the opposite polar geometric relationship between identical image points obtained from different angles (i.e., the same image points are coplanar) to calculate the internal and external parameters of the camera. The self-calibration method is flexible to use, but the calibration accuracy is generally lower than traditional calibration methods. The basic idea is to first establish a constraint equation about the camera's internal parameter matrix through an absolute quadratic curve, called the Kruppa equation. Then, by solving the Kruppa equation, the matrix C (C = $K^{-T}K^{-1}$, where K is the camera's internal parameter matrix) is determined. Finally, the matrix K is obtained through Cholesky decomposition.

Virtual Real Fusion Method

The automatic projection method generally draws inspiration from real-time shadow algorithms, represented by the Shadow Map algorithm [7, 8]. The Shadow Map algorithm has the characteristics of simple computation and hardware friendliness, but due to issues with shadow sampling accuracy, the fusion area is prone to aliasing problems such as jitter and aliasing. The optimization ideas for such fusion quality issues can be divided into improving depth map accuracy and optimizing depth sampling. There are methods to improve the accuracy of depth maps, such as using multi resolution depth maps and changing projection methods. The optimization of deep sampling is mainly solved through various filtering methods.

In addition to aliasing issues, fusion deformation and video overlap also have a significant impact on fusion quality. Fusion deformation mainly includes the distortion effect of the video itself and the projection deformation generated by dynamic targets such as people and cars in the video. Video distortion refers to the deviation phenomenon caused by the camera projecting straight lines, which is often caused by defects in the camera lens itself, as well as intentional situations such as fisheye cameras or wide-angle cameras. After distortion is generated, it will cause the straight lines in the original image to bend, causing the fusion area to shift. This can be reduced or eliminated by introducing a distortion model. For projection deformation caused by moving targets, it can be indirectly eliminated by detecting and extracting the moving targets, estimating the depth of the moving targets, and constructing a bulletin board map. The most direct approach to address the issue of multiple videos simultaneously covering the same area and reducing fusion quality is to divide the coverage area again based on the camera spatial relationship to solve the problem of multiple cameras being visible in the same area at the same time. Although this method avoids the problem of video mixed coloring, it has significant limitations. Multi texture mixing is another commonly used method, and the key to this method is how to determine the optimal mixing coefficient and solve the problem of rendering efficiency.

Virtual and Real Integration Operating Environment

The combination of virtual reality fusion technology and network technology can further expand its application. In the early network environment, the application of virtual and real fusion adopted a dedicated client mode, which had requirements for both software and hardware, limited usage, and could not meet the growing demand for virtual and real fusion. With the rapid development of web technology, the advantages of simple web deployment, low client configuration requirements, and multiuser sharing have become prominent. The development of web-based virtual reality fusion technology has become a practical requirement.

The current virtual reality integration can be divided into client mode, server mode and mixed mode according to the network structure. The idea of the client mode is to treat the server as a pure data source and entrust the fusion rendering to the client for processing. Its development has undergone improvements from plugins to plugins free. The early solution for Web 3D [9] was based on plugin methods, which lacked cross platform capabilities and relied on specific plugins and browsers, resulting in poor compatibility. Browser plugins have hidden dangers that endanger user network security, stability, and performance, and their increased code complexity can also easily lead to vulnerabilities. With the popularization of the HTML5 standard, using WebGL API [10] can achieve high-performance interactive 3D and 2D graphics rendering in any compatible browser, quickly replacing plugin technology, and being widely used. The server-side mode is similar to remote rendering technology, which renders and outputs images or videos on the server side, and then pushes them to the client for display. The remote rendering method has a high transmission volume and requires high network bandwidth. Due to the need for strong computing power on the server to complete the fusion work by accessing videos on the server, it can easily become a performance bottleneck in multi-user and multi-video scenarios, meanwhile it is generally limited to small-scale applications.

The hybrid mode is a new virtual reality fusion network expression method. This method constructs a fusion template to decouple the fusion process, balances the computing tasks of the server and the client, and has good network performance.

3.2 Steps for Solving the Optimization Model of Circular Camera Array Deployment

Establishing a mapping relationship between image/video space and geographic space

For three-dimensional scenes with two-dimensional planes, the homography matrix H solution [11] is used to calibrate the internal and external parameters of the camera; For three-dimensional scenes without two-dimensional planes, the camera's internal and external parameters are self-calibrated by utilizing the special geometric structure in the scene and utilizing the invariance of specific geometric information in perspective projection to establish constraints on the camera's internal and external parameters; For scenarios where the special geometric structure required for self-calibration cannot be obtained, the checkerboard method is first used for internal parameter calibration; Then, manual point extraction or image matching methods are used to obtain control point pairs to calculate the external parameters of the camera. When there are more than 4 corresponding control points, the least squares method is used to solve the homography matrix H. The mapping relationship between the image/video space and geographic space is expressed using the following expression:

$$\lambda_1 = \frac{D}{f_D} \tag{1}$$

$$\lambda_2 = \frac{H_C - H_G}{-f \sin T + y \cos T} \tag{2}$$

$$\lambda_3 = \frac{[(X_G - X_C)\cos P + (Y_G - Y_C)\sin P]\cos T - (H_G - H_C)\sin T}{f} \tag{3}$$

In the formula: λ_1, λ_2, λ_3, represent the transformation coefficients of camera space and geographic space coordinate mapping; f_D represents image distance; D represents object distance; P represents the horizontal azimuth angle of the camera; T represents the camera pitch angle; F represents the focal length of the camera; (XC, YC, HC) represents the camera spatial coordinates; (XG, YG, HG) represents geographic spatial coordinates; (x, y, z) represents the coordinates of the pixel.

Free view image synthesis based on light field reconstruction

The scene is modeled using a differentiable volume rendering formula, and the color of the light is approximated by integrating multiple sample images collected along the light. The calculation process is as follows:

$$C(r) = \sum_{i=1}^{N} T_i(1 - \exp(-\sigma_i\delta_i))c_i \tag{4}$$

$$T_i = \exp\left(-\sum_{j=1}^{i-1}\sigma_j\delta_j\right) \tag{5}$$

In formulas above, C(r) represents the luminous flux, which is obtained by summing each monochromatic light; N represents the number of sampled ray samples; T_i represents the number of light transmitted by ray sample I; σ_i represents the opacity of ray sample I; c_i represents the color of ray sample I; δ_i represents the sampling ray distance.

Optimization of light field reconstruction

Rebuild a sparse voxel table, with each occupied voxel having opacity and spherical harmonic coefficients. By minimizing the mean square error MSE of rendered pixels, optimizing the opacity and spherical harmonic coefficient of voxels, and using TV regularization to help eliminate noise, the calculation process is as follows:

$$\zeta = \zeta_{recon} + \lambda_{TV}\zeta_{TV} \tag{6}$$

$$\zeta_{recon} = \frac{1}{|R|}\sum_{r\in R}\|C(r) - C(r)\|_2^2 \tag{7}$$

$$\zeta_{TV} = \frac{1}{|V|}\sum_{v\in V}\sqrt{\Delta_x^2(v,d) + \Delta_y^2(v,d) + \Delta_z^2(v,d)} \tag{8}$$

In formulas above, ζ_{recon} represents MSE reconstruction losses; ζ_{TV} represents total variable regularization; λ_{TV} is the eigenvalues of the ζ_{TV} matrix; λ_{TV}^{-1} is the inverse matrix of λ_{TV}; R represents the total number of samples collected in the video, v and d represent the opacity and color of the pixel space; Δ_x, Δ_y, Δ_z are the deviations between the values and the average values in the X, Y, and Z directions in the virtual 3D pixel coordinate system. V represents the observed sample in a virtual 3D pixel.

Free View Image Synthesis Based on Depth Information

The reference viewpoint is selected from the sample image, and each pixel on the reference viewpoint is projected into the three-dimensional space using its corresponding depth information and the parameter matrix of the reference camera. According to the parameter matrix of the virtual camera, the points in three-dimensional space are re projected onto the near plane of the virtual camera, and the pixel coordinates of any pixel on the reference viewpoint to the virtual view are solved to obtain the virtual viewpoint image.

After performing free view image synthesis based on depth information, color brightness correction is performed by histogram matching and color space transformation to eliminate artifacts. The Z-buffer blanking algorithm [12] is used to process the virtual viewpoint image to eliminate the overlapping area.

For simplicity, it is assumed that the position of the free view virtual camera is also in the annular space, and when the image overlap rate of adjacent cameras exceeds a certain threshold, the free view image can be synthesized.

For all camera sets $\mathbb{C} = \{C_1, C_2, \ldots, C_n\}$ that can be placed in the annular space, n represents the number of cameras that can be placed, where any camera $C_j\left(C_j \in \mathbb{C}\right)$ is available.

$C_j\left[location\left(X_j, Y_j, H_j\right), posture\left(P_j, T_j\right), inner\left(Size, f_j\right)\right]$ means that if the internal parameters are known, it can be determined by the five parameters of $\left(X_j, Y_j, H_j, P_j, T_j\right)$. The camera parameter space is a continuous five-dimensional space, and the candidate cameras will be obtained in this five-dimensional space by sampling to form a set $\mathbb{C}$.

The target area contains numerous spatial points. To improve the efficiency of optimal deployment, the target area is sampled into a limited number of spatial points to form a set $\mathbb{G} = \{G_1, G_2, \ldots, G_m\}$, where m is the number of sampling spatial points. Mark any point $G_j\left(G_j \in \mathbb{G}\right)$ in the target area covered by the camera C_j as $cover_{c_j}(G_i)$, and $cover_{c_j}$ represents the set of points covered by the camera C_j.

Select subset $\mathbb{C}'\left(\mathbb{C}' \subseteq \mathbb{C}\right)$ of the set of cameras to be placed in the annular space where cameras can be placed, so that the cameras in $\mathbb{C}'$ can cover the set of spatial points in the target area after sampling. Under the condition of ensuring that the overlap rate of adjacent camera images is greater than the threshold γ, the total number of cameras is the least.

Thus, the optimization model of circular array camera deployment can be expressed as the following expression, where $F(\mathbb{C}')$ is the objective function, $card(*)$ is the number of cameras (the same below), and C_S and C_t are the two cameras of $\mathbb{C}'$ in the subset; $C_S.location$ and $C_t.location$ indicates the erection position of cameras C_S and C_t respectively; $overlay\left(C_i, C_j\right)$ is the overlap rate of two cameras C_i and C_j.

$$\min_{\mathbb{C}'} F\left(\mathbb{C}'\right) = card\left(\mathbb{C}'\right), \mathbb{C}' \subseteq \mathbb{C} \tag{9}$$

$$s.t\ \forall G_i \in \mathbb{G}, \exists C_j \in \mathbb{C}', cover_{c_j}(G_i) = 1 \tag{10}$$

$$\forall C_s, C_t \in \mathbb{C}', C_s.location \neq C_t.location \tag{11}$$

$$\forall C_i \in \mathbb{C}', overlay\left(C_i, C_j\right) > \gamma \tag{12}$$

The meaning of this formula is as follows:

Equation (9) is the target: Select a subset $\mathbb{C}'$ from candidate camera set $\mathbb{C}$ to minimize the number of elements in $\mathbb{C}'$;

Equation (10) represents constraint condition 1: All spatial points are covered by at least one camera in $\mathbb{C}'$;

Equation (11) represents constraint condition 2: Only one camera can be installed at the same location.

Equation (12) represents constraint condition 3: The overlap rate of adjacent camera images is greater than the threshold γ.

4 Application and Verification

According to the deployment strategy of the ring sparse array camera described in the article, an experiment was conducted on the real-time scene fusion of power grid digital twins for a Class II substation in a certain area. There are a total of 13 Class II substations in this area. 283 remote signaling and telemetry equipment are deployed in Class II substation in the form of Normal distribution.

To test the advantages of the above data fusion strategy in reducing the number of cameras to control the cost of image acquisition, and to achieve the accuracy, fidelity and real-time of video data, the main tracking indicators are: (1) whether the grid equipment and surrounding environment can be correctly identified; (2) Video texture based on feature point reference image; (3) Service side efficient cache and back-end content generation module speed.

According to the steps and strategies described in this paper, data fusion is carried out under the established components. The results show that the data fusion video generated by this step and strategy (Fig. 1) can solve the integration problem between the facilities and the surrounding environment, and can meet the actual production and operation needs.

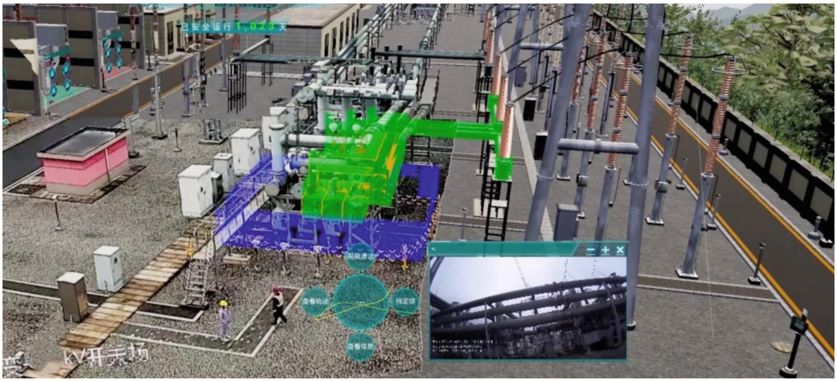

Fig. 1. Video screenshot of digital twin data fusion effect

In terms of fusion efficiency, the data fusion strategy established in this paper can achieve efficient data fusion on the whole. In strict compliance with the requirements and principles of data fusion, the individual characteristics of substation equipment and its ancillary facilities are handled differently. The specific processing parameters are shown in Table 1.

Table 1. Imaging related data based on data fusion strategy

Cycle times	Rendering accuracy	Fusion time(s)
1	0.29	0.27
50	0.11	1.8
200	0.08	3.4
500	0.05	4.3
1000	0.02	5.2

Using Intel i7 12th generation processor for calculation, the fusion time is about 5s. With high accuracy and efficiency, it can meet the needs of engineering applications and effectively support the operation and maintenance of power grid, project construction and early decision-making.

Compared with the existing technology, the operation steps described in this paper can ensure that the sparse camera array can effectively reduce the number of cameras, achieve instantaneous capture of the target during 3D acquisition, save time cost and ensure that the camera cost is controllable; At the same time, free view image synthesis based on light field reconstruction and depth information can effectively improve the accuracy and fidelity of real scene image acquisition, and help to eliminate the deformation problem of virtual and real fusion of video and 3D scene.

5 Conclusion

The construction method and key technologies of digital twin scenes for power transmission and transformation main equipment based on ring sparse camera array real scene replication technology are still the first research in China, and the scientific research results are still in a blank. The circular sparse camera array real scene replication technology studied in this article helps to break the low-level visualization application level of the current digital twin “3D modeling, data hooking, and 3D display” in the power grid. By optimizing the deployment model of the circular camera array, introducing the minimum number of cameras to cover the target area, synthesizing free view images based on light field reconstruction and depth information, multiple free view synthesized images are obtained to compensate for the lack of realism in 3D models. Automatic matching and fusion of real-life data with 3D scenes, achieving true “landing” of 2D real-life videos/images. Construct a bidirectional correlation closed loop between image space, physical space, and virtual space, strengthen the real-time perception and response capabilities of entity states, and better meet the intelligent perception interaction needs of “human machine object” and the goal of “twin synchronization” in the power grid.

References

1. Yin, H., Wang, L., Xiong, J., et al.: Method and System for Status Diagnosis of Substation Automation Equipment Based on Digital Mirroring: CN202210022507.1 [P] 2022. 2nd edn. Publisher, Location (1999)
2. Li, G., Tang, S., Zhang, H., et al.: Research and application of intelligent fault diagnosis system for substation panoramic holography based on big data analysis [J]. Electr World (23), 2 (2019)
3. Hu, G.: Debugging plan for SCADA system of D5000 dispatching platform [J]. Electr. Technol.: Second Half Month (6), 2 (2015)
4. Navarrete, T., Blat, J.: VideoGIS: Segmenting and Indexing Video Based on Geographic Information (2011)
5. Chong, W.K., Naganathan, H., Liu, H., Ariaratnam, S., Kim, J.: Understanding infrastructure resiliency in Chennai, India using Twitter's geotags and texts: a preliminary study[J]. Eng. (English) **004**(002), 54–59 (2018)
6. Wang, J., Hou, Z.: Automatic calibration method for traditional camera calibration methods [J]. Comput. Eng. Appl. **46**(35), 4 (2010)
7. Li, L., Zou, Z.: Real time shadow rendering algorithm based on image and geometric space [J]. Comput. Appl. Softw. **25**(6), 3 (2008)
8. Zhang, F., Xu, L., Tao, C., et al.: Generalized linear perspective shadow map reparameterization [C]. Vrcia Acm International Conference on Virtual Reality Continuum & Its Applications, p. 339. DBLP, (2006)
9. Chittaro, L., Ranon, R.: Web3D technologies in learning, education and training[J]. Comput. Educ. **49**(1), 3–18 (2007)
10. Dovgiy, S.O., Ostapenko, A.O., Bulanchuk, G.G.: Viscous fluid flow modeling with the lattice boltzmann method on graphics processors using WebGL API[J] (2021)
11. Liang, L., Pu, J., Dong, Y., et al.: A Calculation Method for the Homography Matrix H of a Single Line Array Camera
12. Zhou, C.: Research and Implementation of a Z-buffer hidden algorithm [J]. Comput. Aided Eng. **11**(4), 6 (2002)

Research on a Method for Automatically Generating Single Line Maps in Distribution Network GIS

Wei Xiaojing[1], Fan Pengzhan[1], Liu Hu[1], Du Junchao[1], and Cheng Wei[2](✉)

[1] State Grid Corporation of China, Beijing 100031, China
[2] Nanjing NARI Information and Communication Technology Co., Ltd., Nanjing 211106, China
Chengwei5@sgepri.sgcc.com.cn

Abstract. The scale of power grid equipment, the number of power customers and the complexity of grid structure in China are among the highest in the world. In addition, the rapid change of power grid and the frequent transformation of equipment make the automatic generation of single line diagram, especially the single line diagram of distribution network GIS, increasingly difficult. The traditional manual drawing method has the disadvantages of heavy workload, low efficiency and uncontrolled accuracy. At the same time, due to the influence of human drawing habits, the readability of the finished product is low, which cannot meet the requirements of the increasingly updated power grid for its own maintenance and management. In this paper, a specific algorithm is used to determine the flatness of the original drawing, realize orthogonal mapping, and flatten the complex electrical wiring information. Finally, the experimental results show that the algorithm can realize the decoupling of complex wiring diagram, and significantly improve the mapping efficiency and accuracy.

Keywords: Distribution network · Single line diagram · Flatness determination

1 Introduction

With the development of power grid technology, the interaction of various information flows and energy flows increases the difficulty of automatic mapping, and it is difficult to achieve high accuracy. The traditional single line diagram of distribution network is mainly drawn by manual. Although manual drawing has strong controllability and high flexibility, its efficiency is low, the drawing is slow and the drawing style is not uniform, and the readability is not strong. Usually, the single line drawing of distribution network is drawn by CAD, which is off-line and cannot be updated in real time. However, the current power grid is often faced with transformation and new construction, and the change frequency and scale are large, which requires a lot of energy, and the accuracy is greatly affected by the psychology and habits of the rendering personnel, which brings certain difficulties to the daily operation and maintenance of the distribution grid. The accuracy and legibility of the drawings obtained by the maintenance personnel largely determine the progress of the accident treatment [1, 2].

Y. Xue et al. (Eds.): PMF 2023, LNEE 1129, pp. 298–307, 2024.
https://doi.org/10.1007/978-981-99-9251-5_24

At present, most of the automatic mapping algorithms used are relatively single, and they have shortcomings such as poor accuracy and cross mapping [3]. In this paper, combined with the traditional automatic drawing technology of single line diagram, the intelligent algorithm is added, and it is applied to the automatic drawing technology of single line diagram, and has achieved good results.

2 Automatic Mapping Techniques for Single Line Drawings

2.1 Technology Principle

The single line diagram referred to in this paper is the electrical contact diagram of the distribution network, which is mainly used to represent the electrical contact relationship of the complex distribution network wiring. As the density of grid load gradually increases, the demand is also getting higher and higher, and most users are required to use dual power supply to ensure their own electricity consumption [4–6]. The requirement of power supply reliability becomes higher, which directly leads to the complication of electrical contact relationship of distribution network. At present, for rural areas or other areas with low load density, the use of single radiation wiring form; For cities, towns and newly built parks and other areas, the main use of contact wiring form. For a single radiation line, the automatic generation of its single line diagram is usually not error-prone, and it can describe the electrical connection of each node clearly. However, for the line of contact connection mode, it is necessary to accurately identify the affiliation of its contact switch and branch line. Such a pattern of power-intensive development requires that the single-line graph automatic generation technology has stronger adaptability, robustness and accuracy [7].

At present, the automatic generation technology of single line diagram of distribution network is still developing, and a large number of scholars in the field of electric power and computer have made continuous efforts and attempts, and have achieved certain results. Aiming at the drawing goals of the single line diagram of the distribution network, such as orthogonalization, least crossing, as short as possible and beautiful lines [8], if the intelligent algorithm is used for processing, it will inevitably involve multi-objective optimization problems.

2.2 Mapping Principle and Cross Recognition

Distribution network lines are usually controlled according to nodes, such as Manhattan distance [9] and Euclidean distance [10]. Taking Manhattan distance as an example, the Manhattan distance of the total length of the line is:

$$L(G) = \sum_{j=1}^{n} \sum_{j>i} \left(\left|x_i - x_j\right| + \left|y_i - y_j\right|\right)\delta(i,j) \tag{1}$$

Where i and j are the subscripts of two electrical nodes; x_i and y_i are the corresponding coordinate points. $\delta(i,j)$ is the delta function. As the single-line diagram shown in Fig. 1, the value of this function is 1 if there is a direct electrical connection between the two nodes, and 0 otherwise.

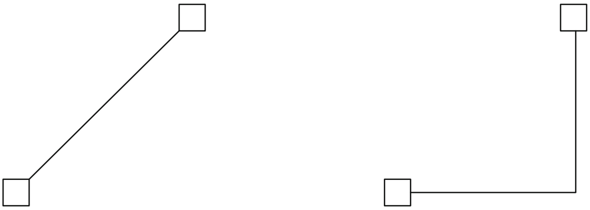

Fig. 1. Single-line plot correlation distance definition.

Normally, it is necessary to reduce the crossing between branches. The target mathematical model is as follows:

$$\min\ C(G) = \sum_{j>i}^{n} c_{ij} \quad i = 1 \ldots n \tag{2}$$

To determine whether branch i and j cross, it is mainly through the method of fast screening and judging the crossing, as follows:

(1) Fast screening to determine whether the rectangles formed by the two branches coincide with each other. However, this method can only quickly and roughly identify the branches that do not meet the requirements.
(2) For the remaining branches that cannot be screened for overlap, the judgment method is crossing discrimination. The basic principle is: if two branches intersect, there must be a situation where one side crosses the other side.

The mathematical models corresponding to the above two steps are merged into the overall goal as follows:

$$\min_{x,y} f = w_1 L(G) + w_2 C(layer) + \ldots + w_n C(layer) \tag{3}$$

In the model above, w is the corresponding weight, which has the greatest influence on the final result. Therefore, it is necessary to use genetic algorithm or particle swarm optimization algorithm to solve the problem when performing line optimization.

3 Algorithms Theory

3.1 Graph Theory

Graph theory is a branch of mathematics that was first introduced by Euler and started the study of graphs. The electrical contact diagram of the distribution network essentially includes lines and nodes, so the single line diagram of the distribution network is divided into points, lines and surfaces [11–13]. Here, points correspond to electrical nodes of the power system, lines correspond to power lines, and faces correspond to a region or the supply area of a high-voltage substation. A surface is composed of points and lines, and the study of the relationship between them is the focus of graph theory.

The definition of a planar connected graph in graph theory is that it can be drawn as a crossing-free planar graph, but not as a planar connected graph. No matter how its path is planned, there are crossings. The principle is shown in Figs. 2 and 3.

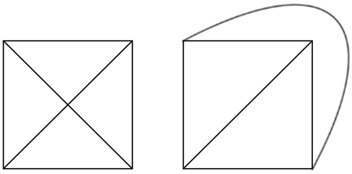

Fig. 2. Planar connectivity

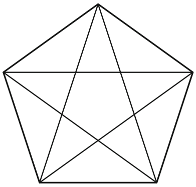

Fig. 3. Nonplanar connectivity

As can be seen from the above figure, the so-called planar connected graph can be adjusted to achieve no cross-connection in the two-dimensional plane by adjusting the connection mode. However, for non-planar connected graphs, no cross-connection can be achieved. Generally, the methods of planarity judgment are divided into: vertex addition method and line addition method.

3.2 The ST-Number Algorithm

The principle of ST-number algorithm can be represented by a connected graph [14]. Firstly, each node in Fig. 4 is numbered by 1 ~ n. After the connection is completed, the number shown in Fig. 4 is called ST-number.

To make better use of the performance of the ST-number algorithm, the cluster form of the ST-number is obtained by sequentially drawing from top to bottom. The following Fig. 5 is the cluster form of Fig. 4.

3.3 The PQ-Tree Algorithm

PQ tree uses nodes P and Q as the connection points of its lines, and the connection is carried out from top to bottom in a tree view. There are two types of nodes: parent node and child node. The parent node refers to the branches connected with it at the lower end; The child node refers to the node with only the upper parent node and no lower terminal node. The function of dividing nodes into these two types is to facilitate the processing of classification and analysis by computer, so as to ensure the accuracy of drawing [15, 16].

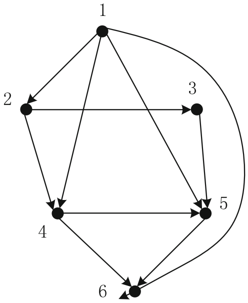

Fig. 4. ST-number example

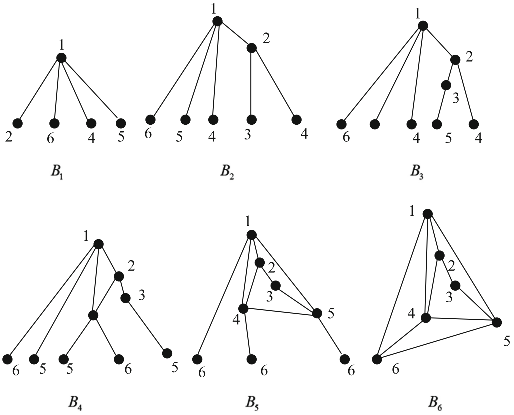

Fig. 5. ST-number expressed in the form of a cluster

There are many advantages after classifying nodes, which are described as follows:

(1) The nodes are classified according to their connection mode and location, which is helpful to reduce the error caused by unknown reference.
(2) The interconnection of child nodes and parent nodes facilitates the computer to fix the attributes of various types of nodes.

To sum up, the idea of PQ tree computer automatic mapping in this paper is similar to that of manual drawing. As shown in Fig. 6, P nodes are represented by dots and Q nodes are represented by rectangles. The ST-number spanning tree is compared with PQ tree.

According to the above drawing and generating methods of PQ-tree, there are two kinds according to whether the original graph can be generated. One is to directly generate the planar graph according to the original algorithm. The other requires a three-dimensional image to be converted into a planar image.

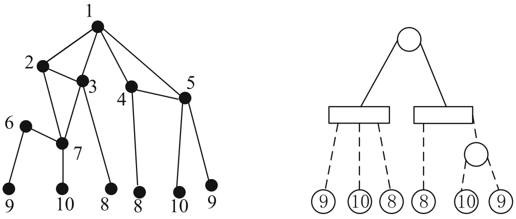

Fig. 6. Bundle form and computer PQ tree

4 Implementation Method

4.1 Main Steps

In this paper, the automatic mapping is carried out in a multi-step decomposition mode, which is mainly divided into two steps: planarization and orthogonalization. The direction of its main data flow is shown in Fig. 7.

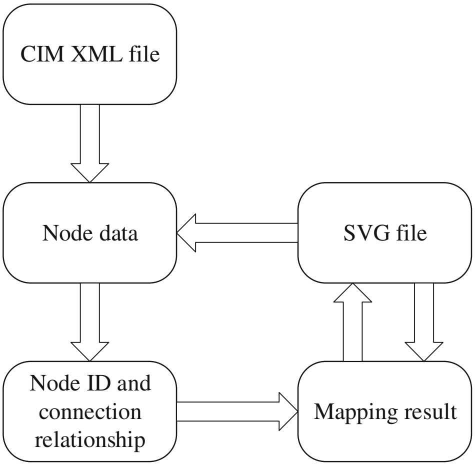

Fig. 7. Main data stream

As shown in Fig. 7, the first step is to extract the data in the CIM XML file and analyze and preprocess the data of each node. Then, according to the node ID and its connection relationship, the initial single line graph is generated, and it is checked with the SVG file. In this way, the existing power grid data can be sorted and checked, and the accurate and usable single line diagram can be generated.

4.2 Planarization Treatment

For planarization, first calculate the number of ST-numbers, and manually select the start point and end point as required. In this process, it is necessary to have several nodes with practical significance. Connecting these nodes constitutes a plan view. This kind of node is generally taken from the bus of the substation in the power system, and the initial starting point is the electrical node with high voltage level and large capacity of the main transformer. If it is impossible to distinguish, the starting point is defined by generating random numbers, and the point with the farthest power supply distance is defined as the end point. Connect the selected start point and end point, and simplify the PQ tree in the order of ST-number. After the calculation, all nodes are matched from bottom to top, and finally the optimal connection topology is selected according to the mapping quality evaluation criteria.

4.3 Orthogonalization Treatment

Orthogonalization processing needs to be carried out on a two-dimensional plane, and the relationship between each point and surface needs to be determined. Sort out the logic of points and surfaces according to the relationship, determine the connection, and then select the optimal path in each connection. The selection of the optimal path should be based on the constraints of points and surfaces, and the optimal orthogonalization scheme should be found on the premise of determining the initial value. The overall process is shown in Fig. 8.

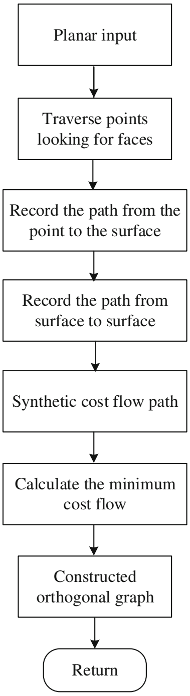

Fig. 8. Orthogonalization process

5 Examples and Numerical Analysis

The IEEE 30-node system is tested according to the mapping scheme described in this paper. On this basis, the complexity of the distribution network is increased, and the IEEE118-node distribution network is selected to test the effectiveness of the orthogonal algorithm.

At the same time, the proposed algorithm and particle swarm optimization are compared and analyzed. The optimization index of the PSO algorithm in this paper is the Manhattan distance between nodes, and the minimum distance and no crossing are the optimal paths and solutions. The main parameters related to PSO mapping are shown in Table 1 and Fig. 9.

Table 1. Data related to particle swarm optimization mapping

Nodes	Cross number	Overlap number	Mapping time/ms
1	26	11	0.25
50	11	5	1.2
200	7	4	2.1
500	5	2	3.5
1000	2	0	4.2

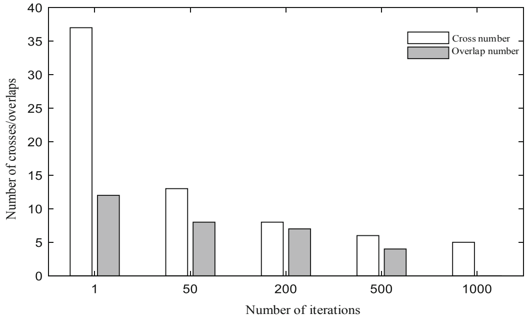

Fig. 9. The relationship between the number of iterations and the number of intersections and overlaps

From the results above, it can be seen that the particle swarm optimization algorithm needs multiple iterations to calculate the results with no crossover or few crossovers. Although it requires relatively long time, the accuracy and efficiency are much higher than that of manual drawing. For the multi-objective decomposition into graphs scheme in the paper, the main data are shown in Table 2.

From the above results, it can be seen that the multi-objective decomposition graph algorithm in this paper not only has higher accuracy than the human working graph, but

Table 2. Main indicators of multi-objective decomposition into graphs scheme

Iterations	Cross number	Overlap number	Mapping time/ms
30	0	0	200
118	0	0	500

also shows significant efficiency advantages compared with the particle swarm optimization algorithm. It has changed from minute level to millisecond level, and the crossing number is 0, so the drawing quality is equivalent to that of manual work.

6 Conclusion

The automatic drawing of single line diagram is of great significance in today's and future distribution network systems, which can replace manual drawing, improve the efficiency of drawing, and increase the accuracy of drawing. In this paper, mathematical statistics and graph theory are combined to generate a single line diagram, which can play their respective advantages and is easier to achieve the goal that needs to be achieved in practice. Finally, a numerical example is used to complete the comparison of the graph characteristics between the proposed algorithm and the particle swarm optimization algorithm, which proves the superiority of the multi-objective decomposition into graphs algorithm. It not only optimizes the effect of graphics rendering, but also broadens the idea of research on mapping technology.

In the future, there will be a larger scale of power asset iot in the distribution network. This kind of system with coupled software and hardware requires more robust single-line diagram automatic generation technology. In addition, the emergence of new elements such as wind power, solar energy, energy storage, and electric vehicle charging stations will also have an impact on the automatic mapping technology of single-line graphs. Therefore, continuous improvements should be made to adapt to the increasingly changing distribution network.

References

1. Boxi, Z., Zhaoyong, M., Hui, J., et al.: Algorithm for borderless cross drawing of distribution feeder single line diagram [J]. J. Power Syst. Autom. **30**(2), 113–118 (2018)
2. Weiguo, Y., Gaomeng, W., Jikeng, L., et al.: A topology verification method for low-voltage distribution networks based on AMI measurement information [J]. China Electric Power **52**(2), 125–133 (2019)
3. Bing, C., Xiaoxu, Z., Weicheng, S., et al.: Implementation of grid based automatic mapping for distribution networks [J]. Electr. Power Eng. Technol. **36**(6), 100–105 (2017)
4. Wang, F., Chen, Z., Hu, B., et al.: Design and implementation of automatic bus coupler switch for dual communication power supply system [J]. Power Syst. Prot. Control **47**(2), 161–166 (2019)
5. Rong Desheng, H., Jushuang, Y.G., et al.: Dual power input magnetic integrated switch inductor Boost converter [J]. J. Power Syst. Autom. **30**(4), 49–56 (2018)

6. Jun, P., Yujie, L., Weijun, H., et al.: Design of dual power intelligent controller based on Internet plus [J]. J. Electr. Power **32**(2), 142–146174 (2017)
7. Wang, J.: Application of GIS technology in county power grid planning [J]. Electron. Sci. Technol. **26**(8), 124–125 (2013)
8. Zhou, H., Meng, J., Zhu, H.: Automatic mapping technology for distribution single line diagrams based on GIS coordinate layout [J]. Power Syst. Autom. **41**(22), 145–150161 (2017)
9. Li, H., Zhang, P., Guo, H.: Adaptive multi-objective particle swarm optimization algorithm based on population Manhattan distance [J]. Comput. Integr. Manuf. Syst. **26**(4), 1019–1032 (2020)
10. Li, K., Lin, Y., Yang, Y.: An improved SDRSMOTE algorithm based on Euclidean distance [J]. Comput. Eng. Sci. **41**(11), 2063–2070 (2019)
11. Chengyu, G., Boxi, Z., Songyi, Z., et al.: Automatic layout algorithm for single line diagrams of regional distribution networks based on genetic algorithm [J]. China Electr. Power **49**(12), 53–57 (2016)
12. Wu, J., Chen, L., Liu, Z.: Design and implementation of bow layout for distribution network main station connection diagram [J]. J. Nanjing Univ. Eng. (Nat. Sci. Ed.) (1), 42–47 (2017)
13. Yansheng, L., Jing, L., Yadi, L., et al.: Topological analysis of large power grids based on graph partitioning [J]. Power Syst. Prot. Control **45**(23), 108–115 (2017)
14. Katzenmoyer, C., Marengo, B.G., Potts, A., et al.: An integrated green infrastructure plan to address combined sewer overflow, stormwater and nutrient reductions in Lancaster city, PA[J]. Proc. Water Environ. Fed. (13), 3107–3124 (2012)
15. Bessy, S., Bord, S.E., Blease, D.P., et al.: Dynamic monopolies for interval graphs with bounded thresholds[J]. Discrete Appl. Math. **26**(7), 256–261 (2019)
16. Chiba, N., Nishizeki, T., Abe, S., et al.: Embedding planar graphs using PQ-tree algorithms[J]. Electron. Commun. Jpn. **67**(7), 12–20 (2010)

Survey of Fault Analysis and Relay Protection of Flexible Low-Frequency Transmission System

Yiwei He(✉), Tonghua Wu, Daojun Zha, Feng Hong, Zhipan Sun, and Feng Long

NARI Group Corporation (State Grid Electric Power Research Institute), Nanjing 211106, China
827983033@qq.com

Abstract. The flexible low-frequency AC transmission technology based on the voltage source AC-to-AC converter makes large-scale networking easy, which can enhance the line transmission capability with its flexible regulation and control functions like power flow regulation, so it is a new transmission technology worthy of in-depth research. The fault characteristics of the flexible low-frequency transmission system (LFTS) are affected by topological structure and control strategies, possibly resulting in a problem of adaptability of conventional protection methods, i.e. relay protection faces a serious challenge. This paper presents an analysis of the basic structure and fault characteristics of the flexible LFTS based on the modular multilevel matrix converter (M3C). On this basis, the adaptability of the relay protection technology to the flexible LFTS is summarized. To solve the problem of adaptability inadequacy of some protection technologies, the research prospect of key protection technologies adapting to the LFTS is made, such as fast amplitude calculation method, sampling value differential protection and time-domain distance protection.

Keywords: Low-frequency transmission · Fault characteristics · Protection principle

1 Introduction

The low-frequency transmission technology utilizes the law of line impedance decreasing pro rata with the frequency so as to shorten the electrical distance of transmission lines and improve transmission power through a reduction in transmission frequency, provided that voltage class is not enhanced. The low-frequency transmission technology is a new generation of low-frequency transmission technology of which the core component is the flexible AC-to-AC converter based on fully-controlled power electronic devices and the theoretical basis is pulse-width modulation (PWM), and it has greater technical and economic advantages in typical scenarios (long-distance large capacity transmission, offshore wind power transmission, island power grid interconnection, urban power grid, etc.) than power frequency AC transmission technology and flexible DC transmission technology [1].

At present, the flexible LFTS research focuses on the control strategies of AC-to-AC converters, such as low-frequency system architecture and modular multilevel matrix

Y. Xue et al. (Eds.): PMF 2023, LNEE 1129, pp. 308–326, 2024.
https://doi.org/10.1007/978-981-99-9251-5_25

converter (M3C), while relatively little research is carried out for fault characteristics and protection principle of the low-frequency system. The flexible LFTS consists of a large number of power electronic devices and its structural characteristics and control methods differ from those of conventional synchronous generator sets, so its fault characteristics are significantly different from those of conventional AC grids. Relay protection is the first "defense line" that ensures the safe operation of the low-frequency system, while the analysis of fault characteristics is the basis for the research into relay protection, so it is crucial that the fault analysis and relay protection of the flexible LFTS are researched.

This paper presents an analysis of the basic structure and fault characteristics of the flexible LFTS based on the modular multilevel matrix converter (M3C); on this basis, the adaptability of the relay protection technology to the flexible LFTS is summarized. To solve the problem of adaptability inadequacy of some protection technologies, the research prospect of key protection technologies adapting to the LFTS is made, such as fast amplitude calculation method, sampling value differential protection and time-domain distance protection.

2 Flexible Low-Frequency Transmission System

M3C combines the conventional matrix converter with the modular cascading mode to realize AC-to-AC conversion, and its topological structure is shown in Fig. 1. For M3C, full-bridge submodules are used to form multiple sets of cascaded multilevel converters with the method of star connection, and each set of converters generates low-frequency voltage through the star (neutral) point to convert 3 phase AC to single phase AC.

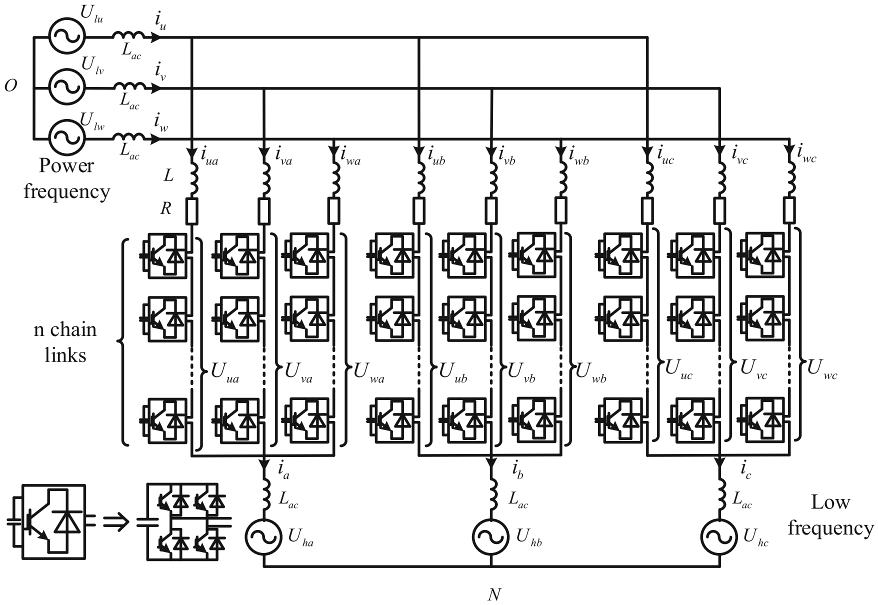

Fig. 1. Schematic diagram of typical M3C topology

M3C uses the multilevel cascading technology which is the same as the modular multilevel converter (MMC). With the direct AC-to-AC conversion without DC links, M3C needs fewer bridge arms, submodules and switching devices than the AC-DC-AC converter topology of back-to-back MMC, with better operation performance of converters in the low-frequency system is better and lower costs, and it is particularly suitable to the flexible low-frequency AC transmission system with a high voltage class and a large capacity [2, 3].

The flexible low-frequency AC transmission technology can use M3C to form a two-phase or three-phase AC transmission system and establish typical system topologies, such as single-ended topology and double-ended topology, with the aim to meet the requirements of different scenarios [4, 5]. And, the single-ended system topology as shown in Fig. 2a can be used for grind connection and transmission of low-frequency power supplies, such as wind power and solar power, and the grid-tie inverter on the power supply side can directly output the low-frequency AC electrical energy, so one AC-to-AC converter station is only required to be built at the power frequency point to realize the large-capacity and long-distance transmission of electric energy. The double-ended system topology as shown in Fig. 2b can realize the interconnection of asynchronous power frequency grids to meet the requirements for cross-regional mutual aid of power flow. The multi-ended system topology illustrated in Fig. 2c can realize the interconnection and complementation of different types of power supplies, loads and stored energy.

3 Fault Characteristics of the Flexible Low-Frequency Transmission System

Figure 3 illustrates the main circuit topology of the LFTS of the double-ended power supply based on M3C. Power Supplies A and B are power frequency power supplies, with a rated voltage of 220 kV, and Power Supply A is the sending-end power supply, while Power Supply B is the receiving-end power supply; power frequency electricity flows through a power-frequency Yg/Δ transformer to reduce the voltage from 220 kV to 60 kV. After flowing through the M3C, it becomes a 20 Hz low-frequency 60kV alternating current. Then the current flows through a low-frequency Δ/Yg transformer to raise the voltage from 60 kV to 220 kV. On the low-frequency side, the receiving end is connected with the sending end through lines.

3.1 Single-Phase Short-Circuit Faults at the Neutral Point of the Low-Frequency Transmission Line

If a Phase A to ground fault occurs at Neutral Point F1 of the low-frequency transmission line of the system illustrated in Fig. 4, the currents on both ends of the line are separately shown in Fig. 3, and Phase A current increases after the 0.04s fault occurs, but due to the control strategy of power electronic devices in M3C, the fault current amplitude is limited to the status similar to the load current before the fault in a short time, which is reflected in weak feeding characteristics.

Figure 5 shows the magnitude-phase characteristics of Phase A current on both ends of the line 20 ms after the occurrence of a Phase A to ground fault at F1. After the fault

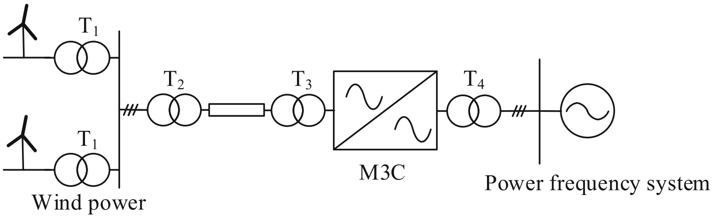

(a) Single-end flexible low-frequency AC transmission

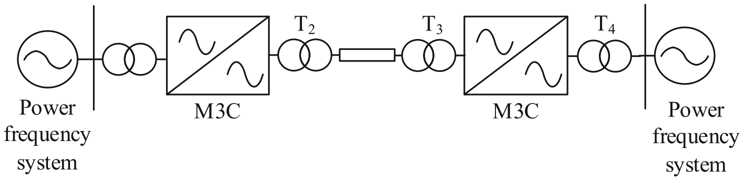

(b) Double-end flexible low-frequency AC transmission

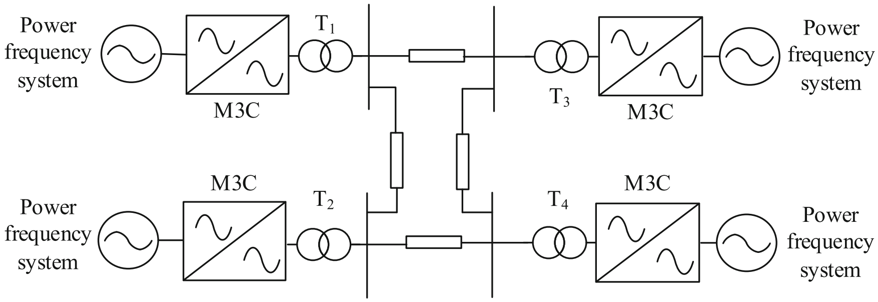

Fig. 2. Typical low-frequency AC transmission system structure

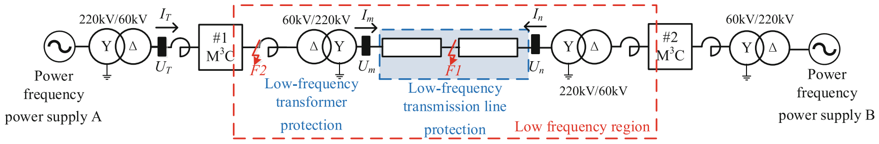

Fig. 3. Typical LFTS topology

happens, the receiving-end power remains basically unchanged, the receiving-end fault current is basically similar to the load current, and the phase angle difference between Phase A currents on both ends is 145°, which shows relatively distinct ride-through characteristics, and the phase angle difference is significantly different from the phase-angle relationship of the currents on both sides when an internal metal fault occurs in the conventional power frequency line.

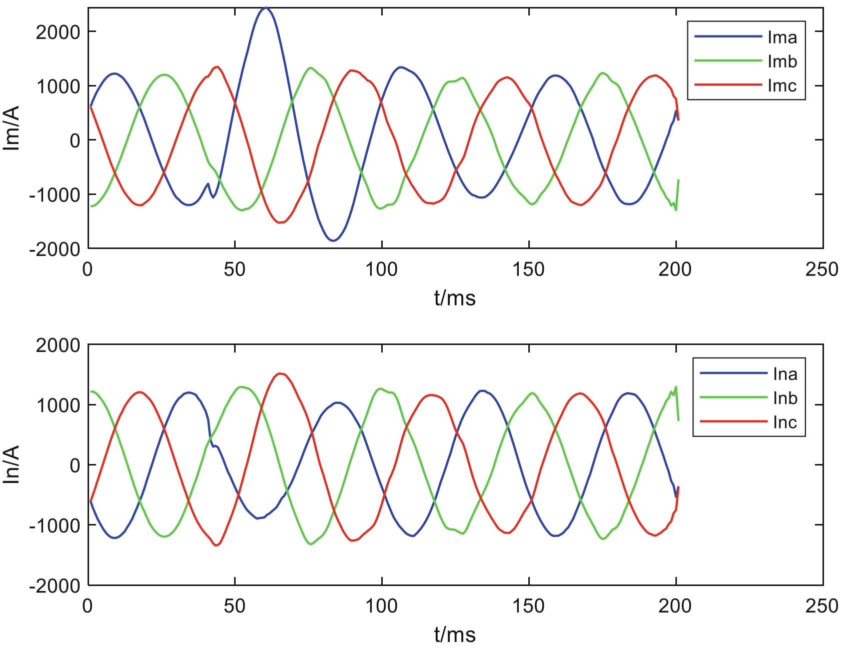

Fig. 4. Current waveforms on both sides of the line before and after the occurrence of a fault at F1

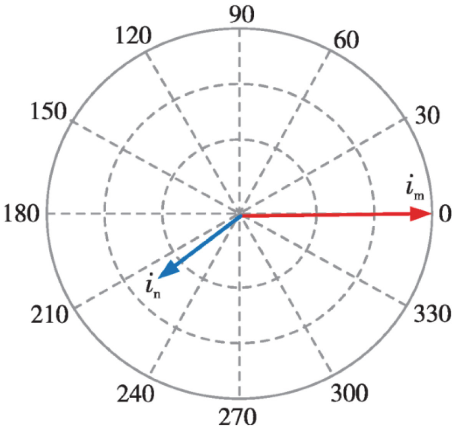

Fig. 5. Phase-angle relationship of the currents on both sides after the occurrence of a fault at F1

3.2 Single-Phase Short-Circuit Faults on the Low-Frequency Low-Voltage Side of the Sending-End Power Supply

Figure 6 shows the aliasing of 50 Hz and 20 Hz of voltage to ground on the power frequency low-voltage side after a fault occurs at F2 on the low-frequency low-voltage side of the sending-end power supply. If a fault occurs on the power frequency low-voltage side, the aliasing of voltage to ground also happens on the low-frequency low-voltage side.

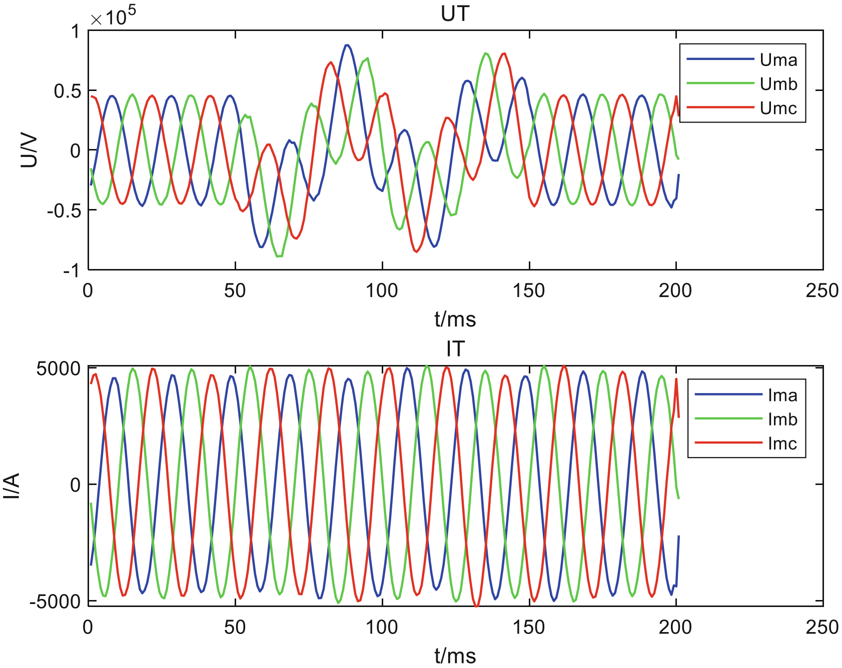

Fig. 6. Current waveforms of voltage to ground on the power frequency low-voltage side before and after the occurrence of a fault

3.3 Single-Phase Grounding Faults on the Low-Frequency Main Transformer Network Side

The fault point setting of the low-frequency system is shown in Fig. 7. Figure 8 shows the differential current on both sides of a fault phase and the second harmonic content of differential current of a fault phase if a permanent BC phase-to-phase short circuit fault occurs at F3 on the simulation low-frequency main transformer (main transformer for short). The current waveform distortion of differential current is obvious and the second harmonic content of differential current is significantly higher than the blocking setting value of magnetizing inrush current within Period 1 after the occurrence of a fault; after Period 1, the second harmonic content is still about 40%; the waveform enters the steady state about 100 ms after the occurrence of the fault, and in this case, the differential current drops to 0.7 p.u (which is subject to the rated secondary current of the transformer) and the second harmonic content of differential current decreases to 20% or below.

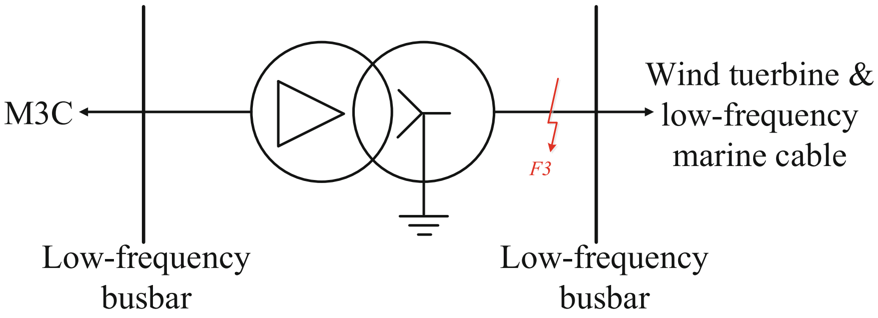

Fig. 7. Single-phase grounding fault point setting on the low-frequency main transformer network side

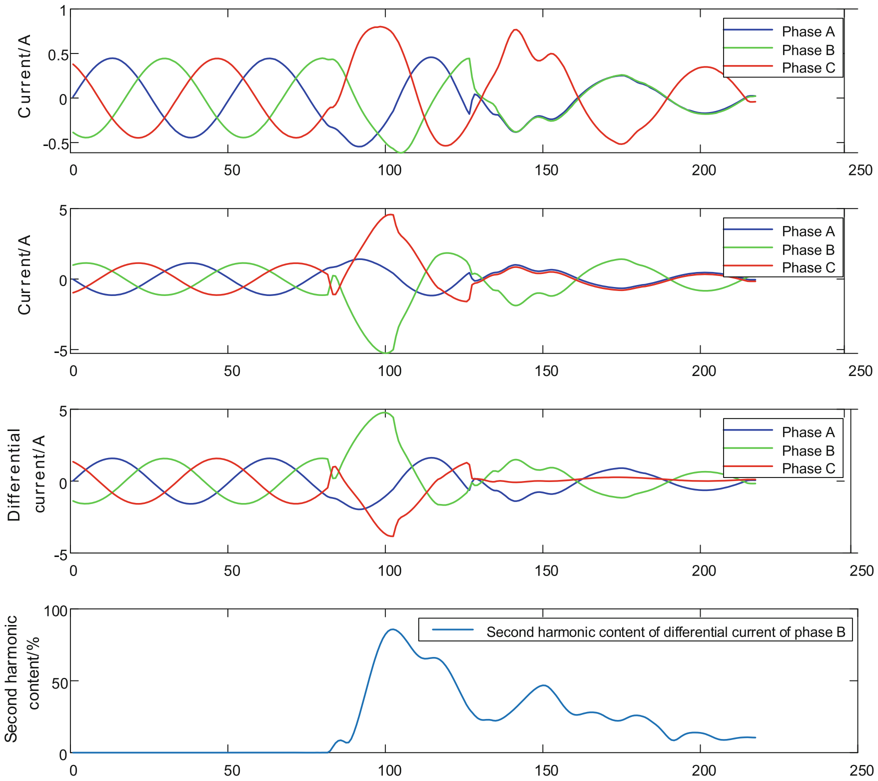

Fig. 8. Differential current and second harmonic case of single-phase ground fault on the net side of low-frequency main transformer

3.4 Summary

To sum up, when a fault occurs in the low-frequency transmission area, the fault characteristics are mainly reflected as follows.

Limit of current amplitude: The fault current amplitude is limited due to the requirements for the safety of M3C devices, which is reflected in weak feeding characteristics.

Current ride-through characteristics: In case of a fault, the control objective of the LFTS is to maintain the original power transmission, and the fault current shows significant ride-through characteristics.

Waveform distortion of voltage to ground: If a grounding short-circuit fault occurs on either side of the M3C converter valve, the aliasing of 50 Hz and 20 Hz of voltage to ground will occur on the other side.

High second harmonic content of differential current of a transformer fault phase: When the LFTS is in the transient state, the capacitor voltage on the bridge arm DC side will show a significant disturbance [6, 7]. The fluctuation in the capacitor voltage on the DC side will further cause the inclusion of other components of non-20 Hz frequencies in the output voltage in addition to normal 20 Hz low frequency, so that the input current on the M3C low-frequency side contains the corresponding harmonic current components.

4 Analysis of the Adaptability of Relay Protection of the Flexible Low-Frequency Transmission System

4.1 Analysis of the Adaptability of Differential Protection

Differential protection is based on Kirchhoff's laws, i.e. calculate and compare the effective values of action current and braking current of the line to different internal faults from external faults. $\dot{I}_m$ and $\dot{I}_n$ denote the currents measured on both ends of the line, respectively. I_{qd1} and I_{qd2} denote the starting currents of a differential relay; K_{r1} and K_{r2} denotes the ratio braking coefficients.

The action current of steady-state differential protection is generally expressed as:

$$I_d = \left|\dot{I}_m + \dot{I}_n\right| \tag{1}$$

The braking current of steady-state differential protection is generally expressed as:

$$I_r = \left|\dot{I}_m - \dot{I}_n\right| \tag{2}$$

The ratio braking properties of a current differential relay of steady-state differential protection current are generally as follows:

$$\begin{array}{l} I_d \geq I_{qd1} \\ I_d \geq K_{r1} I_r \end{array} \tag{3}$$

The action current of variable differential protection is generally expressed as:

$$\Delta I_d = \left|\Delta \dot{I}_m + \Delta \dot{I}_n\right| \tag{4}$$

The braking current of variable differential protection is generally expressed as:

$$\Delta I_r = \left|\Delta \dot{I}_m\right| + \left|\underset{n}{\dot{\Delta I}}\right| \tag{5}$$

The ratio braking properties of a current differential relay of steady-state differential protection current are generally as follows:

$$\begin{aligned} I_d &\geq I_{qd1} \\ \Delta I_d &\geq K_{r2} \Delta I_r \end{aligned} \tag{6}$$

Figure 9 shows the amplitudes of differential current and braking current of Phase A steady-state differential protection after the Phase A grounding fault occurs in 40ms at Neutral Point F1 of the low-frequency transmission line (as shown in Fig. 3). Figure 10 shows the amplitudes of differential current and braking current of Phase A variable differential protection after the Phase A grounding fault occurs at 40ms at Neutral Point F1 of the low-frequency transmission line (as shown in Fig. 3). As regards the steady-state differential protection, the differential current during the fault is far less than the braking current, which cannot meet the requirements for differential protection sensitivity of conventional lines. The variable differential protection shows the characteristics of fault components after the removal of steady-state load current and still has relatively high sensitivity.

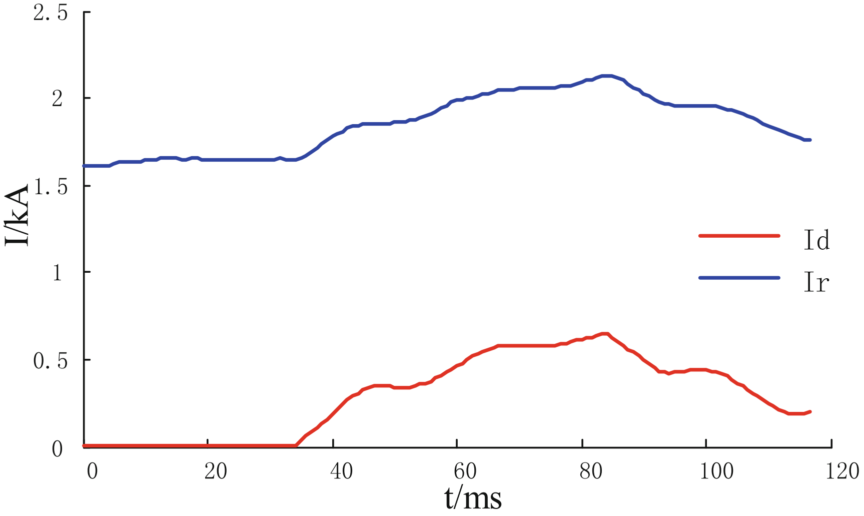

Fig. 9. Differential current and braking current of the steady-state differential protection

4.2 Analysis of the Adaptability of Distance Protection

The action equations of phase-comparison distance protection are as follows:

$$90^\circ < arg\frac{\dot{U}_{OP}}{\dot{U}_P} < 270^\circ \tag{7}$$

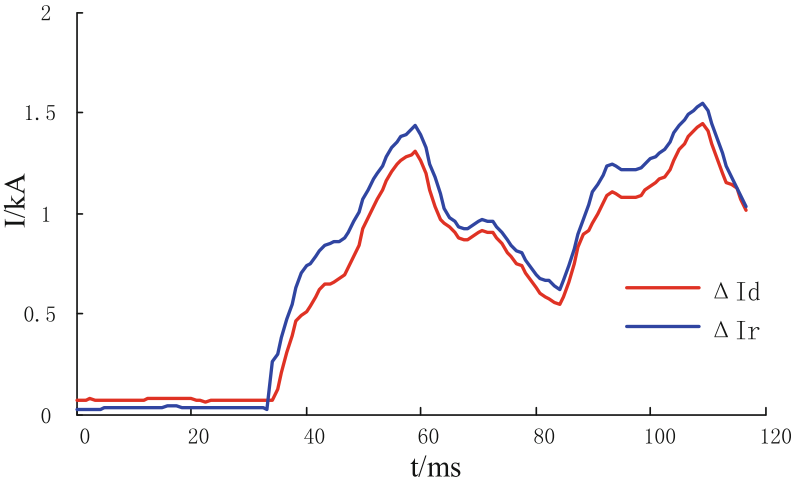

Fig. 10. Differential current and braking current of the variable differential protection

The polarization voltage $\dot{U}_P$ is the positive sequence voltage at the protection installation:

$$\dot{U}_P = \dot{U}_1 \tag{8}$$

For phase-to-phase protection, the working voltage is:

$$\dot{U}_{OP\varphi\varphi} = \dot{U}_{\varphi\varphi} - \dot{I}_{\varphi\varphi} \times Z_{set} \tag{9}$$

For grounding protection, the working voltage is:

$$\dot{U}_{OP\varphi} = \dot{U}_{\varphi} - \left(\dot{I}_{\varphi} + K \times 3\dot{I}_0\right) \times Z_{set} \tag{10}$$

In the above-mentioned equations, φ represents A, B and C.

In the working voltage equation, $\dot{U}_{\varphi}$ denotes the measured voltage of a relay, $\dot{I}_{\varphi}$ denotes the measured current, Z_{set} denotes the set impedance, $\dot{I}_0$ denotes the zero-sequence current, and K denotes the compensation factor of zero-sequence current.

As the polarization voltage is used as the reference phasor of phase comparison, the phase shall remain unchanged before and after the occurrence of various faults, and if a single-phase grounding fault occurs in the low-frequency line area, the polarization reference voltage angle may change abruptly, making the phase-comparison distance protection inapplicable. Figure 11 shows the angle difference between working voltage and polarization voltage after the Phase A grounding fault occurs in 40ms at Neutral Point F1 of the low-frequency transmission line (as shown in Fig. 3).

4.3 Analysis of the Adaptability of Transformer Protection

In case of a fault, the differential protection of a low-frequency main transformer encounters the following problems: small differential current and high second harmonic content.

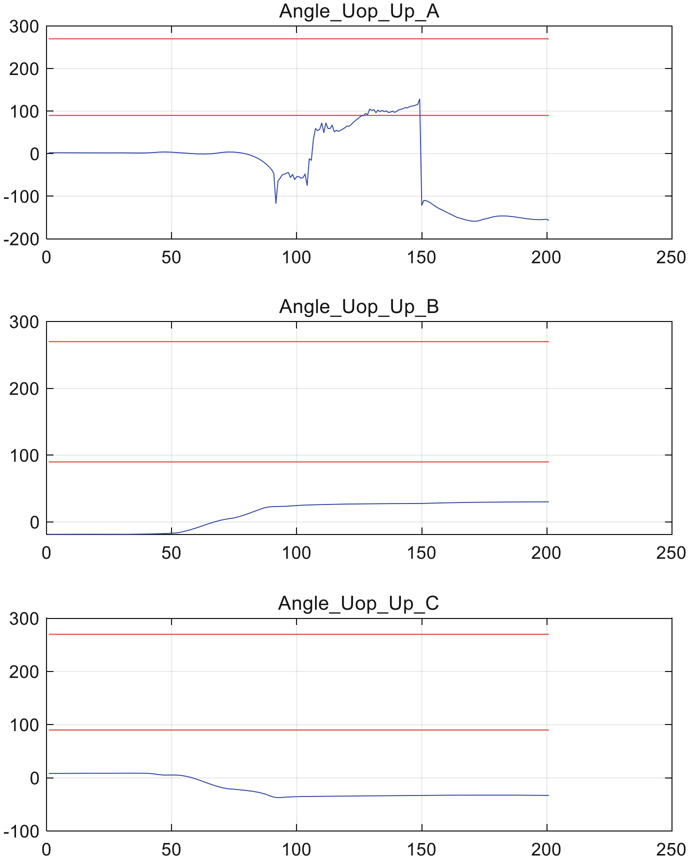

Fig. 11. Polarization voltage angle of single-phase grounding faults in the low-frequency line area

The second harmonic content of the differential current is still higher than the blocking setting value of magnetizing inrush current after Period 1 of the occurrence of the fault, and the magnetizing inrush current criterion cannot be opened.

The failure to open the magnetizing inrush current criterion quickly after an internal fault occurs causes differential protection still to be blocked, the speed of action is relatively slow, and the specification requirements cannot be met.

If a multi-phase evolving fault occurs in the low-frequency main transformer area, for example, a Phase A grounding fault lasts for 20 ms and then a Phase B grounding fault occurs, and the fault current changes multiple times in a short time; In the turning angle calculation process of transformer differential protection, angular difference and zero-sequence component are required to be eliminated, causing the coupling of electrical features of various phases and further aggravating the degree of distortion of the differential current waveform. The above-mentioned factors will slow down the opening speed of magnetizing inrush current criterion and even cause the failure to open the criterion, and differential protection carries the risk of failure to operate.

5 Research Prospect of Protection Technologies Suitable for the Flexible Low-Frequency Transmission System

5.1 Fast Amplitude Calculation Method

If the conventional amplitude algorithm is still used at the working frequency of 20 Hz, the sampling data window will change from 20 ms to 50 ms, which will seriously affect the speed of protection action. To solve this problem, the fast amplitude calculation method suitable for the LFTS needs to be researched. At present, the research into the fast amplitude calculation method is mainly split into two categories: Category I research is aimed at improving the full-cycle Fourier algorithm. The short data window and variable data window Fourier algorithms were separately used in refs. [8] and [9] to accelerate the rate of convergence of algorithms. Reference [10] reduced the computation load of algorithms through a reduction in the order of Fourier algorithms. Reference [11] put forward the Fourier algorithm for adaptive windows. The data window length of this algorithm can change with the length of jump signals to reduce the computation time of the Fourier algorithm. The aforesaid algorithms improve the speed of protection, but the accuracy of computation will be reduced [12]. Category II research refers to the methods based on the periodic signal model, mainly including method of least squares, Kalman Filter method, wavelet transform method, improved recursive least-squares method based on the method of least squares, and adaptive least-squares method, and these algorithms are characterized by relatively high speed and accuracy and are expected to be further researched and applied to the LFTS.

5.2 Sampling Value Differential Protection Based on Low-Frequency Transmission

When steady-state differential protection is applied to the LFTS, its sensitivity is relatively low, and when variable differential protection is applied to the LFTS, the effect of protection will be better, but it can be used for quick protection only, i.e. its application is limited to some extent. Sampling value differential protection is based on the sampling value at each sampling time to distinguish actions. This differential protection is less affected by bad data points and has a relatively short data window, which offers some advantages in terms of reliability and speed.

Reference [13] considered a variety of problems faced by the LFTS relay protection combined with the fault characteristics in the typical low-frequency transmission line area and set different sampling value differential criteria for the fault characteristics of the LFTS to improve the speed and reliability of protection. However, the effect of their application in practical engineering is to be further verified. Reference [14] discussed the differences between sampling value differential protection and instantaneous value differential protection and presented the methods for selecting key parameters of sampling value differential protection in different application objects; Reference [15] analyzed initial phase of sampling, selection of data window length, relationship between setting threshold and number of repeated judgments, and their influence on the performance of protective actions; Reference [16] discussed a trip boundary variation region existing in sampling value differential protection and analyzed the speed suitable for the outlet of sampling value differential protection. The above-mentioned research contents are mainly used in the power frequency transmission system, which is of some reference value to the research into the sampling value differential protection of the LFTS.

5.3 New Principle of Time-Domain Distance Line Protection

For the polarization voltage used in a phase-comparison distance relay, the polarization voltage angle may change abruptly where some types of faults occur inside and outside the line area, making this protection method unsuitable for LFTS protection. To adapt to fault characteristics of the LFTS, such as weak feeding, high harmonic content, and frequency deviation, the relevant scholars put forward the distance protection principle based on the time domain model identification concept.

At present, some research has been conducted into the time-domain distance protection principle for power frequency transmission lines. Reference [17] analyzed the impact of the frequency deviation of wind farm fault current on the power frequency distance protection and pointed out that the method of using the time domain method to solve a differential equation, which was based on the lumped parameter model of the line, was not affected by the characteristics of frequency deviation in principle. Reference [18] presented an algorithm for solving the differential equation for the iterative computation of fault distance based on the digital low-pass filtering and fault point voltage reconstruction, so as to solve the problem of a large error in the power frequency impedance calculation. Reference [19] corrected the boundary of distance protection based on the error in the lumped parameter model of the line and presented a time-domain distance protection scheme for resistance to transient over-reach, with the aim to solve the following problems: the long-distance transmission line was greatly affected by the transient process caused by distributed capacitance and it was prone to transient over-reach of Distance Protection Section I. Reference [20] combined the zero-sequence fault component network with the time-domain full-component network to improve the original time-domain distance protection and enhance the capability of the original time-domain distance protection to resist transition resistance. Reference [21] presented a time-domain distance protection algorithm that could identify the fault direction quickly in case of a zero voltage fault through the analysis of transient voltage caused by a doubly-fed induction generator fault and based on the coefficient of variation between the memory voltage drop and the actual voltage drop under different fault conditions with a view to solving the problem that the conventional time-domain differential equation algorithm is difficult to correctly identify the direction of fault at the outlet of the outgoing line of a wind farm.

The accuracy of computation of the above-mentioned time-domain distance protection schemes is theoretically not affected by the characteristics of weak feeding of fault current and frequency deviation, so these schemes can be better used to protect transmission lines. However, there has been scarcely any research into the relevant principles of time-domain distance protection of low-frequency transmission lines, and further research will be required in the future.

5.4 New Principle of Low-Frequency Transformer Protection Based on Parameter Identification

As the main protection of power transformers, current differential protection reflects an increase in the differential current and operates in case of tripping. To deal with the problems encountered by the differential protection of low-frequency main transformers, such as small differential current, high second harmonic content, and relatively slow speed of differential protection actions caused by the failure to quickly open the magnetizing inrush current criterion after a fault occurs, Chinese and foreign experts and scholars have put forward a range of new transformer protection principles based on equivalent models or parameter variations in order for the performance of power transformer protection to be further improved. The transformer protection based on parameter identification is mainly divided into the transformer protection principle based on the equivalence circuit principle [22, 23] and the transformer protection principle based on the equivalent instantaneous inductance [24–27].

Reference [22] presented a new magnetizing inrush identification algorithm based on the distribution characteristics of normalized equivalent instantaneous inductance to normalize the equivalent instantaneous inductance and make the selection of fixed values for criterion more universal, which was irrelevant to the specific parameter and type of transformers; Reference [23] presented a method that divided the saturated and unsaturated areas of a transformer by differential current and distinguished magnetizing inrush current from short-circuit fault according to the ratio of average equivalent instantaneous inductance in these two areas by using the capability of the instantaneous excitation inductance of a transformer to reflect its degree of saturation; Reference [24] improved the identification method of magnetizing inrush current based on the excitation inductance parameter identification so that this principle could not only be used for single-phase transformers but also for a three-phase transformer (outside the winding) connected with a current transformer on △ wiring side; Reference [25] presented a new transformer protection principle based on the combined impedance of fault components with a view to utilizing the amplitude criterion and direction criterion for the combined impedance of fault components to correctly identify internal faults; Reference [26] utilized the input side data 5ms after the no-load running of a transformer to conduct the parameter identification for the equivalent instantaneous inductance of the transformer, so as to judge whether a fault occurred in the transformer which ran with no load; Reference [27] used the method of least squares to calculate the equivalent excitation inductance within 2 ms, used different numerical features of the equivalent excitation inductance in case of normal operation, core saturation and an internal fault to develop protection schemes, and presented a master scheme for fast transformer protection based on excitation inductance.

Given that the transformer protection schemes based on parameter identification are not influenced by the fault characteristics like small differential current and high second harmonic content of fault current, they can be better used for transformer protection. Nevertheless, the research into the relevant principles of low-frequency transformer protection based on parameter identification is still in its infancy now, so further research will be required in the future.

6 Practice of Flexible Low-Frequency Transmission Projects

6.1 Hangzhou 220 kV Zhongbu-Tingshan Flexible Low-Frequency Transmission Demonstration Project

On May 7, 2021, the 220 kV Zhongbu-Tingshan Flexible Low-frequency Transmission Demonstration Project of State Grid Zhejiang Hangzhou Power Supply Company was officially launched. In this Project, one frequency converter station would be separately built in the 220 kV Zhongbu Substation and the 220 kV Tingshan Substation, each with the capacity of 300 MW/20 Hz and the voltage class of 220 kV. Low-frequency transmission could be realized through the Tingshan-Zhongbu Line, which would interconnect two major load centers in Fuyang and the south part of Xiaoshan to meet the demand for load growth of Fuyang and effectively relieve the power supply pressure of Fuyang. Figure 12 is the schematic diagram of the system structure of this Project.

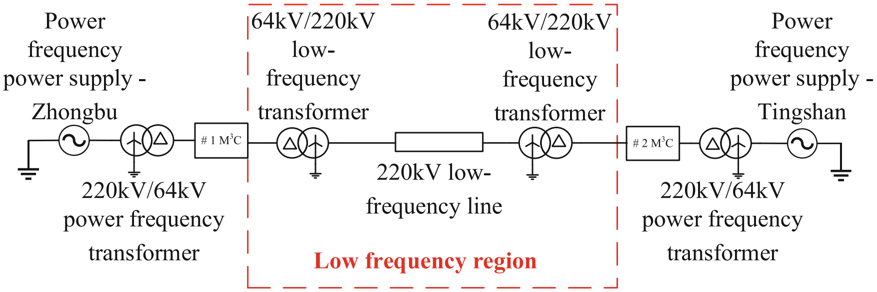

Fig. 12. Schematic diagram of the structure of Hangzhou low-frequency transmission project

6.2 Taizhou 35 kV Flexible Low-Frequency Transmission Demonstration Project

On June 16, 2022, the Taizhou 35 kV Flexible Low-frequency Transmission Demonstration Project was put into operation in Taizhou, Zhejiang. In the Taizhou 35 kV Flexible Low-frequency Transmission Demonstration Project, 20 Hz low-frequency transmission is used, and a 35 kV frequency conversion station was built in Taizhou 35 kV Saltworks Substation to realize the grid-connected transmission of electrical energy from two 1.1 MW low-frequency wind turbines on the Dachen Islands through the new Saltworks-Dachen submarine cable line. The system architecture is shown in Fig. 13.

6.3 Yancheng Dafeng Test and Verification Platform for the Low-Frequency Transmission of Offshore Wind Power

Electric Power Research Institute, State Grid Jiangsu Electric Power Co., Ltd. Has cooperated with domestic wind power generation equipment manufacturers and operators in the joint construction of a test and verification platform for the low-frequency transmission of offshore wind power in Dafeng District, Yancheng City. This platform

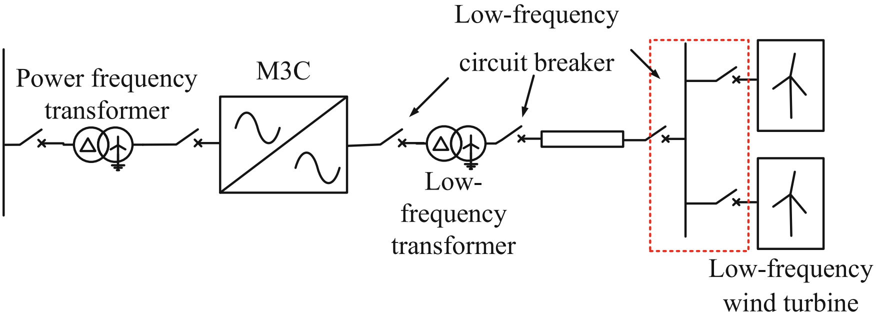

Fig. 13. Zhejiang Taizhou low-frequency transmission demonstration project

includes a 4.5 MW low-frequency wind turbine generator set. It can output 16.7 Hz low-frequency electric energy, pressure is raised to 35 kV with a low-frequency transformer, electric energy is transmitted via the submarine transmission cable line, and finally the low-frequency electric energy is converted into the power frequency via the low-frequency converter (M3C) and then fed into the 35 kV power frequency grid. The system architecture is shown in Fig. 14.

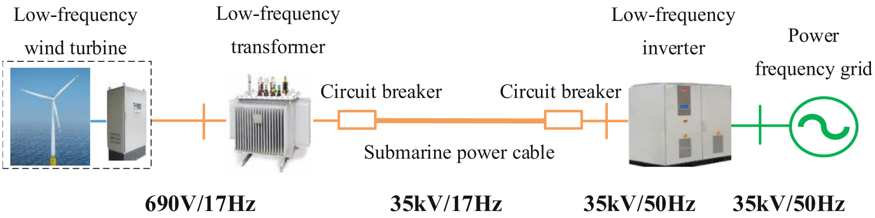

Fig. 14. Yancheng Dafeng test and verification platform for the low-frequency transmission

The aforesaid engineering cases focus mainly on the technical verification of flexible low-frequency transmission from the offshore wind farm. The scale of wind power is relatively small, with voltage classes of 220 kV and below, so there is still a wide gap between it and the low-frequency high-voltage transmission from the future medium and long-distance 1,000,000 kW-class offshore wind farms. Furthermore, various types of protection in the existing engineering cases are mainly based on the existing relay protection principles, and the existing power frequency protection devices are used for adaptability improvement, and whether or not they are still applicable to those low-frequency transmission systems for offshore wind power with a large scale remains to be further researched.

7 Conclusions

In recent years, flexible low-frequency AC transmission technology has garnered widespread attention from the academic world and the industrial world. A large number of technical and economic analyses, control strategy development and experimental prototype research have been conducted for the application of this technology to typical scenarios, and the flexible low-frequency transmission demonstration projects have been successively built in Hangzhou, Taizhou, etc. in Zhenjiang Province. It is believed that the advantages of flexible low-frequency AC transmission technology will be increasing as the system structure is perfected, the relay protection technology is improved and control strategies are optimized, and flexible low-frequency AC transmission is bound to develop at a breakneck pace in the application fields of long-distance large-capacity power transmission, offshore wind power transmission, urban power grid and other typical scenarios.

This paper presents an analysis of the basic structure and fault characteristics of the flexible LFTS based on the modular multilevel matrix converter (M3C); on this basis, the adaptability of the relay protection technology to the flexible LFTS is analyzed, and the research prospect of key protection technologies adapting to the LFTS is carried out to reach conclusions as follows:

A. The M3C can be used to construct the flexible low-frequency AC transmission system with a three-phase topology, with the aim to establish single-ended and multi-ended flexible low-frequency AC transmission grids, increase the flexible control capability of grids and meet the requirements for the development of new electric power systems in the future.
B. Affected by M3C control strategies of the flexible LFTS and other factors, the following fault characteristics different from those of conventional grids occur if the low-frequency system fails, including limited current amplitude, occurrence of current ride-through characteristics, waveform distortion of voltage to ground, and higher second harmonic content of transformer differential current.
C. For the fault characteristics of the flexible LFTS, the adaptability of the relay protection technology to the flexible LFTS is analyzed to draw the following conclusions: the sensitivity of steady-state differential protection is inadequate, the sensitivity of variable differential protection is still relatively high, distance protection is not applicable any more, and the speed of transformer differential protection is not sufficient.
D. To improve the relay protection technology for flexible low-frequency AC transmission, in-depth research into key protection technologies adapting to the LFTS shall be conducted, such as fast amplitude calculation method, sampling value differential protection and time-domain distance protection.

Acknowledgments. This work is supported by Science and Technology Project of State Grid Corporation of China (Relay protection research and equipment development of offshore wind power flexible low-frequency transmission system) (No. SGSH0000DKJS2200477).

References

1. Huang, M., Wang, X., Liu, S., et al.: Technical and economic analysis on fractional frequency transmission system for integration of long-distance offshore wind farm [J]. Autom. Electr. Power Syst. **43**(5), 167–174 (2019)

2. Wu, X., Zhu, H., Dong, Y., et al.: Frequency-division and hierarchical control of modular multilevel matrix converter for flexible low-frequency transmission [J]. Autom. Electr. Power Syst. **45**(18), 131–140 (2021)
3. Tang, Y., Zhang, Z., Xu, Z.: Low-frequency transmission scheme for offshore wind power based on active modular multilevel matrix converter [J]. Autom. Electr. Power Syst. **46**(8), 113–122 (2022)
4. Zhao, G., Chen, W., Deng, Z., et al.: Key technologies and application of flexible low-frequency AC transmission[J]. Autom. Electr. Power Syst. **46**(15), 1–10 (2022)
5. Lin, J., Ni, X., Qiu, P.: Review of flexible low frequency AC transmission technology[J]. Zhejiang Electr. Power **40**(10), 42–50 (2021)
6. Zhu, H., Wu, X., Wang, Y., et al.: A coordinated fault ride-through control for wind turbine through LFTS[J]. Distrib. Utilization **39**(11): 11–17+31 (2022)
7. Gu, Q., Zhang, X., Lyu, H.: Fast differential protection of low-frequency transformer based on fault negative sequence component[J/OL]. Autom. Electr. Power Syst. **47**(07), 184–192 (2023)
8. Zheng, J., Wu, H.: Study of short data window algorithm for microprocessor—based protection set[J]. Autom. Electr. Power Syst. **24**(18): 49–52, 60 (2000)
9. Ding, S., Zhang, C., Gong, Q., et al.: An improved half-wave Fourier algorithm-a new fast algorithm for microprocessor based protection AC sampling[J]. Autom. Electr. Power Syst. **23**(5), 18–20 (1999)
10. Cui, J., Chen, L., Tian, H., et al.: Error research and improvement of traditional DC filter Fourier algorithm [J]. High Voltage Apparatus **54**(7): 260–266 (2018)
11. Huang, Y., He, B.: Study on the optimal noise model of least error square algorithm for relay protection[J]. Autom. Electr. Power Syst. **28**(9), 31–35 (2004)
12. Li, N., Zuo, P., Wang, X., et al.: Inter-harmonic detection based on improved DFT and time-domain quasi-synchronization[J]. Electr. Power Autom. Equipment **37**(4), 170–178 (2017)
13. Pan, W., Qian, Z., Sun, Z., et al.: Research on differential protection of low frequency transmission lines based on differential principle of sampling values[J]. Zhejiang Electr. Power **42**(02), 35–42 (2023)
14. Chen, D., Ma, T., Liu, Pei., et al.: Problems in realization of microcomputer based differential current protection by-sampled values [J]. Electr. Power Autom. Equipment **16**(4): 3–8 (1996)
15. Chen, D., Yin, X., Zhang, Z.: On problems about sampling value differential protection [J]. Electr. Power Autom. Equipment **20**(4), 1–3 (2000)
16. Lin, X., He, Z., Liu, S., et al.: Discussions on some aspects of sampling value differential current protection [J]. Autom. Electr. Power Syst. **25**(19), 27–33 (2001)
17. Zhang, B., Zhang, J., Yuan, B., et al.: Impact of wind farm integration on relay protection(6): analysis of distance protection for wind farm outgoing transmission line [J]. Electr. Power Autom. Equipment **33**(6), 1–6 (2013)
18. Yang, Z., Kong, X., Wang, L., et al.: Distance protection scheme for interconnection line of doubly-fed induction generator based wind farm [J]. Trans. China Electrotechnical Soc. **31**(24), 252–260 (2016)
19. Fan, Y., Hou, J., Chao, Q., et al.: Time-domain equation model deviation correction distance protection for cluster wind power transmission line with anti-transient ability [J]. Electr. Power Autom. Equipment **38**(1), 10–18 (2018)
20. Hou, J., Fan, Y., Wang, Y.: Research on time domain distance protection of parameter identification for cluster wind power transmission line [J]. Power Syst. Prot. Control **46**(5), 46–53 (2018)
21. Chen, Y., Wen, M., Yin, X., et al.: Distance protection for transmission lines of DFIG-based wind power integration system [J]. Int. J. Electr. Power Energy Syst. **100**(SEP.): 438–448 (2018)

22. Zheng, T., Liu, W., Zhuang, H., et al.: A new algorithm based on the distribution of the normalized equivalent instantaneous inductance for the discrimination of inrush [J]. Proc. CSEE **25**(23), 47–53 (2005)
23. Bi, D., Wang, X., Liang, W., et al.: Improved method based on the ratio of average equivalent instantaneous inductance in different zones to identify excitation inrush [J]. Autom. Electr. Power Syst. **29**(17): 49–53, 58 (2005)
24. Kang, X., He, L., Jiao, Z., et al.: Distinguishing magnetizing inrush based on characteristic of excitation inductance [J]. J. Xi'an Jiaotong Univ. **41**(10), 94–98 (2007)
25. Suonan, J., Jiao, Z., Song, G., et al.: A fault component comprehensive impedance based transformer protection principle [J]. Proc. CSEE **19**(7): 1–5, 76 (2008)
26. Zhu, K., Jiang, J., Zhang, T.: Distinguishing magnetizing inrush based on characteristic of equivalent instantaneous inductance [J]. Power Syst. Prot. Control **38**(20), 12–16 (2010)
27. Jiao, Z., Ma, T., Qu, Y., et al.: A novel excitation inductance-based power transformer protection scheme [J]. Proc. CSEE **34**(10), 1658–1666 (2014)

A Coordinated Robust Damping Scheme of STATCOM and Wind Farm Based on H_2/H_∞ Control Considering Communication Delays

Rehan Sadiq, Yu Shan, and Zhen Wang(✉)

College of Electrical Engineering, Zhejiang University, Hangzhou 310027, China
z.wang@zju.edu.cn

Abstract. The proposed work presents a coordinated robust supplementary control scheme for the static synchronous compensator (STATCOM) and wind farm (WNF) to stabilize the multi-machine power network by simultaneously modulating the reactive power of STATCOM and WNF via *d*-axis control loops. The control scheme is solved based on a linear matrix inequality (LMI) framework with multi-objective mixed-H_2/H_∞ output feedback structure, followed by ensuring the predefined damping level of low-frequency modes (LFMs). Furthermore, the design strategy also takes into account multiple input and output channel communication delays. Eigenvalue analysis confirms the significant enhancement in the damping ratio of the dominant mode using the proposed strategy. Finally, time-domain simulations, subject to typical disturbances and uncertainties caused by wind speed and time delays, are used to validate the effectiveness of the strategy.

Keywords: Oscillation damping · Robust H_2/H_∞ control · Wind farm · STATCOM

1 Introduction

Recently, the production of wind energy has become one of the potential energy resources having rapid growth potential. However, because of their distinct dynamic behavior from conventional generation and variable power outputs, large-scale penetration of WNFs with the utility grid poses significant issues [1]. The study reported in Ref. [2] showed that the impact on LFMs is negative with the growing penetration of these renewables, considerably degrading the system's small-signal and transient stability performance. Subsequently, inadequate damping of LFMs decreases the power transfer capability of the transmission lines connecting remote areas, resulting in significant power fluctuations and rotor speed variations for the system undergoing dynamic perturbations [3]. Therefore, owing to the uncertainty caused by intermittent wind power and various disturbances, designing robust controllers is essential to maintain the system's adequate damping level [1, 4, 5].

In this respect, the implementation of a H_∞ controller is examined to damp LFMs, designed by simultaneously modulating the dc-link voltage, rotor speed, and the pitch

Y. Xue et al. (Eds.): PMF 2023, LNEE 1129, pp. 327–338, 2024.
https://doi.org/10.1007/978-981-99-9251-5_26

angle of the permanent magnet synchronous generator (PMSG) [6]. However, the detailed dynamic model of the SGs is not considered. The exploitation of a doubly fed induction generator (DFIG) to alleviate LFMs via LMI-based centralized robust mixed-sensitivity H_∞ method, considering communication delays, is proposed in Ref. [7]. Alternatively, flexible ac transmission system (FACTS) devices can also be employed to accomplish oscillation damping. In this regard, a robust controller is synthesized via a fixed-order loop shaping methodology for the static var compensator (SVC) to stabilize LFMs subject to different uncertainties in a DFIG-based power system [8]. Besides SVCs, STATCOMs have also been widely used for stability enhancement of wind power system by resolving various stability issues including damping of LFMs, and are preferred over SVCs because of their versatile features [9]. Previously, the application of a power oscillation damping (POD) controller for the STATCOM, designed using the phase compensation strategy, is validated for the power system integrated with WNFs [10]. Furthermore, a few authors have also confirmed the efficacy of decentralized POD controllers based on an artificial intelligent (AI) scheme [11] and a heuristic optimization approach [12]. Nevertheless, AI-based model training and tuning controller parameters using heuristic optimization require considerable computational time. Moreover, a nonlinear STATCOM control using the zero-dynamics approach has been discussed in Ref. [13].

Motivated by the above-mentioned studies, the proposed work also aims at stabilizing the LFMs of the power system integrated with the STATCOM and a large-scale WNF. To provide robustness against various power system disturbances and uncertainties due to the intermittent nature of wind speed and time delays of the wide-area communication channels, this paper presents supplementary robust damping control of STATCOM and WNF by coordinatively modulating their reactive power control loops using mixed-H_2/H_∞ control framework [14], followed by ensuring a predefined damping level via LMI-based regional pole placement constraint. In this manner, the design configuration simultaneously considers multiple objectives such as output disturbance rejection, control effort minimizing, and guaranteeing robustness against uncertainties.

2 System Modeling

The entire power system is modeled by representing the dynamics of the synchronous generator (SG), STATCOM, and a wind turbine system. The sixth-order sub-transient model constitutes the dynamic model of each SG in the power network, followed by employing the fast static exciters (*IEEE ST1A*) for all SGs [15].

2.1 STATCOM Model

STATCOM is a VSC-based FACTS device, placed in the power network mainly to deliver dynamic reactive power by generating balanced three-phase AC voltages at the system's frequency with controllable magnitude and phase angle. The injection or absorption of the reactive power from the power network depends upon the magnitude of the STATCOM voltage (V_{st}) relative to the network voltage (V_{pcc}) i.e. the voltage at the bus where STATCOM is connected. If $V_{st} > V_{pcc}$, STATCOM injects reactive power into the AC system, whereas it draws reactive power from the network when $V_{st} < V_{pcc}$. . Besides, it only consumes a little amount of real power to meet the converter's losses. The basic configuration of the STATCOM consists of a DC-link, a VSC (DC to AC), and a grid coupling filter, analogous to the grid-side converter (GSC) of the WNF [9]. By employing a decoupled cascaded-PI control structure (as shown in Fig. 1), STATCOM ensures DC-link voltage (v_{dc}) stability with the q-axis control and provides desired amount of reactive power (Q_{gref}) compensation or directly regulates the bus voltage through the d-axis control [16]. The d-q reference frame-based dynamic model of the STATCOM, aligning the q-axis with the grid voltage, is stated below [17]:

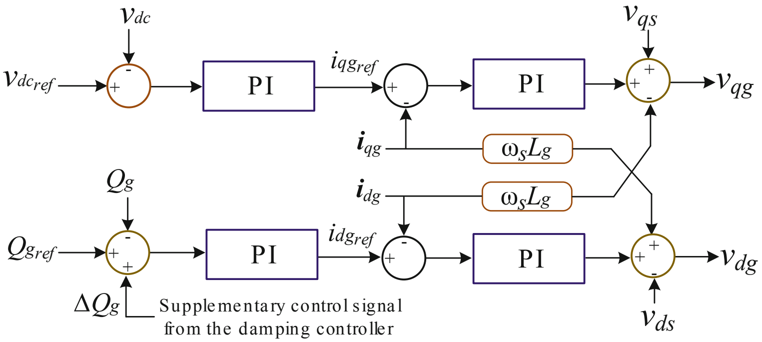

Fig. 1. *dq*-axis control of STATCOM or GSC of PMSG.

$$\begin{aligned}\frac{L_g}{\omega_{el}}\frac{di_{qg}}{dt} &= -R_g i_{qg} + \omega_s L_g i_{dg} + v_{qg} - v_{qs}\\ \frac{L_g}{\omega_{el}}\frac{di_{dg}}{dt} &= -R_g i_{dg} - \omega_s L_g i_{qg} + v_{dg} - v_{ds}\end{aligned} \tag{1}$$

where v_{dg}, v_{qg}, i_{dg}, and i_{qg} stand for d-q axis voltages and currents of the STATCOM, v_{ds} and v_{qs} denote d-q axis components of network voltage, R_g and L_g indicate the resistance and inductance of the grid-side filter, ω_{el} is the system base speed, and ω_s is the synchronous speed. Considering the lossless converter, the DC-link dynamic model can be expressed as:

$$C_{dc}\dot{v}_{dc} = \frac{1}{v_{dc}}\left(v_{qs}i_{qg} + v_{ds}i_{dg}\right) \tag{2}$$

and $Q_g = v_{qs}i_{dg} - v_{ds}i_{qg}$. The variables C_{dc} and v_{dc} represent DC-link capacitance and voltage, respectively.

2.2 PMSG Model

The WNF in the proposed study is modeled as an aggregated PMSG, which includes the dynamics of the turbine, generator, machine side converter (MSC), DC-link capacitor, and the GSC with a filter [18]. The following equations define the *d*-*q* dynamic model of the PMSG [18, 19]:

$$\begin{aligned} \frac{d\psi_q}{dt} &= R_p i_{pq} - \omega_{pr}\psi_d + v_{pq} \\ \frac{d\psi_d}{dt} &= R_p i_{pd} + \omega_{pr}\psi_q + v_{pd} \end{aligned} \tag{3}$$

with

$$\psi_d = -L_d i_{pd} + \phi_m \quad \text{and} \quad \psi_q = -L_q i_{pq}$$

where R_p is the stator resistance, ω_{pr} is the generator speed, and ψ_d, ψ_q, v_{pd}, v_{pq}, i_{pd}, and i_{pq} are the *d*-*q* axis components of the generator flux linkage, stator voltage, and current, respectively. The control structure of the GSC is identical to STATCOM (see Fig. 1) except that the PMSG also injects active power into the grid by maintaining the DC-link voltage. The PMSG and STATCOM provide dynamic reactive power compensation by modulating the *d*-axis control loops via a supplementary damping control signal (ΔQ_g). In this respect, the objective of the proposed study is to synthesize a robust damping controller.

2.3 Time Delay Approximation

The presented work adopts a centralized or wide-area control architecture, which requires communication links for receiving remote feedback signals and transmitting control signals to distant locations. Therefore, communication delay must be considered during the controller's design stage for effective performance against time delays resulting during this remote signal transmission. In the presented work, the time delay (T_d) in both the input ($e^{-sT_{in}}$) and output channels ($e^{-sT_{out}}$) are compensated using the first-order Padé approximation, as illustrated in Fig. 2, which is given as follows:

$$e^{-sT_d} \approx \frac{-\frac{1}{2}sT_d + 1}{\frac{1}{2}sT_d + 1} \tag{4}$$

3 Robust Mixed-H_2/H_∞ Control Framework for Pole Placement

The linearized model of the power system can be characterized by the following state space structure:

$$\begin{aligned} \Delta\dot{x} &= A\Delta x + B\Delta u \\ \Delta y &= C\Delta x + D\Delta u \end{aligned} \tag{5}$$

$$\Delta x = \begin{bmatrix} \Delta x_{SG}^T & \Delta x_{STATCOM}^T & \Delta x_{PMSG}^T \end{bmatrix}^T, \Delta u = \begin{bmatrix} \Delta Q_{statcom} & \Delta Q_{pmsg} \end{bmatrix}^T$$

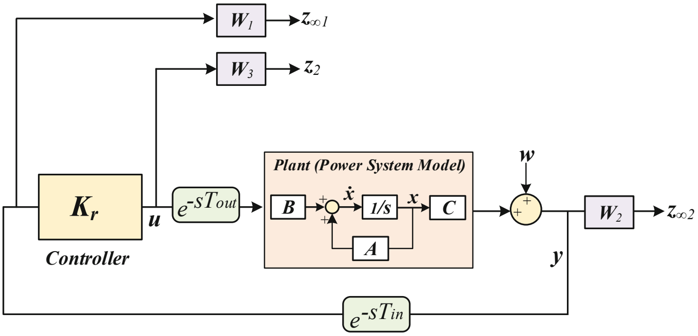

Fig. 2. Multi-objective H_2/H_∞ robust control framework

where x is the state variables, u is a vector of control signals injected into the STATCOM and PMSG via the damping controller, and y denotes the feedback signal of the controller (measured output of the system). Similarly, the structure of the proposed dynamic output feedback controller $u = K_r y$ can be denoted by the following state-space system:

$$\begin{aligned} \dot{x}_k &= A_k x_k + B_k y \\ u &= C_k x_k \end{aligned} \tag{6}$$

In general, different types of disturbances in the power system such as fluctuating wind speed, exciter's action during faults, and variations in generation and load can trigger LFMs in the power system [7]. Therefore, to achieve robust stability under such conditions, the proposed work adopts the multi-objective robust control approach using mixed-H_2/H_∞ synthesis with pole placement constraint. The fundamental presentation of the control framework (multi-objective) is depicted in Fig. 2 and the associated state-space formation of the augmented linear time-invariant (LTI) system is described as follows [14]:

$$\begin{aligned} \dot{x} &= A_i x + B_{1i} w + B_2 i u \\ z_\infty &= C_{\infty i} x + D_{\infty 1 i} w + D_{\infty 2 i} u \\ z_2 &= C_{2i} x + D_{22i} u \\ y &= C_{yi} x + D_{y1i} w + D_{y2i} u \end{aligned} \tag{7}$$

where w denotes external disturbances (e.g., wind speed fluctuations, load variations, etc.) and z implies regulated outputs. The H_∞ performance, which indicates the maximum gain over the complete frequency range, is ensured through z_∞ output channels. On the other hand, the H_2 norm indicating the overall energy of the system's input/output behavior is associated with H_2 output channel [14, 15]. The H_∞ performance channel assures the objectives of disturbance rejection and provides robustness against uncertainties with appropriate selection of weighting functions (i.e., $W_1(s)$ and $W_2(s)$ to be a low-pass and high-pass filter, respectively) to penalize the output channels. Besides, H_2 channel infers optimizing the control effort via a high-pass filter based on the weighting function $W_3(s)$ [15]. In addition, adequate damping performance and better transient response of the power system can be achieved by placing the closed-loop poles inside a specific left-half s-plane, typically characterized as a conic sector by ensuring the damping ratio $\zeta = \cos(\theta/2)$.

Let $(A_{cl,i}, B_{cl,i}, C_{cl\infty,i}, D_{cl\infty,i}, C_{cl2,i}, D_{cl2,i})$ denote the closed-loop state-space system. Then, by representing the transfer function from w to z_∞ and z_2, respectively by $T_{z_\infty w}$ and $T_{z_2 w}$ and considering positive symmetric matrices $X_\infty > 0$, $X_2 > 0$, $Q > 0$, and $X_D > 0$, the multi-objective control involves designing a robust feedback controller $u = K_r y$ by solving the following optimization problem:

$$Min\left(\|T_{z_\infty w}\|_\infty^2 + \|T_{z_2 w}\|_2^2\right) \tag{8}$$

Subject to

$$\begin{pmatrix} A_{cl}X_\infty + X_\infty A_{cl}^T & B_{cl} & X_\infty C_{cl\infty}^T \\ B_{cl}^T & -I & D_{cl\infty}^T \\ C_{cl\infty}X_\infty & D_{cl\infty} & -\varepsilon_\infty^2 I \end{pmatrix} < 0 \quad \text{For } H_\infty \text{ Performance} \tag{9}$$

$$\begin{pmatrix} A_{cl}X_2 + X_2 A_{cl}^T & B_{cl} \\ B_{cl}^T & -I \end{pmatrix} < 0 \quad \text{For } H_2 \quad \text{Performance}$$

$$\begin{pmatrix} Q & C_{cl2}X_2 \\ X_2 C_{cl2}^T & X_2 \end{pmatrix} > 0, trace(Q) < \varepsilon_2^2 \tag{10}$$

$$\begin{pmatrix} \sin\theta\left(A_{cl}X_D + X_D A_{cl}^T\right) & \cos\theta\left(A_{cl}X_D - X_D A_{cl}^T\right) \\ \cos\theta\left(X_D A_{cl}^T - A_{cl}X_D\right) & \sin\theta\left(X_D A_{cl}^T + A_{cl}X_D\right) \end{pmatrix} < 0 \quad \text{Pole Placement} \tag{11}$$

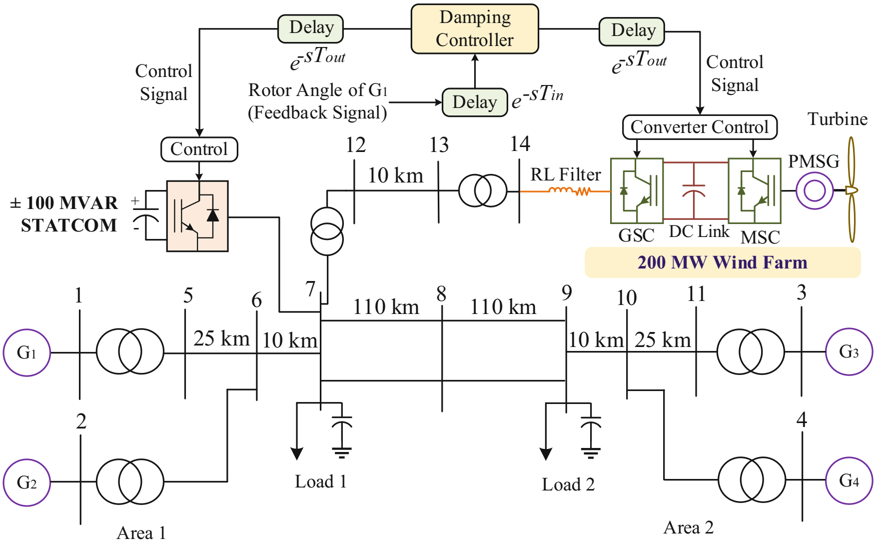

Fig. 3. The modified two-area test system with wind farm

Table 1. Eigenvalues and damping ratios of inter-area mode

Scenario	Eigenvalue	Damping (%)
Without WNF (open loop)	$-0.1717 \pm 3.9707i$	4.32
With WNF (open loop)	$-0.1401 \pm 3.4832i$	4.02
With robust controller	$-0.8043 \pm 3.5724i$	21.96

4 Case Study

4.1 System Study

The complete structure of the test system under study is depicted in Fig. 3 [20]. A 200 MW wind farm is integrated with the two-area power network at bus 7 via a 10 km line. A ± 100 MVAR voltage source converter (VSC) based STATCOM is also installed at bus 7 for stability enhancement purposes. The parameters of the STATCOM and PMSG are referred to [17, 18], respectively.

4.2 Eigenvalue Analysis

The nonlinear model of the studied two-area system with STATCOM and WNF is built using MATLAB/Simulink. After linearization, the most critical mode with the least damping is then identified by conducting the eigenvalue analysis. The two-area test system contains two local modes, corresponding to each area, and one weakly damped inter-area oscillatory mode. Local modes are adequately damped by the typical power system stabilizers. Hence, the focus of this study is on the inter-area mode. The eigenvalues associated with the inter-area mode are listed in Table 1, which shows the reduction in the damping level of mode in the presence of a wind farm. Since the WNF is installed in Area 1 to accommodate the increased load demand in Area 2, a larger amount of the power is transferred through the tie-lines which deteriorates the inter-area mode. As a result, it is required to design a controller to enhance the damping of the critical mode in order to avoid the large oscillation in the system's parameters during transient conditions.

4.3 Controller Design

The initial step in the controller design process is the selection of the most appropriate input feedback signal. Based on the geometric observability measure (GOM) of the various signals such as rotor angles, line currents, and active power flows, the rotor angle (δ_1) of G_1 shows a higher GOM value and is thus selected as a feedback signal [4]. For pole placement constraints, the LMI region is formulated by selecting a conic sector based on the required damping ratio. For a 20% damping ratio, the inner angle is specified as $\theta = 2\cos(0.20)^{-1} = 2.7388$ rad by using MATLAB command '*lmireg*'. To

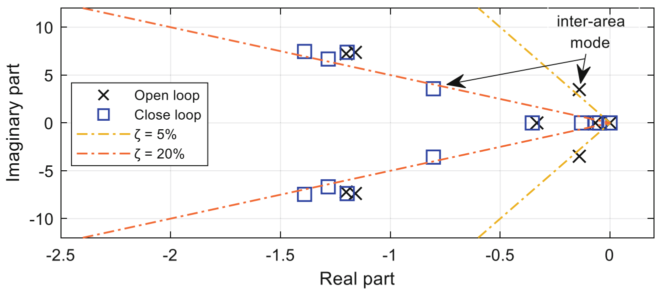

Fig. 4. Eigenvalue plot

synthesize mixed-H_2/H_∞ controller, the function ‘*hinfmix*’ of *LMI Toolbox* is applied [15]. The transfer function of the designed reduced order controller is given as follows:

$$\mathrm{K}_{\mathrm{r\ (PMSG)}} = \frac{12.85s^4 + 43.74s^3 - 449.1s^2 - 23202s - 1469}{s^5 + 81.62s^4 + 589.6s^3 + 5069s^2 + 15940s + 745.2}$$

$$\mathrm{K}_{\mathrm{r\ (STATCOM)}} = \frac{73.72\mathrm{s}^4 + 1482\mathrm{s}^3 - 4094\mathrm{s}^2 - 61654\mathrm{s} - 8686}{\mathrm{s}^5 + 81.62\mathrm{s}^4 + 589.6\mathrm{s}^3 + 5069\mathrm{s}^2 + 15940\mathrm{s} + 745.2}$$

The damping characteristic of the designed controller is first examined by eigenvalue analysis. From Table 1 and the complex eigenvalue plot shown in Fig. 4, it is established the robust controller significantly improves the damping ratio of the critical inter-area mode by guaranteeing the specified damping constraint (pole placement region). Lastly, the eigenvalue results are confirmed by performing non-linear time-domain simulations.

4.4 Simulation Results

The dynamic response of the system is obtained by applying a self-clearing three-phase fault on bus 8 for 100 ms duration at $t = 1\ s$. From Fig. 5a–d, it is demonstrated that the system experiences large oscillations lasting over 20 *s* in the absence of any controller. However, the robust H_2/H_∞ controller delivers significant damping performance and rapidly mitigates the oscillation within 8 *s*. The dynamic reactive power compensations, provided by the STATCOM and PMSG, are shown in Fig. 5e, f. The STATCOM delivers 0.5 pu of reactive power (Q_{STAT}) at steady-state, with the remaining capacity being utilized for transient conditions; where PMSG’s reactive power is limited to a maximum of ± 0.62 pu (Q_{PMSG}) only during disturbances, assuming that the maximum active power supply is 190 MW. Moreover, the intended work focuses on designing a robust controller by simultaneously regulating the Q_{STAT} and Q_{PMSG}; therefore, to emphasize the significance of the proposed scheme, the effectiveness of the coordinated modulation is compared with the uncoordinated approach, accomplished via independently regulating the Q_{STAT} and Q_{PMSG}. Nevertheless, the comparative responses in Fig. 5e, f, evidently show that the coordinated control produces reactive power compensation more efficiently, thereby requiring less control effort.

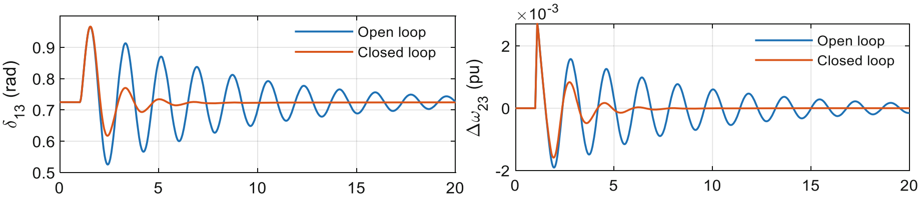

(a) Relative rotor angle (G1-G3)

(b) Speed deviations (G2-G3)

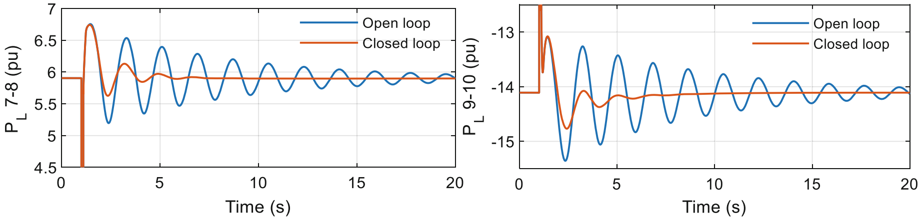

(c) Active power flow (Bus 7 – Bus 8)

(d) Active power flow (Bus 9 – Bus 10)

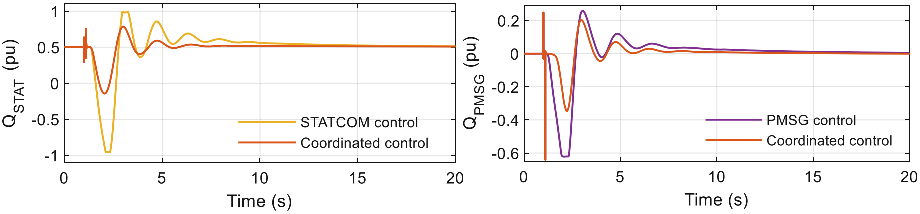

(e) STATCOM-Injected reactive power (pu)

(f) PMSG's compensated reactive power (pu)

Fig. 5. Simulation results for three-phase fault scenario

To confirm the efficiency of the controller at different wind speed and disturbance scenario, initially, it is assumed that the WNF is operating at 50% of its rated capacity. Then, at $t = 1$ s, a sudden load shedding occurs on bus 9 causing 200 MW of permanent load tripping for the remaining simulation interval. The dynamic simulation results, illustrated in Fig. 6a–d, noticeably show the robust damping performance of the controller and settling of the system variables to a new operating point.

Performance Assessment for Time Delays

Lastly, the effectiveness of the controller is validated for wide-area communication delays. The first-order Padé approximation is used to account for a fixed time delay (both in input and output channels) of 150 ms at the controller's design stage. This particular delay value is considered in view of optical fiber based communication links, for which time delay might be in the 100–150 ms range [21]. The transient results, depicted in Fig. 7, corroborate the superior damping performance of the controller designed by considering time delay.

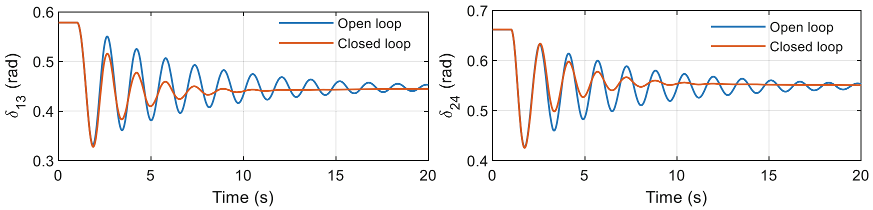

(a) Relative rotor angle (G_1-G_3) (b) Relative rotor angle (G_2-G_4)

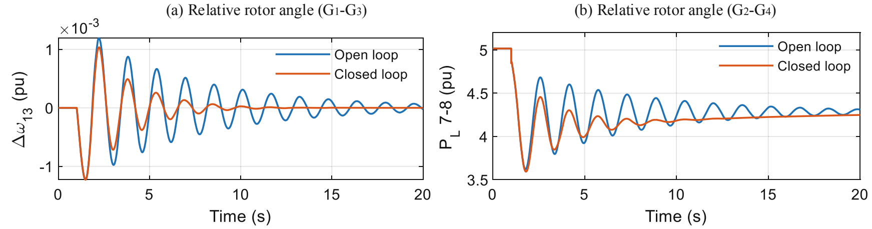

(c) Speed deviations (G_1-G_3) (d) Active power flow (Bus 7 – Bus 8)

Fig. 6. Simulation results for load-tripping fault

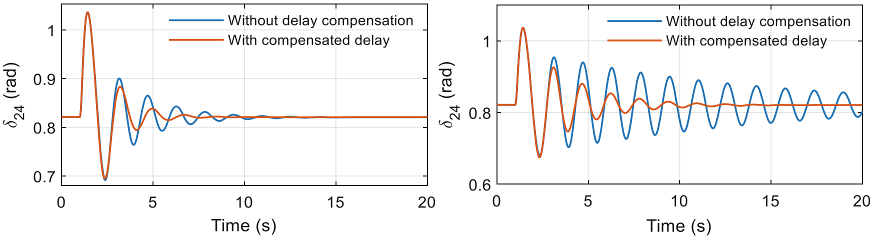

(a) Relative rotor angle (150 ms time delay) (b) Relative rotor angle (250 ms time delay)

Fig. 7. Controller's performance under time delay

5 Conclusion

This article has discussed the stability enhancement of the multi-machine power system connected with a WNF. A supplementary robust coordinated controller for the PMSG and STATCOM, synthesized via mixed-H_2/H_∞ control in the LMI framework is proposed to effectively improve the inter-area mode by assuring constrained pole placement. This is accomplished by modulating the reactive control loop of the STATCOM and PMSG with an additional damping controller, injected to provide dynamic reactive power compensation during transient conditions. The simulation results conclude that the proposed approach can robustly stabilize the power system oscillations subject to different faults, uncertain wind speed, and multi-channel wide area communication delays. Moreover, it is also determined that the coordinated scheme can deliver optimal reactive power compensation compared to an uncoordinated design.

Acknowledgements. This work is supported by the National Nature Science Foundation of China (No. U2166601).

References

1. Setiadi, H., Mithulananthan, N., Shah, R.: Design of wide-area POD with resiliency using modified DEA for power systems with high penetration of renewable energy. IET Renew. Power Gener. **13**(2), 342–351 (2019)
2. Gautam, D., Vittal, V., Harbour, T.: Impact of increased penetration of DFIG-based wind turbine generators on transient and small signal stability of power systems. IEEE Trans. Power Syst. **24**(3), 1426–1434 (2009)
3. Gurung, N., Bhattarai, R.: Optimal oscillation damping controller design for large-scale wind integrated power grid. IEEE Trans. Ind. Appl. **56**(4), 4225–4235 (2020)
4. Ngamroo, I.: Wide-area damping controllers of wind and solar power using probabilistic signal selection. IET Renew. Power Gener. **13**(8), 1351–1359 (2019)
5. Surinkaew, T., Ngamroo, I.: Robust power oscillation damper design for DFIG-based wind turbine based on specified structure mixed H_2/H_∞ control. Renew. Energy 6615–24 (2014)
6. Elhaji, E.M., Hatziadoniu, C.J.: Interarea oscillation damping using H-infinity control for the permanent magnet wind generator. Electr. Power Syst. Res. 151319–328 (2017)
7. Isbeih, Y.J., Shawky, M., Moursi, E., et al.: $H\infty$ mixed-sensitivity robust control design for damping low-frequency oscillations with DFIG wind power generation. IET Gener. Transm. Distrib. **13**(19), 4274–4286 (2019)
8. Abdlrahem, A.A., Hadidi, R., Karimi, A. et al.: Fixed-order loop shaping robust controller design for parametric models to damp inter-area oscillations. Int. J. Electr. Power Energy Syst., 88164–174 (2017)
9. Sadiq, R., Wang, Z., Chung, C.Y., et al.: A review of STATCOM control for stability enhancement of power systems with wind/PV penetration: existing research and future scope. Int. Trans. Electr. Energy Syst. **31**(11), 1–27 (2021)
10. Wang, L., Chang, C.H., Kuan, B.L., et al.: Stability improvement of a two-area power system connected with an integrated onshore and offshore wind farm using a STATCOM. IEEE Trans. Ind. Appl. **53**(2), 867–877 (2017)
11. Zhang, G., Hu, W., Cao, D. et al.: A data-driven approach for designing STATCOM additional damping controller for wind farms. Int. J. Electr. Power Energy Syst., **117** (2020)
12. Morshed, M.J., Fekih, A.: A probabilistic robust coordinated approach to stabilize power oscillations in DFIG-based power systems. IEEE Trans. Ind. Inf. **15**(10), 5599–5612 (2019)
13. Morshed, M.J., Sardoueinasab, Z., Fekih, A.: A coordinated control for voltage and transient stability of multi-machine power grids relying on wind energy. Int. J. Electr. Power Energy Syst., 10995–109 (2019)
14. Li, Y., Rehtanz, C., Member, S., et al.: Wide-area robust coordination approach of HVDC and FACTS controllers for damping multiple interarea oscillations. IEEE Trans. Power Deliv. **27**(3), 1096–1105 (2012)
15. Pal, B., Balarko, C.: Robust Control in Power Systems. Springer, New York (2005)
16. Qiao, W., Harley, R.G., Ganesh, K.V.: Coordinated reactive power control of a large wind farm and a STATCOM using heuristic dynamic programming. IEEE Trans. Energy Convers. **24**(2), 493–503 (2009)
17. Afzalan, E., Joorabian, M.: Analysis of the simultaneous coordinated design of STATCOM-based damping stabilizers and PSS in a multi-machine power system using the seeker optimization algorithm. Int. J. Electr. Power Energy Syst.,531003–1017 (2013)
18. Kunjumuhammed, L., Kuenzel, S., Pal, B.: Simulation of Power System with Renewables, 1st edn. Academic Press, San Diego, CA, Elsevier (2019)
19. Kunjumuhammed, L.P., Member, S., Pal, B.C., et al.: Stability analysis of a PMSG-based large offshore wind farm connected to a VSC-HVDC. IEEE Trans. Energy Convers. **32**(3), 1166–1176 (2017)

20. Kundur, P.: Power System Stability and Control. McGraw-Hill, New York (1994)
21. Bento, M.E.C., Ramos, R.A.: A method based on linear matrix inequalities to design a wide-area damping controller resilient to permanent communication failures. IEEE Syst. J. **15**(3), 3832–3840 (2020)

An Adaptive Dynamic State Estimation of Synchronous Generator Under Unknown Inputs

Dongchen Hou[1,2], Yonghui Sun[1](✉), and Venkata Dinavahi[2]

[1] Hohai University, Nanjing 210098, China
sunyonghui168@gmail.com
[2] University of Alberta, Edmonton 999040, Canada
dinavahi@ualberta.ca

Abstract. The phasor measurement units (PMUs), which are widely distributed at key nodes in the power network, provide a large amount of measurement information for dynamic state estimation. An accurate model is the foundation for ensuring dynamic state estimation. However, due to uncertain factors such as cyber-attacks, aging of device components and differences in operating environments, unknown inputs may exist in the model, seriously affecting the estimation accuracy. To upgrade the estimation performance of cubature Kalman filter (CKF) under unknown inputs, an adaptive CKF method is proposed. By utilizing adaptive factors, the error variance matrix of state variables can be adaptively updated to suppress the impact of unknown inputs on state estimation. Finally, simulations are conducted on the IEEE 39-bus test power system. Compared with traditional unscented Kalman filter (UKF) and CKF, the proposed method has better performance in estimation accuracy and algorithm robustness.

Keywords: Cubature Kalman filter · Dynamic state estimation · Synchronous generators · Unknown inputs

1 Introduction

In modern power systems, a large number of phasor measurement units (PMUs) are installed at critical locations in the power grid, providing valuable measurement information for dynamic state estimation (DSE) [1]. By utilizing dynamic state estimation, operators can monitor the operational states of the power system and develop more scientific and reasonable dispatching strategies and control schemes based on the current system states [2].

To achieve dynamic monitoring, Kalman filtering and its variants have received widespread attention, such extended Kalman filter (EKF), unscented Kalman filter (UKF) and cubature Kalman filter (CKF) [3–5]. By using PMUs data, a real-time DSE method based on EKF was proposed in [6]. Utilizing the hybrid measurement collected from supervisory control and data acquisition (SCADA) and PMUs, an EKF-based DSE method suitable for large-scale systems was proposed in [7]. However, in the process

Y. Xue et al. (Eds.): PMF 2023, LNEE 1129, pp. 339–348, 2024.
https://doi.org/10.1007/978-981-99-9251-5_27

of linearization, EKF abandons the higher-order term of Taylor expansion, resulting in linearization errors between the estimated result and the actual value, which greatly limited its estimation accuracy in nonlinear systems [8].

The derivative free Kalman filter method based on unscented transform and spherical-radial rule has obvious advantages compared with EKF in nonlinear system state estimation [9]. Furthermore, unlike UKF, CKF is not affected by the variable dimensions of state estimation and does not require complex parameter selection, making it more suitable for estimating the state of nonlinear systems, such as modern power systems. Considering the historical measurement, a CKF-based DSE method was developed in [10]. To ensure the performance of the state estimation method in outlier and non-Gaussian environments, a robust CKF method was developed to update the matrix of measurement noise by using M-estimator in [11]. In [12], taking into account the robustness of the CKF under non-Gaussian noise, a robust CKF method based on stochastic event-triggered framework was proposed to suppress tracking performance degradation caused by measurement noise statistical deviation from prior assumptions. To improve the estimation performance of DSE under bad measurement information, a CKF-based nonlinear regression model was constructed in [13]. By using Cauchy kernel functions to calculate the distance between different vectors, a robust CKF method with stronger resilience under DoS attacks was proposed in [14]. In addition, this method can still ensure the effectiveness of DSE in non-Gaussian noise environments. By using the weighted least squares method to estimate unknown input vectors, a derivative free dynamic state estimation method that can separate unknown inputs was proposed in [15].

In this paper, an adaptive cubature Kalman filter (ACKF) is developed to dynamically monitor the states of generators. To avoid complex parameter selection in UKF, the derivative free Kalman filter method based on spherical-radial rule is used to track the state of synchronous generators. Furthermore, taking into account the impact of unknown inputs caused by uncertain factors on dynamic state estimation, an adaptive update method for the error variance matrix of state variables is proposed to correct the estimation bias caused by unknown inputs. Finally, simulations are conducted on the IEEE 39-bus test power system to demonstrate the effectiveness of ACKF.

2 State Estimation Model

Ignoring the sub transient process of direct and quadratic axis windings, the simplified 4th-order model of synchronous generators can be described by

$$\dot{\delta} = \omega - \omega_0 \tag{1}$$

$$\dot{\omega} = \frac{\omega_0}{2H}\left(T_m - T_e - \frac{K_D}{\omega_0}(\omega - \omega_0)\right) \tag{2}$$

$$\dot{e'}_q = \frac{1}{T'_{d0}}\left(E_{fd} - e'_q - \left(x_d - x'_d\right)i_d\right) \tag{3}$$

$$\dot{e'}_d = \frac{1}{T'_{q0}}\left(-e'_d + \left(x_q - x'_q\right)i_q\right) \tag{4}$$

where δ and ω respectively denote rotor angle and speed, H denotes inertia constant, K_D denotes damping coefficient, the subscript d represents the direct axis of synchronous generator rotor, T_m and T_e represent mechanical and electrical torque, the subscript q denotes the quadratic axis of synchronous generator rotor, e' represents the transient voltage, T'_{d0} and T'_{q0} indicate the open circuit time constant of direct axis and quadratic axis, i is the current, E_{fd} is the field voltage, x and x' respectively indicate reactance and transient reactance.

For convenience, the compact matrix form of 4th-order model can be written as

$$\dot{x} = f(x, u) + w, \tag{5}$$

$$z = h(x, u) + v, \tag{6}$$

$$x = \left[\delta^{\mathrm{T}}, \omega^{\mathrm{T}}, e_q'^{\mathrm{T}}, e_d'^{\mathrm{T}} \right]^{\mathrm{T}}, \tag{7}$$

$$u = \left[T_m^{\mathrm{T}}, E_{fd}^{\mathrm{T}}, i_R^{\mathrm{T}}, i_I^{\mathrm{T}} \right]^{\mathrm{T}}, \tag{8}$$

$$z = \left[\delta^{\mathrm{T}}, \omega^{\mathrm{T}}, e_R^{\mathrm{T}}, e_I^{\mathrm{T}} \right]^{\mathrm{T}}. \tag{9}$$

To obtain the state function and measurement function, i_d, i_q, e_R and e_I can be rewritten as

$$i_d = i_R \sin\delta - i_I \cos\delta, \tag{10}$$

$$i_q = i_I \sin\delta + i_R \cos\delta, \tag{11}$$

$$e_R = \left(e_d' + x_q' i_q \right) \sin\delta + \left(e_q' - x_d' i_d \right) \cos\delta, \tag{12}$$

$$e_I = \left(e_q' - x_d' i_d \right) \sin\delta - \left(e_d' + x_q' i_q \right) \cos\delta. \tag{13}$$

where e is the voltage, the subscript R and I respectively denote the real and imaginary parts.

Considering the discrete nature of measurement information, the discrete form of 4th-order model can be given as

$$x_k = f(x_{k-1}, u_{k-1}) + w_{k-1}, \tag{14}$$

$$z_k = h(x_k, u_k) + v_k. \tag{15}$$

3 Proposed Method

3.1 Cubature Kalman Filter

For a n-dimensional model, a set of $2n$ cubature points are selected to capture statistical properties by using spherical-radial rule in CKF. Suppose that the estimation state variable $\hat{x}_{k-1}$ and covariance matrix P_{k-1}. Can be given from static state estimation results. Furthermore, S_{k-1} is the square-rooting matrix of covariance matrix P_{k-1}.

$$P_{k-1} = S_{k-1} S_{k-1}^{\mathrm{T}} \tag{16}$$

$$X_{j,k-1} = \hat{x}_{k-1} + S_{k-1} \xi_j, j = 1, 2, \cdots, 2n \tag{17}$$

where $X_{j,k-1}$ indicates the cubature point set around state variable $\hat{x}_{k-1}$.

Substituting the cubature point set into state function, the state variable $\hat{x}_k$ and the variance matrix $\tilde{P}_k$ can be obtained by

$$X_{j,k}^{*} = f\left(X_{j,k-1}, u_{k-1}\right), j = 1, 2, \cdots, 2n \tag{18}$$

$$\tilde{x}_k = \frac{1}{2n} \sum_{j=1}^{2n} X_{j,k}^{*} \tag{19}$$

$$\tilde{P}_k = \frac{1}{2n} \sum_{j=1}^{2n} X_{j,k}^{*} \left(X_{j,k}^{*}\right)^{\mathrm{T}} - \tilde{x}_k (\tilde{x}_k)^{\mathrm{T}} + Q_{k-1} \tag{20}$$

The square-rooting matrix of covariance matrix $\tilde{P}_k$ can be obtained by

$$\tilde{P}_k = S_k S_k^{\mathrm{T}} \tag{21}$$

$$X_{j,k} = \tilde{x}_k + S_k \xi_j, j = 1, 2, \cdots, 2n \tag{22}$$

Through the measurement function, the predictive measurement $\tilde{z}_k$ and innovation variance matrix $P_{zz,k}$ can be obtained by

$$Z_{j,k} = f\left(X_{j,k}, u_k\right), j = 1, 2, \cdots, 2n \tag{23}$$

$$\tilde{z}_k = \frac{1}{2n} \sum_{j=1}^{2n} Z_{j,k} \tag{24}$$

$$P_{zz,k} = \frac{1}{2n} \sum_{j=1}^{2n} Z_{j,k} Z_{j,k}^{\mathrm{T}} - \tilde{z}_k \tilde{z}_k^{\mathrm{T}} + R_k \tag{25}$$

The cross-covariance matrix and filter gain can be calculated by

$$P_{xz,k} = \frac{1}{2n} \sum_{j=1}^{2n} X_{j,k} Z_{j,k}^{\mathrm{T}} - \tilde{x}_k \tilde{z}_k^{\mathrm{T}} \tag{26}$$

$$K_k = P_{xz,k} P_{zz,k}^{-1} \tag{27}$$

Additionally, the estimation state variable $\hat{x}_k$ and error matrix P_k.can be updated by

$$\hat{x}_k = \tilde{x}_k + K_k (z_k - \tilde{z}_k) \tag{28}$$

$$\hat{P}_k = \tilde{P}_k - K_k P_{zz,k} K_k^T \tag{29}$$

3.2 Unknown Input Correction

Uncertain factors are ubiquitous in the actual power system. The humidity and temperature in the environment can cause varying degrees of aging of equipment components, resulting in mismatches between power system equipment and model assumptions. In addition, the access of malicious cyber-attacks may also lead to device models deviating from assumptions. The unknown input generated by uncertain factors will affect the estimation of all state variables.

Therefore, an adaptive method has been developed to overcome the impact of unknown inputs by utilizing adaptive factors λ_k to correct the state variance matrix.

$$\tilde{P}_k = \lambda_k^{-1} \left[\frac{1}{2n} \sum_{j=1}^{2n} X_{j,k}^* \left(X_{j,k}^* \right)^{\mathrm{T}} - \tilde{x}_k (\tilde{x}_k)^{\mathrm{T}} + Q_{k-1} \right] \tag{30}$$

Theorem 1 Suppose that $\hat{P}_{zz,k}$ is the estimated variance matrix after adding new measurement, $\tilde{P}_{zz,k}$ is the variance matrix obtained by adaptive filtering, $P_{zz,k}$ is the variance matrix obtained based on the law of covariance propagation. The selection of adaptive factors should ensure that the following equation holds.

$$\tilde{P}_{zz,k} = \hat{P}_{zz,k} \tag{31}$$

Then, the adaptive factor λ_k can be calculated by using trace function $tr(\cdot)$.

$$\lambda_k = \frac{tr\left(P_{zz,k} - R_k\right)}{tr\left(\hat{P}_{zz,k} - R_k\right)} \tag{32}$$

Proof The prediction error $\hat{x}_k$ can be expressed as

$$\hat{x}_k = x_k - \tilde{x}_k \tag{33}$$

Furthermore, the filtering residual is

$$r_k = y_k - h\left(\hat{x}_k\right) = y_k - h(x_k - \tilde{x}_k) \tag{34}$$

Based on Taylor expansion, $h(x_k - \tilde{x}_k)$ can be written as

$$h(x_k - \tilde{x}_k) \approx h(x_k) - \left. \frac{\partial h}{\partial x} \right|_{x = \tilde{x}_k} \times \tilde{x}_k = h(x_k) - D_k \tilde{x}_k \tag{35}$$

The filtering residual r_k can be rewritten as

$$r_k = y_k - h(x_k) + D_k\tilde{x}_k = v_k + D_k\tilde{x}_k \tag{36}$$

Based on the law of covariance propagation, the innovation variance matrix $P_{zz,k}$ can be written as

$$\begin{aligned} P_{zz,k} &= \mathrm{E}\left\{r_k r_k^T\right\} \\ &= \mathrm{E}\left\{(v_k + D_k\tilde{x}_k)(v_k + D_k\tilde{x}_k)^T\right\} \\ &= \mathrm{E}\left(D_k\tilde{x}_k\tilde{x}_k^T D_k^T\right) + \mathrm{E}\left(v_k v_k^T\right) \\ &= D_k\tilde{P}_k D_k^T + R_k \end{aligned} \tag{37}$$

By using adaptive factor λ_k, the matrix $\tilde{P}_{zz,k}$ can be obtain by

$$\tilde{P}_{zz,k} = \alpha_k^{-1} D_k\tilde{P}_k D_k^T + R_k \tag{38}$$

According to (31), one further has

$$\hat{P}_{zz,k} = P_{zz,k} = \alpha_k^{-1} D_k\tilde{P}_{x,k} D_k^T + R_k \tag{39}$$

$$\lambda_k\left(\hat{P}_{zz,k} - R_k\right) = D_k P_{x,k} D_k^T = P_{zz,k} - R_k \tag{40}$$

Considering that the value of the adaptive factor should be equal to or less than one, λ_k can be written as

$$\lambda_k = \begin{cases} 1, \ tr\left(P_{zz,k}\right) \geq tr\left(\hat{P}_{zz,k}\right) \\ \frac{tr\left(P_{zz,k} - R_k\right)}{tr\left(\hat{P}_{zz,k} - R_k\right)}, \ tr\left(P_{zz,k}\right) < tr\left(\hat{P}_{zz,k}\right) \end{cases} \tag{41}$$

Ignoring the common term R_k, the expression of the adaptive factor is

$$\lambda_k \approx \begin{cases} 1, \ tr\left(P_{zz,k}\right) \geq tr\left(\hat{P}_{zz,k}\right) \\ \frac{tr\left(P_{zz,k}\right)}{tr\left(\hat{P}_{zz,k}\right)}, \ tr\left(P_{zz,k}\right) < tr\left(\hat{P}_{zz,k}\right) \end{cases} \tag{42}$$

where $P_{zz,k}$ represents the innovation variance matrix and it can be obtained by (25). Based on the residual vector at the current time, the innovation variance matrix $\hat{P}_{zz,k}$ can be obtained by

$$tr\left(\hat{P}_{zz,k}\right) = tr\left(r_k r_k^T\right) = r_k r_k^T \tag{43}$$

4 Numerical Results

Simulations were conducted on the IEEE 39-bus test power system to demonstrate the effectiveness of ACKF. In order to simulate the actual system situation, it is supposed that a three-phase fault has occurred in the test system, and the information of the system and fault parameters can be found in [16]. Additionally, to demonstrate the performance of ACKF for DSE in different scenarios, the estimation results of generator 10 (G10) under unknown inputs and normal conditions are discussed separately.

4.1 Normal Conditions

During normal operation of power system, it is usually assumed that prior statistical information matches actual noise statistics. In order to observe the advantages of ACKF, UKF and CKF are selected as comparative methods. The results of rotor angle and speed of the discussed methods are presented in Fig. 1. The results of *d*- and *q*-axis transient voltage are displayed in Fig. 2. Moreover, the results of average state estimation error are shown in Table 1.

As shown in the figures, the methods discussed above can accurately track the state changes of the generator. However, due to the fact that the noise covariance matrix Q_{k-1} is given and cannot be adaptively updated, there is a small deviation between the estimated result of UKF and the true value when tracking the *d*-axis transient voltage. Additionally, it can be seen from the above results that CKF also has the same problem. Because the adaptive factor corrects the error variance matrix of state variables, which includes the noise covariance matrix Q_{k-1}, the tracking effect of ACKF is better.

Table 1. The results of average estimation error under normal conditions.

Method	δ	ω	e'_q	e'_q
UKF	0.856431	0.001058	0.223119	0.414878
CKF	0.856662	0.001058	0.224217	0.415264
ACKF	0.857656	0.001055	0.216951	0.415431

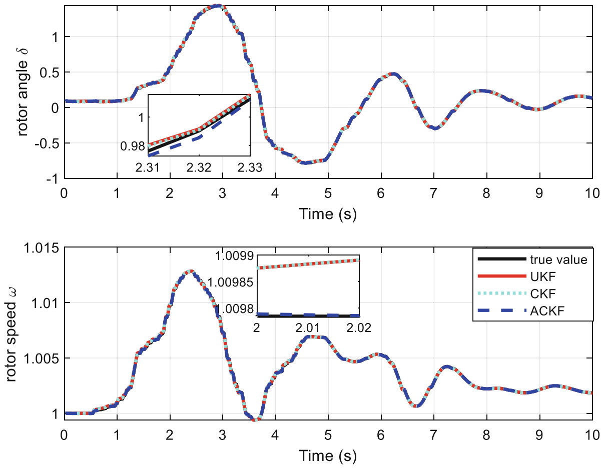

Fig. 1. Estimation results of rotor angle and speed of G10 under normal conditions.

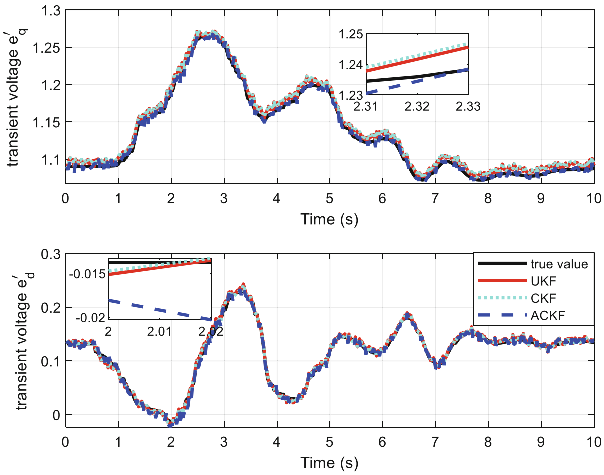

Fig. 2. Estimation results of transient voltages on the direct and quadratic axes of G10 under normal conditions.

4.2 Unknown Inputs

The power system is inevitably affected by uncertain factors during operation, which may lead to estimation bias in dynamic state estimation. The estimation results of G10 are displayed in the Figs. 3 and 4. Moreover, the results of average state estimation error are displayed in Table 2. From the estimation results of transient voltages, it can be seen that the performance of UKF and CKF are affected by unknown inputs and deviate from the actual state, especially for the quadratic axis transient voltage. When the model has unknown inputs, the proposed ACKF can ensure the accuracy of state estimation by adaptively updating the variance matrix of state variables.

Table 2. The results of average estimation error under unknown inputs.

Method	δ	ω	e'_q	e'_q
UKF	0.850392	0.001121	0.263349	0.403610
CKF	0.851262	0.001121	0.269152	0.405064
ACKF	0.851656	0.001055	0.216951	0.401743

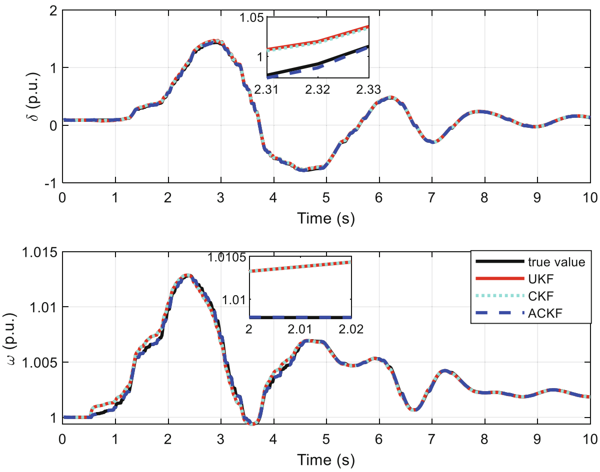

Fig. 3. Estimation results of rotor angle and speed of G10 under unknown inputs.

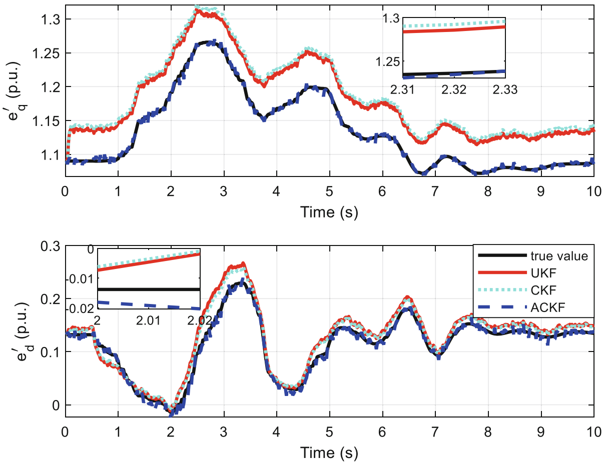

Fig. 4. Estimation results of transient voltages on the direct and quadratic axes of G10 under unknown inputs.

5 Conclusion

An adaptive DSE method was proposed to address the bias in estimation results caused by unknown inputs. In order to avoid complex parameter settings in UKF, a more flexible CKF was chosen for state estimation of synchronous motors. Furthermore, by utilizing adaptive factors to correct the error variance matrix of state variables, the estimation bias caused by unknown inputs was effectively suppressed. Compared with UKF and CKF, ACKF had good estimation performance in both normal operating conditions and unknown input scenarios.

Acknowledgements. This work was supported by the National Natural Science Foundation of China (No. 62073121), the National Natural Science Foundation of China-State Grid Joint Fund for Smart Grid (No. U1966202) and the Natural Sciences and Engineering Research Council (NSERC) of Canada.

References

1. Wang, Y., Sun, Y., Dinavahi, V.: Robust forecasting-aided state estimation for power system against uncertainties. IEEE Trans. Power Syst. **35**(1), 691–702 (2020)
2. Xiao, R., Wang, G., Hao, X., Huang, R., Xiong, Y.: Dynamic state estimation of medium-voltage DC integrated power system with pulse load. J. Modern Power Syst. Clean Energy **8**(4), 689–698 (2020)
3. Chakhchoukh, Y., Lei, H., Johnson, B.: Diagnosis of outliers and cyber attacks in dynamic PMU-based power state estimation. IEEE Trans. Power Syst. **35**(2), 1188–1197 (2020)
4. Tan, B., Zhao, J., Netto, M.: A general decentralized dynamic state estimation with synchronous generator magnetic saturation. IEEE Trans. Power Syst. **38**(1), 960–963 (2023)
5. Wang, Y., Sun, Y., Dinavahi, V., Shi, Q., Hou, D.: Adaptive robust cubature Kalman filter for power system dynamic state estimation against outliers. IEEE Access **7**, 105872–105881 (2019)
6. Fan, L., Wehbe, Y.: Extended Kalman filtering based real-time dynamic state and parameter estimation using PMU data. Electric Power Syst. Res. **103**, 168–177 (2013)
7. Karimipour, H., Dinavahi, V.: Extended Kalman filter-based parallel dynamic state estimation. IEEE Trans. Smart Grid **6**(3), 1539–1549 (2015)
8. Ahmed, M., Harbi, I., Kennel, R., Abdelrahem, M.: Direct power control based on dead-beat function and extended Kalman filter for PV systems. J. Modern Power Syst. Clean Energy **11**(3), 863–872 (2023)
9. Rigatos, G.: A derivative-free Kalman filtering approach to state estimation-based control of nonlinear systems. IEEE Trans. Industr. Electron. **59**(10), 3987–3997 (2012)
10. Zhang, T., Zhang, W., Zhao, Q., Du, Y., Chen, J., Zhao, J.: Distributed real-time state estimation for combined heat and power systems. J. Modern Power Syst. Clean Energy **9**(2), 316–327 (2021)
11. Li, Y., Li, J., Qi, J., Chen, L.: Robust cubature Kalman filter for dynamic state estimation of synchronous machines under unknown measurement noise statistics. IEEE Access **7**, 29139–291487 (2019)
12. Li, Z., Li, S., Li, B., Yu, S., Shi, P.: A stochastic event-triggered robust cubature Kalman filtering approach to power system dynamic state estimation with non-Gaussian measurement noises. IEEE Trans. Control Syst. Technol. **31**(2), 889–896 (2023)
13. Wang, Y., Yang, Z., Wang, Y., Dinavahi, V., Liang, J., Wang, K.: Robust dynamic state estimation for power system based on adaptive cubature Kalman filter with generalized correntropy loss. IEEE Trans. Instrum. Meas. **71**, 9003811 (2022)
14. Wang, Y., Yang, Z., Wang, Y., Li, Z., Dinavahi, V., Liang, J.: Resilient dynamic state estimation for power system using Cauchy-kernel based maximum correntropy cubature Kalman filter. IEEE Trans. Instrum. Meas. **72**, 9002011 (2023)
15. Anagnostou, G., Pal, B.: Derivative-free Kalman filtering based approaches to dynamic state estimation for power systems with unknown inputs. IEEE Trans. Power Syst. **33**(1), 116–130 (2018)
16. Wang, Y., Sun, Y., Dinavahi, V., Wang, K., Nan, D.: Robust dynamic state estimation of power systems with model uncertainties based on adaptive unscented H-infinity filter. IET Gener. Transm. Distrib. **13**(12), 2455–2463 (2019)

Dynamic Transmission Expansion Planning Using Adaptive Robust Optimization Under Uncertainties

Sahar Rahim[1,2], Fan Li[3], Zhen Wang[1](✉), Pan Dai[3], and Hongji Yang[3]

[1] Zhejiang University, Hangzhou 310027, Zhejiang, China
`eezwang@ieee.org`
[2] COMSATS University Islamabad, Wah Campus 47040, Pakistan
[3] Economic Research Institute of State Grid Zhejiang Electric Power Company, Hangzhou 310027, Zhejiang, China

Abstract. The transmission expansion planning (TEP) problem is one of the perilous issues, which allows electricity transmission planners to design a cost-effective and reliable strategic model for the implementation of optimal transmission reinforcements in existing power grid networks. In this paper, a novel TEP model is proposed considering long- and short- term uncertain factors. The three-stage adaptive robust optimization (ARO) method deals with long-term uncertainties while prudently representing short-term uncertain parameters via scenarios. The formulated strategic scheme is elucidated through a modified decomposition algorithm that applies primal cutting planes and focuses on the subproblem feasible solution. The efficacy of the presented model is demonstrated through realistic case studies based on a 6-bus test system.

Keywords: Transmission expansion planning · Robust optimization · Renewable energy · Uncertainty · Decomposition algorithm

1 Introduction

The modernization and electrification of traditional power grid networks have encouraged power system researchers and engineers to predominantly concentrate on proficient, cost-effective, and reliable electricity supply from power generation units to gigantic distribution stations and then to end-users [1]. With adverse climate variations, one of the tenacious challenges is to limit global greenhouse gas (GHG) emissions [2]. In recent years, renewable energy integration has occupied a prominent position in critical agendas of many industrial countries, aiming to reduce carbon dioxide (CO_2) emissions and meet the requirement of intensifying energy demand [3, 4]. The large-scale deployment of renewable energy sources (RESs) and decommission of orthodox energy resources have sparked a flurry of discussion on well-planned power transmission networks under uncertainties for dexterous power system operations. Transmission expansion planning (TEP) provides optimal and strategic decisions for the expansion and/or construction of transmission lines while reducing investment and operational costs of the power system by

Y. Xue et al. (Eds.): PMF 2023, LNEE 1129, pp. 349–363, 2024.
https://doi.org/10.1007/978-981-99-9251-5_28

observing administrative, environmental, and technical requirements [5]. Furthermore, optimization problems related to transmission network expansion compute minimum net investment cost-based expansion plans that can adequately satisfy the forecasted electric load over a pre-defined planning time horizon. Herein, the forecasted load demand and stochastic power recourses have been deliberated as major sources of uncertainty that must be taken into attention in the planning problem. Therefore, the TEP under uncertainty has engrossed ample interest in the past couple of years from the power industry for the formulation of economic robust designs that can significantly tackle all foreseeable values of net injections [6].

In TEP problems, the expansion decisions need to be calculated under the impact of uncertain factors including both long- and short- term uncertain parameters. The long-term uncertainty is usually associated with year-to-year deviations such as variations in future load demand growth and power generation capacity, while the short-term uncertainty belongs to day-to-day variability such as stochastic power production from RESs, electrical demand fluctuations, and equipment failure [7]. In the literature, there are numerous TEP models that are carried out without considering uncertainties [8–10]. For instance, the TEP approach adopted in [8] is based on the DC networks, formulated through mixed-integer non-linear programming (MINLP). In the same way, the authors formulated TEP as a mixed-integer linear programming (MILP) model and solved it via branch-and-cut approaches [9, 10]. As these expansion planning models did not consider uncertain factors, therefore, the accuracy is near to low. Thus, the TEP investment decision-making model must be articulated within an uncertain environment in order to tackle inherited risk factors.

According to recent studies, it is observed that there are various planning formulation schemes that have been attempting to model uncertainties during the analysis of TEP optimization problems [11, 12]. Over the past few years, stochastic programming (SP) and robust optimization (RO) have been vastly adopted for the characterization of uncertainties [13]. The SP approach entails exact probabilistic information and highly depends on computationally complex uncertainty discretization through scenarios. In [14], an SP-based framework is presented to deal with generation and transmission expansion planning problems under the influence of load demand variations. A MILP formulation is proposed to tackle the TEP optimization problem in a pool-based competitive electricity market, whereas, SP is employed for the realization of long-term futuristic load demand fluctuations [15]. The authors in [16] solved MINLP based TEP problem by taking into account future load demand uncertainty via a large number of scenarios by using the SP approach to reduce net investment cost and enhance reliability. In general, the SP is reliant on massive scenarios generation that may lead to computational intractability for multi-dimensional complex real-time optimization problems.

On the contrary, the RO uncertainty modeling technique has a protuberant advantage over the SP approach; all the uncertain factors are represented in the form of robust sets instead of scenarios, therefore the size of the problem does not increase with the number of scenarios [13]. In modern research on TEP optimization problems under uncertainty, the RO approach has gained a lot of interest. Various researchers and engineers have been working on RO-based TEP methodologies. Jabr in [17] presented a RO-based TEP approach, a polynomial uncertainty set is used to deal with load and renewable generation uncertainties. The formulated model is elucidated by a Benders decomposition (BD) algorithm for the minimization of the expansion planning cost of the power transmission systems. Similarly, a three-level robust framework is proposed in [18] by applying a polyhedral uncertainty set to regulate the fluctuation range of uncertain parameters linked with different regions of the power system, while a primal BD algorithm is used to solve the model. Mínguez and García-Bertrand [19] improved computation performance of the TEP problem via a robust polynomial uncertainty set by differentiating between long- and short- term uncertainties. This work formulates a three-level adaptive robust optimization (ARO) based approach to solve MILP problems, while a modified BD algorithm is employed to evaluate the designed approach. In another article [20], the TEP problem is addressed under long- and short- term uncertainty, whereas, the expansion problem is formulated via ARO and solved through the primal BD algorithm to enhance computational efficiency. The authors in [21] suggested ARO constituted the TEP approach by taking into account the impacts of load demand and generation capacity uncertainties. Liang et al. addressed issues of uncertainty set size and uncertainty budget amount by using a novel ARO method while providing protection against the risk associated with wind generation. Furthermore, the RO-based TEP approach is recommended in [22] to determine the optimized uncertainty budget by minimizing the uncertainty set size pertained to the risk of fluctuation in wind power generation.

After a comparative study, it is observed that references [17, 18] focused on the realization of uncertain factors by using complex polyhedral uncertainty set without considering uncertain parameter correlations. On the other hand, article [19] demonstrated that the presented methodology is computationally effective but they omitted the integrality budget uncertainty constraint. Moreover, [20] provides a dynamic robust TEP model with a limitation of the tradeoff between complexity and accuracy. The article [21] proposed an effective static robust model to find out TEP, which may lead to compromise on the accuracy of the expansion plan for the long-term planning horizon, while the work in [22] faced a tradeoff between investment cost and robustness. By keeping in view aforesaid limitations in the existing TEP, this paper introduces a novel data-driven dynamic approach to find out the optimal expansion plan for the transmission network. Our main contributions are stated below:

(1) To design a three-staged dynamic TEP model based on ARO.
(2) Explicitly characterize long-term uncertain factors that commonly involve multi-year financial commitments and short-term variations that include hourly operating decisions to maximize the expected profit.
(3) Modify the decomposition algorithm based on the constraint-and-column generation method [19] to solve the presented multi-level optimization problem.

The rest of this work is structured as follows. In Sect. 2, the mathematical formulation for TEP is provided, whereas Sect. 3 describes the proposed solution algorithm. The results are discussed in Sect. 4 by analyzing a real-time case study on multiple test benches. In the end, the concluding remarks and future research direction are stated in Sect. 5.

2 TEP Problem Formulation

In this section, a detailed mathematical formulation for TEP optimization problem under uncertainty is discussed.

2.1 Framework of ARO-TEP

In the three-layered ARO-based TEP framework, the first stage minimizes the investment cost (decision variables associated with the expansion of an existing line and/or construction of a new one), the second layer considers all the realization of uncertain factors within the ambiguity set (decision variables linked with uncertain parameters), while system operators select decision variables in the third layer for the reduction in operational cost by taking into account outputs from first and second stages. Our focal goal is to attain a cost-effective expansion scheme while satisfying the worst-case uncertainties identified from the uncertainty set. The systematic approach for the recommended ARO-based TEP is illustrated in Fig. 1.

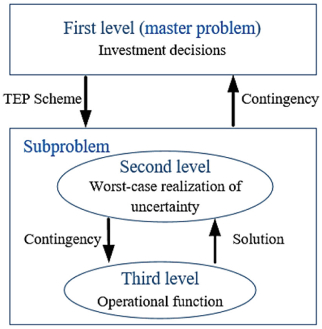

Fig. 1 Framework of ARO-based TEP

2.2 Problem Formulation

The ARO technique represents uncertainties in the form of uncertainty sets, computationally less complex than the SP models [13]. In this work, load demand and power generation resources have been considered as a source of uncertainty in the subjected TEP problem. Thus, the hierarchical structure of the three-layered ARO-based TEP optimization problem is provided below.

$$\min_{\Theta_1} \sum_{l \in \Omega^{L+}} \mathrm{I_l x_l} + \max_{\Theta_2} \sum_{s \in \Omega^{S}} \rho^{\mathrm{S}} \left[\Re\left(\Theta_1, \tilde{\xi} \right) \right] \tag{1}$$

Subject to:

$$\sum_{\mathrm{l} \in \Omega^{\mathrm{L}+}} \mathrm{I_l x_l} \le \Pi^{\mathrm{L,max}} \tag{1a}$$

$$x_l \in \{0, 1\}; x_l \in \Omega^{L+} \tag{1b}$$

$$x_l = 1; x_l \in \frac{\Omega^{\mathrm{L}}}{\Omega^{\mathrm{L}+}} \tag{1c}$$

Subject to:

$$\overline{P}_{g_i}^{T} \in \left[\overline{P}_{g_i}^{T,\min}, \overline{P}_{g_i}^{T,\exp}\right]; \forall g_i \in \Omega^{\mathrm{T}} \tag{1d}$$

$$\frac{\sum_{g_i \in \Omega^Z}\left(\overline{P}_{g_i}^{T,\exp} - \overline{P}_{g_i}^{T}\right)}{\sum_{g_i \in \Omega^Z}\left(\overline{P}_{g_i}^{T,\exp} - \overline{P}_{g_i}^{T,\min}\right)} \leq \Gamma_z^T; \forall z \in \Omega^Z \tag{1e}$$

$$\overline{P}_{g_j}^{R} \in \left[\overline{P}_{g_j}^{R,\min}, \overline{P}_{g_j}^{R,\exp}\right]; \forall g_j \in \Omega^{\mathrm{R}} \tag{1f}$$

$$\frac{\sum_{g_j \in \Omega^Z}\left(\overline{P}_{g_j}^{R,\exp} - \overline{P}_{g_j}^{R}\right)}{\sum_{g_j \in \Omega^Z}\left(\overline{P}_{g_j}^{R,\exp} - \overline{P}_{g_j}^{R,\min}\right)} \leq \Gamma_z^R; \forall z \in \Omega^Z \tag{1g}$$

$$\overline{P}_d \in \left[\overline{P}_d^{\exp}, \overline{P}_{\mathrm{d}}^{\max}\right]; \forall d \in \Omega^{\mathrm{D}} \tag{1h}$$

$$\frac{\sum_{d \in \Omega^Z}\left(\overline{P}_d - \overline{P}_d^{\exp}\right)}{\sum_{d \in \Omega^Z}\left(\overline{P}_d^{\max} - \overline{P}_d^{\exp}\right)} \leq \Gamma_z^D; \forall z \in \Omega^Z \tag{1i}$$

where, l is the index of transmission lines in the set of candidate lines $\Omega^{\mathrm{L}+}$, $\mathrm{I_l}$. is the annualized investment cost of the transmission line and $\mathrm{x_l}$ is the binary variable (i.e. if $\mathrm{x_l} = 1$, then line l is built). The first term of Eq. 1 is the annualized investment cost of building new transmission lines over investment decision variable set ($\Theta_1 = \mathrm{x_l} \in \Omega^{\mathrm{L}+}$). Furthermore, s is the index of operating scenarios in the set Ω^{S} and ρ^{S} is the weight of scenario s. The uncertainty set is denoted by Θ_2 includes uncertain parameters (i.e. $\overline{P}_{g_i}^{T}; \forall g_i \in \Omega^{\mathrm{T}}, \overline{P}_{g_j}^{R}; \forall g_j \in \Omega^{\mathrm{R}}, \overline{P}_d; \forall d \in \Omega^{\mathrm{D}}, ,$) within ambiguity set $\tilde{\xi}$. In this work, the load demand and installed power generating capacity have been considered as long-term uncertainties that are represented by the polyhedral robust sets as in [20]. Constraint (1d-1e) characterizes the uncertainty set of conventional power generation capacity, Constraint (1f-1g) depicts the stochastic power production units, while Constraint (1h-1i) defines the future peak load demand. The long-term uncertain factors for generation capacities $\overline{P}_{g_i}^{T}$ and $\overline{P}_{g_i}^{R}$ that are belonged to the range from minimum level ($\overline{P}_{g_i}^{T,\min}$, $\overline{P}_{g_j}^{R,\min}$) to the expected level ($\overline{P}_{g_i}^{R,\exp}$, $\overline{P}_{g_j}^{R,\exp}$), whereas, the peak load demand $\overline{\mathrm{P}_d}$ at each load node fluctuates between the expected level ($\overline{P}_d^{\exp}$) to its maximum level ($\overline{P}_d^{\max}$). . If there is no case for long-term uncertainty, then no robust protection (i.e. uncertainty budget is 0) is required. With the growth in the uncertainty budget, the uncertainty level increases and higher robust protection is needed. Moreover, the ambiguity set links to predefined geographical zones with index z in Ω^Z. Herein, the value for uncertainty budgets Γ_z^T, Γ_z^R, and Γ_z^D must does not exceed the quantity of generating units and load demand within z zone. Furthermore, $\Re\left(\Theta_1, \tilde{\xi}\right)$ is the recourse function that anticipates operator reactions by ensuring the operating decisions feasibility over the set Θ_1 and all the realizations of uncertainties in $\tilde{\xi}$.

$$R = \min_{\Theta_3} \beta \left(\sum_{\mathrm{g_i} \in \Omega^{\mathrm{T}}} \Lambda_{\mathrm{g_i}}^{\mathrm{T}} \mathrm{P}_{\mathrm{g_i}}^{\mathrm{T,s}} + \sum_{\mathrm{g_j} \in \Omega^{\mathrm{R}}} \Lambda_{\mathrm{g_j}}^{\mathrm{R}} \mathrm{P}_{\mathrm{g_j}}^{\mathrm{R,s}} + \sum_{\mathrm{d} \in \Omega^{\mathrm{D}}} \Lambda_{\mathrm{d}}^{\mathcal{L}} \mathrm{P}_{\mathrm{d}}^{\mathcal{L},\mathrm{s}} \right) \tag{2}$$

Subject to:

$$\sum_{g_i \in \Omega_n^T} P_{g_i}^{T,s} + \sum_{g_j \in \Omega_n^R} P_{g_j}^{R,s} - \sum_{l|s(l) \in \Omega_n} f_l^s + \sum_{l|r(l) \in \Omega_n} f_l^s$$
$$= \sum_{d \in \Omega_n^D} \omega_d^{D,s} \overline{D}_d - \sum_{d \in \Omega_n^D} P_d^{\mathcal{L},s} : \alpha_n^s; \forall n \in \Omega^N, \forall s \in \Omega^S \tag{2a}$$

$$f_l^s - x_l b_l \left(\theta_{s(l)}^s - \theta_{r(l)}^s \right) = 0 : \mu_l^{L,s}; \forall l \in \Omega^L, \forall s \in \Omega^S \tag{2b}$$

$$-f_l^{\max} \le f_l^s \le f_l^{\max} : \gamma_l^{L\min,s}, \gamma_l^{L\max,s}; \forall l \in \Omega^L, \forall s \in \Omega^S \tag{2c}$$

$$0 \le P_{g_i}^{T,s} \le e_{g_i}^{T,s} \overline{\mathrm{P}}_{g_i}^T : \rho_{g_i}^{T\min,s}, \rho_{g_i}^{T\max,s}; \forall g_i \in \Omega^{G^T}, \forall s \in \Omega^S \tag{2d}$$

$$0 \le P_{g_j}^{R,s} \le e_{g_j}^{R,s} \overline{\mathrm{P}}_{g_j}^R : \rho_{g_j}^{R\min,s}, \rho_{g_j}^{R\max,s}; \forall g_j \in \Omega^{G^R}, \forall s \in \Omega^S \tag{2e}$$

$$0 \le P_d^{\mathcal{L},s} \le e_d^{\mathcal{L},s} \overline{\mathrm{P}}_d^D : \psi_d^{D\min,s}, \psi_d^{D\max,s}; \forall d \in \Omega^D, \forall s \in \Omega^S \tag{2f}$$

$$-\pi \le \theta_n^s \le \pi : \delta_n^{\min,s}, \delta_n^{\max,s}; \forall n \in \Omega^N, \forall s \in \Omega^S \tag{2g}$$

$$\theta_n^s = 0 : \varphi_n^s; n : ref, \forall s \in \Omega^S \tag{2h}$$

Here, $\Re$ minimizes the operation cost comprises of power generating cost and load shedding cost, computed over all the short-term scenarios. The set of operating decision variables is Θ_3, defined as $\Theta_3 = P_{gi}^{T,s}, \forall g_i \in \Omega^{G^T}, \forall s \in \Omega^S; P_{gj}^{R,s}, \forall g_j \in \Omega^{G^R}, \forall s \in \Omega^S; P_d^{\mathcal{L},s}, \forall d \in \Omega^D, \forall s \in \Omega^S; f_l^s, \forall l \in \Omega^L, \forall s \in \Omega^S; \theta_n^s, \forall n \in \Omega^N, \forall s \in \Omega^S$. In contrast to the long-term uncertainty throughout the targeted year, the short-term uncertainties pertain to the circadian demand and production variations in every node during a target planning year, represented via scenarios (such as $s \in \Omega^S$). The dual variables linked with each constraint are displayed by a colon. The parameter β denotes the number of functional hours. Moreover, constraint (2a) imposes the power balancing equation at each node n, constraint (2b) calculates the power flow, and constraint (2c) forces the capacity limit of transmission line l. The minimum and maximum limits on demand and production capacities under diverse operational scenarios are denoted by constraints (2d, 2e, and 2f) via factors $e_{gi}^{T,s}$, $e_{gj}^{R,s}$, and $e_d^{\mathcal{L},s}$ respectively. Constraint (2g) bounds the voltage angle θ_n^s at node n in scenario s and constraint (2h) states the reference node by fixing it at zero.

3 Proposed Solution

According to [11, 12], and [13], the ARO-TEP optimization problem under optimization can be mathematically expressed in a compact form as;

$$\min_{x}\left(\mathrm{I}^T x + \max_{u\in U}\ \min_{y\in\Pi(x,u)}\ \mathrm{b}^T y\right) \tag{3}$$

Subject to:

$$\mathrm{I}^T x \le \gamma \tag{3a}$$

$$x \in \{0, 1\} \tag{3b}$$

where x is the first stage vector with binary variables, shows installment states for the transmission line, I is the vector of investment cost, u is the continuous variable of second stage that defines uncertain parameters in the uncertainty set U, vector b includes operating costs, and y is the continuous vector referring to operational variables Moreover, γ represents the investment transmission expansion budget and $\Pi(x, u)$ expresses the feasibility region as a function of x and u for the operating variables y. In the following part, the proposed three-layered optimization problem is transformed into a two stage problem by merging the second and third stage problems. This can be achieved by using the dual of the third-level problem.

3.1 Subproblem

After merging the second and third stage problems in Eq. (1) by employing the KKT conditions, the resultant single level maximization problem in compact form (see [20] for detail formulation) is stated below:

$$F^{dual} = \max_{u,y,\lambda,\mu,\alpha,\varphi}\ \mathrm{b}^T y \tag{4}$$

Subject to:

$$Ax + By = E \tag{4a}$$

$$I_{eq} y = d \tag{4b}$$

$$0 = b + B^T\lambda - G^T\mu + I_{eq}^T\alpha + I_{ineq}^T\varphi \tag{4c}$$

$$0 \le K - Fx - Gy \perp \mu \ge 0 \tag{4d}$$

$$0 \le d - I_{ineq} y \perp \varphi \ge 0 \tag{4e}$$

$$u \in U \tag{4f}$$

where constraint (4c) is obtained from differentiation of the third layer problem Lagrangian with respect to its variables y and constraints (4d) and (4e) represent the complementary conditions linked with inequality constraints.

3.2 Master Problem

The master problem can be expressed as

$$\min_{\Theta_1} \sum_{\mathrm{l}\in\Omega^{\mathrm{L}+}} \mathrm{I_l x_l} + \eta \tag{5}$$

Subject to:

$$\sum_{\mathrm{l}\in\Omega^{\mathrm{L}+}} I_l x_l \leq \Pi^{\mathrm{L,max}} \tag{5a}$$

$$x_l \in \{0, 1\}; x_l \in \Omega^{\mathrm{L}+} \tag{5b}$$

$$x_l = 1; x_l \in \frac{\Omega^{\mathrm{L}}}{\Omega^{\mathrm{L}+}} \tag{5c}$$

$$\begin{aligned} \eta \geq \max_{\Theta_2} \beta \sum_{\mathrm{s}\in\Omega^{\mathrm{S}}} \rho^{\mathrm{S}} \Bigg(& \sum_{\mathrm{g_i}\in\Omega^{\mathrm{T}}} \Lambda^{\mathrm{T}}_{\mathrm{g_i}} P^{T,s,(\nu)}_{g_i} + \sum_{\mathrm{g_j}\in\Omega^{\mathrm{R}}} \Lambda^{\mathrm{R}}_{\mathrm{g_j}} P^{\mathrm{R,s,}(\nu)}_{\mathrm{g_j}} \\ & + \sum_{\mathrm{d}\in\Omega^{\mathrm{D}}} \Lambda^{\mathcal{L}}_{\mathrm{d}} \mathrm{P}^{\mathcal{L},\mathrm{s},(\nu)}_{\mathrm{d}} \Bigg); \forall s \in \Omega^{\mathrm{S}}, \forall \nu \leq k \end{aligned} \tag{5d}$$

$$\begin{aligned} & \sum_{g_i\in\Omega^T_n} P^{T,s,(\nu)}_{g_i} + \sum_{g_j\in\Omega^R_n} P^{R,s,(\nu)}_{g_j} - \sum_{(l|s(l)\in\Omega_n)} f^{s,(\nu)}_l + \sum_{(l|r(l)\in\Omega_n)} f^{s,(\nu)}_l \\ & = \sum_{d\in\Omega^D_n} \omega^{D,s}_d \overline{D}^{(\nu)}_d - \sum_{d\in\Omega^D_n} P^{\mathcal{L},s,(\nu)}_d; \forall s \in \Omega^S, \forall \nu \leq k \end{aligned} \tag{5e}$$

$$-(1 - x_l)M \leq \frac{f^{s,(\nu)}_l}{b_l} - \left(\theta^{s,(\nu)}_{s(l)} - \theta^{s,(\nu)}_{r(l)}\right) \leq (1 - x_l)M; \forall l \in \Omega^L, \forall s \in \Omega^S, \forall \nu \leq k \tag{5f}$$

$$-x_l f^{\max}_l \leq f^{s,(\nu)}_l \leq x_l f^{\max}_l; \forall l \in \Omega^L, \forall \nu \leq k, \forall s \in \Omega^S \tag{5g}$$

$$0 \leq P^{T,s,(\nu)}_{g_i} \leq e^{T,s}_{g_i} \overline{\mathrm{P}}^{T,(\nu)}_{g_i}; \forall g_i \in \Omega^{G^T}, \forall s \in \Omega^S, \forall \nu \leq k \tag{5h}$$

$$0 \leq P^{R,s,(\nu)}_{g_j} \leq e^{R,s}_{g_j} \overline{\mathrm{P}}^{R,(\nu)}_{g_j}; \forall g_j \in \Omega^{G^R}, \forall \nu \leq k, \forall s \in \Omega^S \tag{5i}$$

$$0 \leq P^{\mathcal{L},s,(\nu)}_d \leq e^{\mathcal{L},s}_d \overline{\mathrm{P}}^{D,(\nu)}_d; \forall d \in \Omega^D, \forall s \in \Omega^S, \forall \nu \leq k \tag{5j}$$

$$-\pi \leq \theta^{s,(\nu)}_n \leq \pi; \forall n \in \Omega^N, \forall \nu \leq k, \forall s \in \Omega^S \tag{5k}$$

$$\theta^{s,(\nu)}_n = 0; n : ref, \forall \nu \leq k, \forall s \in \Omega^S \tag{5l}$$

Here, M is a large enough positive constant.

3.3 Solution Algorithm

The proposed algorithm iteratively solved the presented three-layered ARO-TEP optimization problem. At each iteration, the master problem's optimal solution is applied to the subproblem and the optimal solution of the subproblem is used to solve master problem, continues until convergence. The steps of this iterative algorithm are stated below:

1. Set lower and upper bounds to $\mathrm{Z}^{lo} = -\infty$ and $\mathrm{Z}^{up} = +\infty$, respectively.
2. Set the iteration counter to $\nu = 1$.
3. Solve the master problem (5) subject to its constraints (5a) - (5l). The resulting values of decision variables $x^{(\nu)}$ and $\eta^{(\nu)}$.
4. Update the lower bound of the optimal objective function $\mathrm{Z}^{lo} = I^T x^{(\nu)} + \eta^{(\nu)}$.
5. Solve the subproblem for the given value of the x(ν) obtained from (3) to get $P_{gi}^{T,s,(\nu)}$, $P_{gj}^{R,s,(\nu)}$ and $\mathrm{P}_{\mathrm{d}}^{\mathcal{L},s,(\nu)}$
6. Update the upper limit by $\mathrm{Z}^{up} = I^T x^{(\nu)} + F^{dual,(\nu)}$.
7. If $\mathrm{Z}^{up} - \mathrm{Z}^{lo} \leq \in$ then, the algorithm is terminated, else update the iteration counter and continue with step (3).

The data exchange between master and subproblem is depicted in Fig. 1. The investment decision variable x_l is transferred from master to subproblem and from subproblem to master problem, the values of $\overline{P}_{g_i}^{T}; \forall g_i \in \Omega^{\mathrm{T}}$, $\overline{P}_{g_j}^{R}; \forall g_j \in \Omega^{\mathrm{R}}$, $\overline{\mathrm{P}}_d; \forall d \in \Omega^{\mathrm{D}}$ are send.

4 Numerical Case Studies

In this work, all the simulations are done in MATLAB (R2022a) and general algebraic modeling software (GAMS). The CPLEX solver is applied to elucidate the proposed ARO-TEP model on the machine with specifications: Intel (R) Core (TM) i5-CPU M 460@ 2.53 GHz 2.53 GHz with 8 GB installed RAM. Herein, the MILP problem is solved with the optimality gap of 10^{-6}.

4.1 Data

The presented strategic planning methodology is tested to demonstrate its generality on the modified version of the IEEE 6-bus test system comprises of 6 buses, 8 branches, 5 dispatchable energy units, 4 non-dispatchable units, and 5 domestic load. In our model, a set of 6 candidate transmission lines is considered. For the long-term uncertain factor bounds, we have made following assumptions.

1. The maximum futuristic peak load demand is $\overline{D}_{\mathrm{d}}^{\max} = 1.5\overline{D}_{\mathrm{d}}^{\exp}$ in the targeted planning year.
2. Moreover, the minimum future generating capacity of installed conventional power is 80% to its expected bounds such as $\overline{P}_{g_i}^{T,\min} = 0.8\ \overline{P}_{g_i}^{T,\exp}$, whereas the minimum level of future stochastic generating capacity is 50% to its expected limit i.e. $\overline{P}_{g_j}^{R,\min} = 0.5\overline{P}_{g_j}^{R,\exp}$..

In short-term uncertainties, the daily load demand and power production fluctuations at each node of the considered system are taken, represented through scenarios that epitomize operating conditions in every hour of the planning year. Note that by taking into account 8760 h of the target year may lead to intractability. Therefore, this paper adopts a clustering technique, known as the K-means algorithm [23]. In order to circumvent intractability condition, the number of representative hours are selected via K-mean clustering techniques for the sake of simplicity. The historical data related to the Illinois hub for the 2022 year is considered. More specifically, the hourly datasets of the load demand are taken from the MISO [24], while the statistics related to solar and wind energy units are obtained from the NREL and PJM Interconnection [25, 26], as shown in Fig. 2

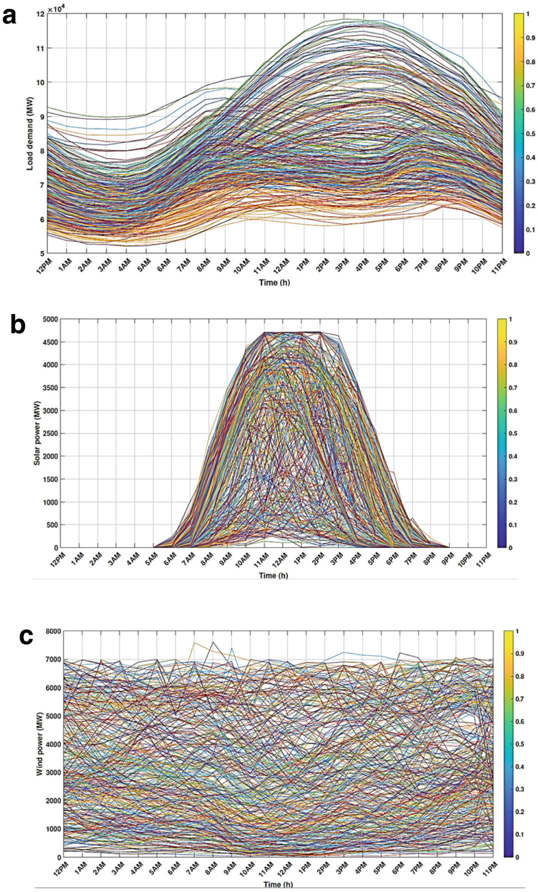

Fig. 2 **a** Hourly historical load demand datasets, **b** Hourly historical datasets for Solar units, **c** Hourly historical datasets for Wind turbine units

After obtaining the required historical datasets, the traditional K-means clustering algorithm is applied to curtail the considered year (2022) into representative days. The variation in the conventional wer production plants (i.e., thermal unit) is much less than the stochastic units, therefore its scenarios are represented by random numbers within bound of [0.85, 1]. Each scenario that signifies a operation condition comprises of $e_{g_i}^{T,s}$, $e_{g_j}^{R,s}$, and $e_{d}^{\mathcal{L},s}$. The generation system is divided into east and west zones with same demand in both regions. For the analysis of uncertainty budget impacts, range of budget for future generating is [0, 9] and for the future peak demand is [0, 90].

4.2 Result

After applying K-mean algorithm, 8 clusters corresponding to 8 representative days and 192 operating conditions have been selected. The acquired data of 24-h-length operational conditions for each representative day is stated in Table. 1.

Additionally, the scenarios weight set is given as $\rho^{\mathrm{S}} = \{0.106, 0.124, 0.140, 0.143, 0.110, 0.138, 0.116, 0.123\}$. Table 2 shows different three investment budgets.

From the Table 2, it is clear that with the increase in the investment budget, I_l is increasing with new lines built in order to relieve transmission congestion and net cost keeps decreasing (also reported in [20]).

5 Conclusion

By considering the theoretical form of the presented ARO-TEP model and stated case study, it can be deduced that the proposed model offers optimal robust transmission plans by providing protection against long- and short- term uncertainties. Through the K-means clustering technique, short-term uncertainties can be accurately represented and formulated model remains tractable. The three-layer ARO-TEP formulation is transferred into a dual-staged problem by using KKT condition and then effectively solved via the primal BD. Results illustrate that TEP decisions highly dependent on realization of uncertain factor and the availability of investment budget. Note that same model can be easily implemented with any case studies such as 12-bus test system, 33-bus test, and 118-bus test system. In the future research directions, we will test our model for other test benches and will enhance the computational efficiency.

Table 1: Resultant data for 24-h-length operational condition.

Variabilities		t_1	t_2	t_3	t_4	t_5	t_6	t_7	t_8	t_9	t_{10}	t_{11}	t_{12}	t_{13}	t_{14}	t_{15}	t_{16}	t_{17}	t_{18}	t_{19}	t_{20}	t_{21}	t_{22}	t_{23}	t_{24}
Demand factor (p.u)	d_1	0.40	0.34	0.31	0.29	0.28	0.30	0.31	0.38	0.40	0.42	0.45	0.51	0.53	0.55	0.55	0.57	0.58	0.58	0.58	0.55	0.50	0.50	0.48	0.47
	d_2	0.29	0.27	0.26	0.25	0.25	0.27	0.32	0.37	0.37	0.36	0.34	0.33	0.30	0.28	0.28	0.27	0.25	0.25	0.29	0.31	0.27	0.27	0.30	0.31
	d_3	0.40	0.38	0.37	0.35	0.36	0.36	0.40	0.45	0.45	0.45	0.44	0.41	0.38	0.35	0.34	0.32	0.32	0.31	0.35	0.39	0.36	0.36	0.38	0.42
	d_4	0.27	0.27	0.24	0.23	0.24	0.29	0.37	0.43	0.40	0.39	0.39	0.35	0.32	0.31	0.29	0.27	0.26	0.27	0.31	0.33	0.30	0.27	0.29	0.30
	d_5	0.48	0.44	0.46	0.38	0.38	0.40	0.43	0.50	0.52	0.56	0.56	0.54	0.50	0.50	0.51	0.51	0.53	0.53	0.53	0.52	0.50	0.49	0.52	0.52
	d_6	0.64	0.57	0.52	0.48	0.48	0.50	0.52	0.58	0.63	0.69	0.76	0.79	0.79	0.79	0.78	0.78	0.80	0.79	0.79	0.78	0.75	0.74	0.74	0.72
	d_7	0.14	0.14	0.14	0.14	0.16	0.20	0.27	0.32	0.28	0.26	0.24	0.21	0.20	0.20	0.18	0.18	0.17	0.16	0.16	0.15	0.14	0.16	0.14	0.15
	d_8	0.15	0.15	0.15	0.14	0.15	0.21	0.29	0.33	0.31	0.31	0.29	0.26	0.24	0.23	0.22	0.20	0.19	0.18	0.19	0.20	0.20	0.19	0.19	0.17
Solar unit capacity factor (p.u)	d_1	0.00	0.00	0.00	0.00	0.00	0.00	0.21	0.37	0.53	0.70	0.64	0.74	0.64	0.70	0.71	0.67	0.70	0.60	0.48	0.33	0.06	0.00	0.00	0.00
	d_2	0.00	0.00	0.00	0.00	0.00	0.00	0.00	0.02	0.13	0.17	0.15	0.19	0.17	0.21	0.16	0.12	0.04	0.00	0.00	0.00	0.00	0.00	0.00	0.00
	d_3	0.00	0.00	0.00	0.00	0.00	0.00	0.00	0.00	0.06	0.10	0.15	0.14	0.17	0.18	0.12	0.08	0.05	0.04	0.02	0.00	0.00	0.00	0.00	0.00
	d_4	0.00	0.00	0.00	0.00	0.00	0.00	0.00	0.03	0.22	0.42	0.57	0.62	0.63	0.59	0.43	0.25	0.16	0.08	0.00	0.00	0.00	0.00	0.00	0.00
	d_5	0.00	0.00	0.00	0.00	0.00	0.00	0.00	0.17	0.39	0.58	0.63	0.73	0.79	0.75	0.61	0.51	0.60	0.36	0.15	0.15	0.00	0.00	0.00	0.00
	d_6	0.00	0.00	0.00	0.00	0.00	0.00	0.09	0.34	0.46	0.60	0.69	0.69	0.64	0.67	0.64	0.62	0.75	0.68	0.50	0.37	0.18	0.00	0.00	0.00
	d_7	0.00	0.00	0.00	0.00	0.00	0.00	0.02	0.35	0.54	0.76	0.87	0.96	0.89	0.90	0.82	0.66	0.51	0.60	0.38	0.09	0.00	0.00	0.00	0.00
	d_8	0.00	0.00	0.00	0.00	0.00	0.00	0.00	0.18	0.51	0.71	0.78	0.87	0.96	0.92	0.82	0.67	0.58	0.38	0.21	0.04	0.00	0.00	0.00	0.00

(continued)

Table 1: (*continued*)

Variabilities		t_1	t_2	t_3	t_4	t_5	t_6	t_7	t_8	t_9	t_{10}	t_{11}	t_{12}	t_{13}	t_{14}	t_{15}	t_{16}	t_{17}	t_{18}	t_{19}	t_{20}	t_{21}	t_{22}	t_{23}	t_{24}
Wind unit capacity factor (p.u)	d_1	0.23	0.20	0.18	0.19	0.19	0.17	0.17	0.15	0.14	0.10	0.10	0.10	0.10	0.11	0.11	0.12	0.14	0.13	0.14	0.13	0.18	0.18	0.21	0.26
	d_2	0.85	0.84	0.83	0.83	0.82	0.82	0.82	0.75	0.76	0.78	0.83	0.84	0.86	0.87	0.84	0.81	0.80	0.78	0.80	0.80	0.83	0.80	0.80	0.80
	d_3	0.35	0.35	0.34	0.34	0.33	0.31	0.32	0.30	0.28	0.29	0.29	0.27	0.26	0.28	0.28	0.28	0.30	0.30	0.31	0.32	0.34	0.34	0.37	0.37
	d_4	0.41	0.38	0.39	0.40	0.38	0.39	0.37	0.31	0.30	0.28	0.26	0.26	0.29	0.32	0.31	0.30	0.30	0.31	0.29	0.30	0.34	0.38	0.40	0.40
	d_5	0.52	0.49	0.48	0.53	0.57	0.56	0.55	0.50	0.50	0.48	0.50	0.47	0.49	0.51	0.52	0.55	0.60	0.64	0.58	0.59	0.65	0.64	0.64	0.66
	d_6	0.15	0.12	0.12	0.13	0.12	0.15	0.15	0.12	0.12	0.09	0.06	0.05	0.05	0.06	0.07	0.10	0.15	0.15	0.13	0.14	0.16	0.16	0.17	0.17
	d_7	0.42	0.40	0.42	0.44	0.47	0.41	0.39	0.31	0.27	0.25	0.26	0.25	0.22	0.23	0.25	0.27	0.27	0.29	0.24	0.24	0.26	0.30	0.39	0.40
	d_8	0.72	0.69	0.72	0.75	0.77	0.77	0.77	0.72	0.70	0.70	0.75	0.75	0.76	0.74	0.76	0.72	0.74	0.75	0.70	0.73	0.75	0.78	0.76	0.73

Table 2: Impact of investment budget

$\Pi^{L,\max}$(M)	1	2	3	4
Lines built	5–6	3–6	2–4, 3–6	3–4, 3–6
$\boldsymbol{I_l}$(M$)	0.7	1.6	3	3.4
Total cost (M$)	1590	1271	1089	1019

Acknowledgement. This work is supported by the Science and Technology Project of State Grid, Zhejiang Electric Power Company (No. 5100-202119559A-0–5-SF).

References

1. Lumbreras, S., Ramos, A.: The new challenges to transmission expansion planning: survey of recent practice and literature review. Electric Power Syst. Res. **134**, 19–29 (2016)
2. Rahim, S., Ahmad, H.: Data-driven multi-layered intelligent energy management system for domestic decentralized power distribution systems. J. Build. Eng. **68**, 106113 (2023)
3. Sarker, E., Seyedmahmoudian, M., Jamei, E., Horan, B., Stojcevski, A.: Optimal management of home loads with renewable energy integration and demand response strategy. Energy **210**, 118602 (2020)
4. Rahim, S., et al.: Exploiting heuristic algorithms to efficiently utilize energy management controllers with renewable energy sources. Energy Build. **129**, 452–470 (2016)
5. Ude, N.G., Yskandar, H., Graham, R.C.: A comprehensive state of- the-art survey on the transmission network expansion planning optimization algorithms. IEEE Access **7**, 123158–123181 (2019)
6. Jabr, R.A.: Robust transmission network expansion planning with uncertain renewable generation and loads. IEEE Trans. Power Syst. **28**(4), 4558–4567 (2017)
7. García-Cerezo, A., Baringo, L., García-Bertrand, R.: Representative days for expansion decisions in power systems. Energies **13**(2), 335 (2020)
8. Romero, R., Monticelli, A., Garcia, A., Haffner, S.: Test systems and mathematical models for transmission network expansion planning. IET Proc.—Gener. Trans. Distribut. **149**(1), 27–36 (2002)
9. Alguacil, N., Motto, A.L., Conejo, A.J.: Trasmission expansion planning: a minxed-integer LP approach. IEEE Trans. Power Syst. **18**(3), 1070–1077 (2003)
10. Binato, S., Pereira, M.V.F., Granville, S.: A new Benders decomposition approach to solve power transmission network design problems. IEEE Trans. Power Syst. **16**(2), 235–240 (2001)
11. Rahim, S., Siano, P.: A survey and comparison of leading-edge uncertainty handling methods for power grid modernization. Expert Syst. Appl. **204**, 117590 (2022)
12. Rahim, S., Wang, Z., Ju, P.: Overview and applications of Robust optimization in the avant-garde energy grid infrastructure: a systematic review. Appl. Energy **319**, 119140 (2022)
13. Conejo, A. J., Baringo, L., Kazempour, S. J., & Siddiqui, A. S. (2016). Investment in electricity generation and transmission. Decision making under uncertainty. Springer
14. López, J.A., Ponnambalam, K., Quintana, V.H.: Generation and transmission expansion under risk using stochastic programming. IEEE Trans. Power Syst. **22**(3), 1369–1378 (2007)
15. de la Torre, S., Conejo, A.J., Contreras, J.: Transmission expansion planning in electricity markets. IEEE Trans. Power Syst. **23**(1), 238–248 (2008)

16. Sima, C.A., Lazaroiu, G.C., Dumbrava, V., Roscia, M., Zaninelli, D., Duquenne, P.: Stochastic programming approach for TEP optimization considering RES integration in electricity market. In *International Conference On Energy and Environment (CIEM)*, pp. 485–489. IEEE (2017)
17. Jabr, R.A.: Robust transmission network expansion planning with uncertain renewable generation and loads. IEEE Trans. Power Syst. **28**(4), 4558–4567 (2013)
18. Ruiz, C., Conejo, A.J.: Robust tranmission expansion planning. Euro. J. Oper. Res. **242**, 390–401 (2015)
19. M´ınguez, R., Garc´ıa-Bertrand, R.: Robust transmission network expansion planning in energy systems: Improving computational performance. Euro. J. Oper. Res., **248**, 21–32 (2016)
20. Zhang, X., Conejo, A.J.: Robust transmission expansion planning representing long-and short-term uncertainty. IEEE Trans. Power Syst. **33**(2), 1329–1338 (2017)
21. Roldán, C., García-Bertrand, R., Mínguez, R.: Robust transmission expansion planning with uncertain generations and loads using full probabilistic information. Electric Power Syst. Res. **189**, 106793 (2020)
22. Liang, Z., Chen, H., Chen, S., Wang, Y., Zhang, C., Kang, C.: Robust transmission expansion planning based on adaptive uncertainty set optimization under high-penetration wind power generation. IEEE Trans. Power Syst. **36**(4), 2798–2814 (2021)
23. Hu, H., Liu, J., Zhang, X., Fang, M.: An effective and adaptable K-means algorithm for big data cluster analysis. Patt. Recogn. **139**, 109404 (2023)
24. "Miso: Actual load - lcg consulting," May 2023. [Online]. Available: http://www.energyonline.com/Data/GenericData.aspx?DataId=10&Amp;MISOActual Load.
25. "Grid data and tools. (Jun 2022). [Online]. Available: https://www.nrel.gov/grid/grid-data-tools.html.
26. "Markets & operations. (Jun 2022). [Online]. Available: https://www.pjm.com/markets-and-operations.

Very Short-Term Forecasting of Wind Power Based on Transformer

Sen Wang[1,2], Yonghui Sun[1](✉), Wenjie Zhang[3], and Dipti Srinivasan[2]

[1] Hohai University, Nanjing 210098, China
senwang@hhu.edu.cn, sunyonghui168@gmail.com
[2] National University of Singapore, Singapore 117583, Singapore
dipti@nus.edu.sg
[3] The Hong Kong Polytechnic University, Hongkong 999999, China
wenjie-ee.zhang@polyu.edu.hk

Abstract. Accurate wind power forecasting is crucial for the stability of modern power systems and fostering wind power utilization. However, very short-term forecasting faces challenges due to its limited input duration, and the utilization of long sequences is rarely employed in this context. The reason behind this limitation lies in the fact that traditional forecasting models often encounter the issues of gradient disappearance or gradient explosion when handling long sequences. Therefore, this paper presents a novel very short-term wind power forecasting model based on Transformer (TF), aiming to explore the feasibility of utilizing long sequences for very short-term forecasting. The proposed model is evaluated through case using real-world engineering data. The obtained numerical results demonstrate that TF is capable of effectively processing long sequences, providing valuable insights for the advancement of future forecasting models.

Keywords: Transformers · Wind power · Very short-term · Deterministic forecasting

1 Introduction

The robust development of renewable energy sources has emerged as a global consensus in the trajectory of energy evolution [1]. Among these sources, wind power (WP) stands out due to its non-polluting, renewable nature and widespread distribution [2–4]. Nevertheless, the climate environment considerably influences WP, imbuing it with elements of randomness, volatility, and instability. The large-scale incorporation of WP into the power grid has consequently altered the grid structure, with renewable energy becoming the predominant energy. This paradigm shift toward a power system predominantly sustained by WP poses significant challenges to its safe and stable operation. Accurate wind power forecasting (WPF) is instrumental in addressing these challenges [5]. The forecasting results aid in various facets such as WP consumption, operational and maintenance activities of stations, dispatching decisions, and transactions in the power market.

Y. Xue et al. (Eds.): PMF 2023, LNEE 1129, pp. 364–374, 2024.
https://doi.org/10.1007/978-981-99-9251-5_29

Currently, the utilization of the recurrent neural network (RNN) [6], specifically the long short-term memory (LSTM) [7], is widespread. LSTM and its various adaptations find extensive employment in the domain of time series forecasting. In [8], a high-precision short-term forecasting of photovoltaic power based on LSTM was achieved by categorizing weather patterns. In [9], a deep residual network was proposed as a solution to address the overfitting issue associated with bidirectional LSTM. This network significantly enhances the accuracy and efficiency of very short-term WPF. In [10], a novel very short-term WPF model was proposed, which integrates multi-task learning with long-term and short-term forecasting approaches. The model considers wind speed forecasting as an auxiliary task, offering a fresh perspective on WPF. This approach aims to enhance the accuracy and reliability of WPF by incorporating both short-term and long-term factors. A novel approach was presented in this paper, wherein an error forecasting model was proposed [11]. This model utilizes a gated recurrent unit (GRU) to enhance the performance of the forecasting model by incorporating error correction mechanisms. However, despite its merits, LSTM also possesses several limitations. One notable drawback is its inability to execute parallel computing, resulting in significant wastage of computational resources. Moreover, LSTM exhibits restricted memory capacity, impeding its effectiveness in extracting long-term dependent features from data.

The Transformer (TF) model is a type of deep learning model widely utilized in natural language processing (NLP). The main characteristic of this model lies in its foundation on the attention mechanism, which allows the model to take into account the relationships between different elements within a sequence while processing sequential data. In forecasting, many researchers have explored. In [12], a TF-based load forecasting model was proposed, which solved the problem of long-term memory loss by introducing an attention mechanism. In [13], a spatio-temporal wind speed forecasting model based on graph neural network and TF was proposed. In [14], TF was used as the main model to realize the forecasting of SO_2 emission concentration. In [15], the TF was used to learn local and global features, which effectively improves the performance of high-speed train wheel wear state forecasting. In [16], a novel multi-view spatial-temporal TF model was proposed. This model can effectively learn complex spatio-temporal domain correlations and latent features from multiple views. In [17], short-term forecasting of highway speeds was proposed based on improved TF. In [18], incorporating high-dimensional meteorological features into the forecasting model, a new airport capacity forecasting method based on the improved TF was proposed. In different forecasting horizons, high accuracy has been achieved. However, the application of TF has not been extensively investigated in the realm of WPF.

The objective of this study is to propose a deterministic forecasting model for very short-term WP based on TF. The advantage of this model is that it can handle longer sequences. Because it does not depend on positional information in the sequence, it reduces the problem of vanishing or exploding gradients due to long sequences.

The remaining sections of this paper are organized as follows: The formulation of WPF based on TF are proposed in Sect. 2. Case studies, results comparisons and analysis are given in Sect. 3. Finally, the conclusions of this paper are drawn in Sect. 4.

2 Forecasting Model

The TF, initially introduced in 2017, combines a fully connected layer with a self-attention mechanism [20]. ChatGPT, which is very popular recently, and TF is its main model. This model structure eliminates redundant loops and relies on global dependencies within the attention mechanism to establish input and output functions. Its remarkable success lies in the field of machine translation, where achieving precise translation requires comprehending extensive long-term dependencies to capture the wealth of contextual information present in the text. The TF effectively addresses this challenge by providing a robust solution.

A further advantage of TF lies in their efficiency compared to other deep learning methodologies such as LSTM, RNN, and GRU [21]. TFT can process all time steps in parallel, markedly reducing computational time. This characteristic renders them particularly suitable for very short-term forecasting, providing a competitive edge in time-sensitive applications.

2.1 Positional Encoding

The TF model requires the use of position embedding in addition to input embedding to accurately depict the position of each element. Unlike RNNs, which rely on sequential information, the TF utilizes global information and thus does not inherently incorporate ordering information, despite its importance. To address this, position embedding is employed by the TF to encode and retain the relative or absolute positions of elements in the sequence.

$$PE_{(pos,2i)} = \sin\left(pos/10000^{2i/d}\right) \tag{1}$$

$$PE_{(pos,2i+1)} = \cos\left(pos/10000^{2i/d}\right) \tag{2}$$

where *pos* is the positional in sequence, d is the dimensions of *PE*.

2.2 Self-Attention

Self-attention in TF is more recognized among the models using attention mechanism. It is better at capturing the internal relevance of the data than the existing attention mechanism. It can better alleviate the deficiency of long-range dependency.

The self-attention employed in this study involves mapping the input sequence into query-key-value format and determining the weight by computing the dot product between a question and all keys. This enables the model to capture the inherent relationship between each data point and the entire sequence, as depicted in Fig. 1. Such an approach proves particularly advantageous for WPF, especially when relying on historical WP data as input for forecasting models, as high-precision meteorological data may not always be available.

For each input X, it is linearly transformed to three different spaces.

$$\begin{cases} Q = W_q X \\ K = W_k X \\ V = W_v X \end{cases} \tag{3}$$

The attentional function is defined as

$$Attention(Q, K, V) = Vsoftmax\left(\frac{QK^T}{\sqrt{D_k}}\right) \tag{4}$$

where Q is the queries vector, K is the keys vector, V is the value vector, $\sqrt{D_k}$ is the magnification or reduction factor, W_* is the weight.

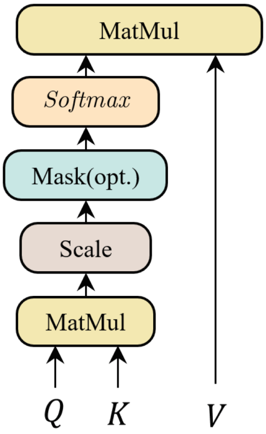

Fig. 1. Scaled Dot-product Attention

2.3 Multi-Head Attention

TF uses multi-head attention to perform parallel operations, not just a single self-attention module. Multi-headed attention allows the model to focus together on information in different subspaces, resulting in more comprehensive attentional information. The structure of multi-Head attention is illustrated in Fig. 2. Figure 3 shows the complete structure of TF.

$$MultiHead(Q, K, V) = W_o[head_1; \cdots ; head_M] \tag{5}$$

where $\forall h \in \{1, \cdots, M\}$, $head_m = Attention(Q_m, K_m, V_m)$.

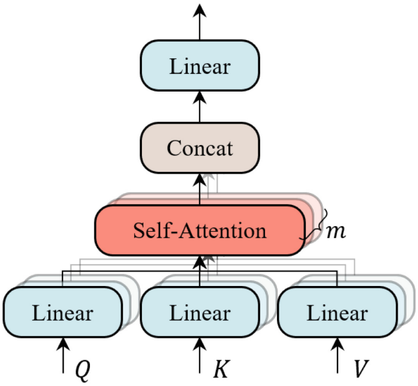

Fig. 2. Multi-head attention

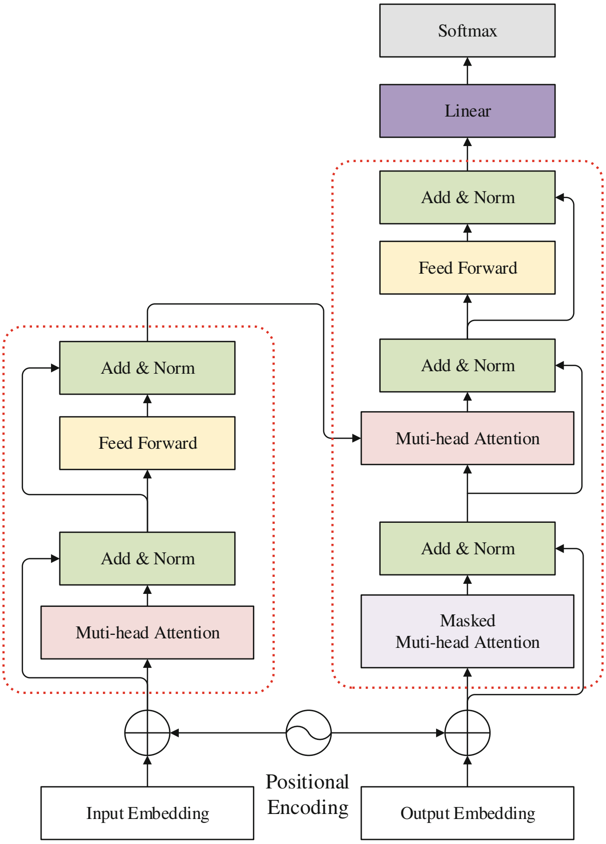

Fig. 3. Framework of TF

3 Case Study

This study draws from the empirical operating data of an offshore wind farm located in Jiangsu, collected within the 2020. The wind farm, boasting an installed capacity of 99MW, presents a time resolution of 15 min. The data has been subdivided into different sets for various purposes: training, validation, and testing. The initial 70% of the dataset forms the training set, designated for the initial model training. The subsequent 25% constitutes the validation set, employed to ascertain the model's performance. This not only helps in preventing overfitting, but also facilitates parameter tuning. The remaining data serves as the test set, utilized to evaluate the model's final performance. Last but not least, the results are analyzed using common evaluation metrics.

3.1 Datasets

In 2020, a comprehensive dataset consisting of 35,136 WP measurements was compiled, with values ranging from 0 to 99 MW. The mean power output was calculated to be 27.0622 MW, demonstrating a standard deviation of 28.1026, indicative of the variability in the power output. The median, 50% quantile, was established at 17.12 MW. There are no outliers in these data. This robust dataset provides a broad perspective on power generation patterns for the given year. The configuration of parameters is a crucial determinant that significantly influences the model's performance. To ensure reproducibility, the important parameters of TF are outlined in Table 1.

Table 1. Important parameters of TF

Name	Number
Input	96
Output	1
Loss function	MSE
Optimization	Adam
Encoder layer	1
Decoder layer	1
Feedforward	64
Multi-head	6
Activation	Relu

3.2 Evaluation Indicator

To comprehensively assess the performance of the proposed model, we employ two evaluation metrics: the Mean Absolute Percentage Error (MAPE) and the Root Mean

Square Error (RMSE). These indicators are utilized to analyze and gauge the accuracy of the forecasting results from various perspectives.

$$e_{MAPE} = \frac{1}{T}\sum_{t=1}^{T}\left|\frac{\hat{p}_t - p_t}{C}\right| \times 100\% \tag{6}$$

where C is the wind farm install capacity, p_t is the actual WP at t, $\hat{p}_t$ is the forecasting WP at t.

$$e_{RMSE} = \sqrt{\frac{1}{T}\sum_{t=1}^{T}\left(\hat{p}_t - p_t\right)^2} \tag{7}$$

3.3 Result Analysis

To comprehensively assess the predictive capabilities of TF from various angles, this study employs RNN, LSTM, GRU, and multi-layer perceptron (MLP) as comparative models. These models have been extensively utilized in the domain of time forecasting. To present the findings, we randomly selected the forecast outcomes for two-day and three-day intervals in the months of November and December 2020.

Figure 4 presents the forecast results for November 30 and December 30, 2020. Sub-figure (a) illustrates that both TF and LSTM have yielded favorable forecasting outcomes in comparison to MLP, which possesses a simplistic structure. However, due to MLP's simple structure, its stability is compromised. As TF and LSTM employ similar parameters, distinguishing between the two models based solely on the figure is challenging. Similar observations can be made from sub-figure (b). Nevertheless, it is worth noting that TF's forecasting effectiveness is subpar at certain instances, indicating that TF's performance is not consistently optimal.

Figure 5 presents the forecast results for three consecutive days, specifically November 13th to 15th, 2020. The figure demonstrates that all three models exhibit favorable predictive performance. Nonetheless, the GRU demonstrates limited robustness in scenarios where power changes continuously and rapidly. While the TF may not achieve optimal forecasting performance at certain instances, it maintains an overall high level of accuracy. To facilitate a comprehensive comparison of the predictive performance among the models on a global scale, Table 2 displays the calculated MAPE and RMSE results for different models.

It can be concluded from Table 2 that there is little difference between the models. To facilitate a more intuitive comparison, we present Table 2 in a visual format, depicted as Fig. 6. The TF demonstrates the highest accuracy based on the MAPE metric. From an RMSE standpoint, although TF is not the optimal model, the discrepancy between TF and the optimal model (GRU) is less than 0.01, which is practically insignificant. This becomes particularly relevant when considering the use of one year of data in this example. It is obvious that TF is the globally optimal model.

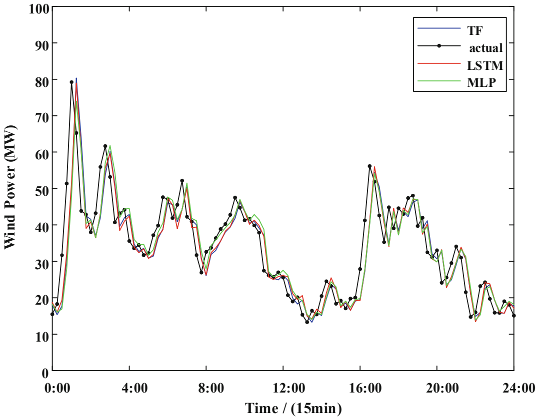

(a) Nov. 30, 2020

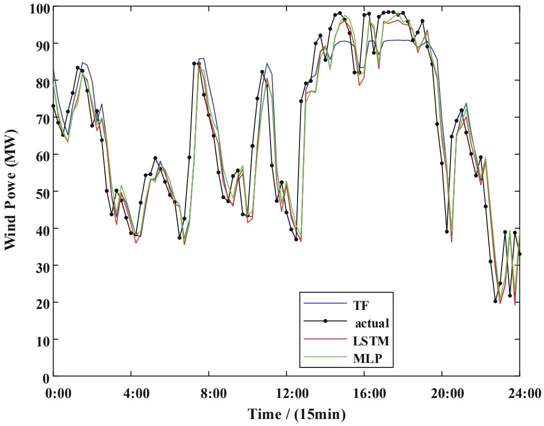

(b) Dec. 30, 2020

Fig. 4. Different model for Nov. 30 and Dec. 30, 2020

4 Conclusion

Accurate forecasting of WP is integral to the secure and steady operation of power systems that rely heavily on renewable energy. In this context, the paper puts forth a TFT-based model designed for very short-term probabilistic forecasting of WP. The primary inferences drawn from the simulations conducted are

(1) TF can handle longer sequences in WPF. Maintains good performance on very short-term forecasts with long inputs.
(2) The TF-based forecasting model proposed in this study demonstrated superior performance in the realm of WPF.

In conclusion, the TF-based WPF model introduced in this study has demonstrated its feasibility, as supported by the promising results obtained from preliminary simulations. Future research could focus on refining this model by incorporating various elements,

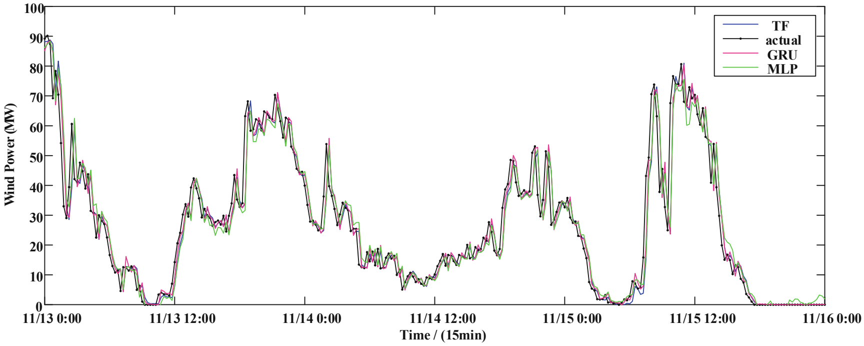

Fig. 5. Different model from Nov. 13 to 15, 2020

Table 2. Comparison of different evaluation indicators

Group	MAPE (%)	RMSE
MLP	4.49	6.9067
RNN	4.41	6.9238
GRU	4.28	6.6868
LSTM	4.34	6.7595
TF	4.26	6.6895

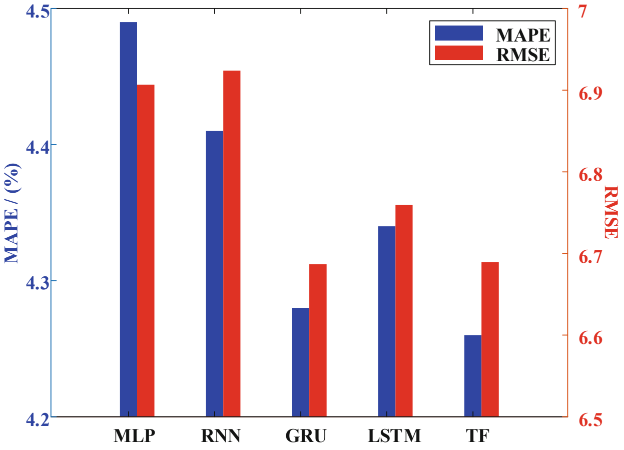

Fig. 6. RMSE and MAPE of different models

such as slope forecasting, seasonal segmentation, and scene recognition, with the aim of enhancing the predictive performance of WP generation.

Acknowledgements. This work was supported by the EMA-PSA, Singapore under Award R-263–000-F04–592 (EMA-EP005-EPJGC-0003), National Natural Science Foundation of China (No. 62073121) and the China Scholarship Council (No. 202206710082).

References

1. Xue, Y., et al.: A review on short-term and ultra-short-term wind power prediction. Autom. Electric Power Syst. **39**(6), 141–151 (2015)
2. Quan, H., Zhang, W., Zhang, W., Li, Z., Zhou, T.: An interval prediction approach of wind power based on skip-gru and blockbootstrap techniques. IEEE Trans. Indus. Appl. (2023) 101109/TIA20233270114
3. Hong, T., Pinson, P., Wang, Y., Weron, R., Yang, D., Zareipour, H.: Energy forecasting: a review and outlook. IEEE Open Access J. Power Energy **7**, 376–388 (2020)
4. Wang, K., Zhang, Y., Lin, F., Wang, J., Zhu, M.: Nonparametric probabilistic forecasting for wind power generation using quadratic spline quantile function and autoregressive recurrent neural network. IEEE Trans. Sustain. Energy **13**(4), 1930–1943 (2022)
5. Zhang, H., Liu, Y., Yan, J., Han, S., Li, L., Long, Q.: Improved deep mixture density network for regional wind power probabilistic forecasting. IEEE Trans. Power Syst. **35**(4), 2549–2560 (2020)
6. Connor, J.T., Martin, R.D., Atlas, L.E.: Recurrent neural networks and robust time series prediction. IEEE Trans. Neural Networks **5**(2), 240–254 (1994)
7. Hochreiter, S., Schmidhuber, J.: Long short-term memory. Neural Comput. **9**(8), 1735–1780 (1997)
8. Gao, M., Li, J., Hong, F., Long, D.: Day-ahead power forecasting in a large-scale photovoltaic plant based on weather classification using LSTM. Energy **187**, 115838–115850 (2019)
9. Ko, M.S., Lee, K., Kim, J.K., Hong, C.W., Dong, Z.Y., Hur, K.: Deep concatenated residual network with bidirectional LSTM for one-hour-ahead wind power forecasting. IEEE Trans. Sustain. Energy **12**(2), 1321–1335 (2020)
10. Wei, J., Wu, X., Yang, T., Jiao, R.: Ultra-short-term forecasting of wind power based on multi-task learning and lstm. Int. J. Electr. Power Energy Syst. **149**, 109073–109084 (2023)
11. Li, C., Tang, G., Xue, X., Saeed, A., Hu, X.: Short-term wind speed interval prediction based on ensemble gru model. IEEE Trans. Sustain. Energy **11**(3), 1370–1380 (2019)
12. Ran, P., Dong, K., Liu, X., Wang, J.: Short-term load forecasting based on CEEMDAN and transformer. Electric Power Syst. Res. **214**, 108885–108893 (2023)
13. Bentsen, L.Ø., Warakagoda, N.D., Stenbro, R., Engelstad, P.: Spatiotemporal wind speed forecasting using graph networks and novel transformer architectures. Appl. Energy **333**, 120565–120578 (2023)
14. Li, R., Zeng, D., Li, T., Ti, B., Hu, Y.: Real-time prediction of SO2 emission concentration under wide range of variable loads by convolution-LSTM VE-transformer. Energy **269**, 126781–126793 (2023)
15. Wang, H., Men, T., Li, Y.F.: Transformer for high-speed train wheel wear prediction with multiplex local–global temporal fusion. IEEE Trans. Instrum. Meas. **71**, 1–12 (2022)
16. Pu, B., Liu, J., Kang, Y., Chen, J., Yu, P.S.: MVSTT: A multiview spatial-temporal transformer network for traffic-flow forecasting. IEEE Trans. Cybernetics (2022). https://doi.org/10.1109/TCYB.2022.3223918
17. Zhang, H., Zou, Y., Yang, X., Yang, H.: A temporal fusion transformer for short-term freeway traffic speed multistep prediction. Neurocomputing **500**, 329–340 (2022)

18. Du, W., Chen, S., Li, H., Li, Z., Cao, X., Lv, Y.: Airport capacity prediction with multisource features: A temporal deep learning approach. IEEE Trans. Intell. Transp. Syst. **24**(1), 615–630 (2023)
19. Wang, S., Sun, Y., Zhang, S., Zhou, Y., Hou, D., Wang, J.: Very short-term probabilistic prediction of PV based on multi-period error distribution. Electric Power Syst. Res. **214**, 108817–108826 (2023)
20. Vaswani, A., Shazeer, N., Parmar, N., Uszkoreit, J., Jones, L., Gomez, A.N., Kaiser, Ł., Polosukhin, I.: Attention is all you need. Adv. Neural Inf. Process. Syst. **30** (2017)
21. Cho, K., Van Merriënboer, B., Gulcehre, C., Bahdanau, D., Bougares, F., Schwenk, H., Bengio, Y.: Learning phrase representations using RNN encoder-decoder for statistical machine translation (2014). arXiv preprint arXiv:1406.1078

Charging and Discharging Model of Electric Vehicle Virtual Power Plant Considering Dynamic Electricity Price in New Power System

Li Mingyang[1,2](✉), Zheng Yukun[3], Wang Yanqian[1,2], Yin Yao[1,2], Dai Yang[1,2], and Cai Kesu[1,2]

[1] NARI Group Corporation (State Grid Electric Power Research Institute), Nanjing 211106, China
781911518@qq.com
[2] NARI Technology Co. Ltd, Nanjing 211106, China
[3] Xi-an Jiaotong-Liverpool University, Suzhou, Jiangsu Province 215123, China

Abstract. Electric vehicles are being used on a large scale, and virtual power plants are redefining electric vehicles. A profit maximization model of EVs charging/discharging is constructed in this paper.The model is aimed at the maximum profits, while being constrained by power/energy storage batteries charging/discharging capacities and the travel needs of EVs.The model also express the charging/discharging decision of EVs very well. An analysis and calculation of the economic benefit and charging distribution of EV charging/discharging have been made by simulating user travel needs with Monte Carlo method. The data of the user travel rule come from NHTS (National Household Travel Survey) in 2021. The results indicate the rational charging/discharging model which can be significantly improved by responding to the TOU(Time Of Use) and RT (Real-Time) electricity price. Meanwhile, due to the cheaper off-peak electricity price at night, the expensive on-peak electricity price during the day, electric vehicles tend to charge at low load time and discharge at peak load time inversely so as to achieve peak load shifting. The power/energy storage batteries storage function of EVs is worth further developing.

Keywords: New power system · Virtual power plant · EV · V2G · Monte Carlo simulation · Peak load shifting

1 Introduction

Electric vehicle charging load forecasting is the basic issue of the electric vehicle charging management. Electric vehicle charging load distribution is defined as the distribution characteristics of the charging load in 24 h a day. If the charging load of the electric vehicles can be arranged in the off-peak periods, it could reduce the construction investment of the distribution network and save plenty of power grid investment costs [2–4].

Recently, scholars around the world have done a lot in the electric vehicle charging load forecasting. According to the parking statistics, reference has further discussed the

Y. Xue et al. (Eds.): PMF 2023, LNEE 1129, pp. 375–384, 2024.
https://doi.org/10.1007/978-981-99-9251-5_30

charging load on different spaces. This kind of research is based on the travel laws of the existing traditional cars and has well solved the forecasting of the charging load distribution of electric vehicles by the travel characteristics of electric vehicles. The concept of a vehicle to grid has been a focus since its proposition. According to the travel statistics of the existing traditional vehicles, a vehicle is moving more than 91% of the time, which makes it possible that its power/energy storage batteries can provide energy to charge in the low load periods and provide peak load shifting, frequency modulation, and steady voltage by V2G in the peak load periods [5–7]. Nowadays, the economic suitability, and the technical feature and management mode of V2G are widely re-searched. However, there is a lack of research into the synthesized impacts on the power load curve of the charging of electric vehicles and the discharging of V2G [8, 13].

This paper has made a decision model to ensure the maximum operating income where charging or V2G discharging is needed. It has also discussed the effects of differently charged electricity prices on the charging load distribution.

2 The Travel Data of EVs

2.1 NHTS (National Household Travel Survey)

The NHTS survey conducted by the Department Of Transportation (DOT) represents millions of vehicles in the United States. It reports on hundreds of thousands of vehicle trips made across the United States in 2021. The vehicle travel behaviour data used in this paper are derived from the 2021 National Household Travel Survey (NHTS). The NHTS data contains four major files, including a daily trip dataset and a vehicle dataset [1, 9–11].

Several processing steps were required in order to prepare the data for input to the model. For each trip, the daily trip file contains the data on the distance travelled, the type of vehicle, the time of departure, and the type of departure. Vehicle-level information, such as the state of the vehicle and the vehicle's age, comes from the vehicle file. From the full survey, we only select trips taken by private vehicles, driver ID and vehicle ID. Table 1 shows a typical daily trip of a vehicle, and the start time, end time, duration, average velocity, and distance [12].

Table 1. A typical daily trip of a vehicle.

Trips	Start time	End time	Time (h)	Duration (km)	Velocity (km/h)
1st	08:48	09:03	0.25	7.2	28.8
2nd	12:28	12:43	0.25	8.0	32.0
3rd	15:00	15:12	0.20	6.8	34.0
4th	17:24	17:45	0.25	6.4	25.6

2.2 Electricity Tariff Structure

To some extent, the EV load demand can be dictated by the electricity tariff structure. Two types of typical electricity tariff structures are taken into consideration: Time-Of-Use (TOU) pricing and Real-Time Pricing (RTP). TOU pricing divides the tariff into three main blocks: peak, flat, and valley price, as shown in Fig. 1 [9, 11]. The latter option provides a real-time rate which varies by season of the year, hour of the day, and by weekday and weekend, as shown in Figs. 1 and 2.

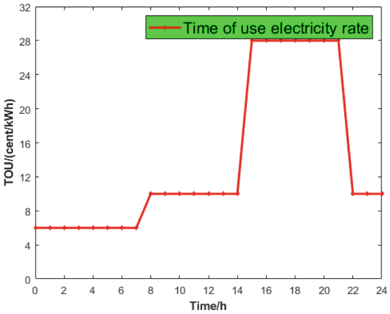

Fig. 1. Time of use electricity rate(TOU).

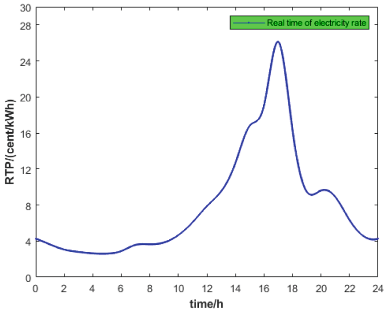

Fig. 2. Real time electricity rate(RT).

3 Charging and Discharging Decision–Making Model of EVs

Electric vehicles are associated with a power grid by the battery charge/discharge, whose key index is the battery state of charge. SOC is the ratio of current electric quantities and the full electric quantities of a battery, which describes the current available in the capacity of a battery by centesimal grade. Battery energy is in kWh, which is denoted by the product of the battery capacity and rated current.

3.1 Calculation of Power Battery SOC and Loss Cost

In this paper, the power/energy storage battery charge/discharge procedure involves the SOC calculation of. To avoid over-discharging, the SOC must be greater than the minimum SOC ($SOC_{\min}$), or else, the discharging must be terminated. Similarly, to avoid the over-charging of a battery, the SOC must be less than the allowed maximum SOC ($SOC_{\max}$), or else, the charging must be terminated. We assume that the initial value of SOC is 0.83 (marked as SOC_S), and the end value of SOC is 0.58 (marked as SOC_e), as shown in Fig. 3 [5, 7].

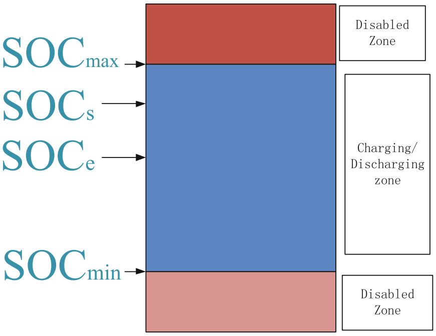

Fig. 3. SOC level available for different application types.

(1) Under the condition that the travelling distance of an electric vehicle is given, its SOC_t cost during the trip can be obtained by the following formula:

$$SOC_{\mathrm{t}} = \frac{\xi_{100}}{100 \cdot C_B} d \tag{1}$$

where ξ_{100} is the power consumption per hundred kilometers of the energy storage battery $(\mathrm{kW} \cdot h/100\mathrm{km})$, d is the travelling distance (km), and C_B is the capacity of energy storage battery $(\mathrm{kW} \cdot h)$.

(2) When charging electric vehicles, the way of fully-charging within six and four hours is adopted, during which time the battery is in the allowed SOC interval and the charging can be regarded as constant current charging. Then, the relationship between the charging time and SOC is

$$SOC_{charge} = \frac{Q^{down}(t)}{C_B} = \eta^{down} \frac{\int_0^{t^{down}} p^{down}(t)}{C_B} \tag{2}$$

where $SOC_{ch\arg e}$ is the SOC after charging, $Q^{down}(t)$ is the charged electric energy $(\mathrm{kW} \cdot h)$, $p^{down}(t)$ is the charge power (kW),t^{down} is the charge time (h) and η^{down} is the charge efficiency.

(3) In the service that electric vehicles supply power to the power grid, we just discuss the peak load shifting, that is the selling power of the stored battery energy. Suppose

that the electric energy of electric vehicles is sold by constant power, then the sold battery SOC is

$$SOC_{V2G} = \frac{Q^{up}(t)}{C_B} = \eta^{up} \frac{\int_0^{t^{up}} P^{up}(t)}{C_B} \tag{3}$$

where SOC_{V2G} is the SOC of the sold batteries of the V2G in the discharging, $Q^{up}(t)$ is the discharged electric energy $(\text{kW} \cdot h)$,$p^{up}(t)$ is the discharge power (kW),t^{up} is the discharge time (h) and η^{up} is the discharge efficiency.

(4) The battery loss cost is the product of equivalent battery loss cost rate ωd per kilowatt-hour and the battery electric energy of charging / discharging.

$$W_{\text{b}} = \frac{1}{2}\omega_d(\lambda^{up}Q^{up} + \lambda^{down}Q^{down}) \tag{4}$$

where ω_d is the loss rate of power batteries $(\$/\text{kW} \cdot h)$, λ^{up} is the discharge power coefficient of V2G, λ^{down} is the charge power coefficient of power batteries, Q^{up} is the discharged electric quantities $(\text{kW} \cdot h)$ and Q^{down} is the charged electric quantities $(\text{kW} \cdot h)$.

3.2 Model

An objective Function.

EV power batteries have charging and discharging genergy processes throughout the course of one day. For example, a vehicle may make m trips during the course of 24 h. The periods of battery SOC may decrease (i.e., electricity consumption) or increase during a period. In ith trip, a dwelling activity takes up a set of segments (i.e., seg(i)).The objective of a charging/discharging problem is to maximize the operating income (minimize the operating cost) subject to the constraints of EV travel. The income function of EV can be represented as described in (5):

$$\begin{aligned}\max F_{profit} = \sum_{i=1}^{m}\sum_{j=1}^{seg(i)} \Bigg\{ & [\eta\eta^{up}g_{i,j}(t) - \frac{1}{2}\omega_d\lambda^{up}] \int_0^{t_{i,j}^{up}} P^{up}(t)dt \\ & - [\eta\eta^{down}f_{i,j}(t) + \frac{1}{2}\omega_d\lambda^{down}] \int_0^{t_{i,j}^{down}} P^{down}(t) \Bigg\}\end{aligned} \tag{5}$$

where $g_{i,j}(t)$ is the charging rate $(\$/kW \cdot h)$,$f_{i,j}(t)$ is the discharging rate $(\$/kW \cdot h)$, and η is the power grid convert efficiency. $t_{i,j}^{down}$, $t_{i,j}^{up}$ are the charging and discharging time of segment j for trip i, respectively. Equality and Inequality Constraints:

(1) The power balance constraints: in a period (usually 24h), the state of charge of the battery in the first stroke equals that in the last stroke, namely the difference of the charge electric quantities and the discharge electric quantities (vehicle discharge and V2G discharge) is zero. The power balancing constraint must be satisfied as follows:

$$\sum_{i=1}^{m}\sum_{j=1}^{seg(i)} \eta[\eta^{down} \int_0^{t_{i,j}^{down}} P^{down}(t) - \eta^{up} \int_0^{t_{i,j}^{up}} P^{up}(t)] - 100\omega_{100} \sum_{i}^{m} d_i = 0 \tag{6}$$

(2) Electric vehicles travel constrains: the dis-charge process must equal the battery SOC in the next trip. That is to say, the initial battery electric quantities of electric vehicles must satisfy the first trip.

$$SOC_{\min} C_A \leq SOC_S C_B - \frac{W_{100}}{100} d_1 \leq SOC_{\max} C_B \tag{7}$$

The electric vehicles start charging/discharging after the kth ($k = 1, 2, \ldots, m$) stroke, but after charging and discharging, the electric quantities of electric vehicles must be satisfied in the (k + 1)th stroke. Therefore, there are m constraints.

$$\begin{aligned} SOC_{\min} C_B \leq SOC_S C_B + \sum_{i=1}^{k} \sum_{j=1}^{seg(i)} \eta[\eta^{down} \int_0^{t_{i,j}^{down}} P^{down}(t) - \eta^{up} \int_0^{t_{i,j}^{up}} P^{up}(t)] \\ - \frac{\omega_{100}}{100} \sum_{i=1}^{k+1} d_i \leq SOC_{\max} C_B \end{aligned} \tag{8}$$

(3) The battery SOC constraints: battery states of charge constraints. The summation of the charged electricity quantities and the minimum allowed electricity quantities is no more than the maximum allowed electricity quantities.

$$\int_0^{t_{i,j}^{down}} P^{down}(t) + SOC_{\max} C_B \leq SOC_{\max} C_B \tag{9}$$

The difference of maximum allowed electricity quantities and the total discharged electricity quantities is no more than the allowed minimum electricity quantities.

$$SOC_{\min} C_B + \int_0^{t_{i,j}^{UP}} P^{\mathrm{up}}(t) \leq SOC_{\max} C_B \tag{10}$$

The electricity quantities after charging/discharging in the lth (l = 1,2,3,…,*seg(i)*) period of the kth (k = 1,2,3,…,m) stroke are not only no less than the minimum allowed electricity quantities but also no more than the maximum allowed electricity quantities. There are such constraints.

$$\begin{aligned} SOC_{\min} C_B \leq SOC_S C_B + \sum_{i=1}^{k} \sum_{j=1}^{l} \eta[\eta^{down} \int_0^{t_{i,j}^{down}} P^{down}(t) - \eta^{up} \int_0^{t_{i,j}^{up}} P^{up}(t)] \\ - \frac{\omega_{100}}{100} \sum_{i=1}^{k} d_i \leq SOC_{\max} C_B \end{aligned} \tag{11}$$

(4) Time constrains: After each stroke, the charging/discharging time of electric vehicles should be less than the time difference between the two periods and be non- negative. In the same period, charging and discharging can only be selected alternatively. Charging and V2G charging are prohibited during the running of electric vehicles.

$$0 \leq t_{i,j}^{down} \leq t_{i,j+1} - t_{i,j} \tag{12}$$

$$0 \leq t_{i,j}^{up} \leq t_{i,j+1} - t_{i,j} \tag{13}$$

$$t_{i,j}^{up} * t_{i,j}^{down} = 0 \tag{14}$$

$$t_{trip=0} \tag{15}$$

where t_{trip} is the electric vehicle travel time.

In this paper, the established orderly charging optimization model for electric vehicles is a mixed programming model and is solved by utilizing the YALMIP toolbox.

4 The Results of Calculation and Simulation

4.1 The Data of EVs

Lithium-ion ferrous phosphate battery is currently the main power battery for EV batteries. Lithium iron phosphate battery has the advantages of low price, safety, long life, big capability and so on. The two types of EVs (BYD E6 and the Tesla model) are using lithium-ion ferrous phosphate in this paper. The capacity, duration of charging process, power demand are different from each other, but the charging/discharging characteristics, efficiency and related battery SOC profiles of the two types of EV are same. The following Table 2 lists the the EV power/energy storage battery.

Table 2. EV power/ energy storage battery

Types	CB	P	ωd	W100
BYD	76.91/kWh	9.5/kWh	4.0/cent/kWh	21.5kWh/100km
Tesla	89.12/kWh	7.0/kWh	4.0/cent/kWh	15.1kWh/100km
Types	SOC_{min}	SOC_{max}	η^{up}/η^{down}	η
BYD	0.12	0.98	0.98	0.92
Tesla	0.12		0.98	0.92

4.2 Monte Carlo Simulation Considering on Electricity Rate and Uncertainty Schedule

Based on Part 2, Monte Carlo simulation is employed to sample the data, considering the change of EV trips, their duration, as well as the start time and the trip's distance. The charging/discharging load curve of all EVs is accumulated and a single EV charging/discharging load curve L is obtained. The entire calculation of charging and discharging decision-making modeling is carried out as described in Fig. 4. The vehicle travel behaviors used in this paper are derived from Sect. 1.1, and the electricity tariff structures are derived from Sect. 1.2. The practical simulation results show that the average benefits remain invariant basically after simulating 5000 times. Considering the accuracy and the calculation speed, the simulation process is repeated for 5000 times.

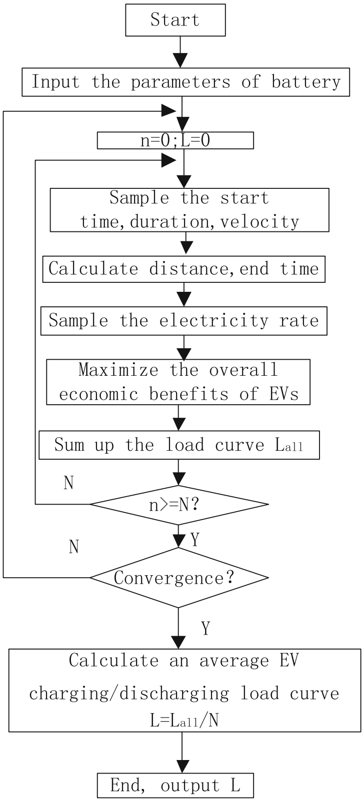

Fig. 4. Flow chart of EV profits maximization algorithm based on Monte Carlo simulation.

4.3 Charging and Discharging (V2G) Profile Base on a Single EV

The TOU electricity rate is employed to determine the most economic starting time of EV battery charging, while the RT electricity price is adopted to discharge (V2G) during the peak time based on the algorithm of Sect. 2.2. In this paper, the peak load time is 15.00–19.59 pm, while the valley load time is 0.00–6.59 am and 22.00–23.59 pm. At last the maximum operating profits of the average electric vehicle are 88.79 cents. An obvious charging load peak appears from 0.00 am to 6.59 am and an obvious discharging (V2G)load peak appears from 16.00 am to 22.59 am. The charging peak and the regular load peak occur during different periods of time, while the discharging peak and the regular load peak almost occur simultaneously. Fig. 5 shows the profile of charging/discharging load based on a single EV. The large scale development of private EVs will impose huge impacts on power grids. From 2021 to 2050, with the popularity of private EVs, the charging and discharging load of EVs increases dramatically. It is a controlled charging/discharging strategy to smooth load the profile of a power grid. The main factor for this phenomenon is the charging and discharging electricity tariff structure. Based on the high level prediction, the large scale development of private EVs will pose huge impacts on power grids.

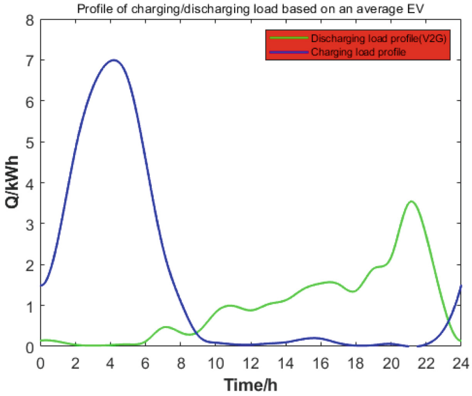

Fig. 5. Profile of charging/discharging load based on an average EV

5 Conclusions

EVs are increasing their great potentials in the global automotive market share. EVs can be regarded as distributed energy storage units, if we can logically and reasonably control and operate them, they have great potentials to contribute to load shifting. The charging/discharging load of EVs is influenced by many factors. Therefore it is difficult to build a deterministic model between the charging demand and these uncertain factors. In this paper, under the constraints of power battery charging/discharging capacity and customer travel needs, an electric vehicle charging/discharging model is proposed to maximize the electric vehicle economic benefits. The vehicle travel behavior's data used are derived from the 2021 NHTS. A Monte Carlo simulation based model is proposed to forecast the charging load and discharging load of a single EV. On the top of that, several conclusions are reached below:

(1) The uncertainties of EVs charging behavior bring great challenges to power grid operation and peak-valley regulation. EVs charging load are mainly determined by EVs ownership, EV types, charging duration, charging modes, charging frequency, battery characteristics, and electricity tariff structure.
(2) While a single EV charging load has spatial temporal uncertainties, a large number of EVs charging behavior obeys certain probability models. Therefore, we can calculate and analysis an EV's charging load, based on Monte Carlo EVs charging load calculation model.
(3) The results of the simulation indicate that with guiding and controlling EV owners' charging behavior, the peak discharging load appears at the same time when the whole grid's load reaches peak value, which further narrows the gap between peak and valley.

References

1. 2021 National Household Travel Survey, User'sGuide
2. Madrid, C., Argueta, J., Smith, J.: Performance characterization-1999 Nissan Altra-EV with lithium-ion battery. Southern California EDISON (1999)
3. Linden, D., Reddy, T.B.: Handbook of Batteries, 3rded. McGraw-Hill, NewYork (2001)
4. Zechun, H.U., Yonghua, S.O.N.G., Zhiwei, X.U., et al.: Reference to a book: impacts and utilization of electric vehicles integration into power systems [J]. Proc. CSEE **32**(4), 1–10 (2012)
5. Lofberg, J.: Modeling and solving uncertain optimization problems in YALMIP[C]. In: Proceedings of the 17th IFAC World Congress, pp. 1337–1341 (2008)
6. Lu, L., Han, X., Li, J., et al.: A review on the key issues for lithium-ion battery management in electric vehicles [J]. J. Power. Sources **226**, 272–288 (2013)
7. Lu, L., Wen, F., Xue, Y., et al.: Economicanaly of ancillary service provision by plug-in electric vehicles [J]. Autom. Electric Power Syst., (2013)
8. Luo, Z., Hu, Z., Song, Y., et al.: Study on plug-in electric vehicles charging load calculating[J]. Autom. Electric Power Syst. **35**(14), 36–42 (2011)
9. Ma, Y., Houghton, T., Cruden, A., et al.: Modeling the benefits of vehicle-to-grid technology to a power system [J]. Power Syst. IEEE Trans. **27**(2), 1012–1020 (2012)
10. Reference to a chapter in an edited book: Lopes, J.A.P., Soares, F.J., Almeida, P.M.R.: Integration of electric vehicles in the electric power system. Proc. IEEE., **99**(1), 168–183 (2011)
11. Weifeng, Y.A.O., Junhua, Z.H.A.O., Fushuan, W.E.N., Yusheng, X.U.E., Fengyun, C.H.E.N., Liang, L.I.: Frequency regulation strategy for electric vehicles with centralized charging [J]. Autom. Electric Power Syst. **38**(9), 69–76 (2014)
12. Zhang, H., Hu, Z., Song, Y., Xu, Z.J.L.: A prediction methodfor electric vehicle charging load considering spatial and temporal distribution[J]. Autom. Electric Power Syst. **38**(1), 13–20 (2014)
13. Zhang, L., Brown, T., Samuelsen, S.: Evaluation of charging infrastructure requirements and operating costs for plug-inelectric vehicles [J]. J. Power. Sources **37**(14), 43–49 (2013)

PV and Energy Storage Siting and Capacity Strategy Based on Dynamic Network Reconfiguration and Cluster Partitioning

Tongzheng Wei[1](✉), Hongwei Du[1], Dong Xia[1], Suyang Zhou[2], and Tao Han[1]

[1] State Grid Electric Power Research Institute Co., Ltd, Nanjing 211106, Jiangsu Province, China
2285581385@qq.com
[2] Southeast University, Nanjing 210096, Jiangsu Province, China

Abstract. For the problem of siting and capacity of PV and energy storage connected to distributed PV distribution network with high penetration rate, a PV energy storage siting and capacity strategy based on dynamic network reconfiguration and cluster division is proposed. The method first proposes a cluster division model considering dynamic reconfiguration for cluster division method, on this basis, a PV energy storage siting and capacity setting model based on dynamic network reconfiguration and cluster division is established, the upper-level planning model takes the equal annual value installation cost, annual operation and maintenance cost, cluster power purchase cost active network loss minimization as the objective function, each cluster DG capacity, ESS capacity and power as the decision variables for The upper-level planning, the lower-level planning model takes network loss minimization as the objective function, and the DG and ESS access capacity and access location of each cluster internal node as the decision variables for the lower-level planning. Finally, the feasibility and effectiveness of the method are verified with the improved IEEE33 node system.

Keywords: Distributed generation · Network reconfiguration · Energy storage · Siting and capacity setting

1 Introduction

In order to promote the "double carbon" goal, "whole county photovoltaic" work in the national orderly promotion, distribution network in the distributed photovoltaic (DPV) as a representative of renewable distributed power The penetration rate is rapidly increasing [1] The penetration of distributed photovoltaic in the distribution grid is rapidly increasing. In order to solve the source-load imbalance problem caused by distributed generation (DG) access and give full play to the active role of DG, the joint expansion planning of DG and energy storage system (ESS) has become a research hotspot.

The flexible restructuring capability of distribution networks has become one of the hallmarks of smart distribution networks [2] Many scholars have studied the impact of network reconfiguration as an active management tool on the optimal configuration

Y. Xue et al. (Eds.): PMF 2023, LNEE 1129, pp. 385–402, 2024.
https://doi.org/10.1007/978-981-99-9251-5_31

of DG. Literature [3] A robust planning model of DG with network reconfiguration is developed with the objective of minimizing the annual integrated cost, which improves the economy and reliability of system operation. Literature [4] A DG siting and capacity optimization method considering network dynamic reconfiguration is proposed for the closed-loop design of distribution networks, which improves the overall economic efficiency of DG consumption capacity and investment cycle. Literature [5] The optimal topology of the distribution network and the optimal charging and discharging method of ESS are presented for distribution networks with high permeability DG and ESS, which effectively reduce the operating cost and improve the operational reliability of the distribution network. Literature [6] A renewable energy planning method considering dynamic network reconfiguration and distribution network uncertainty is proposed. Many studies have shown that network reconfiguration can effectively improve the consumption capacity, operational reliability and economy of distribution grid DG. The current distribution network planning is based on the load characteristics of a fixed scenario and does not consider the change of system contact switch, so there is room for further research on the distribution network planning technology under dynamic topology and time-varying load. Moreover, most of the above distribution network planning with DGs is a centralized planning model, and the complexity of the centralized optimization model will increase dramatically when large-scale DGs are connected to the distribution network, which will lead to "dimensional disaster" [7]. The complexity of the centralized optimization model increases dramatically when large scale DGs are connected to the distribution network, leading to "dimensional disaster". The distributed generation cluster (DGC) is formed by aggregating DGs, energy storage, loads and other control devices that are geographically or electrically close to each other or form complementary relationships. Planning the distribution network in terms of DGCs not only reduces the complexity of the problem, but also greatly increases the DG's capacity to consume because the DGCs take into account the degree of power matching between source and load in the division process [8].

For cluster planning, existing research is divided into two main aspects: cluster delineation and cluster planning. In terms of cluster classification, the existing cluster classification methods are mainly based on electrical modularity [9], active power balance degree [10] and reactive power balance [11] as cluster classification indexes, using association discovery algorithm [12] and intelligent optimization algorithm [13] and clustering algorithm [14] Cluster classification is performed. The existing cluster classification metrics do not consider the impact of cluster size on the subsequent cluster operation control, and the clusters are classified with too large a difference in size, even producing isolated nodes. In terms of cluster planning, existing studies have demonstrated that reasonable cluster classification is beneficial to the planning and configuration of distribution networks [8, 15, 16]. Literature [15] proposed a distributed energy storage capacity planning strategy considering cluster voltage autonomy to improve node voltages based on cluster delineation for distribution networks. Literature [16] developed a distributed PV and energy storage two-layer planning model by using PV capacity and location within the cluster as decision variables. Literature [8] proposed a joint network-source-storage two-layer expansion planning strategy for distribution networks based on cluster division, which reduces the conservativeness of distribution network planning.

All the above studies consider the influence of system contact switch action on cluster division, and the existing cluster division methods still have certain defects.

Considering the shortcomings of existing research cluster delineation methods and the fact that few papers combine cluster delineation with network reconfiguration, this paper proposes a two-tier planning method for PV energy storage based on network reconfiguration and cluster delineation. Firstly, a distributed generation cluster classification method considering dynamic network reconfiguration is proposed, secondly, a two-layer planning model is established based on the above cluster classification results, where the upper-level planning model takes the equal annual value installation cost, annual operation and maintenance cost, cluster power purchase cost, and active network loss minimization as the objective functions, and the DG capacity, ESS capacity and power of each cluster as the decision variables for the upper-level planning, the lower-level planning model takes the network The lower-level planning model uses network loss minimization as the objective function and DG and ESS access capacity and access location of each cluster internal node as the decision variables for lower-level planning, finally, the feasibility and effectiveness of the method are verified with the improved IEEE33 node system.

2 Two-Layer Planning Architecture for PV Energy Storage Considering Dynamic Network Reconfiguration and Cluster Division

For the problem of cluster division and siting and capacity planning of DG distribution network with high penetration rate, a PV energy storage siting and capacity model based on dynamic network reconstruction and cluster division is established, and its architecture diagram is shown in Fig. 1.

In the cluster partitioning method considering dynamic network reconfiguration, the dynamic network reconfiguration optimizes the best network reconfiguration scheme for each time period with the minimum number of device actions and the minimum network loss as the objective function. Based on the reconfiguration scheme for each time period, the cluster division is performed with the objective of maximizing the mean value of the comprehensive cluster division index for all-weather.

Based on the above cluster division results, in the PV and ESS two-level planning model, the upper-level planning model takes the equal annual value installation cost, annual operation and maintenance cost, cluster power purchase cost, and active network loss minimization as the objective function, and the DG capacity, ESS capacity and power of each cluster as the decision variables for the upper-level planning, the lower-level planning model takes the network loss minimization as the objective function, and the DG and ESS of each node within the cluster as the decision variables for the lower-level planning. Access capacity and access location of each cluster are the decision variables for lower-level planning. The decision variables of the upper-level planning model are passed to the lower-level planning model as its initial conditions and constraints, and the lower-level planning is based on the above-mentioned intra-cluster planning, and the active network loss power obtained from the tide calculation is uploaded to the upper-level planning model.

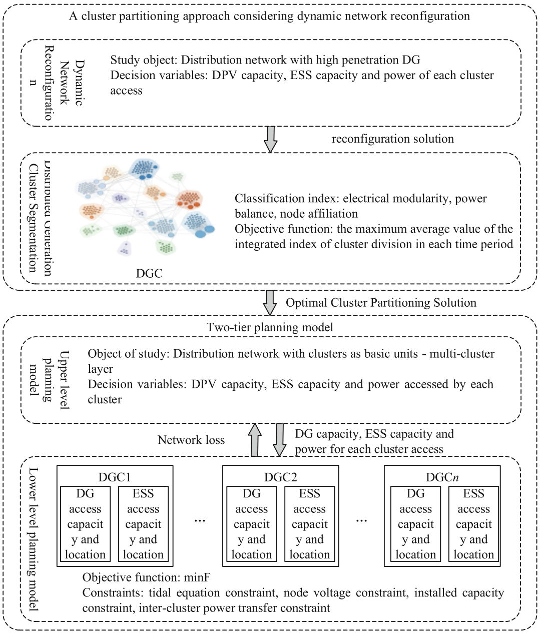

Fig. 1. Architecture diagram of PV energy storage double layer planning considering dynamic network reconfiguration and cluster division

3 Cluster Partitioning Approach Considering Dynamic Network Reconfiguration

3.1 Dynamic Network Reconfiguration

Dividing the network reconfiguration study time period into N time points, the system load corresponding to time point k is $\boldsymbol{X}_k = [X_{k1}, X_{k2}, \cdots, X_{kn}]^T$, where n is the number of nodes, and the daily load can be expressed as $\boldsymbol{X} = [X_1, X_2, \cdots, X_N]^T$. If this matrix is divided into time periods and the data difference between the divided time periods is minimized, let $1 \le \theta_1 \le \theta_2 \le T$, then the segment difference between moment θ_1 and moment θ_2 is

$$\begin{cases} d_{\theta_1\theta_2} = \sum\limits_{k=\theta_1}^{\theta_2} \sum\limits_{j=1}^{n} (x_{kj} - \overline{x_j}) \\ \overline{x_j} = \dfrac{1}{\theta_2 - \theta_1 + 1} \sum\limits_{k=\theta_1}^{\theta_2} x_{kj} \end{cases} \tag{1}$$

Then, after dividing the N moments into k *time periods, the* sum of the differences of each time period is

$$S_d^{N,k} = \sum_{j=1}^{k} \boldsymbol{D}(i_{j-1} + 1, i_j) \tag{2}$$

where: ***D*** is the segment difference matrix, where the *i-th* row and *j-th* column element $\boldsymbol{D}(i,j) = d_{ij}$, $S_d^{N,k}$ as the reconstruction frequency measure, the smaller the division time period k the larger its value.

Through dynamic network topology reconfiguration, the network switching state is changed so as to adjust the network structure, which has the effect of reducing network losses and improving node voltages while satisfying the operating constraints. Combined with the time period division method proposed above, the objective function of dynamic network reconfiguration is

$$f_1 = \max\left[\alpha_1 S_d^{N,k} - \alpha_2 \sum_{i=1}^{24}\sum_{j=1}^{b} r_i (I_i)^2 \Delta T\right] \tag{3}$$

where: α_1, α_2 are the weight coefficients of each target, respectively, r_i is the resistance value of branch *i*, I_i is the current amplitude of branch *i*, ΔT is the duration of each time period, and $\Delta \mathrm{T} = 1\mathrm{h}$ is taken in this paper, b is the number of network branches.

3.2 Cluster Division

The cluster partitioning objective function is

$$f_2 = \max[w_1\rho + w_2\beta + w_3\lambda] \tag{4}$$

where: ρ, β, λ are the electrical modularity index, power balance index, and node affiliation index for cluster classification, respectively, w_1, w_2, w_3 are the weight coefficients of each index, and $w_1 + w_2 + w_3 = 1$. Different weight coefficients are selected according to different cluster classification objectives, and the corresponding cluster classification results can be obtained.

(1) Electrical modularity index

The concept of modularity function was proposed by Newman [17] to quantify the strength of community structure in complex networks. The larger the modularity index, the higher the intra-cluster coupling tightness, the smaller the modularity index, the lower the inter-cluster coupling tightness. The expression of the modularity function is

$$\rho = \frac{1}{2m}\sum_i\sum_j\left(e_{ij} - \frac{k_i k_j}{2m}\right)\varphi(i,j) \tag{5}$$

where: e_{ij} is the weight of the edge between node *i* and j. By changing the definition of e_{ij}, the modularity function will have a different meaning, k_i is the sum of all edge weights of node *i*, m is the sum of edge weights of all nodes in the network, $\varphi(i,j) = 1$ when nodes *i* and *j* are in the same DGC, otherwise $\varphi(i,j) = 0$.

Measuring the structural performance of clusters based only on the topological relationship of distribution networks lacks consideration of the electrical connection between nodes, and most scholars currently use electrical distance to measure the tightness of electrical coupling between nodes, as expressed in the following equation:

$$\Delta \boldsymbol{V} = \boldsymbol{S}_{QV}\Delta \boldsymbol{Q} \tag{6}$$

$$\mathrm{d}_{ij} = \lg \frac{S_{QV,jj}}{S_{QV,ij}} \tag{7}$$

where: $\boldsymbol{S}_{QV}$ is the sensitivity matrix, $S_{QV,\,ij}$ is the element of the *i-th* row and *j-th* column of the matrix, which indicates the value of the change of voltage at node *i* caused by the change of power at node *j*, $\boldsymbol{\Delta Q}$ is the change of reactive power and $\boldsymbol{\Delta V}$ is the change of voltage, d_{ij} is the ratio of the change of voltage at node j to the change of voltage at node *i when the change of* reactive power at node *j* occurs.

Consider that the electrical distance between two nodes is not only related to itself, but also to other nodes in the network. Let the network have *n nodes* and define the electrical distance between node *i* and node j as [18]: the

$$L_{ij} = \sqrt{(d_{i1} - d_{j1})^2 + (d_{i2} - d_{j2})^2 + \cdots + (d_{in} - d_{jn})^2} \tag{8}$$

where: L_{ij} is the electrical distance between node *i* and node *j*. The larger the value means the farther the electrical distance between nodes, the smaller the value of the edge weights in the corresponding modularity function, and vice versa. Accordingly, the expression of the relationship between node edge weights and electrical distance is

$$e_{ij} = 1 - L_{ij}/\max(\boldsymbol{L}) \tag{9}$$

where: $\boldsymbol{L}$ is the electrical distance matrix.

(2) Power balance index

The access of a large number of DGs may cause problems such as power backfeeding and voltage crossing of the distribution network. The power backward transmission will not only increase the line loss sharply, but also has the risk of overloading and burning the equipment. Cluster division should take into account the internal power balance of the cluster, reduce the active power out of the cluster, and have a certain voltage regulation capability when the voltage exceeds the limit. When the voltage exceeds the limit, the voltage level is first restored by adjusting the reactive power, when the reactive power adjustment margin is exceeded, the active power is adjusted to maintain the stable operation of the distribution network. Therefore, the power balance index needs to consider the balance degree of active and reactive power within the cluster, and the larger the active and reactive power balance index is, the higher the power balance degree within the cluster.

$$\beta = (\beta_{\mathrm{P}} + \beta_{\mathrm{Q}})/2 \tag{10}$$

where: β is the power balance index, β_{p} is the total active power balance index of the system, β_{Q} is the total reactive power balance index of the system. The active power balance index is used to describe the balance between active power demand and supply within the cluster, and the calculation formula is calculated as

$$\beta_{\mathrm{P}} = \frac{1}{c}\sum_{i=1}^{c}(1 - \frac{1}{T}\sum_{t=1}^{T}\frac{P_{\mathrm{clu}}(t)_i}{\max(P_{\mathrm{clu}}(t)_i)}) \tag{11}$$

where $P_{\text{clu}}\ (t)_i$ is the net power characteristic of cluster i, T is the typical time-varying scene duration, and c expresses the number of clusters. ˎ

The reactive power balance indicator is used to describe the balance between reactive power demand and supply within the cluster:

$$Q_i = \begin{cases} \dfrac{Q_{\sup,i}}{Q_{\text{need},i}} & Q_{\sup,i} < Q_{\text{need},i} \\ 1 & Q_{\sup,i} \geq Q_{\text{need},i} \end{cases} \tag{12}$$

$$\beta_Q = \frac{1}{c}\sum_{i=1}^{c} Q_i \tag{13}$$

where: $Q_{\sup,i}$, $Q_{\text{need},i}$ are the maximum value of reactive power output and reactive power demand of cluster i, respectively, Q_i is the reactive power balance of cluster i.

(3) Node affiliation metrics

Whether the cluster size is balanced or not affects the difficulty of "intra-cluster autonomy" and "inter-cluster coordination", and improving the balance of cluster size can reduce the complexity of cluster optimization model and improve the regulation ability of set DG. To address the problem of unbalanced cluster size, the paper proposes the node affiliation index to evaluate the reasonableness of each cluster size:

$$\lambda = \frac{\mu(i, V[i])}{\mu(i, V - V[i])} \tag{14}$$

$$\mu(i, V[i]) = \frac{1}{|V[i]|}\sum_{j \in V[i]} e_{ij} \tag{15}$$

$$\mu(i, V - V[i]) = \frac{1}{|V - V[i]|}\sum_{j \in V - V[i]} e_{ij} \tag{16}$$

where: λ *is the* node affiliation metric, the larger the value the more balanced the size of each cluster, $V[i]$ is the cluster where node i is located, $|\ V[i]\ |$ is the sum of the number of edges between all nodes in the cluster, $j \in V[i]$ denotes the nodes in the same cluster as node i and connected, $\mu(i,V[i])$ is the affiliation degree of the nodes in the same cluster as node i and connected in cluster $V[i]$, $V - V[i]$ is the cluster that does not contain node i, $|V - V[i]|$ is the sum of the number of edges between the remaining clusters except cluster $V[i]$, $j \in$ denotes the nodes that are not in the same cluster as node i but connected, $\mu(i,V[i])$ is the affiliation degree o*f* the nodes in the cluster $V[i]$ that are connected to node i, is the cluster that does contains node i, $|V - V[i]|$ is the sum of the number of edges between nodes in the remaining clusters except cluster $V[i]$, $j \in V - V[i]$ denotes a node that is not in the same cluster as node i but is connected, $\mu(i, V - V[i])$ is the degree of affiliation of a node that is not in the same cluster as node i but is connected in cluster.

In terms of cluster division indexes, the existing cluster division indexes mainly include electrical modularity, active power balance and reactive power balance indexes.

None of them consider the impact of cluster size on the subsequent cluster operation control, and the differences in the size of the divided clusters are too large, even generating isolated nodes.

In contrast, the comprehensive cluster division index proposed in this paper can effectively equalize the cluster size, avoid the situation of isolated nodes forming a separate group, and facilitate the subsequent cluster planning.

4 Two-Tier Planning Model

4.1 Upper-Level Planning Model

The upper-level planning model takes the equivalent annual value of DG and ESS installation cost C_1, annual operation and maintenance cost C_2, cluster power purchase cost C_3, and minimum network loss cost C_4 as the objective function, and uses the cluster as the basic unit to optimize the DPV capacity, ESS capacity and power for each cluster access.

4.1.1 Objective Function

$$\min C = C_1 + C_2 + C_3 + C_4 \tag{17}$$

(1) Equivalent annual value installation cost

$$C_1 = \sum_{i=1}^{N_C} \left[\begin{array}{l} C_{\text{DG}} S_{\text{clu}.i}^{\text{DG}} \dfrac{r(r+1)^{y_{\text{DG}}}}{(r+1)^{y_{\text{DG}}} - 1} + C_{\text{E}} S_{\text{clu},i}^{\text{ESS}} \dfrac{r(r+1)^{y_{\text{ESS}}}}{(r+1)^{y_{\text{ESS}}} - 1} \\ + C_{\text{P}} P_{\text{clu}.i}^{\text{ESS}} \dfrac{r(r+1)^{y_{\text{ESS}}}}{(r+1)^{y_{\text{ESS}}} - 1} + C_{\text{IED}} \dfrac{r(r+1)^{y_{\text{IED}}}}{(r+1)^{y_{\text{IED}}} - 1} \end{array} \right] \tag{18}$$

where: N_C is the number of DGCs, C_{DG}, C_{E}, C_{P}, C_{IED} are the DG unit capacity investment cost, ESS unit capacity and power investment cost and intelligent equipment acquisition cost, respectively, $S_{\text{clu}.i}^{\text{DG}}$, $S_{\text{clu},i}^{\text{ESS}}$, $P_{\text{clu}.i}^{\text{ESS}}$ are the DG and ESS installed capacity and ESS inverter rated power of cluster i, respectively, $y_{\text{DG}}, y_{\text{ESS}}, y_{\text{IED}}$ are the service life of DG, ESS and intelligent equipment, respectively, r is the discount rate, and $r = 10\%$ is taken in this paper.

(2) Annual operation and maintenance costs

$$C_2 = \sum_{t=1}^{8760} \sum_{i=1}^{N_C} \left[C_{\text{DG}}^{\text{OM}} P_{\text{clu},i,t}^{\text{DG}} + C_{\text{ESS}}^{\text{OM}} \left| P_{\text{clu},i,t}^{\text{ESS}} \right| + C_{\text{IDE}}^{\text{OM}} \right] \tag{19}$$

where: $C_{\text{DG}}^{\text{OM}}$, $C_{\text{ESS}}^{\text{OM}}$, $C_{\text{IDE}}^{\text{OM}}$ are the annual operation and maintenance costs of DG, ESS and smart devices, respectively, $P_{\text{clu},i,t}^{\text{DG}}$ is the DG output of cluster i at time t, $P_{\text{clu},i,t}^{\text{ESS}}$ is the ESS charging and discharging power of cluster i at time t.

(3) Cluster power purchase cost

$$C_3 = C_t^{in} \sum_{t=1}^{8760} \sum_{i=1}^{N_C} P_{\mathrm{clu},i,t}^{\mathrm{in}} \tag{20}$$

where: C_t^{in} is the real-time electricity price at moment *t*, $P_{\mathrm{clu},i,t}^{\mathrm{in}}$ is the net power flowing into cluster *i* at moment *t*.

(4) Network damage costs

$$C_4 = C_t^{in} \sum_{t=1}^{8760} \sum_{i=1}^{N_C} P_{\mathrm{clu},i,t}^{\mathrm{loss}} \tag{21}$$

where: $P_{\mathrm{clu},i,t}^{\mathrm{loss}}$ is the total active network loss of cluster *i* at time *t*.

4.1.2 Constraints

(1) Cluster Installation Capacity Constraints

$$0 \le P_{\mathrm{clu},i}^{\mathrm{DG}} \le \sum_{i=1}^{n} P_{\mathrm{DG},i,j}^{\max} \tag{22}$$

where: $P_{\mathrm{clu},i}^{\mathrm{DG}}$ is the installed DG capacity of cluster *i*, $P_{\mathrm{DG},i,j}^{\max}$ is the maximum installed DG capacity of cluster *i* node *j*.

(2) Upper grid power backfeed constraint

$$P_{\mathrm{cp},l,t}^{\mathrm{off}} \le P_{\mathrm{cp},l,t}^{\max} \tag{23}$$

where: $P_{\mathrm{cp},l,t}^{\mathrm{off}}$, $P_{\mathrm{cp},l,t}^{\max}$ are the backward power and its maximum allowable backward power on the contact line *l* at time *t, respectively.*

(3) Inter-cluster power transfer constraints

$$\left|P_{\mathrm{clu},l,t}\right| \le P_{\mathrm{clu},i,l,t}^{\max} \tag{24}$$

where: $P_{\mathrm{clu},l,t}$, $P_{\mathrm{clu},i,l,t}^{\max}$ are the transmission power and the maximum allowed transmission power on the inter-cluster contact line *l* at time *t, respectively.*

4.2 Lower Level Planning Model

The lower layer planning model takes the minimum active network loss within the cluster as the objective function, and takes the nodes as the basic unit to optimize the access location and access capacity of DPV and ESS.

4.2.1 Objective Function

$$F = \sum_{i=1}^{24} \sum_{j=1}^{b_{\mathrm{clu},i}} r_i (I_i)^2 \Delta T \tag{25}$$

where: $b_{\mathrm{clu},i}$ is the number of branches of cluster *i*.

4.2.2 Constraints

(1) Tidal equation constraint

$$\begin{cases} P_{i,t} = U_{i,t} \sum_{j \in i} U_{j,t}(G_{ij}\cos\theta_{ij,t} + B_{ij}\sin\theta_{ij,t}) \\ Q_{i,t} = U_{i,t} \sum_{j \in i} U_{j,t}(G_{ij}\cos\theta_{ij,t} - B_{ij}\sin\theta_{ij,t}) \end{cases} \tag{26}$$

where: $P_{i,t}$, $Q_{i,t}$ are the injected active and reactive power at node *i at time t*, respectively, $\theta_{ij,t}$ is the voltage phase angle difference between nodes *i andj* at time *t*, $U_{j,t}$ is the voltage amplitude at node *j* at time *t*, G_{ij}, B_{ij} are the conductance and conductance of branch *ij,* respectively.

(2) Node voltage constraints

$$U_{i,j}^{\min} \leq U_{i,j,t} \leq U_{i,j}^{\max} \tag{27}$$

where: $U_{i,j}^{\min}$, $U_{i,j}^{\max}$ are the upper and lower limits of the voltage amplitude of node *j* in cluster *i*, respectively, $U_{i,j}$ is the voltage amplitude of node *j* in cluster *i* at time *t.*

(3) Node installation capacity constraint

The installation capacity constraint mainly includes node installation capacity constraint and cluster *i* installation capacity constraint.

$$\begin{cases} 0 \leq S_{\mathrm{DG},i,j} \leq S_{\mathrm{DG},i,j}^{\max} \\ \sum_{i=1}^{n} S_{\mathrm{DG},i,j} - S_{\mathrm{clu},i}^{\mathrm{DG}} = 0 \end{cases} \tag{28}$$

where: $S_{\mathrm{DG},i,j}$ and $S_{\mathrm{DG},i,j}^{\max}$ are the installed DG capacity and the maximum installed capacity of node *j in* cluster *i*, respectively, $S_{\mathrm{clu},i}^{\mathrm{DG}}$ is the installed DG capacity in cluster *i* optimized by the upper-level planning model.

(4) Intra-cluster power transfer constraints

$$S_{\mathrm{clu},i,l}^{\min} \leq S_{\mathrm{clu},l,t} \leq S_{\mathrm{clu},i,l}^{\max} \tag{29}$$

where: $S_{\mathrm{clu},i,l}^{\min}$, $S_{\mathrm{clu},i,l}^{\max}$ are the transmission power and the maximum value of transmission power on branch *l in the cluster, respectively*, $S_{\mathrm{clu},l,t}$ is the transmission power on branch *l* in the cluster at time *t.*

(5) ESS operational constraints

$$\begin{gathered} -P_{\mathrm{bess},\mathrm{M}} \leq P_{\mathrm{bess}}^{*}(t) \leq P_{\mathrm{bess},\mathrm{M}} \\ S_{\mathrm{OC,m}} \leq S_{\mathrm{OC}}^{*}(t) \leq S_{\mathrm{OC,M}} \end{gathered} \tag{30}$$

where: $P_{\text{bess },\text{M}}$ is the maximum power limit of ESS, $P^{*}_{\text{bess}}(t)$ is the power of the storage system at time t, $S_{\text{OC,M}}$ and $S_{\text{OC,m}}$ are the upper and lower SOC limits of ESS, SOC,M and SOC,m are the upper and lower SOC limits of ESS, and $S_{\text{OC,M}}$ and $S_{\text{OC,m}}$ are the upper and lower SOC limits of ESS. limits of ESS, and S^{*}_{OC} (t) is the state of charge of the energy storage system at moment t.

(6) DG operational constraints:

$$\begin{cases} 0 \leq P_{i,DG} \leq P^{\max}_{i,\text{DG}} \\ -Q^{\max}_{i,\text{DG}} \leq Q_{i,DG} \leq Q^{\max}_{i,\text{DG}} \end{cases} \tag{31}$$

where: $P_{i,DG}$ is the *i-th* DG active power output, $P^{\max}_{i,\text{DG}}$ and $Q^{\max}_{i,\text{DG}}$ are the *i-th* DG active power output and reactive power output maxima, respectively, In order not to lose generality, this paper adopts the DG power control strategy with constant power factor, $Q^{\max}_{i,\text{DG}} = P^{\max}_{i,\text{DG}} \tan \varphi_k$.

4.3 Two-Level Programming Model Solution Algorithm

For the characteristics of many types and numbers of variables of the proposed two-layer planning model in this paper, the two-layer iterative hybrid particle swarm algorithm is used. The solution is performed. In the two-layer planning model, the upper layer particles represent the installed capacity of DG and ESS and the power of ESS in each cluster, the lower layer particles represent the installed DG and ESS installation locations in each cluster, and its structure is shown in Fig. 2.

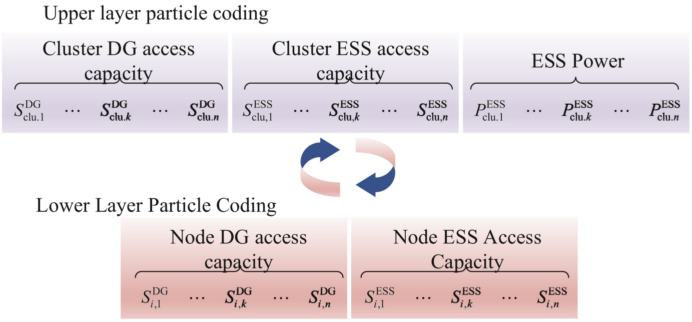

Fig. 2. Particle encoding

The main steps of the two-layer programming model solving algorithm based on the two-layer iterative hybrid particle swarm algorithm are as follows:

Step 1 Parameter initialization. Based on the original data of the distribution network to be planned, preliminary tide calculation is performed to obtain node voltage and branch tide data and initialize the parameters of the particle swarm algorithm.

Step 2 Upper level particle swarm optimization:

(1) Initialization of upper layer particle swarm algorithm. Each particle in the upper layer consists of each cluster DG, ESS access capacity and ESS power. Initialize the velocity, position, individual optimal value and group optimal value of the upper layer particle swarm, and set the current iteration number $i = 0$.
(2) Iterative solving. Update the velocity and position of the upper particles, and when the velocity and position of the particles are the same before and after the update, introduce a random number between (0,1) for the current particle velocity to prevent the algorithm from falling into local optimum, and the number of iterations $i = i + 1$.

Step 3 Lower level particle swarm algorithm optimization.

(1) Initialization of the lower particle swarm algorithm. The upper particle optimization result is used as the initial condition of the lower particle swarm algorithm, initialize the velocity, position, individual optimal value and group optimal value of the lower particles, and set the current iteration number $i^* = 0$.
(2) Parameter update. The lower particle velocity and position updates are the same as (2) in step 2, with iteration number $i^* = i^* + 1$.
(3) Calculate the lower layer particle adaptability. Update the access data of nodes DG and ESS in the distribution network cluster, perform the tide calculation and update the lower layer particle adaptation value.
(4) Update the individual and group fitness of lower level particles. Compare the current individual fitness with the optimal individual fitness, and update the individual optimal value and individual fitness. Similarly, update the population optimum and population fitness.
(5) Iteration number judgment. If the current number of iterations $i^* < i^{*,max}$, then return to step 3 in (2) keep iterating, if the current number of iterations i $i^* \geq {}^{*,max}$, output the population optimal value and the population fitness value is the most optimized result.

Step 4 Update the upper layer particle fitness. Update the access data of each cluster DG, ESS to calculate the upper layer particle fitness, same as (4) in step 3 to update the upper layer particle fitness.

Step 5 Iteration number judgment. If the current number of iterations $i < i^{max}$, then return to step 2 (2) to iterate continuously, otherwise output the result of upper and lower layer double layer planning.

5 Example Analysis

In order to verify the effectiveness of the proposed method, this paper takes the modified IEEE33 system as an example, simulation tests are conducted in MATLAB 2020a environment. The base voltage and base power of this system are 12.66 kV and 10 MV-A, respectively, and the maximum daily load is 3715 + j2300 kVA, and the upper and lower limits of node voltage are set to 1.05 and 0.9, respectively. Among the various costs, the cost of shutting down the operation when the system is reconfigured is 0.5 yuan/time, the peak and valley time-sharing tariffs are 0.7 yuan/(kW-h) and 0.4 yuan/(kW-h), respectively, DG investment cost and operation and maintenance cost are RMB1500/(kVA) and RMB500/(kVA) respectively, ESS investment cost and operation and maintenance cost are RMB1500/(kVA) and RMB500/(kVA) respectively.

5.1 Reconfiguration Scheme and Analysis of Cluster Division Results

According to the time period division method proposed in this paper, the equivalent load of each node is treated with a 24 × 32-dimensional matrix processing, and the improved K-means algorithm is used. The time period division is carried out. The equivalent daily load curve is finally divided into 4 segments, as shown in Fig. 3.

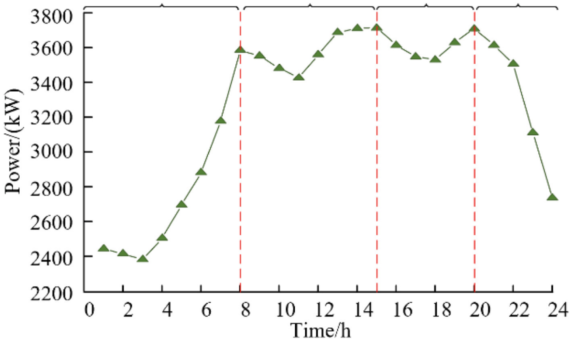

Fig. 3. Load time curve

The network reconfiguration of the distribution network without any optimization measures is carried out in each optimal time period, and the number of individual switch actions is set to be no more than 4, and the total number of switch actions in a single reconfiguration process is no more than 12. In order to further verify the effectiveness and rationality of the time-period-based network reconstruction method proposed in this paper, three different reconstruction schemes are used for comparison and analysis, and the results of network reconstruction for each scheme are shown in Table 1.

Option 1: No time period division of the equivalent daily load curve, and static network reconfiguration within each unit time period.

Option 2: Using the literature [19] The proposed time slot partitioning method combining dual-scale spectral clustering and adaptive time slot algorithm is used for network reconstruction.

Option 3: The time slot partitioning method proposed in this paper equates the daily load curve for time slot partitioning and performs network reconstruction.

As can be seen from Table 1, although the static network reconfiguration method can ensure the best network topology and minimum network loss in each unit time period, it has too many switch actions and excessive equipment losses. Option 2 and Option 3 achieve a balance between network loss and the number of switch actions by considering the constraint on the number of switch actions, reducing the network loss to

Table 1. Comparison chart of different reconfiguration schemes

Restructuring solutions	Reconfiguration time frame	Disconnect switch number	Net loss/ (kW-h)	Switching motion number of jobs
Option 1	Unit Period	Optimal in each time period	1616.7	36
Option 2	00:00–07:00 07:00–15:00 15:00–20:00 20:00–24:00	9, 14, 28, 33, 36 9, 14, 16, 27, 33 9, 14, 20, 27, 30 9, 14, 20, 27, 30	1828.5	14
Option 3	00:00–08:00 08:00–15:00 15:00–21:00 21:00–24:00	9, 14, 28, 33, 36 11, 15, 28, 33, 34 11, 15, 28, 33, 34 9, 14, 20, 27, 30	1775.4	12

a lower level while significantly reducing the number of switch actions. Compared with Option 2, Option 3 reduces the number of switch actions by 2 and the network loss by 53.1 kW. Figure 4 shows the comparison of system node voltages after different network reconfiguration options.

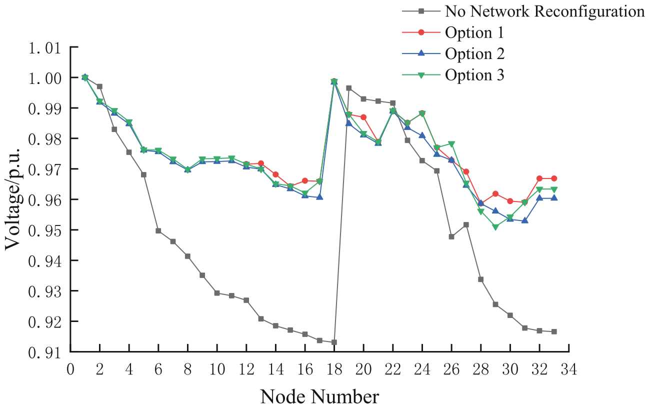

Fig. 4. Node voltage comparison of different solutions

As can be seen from Fig. 4, the node voltages after network reconfiguration are improved compared to those without network reconfiguration. The node voltage amplitude fluctuation is smaller in scenario 1 compared to scenarios 2 and 3 because it is not constrained by the number of switching actions and the network topology is in the optimal state in all time periods. The difference between the node voltage magnitude of Option 2 and Option 3 is not significant, while the number of switching operations and network loss cost of Option 3 are lower than those of Option 2, so Option 3 has better performance compared to Option 2.

Combined with the network topology determined by the above network reconfiguration scheme, the clustering is carried out with the goal of maximizing the mean value of the all-weather comprehensive cluster division index, and the cluster division results are shown in Fig. 5.

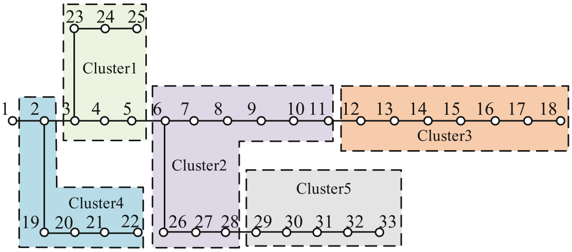

Fig. 5. Distributed generation cluster division results

5.2 Analysis of Planning Results

In order to fully explore the impact of network reconfiguration and cluster division on distribution network planning, this paper constructs three different scenarios to compare and analyze the siting and capacity setting problems of system DG and ESS under different situations and verify the effectiveness and feasibility of the proposed method.

Option 1: Centralized planning scheme for PV and energy storage without network reconfiguration and cluster planning, with nodes as the basic unit for DG and ESS installation capacity, access location and ESS rated power directly.

Option 2: Cluster planning scheme without considering dynamic network reconfiguration, the upper layer optimizes DG access capacity, ESS access capacity and ESS power for each cluster as the basic unit, and the lower layer optimizes DG access capacity and ESS access capacity for each node as the basic unit.

Option 3: Cluster planning scheme considering dynamic network reconfiguration. Based on the cluster partitioning results shown in Fig. 5, the siting and capacity determination of DG and ESS are performed according to the two-layer planning model proposed in this paper.

The distributed PV and energy storage planning results of different schemes are shown in Figs. 6 and 7. Scheme 1 has the largest PV penetration, but the storage planning capacity is higher than both Scheme 2 and Scheme 3, leading to an increase in the capacity of the configured ESS and an increase in the cost of configuring ESS. This is because when the centralized planning method is used for planning, the number of planning nodes is too large for large-scale network belts, and the difficulty of solving increases exponentially with the increase in the number of nodes, and the optimization results are not very satisfactory.

On the basis of Scheme 1, Scheme 2 adopts the cluster planning method, and the number of nodes to be planned in each cluster is much smaller than the total number of nodes in the system, which makes the dimensionality of the optimization variables

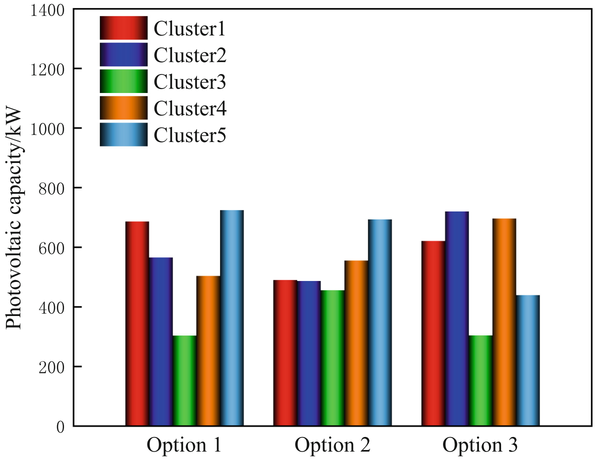

Fig. 6. PV configuration capacity

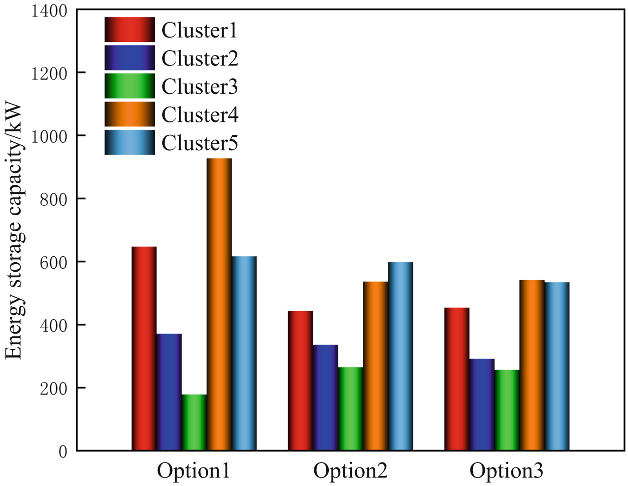

Fig. 7. Configured capacity of each cluster ESS

Table 2. Results of different scenario planning

Programs	PV capacity	ESS Capacity
Option 1	2780.81622	2738.17587
Option 2	2678.07767	2175.617
Option 3	2777.07773	2074.50036

of the upper-level planning model of the two-layer planning model greatly reduced and is conducive to improving the accuracy of the planning solution. As can be seen from Table 2, the clustering planning results of Scheme 2 can significantly reduce the ESS configuration capacity, and the ESS is more evenly distributed in each cluster, which makes the power within each cluster more balanced and the inter-cluster power interaction power less, which makes the network loss also greatly reduced.

6 Conclusion

This paper considers the interplay between network reconfiguration and cluster partitioning, establishes a two-layer planning model for PV and ESS, and draws the following conclusions from a comparative analysis of three different scenarios:

(1) When considering the dynamic reconfiguration of the network, by changing the network switching state, the power balance within the system can be improved and the capacity of ESS configuration can be reduced, while the DG's dissipation capacity can be reduced.
(2) Combining network reconfiguration with cluster planning methods not only helps to improve the accuracy of the planning solution, but also enables the system to improve the voltage level and reduce the network loss in the post-planning operation phase.

Acknowledgement. This work is supported by National Key R&D Program of China (No. 2022YFB2402905).

References

1. Li, J., Sun, D., Zhu, X., et al.: Voltage regulation strategy for distributed energy storage considering coordination among clusters with high penetration of photovoltaics. Auto. Elect. Pow. Syst. **47**(10), 47–56 (2023)
2. Zhang, X., Mo, L., Chen, C., et al.: A two-stage robust optimization model for network reconfiguration and reactive power optimization synergy in hybrid AC-DC distribution networks. Power Syst. Tech. **46**(03), 1149–1162 (2022)
3. Ma, L., Wang, Y., Wang, C.: Robust planning of distributed power sources for active distribution network meshing and network reconfiguration[J]. Automation of Electric Power Systems. **42**(11), 94–101 (2018)
4. Zhu, J., Gu, W., Zhang, H., et al.: An optimization method for siting and capacity setting of distributed power supplies considering dynamic network reconfiguration. Automat. Elect. Pow. Syst. **42**(05), 111–119 (2018)
5. Azizivahed, A., Arefi, A., Ghavidel, S., et al.: Energy management strategy in dynamic distribution network reconfiguration considering renewable energy resources and storage. IEEE Trans. Sustain. Energy. **11**(2), 662–673 (2019)
6. Wang, W., Huang, Y., Yang, M., et al.: Renewable energy sources planning considering approximate dynamic network reconfiguration and nonlinear correlations of uncertainties in distribution network. Int. J. Electr. Power Energy Syst. **36**(02), 335–341 (2016)
7. Ding, M., Zhang, Y., Bi, R., et al.: Coordinated expansion planning of distribution network sources considering cluster division. Proceed. EPSA **33**(01), 136–143 (2021)

8. Shi, B., Xiao, C., Peng, K., et al.: Network-source-storage double-layer joint expansion planning strategy for distribution networks based on cluster partitioning. Automat. Elect. Pow. Syst. **6**(3), 704–711 (2020)
9. Ding, M., Gao, P., Bi, R., et al.: A cluster classification method for renewable energy with high penetration considering flexibility. Proceed. EPSA. **33**(1), 115–172 (2021)
10. Thanh, N., Man, K.: Cluster-based predictive PCC voltage control of large-scale offshore wind farm. IEEE Acc. **15**(1), 173–192 (2021)
11. Huang, S., Wu, Q., Zhao, J., et al.: Distributed optimal voltage control for VSC-HVDC connected large-scale wind farm cluster based on analytical target cascading method. IEEE Trans. Sustain. Energy. **11**(4), 2152–2161 (2020)
12. Zhao, W., Zhang, F., Liu, J.: Advances in community discovery for complex networks. Comp. Sci. **47**(02), 10–20 (2020)
13. Bi R., Liu X., Ding M., et al.: A method for dividing renewable energy generation clusters with the goal of improving consumption capacity, **39**(22), 6583–6592 (2019)
14. Wu, Y., Gao, C., Cao, H., et al.: Clustering analysis of daily load curve based on grey wolf optimization clustering algorithm. Proceed. CSEE **48**(6), 68–76 (2020)
15. Li, G., Li, Y., Liu, J., et al.: A distributed energy storage capacity planning method considering cluster division. Proceed. EPSA **30**(12), 1–10 (2018)
16. Ding, M., Fang, H., Bi, R., et al.: Capacity planning of distributed photovoltaic and energy storage in distribution networks based on cluster division. Proceed. EPSA **39**(8), 2187–2201 (2019)
17. Newman, M.: Finding community structure in networks using the eigenvectors of matrices. Phys. Rev. **74**(3), 036104 (2006)
18. Su S., Zhang Q., Xiong W., et al.: Dynamic network reconfiguration and reactive voltage adjustment for co-optimization with high penetration renewable energy. Power Grids Clean Ener. **39**(1), 100–229 (2023)

The Decomposition Method for Customer Directrix Load Based on Power Customers Load Profile Clustering

Yunfei Shao[1], Haijun Shen[2](✉), Shuai Fan[1], and Guangyu He[1]

[1] School of Electronic Information and Electrical Engineering, Shanghai Jiao Tong University, Shanghai 200240, China
[2] Energy Security Department, Logistics Support Center, Shanghai Jiao Tong University, Shanghai 200240, China
`hjshen@sjtu.edu.cn`

Abstract. Due to the global warming caused by the excessive use of fossil energy, the uncertainty and volatility of new energy have put pressure on the regulation of the power system, resulting in problems such as abandoning wind and light. The customer directrix load has been proposed to define the ideal load curve shape to smooth the fluctuation, and achieve the balance of adjustable resources and non-adjustable resources. However, this method cannot personalize and guide different types of users, and fails to fully tap the user's adjustment potential. Therefore, a customer directrix load decomposition method based on power customers load profile clustering is proposed. Firstly, the research on user clustering and load customer directrix load is analyzed, especially for the problems faced by personalized clustering of users' electricity consumption. Secondly, the decomposition scheme of the customer directrix load, the model of the sub-customer directrix load and the measurement of the effect are proposed, and a set of decomposition mechanism of the sub-customer directrix load is designed based on the clustering algorithm of user characteristics. The results of the example analysis show that compared with the existing mechanism, the sub-customer directrix load decomposition mechanism can fully tap the user's adjustment ability and guide the user closer to the customer directrix load. This mechanism is suitable for different kinds of clusters of spontaneous clustering according to the user power consumption characteristics. Finally, this mechanism can effectively reduce the problem of wind and light abandonment and improve the absorption capacity of new energy.

Keywords: Load profile clustering · Power consumption characteristics · Customer directrix load decomposition · New energy absorption

1 Introduction

1.1 Background

Fossil energy use causes climate change and energy shortages. China promotes new energy to address these issues. However, rapid new energy growth poses power regulation challenges, leading to curtailment and lack of control. Traditional methods are inefficient

Y. Xue et al. (Eds.): PMF 2023, LNEE 1129, pp. 403–421, 2024.
https://doi.org/10.1007/978-981-99-9251-5_32

for high new energy grids [1]. Demand response, through price-based and incentive-based approaches, effectively regulates and absorbs new energy, promoting power system reform [1]. However, issues such as participation, baseline calculation, effectiveness, fairness, and quantification need resolution for large-scale implementation [2].

Customer Directrix Load (CDL) stabilizes new energy fluctuations and provides an ideal load curve for demand response. Literature [1] introduces CDL to improve load curves, while Literature [2] decomposes CDL for large-scale response options, maximizing user potential. Traditional demand response lacks personalization and user potential utilization. Load aggregators decompose the customer directrix load into sub-customer directrix loads, giving users more options and facilitating their response potential exploration [2]. This study proposes an effective method, including decomposition, considering users' electricity consumption behavior. The CDL decomposition mechanism guides users' autonomous response, bringing the total load curve closer to the CDL and offering more options to explore their response potential.

This paper will analyze the limitations of research on electricity consumption characteristics and quasi-linear demand response based on customer clustering, and propose a customer directrix load decomposition method based on users clustering, which realizes individuality by decomposing load directrix guidance and synergistic combination. This method is expected to overcome the limitations of traditional demand response, improve the effect of demand response, and better adapt to the personalized needs of users.

1.2 State-of-the-Art

Current research examines user electricity consumption using questionnaires, power data analysis, and smart meters, employing clustering algorithms like k-means and SOM. A comprehensive clustering method integrating K-means, SOM, and BP neural network is proposed [3], while another study explores various clustering algorithms, distance measures, and evaluation functions for user behavior analysis [4]. Smart grid technology provides users with control and feedback [4]. The power grid center offers real-time information and recommendations through mobile apps to promote energy-saving [4]. Limitations in current research on clustering methods for electricity consumption include data availability, privacy concerns, low user participation, complex user behavior, and social and cultural differences in energy perception and behavior. These limitations encompass: (1) Data availability and privacy: Privacy regulations restrict data acquisition and analysis, posing challenges in data acquisition and analysis [5]. (2) User participation and response: Low user participation and passive response hinder the effectiveness of demand response strategies. (3) Complexity and diversity of user behavior: Numerous factors influence user behavior, making it challenging to predict and intervene in electricity consumption and design personalized strategies [5].

In customer directrix load-based demand response studies, the concept and model of customer directrix load have been proposed, along with an implementation plan. The customer directrix load defines an ideal load curve shape to stabilize system fluctuations, allowing users to adjust their power consumption patterns based on incentives [6]. This achieves a balance between adjustable and non-adjustable resources, especially for accommodating high proportions of new energy. However, there are limitations to the current research. Existing methods lack personalized guidance and user combinations, making it challenging for some users to approach the customer directrix load. Additionally, decomposing the customer directrix load into sub-customer directrixs and ensuring the total load curve aligns with the customer directrix load requires further investigation. Addressing these issues will enhance the effectiveness of customer directrix load demand response and maximize user response potential [7].

1.3 Innovation

This paper presents a customer directrix load decomposition method based on user clustering considering consumer power consumption behavior. Users collaborate and make adjustments to align their combined load curve with the customer directrix load. The load aggregator decomposes the alignment into sub-customer directrix load, providing users with options that match their consumption habits, tapping into their response potential. A diagram illustrates the customer directrix load and two sub-customer directrix loads (sub-customer directrix load 1 and sub-customer directrix load 2). Users visually assess and select a curve that matches their target. Decomposing the guideline enables user autonomy, promoting convergence towards the customer directrix load [2]. Further research is needed to investigate the decomposition methodology and ensure user autonomy in selecting sub-customer directrix load. Effective strategies and mechanisms are explored for users' autonomous decision-making, achieving closer adherence to the customer directrix load [1] (Fig. 1).

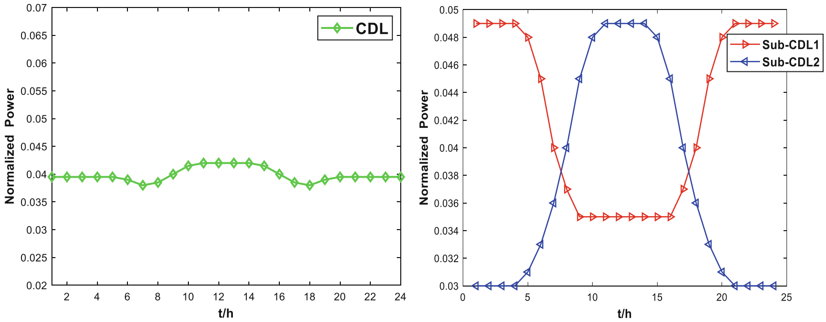

Fig. 1. Schematic diagram of customer directrix load decomposition

2 Solution Method

2.1 Power Customers Load Profile Clustering Method

In this paper, the k-means algorithm is mainly used to cluster the user's electricity consumption characteristics. K-means is a clustering algorithm whose principle is to divide a data set into k clusters such that each data point belongs to the nearest cluster and the center of the cluster is the average of all data points. This algorithm is based on iterative optimization, and each iterative step will update the center point of the cluster until the convergence condition is reached. The basic principle of the K-means clustering algorithm: First, select the data set to be divided into k clusters, and then randomly select k data points as the initial cluster centers. Each data point is then assigned to the nearest cluster center, and each data point can only belong to one cluster. The cluster center points are updated according to the assigned data points, which is achieved by computing the mean of the data points belonging to each cluster. Repeat the above steps until the center point of the cluster no longer changes, or reaches the predetermined number of iterations. Finally, k clusters and the center point of each cluster are obtained.The flow chart of K-Means algorithm is shown in the Fig. 2.

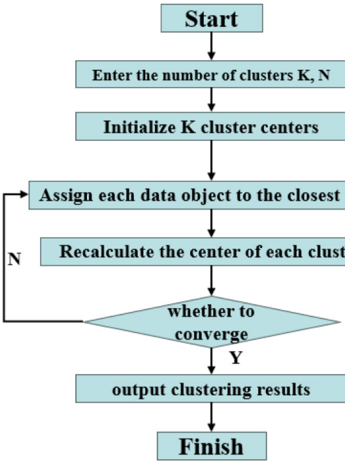

Fig. 2. K-means algorithm flow chart

2.2 Load Shape

The load curve shape is defined by the total electricity recorded during the time period T, denoted as $l(t)$. It is standardized using the reference pair, represented by $\alpha = \sum_{t=1}^{T} l(t)$. Which is standardized by the reference pair, that is

$$l^{*}(t) = f_u(l(t)) = \frac{l(t)}{\alpha} \tag{1}$$

$l^{*}(t)$ is the value of the load curve through the $l(t)$ normalization algorithm $f_u(\cdot)$, so that the characteristics of the magnitude of the load curve are eliminated, and only the characteristics of the curve shape are retained [2] (Fig. 3).

2.3 Customer Directrix Load Model

In terms of directrix calculation, it is considered that most current demand response (DR) projects use load aggregators to integrate loads of a certain magnitude, and cooperate

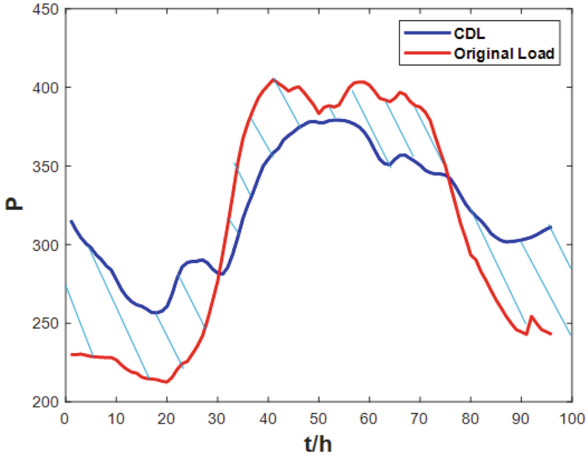

Fig. 3. Schematic diagram of customer directrix load

with power companies for demand response at the macro level. At the system level, the independent system operator (ISO) and the control center of the power company usually act as the demand response center, and its goal is to fully absorb new energy while minimizing operating costs. To achieve economic dispatch, the demand response center sets an objective function [3]:

$$\min \sum_{t=1}^{T} \sum_{i=1}^{N_G} (a_i P_{G,i}^2(t) + b_i P_{G,i}(t) + c_i) + \sum_{t=1}^{T} C_R(P_{R.\max}(t) - P_R(t)) \tag{2}$$

$P_{G,i}(t)$ is the active output of the i-th adjustable generator in the system during the t period, and there are N adjustable generators in total; $P_R(t)$ is the output of all new energy power generation such as photovoltaic and wind power in the system during the t period; $P_{R.\max}(t)$ is the t period The maximum output of new energy can be predicted in advance; a, b, c, are the cost coefficients of the i-th controllable unit, and the first item of the objective function is the sum of the operating costs of all controllable generating units. C_R is the cost of abandoning wind and light, and the second item of the objective function is the cost of not consuming new energy.

In order to fully accommodate new energy, C_R can be set to a very large coefficient, and only when the constraints are difficult to meet will the cost of curtailment of wind and light be generated. In terms of constraints, the traditional balance equation of supply and demand can be transformed into a way in which controllable resources balance uncontrollable resources. This means using adjustable power generation resources and responding demand-side resources to balance non-adjustable new energy generation and non-responsive demand-side resources. Specifically, the constraints can be expressed as the following equations:

$$\sum_{i=1}^{N_G} P_{G,i}(t) - a_D P_D^*(t) = P_C(t) - P_R(t) \tag{3}$$

$P_D(t)$ and $P_C(t)$ are respectively the power consumption of all loads participating in DR and not participating in DR in the system during the t period; a_D is the total power consumption of the loads participating in the DR within the T period. Given that demand response is a process that guides users to change periods of electricity consumption rather than increase or decrease electricity consumption, it can be considered that the amount of electricity consumed within a certain period of time is certain. Therefore, the following constraints need to be considered when conducting demand response:

$$\begin{cases} \sum_{t=1}^{T} P_D^*(t) = 1 \\ 0 \leq P_D^*(t) \leq 1 \end{cases} \tag{4}$$

It should be noted that $P_R(t)$ is recorded as a controllable quantity because power curtailment is allowed, but the cost of power curtailment is very high, and it only occurs when the system is difficult to balance. In addition, constraints such as the upper and lower output constraints of the controllable generator set, the rise and fall slope constraints of the controllable generator set, the spinning reserve constraint, and the output range constraints of new energy sources need to be considered.

2.4 Evaluation Metrics

This article discusses how to quantify how effectively users respond to the customer directrix load, and introduces a metric to measure how similar the shape of the load curve is to the customer directrix load. The expression for this indicator is as follows:

$$\begin{cases} E = e^{-\varepsilon d^2} \\ d = \sqrt{\sum_{t=1}^{T} (l^*(t) - P_D^*(t))^2} \end{cases} \tag{5}$$

Among them, E is the measurement index after converting the Euclidean distance to the (0,1] interval, $l^*(t)$ is the normalized value of the load curve to be measured, and d is the Euclidean distance between the two sequences. Based on this, the actual load curve of the user is compared with The proximity of the guideline is objective and reliable. We can use an objective and reliable indicator to measure the proximity of the user's actual load curve to the guideline. This indicator is called E, which reflects the role of the load curve in promoting new energy consumption. The calculation of incentives for demand response (DR) users is based on the indicator mentioned earlier. When the indicator E is larger, it indicates that users have made greater contributions to promoting new energy consumption. Consequently, users who have actively participated in load adjustment and demonstrated a higher degree of alignment with the desired load patterns will receive greater incentives. This incentivization mechanism rewards users for their efforts in supporting and promoting the adoption of new energy sources. By aligning their electricity consumption with the prescribed load patterns, users contribute to the overall stability and efficiency of the power grid, as well as the integration of new energy resources. The larger the indicator E, reflecting the user's significant contributions to the promotion of new energy consumption, the more incentives they can receive. These incentives serve as a recognition of the user's active involvement in demand response initiatives and their positive impact on the energy system. The calculation of incentives for DR users takes into account the indicator E, which represents the level of contribution made by users towards promoting new energy consumption. By rewarding users with higher incentives for larger E values, it encourages their continued engagement in load adjustment and facilitates the transition towards a more sustainable and new energy future.

2.5 Customer Directrix Load Decomposition

Although the DR center only guides users according to a certain customer directrix load, this method has the advantages of fairness and decoupling. However, for a large number of users, especially residential users, this method lacks personalized guidance and cannot fully tap the user's response potential. It may be difficult for some users to change their own electricity consumption patterns to approach the customer directrix load, but they can combine with other users and make certain changes towards different goals, so that the shape of the combined load curve is close to the customer directrix load.

From a top-down perspective, a load aggregator, serving as a professional DR service provider, has the capability to decompose the customer directrix load provided by the DR center into multiple sub-customer directrix loads. This approach enables users to choose and align their electricity consumption with one of the sub-customer directrix loads that best suits their habits and preferences. Through an effective decomposition mechanism, the collective load curve of all users can be optimized to closely match the desired customer directrix load. By offering users a range of sub-guidelines to choose from, the load aggregator provides them with increased flexibility and options, thereby unlocking the full potential of user response. The key research question in this context is how the load aggregator should decompose the customer directrix load released by the system layer into multiple sub-customer directrix loads while ensuring that a large number of users can independently choose and respond to their preferred load pattern. The ultimate goal is to promote the overall load curve to closely align with the desired customer directrix load. The decomposition process involves careful consideration of various factors such as user preferences, electricity consumption habits, and response potential. The load aggregator aims to devise an effective strategy that allows a significant number of users to make independent choices and adjustments, leading to an aggregated load curve that better reflects the customer directrix load.

From a bottom-up perspective, individual users have the potential to engage in dynamic self-organizing aggregation, allowing them to adjust their load curves with minimal cost and move closer to alignment with the desired load pattern. By leveraging advanced technologies and intelligent systems, users can actively participate in demand response and make real-time adjustments to their electricity consumption. This dynamic self-organizing aggregation enables users to modify their load curves in a way that minimizes the need for significant adjustments and achieves a better alignment with the desired load pattern. Through real-time monitoring, analysis, and feedback mechanisms, users can optimize their energy consumption behavior to match the prescribed load curves more effectively. This bottom-up approach empowers users to take charge of their own load adjustments, considering their individual operational constraints, preferences, and financial considerations. The concept of dynamic self-organizing aggregation recognizes that users possess unique characteristics and consumption patterns. By allowing users to make informed decisions and adjustments based on their specific circumstances, the collective load curve can gradually converge towards the desired alignment. This approach not only minimizes the adjustment costs for individual users but also contributes to the overall stability and efficiency of the power grid. In conclusion, the bottom-up perspective acknowledges the potential for users to engage in dynamic self-organizing aggregation. This approach enables users to adjust their load curves with less adjustment cost, resulting in a closer alignment with the desired load pattern. By empowering users to actively participate in demand response and optimize their energy consumption behavior, this approach promotes a more efficient and flexible utilization of energy resources. Denote the load curves of load x and load y as $l_x(t)$ and $l_y(t)$ respectively, then the load curve shape after load x and y aggregation can be calculated as (Fig. 4):

$$l_{xy}^*(t) = \frac{l_x(t) + l_y(t)}{\sum_{t=1}^{T} (l_x(t) + l_y(t))} \tag{6}$$

As can be seen from the figure, when load x and load y are close to the customer directrix load, a large adjustment cost is required. If the load x and load y are aggregated as a whole, then when the aggregated load curve $l_{xy}^*(t)$ is adjusted with the customer directrix load as the target, the adjustment cost to be paid is significantly reduced, and the user response potential can be better utilized.

According to the research results of the cited literature [8], for the daily load curve of 220,000 residential users (divided into 24 periods), the researchers used the adaptive K-Means algorithm to construct a load dictionary library. Interestingly, the study found that even if only considering the shape characteristics of the load curves, a large number of load curves can be clustered into a certain number of characteristic curve libraries. In addition, research results based on a large amount of data show that the shape characteristics of these load curves are stable over a period of time, and the proportion of daily electricity consumption of each typical load type is usually not much different from historical statistics. Therefore, in the follow-up research, this paper will take this as the default assumption. In this way, the load aggregator can divide the historical electricity consumption data of the users under its jurisdiction into M typical load curves through a certain clustering algorithm, which are recorded as $L_i(t)$ ($t = 1, 2,\ldots T$; $i = 1, 2,\ldots M$), at the same time, also calculate the percentage of daily power consumption of the user group corresponding to various typical load curves, denoted as w_i ($i = 1, 2,\ldots M$), so, according to the M typical load curves, the load aggregator can decompose the received customer directrix load into corresponding M sub-customer directrix load.The following is an introduction on how to decompose the customer directrix load. The goal considered in this paper is to minimize the weighted sum of the adjustment

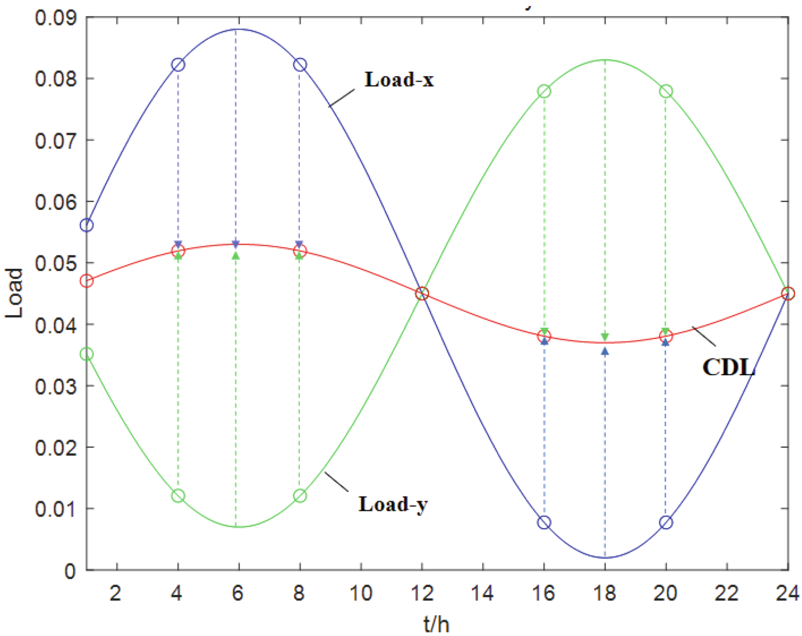

(a) Load-x and Load-y

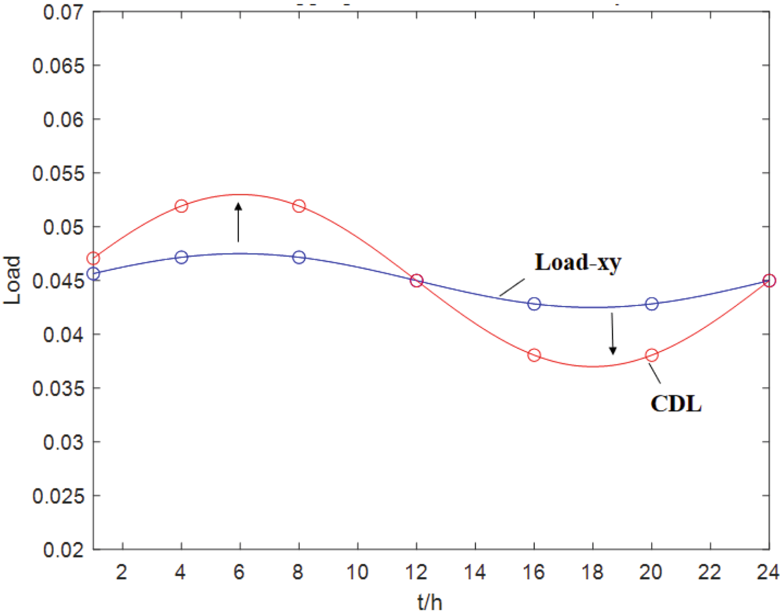

(b) The aggregation of Load-x and Load-y

Fig. 4. Schematic diagram of dynamic self-organization principle

costs of each sub-customer directrix load and its corresponding typical load curve.

$$\min \sum_{i=1}^{M} \sum_{t=1}^{T} w_i (P_{D,i}^*(t) - L_i(t))^2 \tag{7}$$

It should be noted that customer directrix load value $P_D^*(t)$ here is released by the DR center at the system layer, and when the load aggregator decomposes it, $P_D^*(t)$ is taken as a known quantity. The entire process of directrix calculation and sub-directrix decomposition can be expressed as a standard quadratic programming problem, which can be directly solved by mature software packages such as GUROBI.

3 Case Study

3.1 Test System

In order to verify the effectiveness of the mechanism proposed in this chapter, we constructed a power system example with a high proportion of new energy, and considered a large number of users participating in DR. The proposed mechanism is analyzed in detail in this paper. In the calculation example, we used the data of 36 controllable power generation resources provided [9]. In terms of new energy, we selected the new energy output curve of a certain day in 2017 published by PJM and standardized it. This standardized curve is used as the upper limit standard value of the new energy output of the test system, and the total output of new energy is adjusted according to 40% of the total load of the day. In terms of load, the 24h data of user load in a certain area on December 31, 2014 provided by the test questions of the Ninth Electrician Mathematical Modeling Contest [10] is selected. This data is used as the total load curve in this paper. In terms of DR users, this paper uses the user load meter data for the whole year of 2014 provided by the 9th Electrician Modeling Mathematics Contest, and takes 1 h as the collection frequency. In order to simplify the problem, this article uses the data of the last day as the test data, while the previous data is used to divide the sub-customer directrix load. In this paper, it is assumed that all residential loads participating in demand response are handled by a single load aggregator agent [11].

Based on the 24-h data of user load in a certain area on December 31, 2014, we have drawn typical load curves of 30 industrial sub-sectors. In addition, in order to quantify the typical power consumption law of the industry, we defined three indicators, namely, peak-to-valley difference, load rate, and curve similarity to the unified guideline. These indicators can reveal the degree of fluctuation of the curve, the level of load, and the contribution of the industry's own electricity consumption pattern to the power grid's peak-shaving and valley-filling and promotion of new energy consumption. Specifically, the peak-to-valley difference and the load rate measure the degree of fluctuation of the curve, while the similarity of the line reflects the contribution of the industry's electricity consumption pattern to the grid, that is, the higher the similarity, the greater the contribution. Finally, through the analysis of the drawn typical load curves and corresponding indicators, we can gain an in-depth understanding of the power consumption laws of various industries [12].

3.2 The Absorption of New Energy

In this advanced and highly efficient new energy power system, the Demand Response (DR) center plays a crucial role in managing the energy consumption. To achieve this, the center relies on several key inputs, including controllable unit parameters, new energy data, non-DR load data, and the total load that participates in the Demand Response program. These inputs are used to calculate the customer directrix load, which represents the targeted load level for individual customers [13]. The calculation process and the resulting customer directrix load are illustrated in Fig. 5. This figure visually presents the outcome of the calculation, providing valuable insights into the optimal load allocation and energy usage within the system.

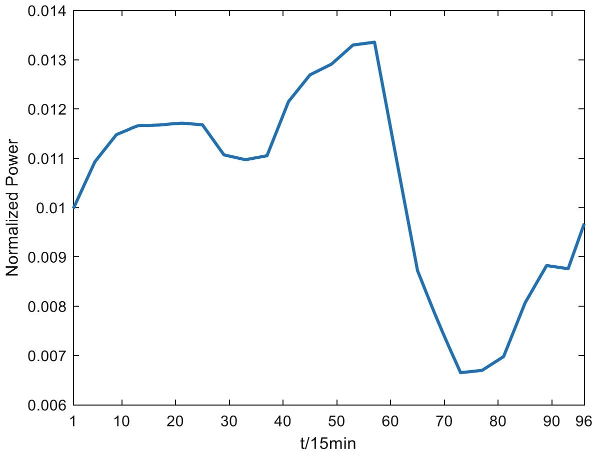

Fig. 5. Residential unified customer directrix load

Once receiving the customer directrix load, aggregators or other large users will try their best to adjust their electricity consumption patterns to improve the similarity between their load curve and the guideline, thereby increasing the index *E* and obtaining more incentives. Simulate the decision-making process of the aggregator, gradually increase *E* until *E* is equal to 1, and get 10 sets of incremental *E* values. After obtaining the shaped load curve, the corresponding amount of curtailed wind and light is calculated by considering the economic dispatch algorithm that prioritizes dispatching new energy. The result is shown in Fig. 6. With the increase of similarity degree *E*, the amount of curtailed wind and light is significantly reduced. When DR users shape the load curve and make it completely consistent with the customer directrix load, new energy can be fully absorbed [14].

3.3 Sub-Customer Directrix Load Decomposition

Upon receiving the customer directrix load issued by the Demand Response (DR) center, the load aggregator takes on the responsibility of decomposing it into multiple sub-customer directrix load. These sub-customer directrix loads are then made available

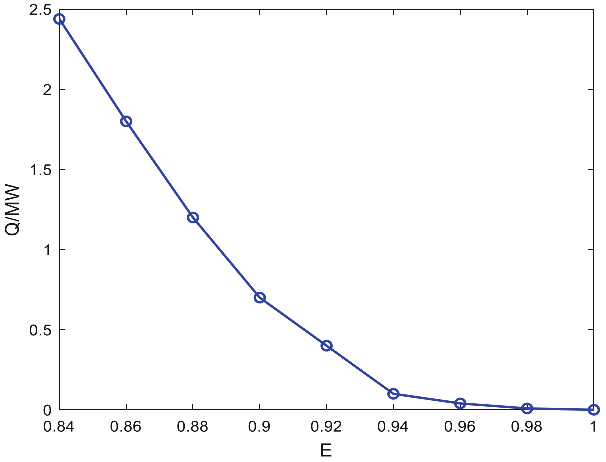

Fig. 6. Trend diagram of the amount of wind and light curtailment (*Q*) with *E*

to the users falling under the aggregator's jurisdiction, offering them alternative target solutions to pursue [9]. This section aims to delve into the significance of decomposing the load directive.

As mentioned earlier, this chapter utilizes a selected dataset, excluding the data from the last day, as the historical data. With *M* set to 30, the residential loads are clustered into 30 categories based on their electricity consumption characteristics. Each category is then assigned a corresponding sub-customer directrix load derived from their characteristic load curve.

Figure 5 visually represents the unified customer directrix load of the system. To ensure equal user participation across all clusters during demand response, the load characteristic curves of the 30 different user load categories are compared with their corresponding sub-customer directrix load. This comparative analysis enables the assessment of how effectively each user load category is guided towards its intended target. By examining the sub-customer directrix load's impact on each category, valuable insights can be gained regarding the effectiveness and suitability of the sub-customer directrix load for different user groups.

Analyzing the alignment of load curves across various user categories provides valuable insights into the effectiveness of the sub-customer directrix load in facilitating the alignment process. By comparing the load characteristic curves with their corresponding sub-customer directrix loads, we can assess how well the decomposition approach enables a closer match between users' load profiles and their sub-customer directrix load targets. This examination allows us to evaluate the degree to which the sub-customer directrix load effectively guides users towards achieving their desired load curves, thereby enhancing the overall success of the demand response strategy. The findings from this analysis contribute to a deeper understanding of the efficacy of the decomposition method in improving the sub-customer directrix load between users' load profiles and their respective targets.

The analysis presented here emphasizes the advantages of decomposing the load directive into sub-guidelines. This approach enables a more detailed and customized strategy for load alignment, taking into account the distinct characteristics and behaviors of different user categories. By providing users with specific sub-customer directrix load, they are empowered to align their load profiles in a more targeted and effective manner. This not only improves the overall effectiveness of demand response initiatives but also promotes a more efficient utilization of energy resources. The availability of sub-customer directrix loads allows for a more personalized and optimized approach, maximizing the potential for users to contribute to load management and create a more sustainable energy system (Fig. 7).

3.4 Evaluation of Demand Response Based on Sub-Customer Directrix Load

(1) User response level

The calculation example aims to provide a comprehensive comparison of the adjustment costs incurred by different users when responding to the unified customer directrix load and the sub-customer directrix load. To visually represent these costs, the adjustment cost is quantified by considering the absolute value of the load adjustment made by the user while fully adhering to the customer directrix load. This means that the adjustment cost increases in proportion to the magnitude of the load adjustment [15].

By adopting this approach, a meaningful assessment can be made regarding the trade-off between the customer directrix load and the associated costs. It enables users to make informed decisions based on their specific operational and financial considerations. Considering the adjustment costs in this manner allows users to better evaluate the economic implications of different customer directrix load options and optimize their load adjustment strategies accordingly. In summary, by quantifying the adjustment costs based on the magnitude of load adjustments, users can gain insights into the financial implications of adhering to different customer directrix load scenarios. This approach facilitates decision-making and empowers users to optimize their load adjustment strategies, taking into account both operational and financial factors.

By considering the absolute value of the load adjustment, this approach offers a straightforward and transparent assessment of the costs involved in aligning users' electricity consumption with the prescribed customer directrix load. This analysis effectively captures the scale and extent of the modifications made by users to match their load curves with the desired targets. A higher absolute value signifies a more significant load adjustment, indicating a greater cost borne by the user.

This quantitative measure provides a clear understanding of the trade-off between load alignment and the associated costs. It facilitates decision-making and strategic planning for users who participate in demand response programs. Users can assess the feasibility and economic implications of aligning their electricity consumption with the customer directrix load by considering the magnitude of load adjustments. This information empowers them to make informed choices and devise effective strategies for optimizing their participation in demand response programs.

The comparison of adjustment costs between the unified customer directrix load and the sub-customer directrix load in the calculation example offers valuable insights into

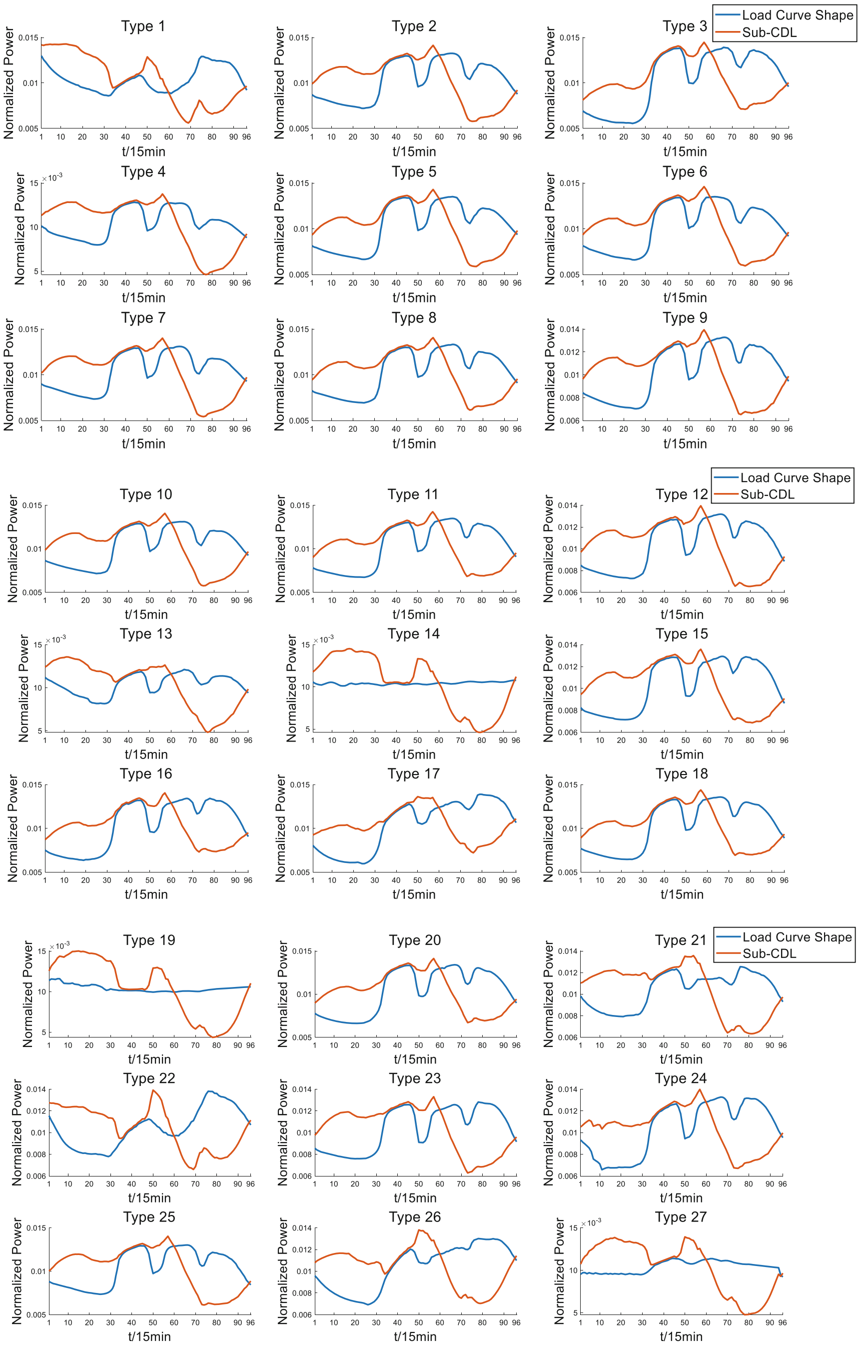

Fig. 7. M = 30 sub-alignment division results and corresponding 30 types of user load characteristic curves

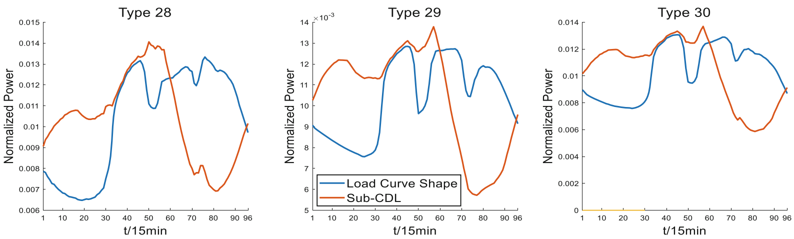

Fig. 7. (*continued*)

the affordability and feasibility of different alignment options. By quantifying the costs associated with load alignment, users can assess the potential financial implications and make informed decisions regarding their preferred approach.

This cost-centric perspective provides a comprehensive understanding of the economic considerations involved in demand response. Users can evaluate the financial implications of their customer directrix load choices, striking a balance between desired alignment outcomes and the costs incurred. This evaluation empowers users to make more informed decisions in load management and demand response, considering both their operational objectives and financial considerations.

By considering the adjustment costs and their impact on the economic viability of demand response initiatives, users can optimize their energy resource utilization and ensure efficient load management. These insights facilitate a more effective utilization of energy resources while ensuring the economic viability of demand response initiatives. It enables users to make strategic decisions that align with their operational goals and financial capabilities, contributing to a sustainable and cost-effective energy consumption strategy (Table 1).

From the perspective of the index of load adjustment, the load adjustment of different types of users classified by M = 30 compared with the sub-customer directrix load is significantly lower than the load adjustment compared with the unified customer directrix load, indicating that different types of users are close to their respective. The price paid for the sub-customer directrix load is far less than the cost of approaching the unified customer directrix load. It is easier for different types of users to approach their respective sub-customer directrix load by adjusting their own electricity consumption habits. The similarity between the user's characteristic curve and the sub-customer directrix load is higher than that of the unified customer directrix load, indicating that the release of the sub-customer directrix load is more conducive to the consumption of new energy.

To sum up, sub-customer directrix load are more accurate and feasible than unified customer directrix load, and can improve the similarity between customer directrix load and various load curves, so that the loads that need to be adjusted for each sub-customer directrix load in the process of carrying out demand response The amount is reduced, and the enthusiasm of various users to participate in demand response is mobilized.

In summary, sub-customer directrix loads prove to be more accurate and feasible than unified customer directrix load. They enhance the similarity between customer directrix load and various load curves, thereby reducing the amount of load adjustment required for each sub-load during the demand response process. This reduction in adjustment

Table 1. M = 30 types of adjustments and similarity of different user comparison with CDL

User clustering and classification results	Load adjustment compared to uniform CDL(MW)	Load adjustment compared to sub-CDL (MW)	Similarity to Uniform CDL	Similarity to sub-CDL
Type 1	68047.36804	67482.65014	0.80	0.80
Type 2	163293.2353	157478.9431	0.70	0.80
Type 3	155211.5587	118151.522	0.66	0.80
Type 4	174943.9574	134464.8161	0.44	0.80
Type 5	190781.6857	180012.5203	0.79	0.80
Type 6	190437.4008	180982.2284	0.65	0.80
Type 7	193776.3273	177076.4103	0.55	0.80
Type 8	188384.1576	182226.5829	0.66	0.80
Type 9	158062.0929	148860.8005	0.46	0.80
Type 10	186382.4978	180795.6825	0.82	0.80
Type 11	181662.2076	164878.798	0.62	0.80
Type 12	168821.6622	166119.7873	0.55	0.80
Type 13	136630.7369	114570.9346	0.77	0.80
Type 14	28411.88971	20100.85002	0.81	0.80
Type 15	157062.4157	148922.5643	0.79	0.80
Type 16	167953.3396	141855.1134	0.78	0.80
Type 17	107105.652	83489.31963	0.77	0.80
Type 18	181758.5032	159266.0977	0.63	0.80
Type 19	33433.6255	22959.13987	0.79	0.80
Type 20	168016.9287	150053.9481	0.82	0.80
Type 21	74405.12358	81694.63753	0.69	0.80
Type 22	50661.11155	44503.55103	0.79	0.80
Type 23	158809.4403	156428.1999	0.81	0.80
Type 24	192464.4657	170690.0102	0.77	0.80
Type 25	199795.2699	187709.8909	0.80	0.80
Type 26	110852.5359	96696.69297	0.81	0.80
Type 27	35906.07343	26235.34532	0.80	0.80
Type 28	101246.0817	89873.52613	0.73	0.80
Type 29	206333.1495	186960.8684	0.71	0.80
Type 30	160634.0486	150711.7086	0.79	0.80

amounts mobilizes the participation of various users in demand response, fostering greater enthusiasm for involvement.

(2) System benefit level

See Table 2.

Table 2. Comparison of total system load indicators before and after demand response

Before response		After response	
Load factor	Peak valley difference (MW)	Load factor	Peak valley difference (MW)
0.93	26025.6	0.95	20000.6

The study examined the changes in load rate and peak-to-valley difference of the system-level load before and after the implementation of sub-customer directrix loads. In the absence of demand response, the load rate of the total system load was measured to be 0.93, with a peak-to-valley difference of 26025.6 MW. However, when different types of users followed the customer directrix load with 80% similarity under the guidance of the sub-customer directrix load, significant improvements were observed. The load rate of the total load increased to 0.95, and the peak-to-valley difference was reduced to 20000.6 MW.

These findings indicate that the participation of different users in demand response can effectively enhance the load rate of the overall system load. By reducing the peak-valley difference of the total load, the power grid's regulation capabilities are enhanced. This demonstrates the potential of demand response programs to optimize electricity consumption patterns and improve the overall stability and efficiency of the power grid.

4 Conclusion

This paper presents a customer directrix load decomposition method that takes into account the characteristics of consumers' electricity consumption. Building upon large-scale directrix demand response, the key focus lies in maximizing the user's adjustment potential and guiding them to approach the directrix more effectively. This is achieved by dividing sub-customer directrix loads based on the electricity consumption characteristics of different users. The research analysis identifies several problems in the current understanding of consumers' electricity consumption characteristics and quasi-linear demand response. To address these issues, this paper proposes a decomposition scheme for the load directrix, a calculation model for the sub-directrix, and a measurement approach for evaluating the response effect. Additionally, a decomposition mechanism for the load directrix is introduced.

Through example analysis conducted on a constructed test system, the results demonstrate that the proposed sub-alignment decomposition mechanism outperforms existing mechanisms. It proves to be suitable not only for different types of clusters formed through users' spontaneous clustering but also for different types of clusters based on users' electricity consumption characteristics, including industry categories. Ultimately, this mechanism effectively mitigates wind and solar curtailment in high-proportion new energy systems and improves the system's capacity to absorb new energy.

Despite the progress made in studying customer directrix load-based demand response considering users' electricity consumption characteristics, there are several areas that warrant further investigation, including:

(1) The research on considering users' electricity consumption characteristics often relies solely on clustering algorithms to classify categories, neglecting the complexity and diversity of user behavior. User behavior is influenced by numerous factors, making it challenging to predict and intervene in their electricity consumption behavior. Designing individual demand response strategies remains a significant challenge.
(2) Determining the appropriate number of decomposition types (M) in the sub-customer directrix load decomposition mechanism requires further research. Adequate subdivision of sub-customer directrix load enhances the system's ability to absorb new energy. However, dividing too many sub-customer directrix load may result in minimal differences between the customer directrix loads, providing little added value for users. Conversely, an excessive number of sub-customer directrix load complicates aggregator management and hinders practical implementation for the majority of users.

Addressing these research directions will contribute to the advancement of customer directrix load-based demand response considering users' electricity consumption characteristics, ultimately improving the effectiveness and practicality of demand response strategies in applications.

References

1. Shuai, F.A.N., Kunqi, J.I.A., Fen, W.A.N.G., et al.: Large-scale demand response based on customer directrix load. Automat. Elect. Pow. Syst. **44**(15), 19–27 (2020). https://doi.org/10.7500/AEPS20191107001
2. Lin, Y.A.N.G.: Incentive mechanisms of the customer directrix load-based demand response. Shanghai Jiao Tong Univ. (2020). https://doi.org/10.27307/d.cnki.gsjtu.2020.001453
3. Bo, Y., Tianxiang, Z., Yifei, W., et al.: Study on electric power system operational decision-making with consideration of large-scale user load directrix demand response. Water Res. Hydropower Eng. **53**(12), 150–159 (2022)
4. Beibei, W.: Research on consumers' response characteristics and ability under smart grid: a literatures survey. Proceed. CSEE **34**(22), 3654–3663 (2014)
5. Yi, D., Hongxun, H., Zhenzhi, L., et al.: Design of business model and market framework oriented to active demand response of power demand side. Automat. Elect. Pow. Syst. **41**(14), 2–9 (2017)
6. Yan, M., Shuai, F., Xiangming, Z., Jucheng, X., Huan, Z., Guangyu, H.: IEEE Power & Energy Society General Meeting (PESGM) (2022)
7. Yan, M., Shaolun, X., Juhua, H., Shuai, F., Jucheng, X., Guangyu, H.: Optimal strategy for customer directrix load based demand response considering comfort and preference of customers. In: IEEE PES Innovative Smart Grid (2022)

8. Mandira, R., Hamed, G., Jessika E. T.: Evaluating low-carbon transportation technologies when demand responds to price. Environ. Sci. Technology (2022)
9. Guangyu, H., Yingyun, S., Shengwei, M., et al.: Multi-indices self-approximate-optimal smart grid. Automat. Elect. Pow. Syst. **33**(17), 1–5 (2009)
10. Yi, T., Zhenzhen, L., Xiangyun, F.: Demand response strategies for promoting consumption of distributed power generation with residential active loads. Automat. Elect. Pow. Syst. **39**(24), 49–55 (2015)
11. Fen, W., Zhiyong, L., Jie, S., Huan, Z., Shuai, F., Guangyu, H.: Self-organizing aggregation operation scheduling method for virtual power plant. Elect. Pow. Const. **42**(4), 79–88 (2021)
12. Shuai, F., Kunqi, J., Bingqing, G., et al.: Collaborative optimal operation strategy for decentralized electric heating loads. Automat. Elect. Pow. Syst. **41**(19), 20–29 (2017)
13. Kwac, J., Flora, J., Rajagopal, R.: Household energy consumption segmentation using hourly data. IEEE Trans. Smart Grid **5**(1), 420–430 (2014)
14. Ma, H., Shahidehpour, S.: Unit commitment with transmission security and voltage constraints. IEEE Trans. Power Syst. **14**(2), 757–764 (1999)
15. Hong, Z., Xin, S., Haoyuan, M., et al.: Research on online optimal dispatching of residential energy consumption based on Multi-Agent asynchronous deep reinforcement learning. In: Proceedings of the CSEE [2019-09-20]. https://doi.org/10.13334/j.0258-8013.pcsee.182498
16. Zexing, C., Yongjun, Z., Zhiheng, X., et al.: Modelling and optimal day-ahead dispatch of district energy centre considering price elasticity of energy load demand. Automat. Elect. Pow. Syst. **42**(12), 27–35 (2018)
17. Fabic, M.S.: What do we demand? responding to the call for precision and definitional agreement in family planning's "demand" and "need" Jargon. Global Heal. Sci. Pract. **10**(1) (2022)

Control Strategies for the PV-Integrated Islanded Microgrid Under Normal and Fault Conditions

Yuping Zheng[1], Shenyun Yao[2], Tonghua Wu[1](✉), Hai Wu[1], Xiaojiang Zheng[1], and Lei Xia[1]

[1] The State Key Laboratory of Smart Grid Protection and Control, NARI Group Corporation, Nanjing, China
1627542261@qq.com
[2] The College of Energy and Electrical Engineering, Hohai University, Nanjing, China

Abstract. This paper describes the corresponding control strategies for the normal and fault operation states of the islanded microgrid system. The islanded microgrid system consists of distributed energy resources (DER) such as photovoltaic (PV), hybrid energy storage (HES) and microturbine (MT) and loads such as pumping unit load (PUL) and equivalent load. In the normal condition, it adopts a voltage and frequency (V-f) control strategy for the inverter of MT to maintain constant voltage and frequency of the whole system and a constant power control strategy for the rest of the power inverters. In the fault condition, the front and rear stages of the PV system adopt constant power control and reactive power compensation priority control respectively, thus realizing low voltage ride-through (LVRT). The proposed control strategies can ensure the stability of voltage and frequency of the microgrid during normal conditions and the ability of the PV system to achieve LVRT during fault conditions. A simulation model of the islanded microgrid system based on PSCAD/EMTDC is constructed and the effectiveness of the control strategies under normal and fault conditions is verified.

Keywords: Microgrid · Two-stage photovoltaic (PV) · Low voltage ride-through (LVRT) · Voltage and frequency (V-f) control · Constant power control

1 Introduction

With the growing energy and environmental crisis, distributed generation (DG) technologies have received widespread attention due to their high energy utilization and low pollution. DG technologies can include photovoltaic (PV), microturbine (MT), and energy storage power generation. Microgrids can combine a series of distributed energy resources (DER) in an orderly and effective way and are a typical application of DG [1]. Different types of DERs in the microgrid have different control characteristics. In order to ensure the stable operation of the microgrid system, it is necessary to reasonably set the control strategy of each micro-source. Microgrids can operate in two modes: grid-connected and islanded mode. In grid-connected mode, the micro-source

Y. Xue et al. (Eds.): PMF 2023, LNEE 1129, pp. 422–436, 2024.
https://doi.org/10.1007/978-981-99-9251-5_33

and load are connected to the grid together, and the system voltage and frequency are determined by the large grid, while in islanded mode, the system voltage and frequency are determined by the way the micro-source is controlled [2–4]. Moreover, if a voltage sag occurs at the point of common coupling (PCC) side of the PV system, it is easy to trigger DC-link overvoltage protection or inverter overcurrent protection and cause the PV system to go directly off-grid, which in turn leads to problems such as power oscillations or insufficient power supply in the microgrid system [5]. Therefore, it is necessary to investigate the low voltage ride-through (LVRT) function of PV systems under microgrid fault conditions.

Unlike traditional single-stage PV power generation systems, two-stage PV power generation systems have an additional DC/DC converter to achieve maximum power point tracking (MPPT) control, however, in the event of an asymmetric voltage sag at PCC, the PV system will face a more serious overvoltage problem in DC side, leading to PV off-grid. Researches on LVRT methods for asymmetric voltage faults in two-stage PV power systems can be divided into two categories: (1) DC-link voltage control, (2) inverter-side current-limiting control. The DC-link voltage control strategy is essentially balancing the power input and output at both ends of the DC bus capacitor and can be divided into two types: hardware-assisted and control strategy improvement. In [6], an LVRT strategy based on a chopper circuit added in the DC link is proposed, where the chopper circuit is put in to suppress the DC-link voltage rise when it crosses the limit, however, this strategy will increase the cost input. In [7, 8], the control strategy of the DC/DC converter is focused, where the system front converter is switched from MPPT control to non-MPPT control after the voltage sag on the network side to ensure DC-link voltage stability. The inverter current-limiting strategy, i.e. controlling the current not to exceed the maximum current limit in case of network-side faults, then distributing active, reactive power according to the maximum current limit. It is necessary to ensure that the inverter can support the grid voltage recovery by outputting reactive power while utilizing its capacity to output active power. As described in [9–13], inverter current limiting primarily improves the control strategy of the PV system's backstage converter. The focus of the above literature is different, but the control strategies of the PV system's front stage and rear stage are independent of each other during the LVRT period, and the front stage converter passively regulates the PV output power according to the DC side voltage value, which is less efficient, so the PV LVRT strategy proposed in this paper is to compute the active power command of the front stage converter as well as the reactive power compensation value of the rear stage inverter according to the grid side dips voltage magnitude to connect the front and rear stage controls, thus further improving the PV LVRT strategy.

As the main contribution of this paper, the control strategies of each DER are proposed for the normal state and fault state of the islanded microgrid system to maintain the stability and safety of the islanded microgrid system. Under the normal condition, the MT adopts the V-f control strategy to maintain the voltage and frequency of the whole system, the PV system adopts the MPPT control strategy to improve the power generation efficiency, and the hybrid energy storage system (HESS) adopts the constant power charging and discharging strategy to maintain the balance of power supply in the system. Under the fault condition, in order to prevent the PV system from going off-grid and other accidents due to voltage sags, this paper proposes a low-voltage ride-through control strategy for the two-stage PV system within the system under asymmetric fault conditions, i.e., the front stage of the PV system adopts constant power control, and the back stage adopts reactive priority compensation control based on the negative-sequence current suppression method. In addition, the active power reference value of the front stage is related to the reactive power compensation value of the rear stage, thus linking the front and rear stage control which can improve the response speed of the control strategy. Finally, an islanded microgrid system model is established based on PSCAD/EMTDC, and the effectiveness of the proposed distributed power control strategy is verified by simulation results.

The paper is organized as follows. In the next section, the mathematical models of each DER and load in the microgrid system are presented. In Section III, the control strategies for each DER in the microgrid system are presented, in which, for the PV system, the control strategies are proposed for normal and fault conditions respectively. Simulation results are shown in Section IV. Finally, conclusions are given in Section V.

2 Modeling of Distributed Power of Generation and Load

2.1 Modeling of PV Array

The photovoltaic cell is the basic unit of the PV system, which can realize the function of converting solar energy into electrical energy. It consists of a photogenerated current source, diode, series and parallel resistors, and its equivalent circuit model is shown in Fig. 1. R_{sr} is the series resistance of the constant current source and R_{sh} is the bypass resistance of the constant current source.

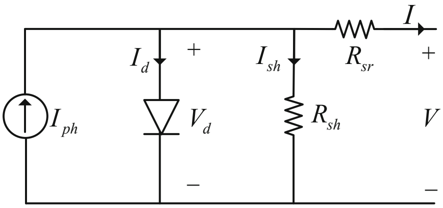

Fig. 1. Photovoltaic cell equivalence model.

According to Kirchhoff's current law, the circuit current equation for a single PV cell is,

$$I = I_{ph} - I_d - I_{sh} \tag{1}$$

where I is the load current, I_{ph} is the photogenerated current, I_d is the diode reverse saturation current and I_r is the diode bypass current.

The photogenerated current I_{ph} is,

$$I_{ph} = \frac{S}{S_r}[I_{sc} + C_T(T - T_r)] \tag{2}$$

where S is the solar radiation, T is the PV cell temperature, I_{sc} is the PV cell short-circuit current measured at the reference solar radiation S_r and the reference cell temperature T_r and C_T is the temperature compensation factor.

The diode reverse saturation current I_d and the diode bypass current I_{sh} are,

$$I_d = I_o\left[\exp\left(\frac{V + IR_{sr}}{kAT/q}\right) - 1\right] \tag{3}$$

$$I_o = I_{or}\left(\frac{T}{T_r}\right)^3 \exp\left[\frac{qE_g}{kA}\left(\frac{1}{T_r} - \frac{1}{T}\right)\right] \tag{4}$$

$$I_{sh} = \frac{V+IR_{sr}}{R_{sh}} \tag{5}$$

where I_o is the reverse saturation current, I_{or} is the dark current at the reference temperature, k is the Boltzmann constant, A is the diode ideal constant, E_g is the band-gap energy of the solar cell material and q is the electron charge.

2.2 Modeling of Hybrid Energy Storage

To balance the benefits of different energy storage units and compensate for their respective drawbacks, a hybrid energy storage system (HESS) combining the supercapacitor (SC) and the vanadium redox battery (VRB) has been adopted. The equivalent circuit models of the supercapacitor and VRB are shown below.

The SC's equivalent model, which can be seen in Fig. 2(a), consists of a series resistor and capacitor, with the equivalent series resistance (ESR) included to reflect energy loss and charging or discharging efficiency.

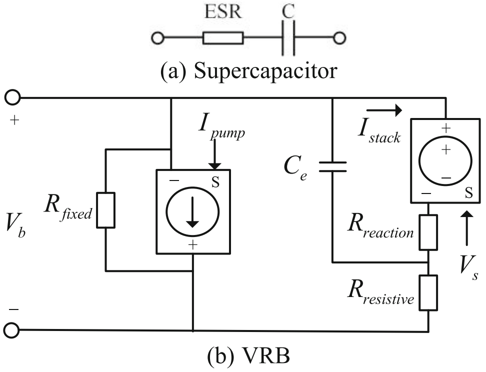

Fig. 2. Hybrid energy storage equivalence model.

Considering the complexity and accuracy of the model, the VRB equivalent loss model is used so that the electrical characteristics of the VRB can be better represented. The VRB equivalent loss model is shown in Fig. 2(b), where the battery stack electric potential V_s is equated to a controlled voltage source influenced by the dynamic variable S_{soc}. The power loss of the VRB is divided into two parts: external loss and internal loss. The internal losses include the loss of resistance $R_{reaction}$ caused by the reaction kinetics and the loss of resistance $R_{resistive}$ caused by mass migration, membranes, solutions, electrodes and bipolar plates, while the external losses include the loss of fixed resistance R_{fixed} and the pumping losses which are equated by a controlled current source and controlled by the pumping current I_{pump}.

2.3 Modeling of Microturbine

In this paper, only the power generation state of the MT is considered, so the gas turbine model with a single shaft and single cycle heavy load proposed by Rowen is used, as shown in Fig. 3, where the exhaust port temperature function f_1, the turbine torque output function f_2, and the transfer functions f_3 of the valve positioner and fuel brake in the fuel system are,

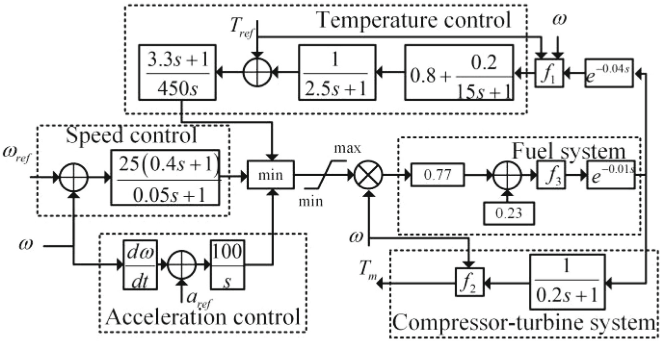

Fig. 3. Microturbine dynamic simulation model.

$$f_1 = T_{ref} - 700\left(1 - \omega_{f_1}\right) + 500(1 - \omega) \tag{6}$$

$$f_2 = 1.3\left(\omega_{f_2} - 0.23\right) + 0.5(1 - \omega) \tag{7}$$

$$f_3 = \frac{1}{(0.05s + 1)(0.4s + 1)} \tag{8}$$

where T_{ref} is the temperature reference, ω_{f_1} and ω_{f_2} are the fuel flow signals, and ω is the actual turbine speed.

From Fig. 3, it can be seen that the simulation model of the MT includes speed and acceleration control system, fuel system, compressor-turbine system, and temperature control system.

2.4 Modeling of Pumping Unit Load

The equivalent model of pumping unit load (PUL) is illustrated in Fig. 4, which is structured as an induction motor driving the pumping unit, where the motor output speed ω_m drives the pumping unit and the pumping unit output load torque T_m is fed back to the motor.

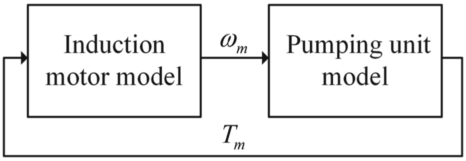

Fig. 4. Equivalent model of pumping unit load.

In the upstroke, the pumping unit lifts the pumping rod and oil column, and the motor runs under a heavy load; in the downstroke, the pumping rod and oil column can move downwards under their gravity, and the pumping unit is lightly loaded or even becomes inverted for power generation. To make the load even, the pumping unit is usually equipped with a balancing block, so the sum of the balancing block and the power of the pumping unit's suspension point is used as the output power of the motor. The PUL model is based on the actual parameters of the pumping unit operation so that the cyclical alternating load characteristics of the pumping unit operation can be simulated.

3 Distributed Power Generation Control Strategies

3.1 PV

The PV modules need to be connected to the grid via converters. For different system states and control objectives, different control strategies need to be implemented for the converter to ensure normal operation under system steady state conditions and LVRT under fault conditions. The control strategies for the front and rear stages of the two-stage PV system are given below for normal and fault conditions.

Normal Condition. In the normal condition of the system, the PV front stage achieves MPPT control and the backstage inverter adopts a constant power control method based on instantaneous power theory, ensuring the efficiency and stability of the PV system.

The control strategy of the pre-stage boost circuit is shown in Fig. 5. To begin with, the PV array port voltage u_{pv} and output current i_{pv} are sampled and used in the MPPT algorithm to calculate the port voltage u_{pv_ref} corresponding to the maximum power output of the PV array. After comparing it with the actual value u_{pv} and performing PI adjustment, the boost switch duty cycle reference value is obtained, which is then used to control the power tube switching in the boost circuit.

Figure 6 gives the control block diagram of the rear DC/AC inverter circuit. U_{dc}, u_{dc_ref} are the actual and reference values of the DC-link voltage respectively, i_d^* is

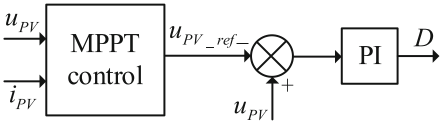

Fig. 5. Block diagram of the Boost circuit control strategy in normal condition.

given by the voltage external loop PI controller and $i_q{}^*$ is given by the reactive power required by the system. i_d, i_q is the dq component of the grid-connected current, ω is the grid fundamental frequency and L is the filter inductor.

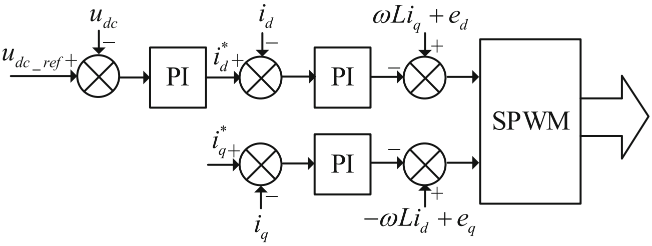

Fig. 6. Block diagram of the PV inverter control strategy in normal condition.

Fault Condition. According to the requirements of the Technical Provisions for grid-connected PV Plants, the grid-connected operation of PV inverters needs to realize LVRT in the event of a system fault, satisfying the following conditions: (1) during a voltage sag, the PV inverter should be able to operate uninterruptedly on the grid while ensuring its safety. (2) the PV inverter should be able to provide reactive power support to the grid during LVRT [14].

Under normal conditions, the DC-link voltage is stable and the PV array output power P_{pv} is equal to the PV input grid power P_{out} if losses are not taken into account, while the output limitation on the AC-side current amplitude during a voltage sag will lead to a reduction in P_{out}, which in turn generates an unbalanced power as shown in Eq. (9),

$$\Delta P = P_c = P_{pv} - P_{out} = \frac{1}{2}\frac{C\left(u_{dc}'^2 - u_{dc}^2\right)}{\Delta t} \tag{9}$$

where P_c is the absorbed power of the DC bus capacitor, u_{dc}, $u_{dc}{}'$ are the DC-link voltage values before and after the voltage sag, and Δt is the duration of the voltage sag.

If the boost circuit still carries out MPPT control at this point, P_{pv} remains stable at the maximum power point (MPP), at which point the energy of the bus capacitors will instantly pile up and the bus voltage continues to rise, resulting in a continuous increase in the active current reference value in Fig. 6, i.e. the output current of the inverter keeps increasing. Given that voltage sags at the PV grid-side can lead to safety hazards such as over-current in the inverter and over-voltage in the DC bus, measures need to be taken to avoid the inverter going off-grid due to self-protection. Therefore, after a voltage sag fault occurs at PCC, this paper adopts a control strategy of constant power control of the front stage boost circuit and priority control of reactive power compensation of the rear stage inverter.

Given that voltage sag faults in power systems are mostly asymmetric faults, the control strategy adopted in this paper focuses on the LVRT control strategy under asymmetric faults in two-stage PV systems. Since positive, negative and zero sequence components are generated for voltage and current during asymmetric faults, while for the three-phase three-wire system without neutral, zero sequence components can be disregarded, second-order generalized integrator (SOGI) is used to separate positive and negative sequence for network-side voltage and current.

In this paper, the inverter side adopts the negative sequence current suppression method, thus suppressing the negative sequence current component of the inverter side output and reducing the unbalance of the PCC side output current. In addition, the inverter needs to deliver a certain amount of reactive power to the grid during the LVRT to support voltage recovery, the specific value of which is [15]

$$i_{qref} = \begin{cases} 0, & U_{pcc} \geq 0.9 \\ 2\left(U_{pcc} - 1\right)I_N & 0.5 < U_{pcc} < 0.9 \\ 1.1I_N & U_{pcc} \leq 0.5 \end{cases} \tag{10}$$

where I_N is the rated output current amplitude of the inverter and U_{pcc} is the parallel network voltage, in pu.

For the inverter reference active power P_{0ref}, it is generally determined by the DC-link voltage control outer loop as shown in the following equation,

$$P_{0ref} = u_{dc\_ref}\left[\left(K_p + \frac{K_i}{s}\right)\left(u_{dc} - u_{dc\_ref}\right)\right] \tag{11}$$

where K_p is the proportional coefficient of the voltage outer loop PI controller and K_i is the integral coefficient of the voltage outer loop PI controller.

It can be known that P_{0ref} obtained from (11) is not only related to the fluctuation value of the DC-link voltage, but also affected by the control parameters. However, the maximum output active DC component of the inverter is constrained by the output current limiting constraints after the grid-side voltage sags, which should be unique and certain. Therefore, in this paper, the active power of the inverter-side control is calculated from the perspective of positive and negative sequence components, and this reference active power value is also the outer loop reference value of the PV front-stage converter, thus linking the front and rear stage control to improve the conversion efficiency of the control strategy.

The expression for the active power P of the inverter is

$$P = \frac{3}{2}\left(u_{gd}i_d + u_{gq}i_q\right) \tag{12}$$

The expressions for the positive and negative sequence voltages and currents when considering asymmetric faults at the PCC side are

$$\begin{cases} u_{gd} = u_{dP} + u_{dN} \\ i_d = i_{dP} + i_{dN} \\ u_{gq} = u_{qP} + u_{qN} \\ i_q = i_{qP} + i_{qN} \end{cases} \tag{13}$$

Combining (12) with (13), and neglecting the diphthong component, the formula for the active power reference command can be obtained as

$$P_{ref} = \frac{3}{2}\left(u_{dP} i_{dPref} + u_{dN} i_{dNref}\right) \tag{14}$$

where u_{dP} and u_{dN} are the positive and negative sequence d-axis components of the PCC voltage respectively, i_{dPref} and i_{dNref} are the positive and negative sequence references of the d-axis currents respectively. i_{dPref} can be uniquely determined from the reactive current i_{qPref} obtained from Eq. (10),

$$i_{dPref} = \sqrt{(1.1 i_N)^2 - i_{qPref}^2} \tag{15}$$

As the inverter side takes the negative sequence current suppression method, i_{dNref}, i_{qNref} are set to 0. In addition, the DC voltage outer loop controls the DC-link voltage to be constant, making the PV the rear inverter input power equal to the front boost circuit output power, from which it can be known that the DC voltage outer loop determines the active power command i_{dPref}. The current i_q related to reactive power is obtained from Eq. (10), thus reactive power compensation can be carried out. This method allows the response power issued to be specified during LVRT and correlates the front and rear stage control to improve the speed of low ride-through response after a voltage sag. The control strategies for the front and rear circuits of the PV generation system during the LVRT are given in Figs. 7 and 8 respectively.

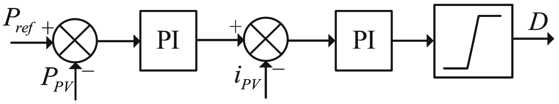

Fig. 7. Block diagram of Boost circuit control strategy during LVRT.

3.2 Hybrid Energy Storage

The hybrid energy storage (HES) front stage buck/boost circuit adopts constant power charging and discharging control of the battery, while the rear stage DC/AC inverter circuit adopts constant power control based on instantaneous power theory, the same control strategy as the PV inverter under normal conditions.

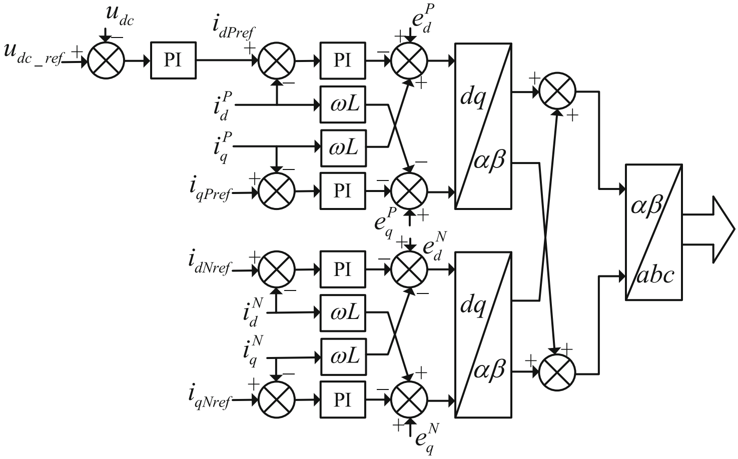

Fig. 8. Block diagram of PV inverter control strategy during LVRT.

3.3 Microturbine

The MT drives the high-speed generator directly and is grid-connected via an AC/DC rectifier and a DC/AC inverter circuit, thereby converting high-frequency AC power to work-frequency AC power. The AC/DC circuit adopts an id = 0 based vector control strategy. As the system in this paper is not connected to the grid and operates independently, a distributed power supply is required to maintain voltage and frequency stability in the microgrid. The microgrid in this paper adopts master-slave control to ensure stable operation of the microgrid in islanded operation mode. In the distributed power supply, the power-adjustable MT is generally used as the main micro-source, i.e. the MT inverter takes V-f control and the other DERs take constant power control.

4 Simulation Results

4.1 Simulation Parameters

In the islanded microgrid system established in this paper, the rated frequency of the system is 50 Hz, and the rated voltage is 0.4/6 kV. The rated power of each micro-source of MT, PV, and HES is 355 kW, 253 kW, and 730 kW respectively. In addition, in HES, SC is rated at 480 kW and operates in discharge mode, while VRB is rated at 250 kW and operates in charge mode. The rated power of the pumping unit load is 45 kW, and the other loads of the system are established by the constant power model, and the rated power is 660 kW.

4.2 Simulation Results

Based on the DERs and load equivalent models and control strategies proposed in this paper, the islanded microgrid system is established in PSCAD/EMTDC. Figures 9 and

10 show the simulation results of the islanded microgrid system under normal and fault conditions, respectively.

From Fig. 9(a) and (b), it can be seen that the RMS voltage on the low-voltage side of the system is maintained at 0.4 kV, and the system frequency is maintained at about 50 Hz, which verifies the feasibility of the V-f strategy adopted by the MT inverter. Figure 9(c)–(e) shows the output power of micro-sources such as PV, HES, and MT respectively. Considering a certain loss, the active power and reactive power output by the PCC side of PV are about 243 kW and 0, respectively. The output active power and reactive power of the PCC side of HES are about 220 kW, 0 respectively. The simulation results show that the PV system operates at MPP, and the HESS realizes constant power charge and discharge control. The active power generated by MT fluctuates with the fluctuation of the load value in the microgrid, and the reactive power value basically remains unchanged. As shown in Fig. 9(f), the PUL absorbs active power during the upstroke, and sends active power back to the system during the downstroke, resulting in the phenomenon of reverse power transmission. Moreover, the fluctuation time and amplitude of the curves for the active power absorbed by the PUL and the active power sent out by the MT are basically consistent.

Assuming that during the operation of the microgrid system for 1 s, a single-phase short circuit fault occurs on the PCC of the PV system, and the fault is cleared after 0.5 s. As shown in Fig. 10(a) and (b), the system voltage drops at 1 s, and after the fault is removed at 1.5 s, the RMS voltage rises briefly, and then returns to a stable operating state after 2 s. Figure 10(c) and (d) show the simulation results of the PV system. During the voltage sag, the PV system switches control strategies to give priority to generating reactive power and try to generate active power on the basis of capacity constraints. At the same time, the DC-link voltage of the PV system is still basically maintained at about 1 kV.

In short, under the control strategies proposed in this paper, the islanded microgrid system can operate stably and maintain power supply balance under the normal condition. In the fault condition, the islanded microgrid system can restore stability after a short time after the fault is removed. And during the voltage sag, the PV system can realize LVRT.

5 Conclusions

This paper presents the control strategies for islanded microgrid systems under normal and fault states respectively. A simulation model of the islanded microgrid with DERs and equivalent loads is built based on PSCAD/EMTDC to verify the effectiveness of the proposed control strategies. The simulation results show that the voltage and frequency of the islanded microgrid system are kept constant under normal conditions due to the V-f control strategy of the main micro-source MT. The other micro-sources adopt constant power control to maintain the balance of power supply in the system. Unlike the normal state, the front stage of the two-stage PV system in the fault condition adopts constant power control to avoid over-voltage of the DC-link voltage due to power imbalance after a voltage sag, and the rear stage adopts reactive power priority compensation control based on the negative sequence current suppression method so that the PV system can

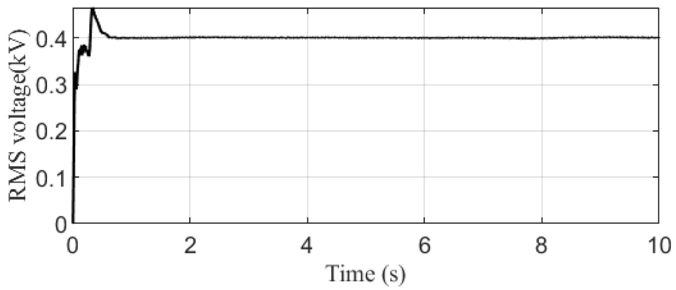

(a) RMS voltage

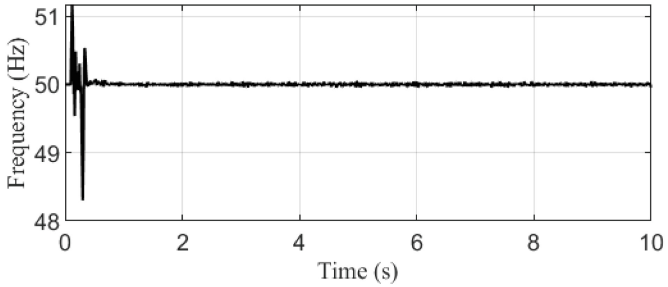

(b) Frequency

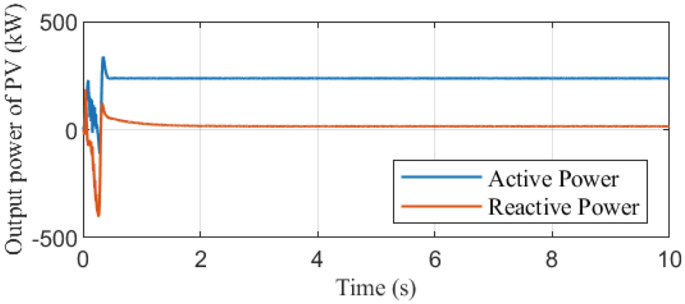

(c) Output power of PV

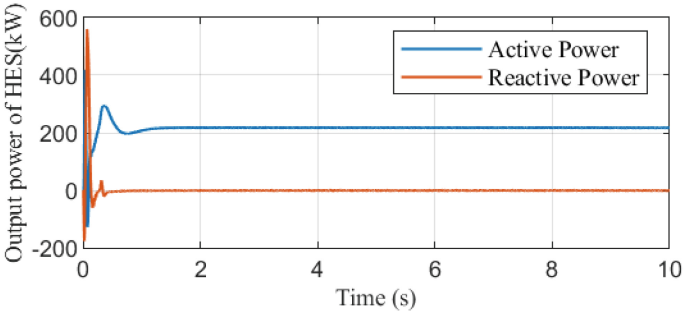

(d) Output power of HES

Fig. 9. Normal condition.

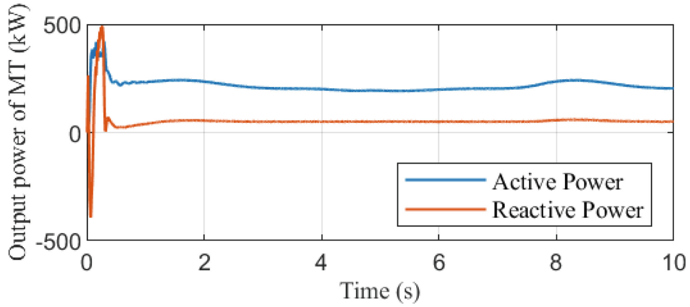

(e) Output power of MT

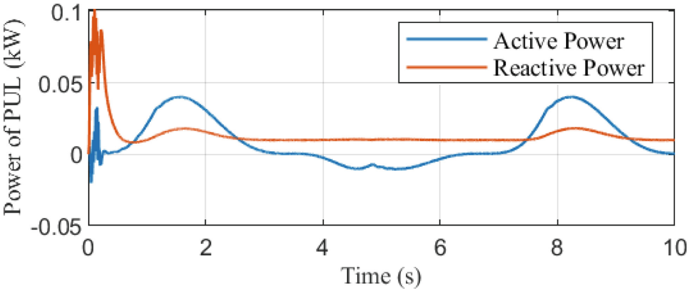

(f) Power of pumping unit load

Fig. 9. (*continued*)

emit specified reactive power to support the system voltage recovery. It can therefore be concluded that the control strategies proposed in this paper achieves the following objectives: the voltage and frequency of the entire system remain stable and the power supply and demand are balanced under normal conditions, and the PV has the capability of LVRT under fault conditions, avoiding off-grid accidents.

In addition, the islanded microgrid strategies proposed in this paper has the following characteristics:

1. When an asymmetrical fault occurs on the grid side of the PV system, the inverter output active power value is calculated based on the output capability of the inverter, which is also passed to the PV front stage DC/DC converter at the same time to realize the sharing of active commands between the front stage and the rear stage controls. This strategy determines the PV output power during the PV LVRT period, which reduces the difficulty of the adjustment of the simulation parameters and improves the efficiency of the switching of the control strategy to a certain extent.
2. The equivalent load in the simulation model of the islanded microgrid system established in this paper is not kept constant power, and the overall load power value within the system will change with the change of the pumping load up and down strokes, which can further verify the effectiveness of the DG constant power control strategies within the system from the side.

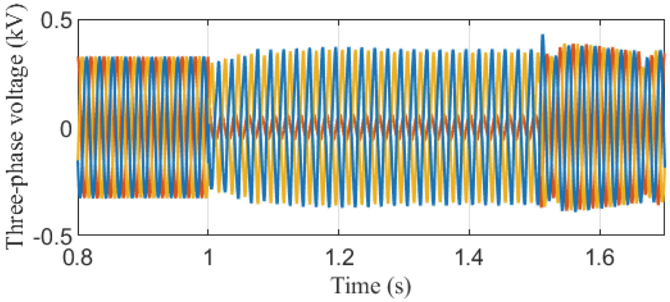

(a) Three-phase voltage

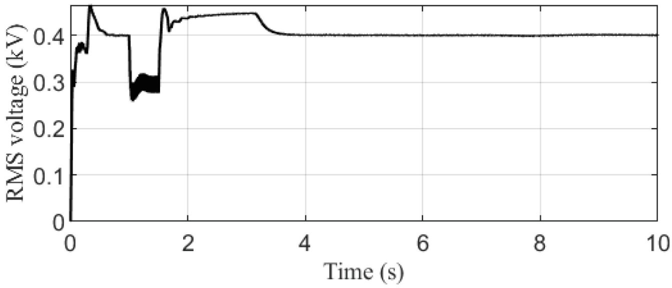

(b) RMS voltage

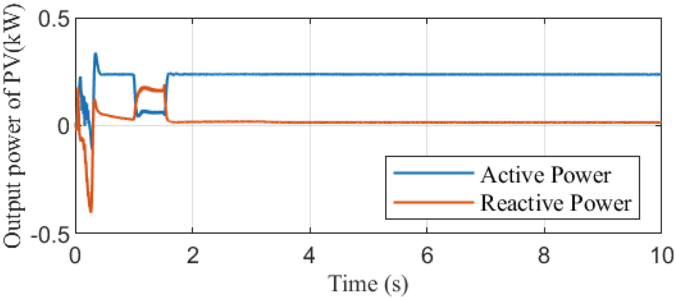

(c) Output power of PV

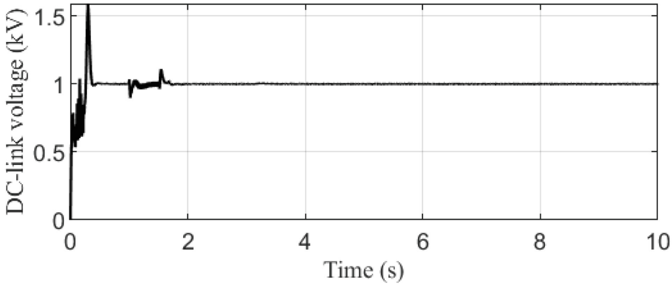

(d) DC-link voltage

Fig. 10. Fault condition.

Acknowledgement. This work was supported by Science and Technology Program of State Grid Corporation of China under Grant 5108-202218280A-2-75-XG.

References

1. Saeed, M.H., Fangzong, W., Kalwar, B.A., Iqbal, S.: A review on microgrids' challenges and perspectives. IEEE Acc. **9**, 166502–166517 (2021)
2. Lopes, J.A.P., Moreira, C.L., Madureira, A.G.: Defining control strategies for microGrids islanded operation. IEEE Trans. Power Syst. **21**(2), 916–924 (2006)
3. Gao, F., Iravani, M.R.: A control strategy for a distributed generation unit in grid-connected and autonomous modes of operation. IEEE Trans. Power Delivery **23**(2), 850–859 (2008)
4. Adhikari, S., Li, F.: Coordinated V-f and P-Q control of solar photovoltaic generators with MPPT and battery storage in microgrids. IEEE Trans. Smart Grid **5**(3), 1270–1281 (2014)
5. Joshi, J., Swami, A.K., Jately, V., Azzopardi, B.: A comprehensive review of control strategies to overcome challenges during LVRT in PV systems. IEEE Acc. **9**, 121804–121834 (2021)
6. Geng, Y., Yang, K., Lai, Z., Zheng, P., Liu, H., Deng, R.: A novel low voltage ride through control method for current source grid-connected photovoltaic inverters. IEEE Acc. **7**, 51735–51748 (2019)
7. Ding, G., et al.: Adaptive DC-link voltage control of two-stage photovoltaic inverter during low voltage ride-through operation. IEEE Trans. Power Electron. **31**(6), 4182–4194 (2016)
8. Mojallal, A., Lotfifard, S.: Enhancement of grid connected PV arrays fault ride through and post fault recovery performance. IEEE Trans. Smart Grid **10**(1), 546–555 (2019)
9. Afshari, E., et al.: Control strategy for three-phase grid-connected PV inverters enabling current limitation under unbalanced faults. IEEE Trans. Ind. Electron. **64**(11), 8908–8918 (2017)
10. Tang, C.-Y., Chen, Y.-T., Chen, Y.-M.: PV power system with multi-mode operation and low-voltage ride-through capability. IEEE Trans. Ind. Electron. **62**(12), 7524–7533 (2015)
11. Talha, M., Raihan, S.R.S., Rahim, N.A., Akhtar, M.N., Butt, O.M., Hussain, M.M.: Multi-functional PV inverter with low voltage ride-through and constant power output. IEEE Acc. **10**, 29567–29588 (2022)
12. Lin, F.-J., Lu, K.-C., Ke, T.-H., Yang, B.-H., Chang, Y.-R.: Reactive power control of three-phase grid-connected PV system during grid faults using Takagi–Sugeno–Kang probabilistic fuzzy neural network control. IEEE Trans. Ind. Electron. **62**(9), 5516–5528 (2015)
13. Camacho, A., Castilla, M., Miret, J., Borrell, A., de Vicuña, L.G.: Active and reactive power strategies with peak current limitation for distributed generation inverters during unbalanced grid faults. IEEE Trans. Ind. Electron. **62**(3), 1515–1525 (2015)
14. Jaalam, N., Rahim, N.A., Bakar, A.H.A., Eid, B.M.: 'Strategy to enhance the low-voltage ride-through in photovoltaic system during multi-mode transition. Sol. Energy **153**, 744–754 (2017)
15. Yang, Y., Enjeti, P., Blaabjerg, F., Wang, H.: Suggested grid code modifications to ensure wide-scale adoption of photovoltaic energy in distributed power generation systems. IEEE Ind. Appl. Soc. Annu. Meeting, Lake Buena Vista, FL, USA, 1–8 (2013)

An Ultra-Short-Term PV Power Prediction Method Based on Meteorological Factors with Weather Fluctuation Level and Historical Power Datasets

Enyu Wang(✉), Chao Lu, Peng Hou, Yiwen Wu, Yang Shen, and Guodong He

Baima Lake Laboratory, Hangzhou 310030, Zhejiang Province, China
`15650759432@163.com`

Abstract. Photovoltaic (PV) power generation has attracted widespread attention due to its environmental friendliness and cost-effectiveness. However, the intermittency and unpredictability of PV power production pose challenges to the reliable operation of the electric power system (EPS), especially in complex weather conditions where the output power of PV becomes even more difficult to predict. Therefore, the development of an accurate ultra-short-term PV power forecasting system is crucial in assisting power system operators in maintaining grid stability and enabling effective energy trading among market participants. This study proposes a novel ultra-short-term power forecasting model that combines the GRU neural network and K-means clustering method. The model integrates the time-series data of various meteorological parameters over a certain period, considering the periodicity and continuity of weather changes. Additionally, it incorporates power time series data to extract information about the operational characteristics of the PV plant. Furthermore, the model defines several variables that measure the level of weather fluctuations, enabling effective classification of weather types on a short-time scale and providing references for the forecasting process. The experimental results demonstrate that the proposed method can improve the accuracy of ultra-short-term photovoltaic power prediction, and its advantages are more prominent in complex weather conditions.

Keywords: Ultra-short-term photovoltaic power prediction · Feature extraction · Weather fluctuation level · K-means method · Gated Recurrent Unit

1 Introduction

The continuously increasing global energy demand is still mostly met by using fossil fuel-based energy sources which incurs various environmental problems. To leverage cleaner and lower carbon sources, a great deal of scholars devotes to the research of renewable energy utilization [1, 2]. Photovoltaic (PV) power generation technology has the advantages of being environmentally friendly and cost-effective, which draws worldwide attention [3]. However, the intermittence and randomness of PV energy production endanger the electrical power system (EPS) operation. Therefore, it is crucial to develop

Y. Xue et al. (Eds.): PMF 2023, LNEE 1129, pp. 437–450, 2024.
https://doi.org/10.1007/978-981-99-9251-5_34

an accurate PV power prediction system that helps the power system operators in stabilizing the grid and facilitates the electricity market participants in trading the energy [4].

PV power prediction can be divided into ultra-short-term (intraday) prediction, short-term prediction, and medium to long-term prediction according to the time scale of prediction. In China, the PV power stations should submit ultra-short-term power prediction curves to power regulatory agencies on time, and the owners will be faced with fines if the accuracy of prediction results doesn't meet the power prediction regulations. In recent years, various ultra-short-term PV power prediction methods have been proposed in the literature. Historically-proposed methods can be generally divided into four categories according to the source of data: historical power data, numerical weather prediction (NWP) data, cloud observation data, and multiple combinations of data. The statistical models based on historical power data use mathematical or statistical models to extract periodic patterns from time series [5, 6]. The statistical models generally consist of linear prediction models [7], autoregressive moving average (ARMA) [8], autoregressive integrated moving average(ARIMA) [9], Markov chain [10], and grey system theory [11]. These prediction models perform better under less fluctuating weather conditions [12], ignoring the impact of meteorological factors on the output of PV power stations. For complex and mutant weather, prediction methods should also take meteorological data into account [13, 14]. The characteristic variables in the NWP data, including irradiation intensity, temperature, and atmospheric pressure, provide critical data support for ultra-short-term PV power prediction [15]. The cloud distribution also affects the irradiation intensity, so the ultra-short-term prediction approach using historical sky images to obtain the cloud distribution in future sky images is proposed in [16]. The accuracy of the prediction models, using only NWP data or cloud observation data regardless of historical power data, can be greatly influenced by inaccurate weather or cloud distribution forecast information [17]. Combining K-means, optimal similar day approach, and long short-term memory (LSTM) network, another hybrid prediction model is proposed in [18], which takes the historical power data and meteorological factors into account.

Apart from the diversity of the source data, the feature extraction technique is also vital to improve prediction accuracy. In [19], a hybrid PV power prediction method combined with path analysis (PA) and phase space reconstruction(PSR) is proposed. PA is employed to identify dominant meteorological factors affecting the PV power fluctuation characteristics, which can adjust the weights of meteorological factors. Then, feature vectors are constructed using the dominant factors, which are used for grouping similar days' datasets according to meteorological conditions. Ref. [17] proposes a hybrid innovative model using an improved K-means approach to cluster the historical power data sets and combines the grey relational analysis (GRA) method to determine the optimal similarity day of the forecasting day. The proposed model adopts meteorological factors and historical power datasets within two years. The existing literature mainly focuses on improving decomposition methods, reconstruction methods, and optimal similarity day methods. The above works also show that the reasonable classification of weather types contributes to the prediction accuracy improvement. However, these methods select days with similar meteorological characteristics to the forecasting day as the input while the weather fluctuation is not taken into account.

This paper proposes a new method that combines meteorological factors with historical power datasets in the feature extraction step and applies it to ultra-short-term PV power prediction. The weather fluctuation level, which includes global irradiance fluctuation, direct irradiance fluctuation, and scattered irradiance fluctuation, is defined to cluster datasets into 4 categories. The classification results are also considered as one of the dominant meteorological factors. The main contributions of this work can be summarized as follows:

a. We propose a new method for ultra-short-term PV power prediction by combing meteorological factors with historical power datasets, which shows higher prediction accuracy than merely relying on meteorological factors or historical power datasets.
b. We propose a novel method to define weather fluctuation level, which calculates the degree of fluctuation based on the natural variations of irradiance.

The paper is organized as follows. Section 2 introduces the methods of the proposed forecasting method. In Sect. 3, the framework of the proposed improved prediction method is presented in detail. In Sect. 4, the experiments and result analysis are presented. Section 5 concludes the paper and introduces our future work.

2 The Methods of PV Power Prediction

2.1 K-means Clustering Method

The K-means clustering method is categorized as a partitioned clustering method [20], partitioning given datasets into clusters and finding the minimum squared error between the various data points in the datasets and the center of each cluster. Then each data point is assigned to the cluster center nearest to it. Mathematically, given a dataset $X = \{x_i\}$, $i = 1, 2,\ldots,n$, X is partitioned into k number of clusters $C = \{c_j\}, j = 1, 2,\ldots,k$. Then, the center of each cluster is re-evaluated. The K-means method process is iteratively performed until the cluster membership is stable. The K-means clustering method aims to minimize the sum of the square error of each cluster, which is demonstrated as follows:

$$\text{Minimize}\, J(C) = \sum_{k=1}^{K} \sum_{x_i \in c_k} \|x_i - \mu_k\|^2 \tag{1}$$

The K-means clustering method process is illustrated in Fig. 1.

2.2 Recurrent Unit

Gated Recurrent Unit(GRU) is a variant of Long Short-term Memory(LSTM) neural network. LSTM is an improved recurrent neural network(RNN) that replaces the hidden layer units of RNN with LSTM cell unit structures, effectively solving the long-term dependence problem existing in RNN. LSTM consists of an input gate, a forgotten gate, and an output gate. GRU merges the input gate and the forgotten gate into one update gate, the output gate is changed to a reset gate, and the training parameters are reduced. GRU has the same prediction accuracy as LSTM, and has the advantages of simpler

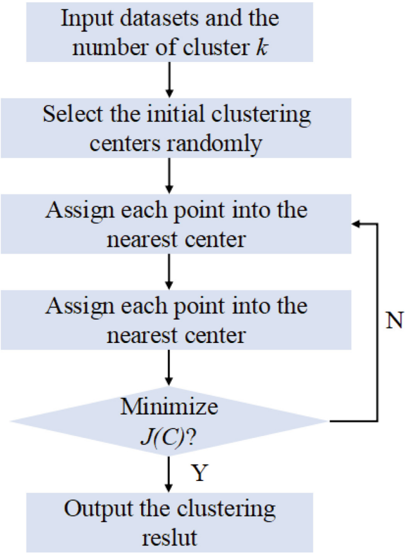

Fig. 1. The K-means clustering method process

structure and faster network training. The network structure diagrams of LSTM and GRU are shown in Fig. 2 for comparison.

It can be seen from Fig. 2(b) that the GRU contains three key parts: the reset gate, the update gate, and the candidate hidden state. The reset gate, rt, can be considered as a controller that determines the retention of historical information based on the input, xt, and the hidden sate of the previous moment ht-1. The update gate, Zt, determines how much new information should be added at the current moment.

2.3 Spearman's Rank Correlation Coefficient

Spearman's rank correlation coefficient is primarily used to measure the correlation between the changing trends of variables. It does not directly operate on the values of variables in each dimension but rather calculates the correlation based on the rankings of the values in each dimension. The formula for calculating Spearman's rank correlation coefficient is:

$$\rho = 1 - \frac{6\sum(x_i - y_i)^2}{n^3 - n} \tag{2}$$

where x_i represents the rank of the *ith* data group of variable X among all X values, and y_i represents the rank of the *ith* data group of variable Y among all Y values.

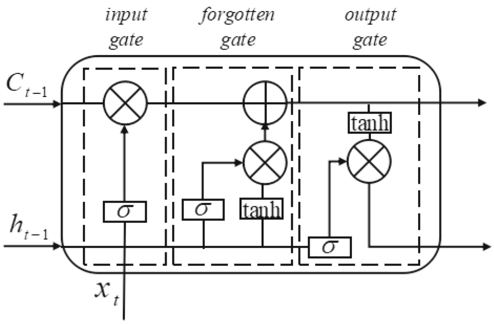

(a) network structure of LSTM

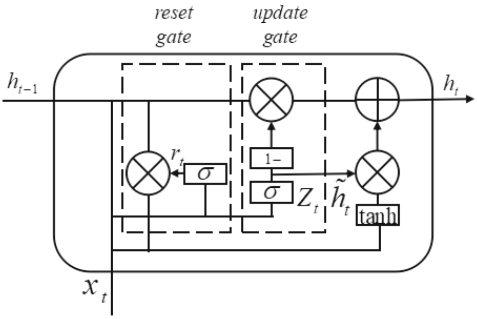

(b) network structure of GRU

Fig. 2. Network structure diagrams of LSTM and GRU

3 Improved Prediction Method Based on GRU and K-means

3.1 Feature Selection

Due to the complexity of the inherent properties of the PV power stations, it is difficult to fully consider all the performance parameters in practice. Thus, selecting suitable features for model training is critical for improving prediction accuracy. Obviously, historical power data is one of the primary factors influencing PV plant generation as it encapsulates the inherent characteristics of the photovoltaic system. Similarly, meteorological data contains information about recent weather trends and periodic weather patterns in the local area. Therefore, feature selection should include both meteorological and power time-series data.

Furthermore, meteorological data contains information on weather types. Under different weather types, future weather development trends can vary. To clarify, a simple example is shown in Fig. 3.

The horizontal axis of Fig. 3 represents time, with a range of one day, and the vertical axis represents the actual power output of a photovoltaic power plant. Figure 3 shows that the PV power curve reaches the highest value around noon under relatively stable weather conditions as shown with blue, green, and red lines. However, under

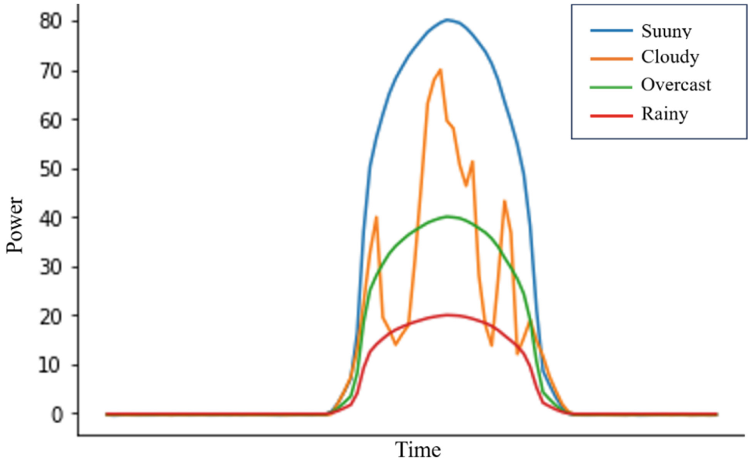

Fig. 3. Power curves of PV stations under several typical weather conditions

non-stationary weather conditions, the PV power curve fluctuates significantly as the orange line shows. These dramatic fluctuations incur the prediction bias and should be fully considered in the feature selection step.

3.2 Weather Fluctuation Level

In general, solar irradiance has the greatest impact on the power generation. Thus, we choose the features that has a higher Spearman's rank correlation coefficient with the power generation to define the weather fluctuation level (WFL) in this work. In other words, global irradiance, direct irradiance, and scattered irradiance are selected to define WFL. The WFL is defined and calculated as follows:

Step 1: Get the theoretical irradiance curve of the local horizontal plane sun without considering the coefficient, which is obtained as follows:

$$G = \sin\delta\ \sin\varphi + \cos\delta\ \cos\varphi\ \cos\omega \tag{3}$$

where, G is the theoretical solar irradiance on the horizontal plane without considering the coefficient in the local area, δ is the declination of the sun, φ is the local latitude and ω is the solar hour angle.

The declination of the sun δ is calculated as follows:

$$\delta = 23.45^\circ \sin\left(2\pi * \frac{284 + N}{365}\right) \tag{4}$$

where, N is the number of days that have passed this year.

The solar hour angle ω is calculated as follows:

$$\omega = \left(\frac{tt}{60} - 12\right) * 15^\circ \tag{5}$$

where, *tt* is the true solar time, which is the time converted by time zone time according to the local longitude.

Step 2: Fit a stable irradiance curve under current weather conditions. Under ideal conditions, the variation trend of the irradiance curve for stable weather should be equivalent to the theoretical curve obtained in **Step 1**. Firstly, translate the theoretical irradiance curve up and down to make its left zero point coincide with the time before the actual irradiance today, in order to eliminate the impact of obstacles, such as mountains on the irradiance at sunrise. Then, calculate the average value of the true irradiance at the four previous moments before time t. The average value is compared with the point on the theoretical curve at the corresponding moment t. A coefficient is obtained to make these two curves coincide.

Step 3: Calculate the weather fluctuation degree. Take the true irradiance values at the four previous moments (1 h) before time t and compare them with the corresponding points on the fitted curve in **Step 2**. Then calculate the absolute value of the difference and accumulate it to obtain the degree of weather fluctuation degree.

Step 4: Calculate the WFL. Global irradiance, direct irradiance, and scattered irradiance are individually incorporated into steps 2 and 3 for calculation, resulting in the weather fluctuation degrees corresponding to the three types of irradiance. By using K-means clustering method, the data at different time points are divided into four categories based on the three types of weather fluctuation degree. These categories are then labeled as 0, 1, 2, and 3, which is referred to as the weather fluctuation levels.

3.3 Evaluation Criteria

According to the "Implementation Rules for Grid-Connected Operation and Management of Power Plants in the Northwest Region," the accuracy of the harmonized average value at the second hour in the ultra-short-term forecast curve for wind power plants and PV power stations should be no less than 75%. The formula for calculating accuracy is as follows:

$$E = 1 - 2 \times \sum_{i=1}^{n} \left(\left| \frac{P_i^r}{P_i^r + P_i^n} - 0.5 \right| \times \frac{\left| P_i^r - P_i^n \right|}{\sum_{i=1}^{n} \left| P_i^r - P_i^n \right|} \right) \tag{6}$$

where:

E is the accuracy.

i represents the number of data points in the ultra-short-term prediction.

n is the prediction window length which is 96.

P_i^n is the predicted power value at the i-th point.

P_i^r is the actual power value at the i-th point.

If both P_i^n and P_i^r are within 3% of the installed capacity, the point is not included in the error calculation. And the higher the assessment score, the greater the penalty imposed on the power plant. If the 75% criterion is not met, each 1% reduction of accuracy will result in a penalty of 0.015 points per 10,000 kilowatts of the total installed capacity.

The indicator score is defined in the following.

$$E = 1 - 2 \times \sum_{i=1}^{n} \left(\left| \frac{P_i^r}{P_i^r + P_i^n} - 0.5 \right| \times \frac{\left| P_i^r - P_i^n \right|}{\sum_{i=1}^{n} \left| P_i^r - P_i^n \right|} \right) \quad (6)$$

3.4 The Framework of the Proposed Improved Prediction Method

The prediction method is illustrated in Fig. 4.

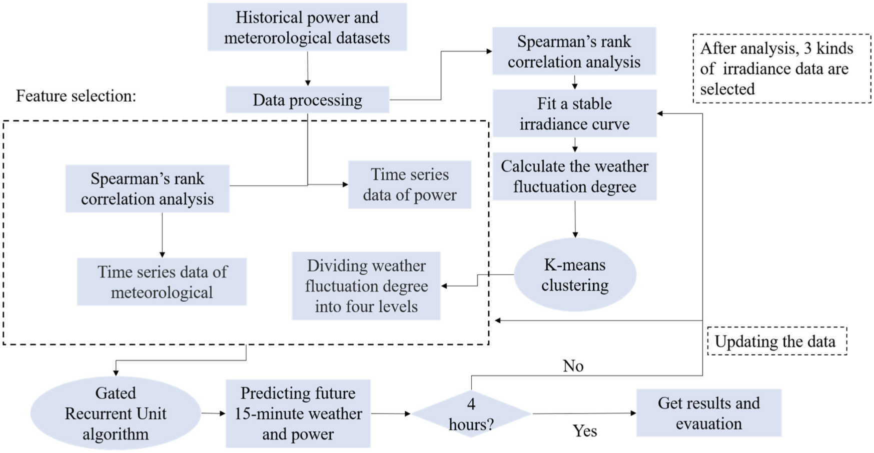

Fig. 4. Flowchart of the prediction method based on GRU and K-means

The implementation procedure of the proposed method is summarized as follows:

Step 1: Preprocess the historical data, which includes removing empty data and eliminating data points that exceed the physical threshold.

Step 2: Perform Spearman's rank correlation analysis, stable irradiance curve fitting, and weather fluctuation Level calculation using the methods described in the third part of the article.

Step 3: By conducting Spearman's rank correlation analysis, we have selected the time-series data of global irradiance, scattered irradiance, direct irradiance and power for the past 24 h.

Step 4: Use a GRU model to perform rolling predictions on the meteorological and power data for the next 15 min. If the prediction horizon does not reach the next 4 h, the current prediction results are returned to Step 2 and 3 as the historical values for the next prediction. If the prediction horizon reaches the next 4 h, the prediction is stopped, and the short-term power forecast for 96 points is obtained.

4 The Experiments and Result Analysis

4.1 Data Acquisition

This paper takes a PV power station in Gansu province as the research object, with a rated capacity of 100MW. The data for the entire year of 2022 is used as the training sample to conduct ultra-short-term forecasting for January and February 2023.

4.2 Spearman's Rank Correlation Analysis

According to the method mentioned in Sect. 2.3, we make a correlation analysis. The results are illustrated in Fig. 5.

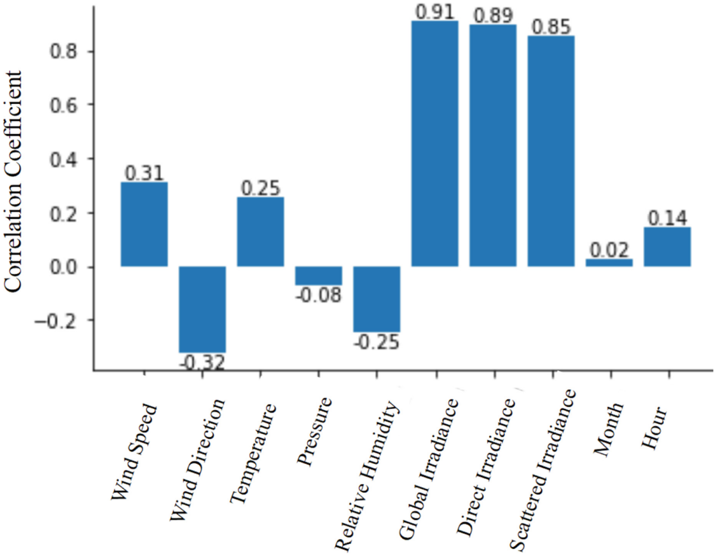

Fig. 5. Spearman's rank correlation coefficients between different meteorological variables and power

The horizontal axis of Fig. 5 represents the different features, and the vertical axis represents the Spearman's rank correlation coefficient. Figure 5 shows that total irradiance, direct irradiance, and scattered irradiance are highly correlated with PV output power which has Spearman's rank correlation coefficients of 0.85 or higher while other meteorological features show lower correlations. This demonstrates the validity of using irradiance to characterize the degree of weather fluctuation, as mentioned in Sect. 3.1.

4.3 WFL Analysis

As an example, we have selected the data from March 25–27, 2022, which is considered representative. The comparison curves of WFL data with the three types of irradiance are shown in Fig. 6.

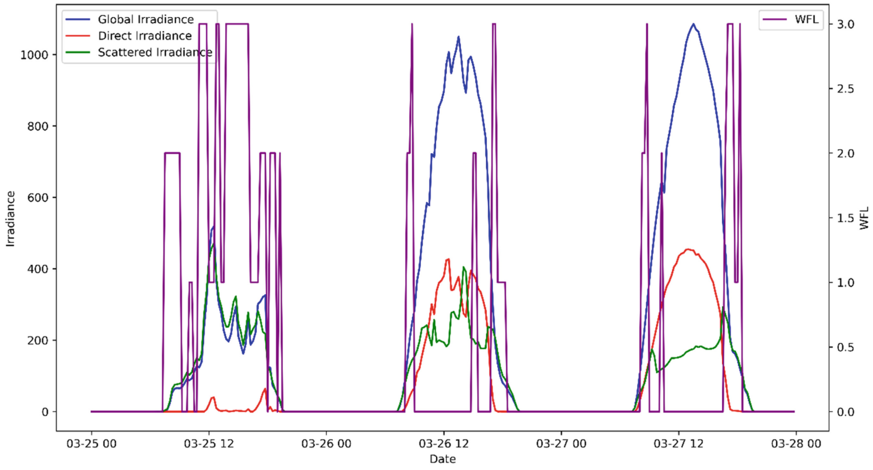

Fig. 6. WFL and irradiance curve

In Fig. 6, the horizontal axis displays the dates, while the left vertical axis represents the irradiance and the right vertical axis represents the WFL. It is evident that on March 25th, the global and scattered irradiance experienced significant fluctuations throughout the morning and afternoon, while the direct irradiance remained close to zero. This indicates a non-stationary rainy day. Despite this, the WFL values remained relatively high throughout the day, consistent with the weather condition. The direct and scattered irradiance on March 26th showed noticeable fluctuations but the global irradiance followed a relatively standard distribution pattern, excluding the morning and evening periods. Consequently, the WFL data remained low for much of the day. The same pattern is visible on March 27th, with the global and direct irradiance curves appearing smoother than on March 26th, suggesting mostly sunny weather, with occasional cloudy periods. The WFL data aligns with the corresponding weather pattern.

4.4 Comparative Analysis

To validate the accuracy of the model after incorporating power time series data and weather fluctuation clustering data, this study employs the following three methods for ultra-short-term forecasting:

Method 1: Power prediction using only historical meteorological data.

Method 2: Power prediction by integrating historical meteorological data with historical power data.

Method 3: Power prediction by integrating historical meteorological data, historical power data, and WFL data.

The simulation result of each method is illustrated in Fig. 7.

The horizontal axis of Fig. 7. Represents the dates, and the vertical axis represents the accuracy of the predictions. It can be seen that method 3 performs better than method 2 in the majority of the scenarios.

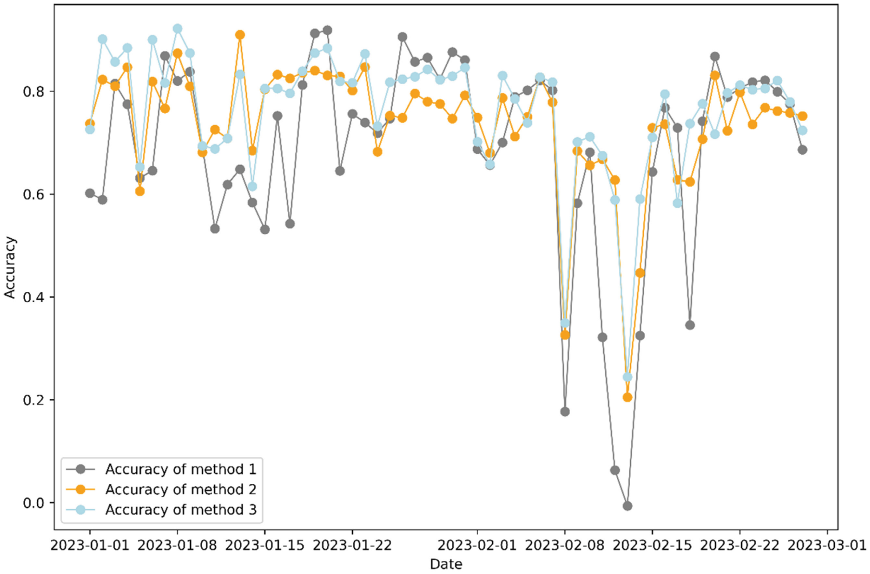

Fig. 7. Comparison of Accuracy for Three Ultra-Short-Term Forecasting Methods

Table 1. Average accuracy and total assessment scores for three methods (Jan. and Feb.)

Evaluation index	Accuracy	Score
Method 1	0.68	83.24
Method 2	0.73	37.94
Method 3	0.76	33.45

The daily accuracy and evaluation scores for the three methods are shown in Table 1. It can be observed that Method 1, which serves as the baseline, has an accuracy of 0.68 and a score of 83.24. Method 2, which incorporates power time series data, shows an accuracy of 0.73, an improvement of 5%, and a score of 37.94, a decrease of 45.3. Method 3, which further includes WFL data on top of Method 2, exhibits an accuracy of 0.76, a further improvement of 3%, with a score of 33.45, a decrease of 4.49.

Table 2. Average accuracy and total assessment scores for three methods (Jan.)

Evaluation index	Accuracy	Score
Method 1	0.74	24.51
Method 2	0.78	6.25
Method 3	0.81	6.14

Table 3. Average accuracy and total assessment scores for three methods (Feb.)

Evaluation index	Accuracy	Score
Method 1	0.62	58.73
Method 2	0.68	31.70
Method 3	0.71	27.31

Table 4. Different WFL time proportion in January and February

Month	0 (stable weather) (%)	1 (relatively stable weather) (%)	2 (relatively variable weather) (%)	3 (variable weather) (%)
1	87.03	1.21	7.26	4.50
2	82.37	0.20	7.48	8.14

To assess the suitability of the model from the perspective of weather fluctuations, the evaluation results are divided into January and February. Table 2 presents the evaluation results for January, while Table 3 presents the evaluation results for February. By applying the WFL method mentioned in Sect. 3.2 to analyze the weather fluctuations in January and February of 2023, the specific results are shown in Table 4. In January, the number of days with WFL index 0 (stable weather) accounts for 87.03%, while in February, it accounts for 82.37%. The number of days with WFL index 3 (variable weather) in January is 4.5%, while in February, it is 8.14%. Clearly, the weather in February is generally more variable compared to January.

Based on the assessment scores, in the relatively stable weather conditions of January, the difference in scores between Method 3, which considers WFL, and Method 2 is only 0.11, indicating a non-significant advantage. However, in the relatively variable weather conditions of February, Method 3 shows a larger advantage with a score 4.39 lower than Method 2.

5 Conclusions and Future Work

This study proposes a photovoltaic power ultra-short-term forecasting model that combines the GRU neural network and K-means clustering method. The model takes into account the periodicity and continuity of weather changes, and it incorporates power time-series data to extract information about the operational characteristics of the PV plant. Additionally, the model integrates clustered weather fluctuation data to effectively classify weather types on a short-time scale and provide references for the forecasting process.

Operational data from a photovoltaic power plant in Gansu Province were used to train the proposed model, and data from January and February 2023 were used for testing.

The model's performance was compared to two other models and found to outperform in terms of prediction accuracy, especially in variable weather conditions.

In future, we will further improve our work by utilizing Ensemble Empirical Mode Decomposition (EEMD) to improve the validity of the data, studying abrupt weather change characterization, identifying additional factors affecting PV plant power generation, and developing appropriate techniques to incorporate them into the feature selection process. Additionally, a weather recognition switch will be designed to adaptively select a prediction model based on the WFL index, and methods of neural network hyperparameter optimization will be explored to improve the efficiency and accuracy of the model.

References

1. Mishra, M., Dash, P.B., Nayak, J., et al.: Deep learning and wavelet transform integrated approach for short-term solar PV power prediction. Measurement **166**(4), 108250 (2020)
2. Ospina, J., Newaz, A., Faruque, M.O.: Forecasting of PV plant output using hybrid wavelet-based LSTM- DNN structure model. IET Renew. Power Gener. **13**(7), 1087–1095 (2019)
3. Tariq, L., Reda, Y., Khalid, B., et al.: Accurate one step and multistep forecasting of very short-term PV power using LSTM-TCN model. Renew. Energy **205**, 1010–1024 (2023)
4. Tawn, R., Browell, J.: A review of very short-term wind and solar power forecasting. Renew. Sustain. Energy Rev. **153** (2022)
5. Raza, M.Q., Nadarajah, M., Ekanayake, C.: On recent advances in PV output power forecast. Sol. Energy **136**, 125–144 (2016)
6. Yang, D., Elynn, W., Kleissl, J.: Operational solar forecasting for the real-time market. Int. J. Forecast. **35**(4), 499–519 (2019)
7. Li, G.Q., Li, X.T., Bian, J., et al.: Multidimensional time series simulation of large-scale photovoltaic power station output based on hourly clear sky index. Power Syst. Tech. **44**(9), 3254–3262 (2020)
8. Zhang, J.L., Liu, Z.Y., Chen, T.: Interval prediction of ultra-short-term photovoltaic power based on a hybrid model. Elect. Pow. Syst. Res. **216**, 109035 (2023)
9. Hakan, A.: A novel approach based on integration of convolutional neural networks and deep feature selection for short-term solar radiation forecasting. Appl. Energy **305**, 117912 (2022)
10. Jianf, F., Wand, Z.Y., Zhang, P.: Prediction of photovoltaic power generation based on gray-weighted Markov chain. Pow. Syst. Protect. Cont. **47**(15), 55–60 (2019)
11. Yang, X.Y., Wang, S.C., Peng, Y., Chen, J.W., et al.: Short-term photovoltaic power prediction with similar-day integrated by BP-AdaBoost based on the Grey-Markov model. Elect. Pow. Syst. Res. **215**, 108966 (2023)
12. Dong, C., Wanf, Z., Bai, J.Y., et al.: Review of ultra-short-term forecasting methods for photovoltaic power generation[J/OL]. High Volt. Eng. https://doi.org/10.13336/j.1003-6520.hve.20220974
13. Larson, D.P., Nonnenmacher, L., Coimbra, C.: Day-ahead forecasting of solar power output from photovoltaic plants in the American Southwest. Renew. Energy **91**, 11–20 (2016)
14. Guijo-Rubio, D., Duran-Rosal, A.M., Gutierrez, P.A., et al.: Evolutionary artificial neural networks for accurate solar radiation prediction. Energy 210 (2020)
15. Kumar, D.S., Yagli, G.M., Kashyap, M., et al.: Solar irradiance resource and forecasting: a comprehensive review. IET Renew. Power Gener. **14**(10), 1641–1656 (2020)
16. Wang, F., Zhen, Z., Liu, C., et al.: Image phase shift invariance based cloud motion displacement vector calculation method for ultra-short-term solar PV power forecasting. Energy Convers. Manage. **157**(1), 123–135 (2018)

17. Lin, P.J., Peng, Z.N., Lai, Y.F., et al.: Short-term power prediction for photovoltaic power plants using a hybrid improved Kmeans-GRA-Elman model based on multivariate meteorological factors and historical power datasets. Energy Convers. Manage. **177**, 704–717 (2018)
18. Bai, R.X., Shi, Y.T., Yue, M., et al.: Hybrid model based on K-means++ algorithm, optimal similar day approach, and long short-term memory neural network for short-term photovoltaic power prediction. Global Ene. Intercon. **6**(2), 184–196 (2023)
19. Zhu, J.B., Li, M.R., Luo, L., et al.: Short-term PV power forecast methodology based on multi-scale fluctuation characteristics extraction. Renew. Energy **208**, 141–151 (2023)
20. Abiodun, M.I., Absalom, E.E., Laith, A., et al.: K-means clustering algorithms: a comprehensive review, variants analysis, and advances in the era of big data. Inf. Sci. **622**, 178–210 (2023)

Calculation of Line Loss in Low Voltage Line with PV Based on Analytical Model

Peng-ju Yang[1], Tao-yun Wang[1], Xiang-hui Guo[2], Fang Yao[1], Chuipan Meng[1], and Zhiyan Zhang[2](✉)

[1] State Grid Shanghai Electric Power Company Jinshan Power Supply Company,
Shanghai 200540, China
[2] School of Electrical and Information Engineering, Zhengzhou University of Light Industry,
Zhengzhou 450002, China
`2004074@zzuli.edu.cn`

Abstract. The rapid development of distributed photovoltaic (PV) is conducive to energy conservation and emission reduction, but its large-scale access also have influence on the low-voltage distribution network line loss. In this paper, a calculation method of low voltage line loss is proposed based on the power flow calculation method of backward-forward substitution. The analytical model of line loss calculation under uniform power network is established, and the relationship between the PV output and the change of line loss is given. An example model of a 15-node low-voltage distribution network with PV is built, and the correctness of the proposed method is verified with the comparison of the analytical model and the simulation model. The influence of three-phase unbalance, PV access capacity and access position on system line loss is analyzed, which provides theoretical basis and decision support for distributed PV access, low-voltage distribution network loss reduction and energy saving.

Keywords: Distributed photovoltaic · Low voltage line · Line loss · Analytical model

1 Introduction

With the increasing global energy shortage and environmental problems, Daoyuan et al. (2021) and Yang and Zhao. (2018) states photovoltaic (PV) generation will become one of the main ways of power supply in the future for a long time, as PV generation is clean and efficient. Earlier studies (He et al. 2014) shows Large-scale of distributed PV grid-connection has great influence on the size and direction of power flow in distribution network, and indirectly affects network loss.

The existing researches on the influence of PV access on line loss mainly focus on the influence of power flow calculation method and three phase unbalance (Ali et al. 2021; Zongbao 2022). In the following studies, they analyzed the influence of PV on line loss by using the backward-forward substitution. Fei and Di (2022) achieved the purpose of reducing network loss by adjusting the reactive power output after PV access. Zhang

Y. Xue et al. (Eds.): PMF 2023, LNEE 1129, pp. 451–462, 2024.
https://doi.org/10.1007/978-981-99-9251-5_35

et al. (2019) provided the optimal access location and access capacity of PV system under typical load distribution. Xu et al. (2017) designed a power flow algorithm containing distributed PV power supply based on the reactive power correction of PV nodes. Subsequent literature analyzed the influence of three-phase unbalance on low pressure line loss. Meifang et al. (2019) built a calculation model of three-phase unbalance line loss based on correction coefficient. He et al. (2017) established a distributed PV multi-objective optimization configuration model, the three phase unbalance degree of PV system is reduced. Li (2020) used the method of balancing three-phase load to solve the problem of three-phase unbalance and loss reduction. Most of the above literatures are applicable to a single scene and are not universal.

Based on the above background, an analytical model based on the calculation method for low voltage line loss containing distributed PV is proposed in this paper. Firstly, the analytical model of line loss calculation for low-voltage lines with PV in typical scenes of homogeneous network is derived. Then, a 15-node low-voltage line simulation model based on MATLAB/SIMULINK is established. With the result comparison of the analytical model and the simulation model, the validity of the analytical model for uniform power network line loss is verified. Finally, the influences of three phase unbalance, PV output variation, PV access location and other factors on low voltage line loss are analyzed.

2 Theoretical Analysis of Line Loss

In order to derive the analytical model for line loss calculation, a low-voltage feeder system with n nodes and n-1 branches was established, as shown in Fig. 1. In Fig. 1, the PV module is connected to the system at node m, the front-end voltage is U_1 and the rated line voltage is U_N.

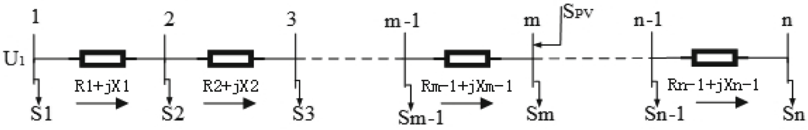

Fig. 1. n node feeder system

In Fig. 1, the load power of node i and the line impedance of the corresponding branch i are respectively written as:

$$\begin{aligned} S_i &= P_i + jQ_i \quad i \in [1, n] \\ Z_i &= R_i + jX_i \quad i \in [1, n-1] \end{aligned} \tag{1}$$

where S_i, P_i, Q_i are respectively the complex power, active power and reactive power of the i node; Z_i, R_i, X_i are respectively the impedance, resistance and reactance of branch i.

While PV power output is excluded, the power loss of all branches after branch i and the influence of voltage drop are ignored, then the single-phase power loss of branch i

is:

$$
\begin{aligned}
\Delta P_i &= \frac{(|S_{i+1}+S_{i+2}+\cdots+S_n|)^2}{U_{\mathrm{N}}^2}R_i \\
\Delta Q_i &= \frac{(|S_{i+1}+S_{i+2}+\cdots+S_n|)^2}{U_{\mathrm{N}}^2}X_i
\end{aligned}
\tag{2}
$$

where ΔP_i, ΔQ_i are active power loss and reactive power loss of branch i respectively; $|S_i|$ represents the modulus of the phasor S_i.

While PV power output is taken into account, the flow power of each branch needs to be superimposed by the load power and PV power output, and the direction of the power flow changes from unidirectional flow to bidirectional flow (Navid et al. 2018; Tong et al. 2019; Prasad et al. 2021). The magnitude and direction of the power on each branch will be determined according to the load power and PV power output. Considering the strong fluctuation of PV power output, the analytical model of line loss calculation under uniform power network are derived in this paper.

Assume that the impedance of all lines in the whole low-voltage feeder system is equal:

$$
\begin{aligned}
&Z_1 = Z_2 = \ldots = Z_i = \cdots = Z_n = Z \\
&Z = R + jX
\end{aligned}
\tag{3}
$$

where Z, R, X are respectively line impedance, resistance and reactance under uniform power network.

While PV is not connected, the line loss of branch i is:

$$
\begin{aligned}
\Delta P_i &= R\frac{\left(\left|\sum_{k=i+1}^{n} S_k\right|\right)^2}{U_{\mathrm{N}}^2} \\
\Delta Q_i &= X\frac{\left(\left|\sum_{k=i+1}^{n} S_k\right|\right)^2}{U_{\mathrm{N}}^2}
\end{aligned}
\tag{4}
$$

where ΔP_{i_1}, ΔQ_{i_1} are respectively the active power loss and reactive power loss of branch i without PV access under a uniform power network.

For the whole feeder system, the total line loss of the system is:

$$
\begin{aligned}
\Delta P &= \sum_{i=1}^{n}\frac{\left(\left|\sum_{k=i+1}^{n} S_{\mathrm{k}}\right|\right)^2}{U_{\mathrm{N}}^2}R \\
\Delta Q &= \sum_{i=1}^{n}\frac{\left(\left|\sum_{k=i+1}^{n} S_{\mathrm{k}}\right|\right)^2}{U_{\mathrm{N}}^2}X
\end{aligned}
\tag{5}
$$

where ΔP, ΔQ are respectively the total active power loss and reactive power loss of the system without PV access under a uniform power network.

Assume that PV is connected to node *m*, and PV power output power is:

$$S_{\mathrm{PV}} = P_{\mathrm{PV}} + jQ_{\mathrm{PV}} \tag{6}$$

where S_{PV} is the total PV power output; P_{PV} 、 Q_{PV} are respectively PV active power output and reactive power output.

At this time, the line loss of the branch *i* is related to the location of the branch and the PV access point. If the branch is behind the PV access point, the line loss of the branch remains unchanged. If the branch is located in front of the PV access point, the line loss of the branch should take into account the impact of PV access:

$$\begin{aligned}
\Delta P_{\mathrm{i\_PV}} &= \begin{cases} \dfrac{\left(\left|\sum\limits_{k=i+1}^{n} S_k - S_{\mathrm{PV}}\right|\right)^2}{U_{\mathrm{N}}^2} R, & i \in [1, m-1] \\ \dfrac{\left(\left|\sum\limits_{k=i+1}^{n} S_k\right|\right)^2}{U_{\mathrm{N}}^2} R, & i \in [m, n-1] \end{cases} \\
\Delta Q_{\mathrm{i\_PV}} &= \begin{cases} \dfrac{\left(\left|\sum\limits_{k=i+1}^{n} S_k - S_{\mathrm{PV}}\right|\right)^2}{U_{\mathrm{N}}^2} X, & i \in [1, m-1] \\ \dfrac{\left(\left|\sum\limits_{k=i+1}^{n} S_k\right|\right)^2}{U_{\mathrm{N}}^2} X, & i \in [m, n-1] \end{cases}
\end{aligned} \tag{7}$$

where ΔP_{i_PV}, ΔQ_{i_PV} respectively refers to the active power loss and reactive power loss of branch *i* after PV access in a uniform power network.

At this time, the total line loss is:

$$\begin{aligned}
\Delta P_{\mathrm{PV}} &= \sum \Delta P_{i\_\mathrm{PV}} = \Delta P - \frac{R|S_{\mathrm{PV}}|}{U_{\mathrm{N}}^2}\left[\left|\sum_{i=1}^{m-1}\left(2\sum_{k=i+1}^{n} S_k - S_{\mathrm{PV}}\right)\right|\right] \\
\Delta Q_{\mathrm{PV}} &= \sum \Delta Q_{i\_\mathrm{PV}} = \Delta Q - \frac{X|S_{\mathrm{PV}}|}{U_{\mathrm{N}}^2}\left[\left|\sum_{i=1}^{m-1}\left(2\sum_{k=i+1}^{n} S_k - S_{\mathrm{PV}}\right)\right|\right]
\end{aligned} \tag{8}$$

where ΔP_{PV}, ΔQ_{PV} are respectively the total active power loss and reactive power loss of the system after PV access under a uniform power network.

Therefore, the variation of line loss caused by PV access is:

$$
\begin{aligned}
\Delta P_{\text{loss}} &= \frac{R|S_{\text{PV}}|}{U_{\text{N}}^2}\left[\left|\sum_{i=1}^{m-1}\left(2\sum_{k=i+1}^{n} S_k - S_{\text{PV}}\right)\right|\right] \\
\Delta Q_{\text{loss}} &= \frac{X|S_{\text{PV}}|}{U_{\text{N}}^2}\left[\left|\sum_{i=1}^{m-1}\left(2\sum_{k=i+1}^{n} S_k - S_{\text{PV}}\right)\right|\right]
\end{aligned}
\tag{9}
$$

where ΔP_{loss}, ΔQ_{loss} are the difference values of active power loss and reactive power loss before and after the system is connected to PV under a uniform power network.

Simplified Eq. (9), and the form shown in Eq. (10) is obtained.

$$
\begin{aligned}
\Delta P_{\text{loss}} &= -\frac{(m-1)R}{U_{\text{N}}^2}|S_{\text{PV}}|^2 + \frac{R\left(\left|2\sum_{i=1}^{m-1}\sum_{k=i+1}^{n} S_k\right|\right)}{U_{\text{N}}^2}|S_{\text{PV}}| \\
\Delta Q_{\text{loss}} &= -\frac{(m-1)X}{U_{\text{N}}^2}|S_{\text{PV}}|^2 + \frac{X\left(\left|2\sum_{i=1}^{m-1}\sum_{k=i+1}^{n} S_k\right|\right)}{U_{\text{N}}^2}|S_{\text{PV}}|
\end{aligned}
\tag{10}
$$

It can be seen from Eq. (10) that the variation of active power line loss is an opening downward quadratic function with PV power output as an independent variable, as shown in Fig. 2.

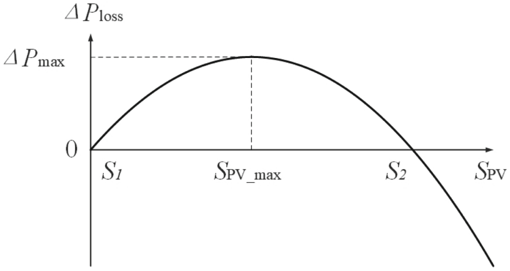

Fig. 2. Relation between variation of active power line loss and PV power output

In Fig. 2, while PV power output is $S_1 = 0$, the initial value of active power line loss change is 0. With the gradual increasing of PV power output, the variation of active power line loss gradually increases. While PV power output increases to $S_{\text{PV\_max}}$, the variation of active power line loss is the maximum value ΔP_{max}. Then, with the further increasing of PV power output, the variation of active power line loss begin to drop back. While the PV power output increases to S_2, the variation of active power line loss dropped to 0. After that, if the PV power output continues to increase, the change of active power line loss will decrease to negative value and continue to decrease.

While the PV power output meets $S_{\text{PV\_max}}$ in Eq. (11), the variation of active power line loss is the maximum $\Delta P_{\max}$.

$$S_{\text{PV\_ max}} = \frac{\left|\sum_{i=1}^{m-1}\sum_{k=i+1}^{n} S_k\right|}{m-1}$$
$$\Delta P_{\max} = \frac{\left[R\left|\sum_{i=1}^{m-1}\sum_{k=i+1}^{n} S_k\right|\right]^2}{(m-1)RU_{\text{N}}^2} \tag{11}$$

While the PV power output meets any of Eq. (12), the active power line loss does not change, ΔP_{loss} is 0.

$$S_1 = 0$$
$$S_2 = \frac{\left|2\sum_{i=1}^{m-1}\sum_{k=i+1}^{n} S_k\right|}{m-1} \tag{12}$$

where $S_{\text{PV\_max}}$ is the PV power output when the change of active power line loss is the largest under uniform power network; S_1 and S_2 are PV power output when the change of active power line loss is zero under uniform power network.

From the above analysis, it can be seen that the variation of active line loss increases first and then decreases with the increasing of PV power output. While the PV power output exceeds the zero point on the right side, that is S_2, the variation of line loss is negative, and line occurs power reversal.

3 Case Study

3.1 Case Descriptions of the 15-Node Low-Voltage Line

Take a 15-node low-voltage distribution line as an example to establish a uniform power network model, and the system topology is shown in Fig. 3. The transformer is an ideal transformer, and a three-phase power supply is used to simulate. The type of distribution lines is JKLYJ-1–185, and each branch length is 20 m. Distributed PV is accessed at node 12, and its output varies with time.

PV power output increases from 6 AM to 11 AM, basically saturation from 11 AM to 2 PM, and then gradually drops to zero at 6 PM. The total load of the system increases first and then decreases with time. The system total load and 24-h PV power output are shown in Fig. 4.

3.2 Analytical Result Analysis and Simulation Verification

According to the topology structure in Fig. 3, the system simulation model is built, and the correctness of the proposed line loss analytical model is verified by comparing the analytical solution of line loss calculation with the simulation results.

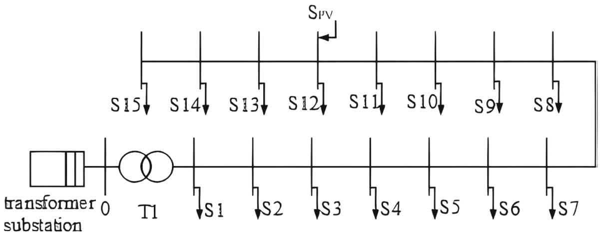

Fig. 3. Topology of a 15-node low-voltage line

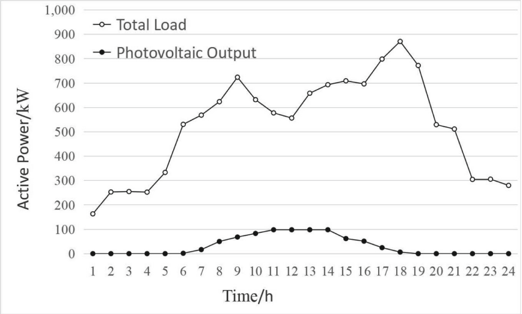

Fig. 4. Total system load and PV power output

(1) Calculation result

According to the 24-h PV power output shown in Fig. 4 and the 24-h power data of each node in the 15-node system, the two methods is set for comparison, and the 24-h system line loss rate before and after PV access is calculated respectively.

Method A: The MATLAB/SIMULINK simulation model of PV access considering the three-phase unbalance;

Method B: Analytical model.

According to the analytic model, three different Scenarios are set up for comparative analysis.

Scenario 1: Analytical model of PV access considering three-phase unbalance;

Scenario 2: Analytical model of PV access in three-phase balance;

Scenario 3: Analytical model with no PV access considering three-phase unbalance.

The line loss rate obtained by the two methods is shown in Table 1.

It can be seen from Table 1 and Fig. 4 that the variation trend of the system line loss rate is basically the same as that of the total load power. The total load reaches its maximum value at 6 PM, and at this moment the line loss rate calculated by the four methods is the maximum value. Similarly, the minimum value of load and line loss occur at 1 AM. In Scenario 1 and Scenario 2 of Method A and Method B, the line loss rate is the minimum value. The particularity of Scenario 2 is actually caused by the consideration of three-phase unbalance after PV connection.

Table 1. The statistical table of line loss rate

Time	Method A (%)	Method B		
		Scenario 1 (%)	Scenario 2 (%)	Scenario 3 (%)
1 AM	3.28	2.22	3.37	2.22
2 AM	3.42	3.41	3.51	3.41
3 AM	3.34	3.44	3.43	3.44
4 AM	3.59	3.39	3.67	3.39
5 AM	4.39	4.42	4.42	4.42
6 AM	6.97	6.79	6.63	6.74
7 AM	6.96	6.80	5.76	7.18
8 AM	6.57	6.50	4.31	7.86
9 AM	7.51	7.20	4.43	8.92
10 AM	5.86	5.88	3.01	7.95
11 AM	4.74	5.02	2.23	7.38
12 AM	4.48	4.73	2.17	7.14
1 PM	5.80	5.85	2.84	8.26
2 PM	6.26	6.18	3.15	8.64
3 PM	7.50	7.17	4.60	8.75
4 PM	7.66	7.32	4.98	8.61
5 PM	9.92	8.99	7.73	9.61
6 PM	11.59	10.21	9.73	10.21
7 PM	11.05	9.25	9.71	9.25
8 PM	8.74	6.63	8.05	6.63
9 PM	6.81	6.52	6.52	6.52
10 PM	5.19	4.02	5.13	4.02
11 PM	4.02	4.08	4.08	4.08
12 PM	3.68	3.75	3.75	3.75
Average	6.23	5.82	4.88	6.60

(2) Simulation verification

In order to verify the correctness of the analytical model for line loss calculation, the influence of three-phase balance on the system should be considered. Under this condition, Scenario 1 in method A and Method B is compared with PV connected to the line. The comparison results are shown in Fig. 5.

It can be seen from Fig. 5 that the analytical results of line loss and the simulation results have the same variation trend. The average error of the two method is 0.46%,

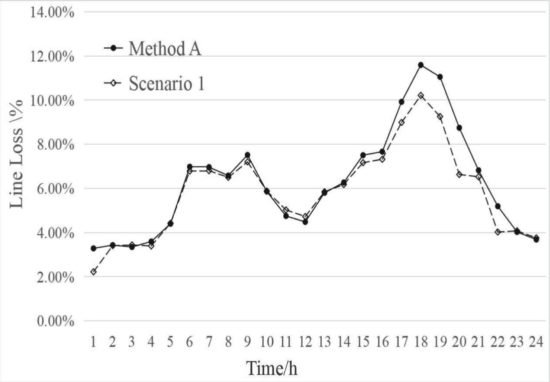

Fig. 5. Comparison of the results of line loss calculation the analytical model and the simulation model

the maximum error is 2.12%, and the minimum error is 0.02%, which indicates that the proposed analytical model of line loss under the uniform power network is correct. Compared with the simulation results, some data are different because the influence of line loss is ignored in the analytical model while calculating the branch power, and the rated voltage is used uniformly while calculating the loss without considering the voltage drop.

3.3 Line Loss Analysis in Different Scenarios

(1) The effect of three phase unbalance on line loss

While the system operates under the three-phase unbalanced scenario, there are a large number of negative sequence components in the voltage, which will affect the voltage in the line and lead to the changes in the system loss. The comparison results of Scenario 1 and Scenario 2 in the analytical model of line loss calculation are shown in Fig. 6.

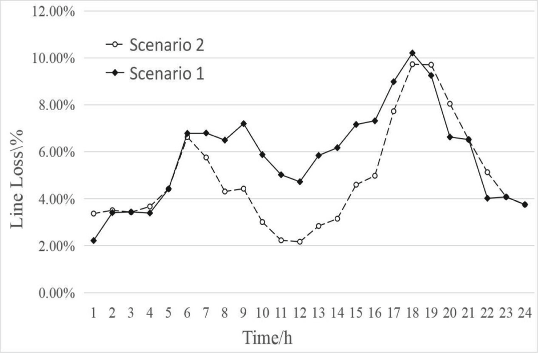

Fig. 6. The influence of three-phase unbalance on line loss

As can be seen from Fig. 6, during the time period from 1 AM to 5 AM and from 7 PM to 12 PM, the PV output is zero, and the average error of the influence of three-phase unbalance on the linear loss rate of the system is 0.5%. Individual time node has a fair-sized differ, and the calculation accuracy is relatively poor while the load is low.

After the PV is connected from 6 AM to 6 PM in Scenario 2, the three-phase voltage and current are asymmetrical due to the unbalance of the three-phase, so the calculated line loss rate has a large deviation from the actual line loss rate, and the deviation increases with the increase of the PV power output. The effect of the three-phase unbalance is corrected, and the linear loss rate data of Scenario 1 is obtained, which is more consistent with the simulation results.

(2) The influence of PV power timing variation on line loss

The time sequence changes of PV power output and load have a certain influence on line loss. The calculation results of the comparison between Scenario 1 and Scenario 3 are shown in Fig. 7.

As can be seen from Fig. 7, the linear loss rate of the system in Scenario 3 shows the same trend with the change of the total load power. The change trend of the system line loss rate in Scenario 1 is the same as that in Scenario 3. However, while the PV power output changes with time, the system line loss rate is smaller than that in Scenario 3 in the same period. From 11 AM to 2 PM, PV power output reaches the maximum, and the difference in line loss rate between the two is 2.41% on average. At 12 AM, the system load is small and PV power output reaches the maximum, resulting in the maximum line loss difference. While the PV power output is small at 6 AM and 6 PM, the difference of line loss rate between them is 0.01% on average. It is easy to know that the increase of PV power output will lead to a gradual decrease in the system line loss rate compared with that PV not connected to the line.

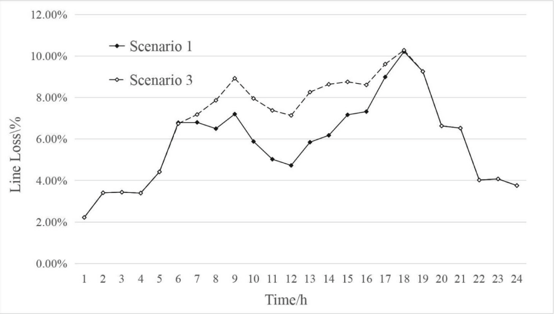

Fig. 7. The influence of PV output on line loss

(3) The influence of PV access location on line loss

In order to study the influence of PV access position on line loss, PV power output data and load data at 12 AM are selected to change the PV access position, and the variation trend of line loss rate is obtained as shown in Fig. 8.

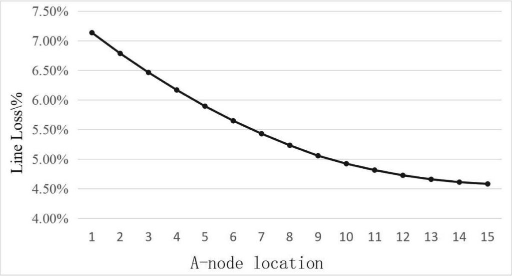

Fig. 8. The influence of PV access position on line loss

As can be seen from Fig. 8, on the premise that PV power output remains unchanged, the closer the PV access location is to the user node, the smaller the system line loss rate and the smaller the active power loss of the whole system. This is because the PV system can be regarded as a power supply after access, and the closer the power supply is to the user side, the lower the line loss. Therefore, the PV power output remains unchanged, and the PV access position in the system will affect the loss of the whole feeder system. The proximity of the PV access point to the user side allows for lower line losses when economy is considered.

4 Conclusion

In this paper, the calculation method of line loss for low-voltage lines considering PV access is proposed, and the analytical model of line loss calculation under a uniform power network is derived. The influences of factors such as before and after PV access, three-phase load unbalance and PV access location on line loss are compared. By comparing the simulation results with the analytical results, the following conclusions are obtained:

(1) The variation of line loss and PV power output of uniform power network accord with the trend of quadratic function. While PV power output gradually increases from zero, the variation of line loss increases first and then decreases until it becomes negative.
(2) The system line loss decreases first and then increases with the increasing of PV power output. While the PV power output is small, all PV power output generation is supplied to the local load for consumption, reducing the system transmission power and line loss. While the PV power output is large, the local load cannot fully absorb the PV power, and a large amount of electric energy is sent back to the system, which lead to the increasing of line loss.

(3) The line loss rate of the system is related to the distance between the PV access point and the load point. While the PV access point is close to the load center, the transmitted power of the system is reduced, and the loss reduction effect is better.

In this paper, the line loss rate of uniform power network is calculated without consideration the line loss rate calculation while the load is distributed irregularly under the non-uniform power network, so the subsequent work will be carried out in combination with more actual situations, and the existing results will be improved.

Acknowledgements. This work was supported in part by the technology project of State Grid Shanghai Electric Power Company (Grant No.: 520932220004-2) and the Science and Technology Project of Henan Province, China (Grant No.: 222102240095).

References

Ali, H.H., El Basuony, G.S., Kamal, N.A.: Maximum power production operation of doubly fed induction generator wind turbine using adaptive neural network and conventional controllers. Inter. J. Comp. Appl. Tech. **65**(2), 173–187 (2021)

Daoyuan, W., et al.: Development of solar photovoltaic industry and market in China, Germany, Japan and the United States of America using incentive policies. Energy Explor. Exploit. **39**(5), 1429–1456 (2021)

Fei, Y., Di, Z.: Loss optimization considering photovoltaic access to low-voltage distribution network. Proceed. CSU-EPSA **11**, 132–136 (2022)

He, H., He, H., Li, X.: Analysis on effect of distribution photovoltaic grid-connection on grid network loss. Modern Elect. Tech. **6**, 158–162 (2014)

He, T., Yang, P., Zheng, C., et al.: Optimal planning of distributed photovoltaic considering three-phase unbalanced degree. In: IECON 2017–43rd Annual Conference IEEE Industrial Electronics Society, Beijing, pp. 2617–2622 (2017)

Li.: Analysis of causes and calculation methods of line loss in distribution network. Electric Pow. Equip. Manage. **9**, 71–72 (2020)

Meifang, W., et al.: Research on the monitoring system design for the line loss of the distribution line based on dynamic three-phase unbalance degree. Proced. Comp. Sci. **155**(C), 815–821 (2019)

Navid, H., et al.: Impact of distributed photovoltaic systems on zone substation peak demand. IEEE Trans. Sustain. Energy **9**(2), 621–629 (2018)

Prasad, H.A., et al.: A novel methodology for power loss allocation of both passive and active power distribution systems. Int. J. Emerging Elect. Pow. Syst. **23**(2), 145–159 (2021)

Tong, X., et al.: Voltage regulation strategy of AC distribution network based on distributed PV grid-connected inverter. J. Eng. **16**, 2525–2528 (2019)

Xu, N., Ying, G., Fan, R., Cao, B., et al.: Power distribution network comprehensive energy-saving potential analysis based on layering index model. In: Proceedings of 2017 4th World Congress on Industrial Materials-Applications, Products, and Technologies (WCIM 2017), pp. 32–41). Information Engineering Research Institute (2017)

Yang F.-F., Zhao, X.-G.: Policies and economic efficiency of China's distributed photovoltaic and energy storage industry. Energy **154**, 221–230 (2018)

Zhang, H., Tong, X., Yin, J.: Influence of distributed photovoltaic power generation on distribution network and the design of optimal access scheme. J. Eng. **16**, 1361–1367 (2019)

Zongbao, W.: A Line loss management method based on improved random forest algorithm in distributed generation system. Distrib. Generation Alternative Energy J. **37**(1), 1–22 (2022)

Two-Stage Optimization Strategy for Managing Electrochemical Energy Storage in Power Grid Peak Shaving and Frequency Regulation

Yongqi Li[1], Man Chen[1], Minhui Wan[1], Yuxuan Li[1], and Jiangtao Li[2](✉)

[1] China Southern Power Grid Power Generation Company Energy Storage Research Institute, Guangdong 510000, China
[2] College of Electrical Engineering, Zhejiang University, Zhejiang 310027, China
22210142@zju.edu.cn

Abstract. Due to the large-scale access of new energy, its volatility and intermittent have brought great challenges to the power grid dispatching operation, increasing the workload and work difficulty of the power grid frequency regulation, and the increase in the installed proportion of new energy has also led to the further expansion of the peak-valley power difference. Electrochemical energy storage has bidirectional adjustment ability, which can quickly and accurately respond to scheduling instructions, but the adjustment ability of a single energy storage power station is limited, and most of the current studies based on the energy storage to participate in a certain type of auxiliary services, which cannot be fully utilized within the range of its life cycle. To solve this problem, a two-stage power optimization allocation strategy is proposed, in which electrochemical energy storage participates in peak regulation and frequency regulation. In the first stage, the adjustment cost, adjustment capacity and health status of each energy storage station in the region are considered, and the output of each energy storage station is determined with the goal of pursuing dispatching economy and reliability. In the second stage, the output of each energy storage power station is sent to each energy storage unit under the power station as the total power, and the goal is to quickly balance the SOC of each energy storage unit, which is conducive to the overall scheduling of the energy storage power station.

Keywords: Power regulation · Peak shaving · Frequency regulation · State of health · State of charge

1 Introduction

With the continuous deepening of the reform of China's electric power system, the transformation of energy cleanliness has entered a critical period, and the electric power system has shown new characteristics such as "high proportion of new energy" and "high proportion of electric electricity" [1–3]. Electrochemical energy storage has the characteristics of fast response speed and high adjustment accuracy, which can provide a powerful means of peak regulation and a fast and reliable means of frequency adjustment

Y. Xue et al. (Eds.): PMF 2023, LNEE 1129, pp. 463–479, 2024.
https://doi.org/10.1007/978-981-99-9251-5_36

and inertia support for the power system [4–7]. In recent years, large-scale electrochemical energy storage has emerged in China and even all over the world, and its regulating and safeguarding role in the power grid cannot be ignored [8, 9].

Considering the randomness of new energy output such as scenery and the electricity consumption on the load side, the increase in the installed proportion of new energy will also lead to excessive peak-valley power difference. However, the adjustment capacity of a single energy storage power station is limited, and it is necessary to coordinate the coordinated output of various energy storage power stations in the region, and the adjustment cost, adjustment capacity and health status (investment years) of each energy storage power station in the region are different. In this case, for different power grid scenarios, the output of each energy storage power station in the region will be faced with the problem, so it is necessary to determine the economic optimization of regional scheduling as the goal to determine the power required by each energy storage power station [10, 11]. At present, the power regulation of battery energy storage stations is mainly based on the SOC difference of BESS for charge and discharge power difference, which makes the SOC of BESS tend to be consistent after long-term operation [12–14]. In [15], aiming at the lifetime model of charge and discharge power-efficiency of BESS, power regulation optimization was realized by solving the objective function of minimum power loss. In [16] proposed a combinational sorting and allocation algorithm for power regulation of various energy storage units of ultra-large scale battery energy storage power station.

To this end, aiming at the joint dispatching problem involving large-scale electrochemical energy storage in the power grid side while participating in the peak regulation and frequency regulation of the power grid, this paper proposes to comprehensively consider the adjustment cost, residual adjustment capacity and health status of the energy storage power station in the first stage of power regulation. In the second stage of power regulation, the goal is to balance the state of charge (SOC) of each energy storage unit, while considering the SOH of each energy storage unit to avoid frequent action of energy storage units with low SOH. The main innovations of this paper are as follows:

1. Consider the energy storage to participate in the joint dispatching of the power grid for peak and frequency modulation, and determine the power required by each energy storage station to achieve the economic optimization of regional dispatching;
2. After each energy storage power station obtains its own determined power value, it will be sent to each energy storage unit under the power station as the total power. In this process, the goal is to quickly balance the SOC of each energy storage unit;
3. Incremental capacity analysis (ICA) [17] is used to evaluate the SOH of each energy storage unit and take it into account in the entire power regulation process. The SOH, SOH range, SOH standard deviation and temperature difference of each energy storage unit are used to comprehensively evaluate the overall SOH of different energy storage power stations.

2 Models and Methods

2.1 Combined Optimization of Peak Shaving and Frequency Regulation

In the day-ahead plan, the output of each power supply is usually optimized on a time scale of 15 min, while the dynamic process of a few seconds to ten seconds after the disturbance appears needs to be considered for fast frequency response. Therefore, when energy storage participates in the joint optimization of peak shaving and frequency regulation, the coordination problem of time scales with wide differences must be considered. The time series of instantaneous output dynamic changes of energy storage participating in frequency response is transformed into the reserve capacity of frequency response in every 15 min, and the frequency regulation of energy storage and peak shaving are optimized under the same time scale in the form of reserve capacity constraint. The model used in the following paper is to determine the output of the traditional unit with a total of 16 time nodes in a cycle of 4 h per day and a point every 15 min at the system scheduling level when the traditional unit and each energy storage jointly participate in peak shaving and frequency regulation.

The essence of the joint optimization of multi-resource (unit + energy storage) and multi-auxiliary services (peak regulation + frequency regulation) is to optimize the allocation of peak shaving and reserved output space for frequency regulation of energy storage. The principle of coordinated frequency response scheduling of energy storage and unit should be: under the premise of giving full play to the unit's response ability, energy storage should supplement the frequency response demand gap. Since this paper focuses on how to distribute peak shaving and frequency regulation instructions among energy storage power stations, the following simplification is made:

1. Forecast the output of each unit on the power source side and the power consumption of users on the load side in a certain regional power grid in the next 4 h of the day, and use 15 min as a time node to calculate the power deficit value required to stabilize at each 16 time points $P_r(t)$.
2. In order to make the joint optimization of peak shaving and frequency regulation be carried out in the same time scale, the second-level time scale of frequency response is transformed into the reserve capacity of frequency response that needs to be kept within 15 min. By predicting the maximum frequency deviation value generated every 15 min in the next 4 h, and according to the maximum frequency deviation value, the frequency response reserve capacity of 16 time points $P_f(t)$ in this period is calculated.

$$P_f(t) = -\frac{1}{R_B}\Delta f(t) \tag{1}$$

In the formula: R_B is the energy storage difference coefficient, $\Delta f(t)$ is the maximum frequency deviation value of the energy storage within a certain period of time.

Therefore, the final required energy storage to stabilize the total power deficit at each time point is:

$$P_{total}(t) = P_r(t) + P_f(t) \tag{2}$$

This paper takes *i* different types of energy storage power stations in a certain regional power grid as the research object. Since the energy storage power stations cannot be charged and discharged at the same time, the charging and discharging flags are set. The determination method is as follows:

$$\begin{cases} \mu_b^c(t) = 1, \mu_b^d(t) = 0, P_{total}(t) < 0 \\ \mu_b^c(t) = 0, \mu_b^d(t) = 1, P_{total}(t) > 0 \\ \mu_b^c(t) = 0, \mu_b^d(t) = 0, P_{total}(t) = 0 \end{cases} \tag{3}$$

The output of each energy storage power station at the *t* moment is related to its charging and discharging state, and according to the principle of power conservation, the total output of each energy storage power station in the region should be equal to the total power deficit, specifically:

$$\begin{cases} P_{b,i}(t) = \mu_b^c(t) \cdot P_{b,i}^c(t) + \mu_b^d(t) \cdot P_{b,i}^d(t) \\ \sum_i^I P_{b,i}(t) = P_{total}(t) \end{cases} \tag{4}$$

$\mu_b^c(t)$, $\mu_b^d(t)$ are the charging and discharging state respectively; $P_{b,i}^c(t)$, $P_{b,i}^d(t)$ are respectively the charging and discharging power of the energy storage station *i*.

2.2 Two-Stage Optimal Distribution Strategy Framework

In view of the differences in the adjustment cost, adjustment capacity, investment years and operating conditions of each energy storage power station in the regional power grid, this paper proposes to comprehensively consider the adjustment cost, residual adjustment capacity and overall SOH of each power station in the first stage of power regulation. In the second stage of power regulation, considering the difference in the depth of charge and discharge of each energy storage unit under the energy storage station, the SOC and SOH of each energy storage unit are different. The inconsistency of SOC will cause the SOC of each energy storage unit to exceed the limit during unified scheduling, resulting in the early withdrawal of some energy storage units from operation, and the SOC of some energy storage units is too high (too low) to facilitate the centralized scheduling of the power station, which greatly restricts the scheduling capability of the energy storage power station. At the same time, since the SOH of the energy storage unit has a "short board effect", in order to extend the service life of the energy storage system as much as possible, frequent action of the energy storage unit with a low SOH should be avoided. To solve the above problems, this paper proposes a two-stage power optimal distribution framework, as shown in Fig. 1,which is as follows:

(1) In the first stage of power regulation, the adjustment cost, residual adjustment capacity and overall SOH of each power station are comprehensively considered, and the local optimal economy and reliability of the regional power grid dispatching level is taken as the goal to determine the power required by each energy storage station.

(2) The output required by each energy storage station in the first stage is sent to each energy storage unit under the power station as the total input. In the second stage of power regulation, the required output of each energy storage unit is determined with the goal of quickly stabilizing the SOC of each energy storage unit. In this process, the difference of SOH of each energy storage unit is considered, and the "energy storage unit with good performance has more and deeper operation" is followed as far as possible. Energy storage units with poor performance move less and move more "principle.

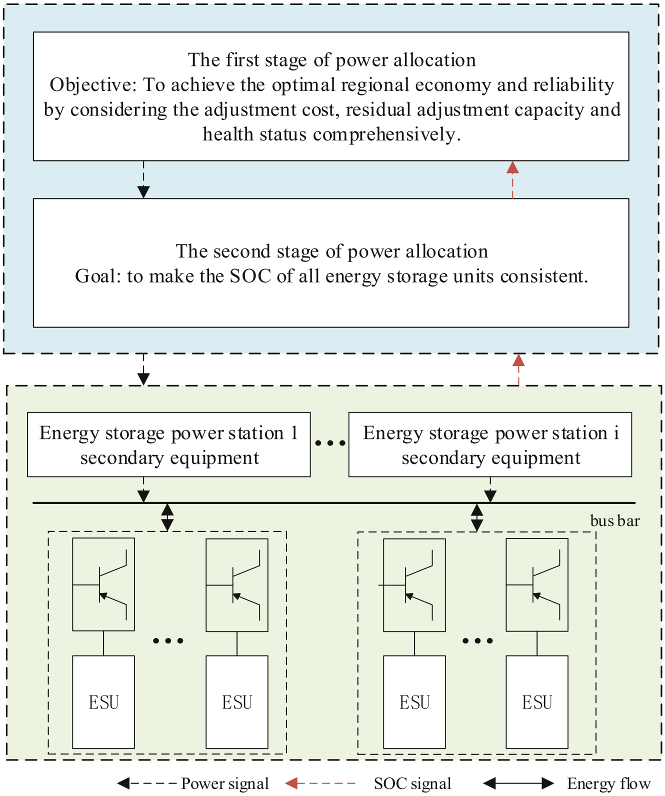

Fig. 1. Two-stage power regulation framework

2.3 First Stage Power Regulation

The first stage of power regulation aims to coordinate the output of each energy storage power station in the regional power grid, and use the output of each power station as the total input to the second stage of power regulation. In order to optimize the adjustment space of the energy storage power station, this paper does not consider the problem of cascading benefits when the energy storage power station participates in peak regulation and frequency regulation at the same time, and aims to minimize the adjustment cost as much as possible. At the same time, since this paper focuses on power regulation among energy storage stations and does not consider power loss during long-distance transmission between stations, the model construction method of power regulation stage is as follows.

In order to facilitate the calculation of the adjustment cost and the complexity of the model, the adjustment cost is simplified into the initial investment cost, energy loss cost and life loss cost, which can reflect the difference of the adjustment cost of different energy storage power stations, as follows:

$$C_{\mathrm{inv},i}^{\mathrm{cost}}(t) = \frac{c_{\mathrm{cap},i} E_{\mathrm{rat},i}}{365 \cdot s} \cdot \frac{r(1+r)^{T_{\mathrm{float}}}}{(1+r)^{T_{\mathrm{float}}} - 1} \tag{5}$$

$$C_{\mathrm{loss},i}^{\mathrm{cost}}(t) = c_{\mathrm{e}} \cdot \Delta t \cdot \left[P_{\mathrm{b},i}^{\mathrm{d}}(t) \cdot \left(\frac{1}{\eta_i^{\mathrm{d}}} - 1 \right) + P_{\mathrm{b},i}^{\mathrm{c}}(t) \cdot \left(1 - \eta_i^{\mathrm{c}}\right) \right] \tag{6}$$

$$C_{\mathrm{life},i}^{\mathrm{cost}}(t) = \left[\left(\frac{\Delta t \cdot P_{\mathrm{b},i}^{\mathrm{d}}(t)}{E_{\mathrm{rat},i} \cdot \eta_i^{\mathrm{d}}} \right)^{k_{\mathrm{p}}} + \left(\frac{\Delta t \cdot P_{\mathrm{b},i}^{\mathrm{c}}(t)}{E_{\mathrm{rat},i}} \cdot \eta_i^{\mathrm{c}} \right)^{k_{\mathrm{p}}} \right] \cdot c_{FR,i} \cdot P_{rate,i} / \left(2N_{0,i}\right) \tag{7}$$

In the formula: $C_{\mathrm{inv},i}^{\mathrm{cost}}(t)$, $C_{\mathrm{loss},i}^{\mathrm{cost}}(t)$, $C_{\mathrm{life},i}^{\mathrm{cost}}(t)$ are the initial investment cost, charge and discharge energy loss cost, and life loss cost of the energy storage power station, respectively; $c_{\mathrm{cap},i}$,$E_{\mathrm{rat},i}$ are the capacity cost and rated capacity respectively;T_{float} is the floating charge life of the energy storage power station, and it is related to the battery type; r is the discount rate, which is 8%;s is the maximum number of dispatching times in a day which is taken as 96;c_e is the on-grid electricity price, which is 520 yuan/(MWh), without considering the influence of time-of-use electricity price;Δt is the scheduling time step, which is 15 min;η_i^c,η_i^d are the charging and discharging efficiency respectively;$c_{FR,i}$,$P_{rate,i}$ are respectively the unit power cost and rated power of the energy storage power station; $N_{0,i}$ is the equivalent number of cycles at 100% charge and discharge depth [18]; k_p is a constant, generally between 0.8 - 2.1, usually 1.

To sum up, the adjustment cost of the energy storage power station i is:

$$C_i(t) = C_{\mathrm{inv},i}^{\mathrm{cost}}(t) + C_{\mathrm{loss},i}^{\mathrm{cost}}(t) + C_{\mathrm{life},i}^{\mathrm{cost}}(t) \tag{8}$$

If only the minimum adjustment cost is considered, the energy storage power station with low adjustment cost but small residual adjustment capacity may assume the adjustment responsibility, and the energy storage power station with high adjustment cost but large residual adjustment capacity does not act, which is not conducive to improving the overall utilization rate of energy storage. Therefore, the resistance coefficient $R_{EF,i}(t)$ is introduced to quantify the residual adjustment capacity of energy storage, which is essentially the residual capacity of the energy storage power station *i* at the *t* moment, defined as follows:

$$\begin{cases} R_{\mathrm{EF}-i}^{\mathrm{c}}(t)\prime = \sum_{j=1}^{J} E_{\mathrm{rate},i,j} \cdot \dfrac{S_{i,j}(t-1) - S_{i,j}^{\min}}{\Delta t} \\ R_{\mathrm{EF}-i}^{\mathrm{d}}(t)\prime = \sum_{j=1}^{J} E_{\mathrm{rate},i,j} \cdot \dfrac{S_{i,j} - S_{i,j}(t-1)}{\Delta t} \end{cases} \tag{9}$$

where, $R_{\mathrm{EF}-i}^{\mathrm{c}}(t)'$ and $R_{\mathrm{EF}-i}^{\mathrm{d}}(t)'$ are the charge and discharge resistance coefficients of the energy storage power station *i* at the *t* moment; $S_{i,j}^{\max}$ and $S_{i,j}^{\min}$ are the upper limit and lower limit of SOC of the energy storage unit in the energy storage power station, $S_{i,j}(t-1)$ is the actual SOC value at the $(t-1)$ moment;$E_{rate,i,j}$ is the rated capacity of the energy storage unit in the energy storage power station; J is the total number of energy storage units in the energy storage power station.

After considering the peak load balancing cost and remaining peak load balancing capacity of the energy storage power station, the overall health status of the energy storage power station should be evaluated, and the SOH, SOH range, SOH standard deviation and temperature range of each energy storage unit should be used as health status evaluation indicators.

Energy storage unit SOH measurement evaluation using the method of incremental capacity analysis (ICA), the method is a method of mathematical model, it contains the battery capacity is highly related features are widely used in lithium batteries SOH evaluation. The relationship between incremental capacity and open circuit voltage can be expressed as follows:

$$\left.\frac{\mathrm{d}Q}{\mathrm{d}U_{\mathrm{oc}}}\right|_{k} \approx \frac{\Delta Q_k}{\Delta U_{\mathrm{oc},k}} = \frac{Q_k - Q_{k-1}}{U_{\mathrm{oc},k} - U_{\mathrm{oc},k-1}} \tag{10}$$

In the formula, Q represents the measured battery capacity, U_{OC} represents the measured open circuit voltage of the battery, and the subscript $k-1, k$ represents two consecutive cycle periods.

A typical incremental capacity (IC) curve can be obtained by conducting constant discharge of small current on each energy storage unit. By extracting the features in the IC curve, the internal health state of the battery can be revealed. For example, the evolution of the peak area, position and amplitude of the IC curve is closely related to the phase transition and phase equilibrium of the lithium and DE lithium processes inside the battery, and the formula is as follows:

$$Q(PA) = \int_{V_{PP}-\Delta V}^{V_{pp}+\Delta V} \mathrm{IC}(v)dv \tag{11}$$

$$SOH = \frac{Q(PA)}{Q_0} \tag{12}$$

where: $Q(PA)$ is the peak area of the IC curve, V_{PP} is the voltage value when the peak value of the IC curve appears, ΔV taking 50 mV, Q_0 as the initial capacity value of the energy storage unit, which can refer to the initial data given by the battery manufacturer.

The overall SOH of an energy storage power station can be evaluated according to the measured SOH, SOH range, SOH standard deviation and temperature range of each energy storage unit according to a certain weight coefficient. The specific calculation formula is:

$$\begin{cases} \Delta \mathrm{SOH}_{\max} = \mathrm{SOH}_i^{\max} - \mathrm{SOH}_j^{\min} \\ \delta_{\mathrm{SOH}} = \sqrt{\dfrac{1}{\mathrm{x}}\displaystyle\sum_{i=1}^{\mathrm{x}}\left(\dfrac{\mathrm{SOH}_i - \mathrm{SOH}_{\mathrm{avg}}}{\mathrm{SOH}_{\mathrm{avg}}}\right)^2} \\ \mathrm{SOH}_{\mathrm{avg}} = \dfrac{1}{\mathrm{x}}\displaystyle\sum_{i=1}^{\mathrm{x}} \mathrm{SOH}_i \\ \Delta \mathrm{T} = \mathrm{T}_i^{\max} - \mathrm{T}_j^{\min} \end{cases} \tag{13}$$

In the formula: $\mathrm{SOH}_i^{\max}$, $\mathrm{SOH}_i^{\min}$, SOH_{avg} are respectively the maximum value and minimum value of the health status of each energy storage unit and the average value of the overall energy storage unit, and X are the number of energy storage units. Divide each indicator into different grades for scoring, and give different weight coefficients according to the importance, and finally get the overall SOH of each power station.

2.4 Second Stage Power Regulation

The second stage of power regulation is the power regulation inside the power station, and the power value is allocated with the goal of balancing SOC. At the same time, the SOH of each energy storage unit is measured to make the energy storage unit with low SOH move less and move less, so as to avoid the SOH of a unit being reduced too much, which affects the overall SOH.

In the actual energy storage power station, in order to more easily manage the energy storage units under its jurisdiction, an energy storage power station will set up about 5 cooperative control units (CCU), and a cooperative control unit will manage about 8 energy storage units. Taking a 100 MW battery energy storage power station in Guangdong Province as an example, an energy storage power station has 4 CCUs, and a CCU manages 6 or 8 energy storage units. Therefore, the power instructions obtained from the first stage of power regulation are first distributed among each CCU to determine the power regulation value of each CCU, and then distributed among each energy storage unit to determine the power regulation value of each energy storage unit.

First, according to the SOC_i of each CCU obtained at the end of the previous scheduling period, Q of N CCUs can be scheduled. SOC_i at $[0,SOC_{\min}]$ when discharging and SOC_i at $[SOC_{\max}, 1]$ when charging cannot be called. Then, combined with the SOC, SOH, and SOC of each CCU, Select T CCUs that participate in scheduling from Q CCUs that can be scheduled, where $\mathrm{T} \le \mathrm{Q} \le \mathrm{N}$.

After the CCU is selected, determine the power of each energy storage unit under the CCU. First of all, the energy storage unit can be determined according to the SOC range of each energy storage unit and SOH, SOH range, SOH standard deviation, and temperature range (specifically, it can be graded according to the first stage of power regulation and given different weight coefficients), and then according to the SOC situation of each energy storage unit, and in order to make the SOC quickly become consistent. The charging and discharging power of each energy storage unit is as follows:

The charge and discharge power regulation coefficients of different energy storage units in different power stations are written in a form related to SOC, as follows:

$$R_{(ij)} = e^{-aSOC_{ij}} \tag{14}$$

$$a = \ln P_{ij\,\max} + \ln N - \ln|P_i| \tag{15}$$

Charging power of the j th energy storage unit in i th CCU:

$$P_{C(ij)} = \frac{\mathrm{e}^{-(\ln P_{\mathrm{ij,max}} + \ln N - \ln|P_i|)SOC_{ij}}}{\sum_{j=1}^{N} \mathrm{e}^{-(\ln P_{\mathrm{ij,max}} + \ln N - \ln|P_i|)SOC_{ij}}} P_i \tag{16}$$

Discharging power of the j th energy storage unit in i th CCU:

$$P_{D(ij)} = \frac{\mathrm{e}^{-(\ln P_{\mathrm{ij,max}} + \ln N - \ln|P_i|)(1 - SOC_{ij})}}{\sum_{j=1}^{N} \mathrm{e}^{-(\ln P_{\mathrm{ij,max}} + \ln N - \ln|P_i|)(1 - SOC_{ij})}} P_i \tag{17}$$

where $R_{(ij)}$ is the distribution coefficient, N is the number of energy storage units, $P_{ij,\max}$ is the maximum charging and discharging power of the energy storage unit, and P_i is the power regulation value of a certain CCU. Finally, the power regulation value of each energy storage unit obtained from the solution is transmitted to the corresponding PCS as a power control command, and each energy storage unit is controlled to operate according to a given power (Fig. 2).

3 Two-Stage Power Regulation Model

3.1 Objective Function

In order to take into account the adjustment cost and the remaining adjustment capacity of each energy storage power station in the region, the objective function is constructed in the first stage of power regulation, aiming at the optimal economy and reliability of the regional power grid, as shown below:

$$F_1 = \min \sum_{t=1}^{T} \sum_{i=1}^{I} R_i(t) C_i(t) \tag{18}$$

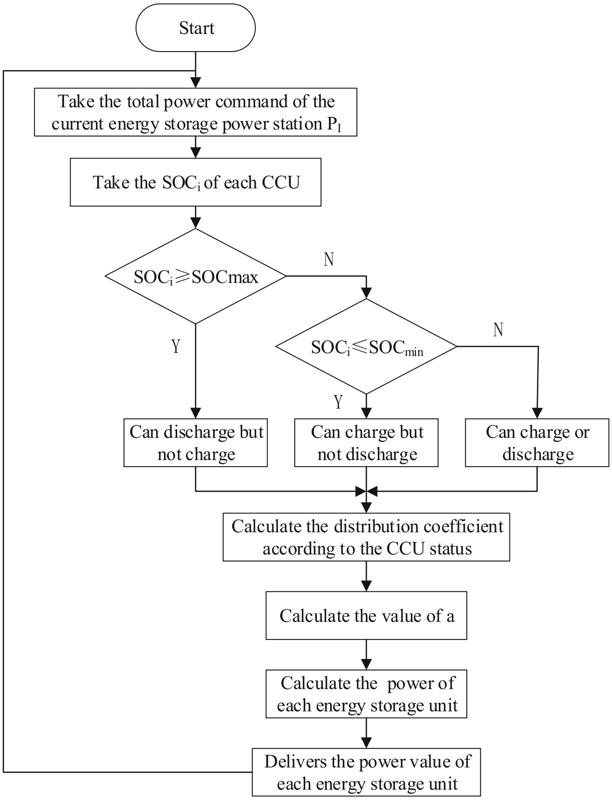

Fig. 2. Flow chart of the second phase of power regulation

For the overall SOH of a power station, if the difference between the overall SOH values of each power station is less than a certain range (3% or 5%), the power required by each power station is determined based on the above objective function. If it exceeds a certain range, the energy storage power station with a higher overall SOH should be preferentially selected to bear the power shortfall, and when the power shortfall is too large, the power station with a smaller "overall SOH" should be invoked to offset the remaining shortfall.

In order to keep the SOC of each energy storage unit of the power station consistent and avoid frequent operation of the energy storage unit with a low SOH, similar to the first-stage consideration of the overall SOH of the power station, when the SOH difference of each energy storage unit is less than a certain range, the output sequence of each energy storage unit is not restricted. On the contrary, the charge and discharge priority is sorted according to the SOH from high to low. The second stage of power regulation takes the minimum variance of each energy storage unit toward an ideal value as the objective function, as shown below:

$$F_2 = \min \sum_{i=1}^{I} \sum_{j=1}^{J} \left(S_{i,j}(t) - S_{ideal}\right)^2 \qquad (19)$$

In the formula, $S_{i,j}(t)$ is the state of charge of the energy storage unit at the t moment, S_{ideal} and is the ideal state SOC value, usually 0.5.

3.2 Constraint Conditions

In the first stage of power regulation, the power required by the energy storage power station must be limited by the rated power of the power station and the remaining adjustment capacity, as follows:

$$\begin{cases} P_{\mathrm{b},i}^{\mathrm{left}}(t) = \mu_{\mathrm{b}}^{\mathrm{c}}(t)P_{\mathrm{b},i}^{\mathrm{c,left}}(t) + \mu_{\mathrm{b}}^{\mathrm{d}}(t)P_{\mathrm{b},i}^{\mathrm{d,left}}(t) \\ \begin{cases} P_{\mathrm{b},i}^{\mathrm{c,left}}(t) = \min\left\{P_{\mathrm{rat},i}, \frac{\left[S_i^{\max} - S_i(t-1)\right]}{\Delta t \cdot \eta_i^{\mathrm{c}}} \cdot E_{\mathrm{rat},i}\right\} \\ P_{\mathrm{b},i}^{\mathrm{d,left}}(t) = \min\left\{P_{\mathrm{rat},i}, \frac{\left[S_i(t-1) - S_i^{\min}\right]}{\Delta t} \cdot E_{\mathrm{rat},i} \cdot \eta_i^{\mathrm{d}}\right\} \end{cases} \end{cases} \tag{20}$$

In the formula: In the formula $P_{b,i}^{c,left}(t)$, $P_{b,i}^{d,left}(t)$ respectively are the charging and discharging remaining frequency regulation capacity of the energy storage power station at the time t.

For each energy storage unit, the following constraints should also be met:

$$\begin{cases} \sum_{j=1}^{J} P_{\mathrm{b},i,j}^{\mathrm{c}}(t) = \mu_{\mathrm{b}}^{\mathrm{c}}(t) \cdot P_{\mathrm{b},i}^{\mathrm{c}}(t) \\ \sum_{j=1}^{J} P_{\mathrm{b},i,j}^{\mathrm{d}}(t) = \mu_{\mathrm{b}}^{\mathrm{d}}(t) \cdot P_{\mathrm{b},i}^{\mathrm{d}}(t) \end{cases} \tag{21}$$

$$\begin{cases} 0 \le P_{\mathrm{b},i,j}^{\mathrm{c}}(t) \le \mu_{\mathrm{b}}^{\mathrm{c}}(t) \cdot P_{\mathrm{rate},i,j} \\ 0 \le P_{\mathrm{b},i,j}^{\mathrm{d}}(t) \le \mu_{\mathrm{b}}^{\mathrm{d}}(t) \cdot P_{\mathrm{rate},i,j} \end{cases} \tag{22}$$

$$\begin{cases} S_{i,j}^{\min} \le S_{i,j}(t) \le S_{i,j}^{\max} \\ \begin{cases} S_{i,j}(t) = S_{i,j}(t-1) + \Delta S_{i,j}(t) \\ \Delta S_{i,j}(t) = \left(\eta_i^{\mathrm{c}} \cdot P_{\mathrm{b},i,j}^{\mathrm{c}}(t) - P_{\mathrm{b},i,j}^{\mathrm{d}}(t)/\eta_i^{\mathrm{d}}\right) \cdot \Delta t / E_{\mathrm{rate},i,j} \end{cases} \end{cases} \tag{23}$$

Formula (21) is the output constraint of the energy storage unit, formula (22) is the rated power constraint, and formula (23) is the upper and lower limit constraint of SOC.

4 Simulation Analysis

4.1 Simulation System Design

In order to verify the effectiveness and practicability of the proposed two-stage power regulation strategy when energy storage participates in the joint optimization of power grid for peaking and frequency modulation, a regional power grid was simulated and analyzed in MATLAB. Assume that there are three different types of electrochemical energy storage power stations in this region, with a total installed capacity of 56 MW/56 MWh. Each energy storage power station consists of 10 energy storage units. The battery type, partial technical parameters and construction cost of each energy storage power station [19] are shown in Table 1, and the SOC value of each energy storage unit in the power station is shown in Table 2.

Table 1. Parameters of example system.

Parameter	Power station 1	Power station 2	Power station 3
Battery type	Liquid flow	Lithium ion	Lead carbon
Charge and dis-charge efficiency	0.83	0.95	0.9
Rated power/MW	16	24	16
Rated capacity/(MWh)	16	24	16
Unit power cost/(Yuan/kW)	2500	1500	1500
Unit capacity cost/(Yuan/(kWh))	5000	3000	900
Float life/year	12	10	10
Cycle life/time	3000	2000	500
SOC upper limit	0.8	0.8	0.8
SOC Lower limit	0.2	0.2	0.2

Table 2. Initial SOC value of the energy storage unit.

ESU	1	2	3	4	5	6	7	8	9	10
SOC	0.05	0.15	0.25	0.35	0.45	0.55	0.65	0.75	0.85	0.95

4.2 Simulation Result Analysis

In the first stage of power regulation, in order to verify the effectiveness of the proposed power regulation strategy aiming at local economy and reliability optimization, the strategy is compared with the traditional dynamic proportional allocation strategy. However, this strategy is improved on the basis of the equal proportional allocation method, and only undertakes the adjustment task according to the remaining adjustment capacity, without considering the lowest adjustment cost as the objective function. The simulation results show that in the traditional dynamic proportional distribution strategy, different energy storage stations have both charging and discharging in the same time period, and the charging or discharging between energy storage stations will increase the power loss, which is not conducive to the economic operation of the system. Under the strategy proposed in this paper, the charging and discharging states of each energy storage power station are consistent in the same period of time, which significantly improves the economy and has practical significance in engineering (Figs. 3 and 4).

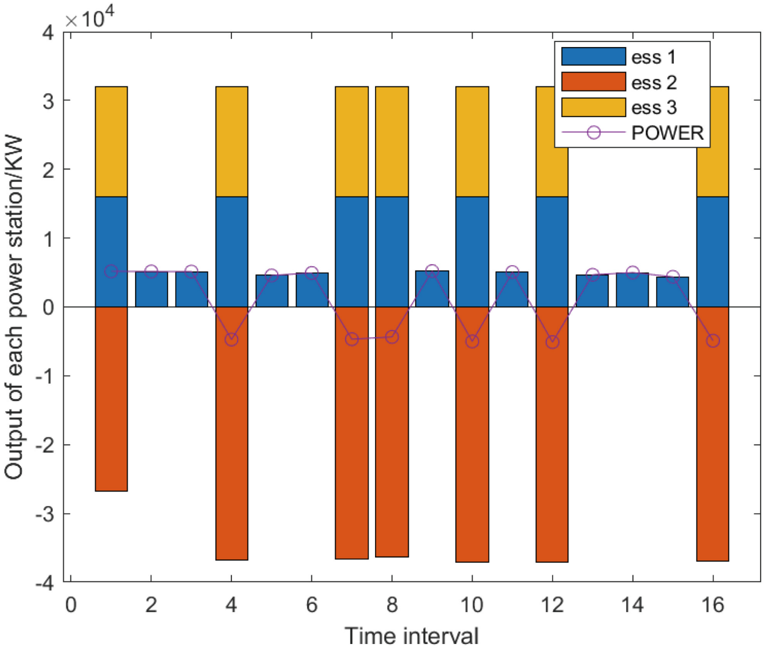

Fig. 3. Output of energy storage power station under traditional strategy

In the second stage of power regulation, the available energy storage unit is first determined according to the state of charge, the charging and discharging state of each energy storage unit is determined according to the total power, and finally the change of the state of charge of each available energy storage unit is obtained. In order to verify the effectiveness of the strategy proposed in this paper, the power regulation strategy proposed in [16] is compared with that proposed in this paper. The experimental simulation results show that compared with the traditional power regulation method, which determines the allocation coefficient according to the proportion of SOC of each energy storage unit in the total SOC. The power regulation strategy proposed in this paper, representing SOC as an exponential form related to power regulation coefficient, can make SOC converge quickly, avoid power redistribution, and is conducive to practical engineering applications. The simulation results are shown in the figure (Figs. 5 and 6).

5 Conclusions

In the future, due to the adjustment of the power supply structure, the proportion of new energy installed capacity will increase, and the demand for auxiliary services such as peak regulation and frequency regulation of the power grid will also increase, and the 100-megawatt energy storage has the advantages of both power and capacity, so it should be more involved in auxiliary services such as peak regulation and frequency regulation on the power grid side to improve the flexibility and reliability of the power grid. At the same time, it will also take advantage of the possible reverse fluctuations between the

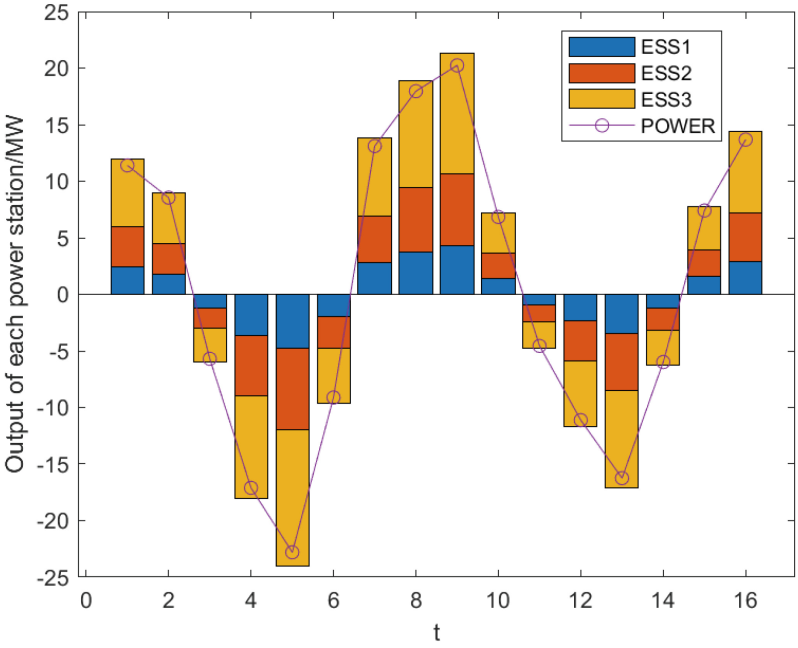

Fig. 4. Output of energy storage power station under improved strategy

demands of different auxiliary services, such as peak regulation and frequency regulation, to expand scheduling resources and make energy storage obtain the overlapping benefits of multiple auxiliary services. However, most of the existing studies focus on the independent participation of energy storage in a certain type of auxiliary services, and less consider the participation in multiple auxiliary services and the collaboration among auxiliary services. The problem is that energy storage alone in a class of auxiliary services will not be fully utilized, and the benefits available over its life cycle will be reduced.

In order to enable energy storage to participate in multiple auxiliary services as much as possible, so that it can obtain more benefits within the whole life cycle, and to reduce the scheduling cost of regional power grid energy storage, the two-stage power regulation strategy proposed in this paper is conducive to increasing the reliability and sustainability of regional energy storage under the premise of considering the local optimal economy and reliability of regional power grid. However, in the second stage of power regulation, as this strategy focuses on SOC balance, no in-depth study has been conducted on the consideration of frequent charge and discharge of energy storage units and the operation efficiency of energy storage units, and further improvement and perfection are needed in the future.

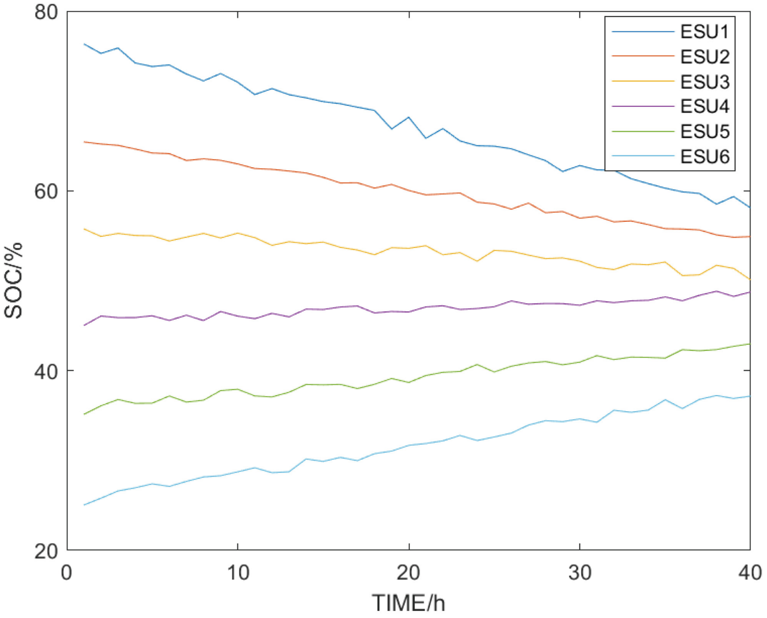

Fig. 5. Reference 20 power regulation strategy simulation curve

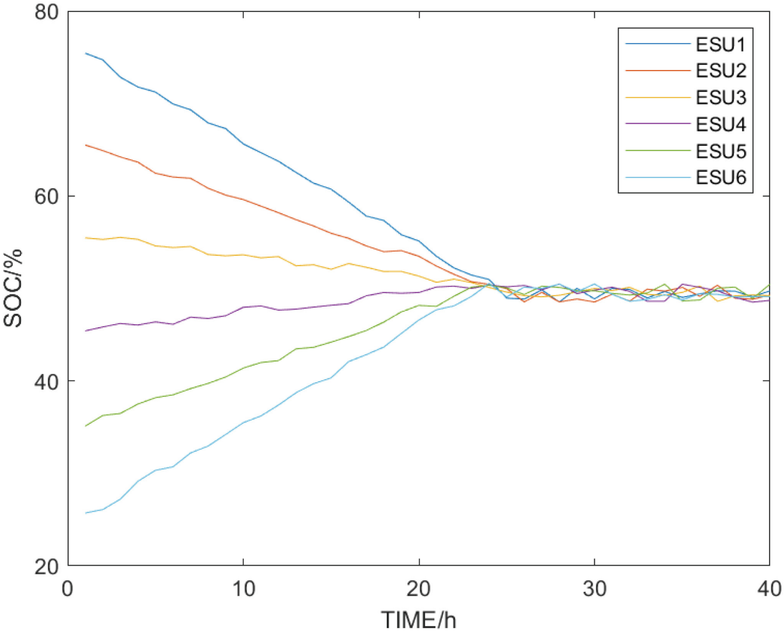

Fig. 6. Improved power regulation strategy simulation curve

Acknowledgments. This work is supported by China Southern Power Grid Power Generation Company Energy Storage Research Institute (020000KK52220002).

References

1. Guoping, C., Yu, D., Zhifeng, L.: Analysis and consideration on high-quality development of new energy with Chinese characteristics in energy transformation. Proceed. CSEE **40**(17), 5493–5506 (2020)
2. Wang, J., Zhong, H., Ma, Z., et al.: Review and prospect of integrated demand response in the multi-energy system. Appl. Energy **202**, 772–782 (2017)
3. Junhui, L., Xichao, F., Gangui, Y., et al.: Research review on frequency modulation of power systems with high wind power penetration. Pow. Syst. Protect. Control **46**(2), 163–170 (2018)
4. Changqing, C., Xinran, L., Xiaolong, L., et al.: Reliability improvement of wind power frequency modulation based on look-ahead control strategy and stage of charge optimization of energy storage. Int. J. Energy Res. **46**(4), 4739–4753 (2022)
5. Hao, Y., Yi, Y., Tang, J., et al.: Active reactive power control strategy based on electrochemical energy storage power station. In: 2019 IEEE 3rd Conference on Energy Internet and Energy System Integration (EI2). IEEE, pp. 90–94 (2019)
6. Zilong, Y., Zhenhao, S., Jing, P., et al.: Coordinated control strategy for distributed photovoltaic/energy storage systems with multiple operation modes. Proceed. CSEE **39**(8), 2213–2224 (2019)
7. Shiqi, L., Junhua, W., Ruixun, Q., et al.: Power coordination control strategy of hybrid energy storage system in auxiliary service market. Power Grid Tech. **46**(9), 3515–3525 (2022)
8. Guiding opinions on accelerating the development of new energy storage (draft for comment). Public Elect. Use **36**(4), 7–9 (2021)
9. Zhou, X., Liu, R., Bao, F.-Z., et al.: Joint optimization model of 100 MW energy storage participating in dual auxiliary service scheduling of power grid. Automat. Elect. Pow. Syst. **45**(19), 60–69 (2021)
10. Li, C., Li, J., Li, J., et al.: Optimization strategy of secondary frequency modulation based on dynamic loss model of the energy storage unit. J. Energy Stor. **51**, 104425 (2022)
11. Shuangming, D., Hang, Y., Cong, L., Mingqi, W., Suya, W., Bo, X.: BESS power regulation strategy considering the consistency of energy storage unit health state and charge state. Auto. Elect. Pow. Syst. **47**(5), 65–73 (2023)
12. Zhu, J., Cui, X., Ni, W.: Model predictive control based control strategy for battery energy storage system integrated power plant meeting deep load peak shaving demand. J. Energy Sto. **46**, 103811 (2022)
13. Xi, L., Yu, L., Xu, Y., et al.: A novel multi-agent DDQN-AD method-based distributed strategy for automatic generation control of integrated energy systems. IEEE Trans. Sustain. Energy **11**(4), 2417–2426 (2019)
14. Singh, P., Lather, J.S.: Dynamic power management and control for low voltage DC microgrid with hybrid energy storage system using hybrid bat search algorithm and artificial neural network. J. Energy Storage **32**, 101974 (2020)
15. Gangui, Y.A.N., Ying, L.I.U., Shuangming, D.U.A.N., et al.: Power regulation strategy for battery energy storage unit group participating in secondary frequency regulation of power system. Auto. Elect. Power Syst. **44**(14), 26–34 (2020). (in Chinese)
16. Xiangjun, L., Lizhi, D., Xuecui, J., et al.: A power regulation method and system for ultra-large scale battery energy storage. Pow. Stat., CN202110232968 **7**[P] (2021-06-25)
17. Li, X., Yuan, C., Wang, Z.: State of health estimation for Li-ion battery via partial incremental capacity analysis based on support vector regression. Energy **203**, 117852 (2020)

18. Zheng, X., Su, Y., Wei, L., et al.: Cost-benefit evaluation for battery energy storage considering degradation and data clustering in performance-based frequency regulation service. In: 2020 IEEE 4th Conference on Energy Internet and Energy System Integration (EI2). IEEE, 279–285 (2020)
19. Jianlin, L., Huimeng, M.A., Dong, H.: Present development condition and trends of energy storage technology in the integration of distributed renewable energy. Trans. China Electrotech. Soc. **31**(14), 1–10, 20 (2016) (in Chinese)

Optimal Dispatch Strategy for Power System with Pumped Hydro Power Storage and Battery Storage Considering Peak and Frequency Regulation

Minjian Cao[1](✉), Tingting Cai[2], and Zechun Hu[1]

[1] Department of Electrical Engineering, Tsinghua University, Beijing, China
`tycmj_scholar@163.com`
[2] State Grid Zibo Power Supply Company, Zibo, China

Abstract. Large-scale new energy access to the power grid provides clean power for the power system, but the uncertainty of new energy output leads to security and stability problems and new energy abandonment in the power system. Pumped storage and battery storage technologies are important means to transfer power and provide power regulation for the system. In this paper, a multi-timescale optimal scheduling model for pumped storage hydropower plants and battery storage systems is developed for large-scale new energy consumption enhancement. The model takes reducing the peak-to-valley difference of the net load curve of the grid and reducing the peaking cost of conventional units as the optimization objectives, and considers the cumulative frequency regulation demand constraints for multiple time periods during the day. By converting the established model into a mixed-integer linear programming (MILP) problem, the optimal scheduling scheme considering the system peak and frequency regulation demands can be solved. A simulation example is carried out with the Beijing-Tianjin-Tangshan power grid to verify the effectiveness of the proposed method.

Keywords: Pumped storage hydro power plants · Energy storage · Optimal dispatch · Peak and frequency regulation

1 Introduction

In recent years, the installed capacity of renewable energy, represented by solar energy, wind energy, small hydropower, etc., has increased dramatically [1, 2]. Since the generation power of renewable energy is generally determined by external meteorological conditions, the output power shows strong intermittency and uncertainty. For this reason, if large-scale new energy is connected to the main grid, it inevitably has an adverse effect on the stability and reliable operation of the power grid [3].

As an effective means to enhance the consumption of renewable energy and reduce the negative impact of fluctuating new energy integrating into the power grid, the research on the application of energy storage technology in the power grid has received widespread

Y. Xue et al. (Eds.): PMF 2023, LNEE 1129, pp. 480–492, 2024.
https://doi.org/10.1007/978-981-99-9251-5_37

attention [4]. By installing energy storage equipment in the power grid and controlling the charging/discharging of energy storage, it can play a role in smoothing the renewable energy power output, reducing the gap between the peak and valley of the system, and improving the economics of power grid operation [5, 6].

Pumped storage is one of the most mature energy storage technologies. It can generate/pump for long time and has large capacity. Pumped storage hydropower power (PSHP) plants have the functions of peak regulation, valley filling, frequency regulation, and accident backup [7]. On the one hand, it can provide fast power support after the failure of large-capacity transmission channels, and on the other hand, it can reduce the amount of abandoned wind and solar energy when the wind farm or PV plants generates a lot. Therefore, it is an effective means of reducing the gap between the peak and the valley of power system as well as ensuring reliable operation [8]. In addition, battery energy storage has high energy density, fast regulation response rate, and the installed capacity has increased significantly in the last decades [9].

The energy storage system can be used as a high-quality regulating resource in the grid to receive the grid's scheduling instructions. By arranging the start and stop of pumped-storage units as well as the charging and discharging of battery storage, the efficiency of the grid can be improved [10–14]. In [10], a PSHP optimal scheduling strategy is proposed to reduce the difference between the peak and valley of net load. In [12], an optimal dispatch model for a combined wind-photovoltaic-water-fire pumped storage system is proposed, with the goal of minimizing the total cost including the generation cost, pollution emission cost, and power abandonment penalty. In the model, various types of unit operation constraints and system operation constraints are considered. In [13], an optimal scheduling problem with the objective of minimizing the total fuel cost, pollutant gas emission, and power purchase cost for a power system containing wind farms and PSHP plants. The model considered the network security constraints under N-1 conditions and optimizes the day-ahead generation schedules for conventional and pumped storage units in the grid. In [14], a PSHP-thermal power hierarchical dispatching strategy and a corresponding optimization model are proposed. The upper model reduces the peak-valley difference of the load by scheduling the operation of pumped-storage units, while the lower model optimizes the dispatch of the units with the objective of minimizing the total system operational cost. The former research only considered the day-ahead optimal scheduling model of the power system with PSHP plants. Besides, frequency regulation for the power system with multi-type energy storage system is not considered as well.

This paper establishes an optimal scheduling model for the power system, aiming at improving the consumption of large-scale renewable energy generation power and reducing the operation cost of the whole power system with PSHP plants and battery storage systems. In order to deal with the changes in frequency demand in daily operation, a rolling optimal scheduling strategy is proposed for the power grid with PSHP and battery storage by considering the changes in demand for frequency regulation.

The outline of this paper is shown as follows. Section 2 models PSHP plants and battery energy storage system. Section 3 proposes optimal scheduling model considering peak and frequency regulation. Section 4 shows the simulation results of the model and Sect. 5 gives the conclusion.

2 Mathematical Modeling of Pumping/Storage Systems

2.1 Pumped Storage Power Plant

Since a PSHP plant generally consists of several reversible pump-turbines, the state of each unit needs to be considered in operation, and also the operating costs are mainly the start-up and shutdown costs of the pumping units in the PSHP plant. For a PSHP that contains conventional units and variable speed units, two types of units are denoted by the symbols s and v, respectively. Therefore, the operating cost of the pumped storage power plant at moment k is shown as follows:

$$C_k^{\mathrm{PH}} = \sum_{j=1}^{M} \left(C_{\mathrm{su}} n_{j,k}^{\mathrm{su}} + C_{\mathrm{sd}} n_{j,k}^{\mathrm{sd}} + C_{\mathrm{vu}} n_{j,k}^{\mathrm{vu}} + C_{\mathrm{vd}} n_{j,k}^{\mathrm{vd}} \right) \tag{1}$$

where n_t^{su}, n_t^{sd} are the number of units turned on and off at time t, and C_{su}, C_{sd} are the start-up and shutdown cost of a single unit at one time.

$$s_k^{c,\varepsilon} \le n_k^{c,\varepsilon} \le s_k^{c,\varepsilon} N_{\mathrm{PH}}^{\varepsilon} \ \varepsilon \in \{\mathrm{sp}, \mathrm{vp}\} \tag{2}$$

$$n_{k+1}^{\mathrm{sp}} = n_k^{\mathrm{sp}} + n_k^{\mathrm{su}} - n_k^{\mathrm{sd}} \tag{3}$$

$$n_{k+1}^{\mathrm{vp}} = n_k^{\mathrm{vp}} + n_k^{\mathrm{vu}} - n_k^{\mathrm{vd}} \tag{4}$$

$$\sum_{k=1}^{T} \left(\mathrm{n}_k^{\mathrm{su}} + \mathrm{n}_k^{\mathrm{sd}} \right) \le 2N_{\mathrm{s}} \tag{5}$$

$$\sum_{k=1}^{T} \left(\mathrm{n}_k^{\mathrm{vu}} + \mathrm{n}_k^{\mathrm{vd}} \right) \le 2N_{\mathrm{v}} \tag{6}$$

$$0 \le n_k^{\mathrm{sp}} \le N_s - n_k^{\mathrm{sg}} \tag{7}$$

$$0 \le n_k^{\mathrm{vp}} \le N_v - n_k^{\mathrm{vg}} \tag{8}$$

$$0 \le n_k^{\mathrm{sp}} \le N_s - n_{k-1}^{\mathrm{sg}} \tag{9}$$

$$0 \le n_k^{\mathrm{vp}} \le N_v - n_{k-1}^{\mathrm{vg}} \tag{10}$$

$$n_k^{\varepsilon} p_{\mathrm{min}^{\varepsilon}} \le P_k^{\varepsilon} \le n_k^{\varepsilon} p_{\mathrm{max}^{\varepsilon}}, \quad \varepsilon \in \{\mathrm{sg}, \mathrm{vg}\} \tag{11}$$

$$n_k^{\mathrm{vp}} p_{\mathrm{min}^{\mathrm{vp}}} \le P_k^{\mathrm{vp}} \le n_k^{\mathrm{vp}} p_{\mathrm{max}^{\mathrm{vp}}} \tag{12}$$

$$P_k^{\mathrm{sp}} = n_k^{\mathrm{sp}} p_0^{\mathrm{sp}} \tag{13}$$

$$P_k^{\mathrm{hg}} = P_k^{\mathrm{sg}} + P_k^{\mathrm{vg}} \tag{14}$$

$$P_k^{\mathrm{hp}} = P_k^{\mathrm{sp}} + P_k^{\mathrm{vp}} \tag{15}$$

Constraints (2–4) describes the constraints of number of pumps in each time. $n_k^{c,\varepsilon}$ is the number of pumps operating in time period k. ε is the type of pump, and sp and vp denote the fixed-speed and variable-speed units, respectively. Constraints (2, 3) denote the number of units working in pump mode in adjacent time periods, where the startup number of units in pump mode for fixed-speed and variable-speed units is n_k^{su}, n_k^{vu}, and the shutdown number of pumps for fixed-speed and variable-speed units is n_k^{sd}, n_k^{vd}. Constraints (5, 6) represent the maximum number of startup and shutdown times in a day for the PSHP plant. Constraints (7–10) means that one unit cannot pump and generate at the same time or shift the mode in adjacent periods. Constraint (11) gives the maximum and minimum generating power for fixed-speed and variable-speed units at time k. For a unit, the pumping power and the maximum and minimum power are p^{ε}, $p_{\min}^{\varepsilon}$, and $p_{\max}^{\varepsilon}$, respectively. Constraint (12) shows the maximum and minimum pumping power for variable-speed units at time k. For a unit, the pumping power and the maximum and minimum power are P_k^{vp}, $P_{\max}^{\mathrm{vp}}$, and $P_{\min}^{\mathrm{vp}}$, respectively. Constraint (13) represents the total pumping power in time period k. Constraints (14, 15) denote the total generating and pumping power of the PSHP at time k, respectively.

The capacity constraints of a PSHP plant can be expressed as

$$V_{k+1}^{\mathrm{u}} = V_k^{\mathrm{u}} - \lambda_g P_k^{\mathrm{hg}} + \lambda_p P_k^{\mathrm{hp}} \tag{16}$$

$$V_{k+1}^{\mathrm{d}} = V_k^{\mathrm{d}} + \lambda_g P_k^{\mathrm{hg}} - \lambda_p P_k^{\mathrm{hp}} \tag{17}$$

$$V_{\min^{\mathrm{u}}} \le V_k^{\mathrm{u}} \le V_{\max^{\mathrm{u}}} \tag{18}$$

$$V_{\min^{\mathrm{d}}} \le V_k^{\mathrm{d}} \le V_{\max^{\mathrm{d}}} \tag{19}$$

$$\delta_{\min^{\mathrm{u}}} \le V_{T_{\mathrm{e}}}^{\mathrm{u}} - V_{T_0}^{\mathrm{u}} \le \delta_{\max^{\mathrm{u}}} \tag{20}$$

where Constraints (16) and (17) describe the continuous operation constraints for the upper and lower reservoir capacities of the pumped storage power plant. V_k^{u} and V_k^{d} denote the upper and lower reservoir capacities at time k, respectively. λ_g and λ_p are coefficients of the power-water conversion in generation and pumping mode, respectively. Constraints (18, 19) denote the capacity range for the upper and lower reservoirs, where the upper and lower capacity limits for the upper reservoir are $V_{\max}^{\mathrm{u}}$ and $V_{\min}^{\mathrm{u}}$. For the lower reservoir are $V_{\max}^{\mathrm{d}}$ and $V_{\min}^{\mathrm{d}}$. . Constraint (20) ensures that after a day's operation, the volume of water in upper reservoir vary within a certain range after a day's operation. In particular, $\delta_{\max}^{\mathrm{u}}$ and $\delta_{\min}^{\mathrm{u}}$ represent the maximum and minimum changes in capacity, respectively.

2.2 Battery Storage System

For battery energy storage systems, the number of charge/discharge times, the charge/discharge power, and charge/discharge depth have impacts on the lifetime, and therefore the impact of lifetime loss needs to be considered. The operating cost of the energy storage system in time t can be expressed as

$$C_t^{OE} = \pi_c p_t^c + \pi_d p_t^d \tag{21}$$

π_c, π_d indicate the unit loss of the energy storage system, and the storage charging and discharging power p_t^c, p_t^d. . Constraint (22) shows the energy constraints of battery storage system:

$$E_t = E_{t-1} + p_t^c \eta_c \Delta t - p_t^d / \eta_d \Delta t \tag{22}$$

During operation, the state of charge (SOC) of the energy storage system needs to be maintained within the upper and lower range, so the energy is constrained as:

$$E_0 \cdot SOC_{\min} \le E_t \le E_0 \cdot SOC_{\max} \tag{23}$$

where E_0 is the rated capacity of the battery storage system. $SOC_{\min}$ and $SOC_{\max}$ represent the upper and lower limits of the charge state for battery, respectively.

3 Optimization Model of PSHP Plant and Battery Storage Participating in Peaking Regulation

3.1 Operation Mode

In order to reduce the gap between peak and valley and minimize the operational cost, this paper proposes an optimal dispatch strategy for grid operation in wide time-scale scheduling.

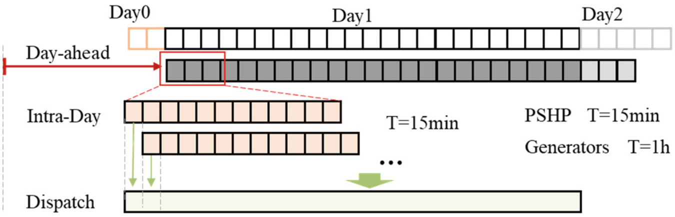

Fig. 1. Multi-timescale rolling dispatch strategy for PSHP and energy storage system from grid-side

The structure diagram of the PSHP-and-battery storage combined system participating in the wide time-scale dispatch of grid operation is shown in Fig. 1. Day-ahead optimal dispatch is adopted at first to determine the startup and shutdown of units. During intraday operation, in order to reduce the error, a time window of 3 h is selected, and a time period of 15 min is used to establish the model. In addition, it is necessary to take into account the frequency regulation in different time periods during the day, and optimize the participation factor of various types of regulation resources in each time period.

3.2 Upper-Level Optimization Scheduling Model

$$\begin{aligned}\min_{t\in \mathrm{T}} \quad & \max\left(P_t^{\mathrm{L,net}} - P_t^{\mathrm{hg}} + P_t^{\mathrm{hp}}\right) \\ & - \min\left(P_t^{\mathrm{L,net}} - P_t^{\mathrm{hg}} + P_t^{\mathrm{hp}}\right)\end{aligned} \tag{24}$$

$$P_t^{\mathrm{L,net}} = P_t^{\mathrm{L}} - \hat{P}_t^{\mathrm{W}} - \hat{P}_t^{\mathrm{S}} \tag{25}$$

$$P_t^{\mathrm{eqL}} = P_t^{\mathrm{L,net}} - P_t^{\mathrm{hg}} + P_t^{\mathrm{hp}} \tag{26}$$

where $P_t^{\mathrm{L,net}}$ represents the net load power of the grid at time t, whose value is the actual load power P_t^{L} minus the forecast wind power $\hat{P}_t^{\mathrm{W}}$ and photovoltaic power $\hat{P}_t^{\mathrm{S}}$. After the end of the dispatch, the actual equivalent load power of the grid can be expressed as P_t^{eqL}.

1. Constraints

The upper-level optimal dispatch model only contains the constraints of PSHP with multiple units. Therefore, the constraints are shown as Constraints (2–20).

3.3 Lower-Level Optimization Scheduling Model

The lower-level model takes into account the battery storage operation loss, the operation cost of conventional units, the penalty for the abandonment of new energy output power, and the mileage regulation cost of frequency regulation resources, with the objective of minimizing the system operation cost.

(1) Objective function

$$\min C_{\mathrm{op},n}^{\mathrm{ESS}} + C_{\mathrm{op},n}^{\mathrm{Gen}} + C_{\mathrm{p},n}^{\mathrm{Re}} + C_n^{\mathrm{mile}} \tag{27}$$

The objective function for intraday operation is to minimize the system operating cost within the dispatch time window, containing four parts: penalty for life loss of battery storage, operating costs of conventional units, the penalty for new energy abandonment, and mileage regulation costs of frequency regulation. The items are shown in Eqs. (28–30), respectively.

$$C_{\mathrm{op},n}^{\mathrm{ESS}} = c_{\mathrm{op}}^{\mathrm{ess}}\left(P_n^{\mathrm{ch}} + P_n^{\mathrm{dis}}\right)\Delta t \tag{28}$$

$$C_{\mathrm{op}}^{\mathrm{Gen}} = \sum_{t\in T}\sum_{i\in G}\left(q_i\left(\overline{P}_{i,n}^{\mathrm{G}}\right)^2 + c_i\overline{P}_{i,n}^{\mathrm{G}}\right)\Delta t \tag{29}$$

$$\overline{P}_{i,n}^{\mathrm{G}} = P_{i,n}^{\mathrm{G}} + \frac{PF_{i,n}\left(E_n^{+} - E_n^{-}\right)}{\Delta t} \tag{30}$$

$$C_n^{\mathrm{mile}} = \phi_i^R \cdot PF_{i,n} \cdot M_n \tag{31}$$

Equation (28, 29) show the life loss for battery and the operation cost of the system. Equation (30) represents the power regulation after considering the participation of conventional units, where $PF_{i,n}$ is the participation factor for unit i in the nth dispatch period. Equation (31) ϕ_i^R denotes the unit mileage cost.

(2) Constraints

$$\sum_{n\in N} P_{i,n}^{\mathrm{G}} - P_n^{\mathrm{ch}} + P_n^{\mathrm{dis}} - P_n^{\mathrm{hp}} + P_n^{\mathrm{hg}} = P_n^{\mathrm{L}} - P_n^{\mathrm{W}} - P_n^{\mathrm{S}} \tag{32}$$

Constraint (32) represents the power balance constraint of the system at time n.

$$U_{i,n}^G P_{i,\min} \le P_{i,n}^{\mathrm{G}} \le U_{i,n}^G P_{i,\max} \tag{33}$$

$$-\Delta\tilde{P}_i^{\mathrm{G}} \le P_{i,n}^{\mathrm{G}} - P_{i,n-1}^{\mathrm{G}} \le \Delta\tilde{P}_i^{\mathrm{G}} \tag{34}$$

Constraint (33) represents the generation power constraint of conventional unit i in time n, where $U_{i,n}^G$ denotes the unit startup and shutdown state of conventional unit i in time period n. Constraint (34) represents the ramp rate of unit in intraday dispatch.

$$0 \le P_n^{\mathrm{W}} \le \hat{P}_n^{\mathrm{W}} \tag{35}$$

$$0 \le P_n^{\mathrm{S}} \le \hat{P}_n^{\mathrm{S}} \tag{36}$$

Constraints (35) and (36) represent the output power constraints of wind and PV units, respectively. $\hat{P}_n^{\mathrm{W}}$ and $\hat{P}_n^{\mathrm{S}}$ denote the intra-day forecasts of wind and PV outputs, respectively.

$$E_n^{E,Da}(1-\delta_{\mathrm{Da}}) \le E_n^{E,\mathrm{Itr}} \le E_n^{E,Da}(1+\delta_{\mathrm{Da}}) \tag{37}$$

$$V^{\mathrm{LR,Da}}(1-\delta_{\mathrm{Da}}) \le V_n^{\mathrm{LR,Itr}} \le V^{\mathrm{LR,Da}}(1+\delta_{\mathrm{Da}}) \tag{38}$$

Operation constraints for PSHP and battery storage are shown in Sect. 2. Constraints (37) and (38) show that the intraday stored energy does not deviate from the day-ahead scheduling for PSHP and battery storage. δ_{Da} shows the maximum relative energy deviation. $V_n^{\mathrm{LR,Da}}$ and $E_n^{E,Da}$ show the volume of water in lower reservoir and energy stored in battery at time n.

$$P_{i,n}^G + PF_{i,n} \cdot MA_n^+ \le P_{i,\max} \tag{39}$$

$$P_{i,n}^G - PF_{i,n} \cdot MA_n^- \ge P_{i,\min} \tag{40}$$

$$P_n^{\mathrm{sg}} + PF_n^{\mathrm{sg}} \cdot MA_n^+ \le N_n^{\mathrm{sg}} \cdot P^{\mathrm{sg,max}} \tag{41}$$

$$P_n^{\mathrm{sg}} - PF_n^{\mathrm{sg}} \cdot MA_n^- \ge N_n^{\mathrm{sg}} \cdot P^{\mathrm{sg,min}} \tag{42}$$

$$P_n^{\mathrm{vg}} + PF_n^{\mathrm{vg}} \cdot MA_n^+ \leq N_n^{\mathrm{vg}} \cdot P^{\mathrm{vg,max}} \tag{43}$$

$$P_n^{\mathrm{vg}} - PF_n^{\mathrm{vg}} \cdot MA_n^- \geq N_n^{\mathrm{vg}} \cdot P^{\mathrm{vg,min}} \tag{44}$$

$$P_n^{\mathrm{vp}} + PF_n^{\mathrm{vp}} \cdot MA_n^+ \leq N_n^{\mathrm{vp}} \cdot P^{\mathrm{vp,max}} \tag{45}$$

$$P_n^{\mathrm{vp}} - PF_n^{\mathrm{vp}} \cdot MA_n^- \geq N_n^{\mathrm{vp}} \cdot P^{\mathrm{vp,min}} \tag{46}$$

$$P_n^{\mathrm{dis}} - P_n^{\mathrm{ch}} + PF_n^{\mathrm{sto}} \cdot MA_n^+ \leq \overline{P}^E \tag{47}$$

$$P_n^{\mathrm{dis}} - P_n^{\mathrm{ch}} - PF_n^{\mathrm{sto}} \cdot MA_n^- \geq \overline{P}^E \tag{48}$$

Constraints (39–48) represent the constraints for AGC signal for each type of frequency regulation resource [15]. MA_n^+ and MA_n^- show the positive and negative maximum AGC signal. PF_n shows the participation factor for units and battery.

$$PF_{i,n} \cdot RR_n^+ \leq rr_i \tag{49}$$

$$PF_{i,n} \cdot RR_n^- \leq rr_i \tag{50}$$

$$PF_n^{\mathrm{sg}} \cdot RR_n^+ \leq N_n^{\mathrm{sg}} \cdot RR^{\mathrm{sg,max}} \tag{51}$$

$$PF_n^{\mathrm{sg}} \cdot RR_n^- \leq N_n^{\mathrm{sg}} \cdot RR^{\mathrm{sg,max}} \tag{52}$$

$$PF_n^{\mathrm{vg}} \cdot RR_n^+ \leq N_n^{\mathrm{vg}} \cdot RR^{\mathrm{vg,max}} \tag{53}$$

$$PF_n^{\mathrm{vg}} \cdot RR_n^- \leq N_n^{\mathrm{vg}} \cdot RR^{\mathrm{vg,max}} \tag{54}$$

$$PF_n^{\mathrm{vp}} \cdot RR_n^+ \leq N_n^{\mathrm{vp}} \cdot RR^{\mathrm{vp,max}} \tag{55}$$

$$PF_n^{\mathrm{vp}} \cdot RR_n^- \leq N_n^{\mathrm{vp}} \cdot RR^{\mathrm{vp,max}} \tag{56}$$

Constraints (49–56) represent the constraints of ramp rate of AGC signal. RR_n^+ and RR_n^- show the positive and negative demand of ramp rate for the power system in the n-th dispatch period. rr_i indicates the ramp rate of generators, and $RR^{\cdot,\max}$ show the maximum ramp rate of units in PSHP.

$$\begin{gathered} V_{n-1}^{\mathrm{u}} - \lambda_g P_n^{\mathrm{hg}} \Delta t + \lambda_p P_n^{\mathrm{hp}} \Delta t \\ -\lambda_g PF_n^{\mathrm{sg}} \left(E_n^+ - E_n^-\right) \Delta t \leq V_{\max}^u \end{gathered} \tag{57}$$

$$\begin{gathered} V_{n-1}^{\mathrm{u}} - \left(\lambda_g P_n^{\mathrm{hg}} \Delta t + \lambda_g PF_n^{\mathrm{sg}} \left(E_n^+ - E_n^-\right) \Delta t\right) \\ +\lambda_p P_n^{\mathrm{hp}} \Delta t - \lambda_g PF_n^{\mathrm{sg}} \left(E_n^+ - E_n^-\right) \Delta t \leq V_{\max^{\mathrm{u}}} \end{gathered} \tag{58}$$

$$\begin{aligned} & E_{n-1}^{\mathrm{E}} - \left(P_n^{\mathrm{dis}} \Delta t - P_n^{\mathrm{ch}} \Delta t + PF_n^{sto} \cdot \left(E_n^{+} - E_n^{-}\right)\right)\eta_{\mathrm{ch}} \\ & \le E_0 \cdot SOC_{\max} \end{aligned} \tag{59}$$

$$\begin{aligned} & E_{n-1}^{\mathrm{E}} - \left(P_n^{\mathrm{dis}} \Delta t + PF_n^{sto} \cdot E_n^{+}\right)/\eta_{dis} \\ & + \left(P_n^{\mathrm{ch}} \Delta t + PF_n^{sto} \cdot E_n^{-}\right) \cdot \eta_{ch} \ge E_0 \cdot SOC_{\min} \end{aligned} \tag{60}$$

Constraints (57, 58) denote the upper reservoir storage operation constraints for the PSHP plant considering the demand for frequency regulation. Only by satisfying the above constraints can it be ensured that the PSHP plant has enough capacity of water to satisfy the demand for frequency regulation in each time period. Similarly, Constraints (59, 60) denote the constraints for battery storage considering the demand for frequency regulation.

$$\sum PF_{i,n} = 1 \tag{61}$$

$$0 \le PF_{i,n} \le 1 \tag{62}$$

Constraint (61) indicates that the sum of the participation factors of the frequency regulation performed by all resources in the grid is 1. According to (62), the participation factor of each resource needs to be between 0 and 1.

4 Case Studies

4.1 Simulation Settings and Parameters

The Beijing-Tianjin-Tangshan power grid is selected as the research object, with a wind power capacity of 20,350 MW and a photovoltaic capacity of 11,060 MW. A typical day of new energy output is selected as an example for analysis. The time PJM historical AGC data are used to generate the frequency regulation demand for the power system [16]. Frequency regulation demand is analyzed by choosing 15 min as the intraday scheduling time period.

In addition, the coefficient of deviation between the volume of water in the day-ahead and intraday operation is 0.15, and the deviation coefficient between day-ahead and intraday SOC of battery storage is 0.05 [17]. The mileage costs of frequency regulation for Shisanling PSHP plant, Panjiakou PSHP plant, and Fengning PSHP plant are 8 ¥/MW, 4 ¥/MW, and 10 ¥/MW, respectively. The mileage cost of frequency regulation for battery storage is 50 ¥/MW [18]. The mileage cost for the remaining conventional units ranges from 7 ¥/MW to 35 ¥/MW, according to IEEE 118-Bus Test System [19].

Numerical simulations are performed by using the CVX toolbox and GUROBI 9.1.0 solver in the MATLAB environment [20].

4.2 Demand for Frequency Regulation

Based on the statistical variables of frequency regulation signal shown in [15], we analyze and evaluate the demand for frequency regulation in 15 min time period of a typical day.

1. Accumulated Regulation Energy

On the typical day, the average of the positive accumulated regulation energy is 13.21 MWh, while the standard deviation is 10.5 MWh. The average of the negative accumulated regulation energy is 19.22 MWh, while the standard deviation is 9.98 MWh. The fluctuation of the positive accumulated regulation energy is greater than the negative counterpart.

2. Accumulated Regulation Mileage

The average value of the accumulated regulation mileage is 6703.97 MW, while the standard deviation of mileage regulation is 831.44 MW. The average value of the accumulated regulation mileage is larger at night.

3. Maximum/Minimum Frequency Regulation Demand

The average of the positive regulation power on the typical day is 300.04 MW. The maximum value is 636.04 MW, and the minimum value is 144.52 MW. The average of negative regulation power is 365.76 MW.

4. Maximum/Minimum Change of Regulation Demand

The average of positive ramping power in the typical day is 1576.46 MW/min, while the average value of negative ramping power is 1579.68 MW/min. The ramping power demand is smooth most of the time in daily operation.

4.3 Simulation Results

The startup and shutdown state of the units, the volume of water in the upper reservoir, and energy stored in the battery storage system are determined by solving the day-ahead dispatch model. According to the results solved by the day-ahead dispatch model, the total cost is 274.0 M¥, with the operational cost and startup/shutdown cost for generators accounting for 273.8 M¥ and 0.2 M¥, respectively.

Figure 2 shows the net load curve after the day-ahead dispatch with the PSHP plant. When the PSHP plant is not scheduled, the maximum difference in the net load is 24,298 MW. The PSHP plants pump when the net load is low, and generate when the net load is high. After solving the day-ahead dispatch model, the maximum difference of the net load is 16,120 MW.

After the intraday dispatch, the total operation cost of the system is 274.2 M¥. Apart from the operation cost, the frequency regulation cost is also calculated in the intraday dispatch model. The total mileage regulation cost is 9.3 M¥. Among them, the mileage regulation cost of generators is 7.3 M¥. The mileage regulation costs of the PSHP plants and the battery storage system are 1.8 M¥ and 0.2 M¥, respectively.

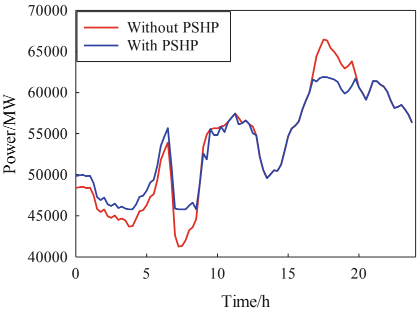

Fig. 2. Net load of the grid before and after day-ahead dispatch with PSHP plant

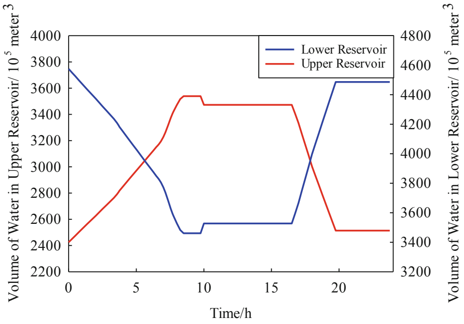

Fig. 3. Volume of water of Fengning PSHP

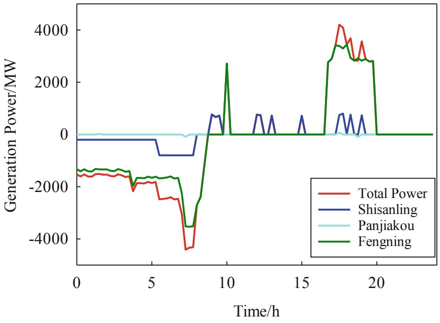

Fig. 4. Generation power of PSHP

The storage capacity of Fengning PSHP plants is shown in Fig. 3. The generation power of each PSHP plant is shown in Fig. 4. The generation power of PSHP in the intraday dispatch approximates the results of the day-ahead dispatch. The deviation is primarily used to participate in the frequency regulation.

The participation factors of the frequency regulation at different moments in the daily operation are shown in Fig. 5. It can be seen that most of the time conventional

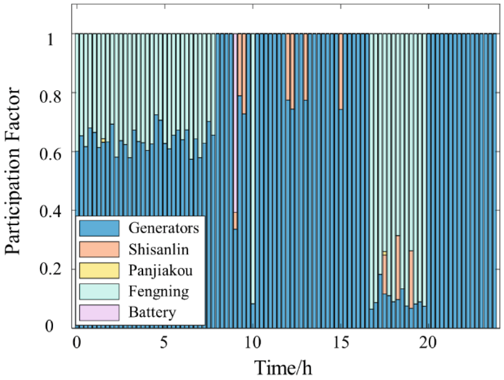

Fig. 5. Participation factors for different units in daily operation

units and the Fengning PSHP plant play the most important role in frequency regulation. Shisanling PSHP, Panjiakou, and the battery storage system only participate in the frequency regulation for several periods, considering the little amount of capacity and high mileage costs of frequency regulation. In addition, the capability of participating in frequency regulation for PSHP plants is strongly impacted by the operation state of units. When the fixed-speed unit is shutdown or in a pumping state, the unit cannot provide frequency regulation capability. When the more number of units in in the generation state, the more capability of frequency regulation can be provided by the PSHP.

5 Conclusion

This paper proposes an optimal dispatch strategy for minimizing the operation cost for power systems with PSHP plants and battery storage considering peak and frequency regulation. The dispatch strategy consists of a day-ahead dispatch model and an intraday dispatch model. In the day-ahead model, a bi-level dispatch model is proposed, with the goal of minimizing the peak-to-valley of net load in the upper-level model and minimizing the operation cost in the lower level. Based on the results solved by the day-ahead dispatch model, demand for frequency regulation is introduced into the intraday dispatch model. The optimal operation state of the system and participation factors of frequency regulation resources are determined by solving the rolling intraday dispatch model. Simulation results show that the difference between the maximum and minimum of the net load can be minimized, and the frequency regulation resources are economically distributed. Future work will formulate the model considering the uncertainty of frequency regulation demand.

Acknowledgment. This work was supported in part by National Natural Science Foundation of China under Grant 52107105.

References

1. Outlook, I. G.R.: Energy transformation 2050. International Renewable Energy Agency (IRENA) (2020)
2. Kaur, D., Cheema, P.S.: Software tools for analyzing the hybrid renewable energy sources: a review. In: 2017 International Conference on Inventive Systems and Control (ICISC) (2017)
3. IRENA.: Global Renewables Outlook. IRENA, Abu Dhabi (2020)
4. Smart grid demonstration program [EB/OL]. http://www.smartgrid.gov/recovery_act/overview/art_grid_demonstration_program.2007/12
5. Hu, J., Yang, S., Hou, C., et al.: Present condition analysis on typical demonstration application of large-scale energy storage technology and its enlightenment. Power Syst. Tech. **39**(4), 879–885 (2015)
6. Yuan, X., Cheng, S., Wen, J.: Prospects analysis of energy storage application in grid integration of large scale wind power. Autom. Elect. Power Syst. **37**(1), 14–18 (2013)
7. Gomes, J.G., Telhada, J., Xu, H., et al.: Optimal operation scheduling of a pump hydro storage system coupled with a wind farm. IET Renew. Power Gener. **15**(1), 9–17 (2021)
8. Tiwari, S, Schelly, C, Sidortsov, R.: Developing a legal framework for energy storage technologies in the U.S: The case of pumped underground storage hydro. Elect. J. **34**(10), 107048–107053 (2021)
9. Pan, X, Khezri, R., Mahmoudi, A., et al.: Optimal planning of solar PV and battery storage with energy management systems for time-of-use and flat electricity tariffs. IET Renew. Power Gene. (2022)
10. Liu, B., Lund, J.R., Liao, S., et al.: Optimal power peak shaving using hydropower to complement wind and solar power uncertainty. Energy Convers. Manage. **209**, 112628 (2020)
11. Liu, B., Lund, J.R., Liao, S., et al.: Peak shaving model for coordinated Hydro-Wind-Solar system serving local and multiple receiving power grids via HVDC transmission lines. IEEE Acc. **8**, 60689–60703 (2020)
12. Zhang, G., Chen, Y., Zhang, J., et al.: Research on optimization of day-ahead dispatching of wind power-photovoltaic-hydropower-thermal power-pumped storage combined power generation system. ACTA Energy Solar. Sin. **41**(8), 79–85 (2020)
13. Huang, S., Lin, S., Liu, M.: Multi-objective security constrained dynamic optimal dispatch with wind farms and pumped storage stations. Proceed. CSEE **36**(1), 112–121 (2016)
14. Lin, L., Yue, X., Xu, B., et al.: Sequence and strategy of pumped storage-thermal combined peak shaving considering benefits of pumped storage and deep regulation of thermal power. Power Syst. Tech. **45**(1), 20–29 (2021)
15. Liu, L., Hu, Z., Duan, X., et al.: Data-driven distributionally robust optimization for real-time economic dispatch considering secondary frequency regulation cost. IEEE Trans. Power Syst. https://doi.org/10.1109/TPWRS.2021.3056390
16. Zhang, X., Tan, T., Zhou, B., et al.: Adaptive distributed auction-based algorithm for optimal mileage based AGC dispatch with high participation of renewable energy. Int. J. Electr. Power Energy Syst. **124**, 106371 (2020)
17. Fernandez-Munoz, D., Perez-Diaz, J.I.: Contribution of non-conventional pumped-storage hydropower plant configurations in an isolated power system with an increasing share of renewable energy. IET Renew. Power Gene. **14**(4), 658–670 (2019)
18. Peña, I., Martinez-Anido, C.B., Hodge, B.-M.: An extended IEEE 118-bus test system with high renewable penetration. IEEE Trans. Power Syst. **33**(1), 281–289 (2018)
19. Grant, M., Boyd, S.: CVX: Matlab software for disciplined convex programming, version 2.1 (2014)
20. Xu, Y., Lei, Y., Xiang, M., et al.: AGC command allocation coordinating frequency performance and anti-vibration of hydropower units. In: 2022 Asian Conference on Frontiers of Power and Energy (ACFPE). IEEE, 151–157 (2022)

Author Index

Y. Xue et al. (Eds.): PMF 2023, LNEE 1129, pp. 493–495, 2024.
https://doi.org/10.1007/978-981-99-9251-5